CO_2 Capture by Aqueous Absorption

Summary of Fourth Quarterly Progress Reports 2011

by Gary T. Rochelle

Supported by the Luminant Carbon Management Program

and the

Industrial Associates Program for CO_2 Capture by Aqueous Absorption

Department of Chemical Engineering

The University of Texas at Austin

January 31, 2012

Introduction

This research program is focused on the technical obstacles to the deployment of CO_2 capture and sequestration from flue gas by alkanolamine absorption/stripping and on integrating the design of the capture process with the aquifer storage/enhanced oil recovery process. The objective is to develop and demonstrate evolutionary improvements to monoethanolamine (MEA) absorption/stripping for CO_2 capture from coal-fired flue gas. The Luminant Carbon Management Program and the Industrial Associates Program for CO_2 Capture by Aqueous Absorption support 17 graduate students and one visiting scholar. Most of these students have prepared detailed quarterly progress reports for the period October 1, 2011 to December 30, 2011.

Conclusions

Thermodynamics and Rates

Two blends of amine and PZ, 6 m PZ/2 m Y and 6 m PZ/2 m Z, have a high heat of absorption, 79 kJ/mol, which is about 13% greater than 7 m MEA. The blends have a good absorption rate, about 9% lower than 8 m PZ and 60% higher than 7 m MEA. The capacity of 6 m PZ/2 m Y (0.55 mol CO_2/kg) and 6 m PZ/2 m Z (0.62 mol CO_2/kg) is about 25% less than 8 m PZ.

The hindered amine blends, 5 m PZ/2 m W and 5 m PZ/2.3 m AMP, have competitive absorption rates compared to 8 m PZ. Both hindered amine blends have 0.66 mol/kg cyclic capacity, which is slightly higher than the primary amine blends and 16% less than 8 m PZ. The heat of absorption for 5 m PZ/2 m W is 72 kJ/mol, which is slightly higher than 7 m MEA. The PZ/AMP blend has a high heat of absorption at 78 kJ/mol.

Among the four new PZ blends, 5 m PZ/2.3 m AMP has the best overall properties. Also, 5 m PZ/2 m W has the highest absorption rate, which is 5% higher than 8 m PZ.

The 2011 8 m PZ pilot plant sample has distinct properties which differ from fresh 8 m PZ solvent. The absorption rate of the pilot plant sample is similar to 8 m PZ. The capacity of the sample is lower than 8 m PZ by about 11%. The heat of absorption of the pilot plant sample is 23% higher than 8 m PZ and 12% higher than 7 m MEA.

The absorption rate of 5 m MDEA/5 m PZ has no temperature dependence between 10 and 40 ˚C. The measured CO_2 solubility at low temperatures agrees well with previous high temperature data.

Careful regression of CO_2 solubility data and heat capacity data in PZ solution gives a well-behaved, thermodynamically consistent prediction of the heat of CO_2 absorption. At 0.3 mol/equiv PZ, the heat of CO_2 absorption varies from 65 kj/mol at 40 ^oC to 83 kJ/mol at 140 ^oC.

Even though 6.5 m PZ/3 m AMP has a similar operating window to 8 m PZ, it has nearly twice the viscosity of 8 m PZ. The blend, 6 m PZ/4 m AMP, is not desirable because of its narrow operating window.

With 5 m PZ/2.3 m AMP, solids are precipitated when the loading is lower than 0.3, but no solids are observed even at a CO_2 loading of 0.5.

The performance of 5 m PZ/2.3 m AMP is similar to 8 m PZ in terms of viscosity, heat of absorption, and the lean and rich loading. Due to lower total alkalinity, the CO_2 capacity is lower.

The mass transfer rates in 5 m PZ/2.3 m AMP is higher than in 8 m PZ when the loading is rich.

Modeling

Replacement of the high pressure cross-exchanger in the pilot plant resulted in a heat duty of 1390 BTU/lb CO_2, a 13% improvement over the first flash skid campaign and was similar in value to the heat duty of the 2010 MEA intercooler campaign.

The cold rich bypass to the low pressure gas-liquid separator successfully reduced the amount of volatile PZ in the condensate by a factor of five.

The effective area model has been modified for random packing to include the gas flow rate influence: $\frac{a_e}{a_P} = C[(\frac{\rho_L}{\sigma})g^{1/3}(\frac{Q}{A} * \frac{1}{a_P})^{4/3}]^{0.116}(\frac{u_G \rho_G}{a_P \mu_G})^n$. The exponent n varies from 0.1 to 0.22 for three random packings. This is comparable to the exponent 0.116 used by Tsai to model the effect of liquid rate in structured packing.

Pressure drop measurements at SRP appear to be 16 to 32% less than other reported measurements in Mellapak 2X, 1” plastic Pall Rings.

Area measurements at SRP appear to be 9 to -9% less than other reported measurements for RSR#5, RSR#7, and Mellapak 2X, even when the other measurements are corrected for gas-side resistance.

$K_l a$ measurements at SRP appear to be 29 to 33% less than Raschig measuremetns with RSR#5 and RSR#7 after corrections for the chemical systems used.

$k_G a$ measurements at SRP appear to 40% greater than Rashchig measurement with RSR#5.

With two cross-exchangers in series, the pilot plant achieved an equivalent work of 34 kJ/mol CO_2 using the two-stage flash with aged 8 m PZ.

Compared to no bypass, using cold, rich bypass to a high pressure and a low pressure flash reduces the equivalent work by 4.9% for 8 m PZ.

The largest component of equivalent work is the reboiler duty of each flash, and so the optimal amount of bypass occurs when the two duties are nearly equal. This was at a bypass of 3% high pressure and 5% low pressure.

Successful control strategies appear to use ratio control for solvent rate to flue gas rate and for steam rate to rich solvent rate.

It is more important to control the ratio L/G to maintain a stable system than the absolute flow rates themselves.

Total system hold-up is an important factor in response times to set point changes.

A control strategy for water make-up must be developed to maintain the system water balance.

Under appropriate market conditions, flexible CO_2 capture can reduce electricity dispatch costs and improve the ability of a facility to earn revenue from ancillary service procurements.

If reboiler steam load is reduced without a reduction in boiler load, the equivalent work is minimized by reducing the speed of the compressor. Active anti-surge control is necessary and provides the best energy performance at steam load from 20 to 60%. At 20% steam load, W_{eq} decreases 10%, and stripper pressure increases a factor of two.

As boiler load decreases, variable compressor speed and optimized system conditions maintain practically constant equivalent work requirement. Load reduction to less than 60% will require use of compressor surge control.

Heat loss measurements predicted in Aspen Plus® via data-fitting of pilot plant data were within 10% of independent calculation using an overall heat transfer coefficient.

Skin temperature measurements at RTD locations on the pilot plant absorber column were, on average, within 2 °C of RTD readings within the column, validating the use of RTD temperatures for heat loss prediction.

Skin temperature measurements indicated as much as 5 °C variation in radial column temperatures at a fixed height.

Solvent Management

Kinetic study of the reaction between nitrite and PZ has been performed from 20 to 150 °C. Nitrite consumption is modeled as a first order reaction in nitrite. MNPZ is produced at temperatures greater than 75 ^{o}C and then decomposes at 100 to 150 ^{o}C.

Ammonia was produced at 3–4 mMol/hr in the miniplant with clean MEA; for used MEA the rate was 20–24 mMol/hr. No chemical inhibitors of MEA oxidation were able to significantly reduce ammonia production in a mini CO_2 capture plant (tested DTPA, HEDP, DMcT, Inh A).

The activation energy of ammonia production from the absorber in the miniplant was 29 kJ/mol, indicating that air bubble entrainment may be responsible for 72% of oxidation.

UV degradation of NDELA was four times faster in the CATO water-wash solution (-0.52 mMol/kg/hr) than in the absorption liquid (-0.13 mMol/kg/hr). The rate of UV degradation of NDELA and MNPZ in water was zero-order in nitrosamine over several orders of magnitude. The presence of impurities reduced the degradation rate by a factor of 4.3x; pH and amine concentration did not significantly affect the degradation rate.

Thermal degradation of nitrosamines occurred at rates from 3.6 to 21.4 mMol/kg/hr at high temperatures (160 to 200 °C). The rate was lower than expected at lower pressure and in the presence of oxygen

The volatility of MNPZ from the absorber in the miniplant was roughly the same (1.02x) as the volatility of PZ at the absorber conditions. The MNPZ emissions were not the result of mechanical entrainment.

8 m 1,4-diaminobutane at a loading of 0.4 mol CO_2/mol alkalinity has a degradation rate of around $750*10^{-9}$ 1/sec at 175 ^oC. 1,4-diaminobutane degrades twice as fast when blended with PZ.

The principal thermal degradation products of 1,4-diaminobutane are ammonia and pyrrolidine. 1,4-diaminobutane appears to reach equilibrium with pyrrolidine after two weeks. This behavior was not seen when 1,4-diaminobutane was blended with PZ.

8 m 2-(Diamino)ethyl ether at a loading of 0.4 mol CO_2/mol alkalinity has a degradation rate of around $200*10^{-9}$ 1/sec at 175 ^oC. Degradation rates of 2-(Diamino)ethyl ether are not enhanced when blended with PZ.

PZ/Y has a greater solid solubility than PZ. At 20 ^oC, solids form at a CO_2 loading of 0.24 in 8 m PZ, 0.19 in 5 m PZ/2 m Y, and 0.13 in 3 m PZ/3.33 m Y.

No precipitates were observed at greatest CO_2 loading provided by the loader at 1 atm CO_2.

The viscosity of loaded 5 m PZ/2 m Y is comparable to that of loaded 8 m PZ.

Mononitrosopiperazine (MNPZ) has maximum UV absorption peaks at 237 and 341 nm. Nitrosodiethanoalamine (NDELA) has maximum absorption peaks at 232 and 345 nm. MNPZ is a much stronger UV absorber than NDELA.

At water wash conditions, 1 kPa CO_2, 40 ^oC, and 0.15 m PZ, the equilibrium CO_2 solubility is 0.42 mol CO_2/equiv PZ. The Fawkes model accurately predicts CO_2 solubility of PZ solutions at low amine concentrations.

The Pickle Research Campus pilot plant campaign (with air/CO_2) solvent contained 7.6 ppm mononitrosopiperazine (MNPZ) at the end of the campaign

After 60 days of operation, Pilot Plant 2 with coal-fired flue gas after SCR accumulated a steady-state of about 100 ppm MNPZ. MNPZ in the water wash system of Pilot Plant 2 was never higher than 10 ppm.

The first order rate constant for nitrosation of 8 m PZ at 120 ^oC and a CO_2 loading of 0.3 is approximately $4*10^{-4}$ s^{-1}. The first order rate constant of MNPZ decomposition under the same conditions is approximately $3.6*10^{-6}$ s^{-1}, which is 100 times slower than PZ nitrosation.

The MNPZ steady state concentration would be 5 mM with a sump operating at 120 ^oC, a sump residence time of 10 minutes, and a flue gas NO_2 concentration of 0.01 millimols/mol CO_2 removed (about 1 ppm NO_2).

Future Work

In 2011 we expect to complete the following milestones in the Luminant Carbon Management Program. A major product has been included for each student.

Students	Q1	Q2	Q3	Q4
Nguyen		Ph.D. Dissertation on Amine volatility		
L. Li	Rate evaluation of common amino acids			
Du			Evaluation of PZ/AEP	
H. Li		Thermo model of AMP/PZ		
Namjoshi				Thermal Degradation of PZ/Diamines
Nielsen		Evaluation of 2 Pilot Plant samples from Fall 2011		
Ashouri		MS Thesis on MNPZ decomposition		
Fine				Nitrosamine thermal decomposition with other sec. amines
Voice			High T cyclic MEA degradation	
Wang				Area, kla, & kga model structured packing
Fulk	Model of water wash performance			
Frailie	Additional stripper options for PZ			
Walters				Stripper dynamic model for control
Sherman				System model of PZ/2MPZ
Sachde			Reconciliation of absorber F11 data	
Madan			Reconciliation of stripper F11 data	
Cohen		Ph.D. dissertation on flexible operation		
Ziaii		Ph.D. dissertation on dynamic modeling		

1. Solvent Screening by the Wetted Wall Column *p. 17*

by Le Li

Four PZ-based blends were screened using the wetted wall column (WWC) during this quarter. Absorption rate and CO_2 solubility of each blend were measured at five CO_2 loadings across the lean and rich operating range and at 20, 40, 60, 80, and 100 ˚C. Two blends of other amines and PZ blends, 6 m PZ/2 m Y and 6 m PZ/2 m Z, have high heats of absorption at 79 kJ/mol. Both blends have good absorption rates, which are only 9% lower than 8 m PZ. PZ/Y has a lower capacity at 0.55 mol/kg. The capacity of PZ/Z is slightly higher at 0.62 mol/kg, which is still lower than 8 m PZ. The high pKa values and carbamate formation reactions of the other amines contribute to the high heat of absorption of the blends. At the same time, the high pKa values result in high operating lean and rich loadings and low CO_2 solubility at rich loadings, which result in reduced capacity of the blends. Two hindered amine and PZ blends, 5 m PZ/2 m W and 5 m PZ/2.3 m AMP, have more competitive absorption rates than 8 m PZ and cyclic capacity of 0.66 mol/kg. PZ/W has low CO_2 solubility at rich loadings, which results in a lower capacity than 8 m PZ. PZ/W has similar heat of absorption to amine W, which is 72 kJ/mol and 12% higher than 8 m PZ. The lower capacity of PZ/AMP is the result of low alkalinity of the blend. PZ/AMP has a high heat of absorption at 78 kJ/mol. Of the four new PZ blends, 5 m PZ/2.3 m AMP has the best overall properties.

The absorption rate of the lean amine sample from the 2011 8 m PZ pilot plant campaign was measured at 40, 60, 80, and 100 ˚C. The sample was tested at the collected loading and two higher loadings. The calculated capacity of the pilot plant sample is approximately 10% less than fresh 8 m PZ. The heat of absorption of the sample is higher than 8 m PZ by 19%. The $k_g'_{avg}$ for the pilot plant sample is slightly higher than 8 m PZ. The distinct properties of the pilot plant sample suggest changes in active species from 8 m PZ as results of possible solvent degradation during the campaign.

5 m MDEA/5 m PZ was measured in the WWC at 10, 20, 30, and 40 ˚C to expand the range of available data for the blend. The absorption rate of 5 m MDEA/5 m PZ has no temperature dependence between 10 and 40 ˚C. The measured CO_2 solubility at low temperature agrees well with previous high temperature data.

2. MDEA/PZ Fawkes Model Upgrade *p. 54*

by Thu Nguyen

This report discusses the effort to upgrade the Fawkes MDEA/PZ model to better match amine volatility and speciation while accurately maintaining CO_2 solubility predictions. The best possible combination of parameter values to match the different types of blend data, as used in this model revision, includes regressed values for H_2O interaction with ion pairs, default values for MDEA and PZ interactions with ion pairs (10 for amine to ion pairs, -2 for ion pairs to amine), default values for the zwitterion H^+PZCOO^- interaction with ion pairs set to mimic default water interaction values (8 for zwitterions to ion pairs, -4 for ion pairs to zwitterion), and the non-randomness factor for zwitterion to MDEA interaction fixed at 0.3.

The MDEA and PZ volatilities, as a function of loading and temperature, were adequately represented in this model revision. This is most likely due to the fact that the H_2O-MDEA and H_2O-CO_2-MDEA parameters were regressed again in this version to properly match experimental unloaded MDEA volatility data and CO_2 solubility. Speciation was also matched

successfully in this model upgrade. This is because the H_2O and MDEA interactions with ion pairs involving HCO_3^- were regressed again along with the introduction of the CO_3^{2-} species. These changes made it possible to obtain noticeably improved fits of CO_2 solubility and MDEA volatilities, which resulted in accurate speciation predictions. The model is able to predict well-behaved heats of absorption that match expectation and are internally consistent overall. For both blends, the CO_2 heats of absorption flip temperature behaviors at loadings that correspond to the critical loadings where PZ is saturated in both MDEA/PZ systems (loading ~ 0.18 for 7 m MDEA/2 m PZ; ~0.33 for 5 m MDEA/5 m PZ). Over a range of loading up to ~0.5 mol CO_2/mol total alkalinity, the CO_2 heat of absorption is estimated to be 40–90 kJ/mol CO_2 for 60–150 ˚C, which is comparable to that of 8 m PZ.

3. Characterization of AMP/PZ *p. 73*

by Han Li

Solid solubility, CO_2 solubility, viscosity, mass transfer rate, and volatility were measured for three different ratios of PZ to AMP. These blends were 6 m PZ/4 m AMP, 6.5 m PZ/3 m AMP, and 5 m PZ/2.3 m AMP. Compared to 8 m PZ, the solid solubility window of 6 m PZ/4 m AMP is much narrower, while 6.5 m PZ/3 m AMP exhibits similar results, and 5 m PZ/2.3 m AMP shows similar lean boundary but with no rich boundary. To avoid high viscosity, 5 m PZ/2.3 m AMP was chosen as a promising blend over 6.5 m PZ/3 m AMP.

The mass transfer rate for 5 m PZ/2.3 m AMP is greater than 8 m PZ at rich loading, while the CO_2 capacity is a little lower because of lower total alkalinity. This blend has comparable heat of absorption to 8 m PZ, but high volatility of AMP may produce more solvent loss.

4. Modeling MDEA/PZ Thermodynamics, Hydraulics, and Kinetics *p. 97*

by Peter Frailie

The goal of this study is to evaluate the performance of an absorber/stripper operation that utilizes MDEA/PZ. A thermodynamic, hydraulic, and kinetic model for 8 m PZ, 7 m MDEA/2 m PZ, and 5 m MDEA/5 m PZ has been regressed in Aspen Plus® (the Fawkes model). This model has already been applied to quantify the potential energy benefits of intercooling and a colder absorber. It has been concluded that intercooling always improves solvent capacity, and a colder absorber has the potential to improve solvent capacity, especially for the 7 m MDEA/2 m PZ blend. Stripper models have been constructed to compare the energy performance of a simple stripper, two-stage flash, and interheated stripper. The Aspen Plus® thermodynamic model has been modified to include recently acquired experimental data and to generate more accurate heat capacity and CO_2 solubility predictions. The goal for the next quarter is to continue to regress the thermodynamics of MDEA/PZ and to incorporate the kinetics for all solvents relevant to this study.

5. Pilot Plant Testing of Advanced Process Concepts using Concentrated Piperazine

by Dr. Eric Chen

In this reporting period, the second pilot plant campaign with the modified two-stage flash skid was completed. The pilot plant was operated for 2.5 weeks and 11 runs were completed. During the heat loss test with distilled water, a leak was discovered in the low pressure cross-exchanger. The low pressure cross-exchanger was taken out of service for repair and bypass piping was

fabricated and installed. The pilot plant was operated with only the high pressure cross-exchanger in Runs 1 to 3 and Runs 8 to 11. In Runs 4 to 7, it was operated with both cross-exchangers.

The absorber column was operated at three gas rates: 350, 475, and 675 ft^3/min. The liquid to gas ratio (L/G) was varied between 3.0 to 4.2 lb/lb. The absorber was packed with 20 feet of GTC 350Z structured packing divided into two beds. The absorber liquid stream was intercooled to 40 °C. The piperazine concentration in the solvent varied from 38.4 to 40.4 wt % and the lean loading varied from 0.24 to 0.26 mol CO_2/equiv PZ. The CO_2 composition of the inlet flue gas was 12 mol % and the CO_2 removal rate in the absorber varied from 72.0 to 92.5%. The inlet feed temperatures to the high and low pressure separator vessels were maintained at a set point of 150 °C. The high and low pressure separators were operated from 10.3 to 14.4 bar, and 6.5 to 7.4 bar, respectively. The pressure ratio between the two flash tanks was between 1.5 and 2.

During Runs 1 to 3, the pilot plant was operated with only the high pressure cross-exchanger, and the log mean approach temperature was between 9.05 and 10.2 °C. Both the low and high pressure cross-exchangers were operated during Runs 4 to 7 and the log mean approach temperature varied between 2.4 and 3.9 °C. In Runs 8 to 11, the LP cross-exchanger was bypassed and the approach temperature for the high pressure cross-exchanger was between 10.5 and 11.3 °C. Replacement of the high pressure cross-exchanger resulted in a heat duty of 1390 BTU/lb CO_2, a 13% improvement over the first flash skid campaign and was similar in value to the heat duty of the 2010 MEA intercooler campaign.

The cold rich bypass to the low pressure gas-liquid separator successfully reduced the amount of volatile PZ in the condensate by a factor of five. Without the bypass in operation, the PZ concentration in the condensate was 2.5 wt %. With the operation of the bypass, the PZ condensate concentration was reduced to 0.5 wt %. Also, fogging was not observed in the sight glasses with the bypass in operation. A new temperature measurement was added inside the low pressure separator during the middle of the campaign.

Cold startup of the flash skid was much smoother with the addition of the new skid return pump and pre-charging the flash tanks with 80 psig nitrogen. Operation of the flash skid was also more stable with the addition of the static pressure measurement at the suction of the high pressure skid pump. The transmitter provided a pressure measurement that could be used to control the variable speed drive of the two upstream absorber rich pumps and not exceed the relief valve set point of 150 psig at the skid high pressure pump suction.

To improve performance of the flash skid, it is recommended that a new temperature measurement be installed in the high pressure separator. Also, additional packing and a proper liquid distributor should be added to the low pressure separator to enhance performance of the cold rich bypass. The heat transfer capacity of the high pressure cross-exchanger should be increased to avoid use of the low pressure cross-exchanger by adding more plates or a complete replacement with a new cross-exchanger. Pressure transmitters should be added to the discharge of the two absorber rich pumps. Finally, temperature transmitters that provide a radial temperature distribution should be installed in the absorber column to provide more information on absorber performance.

6. Absorber Modeling and Pilot Plant Validation *p. 105*

by Darshan Sachde

During the past quarter, Aspen Plus® absorber models were validated using pilot plant data from the J.J. Pickle Research Campus (PRC). The models incorporated heat loss to account for operating conditions at the pilot plant. Independent heat loss calculations by an overall heat transfer coefficient were within approximately 10% of heat loss predicted by data-fitting of pilot plant data in Aspen Plus®. In addition, skin temperature measurements at the pilot plant confirmed the validity of RTD measurements as accurate representations of column inner wall temperatures for modeling and heat loss calculation purposes. Skin temperature measurements also confirmed possible radial temperature profile variation in the pilot plant absorber, highlighting the need for improved measurement and modeling of the column cross-section.

Finally, the validated absorber model was used to develop base case designs for economic evaluation. Part of the base case design included confirmation of a stable operating range for 8 m piperazine (PZ) spanning a lean loading range of 0.27 to 0.3 when operated at 1.1 times the minimum solvent rate.

7. Measurement of Packing Effective Area and Mass Transfer Coefficients *p. 115*

by Chao Wang

In this quarter, most work has been focused on analysis of previous results. The influence of the superficial gas velocity (u_G) on effective area (a_e) has been explored. For random packing, the influence of gas velocity is as large as liquid velocity. The exponent of effective area on gas velocity is 0.218 for 1" plastic Pall Rings compared with 0.248 on liquid velocity. For Raschig Super Rings #0.5, the exponent is 0.174 for gas velocity and 0.202 for liquid velocity. It is reasonable to include gas velocity influence in the existing area model.

The effective area model has been modified with consideration of gas flow influence for random packings. Gas phase Reynolds number is chosen to represent the gas flow influence. The modified area model is: $\frac{a_e}{a_P} = C[(\frac{\rho_L}{\sigma})g^{1/3}(\frac{Q}{A}*\frac{1}{a_P})^{4/3}]^{0.116}(\frac{u_G\rho_G}{a_P\mu_G})^n$

where:

C is packing constant, and
n is exponent for gas flow rate.

Four data sets from outside sources have been found to compare with data measured by SRP. For 1" plastic Pall Rings, the outside source data is from Pall Ring Product Bulletin 350 by Raschig-Jaeger Products, Inc. The pressure drop measurements for air-water compare fairly well with the SRP data, with an average deviation of 24%. The effective area provided by the Product Bulletin is based on the absorption of 1% CO_2 into 1 gmol/L NaOH. Since the NaOH concentration is large, the gas phase mass transfer resistance cannot be ignored. Their effective area has been corrected by subtracting the gas side resistance and it compares well with the SRP measurements with an average deviation of 18%.

For Raschig Super Rings #0.5 and #0.7, the effective area data are obtained from Kolev (2006), who absorbed 1% CO_2 into 1 gmol/L NaOH. The data are again corrected for gas side resistance and compare well with average deviations of 7.2% and 6% for RSR#0.5 and RSR#0.7 respectively. Film mass transfer coefficient (k_Ga and k_La) data are from Product Bulletin 250 by Raschig-Jaeger Products. For k_Ga, Raschig used the absorption of NH_3 from water into air and

observed a deviation of 40% from the SRP RSR#0.5 data. For k_La, Raschig used the desorption of CO_2 into water from air with a 33% deviation from SRP RSR#0.5 data and 29% from SRP RSR#0.7 data.

For Mellapak 2X, two outside sources of data have been found. One is from Ali Zakeri at NTNU (2011) and the other from Sulzer Chemtech (2011). The system used for pressure drop measurements is air-water for both sources. The average deviation from SRP data is 32% for NTNU data and 16% for Sulzer data. The system used for effective area measurements is the absorption of CO_2 into NaOH. The deviation from SRP data is 9.2% for the NTNU data and 9.4% for the Sulzer data.

8. Pilot Plant Modeling of CO_2 Stripping using Piperazine p. 127

by Tarun Madan

Following previous campaigns utilizing the two-stage flash skid for stripping the absorbed CO_2 using concentrated 8 m piperazine (PZ), fresh steady state runs were performed in the pilot plant during October 2011. The results generated from the steady state runs were simulated in Aspen Plus® using the Fawkes model. A Microsoft Excel®-based model was also prepared for equilibrium analysis and quick material balance calculations along with rigorous Aspen Plus® simulation.

The result shows good VLE approach for both the vessels. Also, simulations based on existing model showed a mean deviation of 3% for most values but had much larger inconsistencies for CO_2 stripping rate (deviation of 21%). Both models were updated to consider a shift in loading to take into account the adverse effect of solvent degradation. The resulting models showed significant improvement with a shift in loading of magnitude 0.015–0.03, bringing the CO_2 stripping rate deviation to 3%.

Equivalent work calculations demonstrated better performance than previous trials, giving values as low as 34 kJ/mol CO_2. The simulations will be further analyzed for improvement of model, especially for energy balance.

9. Cold, Rich Bypass to Reduce Stripper Equivalent Work p. 137

by Brent Sherman

Cold, rich bypass with two-stage flash was explored to determine the optimal bypass for minimizing equivalent work (W_{eq}). 8 m PZ with a rich/lean loading of 0.386/0.27 was used with a pressure ratio between the flashes of 1.5. The minimum W_{eq} was 30.9 kJ/gmol CO_2 with a 3% bypass to the high-pressure tank and a 5% bypass to the low-pressure tank. This is a 4.9% improvement over the W_{eq} of 32.5 kJ/gmol CO_2 with the no bypass base case.

10. Steady State Optimization of Partial Load Operations in CO_2 capture p. 142

by Sepideh Ziaii

Co-supervised by Thomas Edgar

This work is devoted to exploring energy efficient control strategies for a capture plant designed to remove 90% of inlet CO_2 using aqueous MEA solution in response to two load reduction scenarios over a wide range of operation: power plant load reduction and reboiler steam rate reduction.

The absorption/stripping dynamic model is integrated with the steady state model of power cycle steam turbines and general performance curves of the CO_2 compressor to take into account operational interactions. The simulation and optimization of those operational scenarios at new steady state condition in the presence of operational limitations existing for pumps and the compressor provide the following results:

Based on equivalent work minimization, when the power plant is operated at 60%, 80%, and 90% of load, the MEA plant initially designed for 90% removal can remove up to 94% of inlet CO_2 by increasing the compressor speed up to 120% of the rated speed. For low load such as 40%, recycling gas through surging stages is the only way to prevent the compressor from surging during low power plant load operation.

Reboiler steam load reduction would be optimum if the reboiler temperature remained at 120 °C At steam loads above 60% it is not necessary to run the reboiler at 120 °C. At loads lower than 60%, where the compressor starts to surge, a surge control strategy should be applied. Two surge control strategies are identified and compared:

1. Anti-surge control on the compressor package;
2. Adjusting compressor speed and solvent rate to save compressor from surging.

Comparing the strategies shows that anti-surge control has more advantages with respect to operation and minimum lost work and would be preferable during partial reboiler steam load operation. The following are the main reasons for this statement:

1. Although there is an additional energy loss associated with anti-surge control because of recompressing recycled gas, the total lost work is still lower than the second strategy since it lets the reboiler run at 120 °C and the CO_2 compressor compress the gas at higher suction pressure and consequently lower compression ratio.
2. Anti-surge control strategy has the capability of operating the plant at a wider range of steam load (20–100%) while the second strategy could not operate the plant below a 40% load.

11. A Review of Dynamic Modeling for Post-Combustion Amine Scrubbing *p. 168*

by Matt Walters

Co-supervised by Thomas Edgar

While steady state models for post-combustion amine scrubbing have been extensively studied, there are limited examples of dynamic models that can simulate the process in the presence of disturbances or set point changes. An accurate dynamic model will be necessary to optimally design and operate a process with a minimum energy requirement, maximum economic return, and fast, stable responses to changes in the system. This report presents a review on the dynamic models for carbon capture that have been created and published, and discusses their scope, complexity, and control strategies. The models presented here provide valuable insights into potential variables that can be controlled, measured, and manipulated in order to operate the process optimally. The dynamic models that have been developed to this point provide a solid foundation for work within the field; however none of the models presented here encompass the entire scope of the CO_2 capture and sequestration process and often include simplifying assumptions that decrease model complexity. There is much room for future work in dynamic modeling for post-combustion carbon capture.

12. Electric Grid-Level Implications of Flexible CO_2 Capture Operation p. 178

by Stuart Cohen

Co-supervised by Michael Webber

Flexible post-combustion absorption/stripping that vents carbon dioxide (CO_2) or stores rich solvent at partial or zero load could add value to facilities with CO_2 capture, with one reason being an increased ability to perform grid reliability services (ancillary services, or AS). The Electric Reliability Council of Texas (ERCOT) electric grid operates four AS markets, and these markets could become more lucrative as the already substantial ERCOT wind capacity increases. The new grid-level electricity dispatch model introduced in the third quarterly report of 2011 has now been tested with flexible CO_2 capture facilities and with up to 144 individually represented facilities. The model uses performance parameters for each generation facility, electricity demand, wind-based electricity production, and AS requirements to determine the power plant operation that minimizes total dispatch costs. It is intended to determine whether flexible CO_2 capture increases AS revenues and improves grid reliability.

Major conclusions from this quarter include the following.

- The grid-level dispatch model successfully demonstrates venting-only flexible CO_2 capture, but ensuring functionality of solvent storage systems requires further testing.
- Under appropriate market conditions, flexible CO_2 capture can reduce electricity dispatch costs and improve the ability of a facility to earn revenue from ancillary service procurements.
- The grid-level model functions properly and has reasonable computation time with up to 144 individually represented power generation facilities.
- Minimum load requirements on power systems can cause over-procurement of high-value AS such as regulation up and a corresponding under-procurement of lower-value AS such as responsive reserves.
- Despite relatively high plant-level resolution and generous ramp rates, electricity prices can still spike to the $3,000 per megawatt-hour offer cap when online units cannot ramp up or down fast enough to respond to changes in demand.

13. Nitrosamine formation in CO_2 capture process using piperazine p. 198

by Mandana Ashouripashaki

Nitrosamines are formed from the reaction between secondary amines and nitrite and they are thought to be carcinogenic. Piperazine (PZ) is an amine of interest in our study and nitrosation products of PZ are N-nitrosopiperazine (MNPZ) and N,N'-dinitrosopiperazine (DNPZ).

The available methods for detecting nitrosamines are not applicable for DNPZ because of its lack of volatility. Hence, a method has been developed for quantifying DNPZ using liquid chromatography followed by mass spectrometry (LC-MS). Results show that the amount of DNPZ produced is negligible, and as the temperature of the reaction increases, DNPZ will disappear.

A new method for quantifying MNPZ has been developed using HPLC with a standard reverse phase column using 5% to 50% acetonitrile in water buffered with ammonium carbonate. A calibration curve has been established for MNPZ.

Kinetic study of the reaction between nitrite and PZ has been performed from of 20 to 150 °C. Nitrite consumption is modeled as a first order reaction in nitrite. MNPZ is produced at temperature greater than 75 ^{o}C and then decomposes at 100 to 150 ^{o}C.

14. Thermal Degradation of PZ blends *p. 252*

by Omkar Namjoshi

Thermal degradation of 8 m 1,4-diaminobutane (DAB, previously referred to as Amine Y) and 8 m 2-(Diamino)ethyl ether (DEE, previously referred to as Amine Z) at a CO_2 loading of 0.4 mol CO_2/mol alkalinity was studied at 175 ^{o}C.

The degradation rate of loaded 8 m DEE is fairly close to that of loaded 6 m PZ/2 m DEE. This confirms that blend synergism (enhancement of degradation rates) is not taking place with 2-(Dimethylamino)ethyl ether. On the other hand, the degradation rate of loaded 8 m DAB is about half that of 6 m PZ/2 m DAB.

The primary degradation pathway of DAB appears to be ring closing. The ring closing mechanism does not appear to be the dominant degradation pathway for DEE.

15. Characterization of PZ/Y *p. 260*

by Yang Du

The novel piperazine-based blended amine solvent PZ/Y is being investigated as a possible alternative to the standard 30 wt % MEA for CO_2 capture from coal-fired flue gas. The solid solubility of PZ/Y with variable amine concentration (5/2, 4/2.67, 3/3.33) and 0–3 mol CO_2/mol alkalinity was measured. The viscosity of loaded 5 m PZ/2 m Y blends was measured from 20 to 60 °C. A long-term thermal degradation experiment for 5 m PZ/2 m Y with 0.3 mol CO_2/mol alkalinity is being conducted at 150 °C and 175 °C.

PZ/Y has a greater solid solubility than pure PZ with equal total alkalinity. The highest CO_2 loading at room temperature and 1 atm is 0.39 mol/mol alkalinity for 5 m PZ/2 m Y, 0.38 mol/mol alkalinity for 4 m PZ/2.67 m Y, and 0.38 mol/mol alkalinity for 3 m PZ/3.33 m Y. No precipitates were observed at high CO_2 loading. The viscosity of 5 m PZ/2 m Y blend is comparable to that of 8 m PZ. No data are yet available for thermal degradation.

16. Degradation and Contamination in Amine Solutions for CO_2 Capture *p. 265*

by Alex Voice
also supported by TNO

Miniplant with MEA

The degradation of monoethanolamine (MEA) was studied in a miniature CO_2 capture plant (miniplant). Ammonia was produced at a rate of 8.5–23 mmol/hr. Some inhibitors identified in previous work, including 1,2dimercapto-1,3,4-thiadiazole (DMcT), diethylenetriamine pentaacetic acid (DTPA), hydroxyethilidene diphosphonic acid (HEDP), and Inhibitor A (Inh A) were ineffective at reducing ammonia production.

Ammonia production rates from MEA were assessed under various conditions. Ammonia was not produced in the absence of oxygen. The introduction of metals into the system (by blending a used MEA solution with the fresh solution) increased ammonia production in the presence of

air and CO_2. Reducing the absorber temperature reduced the rate of ammonia production; the activation energy of this process was 33 kJ/mol.

Miniplant with PZ

Formation and degradation of mono-nitrosopiperazine (MNPZ) in 10 wt % piperazine (PZ) was also studied in the miniplant. Reaction of 10 wt % PZ with 8.6 mMol/kg potassium nitrite produced MNPZ at an initial rate of 0.56 mMol/kg/hr. Thermal degradation of MNPZ occurred at a rate of 0.027 mMol/kg/hr at 120 °C; in the presence of oxygen, the rate was only 0.014 mMol/kg/hr. The rate was zero order in MNPZ concentration. The addition of 0.5 wt % ascorbic acid to the system had little impact on the yield of MNPZ from addition of potassium nitrite; however it resulted in an ammonia production rate of 5.6 mmol/hr from the solution and visibly changed the solution color from pale yellow to brown.

MNPZ was also measured in the condensate from the miniplant; the relative volatility of MNPZ was determined to be 1.02 times the volatility of PZ. No significant amount of potassium was found in the condensate, indicating that the MNPZ was in the gas phase, and not the result of mechanical entrainment.

UV Degradation of Nitrosamines

Destruction of MNPZ in 40 wt % PZ by ultraviolet (UV) light was studied in a circulating batch system with 15% hold-up in an 11 W lamp. The rate of UV degradation of MNPZ in PZ was -0.34 to -0.45 mol/kg/hr in this system, which is equivalent to 28–36 J/mol CO_2 for flue gas containing 5 ppm_v NO_2 and 12% CO_2, and a UV light with 1% hold-up. The degradation rate was zero order in MNPZ concentration, and it did not vary significantly with the CO_2 loading, the presence of oxygen, or the presence of dissolved metals. The rate of PZ degradation was 3.3 mmol/kg/hr in this system.

Destruction of NDELA in water and MEA with UV light was also studied in the same system. The rate of destruction in water and amine solutions at basic conditions was between -0.13 and -0.83 mmol/kg/hr and was not obviously affected by the pH. The rate was zero order in NDELA from 1000 ug/g to below 0.1 ug/g. The presence of degradation products that competed for UV light significantly reduced the rate of destruction.

Thermal Degradation of Nitrosamines

MNPZ in 40 wt % PZ was thermally degraded in a once-through reactor at high temperatures (160–180 °C) and pressure (200 bar). The results from this work indicate that the activation energy of thermal degradation is 78–90 kJ/mol. However, the rates observed at high pressure did not agree with measurements at low pressure, indicating that pressure may be a variable of interest in thermal degradation of nitrosamines.

17. Volatile Emission Control in CO_2 Capture *p. 290*

by Steven Fulk

In this quarter, an Ultraviolet-Visible (UV-VIS) absorption spectroscopy method was developed to locate characteristic absorption bands for pure compounds and aqueous solutions. Mononitrosopiperazine (MNPZ) and N-Nitrosodiethanolamine (NDELA) absorption spectra were measured to determine the efficacy of UV techniques for nitrosamine destruction. MNPZ showed two strong absorption peaks at wavelengths of 237 and 341 nm. NDELA showed two

strong absorption peaks at wavelengths of 232 and 345 nm. Amber vials will prevent UV degradation of nitrosamines in samples because nitrosamines absorb only in the UV region.

CO_2 solubility was measured for 8 and 0.15 m PZ solutions between 40–70 °C. Measured CO_2 partial pressures agree closely with predictions using the Fawkes model, further validating speciation predictions and steady-state loading estimations from previous water wash modeling work.

A combined water wash/absorber column was designed in Aspen Plus® using the Fawkes thermodynamic and kinetic framework. The water wash and absorber column were combined to prevent the gas exiting the absorber from flashing prior to entering the water wash packed section.

Goals for next quarter include sensitivity analysis of the combined absorber/water wash column to determine the effects of process variables on column physical dimensions and temperature profiles/aerosol formation driving forces. Degradation compound absorption spectra will be measured using UV-VIS spectroscopy to locate absorption spectral overlap with nitrosamine compounds.

18. Piperazine Degradation in Pilot Plants *p. 298*

by Paul Nielsen

This progress report discusses the findings made in solvent degradation characterization at the pilot-plant scale. In the fall of 2011, pilot plant campaigns were run at the Pickle Research Campus (PRC) and "Pilot Plant 2" using 8 m piperazine (PZ). Data from these campaigns can be used to determine the degradation rate of PZ and the formation of harmful byproducts, including N-nitrosopiperazine (MNPZ), a known carcinogen. MNPZ was shown to form in both pilot plants, but at a very small concentration of no more than 8 ppm at (PRC) and 324 ppm at Pilot Plant 2. After an initial spike within the first month of startup at Pilot Plant 2, MNPZ concentration settled at a steady state of approximately 100 ppm for the following 6 weeks.

Solvent reclaiming was also tested at Pilot Plant 2. This seemed to halt the formation of additional degradation products but did not reduce the concentration of degradation products already present in the solvent.

Goals for next quarter include a more complete determination of the degradation products and rates from the pilot plant samples.

19. Formation/Decomposition of N-Nitrosopiperazine at 120 ^oC *p. 307*

by Nathan Fine

Nitrosamines are a harmful degradation product formed by the nitrosation of amines used in CO_2 capture. A large majority of nitrosamines are carcinogenic, producing alkylating agents that react with the guanine amine in DNA. The DNA mutation has been shown to cause tumor growth in target organs of humans.

N-Nitrosopiperazine (MNPZ) is a nitrosamine formed by the nitrosation of piperazine (PZ), a promising amine for carbon capture. The rates of MNPZ formation and subsequent decomposition were measured for 8 m PZ at 120 ^oC using $NaNO_2$ as the nitrite source. MNPZ formation was two orders of magnitude faster than MNPZ decomposition. Both rates were found to be first order with respect to the reactants, and irreversible at these conditions.

The rate constants were then used to calculate a first order approximation of the steady state MNPZ concentration in a carbon capture absorption-stripping unit. The steady state concentration can be lowered by increasing the residence time in the stripping sump, decreasing available nitrite from the flue gas, or increasing the temperature in the sump.

Attachments:

Xu, Qing *Thermodynamics of CO_2 Loaded Aqueous Amines*. Ph.D. Dissertation, December 2011. p. 314

Plaza, J.M. *Modeling of CO_2 Absorption using Aqueous Monoethanolamine, Piperazine and Promoted Potassium Carbonate.* Ph.D. Dissertation, May 2012. at http://www.che.utexas.edu/rochelle_group/Pubs/plaza_Dissertation-finalv3.pdf

Solvent Screening by the Wetted Wall Column

Quarterly Report for October 1 – December 31, 2011

by Le Li

Supported by the Luminant Carbon Management Program

Department of Chemical Engineering

The University of Texas at Austin

January 31, 2012

Abstract

Four PZ-based blends were screened using the wetted wall column (WWC) during this quarter. Absorption rate and CO_2 solubility of each blend were measured at five CO_2 loadings across the lean and rich operating range and at 20, 40, 60, 80, and 100 ˚C. Two blends of other amines and PZ, 6 m PZ/2 m Y and 6 m PZ/2 m Z, have high heats of absorption at 79 kJ/mol. Both blends have good absorption rates, which are only 9% lower than 8 m PZ. PZ/Y has a lower capacity at 0.55 mol/kg. The capacity of PZ/Z is slightly higher at 0.62 mol/kg, which is still lower than 8 m PZ. The high pKa values and carbamate formation reactions of the other amines contribute to the high heat of absorption of the blends. At the same time, the high pKa values result in high operating lean and rich loadings and low CO_2 solubility at rich loadings, which result in reduced capacity of the blends. Two hindered amine and PZ blends, 5 m PZ/2 m W and 5 m PZ/2.3 m AMP, have more competitive absorption rates than 8 m PZ and cyclic capacity of 0.66 mol/kg. PZ/W has low CO_2 solubility at rich loadings, which results in a lower capacity than 8 m PZ. PZ/W has similar heat of absorption to amine W, which is 72 kJ/mol and 12% higher than 8 m PZ. The lower capacity of PZ/AMP is the result of low alkalinity of the blend. PZ/AMP has a high heat of absorption at 78 kJ/mol. Among the four new PZ blends, 5 m PZ/2.3 m AMP has the best overall properties.

The absorption rate of the lean amine sample from the 2011 8 m PZ pilot plant campaign was measured at 40, 60, 80, and 100 ˚C. The sample was tested at the collected loading and two higher loadings. The calculated capacity of the pilot plant sample is approximately 10% less than 8 m PZ. The heat of absorption of the sample is higher than 8 m PZ by 19%. The $k_g'_{avg}$ for the pilot plant sample is slightly higher than 8 m PZ. The distinct properties of the pilot plant sample suggest changes in active species from 8 m PZ as results of possible solvent degradation during the campaign.

5 m MDEA/5 m PZ was measured in the WWC at 10, 20, 30, and 40 ˚C to expand the range of available data for the blend. The absorption rate of 5 m MDEA/5 m PZ has no temperature dependence between 10 to 40 ˚C. The measured CO_2 solubility at low temperature agrees well with previous high temperature data.

Introduction

To improve the performance of 8 m PZ, four PZ-based blends were screened using the WWC this quarter. As the new base case solvent, 8 m PZ is better than the old standard 7 m MEA with

twice the absorption rate, double the CO_2 working capacity, and higher resistance to oxidative and thermal degradation. However, 8 m PZ is still limited by a small solid solubility window (Freeman, 2011). Also, 8 m PZ has a relatively low heat of absorption compared to 7 m MEA, which will translate into a disadvantage in the energy optimization of the process (Oyenekan, 2006). Blending PZ with other amines can potentially maintain the attractive properties of PZ, while at the same time improve its limitations. The tested blends are 6 m PZ/2 m Y, 6 m PZ/2 m Z, 5 m PZ/2 m W, and 5 m PZ/2.3 m AMP. Amine Y and amine Z have a high heat of absorption by themselves, so the blends are expected to inherit similar properties (Rochelle, 2011b). Also, these amines and PZ are expected to maintain CO_2 absorption capacity even as the blend becomes thermally degraded. Amine W is a PZ derivative with a hindered amine group, and 2-amino-2-methyl-propanol (AMP) is a primary hindered amine. Hindered amines have large working capacities and relatively high heats of absorption, which suggest potential good performances for the blends. The concentration of each blend was chosen to maximize total alkalinity of the solvent, at the same time maintaining reasonable solid solubility windows and low viscosities. For each blend, the WWC is used to measure absorption rates and CO_2 solubility at five CO_2 loadings at temperatures from 20 ˚C to 100 ˚C. The CO_2 capacity and heat of absorption are calculated using the measured CO_2 solubility results. The measured properties are then compared against results for 8 m PZ and 7 m MEA (Dugas, 2009).

A sample from the 2011 8 m PZ pilot plant campaign was tested to verify pilot plant results. The amine solvent at its operating lean loading was collected from the pilot plant skid. The WWC was used to test the sample at the collected CO_2 loading and two higher CO_2 loadings. The measured absorption rates and CO_2 solubility at these three loadings were compared to results of 8 m PZ.

5 m MDEA/5 m PZ was tested in the WWC at four CO_2 loadings and four temperatures from 10 ˚C to 40 ˚C. Measurements of CO_2 solubility at low temperatures can be used in the MDEA/PZ thermodynamic model in Aspen Plus®. Low temperature data will improve model consistency over a wider temperature range, which can improve model prediction of temperature dependent properties. Absorption rate data at low temperatures can be used to better model absorber performance in cold geographical areas. Additional rate measurements can also verify regressed rate parameters in model.

Experimental Methods

The absorption rate and CO_2 solubility for each solvent were measured using a wetted wall column apparatus. The method is identical to that used by Chen (2011b).

Materials

The solvent blends were prepared by mixing chemicals gravimetrically. The chemical species in 5 m MDEA/5 m PZ are listed in Table 1. To achieve each CO_2 loading condition, CO_2 was added to the solvents by bubbling gaseous CO_2 (99.99%, Matheson Tri-Gas) into the liquid. Some of the chemicals used are listed in Table 2.

The 2011 8 m PZ pilot plant experiment used the absorber lean amine sample collected from the skid. The two high loading conditions were achieved by bubbling CO_2 (99.99%, Matheson Tri-Gas) into the collected sample. The measured CO_2 content and alkalinity in the WWC samples are reported in Table 3.

Table 1: Chemical Species in 5 m MDEA/5 m PZ

	Mass (g)	wt %
MDEA	541.7	0.294
PZ	391.6	0.213
Water	908.9	0.493

Table 2: Materials Used for Solvent Preparation

Chemical	Purity	Source
2-amino-2-methyl-propane	99%	Acros Organics
Piperazine	98%	Sigma-Aldridge
Methyldiethanolamine	98.5%	Huntsman
DDI Water	100.00%	Millipore, Direct-Q

Table 3: Measured content in 2011 8 m PZ pilot plant WWC samples

	Total Alkalinity mol/kg	CO_2 mol/kg	CO_2 loading mol/mol Alk
1st loading	8.15	2.37	0.291
2nd loading	7.65	2.53	0.330
3rd loading	7.79	3.09	0.397

Analytical methods

The CO_2 content in the 2011 8 m PZ pilot plant samples was measured using the total inorganic carbon method. The total alkalinity in the samples was measured using the acid titration method. The apparatus and procedure of both methods are identical to those used by Freeman (2011).

Results and discussion

Piperazine (PZ) blends

Absorption/desorption rates

The liquid film mass transfer coefficient (kg') was measured for 6 m PZ/2 m Y at five loadings across the lean and rich loading range (Figure 1). Four temperatures from 20 ˚C to 80 ˚C were tested. Data were not collected at 100 ˚C for this blend due to the high CO2 partial pressure at high temperature which exceeded the measureable range of the apparatus. Compared at 40 ˚C, the measured kg' of this blend is slightly lower than 8 m PZ at low loading. At rich loading the absorption rates of the blend is the same as 8 m PZ. The kg' of this blend has no temperature dependence at low loading and low temperature. Temperature dependence becomes significant as temperature and loading increase. Absorption rate decreases with increase in temperature.

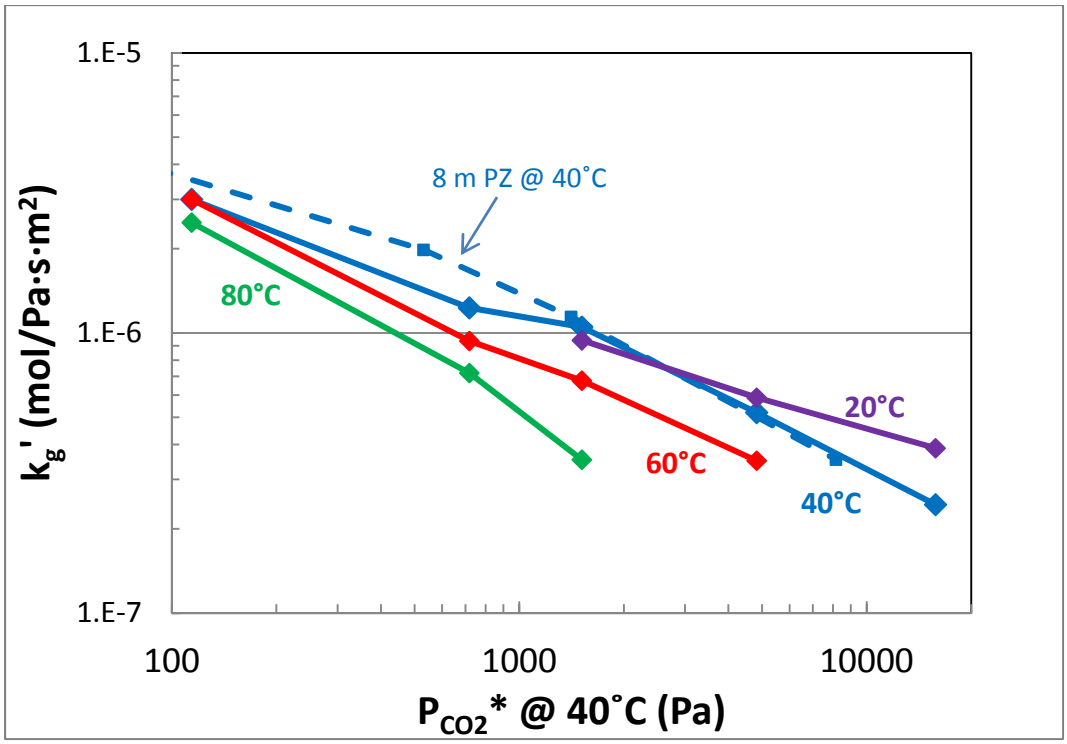

Figure 1: CO_2 Liquid Phase Mass Transfer Coefficient (k_g') in 6 m PZ/2 m Y

It is important to note that 6 m PZ/2 m Y has unique surface tension property which inhibits formation of smooth and stable liquid film on the WWC. At the typical liquid flowrate of approximately 240 mL/min (Chen, 2011a), a significant portion (10–20%) of the WWC surface area was dry. Therefore, the experiments operated with liquid flowrate 1.5 to 2 times higher than the typical set point. While this adjustment ensured the WWC is wetted in its entirety during the measurements, the liquid film on the WWC exhibits visible ripples at this new condition. The higher liquid flowrate will result in a higher physical mass transfer coefficient (kl◦) in the liquid film, which contributes to the values of kg'. The effect of liquid flowrate is more significant at rich loading conditions, where diffusion of species becomes important in the mass transfer in the liquid film. The observed ripples increase the surface area for mass transfer, which results in a higher measured CO2 flux and in turn a higher kg'. Therefore, the reported kg' values for this blend are potentially higher than their true values (if measured at typical conditions), and this effect is more significant at rich loadings. Also, this observed physical property suggests similar behavior of the solvent in an absorber, where a high liquid flowrate will be necessary for proper wetting of the packing.

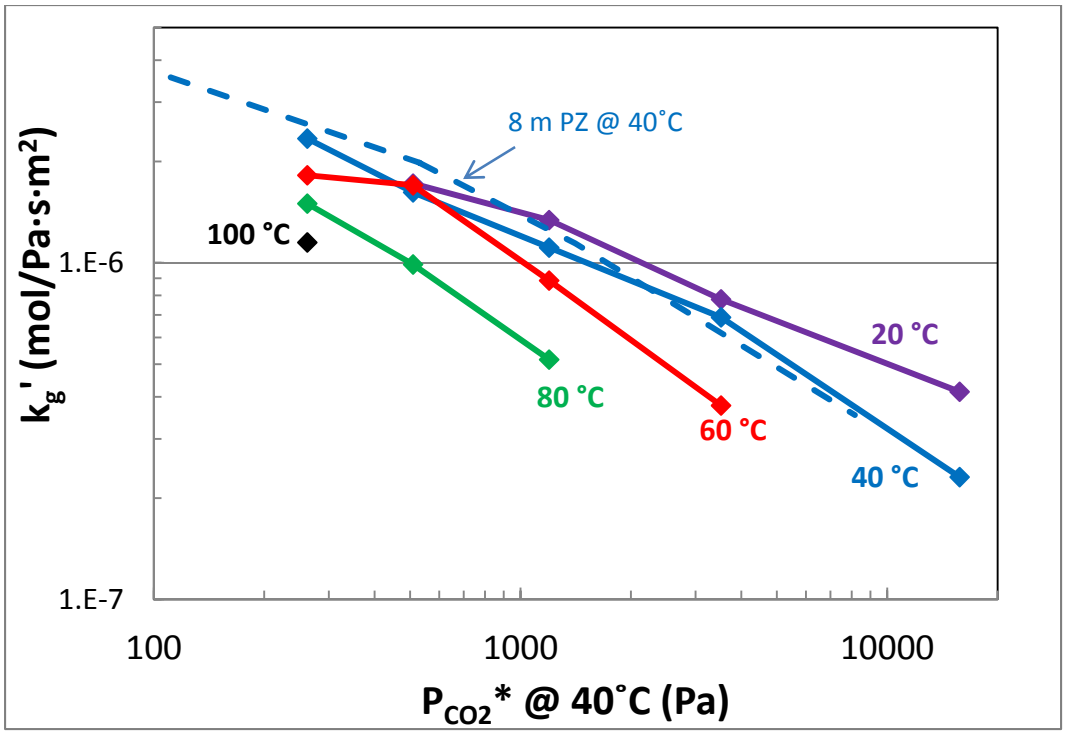

Figure 2: CO_2 Liquid Phase Mass Transfer Coefficient (k_g') in 6 m PZ/2 m Z

The absorption rates for 6 m PZ/2 m Z were measured at five CO_2 loadings and five temperatures from 20 ˚C to 100 ˚C (Figure 2). The blend has similar k_g' values to 8 m PZ at 40 ˚C across the CO_2 loading range of the experiment. Thus, amine Z is likely to have similar rate performance to PZ. The absorption rate of the blend decreases with increase in temperature at all loadings except 0.362. In general, the temperature dependence of k_g' for this blend is more significant at rich loadings and at temperatures between 40 ˚C and 100 ˚C.

For 5 m PZ/2 m W, absorption rates were measured at five loadings across the lean and rich operating range (Figure 3). Five temperatures between 20 ˚C and 100 ˚C were measured. At 40 ˚C, the blend has rates similar to 8 m PZ at lean loadings. At rich loadings, the rates of the blend are higher than 8 m PZ. The addition of amine W resulted in more highly reactive species in the blend at rich loadings than 8 m PZ. The absorption rate of the blend does not change with temperature between 20 ˚C and 40 ˚C at all measured loadings. At 60 ˚C, the measured rate decrease significantly only at the highest loading. Between 80 ˚C and 100 ˚C, more significant temperature dependence of absorption rate is observed, particularly with an increase in CO_2 loading.

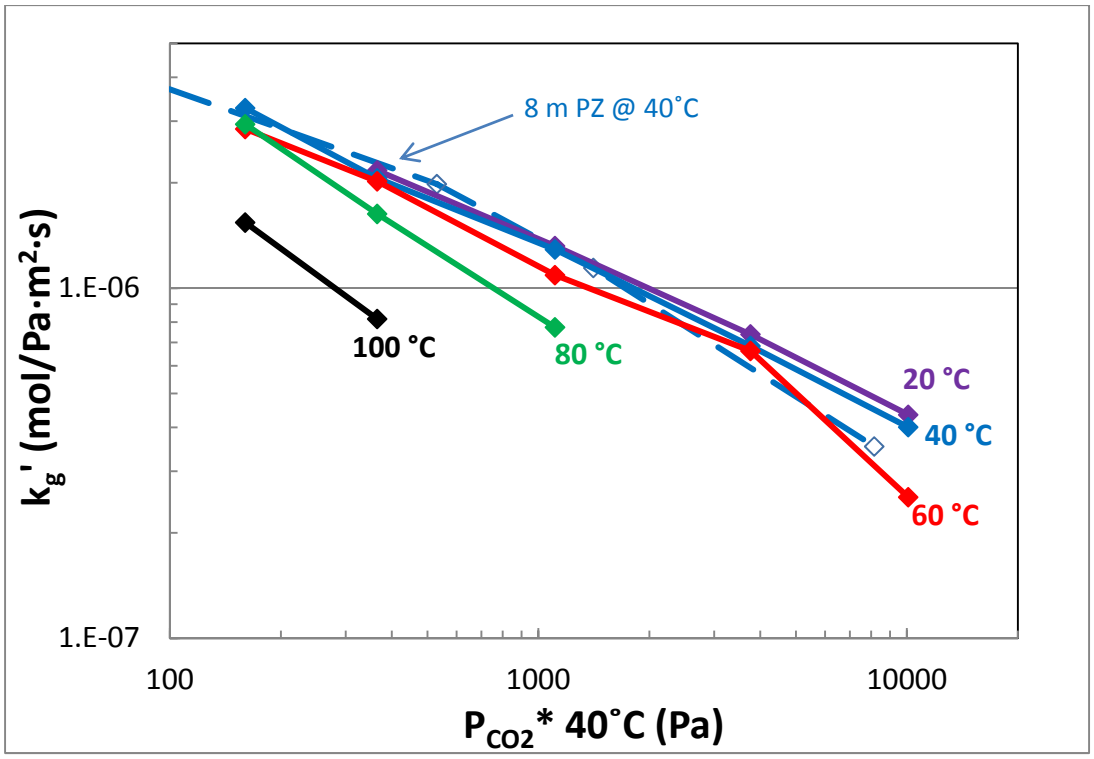

Figure 3: CO_2 Liquid Phase Mass Transfer Coefficient (k_g') in 5 m PZ/2 m W

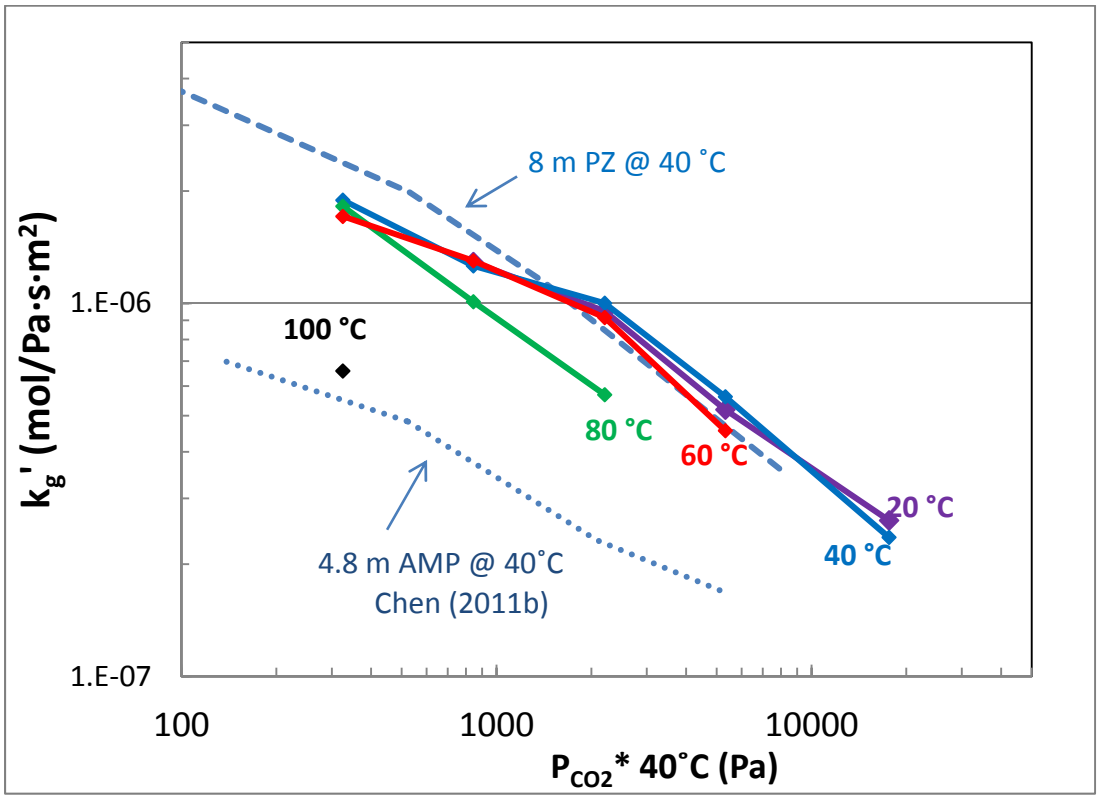

Figure 4: CO_2 Liquid Phase Mass Transfer Coefficient (k_g') in 5 m PZ/2.3 m AMP

The k_g' for 5 m PZ/2.3 m AMP was measured at five CO_2 loadings across the lean and rich operating conditions. At 40 ˚C, the absorption rate of the blend is slightly lower than 8 m PZ at the two lower loadings. At the three high CO_2 loadings, the k_g' of the blend is higher than 8 m PZ. Since the absorption rate of pure AMP is much lower than 8 m PZ and the blend (Chen, 2011b), the increase in rate of the blend at rich loadings is likely the result of a change in the speciation in the blend. The addition of AMP, which has a high pKa amino group, can result in more free PZ and PZ carbamate for reaction with CO_2 at rich loadings. The absorption rate of this blend exhibits no temperature dependence from 20 ˚C to 60 ˚C. At 80 ˚C and high loadings, k_g' is lower than the lower temperature measurements. Also, the absorption rate at 100 ˚C is much lower than at other temperatures.

To compare the rate performance of the solvents in an absorber, the parameter of $k_g'_{avg}$ is used to simplify the dynamic behavior in a column into an average rate (Equation 1).

$$k'_{g\,avg} = \frac{(Flux_{CO_2,top} - Flux_{CO_2,bottom})/Ln(\frac{Flux_{CO_2,top}}{Flux_{CO_2,bottom}})}{[(P_{CO_2,top} - P^*_{CO_2,lean}) - (P_{CO_2,bottom} - P^*_{CO_2,rich})/Ln(\frac{(P_{CO_2,top} - P^*_{CO_2,lean})}{(P_{CO_2,bottom} - P^*_{CO_2,rich})}]} \quad (1)$$

The approximation in the $k_g'_{avg}$ assumes an isothermal absorber operating at 40 ˚C and log mean average between the top and bottom of the absorber column. The approximation is more accurate in the case where the CO_2 equilibrium curve is close to linear on a log scale. Nonetheless, the $k_g'_{avg}$ concept is useful to compare rate performance of solvents on a first order basis. The calculated values of $k_g'_{avg}$ for the four blends are listed in Table 5.

CO_2 solubility

The equilibrium CO_2 partial pressures (P_{CO2}*) for each PZ blend were measured at five CO_2 loadings and temperatures from 20 ˚C to 100 ˚C. A semi-empirical vapor liquid equilibrium model is generated for each solvent by regressing the measured P_{CO2}* results using Equation 2.

$$\ln(P^*_{CO_2}) = a + \frac{b}{T} + c \cdot ldg + d \cdot \frac{ldg}{T} + e \cdot ldg^2 + f \cdot \frac{ldg^2}{T} \quad (2)$$

The regressed model parameters for each blend are summarized in Table 4.

To calculate cyclic capacity, the solvent lean and rich loadings are first found using the VLE model (Equation 2). The lean and rich loadings corresponds to P_{CO2}* of 0.5 and 5 kPa at 40 ˚C, respectively. These values are then used in Equation 3 to give the capacity of the solvent. A large difference between the rich and lean loading values will result in a high cyclic capacity.

$$Capacity = (rich\ ldg - lean\ ldg) \cdot \frac{mol\ Alkalinity}{kg\ solvent} \quad (3)$$

The semi-empirical VLE model (Equation 2) can also predict solvent heat of absorption. Theoretically, the heat of absorption of CO_2 is defined as the temperature dependence of the thermodynamic equilibrium of CO_2 in the solvent. This thermodynamic relationship is expressed is Equation 4.

$$H_{abs} = -R \cdot \frac{\partial(lnP^*_{CO_2})}{\partial(\frac{1}{T})} = -R \cdot (b + d \cdot ldg + f \cdot ldg^2) \quad (4)$$

The calculated cyclic capacity and heat of absorption at the midpoint of the loading range (P_{CO2}* = 1.5kPa) for each solvent are summarized in Table 5.

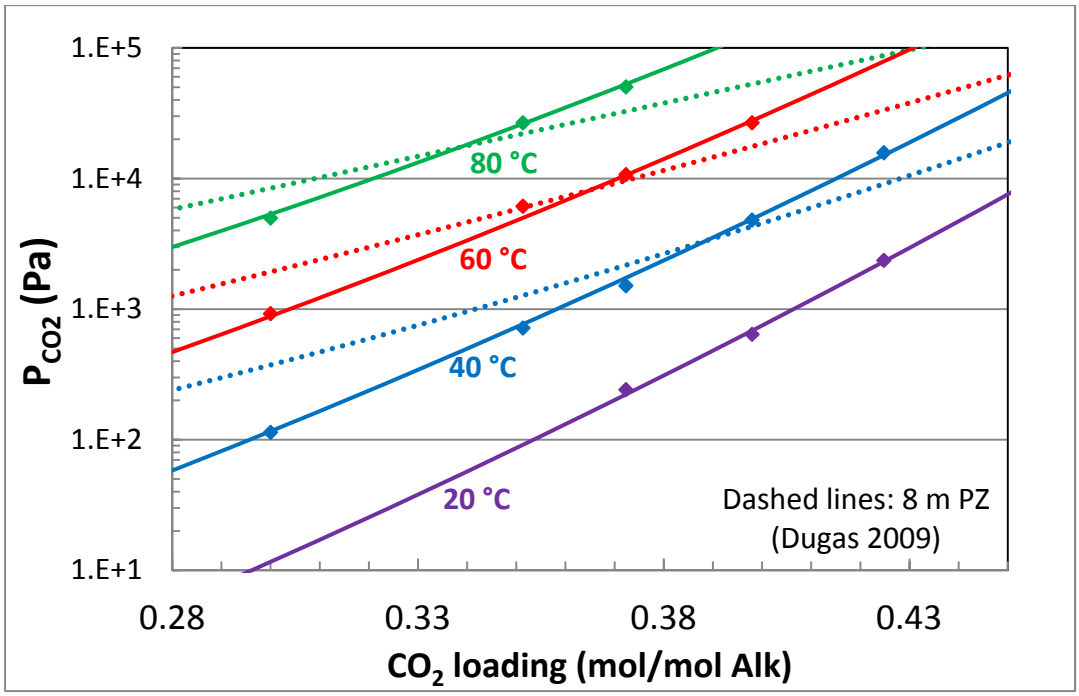

Figure 5: CO_2 solubility of 6 m PZ/2 m Y

The measured P_{CO2}* and the regressed semi-empirical VLE model for 6 m PZ/2 m Y are plotted in Figure 5 and compared against 8 m PZ (dashed lines). CO_2 is more soluble in the blend than 8 m PZ at low loadings, but less soluble at rich loadings. The high CO_2 solubility at low loadings could be attributed to the free amine Y in the blend, which has a high pKa value. As loading increases, free amine Y is consumed by protonation and formation of carbamate. At rich loadings, the second amine group on the carbamate of amine Y and protonated amine Y is likely the dominating CO_2 absorbing species. The low CO_2 solubility at rich loading suggests low CO_2 capacity of the second amine group on amine Y, which could be the result of low pKa value. The addition of amine Y results in a large change of P_{CO2}* with increased CO_2 loading, and thus a lower solvent capacity. However, with two carbamate-forming amine groups, amine Y contributes to the heat of absorption of the solvent which results in a high heat of absorption for the blend.

The CO_2 solubility results for 6 m PZ/2 m Z (Figure 6) exhibit similar trends to PZ/Y but to a lesser extent. The first amine group of amine Z has a lower pKa value than amine Y, while the pKa of the second amine group is likely higher than that of amine Y. Therefore, the CO_2 solubility curve of PZ/Z is more similar to 8 m PZ than the PZ/Y blend. Since the slope of the CO_2 solubility curve is lower for PZ/Z than for PZ/Y, PZ/Z has higher cyclic capacity. Both of the amine groups in amine Z react with CO_2 to form carbamates, which results in a high heat of absorption of the blend similar to PZ/Y.

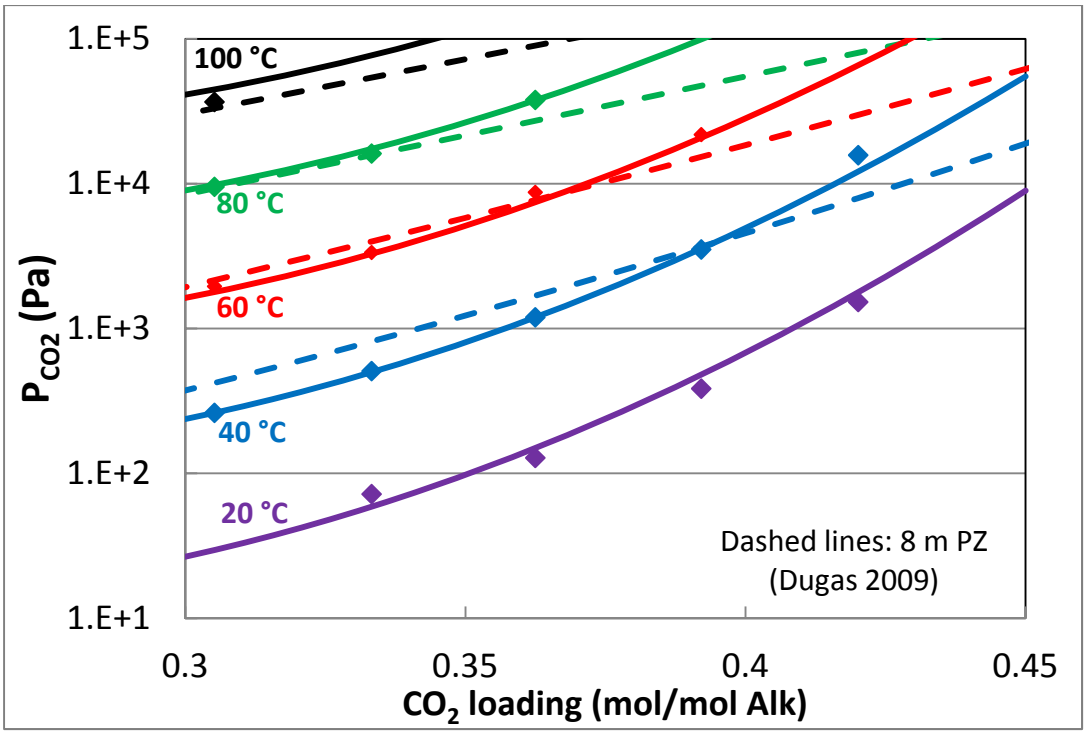

Figure 6: CO_2 solubility of 6 m PZ/2 m Z

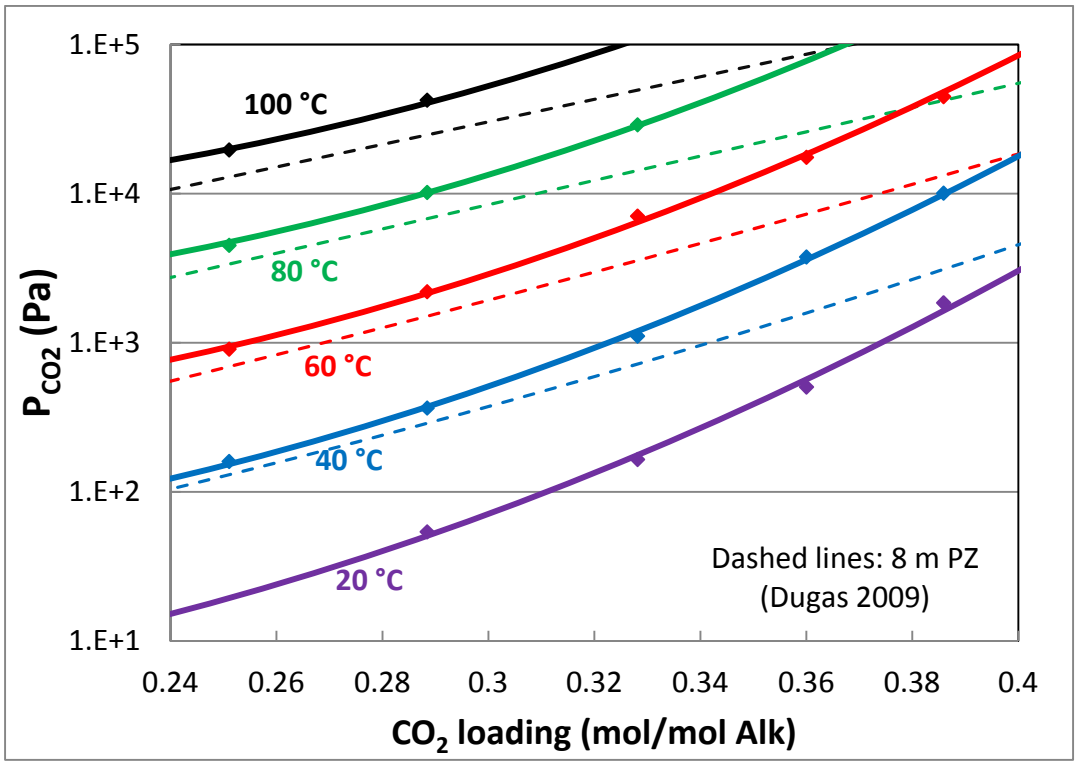

Figure 7: CO_2 solubility of 5 m PZ/2 m W

The P_{CO2}* for 5 m PZ/2 m W is higher than 8 m PZ across the operating loading range and all temperatures (Figure 7). The low CO_2 solubility of the blend is because CO_2 is less soluble in

amine W than in PZ. At low loadings, the measured P_{CO2}* for the blend is similar to 8 m PZ since a significant amount of PZ is available for CO_2 absorption. As loading increases, PZ is consumed by absorbed CO_2, and amine W and derivatives become the active species in the blend, which results in much lower CO_2 solubility of the blend at high loadings. The large increase in P_{CO2}* at high loadings results in a steep slope for the CO_2 solubility curve, which contributes to a lower capacity for this blend than 8 m PZ.

5 m PZ/2.3 m AMP has CO_2 solubility curves with similar shapes to 8 m PZ (Figure 8). The presence of AMP species does not affect the CO_2 solubility dependence on loading. Therefore, PZ/AMP has similar lean and rich loadings to 8 m PZ. However, the capacity of the blend is lower than 8 m PZ due to a lower total alkalinity of the blend. The addition of AMP does have significant effect on the heat of absorption of the blend. Due to the high pKa of AMP, the blend has much higher heats of absorption than 8 m PZ.

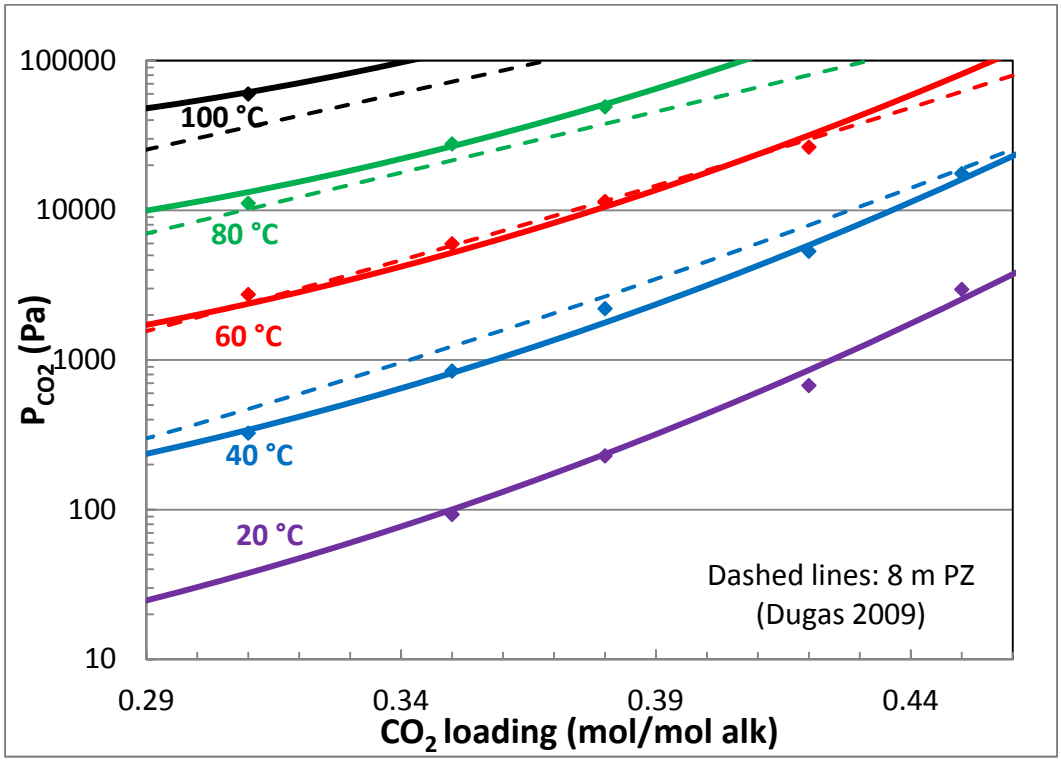

Figure 8: CO_2 solubility of 5 m PZ/2.3 m AMP

Table 4: Regressed semi-empirical VLE model parameters for PZ blends

Amines	Concentration (m)	a Intercept	b 1/T	c Loading	d ldg/T	e ldg^2	f ldg^2/T
PZ/Y	6 / 2	45.7	-15287.6	-33.2	15702.5	30.4	/
PZ/Z	6/ 2	37.5	/	-8410.2	-16668.0	/	37391.1
PZ/W	5 / 2	42.0	-11781.6	-45.3	9154.8	73.7	/
PZ/AMP	5 / 2.3	49.2	-13772.2	-53.0	11802.5	56.4	/

Properties of the new PZ blends are compared against 8 m PZ, 7 m MEA, and 6 m PZ/2 m X. All four PZ blends have competitive absorption rates compared to 8 m PZ, with 5 m PZ/2 m W having the highest and 6 m PZ/2 m Y the lowest rate. The cyclic capacities of the four blends are lower than 8 m PZ by 15–20%. The two hindered amine blends, 5 m PZ/2 m W and 5 m PZ/2.3 m AMP, have the higher capacities at 0.66 mol/kg, which is 10% higher than 7 m MEA. The heats of absorption of 6 m PZ/2 m Y, 6 m PZ/2 m Z, and 5 m PZ/2.3 m AMP are higher than both 8 m PZ and 7 m MEA by about 10–12%. 5 m PZ/2 m W has a heat of absorption slightly higher than 7 m MEA, which is about 5% higher than 8 m PZ. Compared to 6 m PZ/2 m X, the two new amine blends have higher absorption rates (60%), slightly higher capacities, and higher heats of absorption (18%). Based on the three measured properties, the blend of 5 m PZ/2.3 m AMP has the best overall properties, which are better than 7 m MEA and competitive against 8 m PZ in terms of rates and heat of absorption.

Table 5: Measured performance properties of PZ blends

Amines	Concentration (m)	$k_g'_{avg}$ X10^7 (mol/s·Pa·m^2)	Capacity mol/kg	$-H_{abs}$ kJ/mol
PZ/Y	6/2	7.68	0.55	79
PZ/Z	6/2	8.03	0.62	79
PZ/W	5/2	8.92	0.66	72
PZ/AMP	5/2.3	8.50	0.67	78
PZ/X (Rochelle, 2011a)	6/2	4.90	0.53	67
PZ (Dugas, 2009)	8	8.46	0.79	64
MEA (Dugas, 2009)	7	4.30	0.47	70

The measured absorption rates and CO_2 solubility values for the blends are listed in Tables 6–9.

Table 6: CO_2 solubility and absorption rates of 6 m PZ/2 m Y blend

Temperature ˚C	CO_2 loading mol/mol alk	k_g' X10^7 (mol/s·Pa·m^2)	P_{CO2} kPa
20	0.372	9.42	0.242
20	0.398	5.88	0.642
20	0.425	3.88	2.364
40	0.300	30.00	0.114
40	0.351	12.30	0.718
40	0.372	10.50	1.513
40	0.398	5.20	4.821
40	0.425	2.44	15.77
60	0.300	30.00	0.924
60	0.351	9.37	6.148
60	0.372	6.76	10.73
60	0.398	3.50	26.79
80	0.300	24.80	4.982
80	0.351	7.20	26.74
80	0.372	3.53	50.32

Table 7: CO_2 solubility and absorption rates of 6 m PZ/2 m Z

Temperature	CO_2 loading	k_g'	P_{CO2}
˚C	mol/mol alk	X10^7 (mol/s·Pa·m^2)	kPa
20	0.333	17.20	0.072
20	0.362	13.40	0.128
20	0.392	7.79	0.385
20	0.420	4.14	1.527
40	0.305	23.40	0.262
40	0.333	16.20	0.509
40	0.362	11.10	1.196
40	0.392	6.89	3.519
40	0.420	2.31	15.75
60	0.305	18.20	1.958
60	0.333	17.00	3.355
60	0.362	8.86	8.729
60	0.392	3.77	21.84
80	0.305	15.00	9.523
80	0.333	9.89	16.17
80	0.362	5.16	37.92
100	0.305	11.50	36.72

Table 8: CO_2 solubility and absorption rates of 5 m PZ/2 m W

Temperature	CO_2 loading	k_g'	P_{CO2}
˚C	mol/mol alk	X10^7 (mol/s·Pa·m^2)	kPa
20	0.288	21.70	0.054
20	0.328	13.20	0.165
20	0.360	7.38	0.505
20	0.386	4.35	1.854
40	0.251	32.70	0.16
40	0.288	20.60	0.365
40	0.328	12.90	1.109
40	0.360	6.84	3.763
40	0.386	4.01	10.08
60	0.251	28.50	0.907
60	0.288	20.20	2.201
60	0.328	10.90	7.075
60	0.360	6.62	17.54
60	0.386	2.53	44.81
80	0.251	29.40	4.505
80	0.288	16.30	10.20
80	0.328	7.73	28.99
100	0.251	15.40	19.65
100	0.288	8.17	42.43

Table 9: CO_2 solubility and absorption rates of 5 m PZ/2.3 m AMP

Temperature	CO_2 loading	k_g'	P_{CO2}
˚C	mol/mol alk	X10^7 (mol/s·Pa·m^2)	kPa
20	0.35	12.90	0.093
20	0.38	9.53	0.229
20	0.42	5.19	0.676
20	0.45	2.62	2.963
40	0.31	18.90	0.325
40	0.35	12.60	0.844
40	0.38	10.01	2.204
40	0.42	5.62	5.325
40	0.45	2.36	17.62
60	0.31	17.10	2.742
60	0.35	13.00	5.979
60	0.38	9.16	11.46
60	0.42	4.56	26.45
80	0.31	18.20	11.15
80	0.35	10.10	27.78
80	0.38	5.69	49.17
100	0.31	6.59	59.91

2011 8 m PZ pilot plant campaign

The absorption rate of the lean amine sample from the 2011 8 m PZ pilot plant campaign was measured at 40, 60, 80, and 100 ˚C (Figure 9). The sample was tested at the collected loading and two higher loadings. At 40 ˚C, the pilot plant sample has a similar absorption rate to 8 m PZ. Only the 40 ˚C k_g' measured at the initial loading is slightly higher than 8 m PZ. At all three loadings, the absorption rate of the pilot plant sample exhibits more significant temperature dependence than 8 m PZ. This temperature dependence in k_g' could be a result of a change in physical properties of the solvent which will affect the mass transfer of CO_2.

The CO_2 solubility of the pilot plant sample distinctly differs from 8 m PZ (Figure 10). At rich loadings, P_{CO2}* is higher in the pilot plant sample than 8 m PZ. The decrease of CO_2 solubility in the pilot plant samples suggests changes in active species in solution from 8 m PZ. As a result, the cyclic capacity of the pilot plant sample is lower than that of 8 m PZ.

Using the semi-empirical VLE model regressed from the solubility data, the capacity and heat of absorption of the sample were calculated (Table 10). The calculated capacity of the pilot plant sample is approximately 10% less than 8 m PZ. The heat of absorption of the sample is higher than 8 m PZ by 19%. The $k_g'_{avg}$ for the pilot plant sample is slightly higher than 8 m PZ.

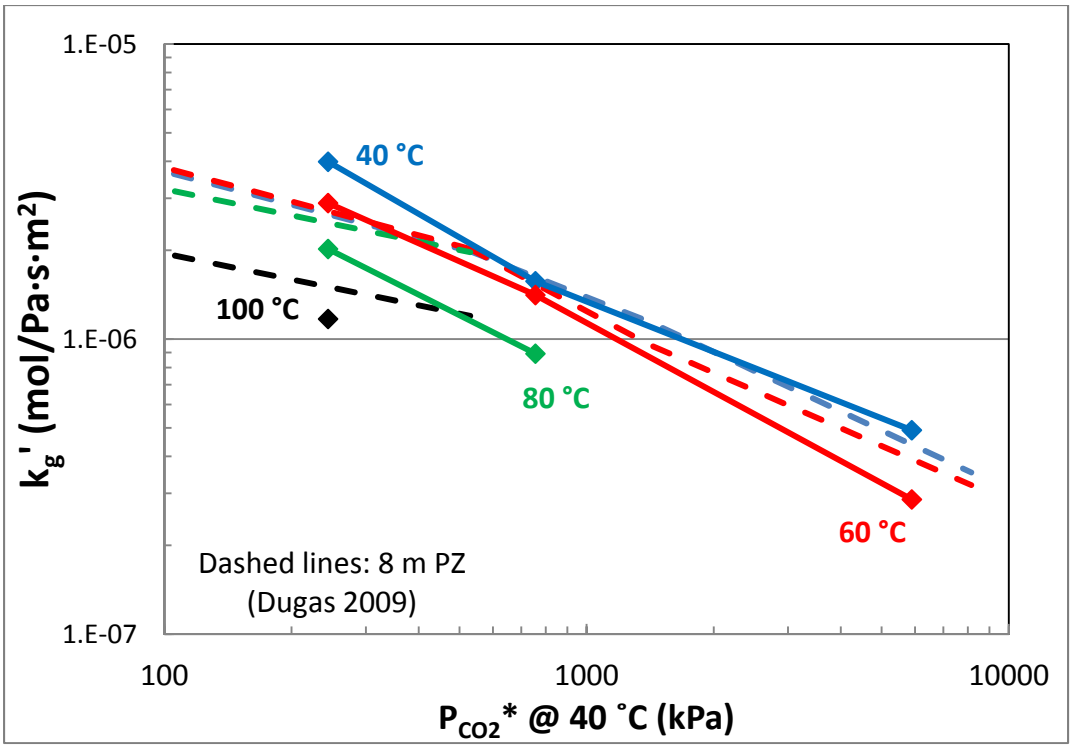

Figure 9: CO_2 Liquid Phase Mass Transfer Coefficient (k_g') in 2011 8 m PZ pilot plant sample

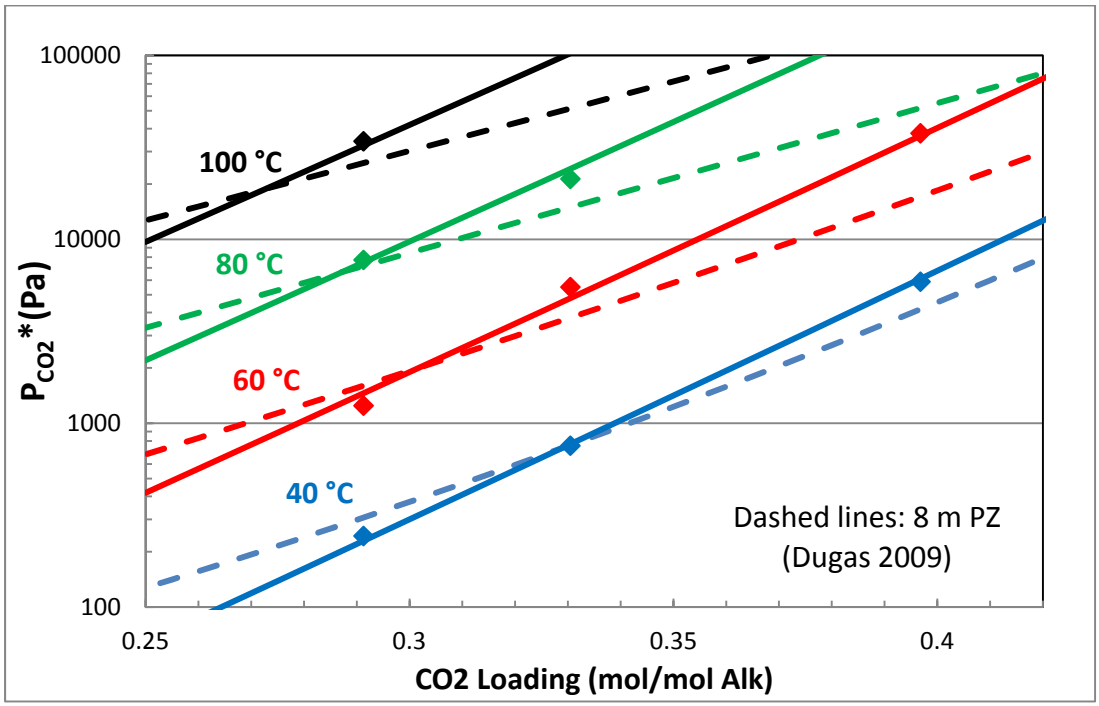

Figure 10: CO_2 solubility in 2011 8 m PZ pilot plant sample

Table 10: Measured properties of the 2011 PZ pilot plant sample

Solvent	$k_g'_{avg}$ X 10^7 (mol/s·Pa·m^2)	Capacity mol/kg	$-H_{abs}$ kJ/mol
2011 8 m PZ Pilot Plant Campaign	8.89	0.70	79
8 m PZ (Dugas, 2009)	8.46	0.79	64

Table 11: CO_2 solubility and absorption rates of 2011 8 m PZ pilot plant campaign

Temperature ˚C	CO_2 loading mol/mol Alk	k_g' X10^7 (mol/s·Pa·m^2)	P_{CO2} kPa
40	0.291	39.90	0.24
40	0.330	15.70	0.76
40	0.397	4.91	5.89
60	0.291	28.90	1.25
60	0.330	14.10	5.51
60	0.397	2.86	37.79
80	0.291	20.20	7.74
80	0.330	8.92	21.35
100	0.291	11.70	34.20

Low temperature results for 5 m MDEA/5 m PZ

The absorption rate of 5 m MDEA/5 m PZ at 10, 20, 30, and 40 ˚C is approximately the same (Figure 11). At low temperature, high solvent viscosity should significantly reduce the diffusivity of all species in solution, but physical solubility of CO_2 will be greater compared to previous rate measurements of the blend at 40 ˚C, the new values are slightly lower at lean loadings. The rate at rich loadings agrees well with previous data.

The P_{CO2}* measured at low temperature is plotted together with previously measured high temperature data (Figure 12). The new equilibrium measurements agree well with the high temperature data. The two sets of data were regressed together and the resulting VLE model fits the experimental data well over the entire temperature range.

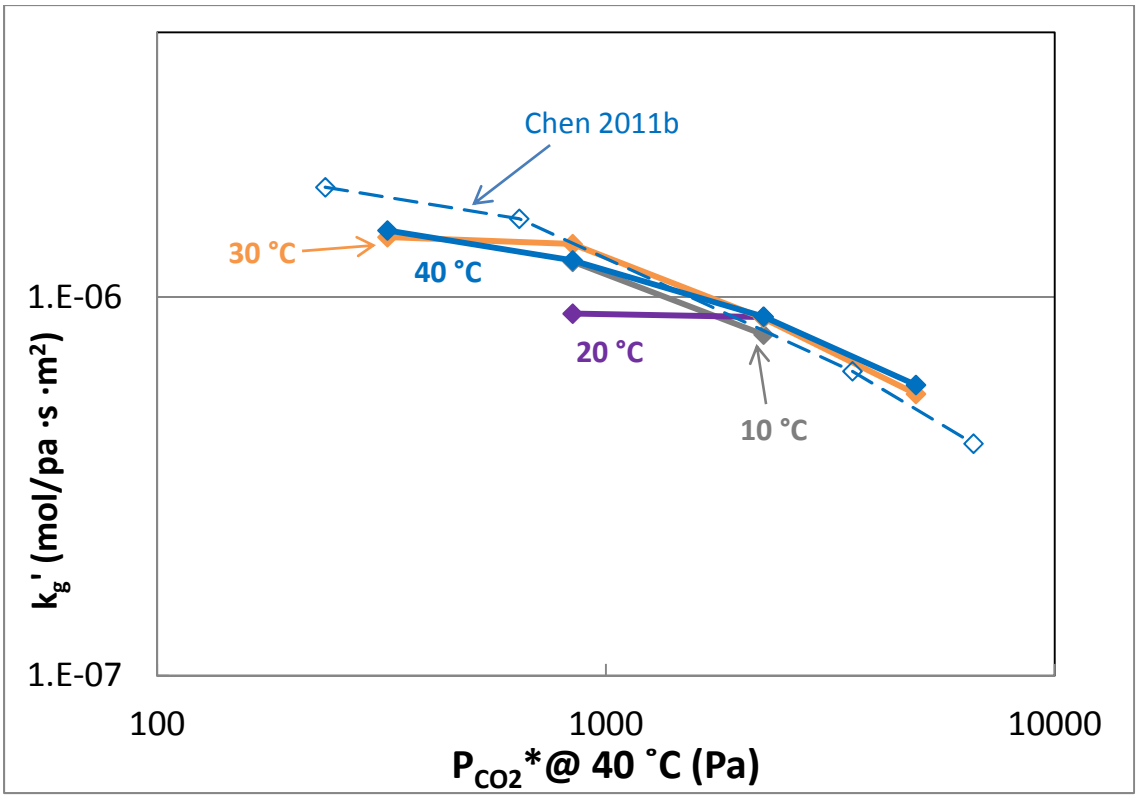

Figure 11: CO_2 Liquid Phase Mass Transfer Coefficient (k_g') at low temperature in 5 m MDEA/5 m PZ

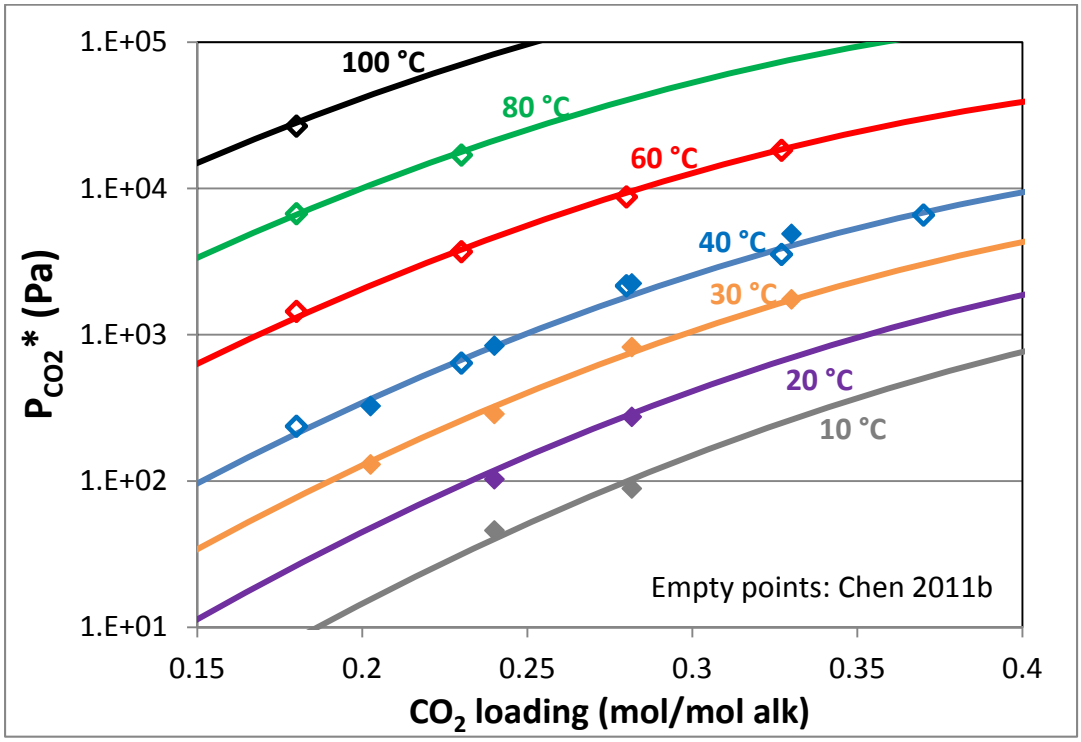

Figure 12: CO_2 solubility in 5 m MDEA/5 m PZ

Table 12: CO_2 solubility and absorption rate of 5 m MDEA/5 m PZ at low temperature

Temperature ˚C	CO_2 loading mol/mol alk	k_g' X10^7 (mol/s·Pa·m^2)	P_{CO2} kPa
10	0.24	12.4	0.046
10	0.28	7.96	0.089
20	0.24	9.04	0.103
20	0.28	8.85	0.275
30	0.20	14.4	0.13
30	0.24	13.8	0.288
30	0.28	8.79	0.825
30	0.33	5.55	1.749
40	0.20	15	0.326
40	0.24	12.5	0.843
40	0.28	8.88	2.245
40	0.33	5.86	4.906

Conclusions

Two blends of other amines and PZ, 6 m PZ/2 m Y and 6 m PZ/2 m Z, have high heat of absorption, 79 kJ/mol, which is about 13% greater than 7 m MEA. The blends have good absorption rate, about 9% lower than 8 m PZ and 60% higher than 7 m MEA. The capacity of 6 m PZ/2m Y (0.55 mol CO_2/kg) and 6 m PZ/2 m Z (0.62 mol CO_2/kg) is about 25% less than 8 m PZ.

The hindered amine blends, 5 m PZ/2 m W and 5 m PZ/2.3 m AMP, have competitive absorption rate compared to 8 m PZ. Both hindered amine blends have 0.66 mol/kg cyclic capacity, which is slightly higher than the other amine blends and 16% less than 8 m PZ. The heat of absorption for 5 m PZ/2 m W is 72 kJ/mol, which is slightly higher than 7 m MEA. The PZ/AMP blend has a high heat of absorption at 78 kJ/mol.

Among the four new PZ blends, 5 m PZ/2.3 m AMP has the best overall properties. Also, 5 m PZ/2 m W has the highest absorption rate, which is 5% higher than 8 m PZ.

The 2011 8 m pilot plant sample has distinct properties which differ from fresh 8 m PZ solvent. The absorption rate of the pilot plant sample is similar to 8 m PZ. The capacity of the sample is lower than 8 m PZ by about 11%. The heat of absorption of the pilot plant sample is 23% higher than 8 m PZ and 12% higher than 7 m MEA.

The absorption rate of 5 m MDEA/5 m PZ has no temperature dependence between 10 to 40 ˚C. The measured CO_2 solubility at low temperatures agrees well with previous high temperature data.

Future Work

Solvent screening using the WWC will continue during the next quarter. A new di-amino acid solvent will be tested as part of the amino acid screening work. Additional PZ-based blends will be tested for application objectives. New amines and blends will be tested to expand

understanding of the relationship between amine structure and solvent absorption rate. The FTIR will be set up as the analyzer for the WWC in order to perform NO_2 absorption rate measurements. Writing will begin for Ph.D. proposal on this work, which will focus on the mass transfer of CO_2 into amino acids, amines, and amine blends.

References

Chen X, Closmann F, Rochelle GT. "Accurate screening of amines by the wetted wall column." *Energy Proc*. 2011a;4:101–108.

Chen X. *Carbon dioxide thermodynamics, kinetics, and mass transfer in aqueous piperazine derivatives and other amines*. The University of Texas at Austin. Ph.D. Dissertation. 2011b.

Dugas RE. *Carbon dioxide absorption, desorption, and diffusion in aqueous piperazine and monoethanolamine*. The University of Texas at Austin. Ph.D. Dissertation. 2009.

Freeman SA. *Thermal degradation and oxidation of aqueous piperazine for carbon dioxide capture*. The University of Texas at Austin. Ph.D. Dissertation. 2011.

Oyenekan BA, Rochelle GT. "Energy Performance of Stripper Configurations for CO_2 Capture by Aqueous Amines." *Ind Eng Chem Res*. 2006;45(8):2457-2464.

Rochelle GT et al. "CO_2 Capture by Aqueous Absorption, First Quarterly Progress Report 2011." Luminant Carbon Management Program. The University of Texas at Austin. 2011a.

Rochelle GT et al. "CO_2 Capture by Aqueous Absorption, Fourth Quarterly Progress Report 2010." Luminant Carbon Management Program. The University of Texas at Austin. 2011b.

Appendix

Table A-1: Detailed WWC data for 6 m PZ/2 m Y

PZ/Y		CO_2 ldg	P^*_{CO2}	T	P	Gas_{Dry}	Gas	$P_{CO2in, dry}$	$P_{CO2in, wet}$	$P_{CO2out, dry}$	$P_{CO2out, wet}$	CO_2 flux	K_G	k_g	K_G/k_g	k_g'
m		mol CO_2/mol alk	Pa	C	psig	Std L/min	Std L/min	Pa	Pa	Pa	Pa	mol/s cm2	mol/s Pa cm^2	mol/s Pa cm^2		mol/s Pa cm^2
6	2	0.301	114	40	20	5	5.16	0.00	0.00	41.86	40.57	-1.69E-08	1.81E-10	4.57E-10	0.40	3.00E-10
								28.70	27.82	58.60	56.79	-1.21E-08				
								46.64	45.20	73.19	70.93	-1.07E-08				
								154.27	149.51	138.49	134.21	6.37E-09				
								177.47	172.00	156.90	152.06	8.30E-09				
								193.02	187.06	167.67	162.49	1.02E-08				
6	2	0.301	924	60	20	5	5.45	0.00	0.00	349.21	320.11	-1.41E-07	1.85E-10	4.83E-10	0.38	2.99E-10
								275.06	252.14	519.03	475.77	-9.85E-08				
								550.12	504.28	703.20	644.60	-6.18E-08				
								1614.48	1479.94	1427.92	1308.92	7.53E-08				
								1860.84	1705.77	1566.64	1436.09	1.19E-07				
								2116.76	1940.36	1724.50	1580.79	1.58E-07				
6	2	0.301	4982	80	40	5	5.72	0.00	0.00	2103.88	1839.54	-5.39E-07	1.40E-10	3.21E-10	0.44	2.48E-10
								1402.59	1226.36	3136.97	2742.82	-4.44E-07				
								2820.25	2465.90	3872.19	3385.67	-2.69E-07				
								8528.63	7457.05	7510.62	6566.95	2.61E-07				
								9810.56	8577.92	8189.29	7160.35	4.15E-07				
								11356.42	9929.55	9207.30	8050.45	5.50E-07				
6	2	0.351	718	40	20	5	5.16	0.00	0.00	205.49	201.46	-5.26E-08	8.61E-11	2.87E-10	0.30	1.23E-10
								145.91	143.06	321.61	315.32	-4.50E-08				
								412.48	404.41	495.81	486.10	-2.13E-08				
								779.72	764.45	754.83	740.06	6.37E-09				
								923.75	905.66	864.93	848.00	1.51E-08				
								1082.10	1060.92	993.50	974.05	2.27E-08				
								1266.10	1241.31	1119.81	1097.89	3.75E-08				
6	2	0.351	6148	60	40	5	5.28	0.00	0.00	1696.68	1606.98	-4.34E-07	7.13E-11	2.98E-10	0.24	9.37E-11
								1440.29	1364.15	2699.60	2556.89	-3.22E-07				
								2933.37	2778.29	3687.44	3492.51	-1.93E-07				
								8965.99	8492.01	8211.92	7777.80	1.93E-07				
								11831.49	11206.03	10398.74	9849.02	3.67E-07				
								23632.82	22383.48	19824.73	18776.70	9.75E-07				

Table A-2: Detailed WWC data for 6 m PZ/2 m Y

PZ/Y		CO_2 ldg	P^*_{CO2}	T	P	Gas_{Dry}	Gas	$P_{CO2in, dry}$	$P_{CO2in, wet}$	$P_{CO2out, dry}$	$P_{CO2out, wet}$	CO_2 flux	K_G	k_g	K_G/k_g	k_g'
m		mol CO_2/mol alk	Pa	C	psig	Std L/min	Std L/min	Pa	Pa	Pa	Pa	mol/s cm2	mol/s Pa cm^2	mol/s Pa cm^2		mol/s Pa cm^2
6	2	0.351	26739	80	40	5	5.72	0.00	0.00	5866.73	5129.61	-1.50E-06	5.88E-11	3.21E-10	0.18	7.20E-11
								5776.24	5050.49	10059.41	8795.50	-1.10E-06				
								31437.54	27487.57	30947.38	27059.01	1.25E-07				
								36565.27	31971.04	35358.74	30916.10	3.09E-07				
								41806.12	36553.40	40147.14	35102.87	4.25E-07				
6	2	0.372	242	20	40	5	5.03	0.00	0.00	60.33	59.95	-1.54E-08	7.06E-11	2.82E-10	0.25	9.42E-11
								60.33	59.95	105.19	104.54	-1.15E-08				
								117.64	116.91	144.41	143.51	-6.85E-09				
								227.35	225.95	233.39	231.94	-1.54E-09				
								429.45	426.79	380.06	377.70	1.26E-08				
								627.02	623.13	538.04	534.70	2.28E-08				
								835.14	829.97	627.02	623.13	5.33E-08				
6	2	0.372	1513	40	40	5	5.10	0.00	0.00	429.82	421.41	-1.10E-07	7.67E-11	2.87E-10	0.27	1.05E-10
								395.14	387.40	665.85	652.82	-6.93E-08				
								774.82	759.65	957.68	938.93	-4.68E-08				
								1851.26	1815.02	1734.38	1700.43	2.99E-08				
								2209.45	2166.20	2051.09	2010.94	4.05E-08				
								2556.33	2506.28	2322.56	2277.10	5.99E-08				
6	2	0.372	10734	60	40	5	5.28	0.00	0.00	2262.24	2142.64	-5.79E-07	5.51E-11	2.98E-10	0.18	6.76E-11
								4441.52	4206.72	5610.34	5313.76	-2.99E-07				
								8890.59	8420.59	9305.33	8813.41	-1.06E-07				
								16016.63	15169.92	14998.62	14205.73	2.61E-07				
								20427.99	19348.07	18693.61	17705.38	4.44E-07				
								24763.94	23454.81	22464.00	21276.45	5.89E-07				
6	2	0.372	50322	80	70	5	5.44	0.00	0.00	9475.48	8706.62	-1.57E-06	3.00E-11	1.99E-10	0.15	3.53E-11
								13708.21	12595.89	19546.46	17960.41	-9.65E-07				
								25384.71	23324.93	29179.57	26811.87	-6.27E-07				
								73958.95	67957.74	70397.62	64685.38	5.89E-07				
								86803.10	79759.68	82015.74	75360.78	7.92E-07				
								96669.74	88825.72	90831.49	83461.20	9.65E-07				
6	2	0.398	642	20	40	5	5.03	0.00	0.00	118.01	117.28	-3.02E-08	4.86E-11	2.82E-10	0.17	5.88E-11
								196.81	195.59	265.44	263.79	-1.76E-08				
								368.37	366.08	417.01	414.42	-1.25E-08				
								1123.95	1116.99	1041.38	1034.93	2.11E-08				
								1286.08	1278.11	1177.12	1169.82	2.79E-08				
								1471.21	1462.09	1329.44	1321.20	3.63E-08				

Table A-3: Detailed WWC data for 6 m PZ/2 m Y

PZ/Y		CO_2 ldg	P^*_{CO2}	T	P	Gas_{Dry}	Gas	$P_{CO2in, dry}$	$P_{CO2in, wet}$	$P_{CO2out, dry}$	$P_{CO2out, wet}$	CO_2 flux	K_G	k_g	K_G/k_g	k_g'
m		mol CO_2/mol alk	Pa	C	psig	Std L/min	Std L/min	Pa	Pa	Pa	Pa	mol/s cm2	mol/s Pa cm^2	mol/s Pa cm^2		mol/s Pa cm^2
6	2	0.398	4821	40	40	5	5.10	0.00	0.00	833.26	816.94	-2.13E-07	4.40E-11	2.87E-10	0.15	5.20E-11
								1425.21	1397.31	1953.06	1914.83	-1.35E-07				
								2895.66	2838.98	3121.89	3060.77	-5.79E-08				
								8815.18	8642.61	8211.92	8051.16	1.54E-07				
								10172.52	9973.38	9418.44	9234.06	1.93E-07				
								11756.08	11525.95	10662.67	10453.94	2.80E-07				
6	2	0.398	26787	60	40	5	5.28	0.00	0.00	3713.84	3517.51	-9.51E-07	3.13E-11	2.98E-10	0.11	3.50E-11
								9075.34	8595.57	10847.42	10273.98	-4.54E-07				
								17521.02	16594.78	18312.80	17344.70	-2.03E-07				
								36787.72	34842.96	35618.90	33735.93	2.99E-07				
								45836.67	43413.53	43913.77	41592.29	4.92E-07				
								54093.83	51234.18	51605.37	48877.27	6.37E-07				
6	2	0.425	2364	20	40	5	5.03	0.00	0.00	320.48	318.50	-8.21E-08	3.41E-11	2.82E-10	0.12	3.88E-11
								565.56	562.05	784.24	779.38	-5.60E-08				
								1108.50	1101.62	1240.46	1232.77	-3.38E-08				
								3268.93	3248.67	3152.05	3132.51	2.99E-08				
								3826.95	3803.23	3653.51	3630.87	4.44E-08				
								4377.43	4350.29	4136.12	4110.48	6.18E-08				
6	2	0.425	15774	40	40	5	5.10	0.00	0.00	1504.39	1474.94	-3.85E-07	2.23E-11	2.87E-10	0.08	2.42E-11
								4520.70	4432.20	5414.28	5308.29	-2.29E-07				
								9045.17	8868.10	9459.92	9274.73	-1.06E-07				
								25031.64	24541.61	24239.86	23765.33	2.03E-07				
								29405.29	28829.65	28274.18	27720.67	2.90E-07				
								33778.95	33117.69	32459.31	31823.88	3.38E-07				

Table B-1: Detailed WWC data for 6 m PZ/2 m Z

PZ/Z		CO_2 ldg	P^*_{CO2}	T	P	Gas_{Dry}	Gas	$P_{CO2in,\ dry}$	$P_{CO2in,\ wet}$	$P_{CO2out,\ dry}$	$P_{CO2out,\ wet}$	CO_2 flux	K_G	k_g	K_G/k_g	k_g'
m		mol CO_2/mol alk	Pa	C	psig	Std L/min	Std L/min	Pa	Pa	Pa	Pa	mol/s cm2	mol/s Pa cm^2	mol/s Pa cm^2		mol/s Pa cm^2
6	2	0.305	262	40	20	5	5.16	0	0	86	83	-3.47E-08	1.55E-10	4.57E-10	0.34	2.34E-10
								62	61	126	122	-2.58E-08				
								120	117	166	160	-1.82E-08				
								439	425	384	373	2.20E-08				
								491	475	423	410	2.71E-08				
								547	531	463	449	3.42E-08				
6	2	0.305	1958	60	20	5	5.45	0	0	492	451	-1.99E-07	1.32E-10	4.83E-10	0.27	1.82E-10
								567	520	1028	943	-1.86E-07				
								1112	1020	1409	1291	-1.20E-07				
								2973	2725	2786	2554	7.53E-08				
								3322	3045	2930	2686	1.58E-07				
								3887	3563	3463	3175	1.71E-07				
6	2	0.305	9523	80	40	5	5.72	0	0	3137	2743	-8.03E-07	1.02E-10	3.21E-10	0.32	1.50E-10
								3039	2657	5591	4889	-6.54E-07				
								6116	5347	7239	6330	-2.88E-07				
								17702	15478	15779	13797	4.92E-07				
								20756	18148	18305	16005	6.27E-07				
								23923	20917	19663	17192	1.09E-06				
6	2	0.305	36717	100	40	5	6.84	0	0	11292	8258	-2.89E-06	8.80E-11	3.76E-10	0.23	1.15E-10
								6881	5032	17023	12449	-2.60E-06				
								12914	9443	20492	14985	-1.94E-06				
								64568	47217	61401	44901	8.11E-07				
								76709	56095	70865	51821	1.50E-06				
6	2	0.333	72	20	20	5	5.05	0	0	21	21	-8.59E-09	1.24E-10	4.46E-10	0.28	1.72E-10
								15	14	29	29	-5.99E-09				
								25	25	36	36	-4.44E-09				
								194	192	162	160	1.28E-08				
								227	225	188	186	1.59E-08				
								182	181	153	151	1.20E-08				

Table B-2: Detailed WWC data for 6 m PZ/2 m Z

PZ/Z		CO_2 ldg	P^*_{CO2}	T	P	Gas_{Dry}	Gas	$P_{CO2in,\ dry}$	$P_{CO2in,\ wet}$	$P_{CO2out,\ dry}$	$P_{CO2out,\ wet}$	CO_2 flux	K_G	k_g	K_G/k_g	k_g'
m		mol CO_2/mol alk	Pa	C	psig	Std L/min	Std L/min	Pa	Pa	Pa	Pa	mol/s cm2	mol/s Pa cm^2	mol/s Pa cm^2		mol/s Pa cm^2
6	2	0.333	509	40	20	5	5.16	0	0	136	132	-5.48E-08	1.20E-10	4.57E-10	0.26	1.62E-10
								106	102	204	198	-3.98E-08				
								206	199	287	279	-3.30E-08				
								975	945	864	837	4.49E-08				
								1061	1028	923	894	5.58E-08				
								1155	1120	1001	970	6.25E-08				
6	2	0.333	3355	60	40	5	5.28	0	0	1191	1128	-3.05E-07	1.08E-10	2.98E-10	0.36	1.70E-10
								577	546	1576	1493	-2.56E-07				
								1127	1068	1908	1807	-2.00E-07				
								4457	4221	4023	3810	1.11E-07				
								5007	4742	4562	4321	1.14E-07				
								5569	5274	4969	4707	1.53E-07				
6	2	0.333	16170	80	40	5	5.72	0	0	4400	3847	-1.13E-06	7.56E-11	3.21E-10	0.24	9.89E-11
								4313	3771	7480	6541	-8.11E-07				
								7971	6969	10157	8881	-5.60E-07				
								30216	26419	27577	24112	6.76E-07				
								33911	29650	30631	26782	8.40E-07				
								37417	32716	32931	28793	1.15E-06				
6	2	0.362	128	20	20	5	5.05	0	0	29	29	-1.17E-08	1.03E-10	4.46E-10	0.23	1.34E-10
								26	25	47	46	-8.59E-09				
								50	49	70	69	-8.11E-09				
								183	181	169	167	5.60E-09				
								206	204	192	190	5.79E-09				
								227	225	204	202	9.36E-09				
6	2	0.362	1196	40	20	5	5.16	0	0	257	249	-1.04E-07	8.92E-11	4.57E-10	0.20	1.11E-10
								260	252	432	419	-6.93E-08				
								506	491	644	624	-5.55E-08				
								1923	1863	1781	1726	5.70E-08				
								2531	2452	2289	2218	9.75E-08				
								2655	2573	2528	2450	5.12E-08				

Table B-3: Detailed WWC data for 6 m PZ/2 m Z

PZ/Z		CO_2 ldg	P^*_{CO2}	T	P	Gas_{Dry}	Gas	$P_{CO2in, dry}$	$P_{CO2in, wet}$	$P_{CO2out, dry}$	$P_{CO2out, wet}$	CO_2 flux	K_G	k_g	K_G/k_g	k_g'
m		mol CO_2/mol alk	Pa	C	psig	Std L/min	Std L/min	Pa	Pa	Pa	Pa	mol/s cm2	mol/s Pa cm^2	mol/s Pa cm^2		mol/s Pa cm^2
6	2	0.362	8729	60	40	5	5.28	0	0	2176	2061	-5.57E-07	6.83E-11	2.98E-10	0.23	8.86E-11
								1497	1418	3163	2996	-4.27E-07				
								3062	2900	4374	4142	-3.36E-07				
								15240	14434	13732	13006	3.86E-07				
								16635	15756	15127	14327	3.86E-07				
								18068	17113	16107	15256	5.02E-07				
6	2	0.362	37920	80	40	5	5.72	0	0	6523	5703	-1.67E-06	4.45E-11	3.21E-10	0.14	5.16E-11
								25793	22552	27754	24267	-5.02E-07				
								50301	43981	48906	42761	3.57E-07				
								64741	56607	62253	54431	6.37E-07				
6	2	0.392	385	20	20	5	5.05	0	0	58	58	-2.36E-08	6.63E-11	4.46E-10	0.15	7.79E-11
								108	107	149	148	-1.68E-08				
								202	200	232	229	-1.21E-08				
								683	676	636	630	1.88E-08				
								780	772	720	713	2.39E-08				
								874	866	804	796	2.85E-08				
6	2	0.392	3519	40	20	5	5.16	0	0	505	489	-2.04E-07	5.99E-11	4.57E-10	0.13	6.89E-11
								749	726	1179	1143	-1.74E-07				
								1461	1416	1720	1667	-1.04E-07				
								3030	2937	3052	2958	-8.69E-09				
								6747	6539	6365	6168	1.54E-07				
								7513	7281	6987	6771	2.12E-07				
								8182	7930	7704	7466	1.93E-07				
6	2	0.392	21838	60	40	5	5.28	0	0	3133	2968	-8.02E-07	3.35E-11	2.98E-10	0.11	3.77E-11
								6715	6360	8487	8038	-4.54E-07				
								12748	12074	13539	12824	-2.03E-07				
								37293	35321	35408	33536	4.83E-07				
								43929	41607	41780	39571	5.50E-07				
								49924	47285	46832	44356	7.92E-07				

Table B-4: Detailed WWC data for 6 m PZ/2 m Z

PZ/Z		CO_2 ldg	P^*_{CO2}	T	P	Gas_{Dry}	Gas	$P_{CO2in,\ dry}$	$P_{CO2in,\ wet}$	$P_{CO2out,\ dry}$	$P_{CO2out,\ wet}$	CO_2 flux	K_G	k_g	K_G/k_g	k_g'
m		mol CO_2/mol alk	Pa	C	psig	Std L/min	Std L/min	Pa	Pa	Pa	Pa	mol/s cm2	mol/s Pa cm^2	mol/s Pa cm^2		mol/s Pa cm^2
6	2	0.420	1527	20	20	5	5.05	0	0	148	147	-5.98E-08	3.79E-11	4.46E-10	0.08	4.14E-11
								205	203	317	314	-4.52E-08				
								399	395	493	489	-3.81E-08				
								2001	1982	1963	1944	1.54E-08				
								2131	2110	2083	2062	1.93E-08				
								2300	2278	2229	2207	2.90E-08				
6	2	0.420	15745	60	40	5	5.28	0	0	926	897	-3.74E-07	2.20E-11	4.57E-10	0.05	2.31E-11
								2830	2742	3461	3354	-2.55E-07				
								5174	5014	5700	5524	-2.12E-07				
								24954	24184	24499	23743	1.83E-07				
								27537	26687	26939	26108	2.41E-07				
								29953	29028	29283	28379	2.70E-07				

Table C-1: Detailed WWC data for 5 m PZ/2 m W

PZ/W		CO_2 ldg	P^*_{CO2}	T	P	Gas_{Dry}	Gas	$P_{CO2in,\ dry}$	$P_{CO2in,\ wet}$	$P_{CO2out,\ dry}$	$P_{CO2out,\ wet}$	CO_2 flux	K_G	k_g	K_G/k_g	k_g'
m		mol CO_2/mol alk	Pa	C	psig	Std L/min	Std L/min	Pa	Pa	Pa	Pa	mol/s cm2	mol/s Pa cm^2	mol/s Pa cm^2		mol/s Pa cm^2
5	2	0.251	160	40	20	5	5.16	0.0	0.0	65.3	63.3	-2.64E-08	1.91E-10	4.57E-10	0.417	3.27E-10
								59.8	58.0	91.4	88.5	-1.27E-08				
								116.2	112.7	135.6	131.4	-7.82E-09				
								223.2	216.3	199.5	193.3	9.56E-09				
								325.0	315.0	271.5	263.1	2.16E-08				
								426.7	413.5	327.9	317.8	3.99E-08				
5	2	0.251	907	60	20	5	5.45	0.0	0.0	316.9	290.5	-1.28E-07	1.79E-10	4.83E-10	0.371	2.85E-10
								104.0	95.4	425.0	389.6	-1.30E-07				
								201.2	184.4	456.6	418.5	-1.03E-07				
								1226.0	1123.9	1132.8	1038.4	3.76E-08				
								1302.6	1194.0	1202.1	1102.0	4.05E-08				
								1398.3	1281.7	1269.1	1163.3	5.21E-08				
5	2	0.251	4505	80	40	5	5.72	0.0	0.0	2077.5	1816.5	-5.32E-07	1.54E-10	3.21E-10	0.478	2.94E-10
								1417.7	1239.5	2967.3	2594.5	-3.97E-07				
								2899.4	2535.1	3804.3	3326.3	-2.32E-07				
								7359.8	6435.1	6507.7	5690.0	2.18E-07				
								8830.3	7720.8	7322.1	6402.1	3.86E-07				
								10263.0	8973.5	8151.6	7127.4	5.41E-07				
5	2	0.251	19649	100	40	5	6.84	0.0	0.0	6884.7	5034.6	-1.76E-06	1.09E-10	3.76E-10	0.290	1.54E-10
								5942.1	4345.3	11544.9	8442.5	-1.43E-06				
								11846.6	8663.1	16031.7	11723.6	-1.07E-06				
								37259.0	27246.6	35373.8	25868.0	4.83E-07				
								38314.7	28018.6	34959.1	25564.7	8.59E-07				
								44762.1	32733.4	40539.3	29645.3	1.08E-06				
								49814.4	36428.0	42650.7	31189.4	1.83E-06				
5	2	0.288	54	20	20	5	5.05	0.0	0.0	17.9	17.8	-7.24E-09	1.46E-10	4.46E-10	0.328	2.17E-10
								11.5	11.4	23.4	23.2	-4.83E-09				
								24.9	24.6	33.5	33.2	-3.48E-09				
								92.8	91.9	81.6	80.8	4.54E-09				
								114.8	113.7	96.6	95.7	7.34E-09				
								116.0	114.9	97.8	96.9	7.34E-09				

Table C-2: Detailed WWC data for 5 m PZ/2 m W

PZ/W		CO_2 ldg	P^*_{CO2}	T	P	Gas_{Dry}	Gas	$P_{CO2in,\ dry}$	$P_{CO2in,\ wet}$	$P_{CO2out,\ dry}$	$P_{CO2out,\ wet}$	CO_2 flux	K_G	k_g	K_G/k_g	k_g'
m		mol CO_2/mol alk	Pa	C	psig	Std L/min	Std L/min	Pa	Pa	Pa	Pa	mol/s cm2	mol/s Pa cm^2	mol/s Pa cm^2		mol/s Pa cm^2
5	2	0.288	365	40	20	5	5.16	0.0	0.0	110.7	107.3	-4.47E-08	1.42E-10	4.57E-10	0.310	2.06E-10
								79.9	77.4	165.5	160.4	-3.46E-08				
								152.8	148.1	216.0	209.3	-2.55E-08				
								534.6	518.1	479.8	465.0	2.21E-08				
								605.8	587.2	547.2	530.4	2.37E-08				
								669.2	648.6	585.0	567.0	3.40E-08				
5	2	0.288	2201	60	40	5	5.28	0.0	0.0	833.3	789.2	-2.13E-07	1.21E-10	2.98E-10	0.404	2.02E-10
								573.1	542.8	1180.1	1117.7	-1.55E-07				
								1116.0	1057.0	1576.0	1492.7	-1.18E-07				
								3310.4	3135.4	2967.3	2810.4	8.78E-08				
								3845.8	3642.5	3299.1	3124.7	1.40E-07				
								4392.5	4160.3	3634.7	3442.5	1.94E-07				
5	2	0.288	10201	80	60	5	5.51	0.0	0.0	4093.4	3716.8	-7.67E-07	9.49E-11	2.28E-10	0.417	1.63E-10
								2811.3	2552.7	5890.4	5348.5	-5.77E-07				
								6065.5	5507.4	7991.2	7256.0	-3.61E-07				
								17727.9	16096.8	15513.8	14086.5	4.15E-07				
								20611.3	18715.0	17213.0	15629.3	6.37E-07				
								24009.6	21800.6	19118.1	17359.1	9.17E-07				
5	2	0.288	42428	100	50	5	6.47	13610.9	10518.7	22128.9	17101.4	-1.84E-06	6.44E-11	3.03E-10	0.212	8.17E-11
								25250.7	19514.0	31003.7	23959.9	-1.25E-06				
								37113.4	28681.6	41038.0	31714.5	-8.50E-07				
								62355.2	48188.7	61017.3	47154.7	2.90E-07				
								82290.0	63594.4	76492.4	59114.0	1.25E-06				
5	2	0.328	165	20	20	5	5.05	0.0	0.0	37.6	37.2	-1.52E-08	1.02E-10	4.46E-10	0.228	1.32E-10
								60.8	60.2	83.5	82.7	-9.17E-09				
								118.6	117.5	128.9	127.7	-4.15E-09				
								226.5	224.3	212.6	210.6	5.60E-09				
								279.6	276.9	255.2	252.7	9.85E-09				
								333.2	329.9	296.6	293.7	1.48E-08				
5	2	0.328	1109	40	40	5	5.10	0.0	0.0	330.7	324.2	-8.47E-08	8.89E-11	2.87E-10	0.309	1.29E-10
								262.8	257.7	517.7	507.5	-6.53E-08				
								499.6	489.8	679.4	666.1	-4.60E-08				
								1462.9	1434.3	1348.7	1322.3	2.93E-08				
								1917.2	1879.7	1687.3	1654.2	5.89E-08				
								2151.0	2108.9	1872.0	1835.4	7.14E-08				

Table C-3: Detailed WWC data for 5 m PZ/2 m W

PZ/W		CO_2 ldg	P^*_{CO2}	T	P	Gas_{Dry}	Gas	$P_{CO2in,\ dry}$	$P_{CO2in,\ wet}$	$P_{CO2out,\ dry}$	$P_{CO2out,\ wet}$	CO_2 flux	K_G	k_g	K_G/k_g	k_g'
m		mol CO_2/mol alk	Pa	C	psig	Std L/min	Std L/min	Pa	Pa	Pa	Pa	mol/s cm2	mol/s Pa cm^2	mol/s Pa cm^2		mol/s Pa cm^2
5	2	0.328	7075	60	40	5	5.28	0.0	0.0	1855.0	1757.0	-4.75E-07	8.00E-11	2.98E-10	0.268	1.09E-10
								1489.3	1410.6	3072.9	2910.4	-4.05E-07				
								3008.8	2849.7	4166.3	3946.0	-2.96E-07				
								12792.9	12116.7	11360.2	10759.6	3.67E-07				
								13810.9	13080.8	12302.8	11652.4	3.86E-07				
								15055.2	14259.3	13056.9	12366.6	5.12E-07				
5	2	0.328	28989	80	40	5	5.72	0.0	0.0	6213.6	5432.9	-1.59E-06	6.23E-11	3.21E-10	0.194	7.73E-11
								6854.6	5993.3	12227.4	10691.1	-1.38E-06				
								12981.5	11350.4	16450.2	14383.3	-8.88E-07				
								51100.1	44679.7	48310.0	42240.1	7.14E-07				
								57321.3	50119.2	53098.4	46426.9	1.08E-06				
								64522.7	56415.8	57660.6	50415.9	1.76E-06				
5	2	0.360	505	20	20	5	5.05	0.0	0.0	75.1	74.4	-3.03E-08	6.33E-11	4.46E-10	0.142	7.38E-11
								105.0	104.0	163.8	162.2	-2.37E-08				
								197.6	195.6	241.1	238.7	-1.76E-08				
								758.7	751.3	716.4	709.4	1.71E-08				
								852.9	844.6	806.8	798.9	1.86E-08				
								940.0	930.8	880.9	872.3	2.38E-08				
5	2	0.360	3763	40	40	5	5.10	0.0	0.0	761.6	746.7	-1.95E-07	5.53E-11	2.87E-10	0.192	6.84E-11
								576.9	565.6	1183.9	1160.7	-1.55E-07				
								1104.7	1083.1	1617.5	1585.8	-1.31E-07				
								4358.6	4273.2	4219.1	4136.5	3.57E-08				
								5436.9	5330.5	5161.7	5060.6	7.05E-08				
								6549.2	6421.0	6036.4	5918.2	1.31E-07				
5	2	0.360	17534	60	40	5	5.28	0.0	0.0	3514.0	3328.2	-9.00E-07	5.42E-11	2.98E-10	0.182	6.62E-11
								6598.2	6249.4	8604.0	8149.2	-5.14E-07				
								12600.7	11934.5	13467.8	12755.9	-2.22E-07				
								37070.5	35110.8	34129.6	32325.4	7.53E-07				
								49362.0	46752.5	43668.7	41360.2	1.46E-06				
								63086.2	59751.2	54866.8	51966.3	2.10E-06				

Table C-4: Detailed WWC data for 5 m PZ/2 m W

PZ/W		CO_2 ldg	P^*_{CO2}	T	P	Gas_{Dry}	Gas	$P_{CO2in,\ dry}$	$P_{CO2in,\ wet}$	$P_{CO2out,\ dry}$	$P_{CO2out,\ wet}$	CO_2 flux	K_G	k_g	K_G/k_g	k_g'
m		mol CO_2/mol alk	Pa	C	psig	Std L/min	Std L/min	Pa	Pa	Pa	Pa	mol/s cm2	mol/s Pa cm^2	mol/s Pa cm^2		mol/s Pa cm^2
5	2	0.386	1854	20	20	5	5.05	0.0	0.0	177.0	175.3	-7.14E-08	3.97E-11	4.46E-10	0.089	4.35E-11
								741.5	734.2	841.9	833.7	-4.05E-08				
								1026.1	1016.1	1102.6	1091.9	-3.09E-08				
								2980.2	2951.1	2875.0	2846.9	4.25E-08				
								4436.8	4393.5	4212.0	4170.8	9.07E-08				
								5915.0	5857.2	5532.3	5478.2	1.54E-07				
5	2	0.386	10083	40	40	5	5.10	0.0	0.0	1285.7	1260.5	-3.29E-07	3.52E-11	2.87E-10	0.123	4.01E-11
								2816.5	2761.3	3774.2	3700.3	-2.45E-07				
								5964.8	5848.0	6421.0	6295.3	-1.17E-07				
								20484.5	20083.5	19391.1	19011.5	2.80E-07				
								23274.6	22819.0	21691.1	21266.4	4.05E-07				
								29307.3	28733.5	26743.4	26219.9	6.56E-07				
5	2	0.386	44806	60	40	5	5.10	0.0	0.0	4505.6	4267.4	-1.15E-06	2.33E-11	2.98E-10	0.078	2.53E-11
								12902.3	12220.2	15466.2	14648.5	-6.56E-07				
								25042.9	23719.1	26324.9	24933.2	-3.28E-07				
								63387.8	60036.9	62030.5	58751.3	3.48E-07				
								69571.3	65893.4	67987.7	64393.6	4.05E-07				
								74849.8	70892.9	72587.6	68750.3	5.79E-07				

Table D-1: Detailed WWC data for 5 m PZ/2.3 m AMP

PZ/AMP		CO_2 ldg	P^*_{CO2}	T	P	Gas_{Dry}	Gas	$P_{CO2in,\ dry}$	$P_{CO2in,\ wet}$	$P_{CO2out,\ dry}$	$P_{CO2out,\ wet}$	CO_2 flux	K_G	k_g	K_G/k_g	k_g'
m		mol CO_2/mol alk	Pa	C	psig	Std L/min	Std L/min	Pa	Pa	Pa	Pa	mol/s cm2	mol/s Pa cm^2	mol/s Pa cm^2		mol/s Pa cm^2
5	2.3	0.31	325	40	20	5	5.16	0.00	0.00	93.04	90.17	-3.76E-08	1.34E-10	4.57E-10	0.292	1.89E-10
								62.90	60.96	138.01	133.75	-3.03E-08				
								109.31	105.93	170.78	165.51	-2.48E-08				
								475.49	460.82	432.44	419.10	1.74E-08				
								527.40	511.12	477.65	462.91	2.01E-08				
								570.21	552.61	507.07	491.42	2.55E-08				
5	2.3	0.31	2742	60	20	5	5.45	0.00	0.00	755.82	692.83	-3.05E-07	1.27E-10	4.83E-10	0.262	1.71E-10
								557.29	510.85	1131.33	1037.05	-2.32E-07				
								1112.20	1019.51	1604.91	1471.17	-1.99E-07				
								3274.40	3001.53	3233.74	2964.26	1.64E-08				
								3826.91	3508.00	3590.12	3290.94	9.56E-08				
5	2.3	0.31	11146	80	40	5	5.72	0.00	0.00	4098.42	3583.47	-1.05E-06	1.16E-10	3.21E-10	0.361	1.82E-10
								4441.52	3883.47	7065.72	6177.95	-6.72E-07				
								8019.63	7012.00	9490.08	8297.70	-3.76E-07				
								12732.62	11132.83	12921.14	11297.66	-4.83E-08				
								23704.46	20726.12	20575.03	17989.89	8.01E-07				
								27474.85	24022.78	22837.27	19967.89	1.19E-06				
								31132.13	27220.55	24571.65	21484.35	1.68E-06				
5	2.3	0.31	59912	100	60	5	6.22	0.00	0.00	16250.13	13052.47	-3.05E-06	5.23E-11	2.54E-10	0.206	6.59E-11
								25981.67	20869.07	33859.59	27196.79	-1.48E-06				
								50233.30	40348.52	55330.77	44442.92	-9.56E-07				
								89005.00	71490.82	86533.49	69505.65	4.63E-07				
								95492.69	76701.88	91270.54	73310.56	7.92E-07				
								102598.26	82409.24	92403.31	74220.43	1.91E-06				
5	2.3	0.35	93	20	20	5	5.05	0.00	0.00	21.29	21.08	-8.59E-09	1.00E-10	4.46E-10	0.224	1.29E-10
								22.00	21.79	37.55	37.18	-6.27E-09				
								34.44	34.11	47.84	47.37	-5.41E-09				
								59.56	58.97	65.78	65.13	-2.51E-09				
								141.84	140.45	130.83	129.55	4.44E-09				
								191.11	189.24	170.78	169.11	8.21E-09				

Table D-2: Detailed WWC data for 5 m PZ/2.3 m AMP

PZ/AMP		CO_2 ldg	P^*_{CO2}	T	P	Gas_{Dry}	Gas	$P_{CO2in,\ dry}$	$P_{CO2in,\ wet}$	$P_{CO2out,\ dry}$	$P_{CO2out,\ wet}$	CO_2 flux	K_G	k_g	K_G/k_g	k_g'
m		mol CO_2/mol alk	Pa	C	psig	Std L/min	Std L/min	Pa	Pa	Pa	Pa	mol/s cm2	mol/s Pa cm^2	mol/s Pa cm^2		mol/s Pa cm^2
5	2.3	0.35	844	40	20	5	5.16	0.00	0.00	186.32	180.57	-7.52E-08	9.85E-11	4.57E-10	0.215	1.26E-10
								202.59	196.34	324.81	314.79	-4.93E-08				
								385.80	373.90	486.50	471.48	-4.06E-08				
								758.21	734.81	793.61	769.12	-1.43E-08				
								1124.63	1089.93	1098.32	1064.43	1.06E-08				
								1486.04	1440.18	1344.92	1303.42	5.70E-08				
								1832.85	1776.29	1619.98	1569.99	8.59E-08				
5	2.3	0.35	5979	60	40	5	5.28	0.00	0.00	1760.77	1667.69	-4.51E-07	9.06E-11	2.98E-10	0.304	1.30E-10
								1474.22	1396.29	2846.65	2696.16	-3.51E-07				
								2933.37	2778.29	3940.06	3731.77	-2.58E-07				
								9033.86	8556.29	8317.49	7877.79	1.83E-07				
								10391.20	9841.88	9184.68	8699.13	3.09E-07				
								11823.95	11198.88	10240.39	9699.03	4.05E-07				
5	2.3	0.35	27778	80	40	5	5.72	0.00	0.00	8095.03	7077.94	-2.07E-06	7.70E-11	3.21E-10	0.240	1.01E-10
								6786.71	5933.99	11903.13	10407.56	-1.31E-06				
								12732.62	11132.83	17143.98	14989.93	-1.13E-06				
								37466.39	32758.94	36222.16	31671.04	3.19E-07				
								49870.99	43604.96	44818.66	39187.43	1.29E-06				
								63142.77	55209.21	56582.29	49473.02	1.68E-06				
5	2.3	0.38	229	20	20	5	5.05	0.00	0.00	43.05	42.63	-1.74E-08	7.85E-11	4.46E-10	0.176	9.53E-11
								59.56	58.97	88.26	87.40	-1.16E-08				
								116.00	114.87	134.90	133.58	-7.63E-09				
								328.40	325.19	308.78	305.77	7.92E-09				
								378.63	374.93	354.23	350.77	9.85E-09				
								429.09	424.90	395.61	391.74	1.35E-08				
5	2.3	0.38	2204	40	20	5	5.16	0.00	0.00	406.61	394.06	-1.64E-07	8.23E-11	4.57E-10	0.180	1.00E-10
								727.11	704.68	1002.17	971.25	-1.11E-07				
								1449.44	1404.71	1583.39	1534.52	-5.41E-08				
								3011.30	2918.38	2906.06	2816.38	4.25E-08				
								3736.03	3620.73	3501.63	3393.57	9.46E-08				
								4470.31	4332.36	4039.79	3915.12	1.74E-07				
5	2.3	0.38	11464	60	40	5	5.28	0.00	0.00	2752.39	2606.88	-7.05E-07	7.01E-11	2.98E-10	0.235	9.16E-11
								2925.82	2771.15	4905.28	4645.97	-5.07E-07				
								6021.32	5703.00	7491.77	7095.72	-3.76E-07				
								17634.13	16701.91	16616.12	15737.72	2.61E-07				
								20537.33	19451.63	18576.73	17594.68	5.02E-07				
								23440.53	22201.36	20688.15	19594.48	7.05E-07				

Table D-3: Detailed WWC data for 5 m PZ/2.3 m AMP

PZ/AMP		CO_2 ldg	P^*_{CO2}	T	P	Gas_{Dry}	Gas	$P_{CO2in,\ dry}$	$P_{CO2in,\ wet}$	$P_{CO2out,\ dry}$	$P_{CO2out,\ wet}$	CO_2 flux	K_G	k_g	K_G/k_g	k_g'
m		mol CO_2/mol alk	Pa	C	psig	Std L/min	Std L/min	Pa	Pa	Pa	Pa	mol/s cm2	mol/s Pa cm^2	mol/s Pa cm^2		mol/s Pa cm^2
5	2.3	0.38	49169	80	50	5	5.59	0.00	0.00	11265.15	10068.51	-2.44E-06	4.69E-11	2.67E-10	0.176	5.69E-11
								12915.23	11543.31	19337.17	17283.07	-1.39E-06				
								25268.54	22584.38	29282.25	26171.74	-8.69E-07				
								75796.70	67745.18	72987.10	65234.03	6.08E-07				
								82129.44	73405.23	78338.71	70017.17	8.21E-07				
								88997.35	79543.59	81817.26	73126.21	1.55E-06				
5	2.3	0.42	676	20	20	5	5.05	0.00	0.00	75.58	74.84	-3.05E-08	4.65E-11	4.46E-10	0.104	5.19E-11
								107.39	106.34	168.62	166.98	-2.47E-08				
								200.20	198.24	250.90	248.45	-2.05E-08				
								960.08	950.70	929.94	920.85	1.22E-08				
								1136.35	1125.25	1086.84	1076.22	2.00E-08				
								1314.55	1301.70	1247.57	1235.38	2.70E-08				
5	2.3	0.42	5325	40	20	5	5.16	0.00	0.00	662.53	642.09	-2.67E-07	5.01E-11	4.57E-10	0.109	5.62E-11
								734.29	711.63	1260.49	1221.59	-2.12E-07				
								1475.75	1430.21	1896.71	1838.18	-1.70E-07				
								8911.93	8636.91	8529.24	8266.03	1.54E-07				
								9581.64	9285.95	9127.19	8845.53	1.83E-07				
								10299.18	9981.36	9749.06	9448.21	2.22E-07				
5	2.3	0.42	26451	60	40	5	5.28	0.00	0.00	3989.08	3778.20	-1.02E-06	3.96E-11	2.98E-10	0.133	4.56E-11
								6809.33	6449.36	9448.60	8949.11	-6.76E-07				
								12841.96	12163.07	14727.15	13948.61	-4.83E-07				
								24982.62	23661.93	25397.37	24054.75	-1.06E-07				
								43570.66	41267.32	41836.28	39624.62	4.44E-07				
								50168.85	47516.70	47303.35	44802.68	7.34E-07				
								62988.18	59658.34	57860.45	54801.68	1.31E-06				
5	2.3	0.45	2963	20	20	5	5.05	0.00	0.00	196.13	194.21	-7.92E-08	2.48E-11	4.46E-10	0.056	2.62E-11
								751.03	743.69	875.41	866.85	-5.02E-08				
								1112.20	1101.33	1219.83	1207.91	-4.34E-08				
								2190.91	2169.50	2222.00	2200.29	-1.25E-08				
								5895.84	5838.23	5728.41	5672.44	6.76E-08				
								6709.06	6643.51	6493.80	6430.35	8.69E-08				
								7450.52	7377.73	7187.42	7117.20	1.06E-07				

Table D-4: Detailed WWC data for 5 m PZ/2.3 m AMP

PZ/AMP		CO_2 ldg	P^*_{CO2}	T	P	Gas_{Dry}	Gas	$P_{CO2in,\ dry}$	$P_{CO2in,\ wet}$	$P_{CO2out,\ dry}$	$P_{CO2out,\ wet}$	CO_2 flux	K_G	k_g	K_G/k_g	k_g'
m		mol CO_2/mol alk	Pa	C	psig	Std L/min	Std L/min	Pa	Pa	Pa	Pa	mol/s cm2	mol/s Pa cm^2	mol/s Pa cm^2		mol/s Pa cm^2
5	2.3	0.45	17617	40	40	5	5.10	0.00	0.00	1564.71	1534.08	-4.01E-07	2.18E-11	2.87E-10	0.076	2.36E-11
								6692.45	6561.43	7484.23	7337.72	-2.03E-07				
								10085.80	9888.36	10651.36	10442.85	-1.45E-07				
								24828.04	24342.00	24337.89	23861.44	1.25E-07				
								30898.37	30293.50	29842.66	29258.45	2.70E-07				
								37421.15	36688.58	35875.29	35172.99	3.96E-07				

Table E-1: Detailed WWC data for 2011 8 m PZ pilot plant campaign sample

Alkalinity	[CO2]	CO_2 ldg	P^*_{CO2}	T	P	Gas_{Dry}	Gas	$P_{CO2in,\ dry}$	$P_{CO2in,\ wet}$	$P_{CO2out,\ dry}$	$P_{CO2out,\ wet}$	CO_2 flux	K_G	k_g	K_G/k_g	k_g'
mol alk/kg	mol/kg	mol CO_2/mol alk	Pa	C	psig	Std L/min	Std L/min	Pa	Pa	Pa	Pa	mol/s cm^2	mol/s Pa cm^2	mol/s Pa cm^2		mol/s Pa cm^2
0.351	0.104	0.291	244	40	40	5	5.10	0.0	0.0	86.3	84.7	-2.21E-08	1.67E-10	2.87E-10	0.581	3.99E-10
								95.8	93.9	170.4	167.1	-1.91E-08				
								184.0	180.4	202.8	198.9	-4.83E-09				
								431.3	422.9	355.2	348.2	1.95E-08				
								523.7	513.5	403.1	395.2	3.09E-08				
								735.2	720.8	494.7	485.0	6.16E-08				
0.351	0.104	0.291	1248	60	40	5	5.28	0.0	0.0	565.2	535.3	-1.45E-07	1.47E-10	2.98E-10	0.493	2.89E-10
								300.9	285.0	712.2	674.6	-1.05E-07				
								576.1	545.7	885.7	838.8	-7.93E-08				
								1853.5	1755.5	1623.5	1537.7	5.89E-08				
								2113.7	2001.9	1793.2	1698.4	8.21E-08				
								2392.7	2266.2	1936.5	1834.1	1.17E-07				
0.351	0.104	0.291	7740	80	40	5	5.72	0.0	0.0	3023.9	2643.9	-7.74E-07	1.24E-10	3.21E-10	0.386	2.02E-10
								2217.0	1938.4	4603.6	4025.2	-6.11E-07				
								4471.7	3909.8	5953.5	5205.4	-3.79E-07				
								10361.0	9059.2	9720.1	8498.8	1.64E-07				
								12510.2	10938.3	11303.6	9883.4	3.09E-07				
								14621.6	12784.5	12661.0	11070.2	5.02E-07				
0.351	0.104	0.291	34204	100	40	5	6.47	0.0	0.0	10560.5	8161.3	-2.29E-06	8.45E-11	3.03E-10	0.278	1.17E-10
								11095.7	8574.8	20817.8	16088.2	-2.10E-06				
								24920.7	19258.9	30138.5	23291.3	-1.13E-06				
								61846.8	47795.8	57075.0	44108.0	1.03E-06				
								74824.5	57825.0	66574.1	51449.0	1.79E-06				
								87757.6	67819.8	76608.4	59203.6	2.41E-06				
0.329	0.111	0.330	756	40	20	5	5.16	0.0	0.0	191.3	185.4	-7.72E-08	1.17E-10	4.57E-10	0.256	1.57E-10
								152.8	148.1	300.9	291.6	-5.98E-08				
								268.6	260.3	400.6	388.3	-5.33E-08				
								941.9	912.8	900.0	872.3	1.69E-08				
								1070.1	1037.1	999.8	968.9	2.84E-08				
								1202.6	1165.5	1100.0	1066.1	4.14E-08				

Table E-2: Detailed WWC data for 2011 8 m PZ pilot plant campaign sample

Alkalinity	[CO2]	CO_2 ldg	P^*_{CO2}	T	P	Gas_{Dry}	Gas	$P_{CO2in,\ dry}$	$P_{CO2in,\ wet}$	$P_{CO2out,\ dry}$	$P_{CO2out,\ wet}$	CO_2 flux	K_G	k_g	K_G/k_g	k_g'
mol alk/kg	mol/kg	mol CO_2/mol alk	Pa	C	psig	Std L/min	Std L/min	Pa	Pa	Pa	Pa	mol/s cm^2	mol/s Pa cm^2	mol/s Pa cm^2		mol/s Pa cm^2
0.329	0.111	0.330	5510	60	20	5	5.45	0.0	0.0	1284.4	1177.4	-5.18E-07	1.09E-10	4.83E-10	0.225	1.41E-10
								1439.9	1319.9	2458.8	2253.9	-4.11E-07				
								2963.5	2716.5	3635.6	3332.6	-2.71E-07				
								7362.0	6748.5	7098.9	6507.3	1.06E-07				
								10208.3	9357.6	9299.4	8524.4	3.67E-07				
								11643.4	10673.1	10375.7	9511.1	5.12E-07				
0.329	0.111	0.330	21352	80	40	5	5.72	0.0	0.0	5421.8	4740.6	-1.39E-06	6.98E-11	3.21E-10	0.217	8.92E-11
								6703.8	5861.5	10398.7	9092.2	-9.46E-07				
								12849.5	11235.0	14998.6	13114.1	-5.50E-07				
								37055.4	32399.6	34529.3	30190.8	6.47E-07				
								42861.8	37476.5	38978.3	34080.9	9.94E-07				
								49573.1	43344.5	44181.5	38630.3	1.38E-06				
0.336	0.136	0.397	5891	40	20	5	5.16	0.0	0.0	653.0	632.8	-2.64E-07	4.44E-11	4.57E-10	0.097	4.91E-11
								2167.0	2100.1	2561.6	2482.6	-1.59E-07				
								4345.9	4211.8	4477.5	4339.3	-5.31E-08				
								8627.3	8361.1	8340.3	8082.9	1.16E-07				
								12813.0	12417.6	12167.2	11791.7	2.61E-07				
0.336	0.136	0.397	37794	60	40	5	5.28	0.0	0.0	4317.1	4088.9	-1.11E-06	2.61E-11	2.98E-10	0.087	2.86E-11
								6737.7	6381.5	9527.8	9024.1	-7.14E-07				
								12544.1	11881.0	14542.4	13773.6	-5.12E-07				
								48928.4	46341.8	48212.0	45663.3	1.83E-07				
								55036.4	52127.0	53415.2	50591.4	4.15E-07				
								61408.4	58162.1	59674.0	56519.4	4.44E-07				

Table F-1: Detailed WWC data for 5 m MDEA/5 m PZ

MDEA/PZ		CO_2 ldg	P^*_{CO2}	T	P	Gas_{Dry}	Gas	$P_{CO2in,\ dry}$	$P_{CO2in,\ wet}$	$P_{CO2out,\ dry}$	$P_{CO2out,\ wet}$	CO_2 flux	K_G	k_g	K_G/k_g	k_g'
m		mol CO_2/mol alk	Pa	C	psig	Std L/min	Std L/min	Pa	Pa	Pa	Pa	mol/s cm^2	mol/s Pa cm^2	mol/s Pa cm^2		mol/s Pa cm^2
5	5	0.202	130	30	20	5	5.09	0.00	0.00	26.55	26.08	-1.07E-08	1.09E-10	4.50E-10	0.24	1.44E-10
								59.80	58.74	80.60	79.18	-8.40E-09				
								110.74	108.78	118.16	116.06	-2.99E-09				
								209.52	205.81	191.11	187.72	7.43E-09				
								259.03	254.44	229.61	225.54	1.19E-08				
								302.09	296.73	260.95	256.32	1.66E-08				
5	5	0.202	326	40	20	5	5.16	0.00	0.00	79.17	76.73	-3.20E-08	1.13E-10	4.57E-10	0.25	1.50E-10
								93.28	90.40	151.88	147.19	-2.37E-08				
								140.16	135.84	189.19	183.35	-1.98E-08				
								377.67	366.01	365.47	354.19	4.92E-09				
								450.38	436.48	422.63	409.59	1.12E-08				
								499.41	484.00	462.10	447.84	1.51E-08				
5	5	0.242	46	10	20	5	5.03	0.00	0.00	14.11	14.04	-5.70E-09	9.68E-11	4.42E-10	0.22	1.24E-10
								13.87	13.80	17.46	17.37	-1.45E-09				
								27.03	26.89	29.66	29.51	-1.06E-09				
								78.69	78.29	71.75	71.39	2.80E-09				
								92.09	91.61	83.95	83.52	3.28E-09				
								104.52	103.99	90.65	90.18	5.60E-09				
5	5	0.242	103	20	20	5	5.05	0.00	0.00	19.37	19.18	-7.82E-09	7.52E-11	4.46E-10	0.17	9.04E-11
								32.05	31.74	43.29	42.87	-4.54E-09				
								59.56	58.97	66.73	66.08	-2.90E-09				
								166.47	164.84	154.51	153.00	4.83E-09				
								217.89	215.77	198.28	196.34	7.92E-09				
								316.92	313.82	282.23	279.48	1.40E-08				
5	5	0.242	288	30	20	5	5.09	0.00	0.00	66.01	64.84	-2.66E-08	1.06E-10	4.50E-10	0.23	1.38E-10
								61.47	60.38	116.96	114.89	-2.24E-08				
								114.81	112.77	152.84	150.13	-1.53E-08				
								315.24	309.65	309.26	303.78	2.41E-09				
								372.65	366.04	356.62	350.30	6.47E-09				
								419.29	411.85	390.11	383.19	1.18E-08				
5	5	0.242	843	40	20	5	5.16	0.00	0.00	182.74	177.10	-7.38E-08	9.75E-11	4.57E-10	0.21	1.24E-10
								297.30	288.13	418.81	405.88	-4.90E-08				
								567.10	549.60	627.61	608.25	-2.44E-08				
								1099.28	1065.36	1047.86	1015.52	2.08E-08				
								1390.37	1347.46	1282.73	1243.15	4.34E-08				
								1557.79	1509.72	1416.68	1372.96	5.70E-08				

Table F-2: Detailed WWC data for 5 m MDEA/5 m PZ

MDEA/PZ		CO_2 ldg	P^*_{CO2}	T	P	Gas_{Dry}	Gas	$P_{CO2in,\ dry}$	$P_{CO2in,\ wet}$	$P_{CO2out,\ dry}$	$P_{CO2out,\ wet}$	CO_2 flux	K_G	k_g	K_G/k_g	k_g'
m		mol CO_2/mol alk	Pa	C	psig	Std L/min	Std L/min	Pa	Pa	Pa	Pa	mol/s cm^2	mol/s Pa cm^2	mol/s Pa cm^2		mol/s Pa cm^2
5	5	0.282	89	10	20	5	5.03	0.00	0.00	14.11	14.04	-5.70E-09	6.75E-11	4.42E-10	0.15	7.96E-11
								57.88	57.59	61.95	61.63	-1.64E-09				
								213.83	212.73	197.33	196.31	6.66E-09				
								238.46	237.24	213.59	212.49	1.00E-08				
5	5	0.282	275	20	20	5	5.05	0.00	0.00	54.77	54.24	-2.21E-08	7.40E-11	4.46E-10	0.17	8.87E-11
								59.80	59.21	87.54	86.69	-1.12E-08				
								110.50	109.42	136.81	135.48	-1.06E-08				
								459.71	455.22	429.33	425.14	1.23E-08				
								504.44	499.51	468.08	463.51	1.47E-08				
5	5	0.282	825	30	20	5	5.09	0.00	0.00	136.33	133.92	-5.50E-08	7.36E-11	4.50E-10	0.16	8.79E-11
								236.79	232.59	346.81	340.66	-4.44E-08				
								454.45	446.39	507.07	498.08	-2.12E-08				
								1609.70	1581.15	1482.93	1456.64	5.12E-08				
								1848.88	1816.10	1683.84	1653.99	6.66E-08				
								2045.01	2008.75	1848.88	1816.10	7.92E-08				
5	5	0.282	2245	40	20	5	5.16	0.00	0.00	310.94	301.34	-1.25E-07	7.43E-11	4.57E-10	0.16	8.88E-11
								571.65	554.00	863.45	836.80	-1.18E-07				
								1097.85	1063.97	1289.19	1249.41	-7.72E-08				
								3245.70	3145.54	3090.23	2994.87	6.27E-08				
								3532.72	3423.70	3341.37	3238.26	7.72E-08				
								3807.78	3690.27	3561.42	3451.52	9.94E-08				
5	5	0.329	1749	30	20	5	5.09	0.00	0.00	196.13	192.65	-7.92E-08	4.94E-11	4.50E-10	0.11	5.55E-11
								710.37	697.78	837.14	822.29	-5.12E-08				
								1439.88	1414.35	1478.15	1451.94	-1.54E-08				
								2922.81	2870.98	2798.43	2748.81	5.02E-08				
								3666.66	3601.65	3451.40	3390.20	8.69E-08				
								4415.30	4337.01	4113.93	4040.99	1.22E-07				
5	5	0.329	4906	40	20	5	5.16	0.00	0.00	583.60	565.59	-2.36E-07	5.20E-11	4.57E-10	0.11	5.86E-11
								1447.05	1402.40	1853.66	1796.46	-1.64E-07				
								2953.90	2862.74	3240.92	3140.91	-1.16E-07				
								8789.94	8518.69	8335.50	8078.27	1.83E-07				
								10177.20	9863.14	9579.24	9283.64	2.41E-07				
								11612.29	11253.95	10846.91	10512.18	3.09E-07				

MDEA/PZ Fawkes Model Upgrade

Quarterly Report for October 1 – December 31, 2011

by Thu Nguyen

Supported by the Luminant Carbon Management Program

Department of Chemical Engineering

The University of Texas at Austin

January 31, 2012

Abstract

This report discusses the effort to upgrade the Fawkes MDEA/PZ model to better match amine volatility and speciation while accurately maintaining CO_2 solubility predictions. The best possible combination of parameter values to match the different types of blend data, as used in this model revision, includes regressed values for H_2O interaction with ion pairs, default values for MDEA and PZ interactions with ion pairs (10 for amine to ion pairs, -2 for ion pairs to amine), default values for the zwitterion H^+PZCOO^- interaction with ion pairs set to mimic default water interaction values (8 for zwitterions to ion pairs, -4 for ion pairs to zwitterion), and the non-randomness factor for zwitterion to MDEA interaction fixed at 0.3.

The MDEA and PZ volatilities, as a function of loading and temperature, were adequately represented in this model revision. This is most likely due to the fact that the H_2O-MDEA and H_2O-CO_2-MDEA parameters were regressed again in this version to properly match experimental unloaded MDEA volatility data and CO_2 solubility. Speciation was also matched successfully in this model upgrade. This is because the H_2O and MDEA interactions with ion pairs involving HCO_3^- were regressed again along with the introduction of the CO_3^{2-} species. These changes made it possible to obtain noticeably improved fits of CO_2 solubility and MDEA volatilities, which consequently resulted in accurate speciation predictions. The model is able to predict well-behaved heats of absorption that match expectation and are internally consistent overall. For both blends, the CO_2 heats of absorption flip temperature behaviors at loadings that correspond to the critical loadings where PZ is saturated in both MDEA/PZ systems (loading ~ 0.18 for 7 m MDEA/2 m PZ; ~0.33 for 5 m MDEA/5 m PZ). Over a range of loading up to ~0.5 mol CO_2/mol total alkalinity, the CO_2 heat of absorption is estimated to be between 40-90 kJ/mol CO_2 for 60 ˚-150 ˚C which is comparable to that of 8 m PZ solvent.

Introduction

Work continued this quarter on upgrading the existing MDEA/PZ Fawkes thermodynamic model to better match key experimental data for amine volatility and speciation. The PZ part of the system was also reworked by Frailie to better match CO_2 solubility at 40 ˚C and speciation. The quaternary system, MDEA-PZ-CO_2-H_2O, is now upgraded using additional experimental data. For the unloaded blend, the amine volatility data could be adequately matched without regressing any cross parameter for MDEA-PZ interaction. This is due to the fact that the binary MDEA-H_2O parameters were properly regressed at the earlier stage, and also that the MDEA-PZ interactions were not significant. In order to match all the different types of loaded blend data, both the C and E parameters of (H_2O, $MDEAH^+$/$PZCOO^-$) and (H_2O, MDEAH+/$PZCOO_2^-$) were

regressed to fit CO_2 solubility data for 7 m MDEA/2 m PZ, 7.7 m MDEA/1.1 m PZ, and 5 m MDEA/5 m PZ. In addition, the C parameters for amine to ion pair interactions were fixed at default values. The combination of parameters used above enabled proper fitting of loaded amine volatility and speciation data as well.

Experimental Methods

Amine Volatility Measurements

Amine volatility was measured in a stirred reactor coupled with a hot gas FTIR analyzer (Fourier Transform Infrared Spectroscopy, Temet Gasmet Dx-4000) as shown in Figure 1.

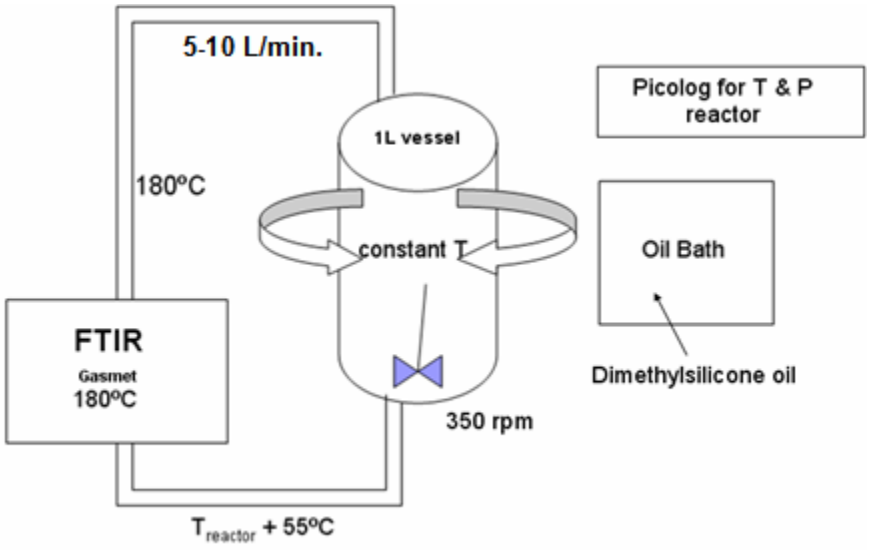

Figure 1: Amine Volatility Experimental Setup

The 1 L glass reactor was agitated at 350 rpm. Temperature in the reactor was controlled by circulating dimethylsilicone oil. The reactor was insulated with thick aluminum insulation material. Vapor from the headspace of the reactor, primarily 5–10 L/min., was circulated by a heated sample pump to the FTIR through a heated Teflon line. Both the line and analyzer were maintained at 180 ºC to prevent possible condensation or adsorption of amine. The FTIR measured amine, CO_2, and water concentration in the gas. After the gas passed through the FTIR, it was returned to the reactor through a heated line maintained ~55 ºC hotter than the reactor. It was determined that the 55 ºC difference is sufficient to ensure that the return gas does not upset the solution that is in equilibrium with the gas inside the reactor, and to prevent potential heat loss at the bottom of the reactor.

Amine Concentration

The amine concentration was determined by acid titration (Hilliard, 2008) with an automatic Titrando series titrator with an automatic equivalence point detection. A 300X diluted sample was titrated with 0.1 N H_2SO_4 to a pH of 2.4. The amount of acid needed to reach the equivalence point at a pH of 3.9 was used to calculate the total amine concentration.

Loading Verification

The CO_2 loading was verified by Total Inorganic Carbon (TIC) analysis. The samples were diluted in H_2O and subsequently dissolved in 30 wt % H_3PO_4 to release aqueous CO_2-containing products. The CO_2 was carried by an N_2 stream to an infrared detector which analyzes and records the CO_2 composition as volts. The resulting voltage peaks are integrated and correlated to CO_2 concentrations using a 1000 ppm inorganic carbon standard made from a mixture of potassium carbonate and potassium bicarbonate (Ricca Chemical, Pequannock, NJ).

Theory

MDEA-PZ-CO_2-H_2O

The parameter values which account for the interaction of either H_2O, MDEA, PZ, and the zwitterions H^+PZCOO^- with cation or anion pairs ($MDEAH^+/HCO_3^-$ for example) are given by the following expressions:

$$\tau_{m,ca} = A_{m,ca} + \frac{B_{m,ca}}{T} + C_{m,ca}\left[\frac{\left(T^{ref} - T\right)}{T} + \ln\left(\frac{T}{T^{ref}}\right)\right]$$

$$\tau_{ca,m} = A_{ca,m} + \frac{B_{ca,m}}{T} + C_{ca,m}\left[\frac{\left(T^{ref} - T\right)}{T} + \ln\left(\frac{T}{T^{ref}}\right)\right] \quad (1)$$

Where $\tau_{m,ca} \neq \tau_{ca,m}$. The A, B, C constants in the above expression correspond to pair parameters GMELCC, GMELCD, and GMELCE, respectively.

Data

The data sets used to regress the MDEA-PZ-CO_2-H_2O system are provided in the following tables.

Table 1 shows the CO_2 solubility for 7 m MDEA/2 m PZ from 40–160 ˚C. The data from 40–100 ˚C were obtained from Chen (2010) and those from 120–160 ˚C were taken from Xu (2010). Chen measured CO_2 solubility using a wetted wall column. Xu obtained the data using a high temperature FTIR setup. The measured temperature was assigned an experimental uncertainty of ±1% and the CO_2 solubility was given a ±1% error.

Table 1: CO_2 Solubility for 7 m MDEA/2 m PZ from 40–160 ˚C (Chen and Xu)

Temperature (C)	Loading	PCO_2 (kPa)	xMDEA	xPZ	xCO_2	xH_2O
40	0.093	0.19	0.107	0.030	0.016	0.847
40	0.166	0.95	0.105	0.030	0.028	0.837
40	0.237	2.8	0.104	0.030	0.039	0.827
40	0.286	5.3	0.103	0.030	0.046	0.821
60	0.093	1.3	0.107	0.030	0.016	0.847

60	0.166	4.4	0.105	0.030	0.028	0.837
60	0.237	13.5	0.104	0.030	0.039	0.827
60	0.273	19.6	0.104	0.030	0.044	0.822
80	0.027	1.27	0.108	0.031	0.005	0.857
80	0.093	5.62	0.107	0.030	0.016	0.847
80	0.166	17.6	0.105	0.030	0.028	0.837
100	0.027	5.21	0.108	0.031	0.005	0.857
100	0.093	19.8	0.107	0.030	0.016	0.847
120	0.132	137	0.103	0.029	0.021	0.846
120	0.226	628	0.092	0.026	0.033	0.849
140	0.125	356	0.100	0.029	0.020	0.852
140	0.206	1362	0.090	0.026	0.029	0.855
160	0.113	785	0.098	0.028	0.017	0.857
160	0.178	2452	0.088	0.025	0.025	0.862

Table 2 gives the CO_2 solubility for 5 m MDEA/5 m PZ from 40–160 ˚C. The data from 40–100 ˚C were obtained from Chen (2011) and those from 120–160 ˚C were taken from Xu (2011). The measured temperature was assigned an experimental uncertainty of ±1% and the solubility data had a ±1% error.

Table 2: CO_2 Solubility for 5 m MDEA/5 m PZ from 40–160 ˚C (Chen and Xu)

Temperature (C)	Loading	PCO_2 (kPa)	xMDEA	xPZ	xCO_2	xH_2O
40	0.18	0.24	0.073	0.073	0.040	0.814
40	0.23	0.64	0.072	0.072	0.050	0.805
40	0.28	2.2	0.072	0.072	0.060	0.796
40	0.33	3.5	0.071	0.071	0.070	0.788
40	0.37	6.6	0.070	0.070	0.078	0.781
60	0.18	1.5	0.073	0.073	0.040	0.814
60	0.23	3.7	0.072	0.072	0.050	0.805
60	0.28	8.8	0.072	0.072	0.060	0.796
60	0.33	18.3	0.071	0.071	0.070	0.788
60	0.37	28.2	0.070	0.070	0.078	0.781
80	0.18	6.7	0.073	0.073	0.040	0.814
80	0.23	16.9	0.072	0.072	0.050	0.805
100	0.22	39.9	0.073	0.073	0.048	0.806
100	0.28	109	0.072	0.072	0.060	0.797
120	0.22	169	0.073	0.073	0.048	0.807
120	0.27	343	0.072	0.072	0.058	0.798
140	0.21	478	0.073	0.073	0.046	0.808
140	0.26	885	0.072	0.072	0.056	0.800
160	0.20	1122	0.073	0.073	0.043	0.811
160	0.24	1746	0.072	0.072	0.052	0.803

Table 3 shows the CO_2 solubility for both 7 m MDEA/2 m PZ and 5 m MDEA/5 m PZ, at 40 and 60 ˚C, obtained from this work. The measured temperature was assigned a ±1% and the CO_2 pressure was assumed to have a ±1% uncertainty.

Table 3: CO_2 Solubility for 7 m MDEA/2 m PZ and 5 m MDEA/5 m PZ at 40 and 60 ˚C (This Work)

Temperature (C)	Loading	PCO_2 (kPa)	xMDEA	xPZ	xCO_2	xH_2O
40	0.14	0.52	0.106	0.030	0.024	0.840
40	0.19	1.43	0.105	0.030	0.032	0.833
40	0.24	3.56	0.104	0.030	0.039	0.827
60	0.14	2.54	0.106	0.030	0.024	0.840
60	0.19	7.35	0.105	0.030	0.032	0.833
60	0.24	17.6	0.104	0.030	0.039	0.827
40	0.22	0.58	0.073	0.073	0.049	0.806
40	0.34	6.83	0.071	0.071	0.072	0.786
40	0.37	11.7	0.070	0.070	0.078	0.781
60	0.22	2.83	0.073	0.073	0.049	0.806
60	0.34	26.8	0.071	0.071	0.072	0.786
60	0.37	39.1	0.070	0.070	0.078	0.781

Table 4 summarizes the CO_2 solubility for the 7.7 m MDEA/1.1 m PZ system at 40 and 70 ˚C as taken from Bishnoi (2000). The measured temperature was assigned a ±1% and the CO_2 pressure was assumed to have a ±1% uncertainty.

Table 4: CO_2 Solubility for 7.7 m MDEA/1.1 m PZ at 40 and 70 ˚C (Bishnoi, 2000)

Temperature (C)	Loading	PCO_2 (kPa)	xMDEA	xPZ	xCO_2	xH_2O
40	0.02	0.033	0.119	0.017	0.004	0.860
40	0.05	0.115	0.119	0.017	0.008	0.856
40	0.06	0.236	0.118	0.017	0.010	0.855
40	0.08	0.367	0.118	0.017	0.012	0.853
40	0.12	1.1	0.117	0.017	0.019	0.847
40	0.12	1.3	0.117	0.017	0.019	0.847
40	0.17	2.6	0.117	0.017	0.025	0.842
40	0.25	7.5	0.115	0.016	0.038	0.831
70	0.01	0.034	0.120	0.017	0.001	0.863
70	0.01	0.241	0.119	0.017	0.002	0.862
70	0.02	0.491	0.119	0.017	0.003	0.861
70	0.04	0.78	0.119	0.017	0.006	0.858
70	0.08	3.6	0.118	0.017	0.013	0.852

Tables 5 and 6 display the volatilities of MDEA and PZ in 7 m MDEA/2 m PZ and 5 m MDEA/5 m PZ, respectively, for a range of nominal lean to rich loadings at 40–70 ˚C.

Table 5: Volatilities of 7 m MDEA/2 m PZ System at Nominal Loadings from 40–70 ˚C

T (C)	Ldg	P_{PZ} (Pa)	P_{MDEA} (Pa)
40	0	1.07	0.46
40	0.143	0.30	0.47
40	0.193	0.15	0.44
40	0.24	0.13	0.47
45	0	1.61	0.81
45	0.143	0.40	0.72
45	0.193	0.23	0.65
45	0.24	0.18	0.65
50	0	2.50	1.15
50	0.143	0.59	1.10
50	0.193	0.34	1.03
50	0.24	0.25	1.18
55	0	3.80	1.62
55	0.143	0.99	1.63
55	0.193	0.57	1.66
55	0.24	0.33	1.65
60	0	5.48	1.91
60	0.143	1.47	2.16
60	0.193	0.78	2.16
60	0.24	0.49	2.02
65	0	8.48	2.83
65	0.143	2.28	3.44
65	0.193	1.33	3.29
65	0.24	0.85	3.08
70	0	11.73	4.23
70	0.143	3.63	5.62
70	0.193	1.93	4.85
70	0.24	1.30	4.68

Table 6: Volatilities of 5 m MDEA/5 m PZ at Nominal Loadings from 40–70 ˚C

T (C)	Ldg	P_{PZ} (Pa)	P_{MDEA} (Pa)
40	0	5.04	0.36
40	0.221	0.51	0.45
40	0.307	0.24	0.37
40	0.362	0.16	0.30
45	0	6.45	0.50
45	0.221	0.72	0.61

45	0.307	0.27	0.52
45	0.362	0.20	0.41
50	0	8.75	0.64
50	0.221	1.22	0.91
50	0.307	0.37	0.77
50	0.362	0.23	0.59
55	0	12.11	0.99
55	0.221	1.81	1.34
55	0.307	0.54	1.11
55	0.362	0.35	0.88
60	0	17.78	1.45
60	0.307	0.91	1.64
60	0.362	0.54	1.32
60.3	0.221	2.85	1.75
65	0	27.81	2.22
65	0.221	4.37	2.69
65	0.307	1.50	2.22
65	0.362	1.00	2.13
70	0	44.77	2.78
70	0.221	6.78	4.07
70	0.307	2.52	3.42

Tables 7 and 8 show the speciation results for 7 m MDEA/2 m PZ and 5 m MDEA/5 m PZ, respectively, at 40 ˚C.

Table 7: Experimental NMR Speciation for 7 m MDEA/2 m PZ at 40 ˚C

Ldg	**0.07**	**0.095**	**0.15**	**0.16**
$MDEA/MDEAH^+$	0.1053	0.1066	0.1052	0.1087
PZ/PZH^+	0.0211	0.0171	0.0138	0.0109
$PZCOO^-/H^+$	0.0094	0.0120	0.0157	0.0155
$PZ(COO)_2^-$	0.0009	0.0018	0.0044	0.0052
HCO_3^-	0.0005	0.0007	0.0017	0.0021

Table 8: Experimental NMR Speciation for 5 m MDEA/5 m PZ at 40 ˚C

Ldg	**0.096**	**0.18**	**0.36**
$MDEA/H^+$	0.0745	0.0732	0.0701
PZ/H^+	0.0558	0.0395	0.0159
$PZCOO^-/H^+$	0.0185	0.0290	0.0416
$PZ(COO)_2^-$	0.0015	0.0052	0.0157
HCO_3^-	0.0005	0.0010	0.0060

Results

Fawkes Model Upgrade: MDEA-PZ-H_2O System

No parameter had to be used to match the MDEA/PZ volatility for either 7 m MDEA/2 m PZ or 5 m MDEA/5 m PZ from 40–60 ˚C. This is because the binary MDEA-H_2O parameters were properly regressed at the earlier stage, and also that the MDEA-PZ interactions were not significant. Figures 2 and 3 show the Flash predictions of the volatilities for 7 m MDEA/2 m PZ and 5 m MDEA/5 m PZ, respectively, in comparison to experimental data.

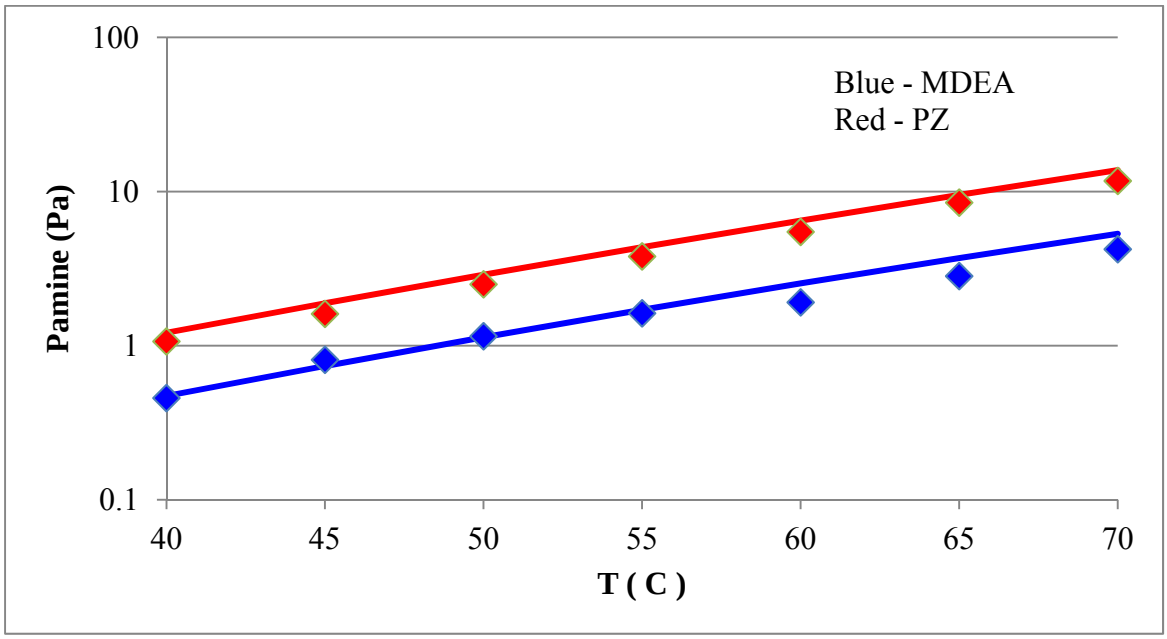

Figure 2: MDEA and PZ Volatility for 7 m MDEA/2 m PZ for 40–70 ˚C

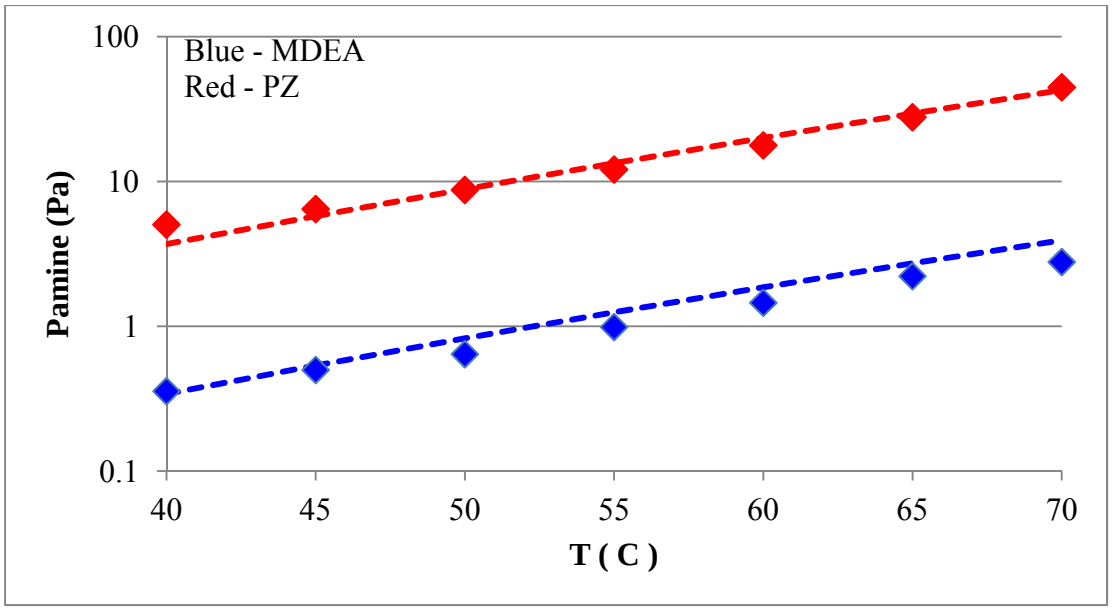

Figure 3: MDEA and PZ Volatility for 5 m MDEA/5 m PZ for 40–70 ˚C

The updated Fawkes model now adequately matches experimental volatility data for the two unloaded blends. This is a key improvement over the older version.

Fawkes Model Upgrade: MDEA-PZ-CO_2-H_2O System

CO_2 solubility data for 7 m MDEA/2 m PZ, 5 m MDEA/5 m PZ, and 7.7 m MDEA/1.1 m PZ were used in the regression of MDEA, PZ, and the zwitterion H^+PZCOO^- interactions with ion pairs in solution. Twelve tau parameters were regressed to fit all the types of experimental data available for the blend, which include CO_2 solubility, amine volatility, speciation, and heat capacity. The best possible combination of parameter values used to match the different types of data includes regressed values for H_2O interaction with ion pairs, default values for MDEA and PZ interactions with ion pairs (10 for amine to ion pairs, -2 for ion pairs to amine), default values for the zwitterion H^+PZCOO^- interaction with ion pairs set to mimic default water interaction values (8 for zwitterions to ion pairs, -4 for ion pairs to zwitterion), and the non-randomness factor for zwitterion to MDEA interaction fixed at 0.3.

Figure 4 shows the upgraded model predictions of CO_2 solubility in comparison to experimental data for 7 m MDEA/2 m PZ from 40–160 ˚C.

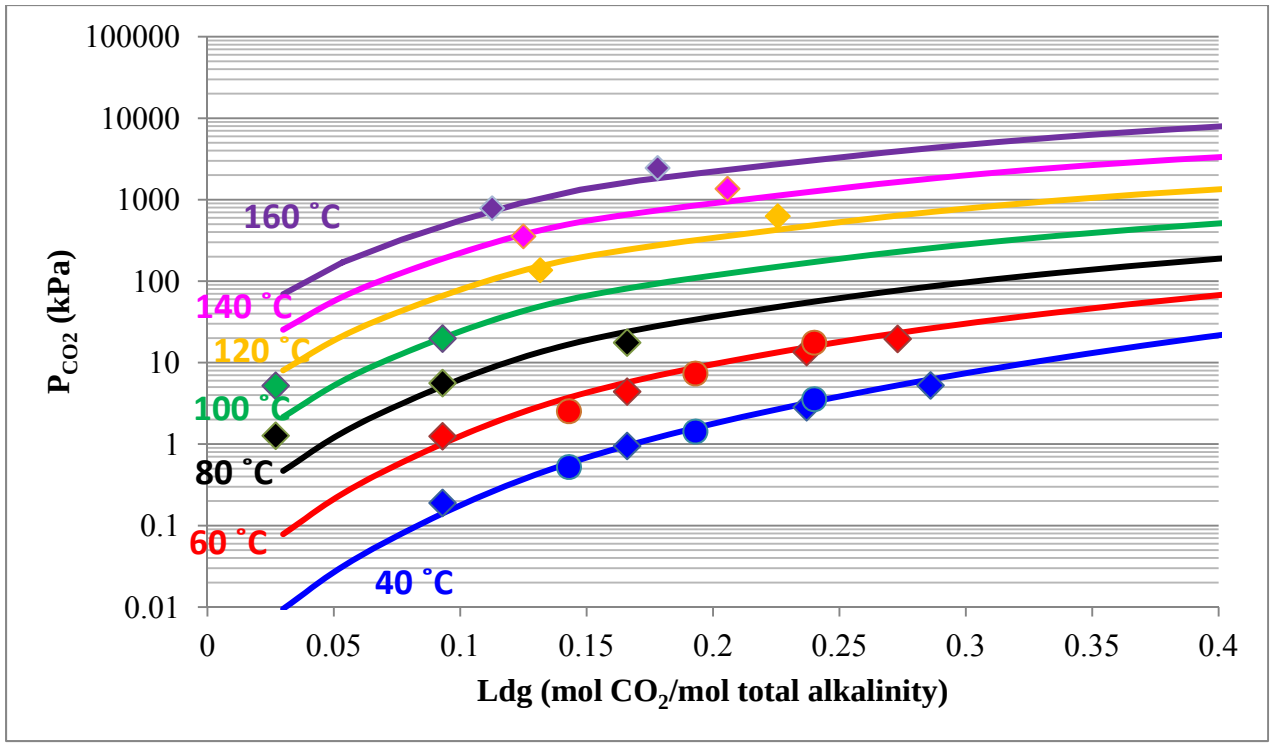

Figure 4: CO_2 Solubility Predictions for 7 m MDEA/2 m PZ from 40–160 ˚C

The upgraded Fawkes model adequately matches CO_2 solubility data for 7 m MDEA/2 m PZ for a wide range of temperature. Experimental data for the very lean loadings (less than 0.05 mol CO_2/mol total alkalinity) appear to be experimental outliers.

Figure 5 displays the upgraded model predictions of CO_2 solubility in comparison to experimental data for 5 m MDEA/5 m PZ from 40–160 ˚C.

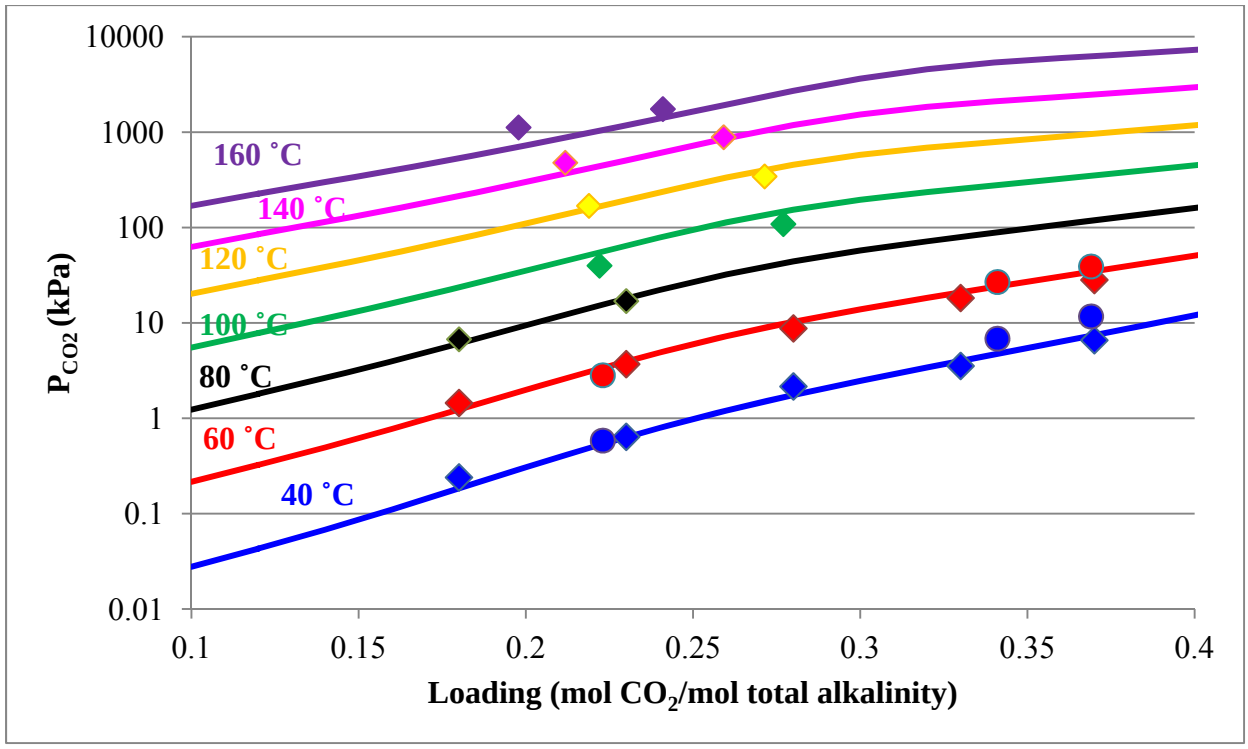

Figure 5: CO2 Solubility Predictions for 5 m MDEA/5 m PZ from 40–160 ˚C

The new model sufficiently represents the CO_2 solubility data for 5 m MDEA/5 m PZ for the wide temperature range of interest.

Figure 6 shows the model prediction of CO_2 solubility for 7.7 m MDEA/1.1 m PZ at 40 and 70 ˚C. Again, the model extrapolates well in predicting the CO_2 solubility at this blend concentration.

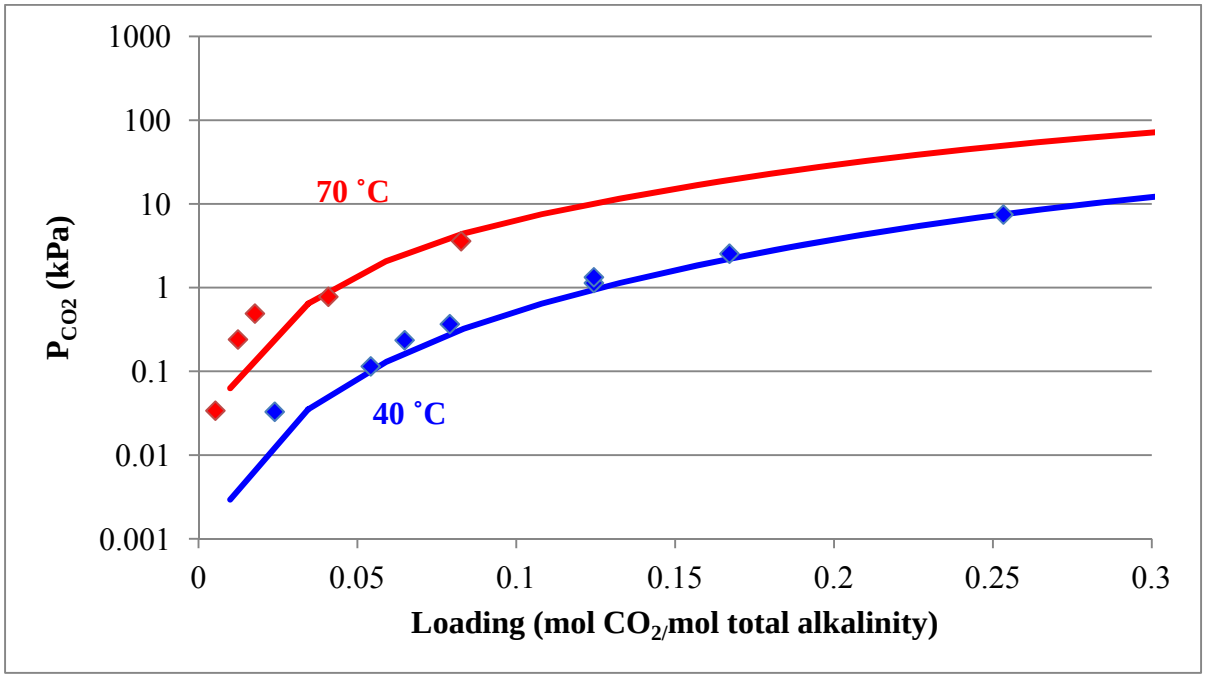

Figure 6: CO_2 Solubility Predictions for 7.7 m MDEA/1.1 m PZ at 40–70 ˚C

Figures 7 and 8 show the upgraded model prediction of MDEA and PZ volatility for 7 m MDEA/2 m PZ and 5 m MDEA/5 m PZ, respectively, for nominal loadings at 40 and 60 ˚C.

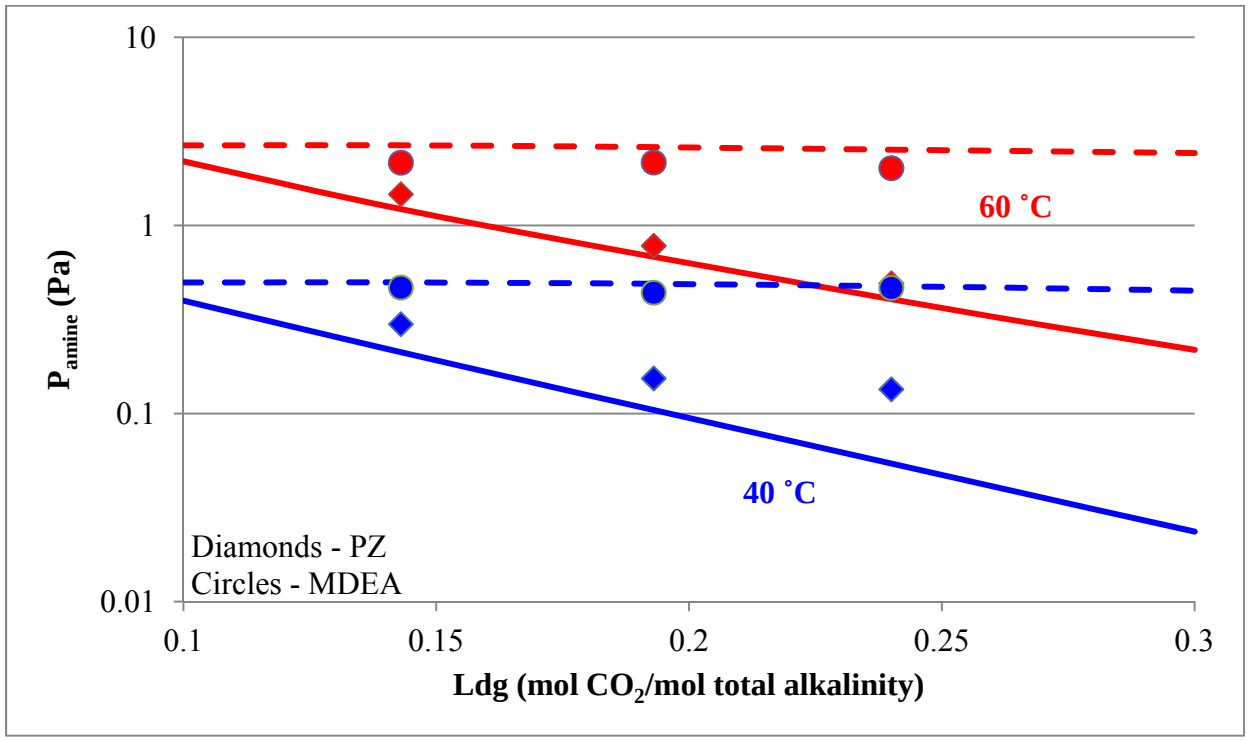

Figure 7: Amine Volatility Predictions for 7 m MDEA/2 m PZ at 40 and 60 ˚C

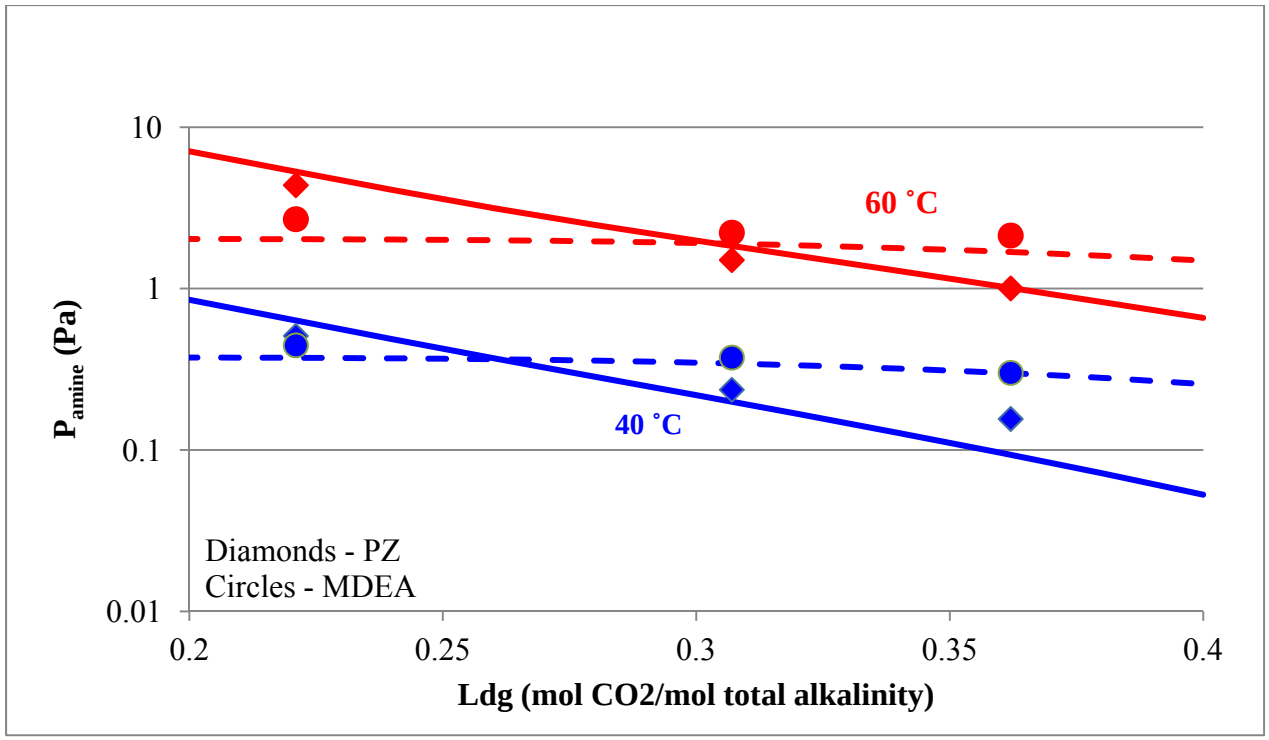

Figure 8: Amine Volatility Predictions for 5 m MDEA/5 m PZ at 40 and 60 ˚C

The upgraded model successfully captures the volatilities of both MDEA and PZ as a function of loading for both temperatures shown. Much of this success is due to the fact that the H_2O-MDEA and H_2O-CO_2-MDEA parameters were regressed again in this version to match experimental unloaded MDEA volatility data and CO_2 solubility. Matching volatility data for the blend is a high priority for this model revision. The largest disparity between experimental and model prediction occurs in the case of the 7/2 blend at 40 ˚C, particularly at high loading, where there is a high degree of uncertainty in the accuracy of the data as this condition is at the detection limit of the FTIR apparatus. Because the model represents the data very well at all other conditions shown, it is trustworthy at this operating condition. The MDEA volatility is not sensitive to changes in loading over the range observed because CO_2 reacts preferentially with PZ, and not MDEA, due to the fact that the former is the stronger base and has two amine groups that can directly react with CO_2.

Figures 9 and 10 show the speciation for 7 m MDEA/2 m PZ and 5 m MDEA/5 m PZ, respectively, at 40 ˚C. The experimental NMR data was obtained by using a Varian Inova 500 MHz NMR spectrometer.

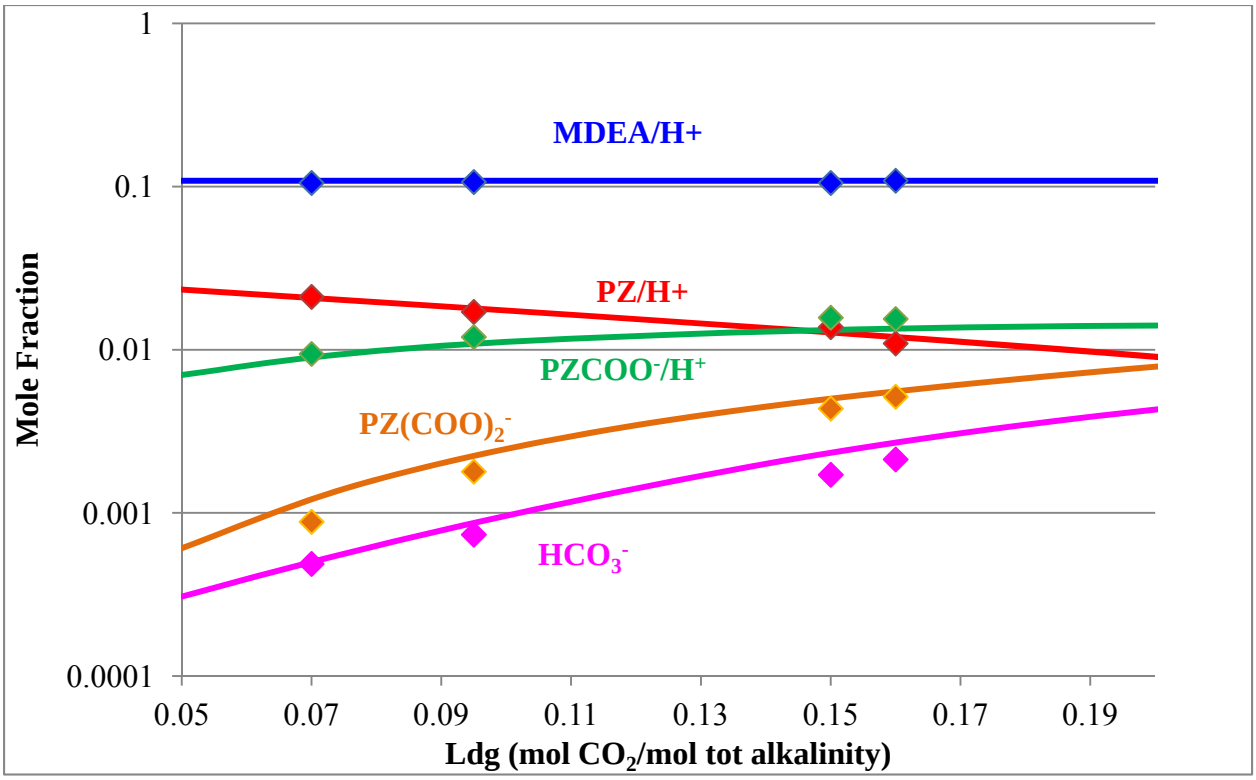

Figure 9: Speciation for 7 m MDEA/2 m PZ at 40 ˚C

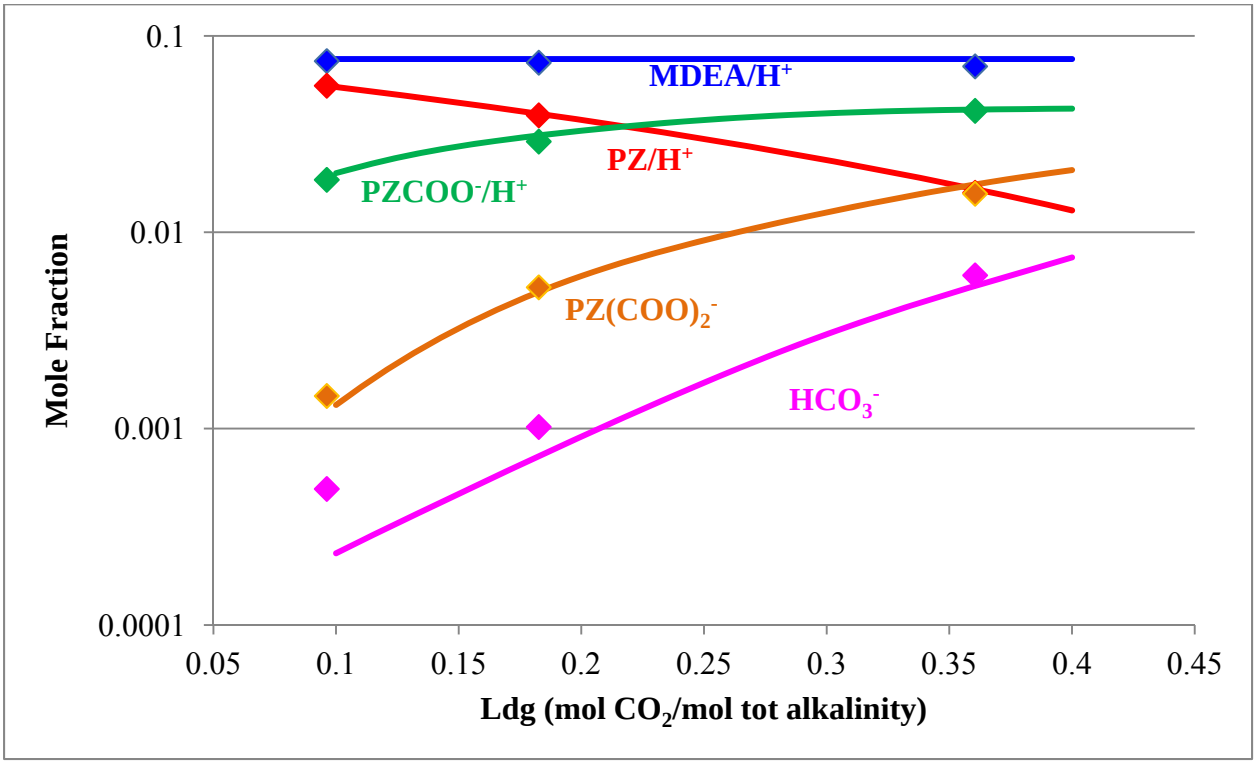

Figure 10: Speciation for 5 m MDEA/5 m PZ at 40 ˚C

The upgraded model adequately matches speciation for both 7 m MDEA/2 m PZ and 5 m MDEA/5 m PZ as shown. In the previous model, the predictions underestimated the amount of $PZ(COO)_2^-$ formed while overestimating the HCO_3^- amount. In this revision, the H_2O and MDEA interactions with ion pairs involving HCO_3^- were regressed again along with the introduction of CO_3^{2-} species. These changes made it possible to obtain noticeably improved fits of CO_2 solubility and MDEA volatilities, which resulted in accurate speciation predictions. The bicarbonate prediction for the blend at low loading is accurate due to the addition of the carbonate species, whereas the prediction at high loading is accurate because of the use of adequate MDEA interaction parameters resulting from the regression of the tertiary MDEA-CO_2-H_2O system. Matching speciation without upsetting CO_2 solubility was a priority for this revision.

Figure 11 and 12 show the predicted CO_2 heats of absorption for 7 m MDEA/2 m PZ and 5 m MDEA/5 m PZ, respectively, from 60–150 ˚C.

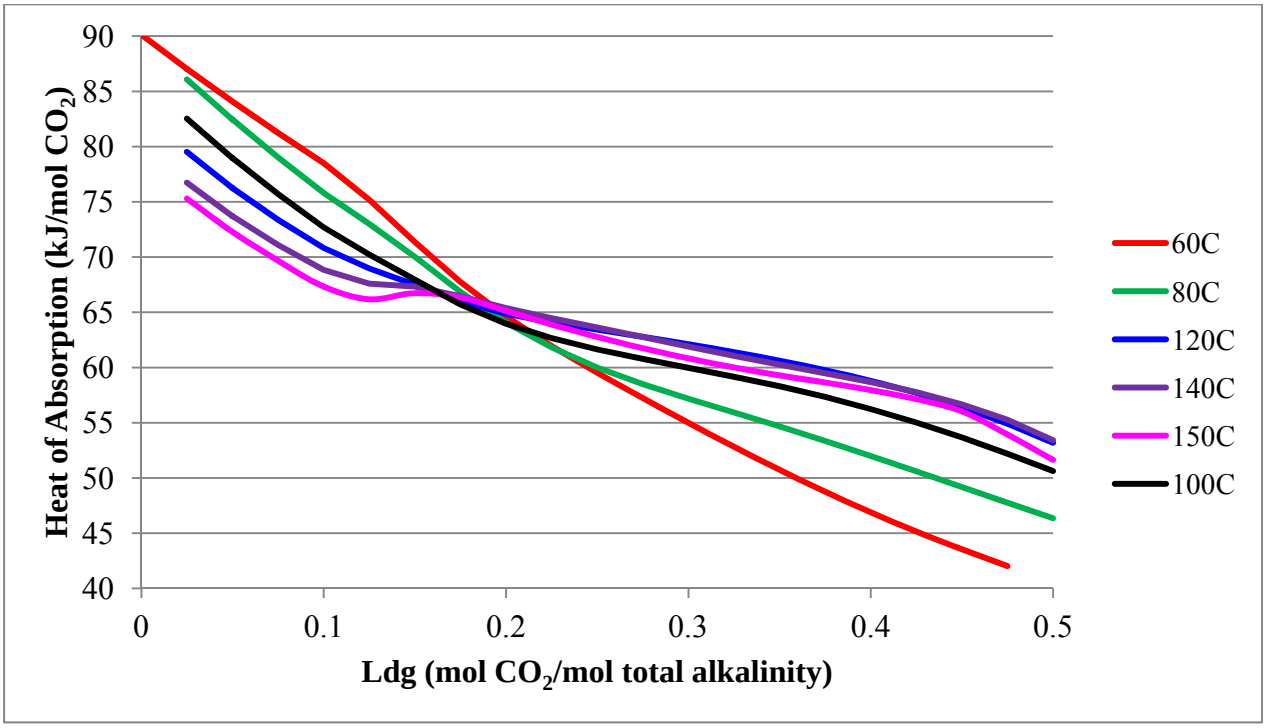

Figure 11: CO_2 Heat of Absorption for 7 m MDEA/2 m PZ from 60–150 ˚C

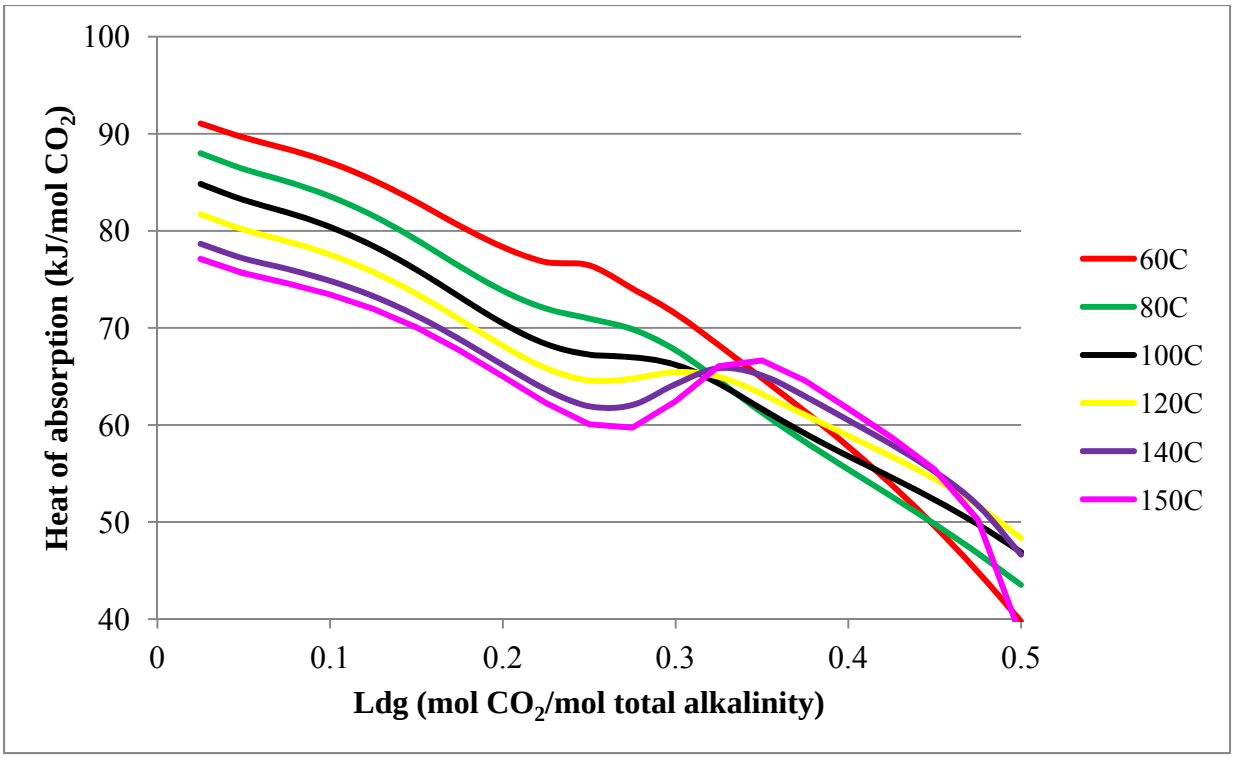

Figure 12: CO_2 Heat of Absorption for 5 m MDEA/5 m PZ from 60–150 ˚C

There are no experimental data available for the heat of CO_2 absorption in MDEA/PZ. Nevertheless, the model predicts well-behaved heat of absorption that matches expectations and is internally consistent. For both blends, the heat of CO_2 absorption prediction flips temperature behavior at the critical loading where PZ is saturated in both systems (loading ~ 0.18 for 7/2; ~0.33 for 5/5). Before reaching the critical loading point, CO_2 reacts primarily with PZ, not MDEA, in an exothermic reaction. Since PZ reaction with CO_2 is exothermic, increasing the system temperature would tend to work against this effect and result in a lower drive for the reaction to occur which is reflected in smaller heat of CO_2 absorption. This is the reason that absorbers require intercooling to reduce the column temperature and improve CO_2 solubility, which manifests in greater values of heat of absorption. After the critical loading where most of the PZ is saturated, CO_2 now reacts with MDEA instead which has a different heat of absorption compared to PZ. At less than 140 ˚C, the heat of absorption tends to decrease with loading because there is less free amine available to react with CO_2. In other words, the drive for CO_2 reaction is much less at greater loading; and the heat of absorption decreases. At temperature higher than 140 ˚C, there is a competing effect between speciation and temperature on the heat of absorption, with the latter overriding the former, particularly for MDEA where the reaction with CO_2 is less exothermic. This behavior is so strong that it compensates for the drop in ΔH_{CO2} due to lack of free amine (PZ); however, if one were to project past a high enough loading (greater than 0.5), the heat of absorption would naturally decline again due to the MDEA running out and not being able to react with CO_2. In other words, speciation would dominate again as it tends to overall. Lastly, predicting CO_2 heat of absorption is not the primary scope of this work, but is secondary to the needs of matching volatility and speciation.

Figures 13 and 14 illustrate the heat capacity predictions for 7 m MDEA/2 m PZ and 5 m MDEA/5 m PZ, respectively, from 40–120 ˚C. The experimental heat capacity data were obtained by using a Differential Scanning Calorimeter apparatus.

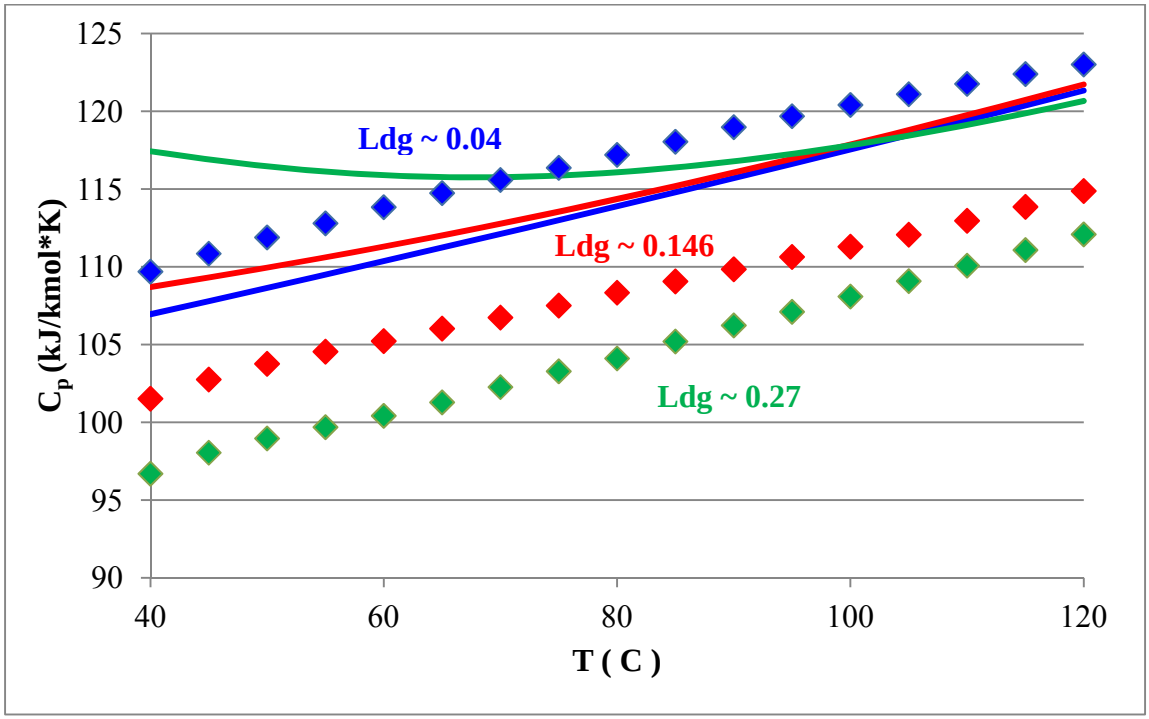

Figure 13: C_p Predictions for 7 m MDEA/2m PZ from 40–120 ˚C

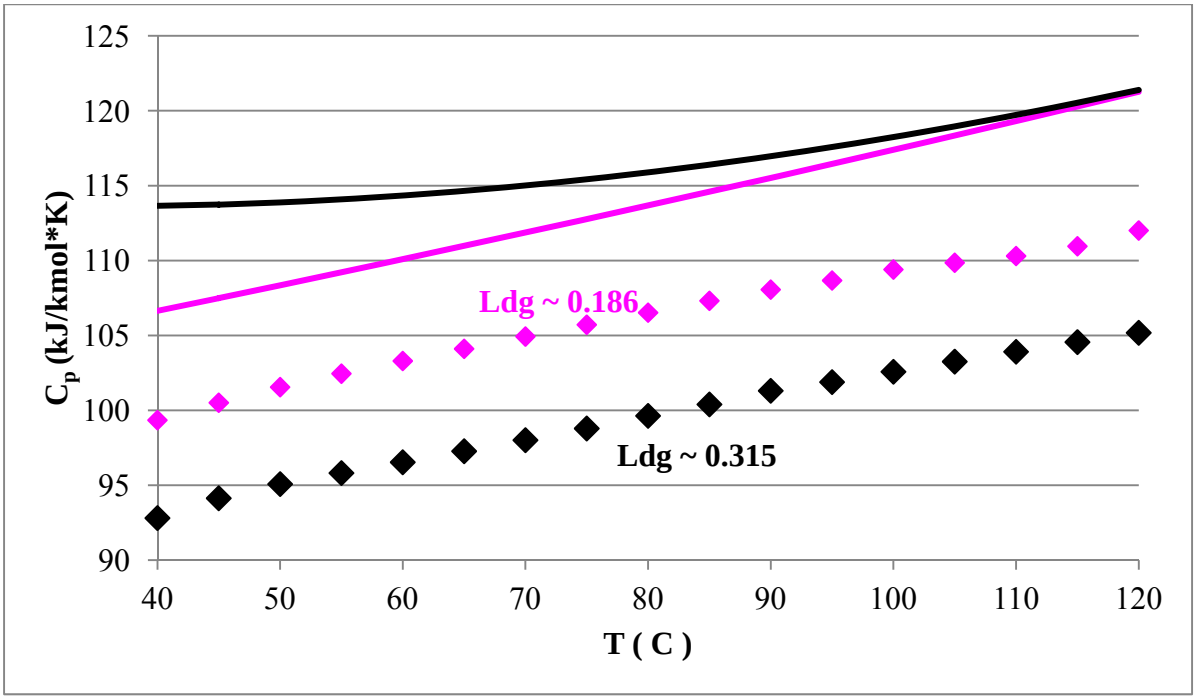

Figure 14: C_p Prediction for 5 m MDEA/5 m PZ from 40–120 ˚C

The experimental C_p for the blends decreases with loading as the CO_2 heat capacity is believed to be negligible, thus increasing the amount of CO_2 in the system results in a decrease of the total

C_p. As seen, the model does not properly match the blend heat capacities. However, the need to represent experimental C_p was not a priority, compared to matching speciation and volatility, from the start. It is interesting that the model matches speciation very well but not C_p, which means that at the very least the heat of reaction prediction is adequate but not the total heat. This suggests that the free energies or enthalpies of formation for some of the electrolyte species could be better optimized. It is also important that the regression uses a reduced set of reactions instead of the full set; thus, certain reactions which may not be significant enough to impact speciation may turn out to be highly relevant for C_p.

Conclusions

1. The amine volatilities for the MDEA/PZ blends at zero loading (MDEA-PZ-H_2O) can be represented successfully without the need to regress any cross parameter for MDEA-PZ interaction. This shows that the MDEA-H_2O and PZ-H_2O interaction parameters were adequately regressed at the binary stage and represent both amine interactions in the blend. Moreover, since the MDEA-PZ interaction, and vice versa, was not regressed, this suggests that MDEA interacts with PZ just as if it were interacting with itself.

2. The best possible combination of parameter values used to match the different types of blend data, as used in this model revision, includes regressed values for H_2O interaction with ion pairs, default values for MDEA and PZ interactions with ion pairs (10 for amine to ion pairs, -2 for ion pairs to amine), default values for the zwitterion H^+PZCOO^- interaction with ion pairs set to mimic default water interaction values (8 for zwitterions to ion pairs, -4 for ion pairs to zwitterion), and the non-randomness factor for zwitterion to MDEA interaction fixed at 0.3.

3. The amine volatilities for loaded 7/2 and 5/5 MDEA/PZ are successfully matched in this revision. Much of this success is due to the fact that the H_2O-MDEA and H_2O-CO_2-MDEA parameters were regressed again in this version to properly match experimental unloaded MDEA volatility data and CO_2 solubility. The model deviates the most from the experimental data for low total PZ, low temperature, and high loading. This condition pushes the detection limit of the FTIR and thus the experimental data itself are suspect.

4. The speciation for both blends is adequately represented in the upgraded model, because the H_2O and MDEA interactions with ion pairs involving HCO_3^- were regressed again along with the introduction of CO_3^{2-} species. These changes made it possible to obtain noticeably improved fits of CO_2 solubility and MDEA volatilities, which resulted in accurate speciation predictions**.**

5. The model predicts well-behaved heats of absorption that match expectations and are internally consistent. For both blends, the predicted heat of CO_2 absorption changes temperature behavior at the critical loading where PZ is saturated in both systems (loading ~ 0.18 for 7/2; ~0.33 for 5/5). At less than the critical loading, PZ reacts primarily with CO_2 in an exothermic reaction. At greater than the critical loading, MDEA reacts with CO_2 in with a reduced heat of absorption than with PZ.

Future Work

The model for binary amine-water systems is being finalized. An effort will be made to understand and predict the results of amine volatility for several solvents that were screened at nominal lean loadings for potential industrial applications. Amine volatility for MDEA-PZ at water wash condition will be investigated.

References

Bishnoi S. *Carbon Dioxide Absorption and Solution Equilibrium in Piperazine Activated Methyldiethanolamine*. Ph.D. Dissertation. The University of Texas at Austin. 2000.

Chen X. *Carbon Dioxide Thermodynamics, Kinetics, and Mass Transfer in Aqueous Piperazine Derivatives and other Amines*. Ph.D. Dissertation. The University of Texas at Austin. 2011.

Characterization of AMP/PZ

Quarterly Report for October 1 – December 31, 2011

by Han Li

Supported by the Luminant Carbon Management Program

Department of Chemical Engineering

The University of Texas at Austin

January 31, 2012

Abstract

Solid solubility, CO_2 solubility, viscosity, mass transfer rate, and volatility were measured for three different ratios of PZ to AMP. These blends were 6 m PZ/4 m AMP, 6.5 m PZ/3 m AMP and 5 m PZ/2.3 m AMP. Compared to 8 m PZ, the solid solubility window of 6 m PZ/4 m AMP is much narrower, while 6.5 m PZ/3 m AMP exhibits similar results, and 5 m PZ/2.3 m AMP shows similar lean boundary but with no rich boundary. To avoid high viscosity, 5 m PZ/2.3 m AMP was chosen as a promising blend instead of 6.5 m PZ/3 m AMP.

The mass transfer rate for 5 m PZ/2.3 m AMP is greater than 8 m PZ at rich loading, while the CO_2 capacity is a little lower because of lower total alkalinity. This blend has comparable heat of absorption to 8 m PZ, but high volatility of AMP may produce more solvent loss.

Introduction

Piperazine (PZ) is a cyclic amine with two secondary amine nitrogens, which has the advantages of high reaction rate, greater absorption capacity, and resistance to oxidation and thermal degradation. 8 m PZ is a promising solvent for CO_2 capture, but the operating range between lean loading and rich loading is limiting, at 0.31–0.39 (Freeman, 2010). In this quarter, AMP was examined as an additive to aqueous PZ.

2-amino-2-methyl-1-propanol (AMP) is a hindered amine, which has the advantages of high absorption capacity, resistance to oxidation and thermal degradation, and low regeneration heat. 4.8 m AMP has been investigated and the operating range between lean loading and rich loading is 0.27–0.56 (Chen, 2011).

The blend is expected to have a larger operating range than 8 m PZ. Since concentrated AMP can precipitate solids, the focus of this quarter was to find a usable proportion of PZ to AMP. The properties of three different ratios – 6 m PZ/4 m AMP, 6.5 m PZ/3 m AMP, and 5 m PZ/2.3 m AMP – were examined as a function of solid solubility, CO_2 solubility, viscosity, mass transfer rates, and volatility.

Literature Review

There are 12 references related to PZ/AMP blends. Seo (2000) studied PZ/AMP/H_2O/CO_2 and reported CO_2 absorption rate, CO_2 solubility, heat capacity, and physical properties such as density and viscosity. They also focus on modeling of the mass transfer process.

Physical Properties

The physical properties of blends of AMP and PZ, as measured in the literature, are listed in Table 1. In addition to density and viscosity, Sun (2002) also measured the diffusivity of N_2O in these solutions and these measurements are applied to estimate CO_2 diffusivity. This experiment was performed in a wetted wall column with a reported error of 2%. Paul (2006) and Samanta (2006) correlated the results as a function of temperature and amine concentration, while Ghulam Murshid (2011) regressed them as a function of temperature.

Table 1: Physical properties measured in literature

Author Year	Properties	Temperature/K	Concentration
Sun 2002	Density Viscosity	303.15-313.15	AMP: 1.0, 1.5 M PZ: 0.1-0.4 M
Paul 2006	Density Viscosity	288-333	Total: 30 wt % PZ: 3-12 wt %
Samanta 2006	Density Viscosity	298-333	Total: 30 wt % PZ: 2-8 wt %
Dash 2011	Density Viscosity	303-323	Total: 40 wt % PZ: 2-8 wt %
Murshid 2011	Density Viscosity Surface tension Refractive index	298.15-333.15	Total: 30 wt % PZ: 1.74-10.35 wt %
Chen 2009	Heat capacity	303.2-353.2	14 different concentrations

Chen (2010) reported heat capacity data for the system (AMP-PZ-H_2O) and applied the Redlich-Kister-type model to estimate excess molar heat capacities, keeping the mole fractions of water at 0.6, 0.7, 0.8, and 0.9. All the solutions are investigated without CO_2 $loadin_g$.

Reaction kinetics

Table 2 lists research on the reaction kinetics in PZ/AMP. PZ was in all cases regarded as an activator.

Table 2: Reaction Kinetics Summary in Literature

Amines	Rate Constants $k_{2,AMP}$ $m^3/kmol/s$	Temperature	Concentration	CO_2 partial pressure	Author Year
HMDA+AMP **MDEA+AMP** **PZ+AMP**	$k_H=3.84\times10^{10}\exp\left(-\frac{5361}{T/K}\right)$ $k_M=6.60\times10^{9}\exp\left(-\frac{4959}{T/K}\right)$ $k_P=9.09\times10^{9}\exp\left(-\frac{5058}{T/K}\right)$	303-343K	1 wt %, 3 wt %, 5 wt % additives + 30 wt % AMP	/	Choi 2007
PZ+AMP	/	298-313K	2-8 wt % PZ added to keep the total 30 wt %	2-14kPa	Samanta 2008
AMP **AMP+PZ**	AMP: 1150 at 303K 1241 at 313K AMP+PZ: 1500 at 303K 1771 at 313K	303-313K	0.55-3.35 M AMP + 0.115-0.233 M PZ	/	Seo 2000
PZ **PZ+AMP**	$3.13\times10^{7}\exp\left(-\frac{3034}{T/K}\right)$	303.15-313.15K	1-1.5 M AMP + 0.1-0.4 M PZ	/	Sun 2002
PZ+AMP	/	303-323K	2-8 wt % PZ added to keep the total 40 wt %	5-15kPa	Dash 2011

The zwitterion mechanism is generally accepted as the reaction mechanism between CO_2 and PZ-activated aqueous AMP. The reaction of CO_2 and AMP is second order. Choi (2007) conducted the measurements in a stirred cell reactor and compared the enhancement of absorption rate by different additives. The results showed that HMDA promoted the rate most.

Samanta (2008) developed a coupled mass transfer-reaction kinetics-equilibrium model according to Higbie's penetration theory, to predict the absorption rates and enhancement factors. The predicted results were compared with experimental data of absorption of CO_2 into AMP+PZ in a wetted wall contactor. By parametric sensitivity analysis, the author suggests that formation of PZ-dicarbamate is important in the overall kinetics of CO_2-AMP-PZ. Seo (2000) used a wetted sphere absorber. Sun (2002) modeled the kinetic data with a hybrid reaction rate model, a second-order reaction for the reaction of CO_2 with PZ, and a zwitterion mechanism for the reaction of CO_2 with AMP. The overall pseudo first-order reaction rate constants were obtained through measurements in a wetted wall absorber. The author's calculation showed that there was a small difference between the

overall and apparent rate constant. Dash (2011) modeled the mass transfer process through Aspen Plus® to predict CO_2 absorption rate and enhancement factor. The results showed that 35 wt % AMP + 5 wt % PZ appeared to produce the optimum absorption rate.

CO_2 Solubility

Yang (2009) measured CO_2 solubility in an aqueous mixture of PZ and AMP, in which PZ acts as a promoter. The apparatus used was a 1.0 L stainless steel vapor-recirculation equilibrium cell. The temperature and pressure were controlled at the range of 313.2–353.2 K and up to 152 kPa. The concentrations of AMP were 2 and 3 M, while those of PZ were 0.5–1.5 M. The Kent-Eisenberg model was adapted to represent the data. Dash (2011) also measured CO_2 solubility with a high pressure stainless steel stirred equilibrium cell at 303–323 K and 298–328 K respectively. The CO_2 partial pressure was controlled at 0.1–140 kPa and 0.1–1450 kPa. 2–8 wt % PZ was added to the aqueous AMP solutions to keep the total concentration at 30 wt % and 40 wt %. An e-NRTL model was adapted in Aspen Plus® modeling. This model was then used to predict speciation, heat of absorption, pH of the CO_2 loaded solution, and amine volatility, but the model was not verified.

Experimental Methods

Solvents used in this research are listed in Table 3.

Table 3: Chemical Species Used for Solvents Preparation

Chemical	Purity	Source	CAS#
Piperazine	98%	Sigma-Aldridge	110-85-0
2-amino-2-methyl-1-propanol	99%	Acros Organics	124-68-5

Solid solubility experiments were conducted in a water bath with the temperature maintained within the range of 0–80 °C. The solution was prepared at loadings of 0.05, 0.1, 0.15, 0.2, 0.25, 0.3, 0.35, 0.4, and 0.45 mol CO_2/equiv amine. The loaded and unloaded samples were set at 40 °C, 30 °C, and 25 °C overnight to have a feel for what the transition temperature is.

The temperature of the water bath was then carefully increased to melt the slurry. The melting temperature is regarded as the transition temperature.

Two experiments on aqueous AMP solution were performed in a jacketed loader with a stirring bar. The initial concentrations of the experiments were 12 m AMP and 10 m AMP. The solution was loaded until solids precipitated. Then the temperature was increased to 35 °C, 40 °C, 50 °C, 60 °C and samples were taken at each point. 8 to 10 hours were given to reach the solid-liquid equilibrium. The samples were immediately diluted in DDI water to prevent crystallization.

The low temperature CO_2 solubility data and mass transfer rates from 20 to 100 °C were measured using the wetted wall column. The method is identical to that used by Hilliard (2008).

The high temperature CO_2 solubility data were obtained from total pressure measurement with a sealed autoclave. The experimental method can be found from Xu's progress report (Rochelle, 2010).

Amine volatility measurements were performed in a volatility apparatus equipped with a heat-insulated glass reactor and an FTIR to analyze the gas composition, and a computer to record the FTIR results online. The detailed operation is referred to Hilliard's dissertation (2008).

The CO_2 loading and concentration of the samples were obtained through cation chromatography, acid titration and total inorganic carbon analyzer. The details of these analytical methods can be found in Hilliard (2008).

Results and Discussion

Aqueous AMP solution

Solid solubility of loaded aqueous AMP solutions is shown in Table 4. As the most concentrated solution used in previous research is 4.8 m, no solid issues are reported.

Table 4: Solid solubility of loaded AMP aqueous solution

T °C	α mol CO_2/mol alkalinity	AMP mol AMP/kg H_2O
21	0.11	11.01
35	0.31	5.22
35	0.47	6.69
40	0.398	8.23
40	0.474	6.67
50	0.40	8.90
60	0.394	9.36

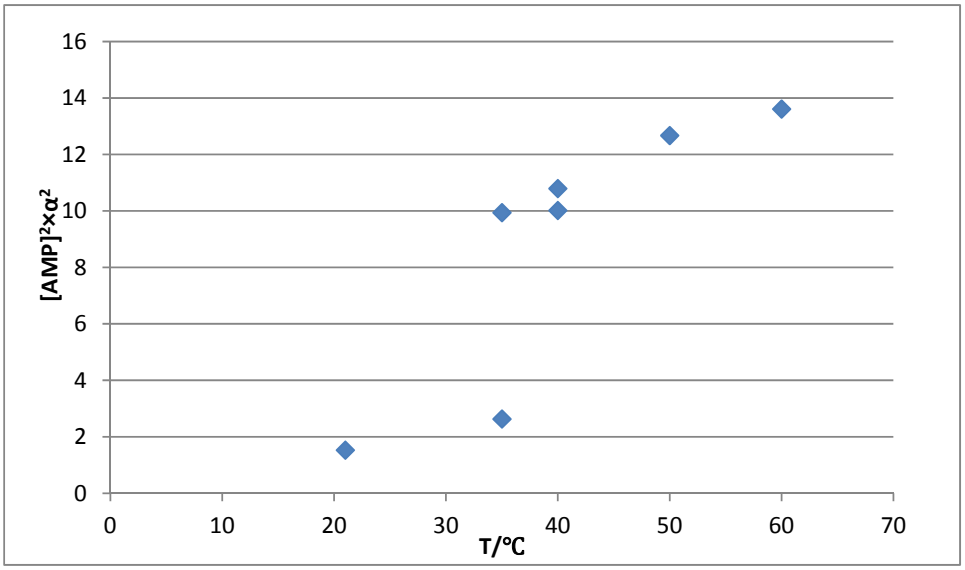

Figure 1: Relationship between $\alpha^2 * [AMP]^2$ and temperature

As AMP-carbamate is not stable, we can ignore its existence. We assume that the composition of the loaded solution includes $AMPH^+$, HCO_3^-, and free AMP. The solid may be $(AMPH^+)(HCO_3^-)$, whose equilibrium in solution is as follows:

$$(AMPH^+)(HCO_3^-) \overset{K_{sp}}{\Leftrightarrow} AMPH^+ + HCO_3^-$$

Then K_{sp}, which is a function of temperature, can be expressed as $K_{sp} = [AMPH^+] * [HCO_3^-]$, in which:

$$[HCO_3^-] = [AMPH^+] = \alpha * [AMP]$$

The relationship between $\alpha^2 * [AMP]^2$ and temperature is shown in Figure 1.

The results in Figure 1 are not consistent with assumption that the solid is $(AMPH^+)(HCO_3^-)$. There may be two different solid phases, one at high temperature and one at low temperature respectively, which need additional investigation.

6 m PZ/4 m AMP

The transition temperature of loaded 6 m PZ/4 m AMP and 6.5 m PZ/3 m AMP is listed in Table 5. The comparison of solubility window with 8 m PZ (Freeman, 2011) is shown in Figure 2.

Table 5: Transition temperature of loaded 6 m PZ/4 m AMP

α **mol CO_2/mol alkalinity**	**Transition** **T/℃**
0	37.0
0.043	34.0
0.097	30.0
0.145	26.0
0.163	24.0
0.225	15.0
0.292	3.0
0.309	0.0
0.337	0.0
0.341	40.0

Figure 2 shows that substituting 2 m PZ with 4 m AMP will narrow the solubility window and present a smaller rich loading boundary, which will also reduce the operating range. To find a possible concentration that will not precipitate at room temperature, the supernatant of the slurry with a total 0.41 loading at room temperature was analyzed. The results from cation chromatography and total inorganic carbon analyzer showed that 6 m PZ/3.2 m AMP with a loading of 0.44 will be soluble.

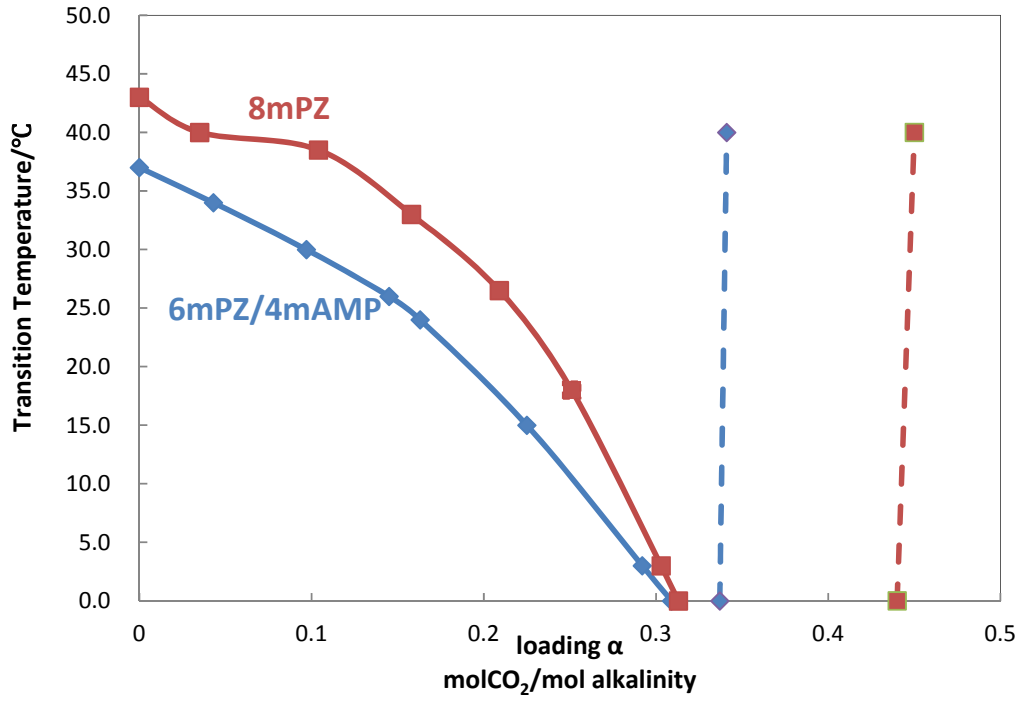

Figure 2: Comparison of solubility window between 6 m PZ/4 m AMP and 8 m PZ

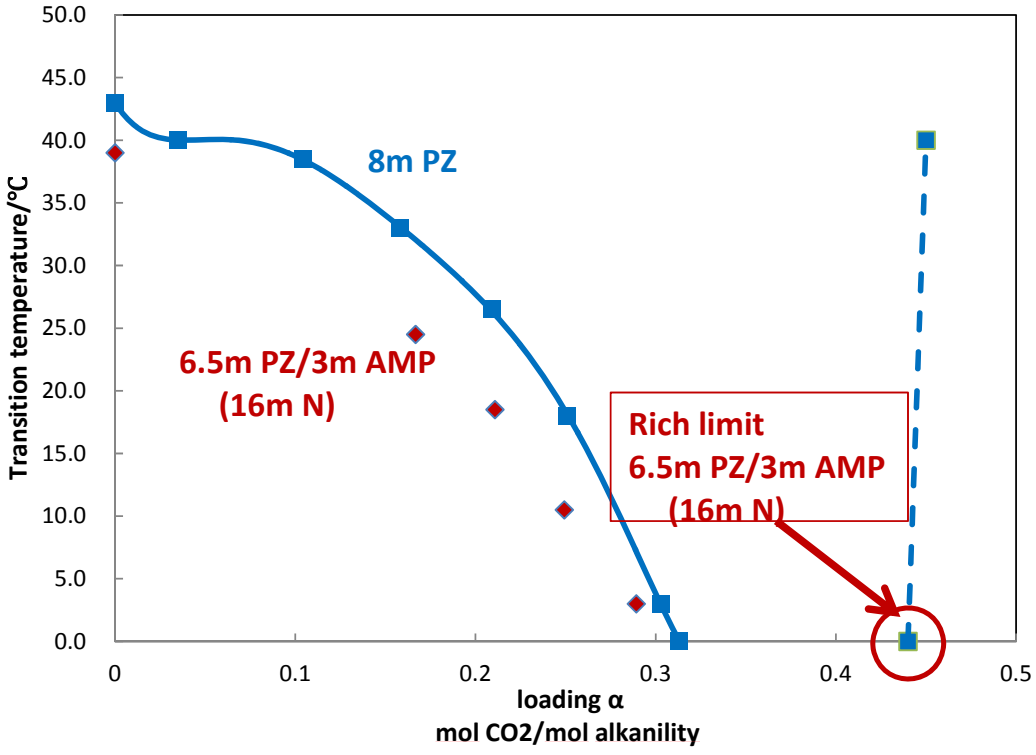

Figure 3: Comparison of solubility window between 6.5 m PZ/3 m AMP and 8 m PZ

6.5 m PZ/3 m AMP

To obtain a comparable CO_2 capacity with 8 m PZ, 16 m alkalinity is kept when preparing the

blend. Thus 6.5 m PZ/3 m AMP was chosen as the second blend to be researched. The transition temperature of loaded solution is listed in Table 6.

Table 6: Transition temperature of loaded 6.5 m PZ/3 m AMP

6.5 m PZ/3 m AMP	
α **mol CO_2/mol alkalinity**	**Transition T/℃**
0	39.0
0.167	24.5
0.211	18.5
0.249	10.5
0.289	3.0
0.445	0

Figure 2 shows the comparison of solid solubility window between this blend and 8 m PZ. They have similar lean and rich boundary at 0 °C.

The total pressure over the loaded blend was measured at 100–160 °C. The partial pressure of CO_2 was calculated by subtracting the partial pressure of N_2 and water from the pressure. P_{water} was assumed to follow the Raoult's Law and P_{amine} was neglected.

Table 7: Total pressure and CO_2 partial pressure in 6.5 m PZ/3 m AMP

PZ/AMP		T	CO_2 ldg	Pt	P_{CO2}	PZ/AMP		T	CO_2 ldg	Pt	P_{CO2}
m		C	mol/mol alk	Pa	Pa	m		C	mol/mol alk	Pa	Pa
6.5	3	100	0.271	102214	21190	6.5	3	150	0.291	1141449	764197
6.5	3	120	0.270	243543	84881	6.5	3	160	0.283	1688446	1198651
6.5	3	130	0.269	369987	154178	6.5	3	100	0.440	469430	391664
6.5	3	140	0.266	579748	291094	6.5	3	120	0.429	1052190	899905
6.5	3	150	0.263	881545	501402	6.5	3	130	0.418	1672737	1465603
6.5	3	160	0.257	1310666	817117	6.5	3	140	0.409	2227888	1950836
6.5	3	120	0.303	292918	135462	6.5	3	150	0.393	3192774	2827911
6.5	3	130	0.300	470316	256149	6.5	3	160	0.378	4131738	3658027
6.5	3	140	0.297	733516	447057						

The liquid composition has been corrected for 100–160 °C data because the CO_2 loading in the liquid phase differs significantly from that measured at room temperature, especially at high temperature and high loading.

The total pressure and CO_2 partial pressure of this blend were listed in Table 7. An empirical model was developed by regressing CO_2 partial pressure as a function of temperature and CO_2 loading in the liquid phase.

$$lnP_{CO2} = (42.4 \pm 1.2) + (-16.5 \pm 3.5)\alpha + \frac{(-13811 \pm 487)}{T} + (12433 \pm 1408)\frac{\alpha}{T} \quad (1)$$

The heat of absorption can be derived from the CO_2 partial pressure model according to the Gibbs-Helmholtz Equation.

$$\Delta H_{abs} = -R\frac{\partial lnP_{CO2}}{\partial \frac{1}{T}} = -R(-13811 + 12433\alpha) \quad (2)$$

The CO_2 loading at 40℃ when the CO_2 partial pressure is 0.5 kPa and 5.0 kPa can also be predicted from the CO_2 partial pressure model, which is exactly the definition of lean and rich loading. Then the CO_2 capacity of this blend can be obtained.

$$Capacity = mol\ CO_2/kg\ solvent = \frac{(\alpha_{rich} - \alpha_{lean}) \cdot mol\ alkalinity}{kg\ solvent} \quad (3)$$

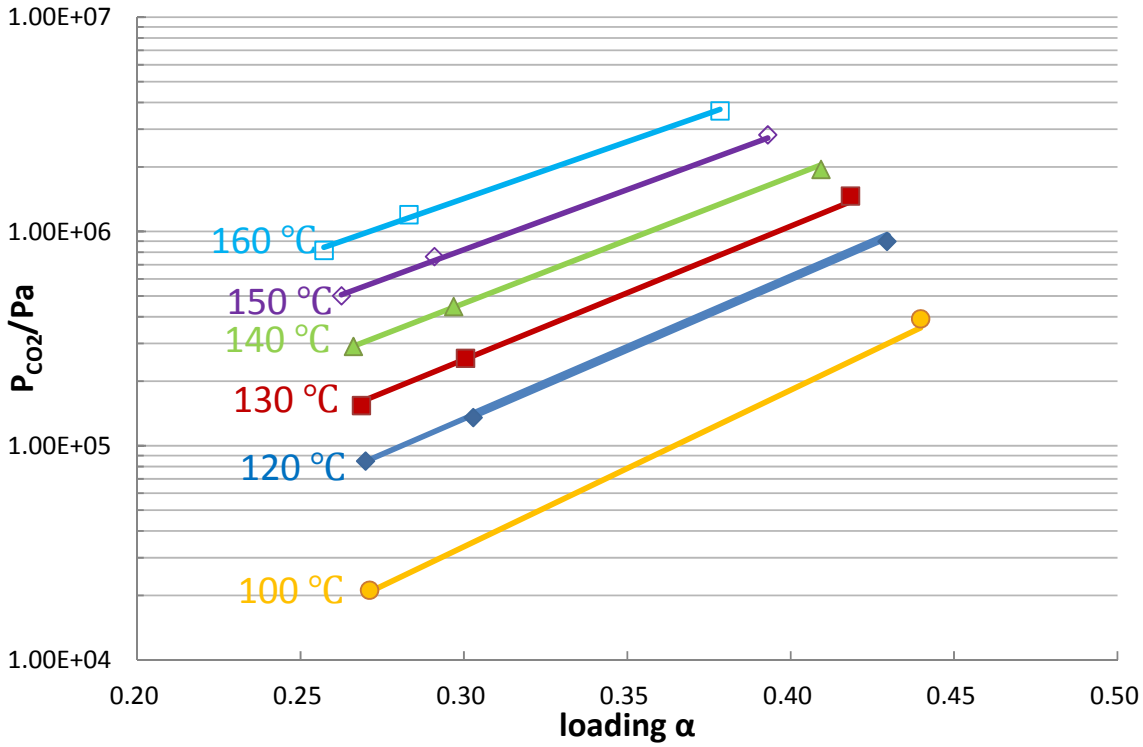

Figure 4: CO_2 solubility in aqueous 6.5 m PZ/3 m AMP [Points: experimental data. Lines: model (Equation 1)]

Figure 4 gives the CO_2 partial pressure from 100 to 160 °C at variable loading. The model fits the data well. The predicted CO_2 capacity, lean and rich loading and heat of absorption are listed in Table 8.

Table 8: Predicted properties of 6.5 m PZ/3 m AMP

CO_2 Capacity (mol CO_2/kg solvent)	0.87
Lean loading (mol CO_2/mol alkalinity)	0.342
Rich loading (mol CO_2/mol alkalinity)	0.441
$-\Delta H_{abs}$ @P_{CO2}=1.5 kPa (kJ/mol)	75

Table 9: Viscosity of loaded 6.5 m PZ/3 m AMP

T (℃)	25	40	60	80
CO_2 ldg (mol CO_2/mol alk)	**μ(cP)**	**μ(cP)**	**μ(cP)**	**μ(cP)**
0.448	37.96	22.05	11.29	6.95
0.305	27.54	15.35	7.53	4.57
0.271	29.83	15.82	8.93	4.83

The viscosity of 6.5 m PZ/3 m AMP at rich loading when the temperature is 40 °C is 22 cP, as listed in Table 9, while that of 8 m PZ at the same condition is 12 cP. But the viscosity is expected to be not much higher than 8 m PZ because high viscosity may reduce the mass transfer rate and affect the performance of heat exchanger.

5 m PZ/2.3 m AMP

To gain a lower viscosity than 6.5 m PZ/3 m AMP without largely decreasing the CO_2 capacity and heat of absorption, the 6.5 m PZ/3 m AMP blend was diluted by 80%. The new blend was obtained as 5 m PZ/2.3 m AMP.

Viscosity

The viscosity of this blend was shown in Table 10. When the temperature is 40 °C, the viscosity is 11.63 cP at rich loading, which is acceptable.

Solid Solubility Observation

No solids were observed even when the loading was 0.5 at 0 °C, which means that there may be no rich boundary in this blend. But the solids started being precipitated when the loading was lower than 0.3. The operating window is a little wider than 8 m PZ.

Table 10: Viscosity of loaded 5 m PZ/2.3 m AMP

T (°C)	40	60	80
CO_2 ldg (mol CO_2/mol alk)	μ(cP)	μ(cP)	μ(cP)
0.482	11.63		
0.387	10.37	5.79	3.93
0.302	8.53	4.85	3.19

CO_2 Solubility

The total pressure over the loaded blend was measured at 100–160 °C. The partial pressure of CO_2 was calculated by subtracting the partial pressure of N_2 and water from the pressure. P_{water} was assumed following the Raoult's Law and P_{amine} was neglected.

Table 11: Total pressure and CO_2 partial pressure in 5 m PZ/2.3 m AMP

PZ/AMP		Temp	CO_2 ldg	Pt	P_{CO2}	PZ/AMP		Temp	CO_2 ldg	Pt	P_{CO2}
m		C	mol CO_2/mol alk	Pa	Pa	m		C	mol CO_2/mol alk	Pa	Pa
5	2.3	120	0.297	285174	119411	5	2.3	100	0.436	346514	263921
5	2.3	130	0.295	447459	221991	5	2.3	110	0.432	529564	412828
5	2.3	140	0.291	679857	378283	5	2.3	120	0.427	822879	661143
5	2.3	150	0.286	1023079	625922	5	2.3	130	0.418	1254771	1034782
5	2.3	160	0.279	1489712	974074	5	2.3	140	0.410	1730410	1436163
5	2.3	120	0.382	530992	367829	5	2.3	150	0.397	2424693	2037185
5	2.3	130	0.376	838986	617056	5	2.3	100	0.494	750970	669627
5	2.3	140	0.369	1246288	949446	5	2.3	130	0.466	2118823	1902161
5	2.3	150	0.359	1820621	1429694	5	2.3	150	0.439	3619144	3237497
5	2.3	160	0.347	2527706	2020157						

The liquid composition has been corrected for 100–160 °C data because the CO_2 loading in the liquid phase differs significantly from that measured at room temperature, especially at high temperature and high loading.

The total pressure and CO_2 partial pressure of this blend from 100 to 160 °C are listed in Table 11.

Table 12: CO_2 partial pressure in 5 m PZ/2.3 m AMP from wetted wall column

PZ/AMP		Temp	CO_2 ldg	P_{CO2}	PZ/AMP		Temp	CO_2 ldg	P_{CO2}
m		C	mol CO_2/mol alk	Pa	m		C	mol CO_2/mol alk	Pa
5	2.3	40	0.310	325	5	2.3	40	0.380	2204
5	2.3	60	0.310	2742	5	2.3	60	0.380	11464
5	2.3	80	0.310	11146	5	2.3	80	0.380	49169
5	2.3	100	0.310	59912	5	2.3	20	0.420	676
5	2.3	20	0.350	93	5	2.3	40	0.420	5325
5	2.3	40	0.350	844	5	2.3	60	0.420	26451
5	2.3	60	0.350	5979	5	2.3	20	0.465	2963
5	2.3	80	0.350	27778	5	2.3	40	0.465	17617
5	2.3	20	0.380	229					

Together with the low temperature data from 20 to 100 °C, which are shown in Table 12, an empirical model was generated by regressing CO_2 partial pressure as a function of temperature and CO_2 loading in the liquid phase.

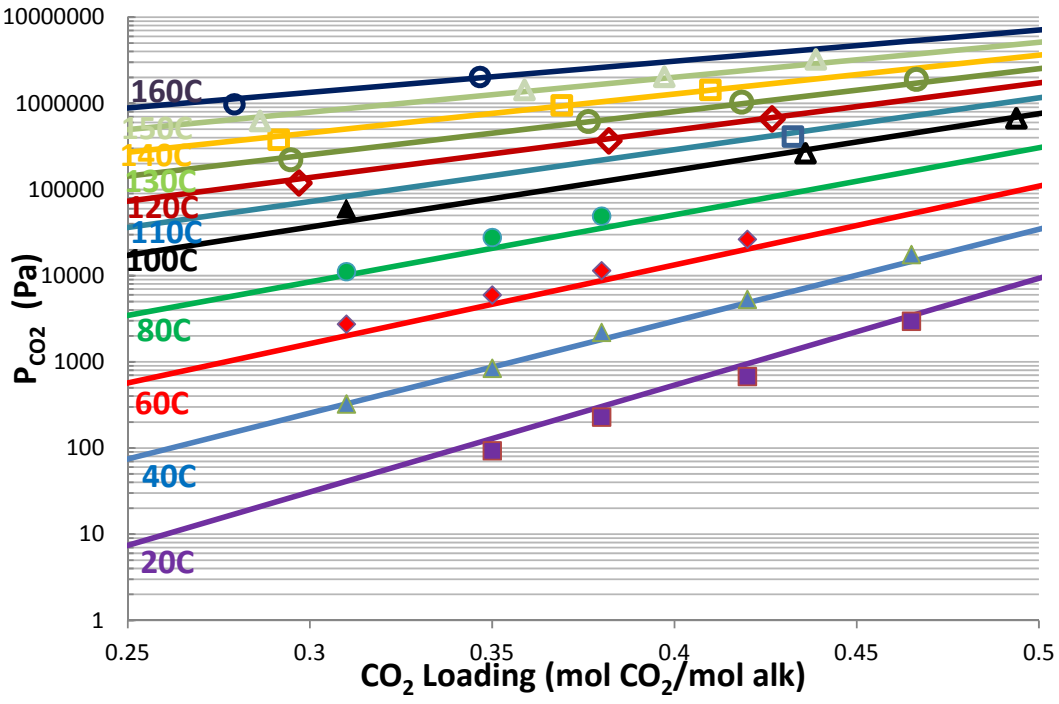

Figure 5: CO_2 Solubility for 5 m PZ/2.3 m AMP [Filled points: from wetted wall column. Empty points: from total pressure measurement. Lines: Equation 4]

$$lnP_{CO2} = (46.7 \pm 2.6) + (-34.0 \pm 6.7)\alpha + \frac{(-15186 \pm 958)}{T} + (18338 \pm 2500)\frac{\alpha}{T} \quad (4)$$

The heat of absorption can be derived from the CO_2 partial pressure model according to the Gibbs-Helmholtz Equation.

$$\Delta H_{abs} = -R\frac{\partial lnP_{CO2}}{\partial \frac{1}{T}} = -R(-15186 + 18338\alpha) \quad (5)$$

The CO_2 loading at 40 °C when the CO_2 partial pressure is 0.5 kPa and 5.0 kPa can also be predicted from the CO_2 partial pressure model, which is exactly the definition of lean and rich loading. Then the CO_2 capacity of this blend can be obtained by Equation 3.

The comparison of CO_2 capacity, loading range and heat of absorption between 5 m PZ/2.3 m AMP and 8 m PZ and 4.8 m AMP is shown in Table 13. This blend has, unexpectedly, a lower CO_2 capacity than other two solvents. Noticing that the delta loading of this blend is slightly greater than 8 m PZ, the loss of CO_2 capacity is because of the lower total alkalinity in this blend. The heat of absorption of the three solvents is comparable when the equilibrium partial pressure of CO_2 is 1.5 kPa.

Table 13: Comparison between 5 m PZ/2.3 m AMP, 8 m PZ, and 4.8 m AMP

	5 m PZ/2.3 m AMP	**8 m PZ**	**4.8 m AMP**
CO_2 Capacity (mol CO_2/kg solvent)	0.71	0.79	0.96
Lean loading (mol CO_2/mol alkalinity)	0.328	0.31	0.27
Rich loading (mol CO_2/mol alkalinity)	0.422	0.39	0.56
$-\Delta H_{abs}$ @P_{CO2}=1.5 kPa (kJ/mol)	69	70	73

CO_2 mass transfer rates

As a complement to Table 12, Table 14 lists the CO_2 mass transfer rates in 5 m PZ/2.3 m AMP.

The detailed wetted wall column results are included in the Appendix.

Figure 6 compares the CO_2 mass transfer rates between this blend and 8 m PZ and 4.8 m AMP (Chen, 2011). The rates of this blend are always much higher than those of 4.8 m AMP, but a little bit lower than those of 8 m PZ when the CO_2 loading is low. As the CO_2 loading gets richer, the difference of rates between this blend and 8 m PZ becomes smaller, and this blend transfers CO_2 faster than 8 m PZ after a certain loading point.

Table 14: k_g' Measured for 5 m PZ/2.3 m AMP

CO_2 loading	Temperature	k_g'
mol CO_2/mol alk	°C	$\times 10^7$ (mol/s·Pa·m^2)
0.350	20	12.90
0.380	20	9.53
0.420	20	5.19
0.465	20	2.62
0.310	40	18.90
0.350	40	12.60
0.380	40	10.00
0.420	40	5.62
0.465	40	2.36
0.310	60	17.10
0.350	60	13.00
0.380	60	9.16
0.420	60	4.56
0.310	80	18.20
0.350	80	10.10
0.380	80	5.69
0.310	100	6.59

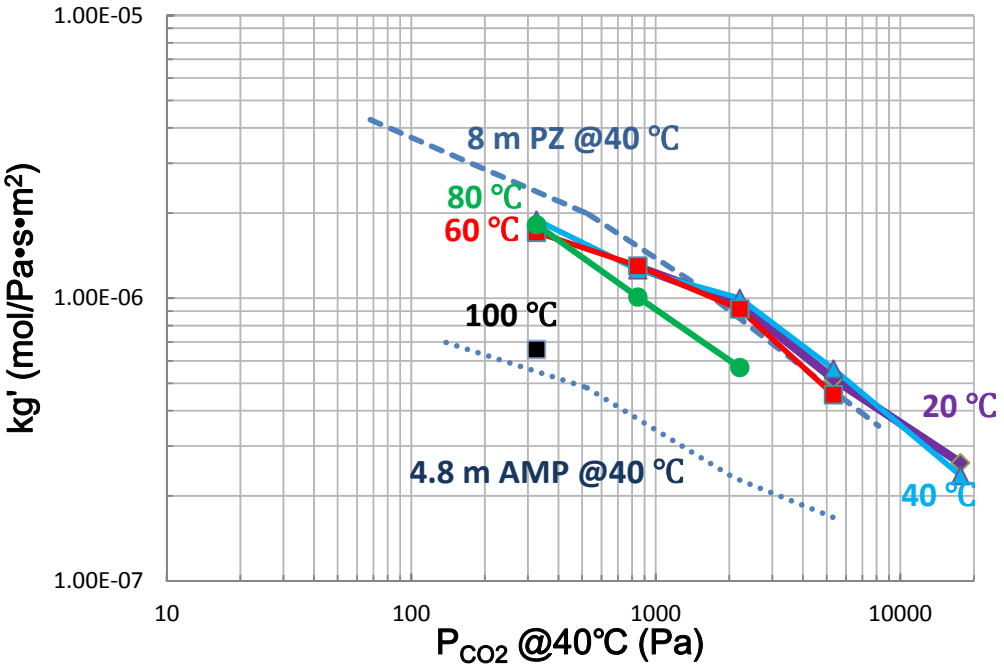

Figure 6: CO_2 Liquid Phase Mass Transfer Coefficient (k_g') in 5 m PZ/2.3 m AMP Volatility

Partial pressures for amine, water, and carbon dioxide are calculated using the concentration readings from the FTIR multiplied by atmospheric pressure.

$$P_{amine} = P_{atm} \times \frac{\text{amine [ppm]}}{1{,}000{,}000}$$

$$P_{H_2O} = P_{atm} \times \frac{H_2O \text{ [ppm]}}{1{,}000{,}000}$$

$$P_{CO_2} = P_{atm} \times \frac{CO_2 \text{ [ppm]}}{1{,}000{,}000}$$

After calculation, the volatility and CO_2 solubility for unloaded and loaded 5 m PZ/2.3 m AMP are shown in Table 15.

Table 15: Volatility and CO_2 solubility for unloaded and loaded 5 m PZ/2.3 m AMP

PZ/AMP		T	CO_2 ldg	P_{PZ}	P_{AMP}	P_{H2O}	P_{CO2}
m		C	mol/mol alk	Pa	Pa	Pa	Pa
5	2.3	40.1	0	4.78	12.15	5911	0
5	2.3	45	0	5.21	13.80	7130	0
5	2.3	50	0	8.46	21.06	9449	0
5	2.3	55	0	13.52	31.06	12203	0
5	2.3	60	0	15.46	40.17	15378	0
5	2.3	40	0.299	0.60	5.71	5723	244
5	2.3	45	0.299	0.65	8.24	7310	407
5	2.3	50.1	0.299	1.23	12.57	9757	677
5	2.3	55.1	0.299	1.90	17.65	12568	914
5	2.3	60	0.299	2.69	23.44	15822	1338
5	2.3	65	0.299	4.14	34.35	20050	2190

Figures 7–8 demonstrate that AMP is much more volatile than PZ. The volatility of PZ and AMP both decrease when CO_2 is loaded into the solution because of the decreasing concentration of free amine. But the volatility of PZ decreases faster than that of AMP, which suggests that CO_2 first reacts with PZ.

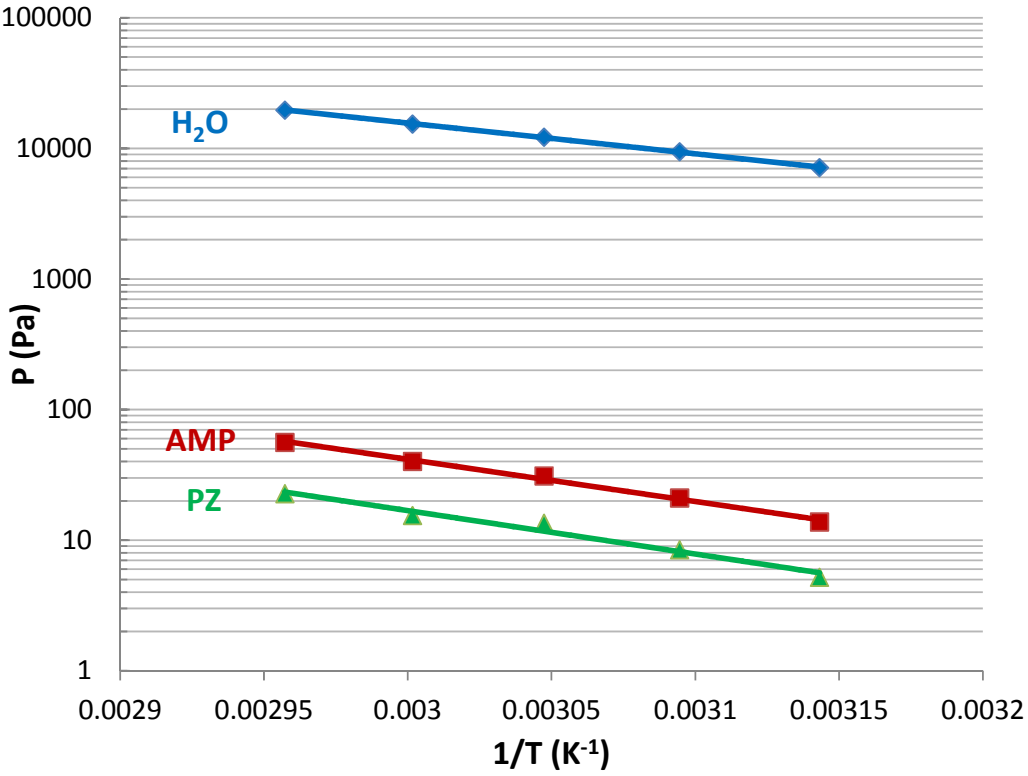

Figure 7: Amine volatility in aqueous unloaded 5 m PZ/2.3 m AMP

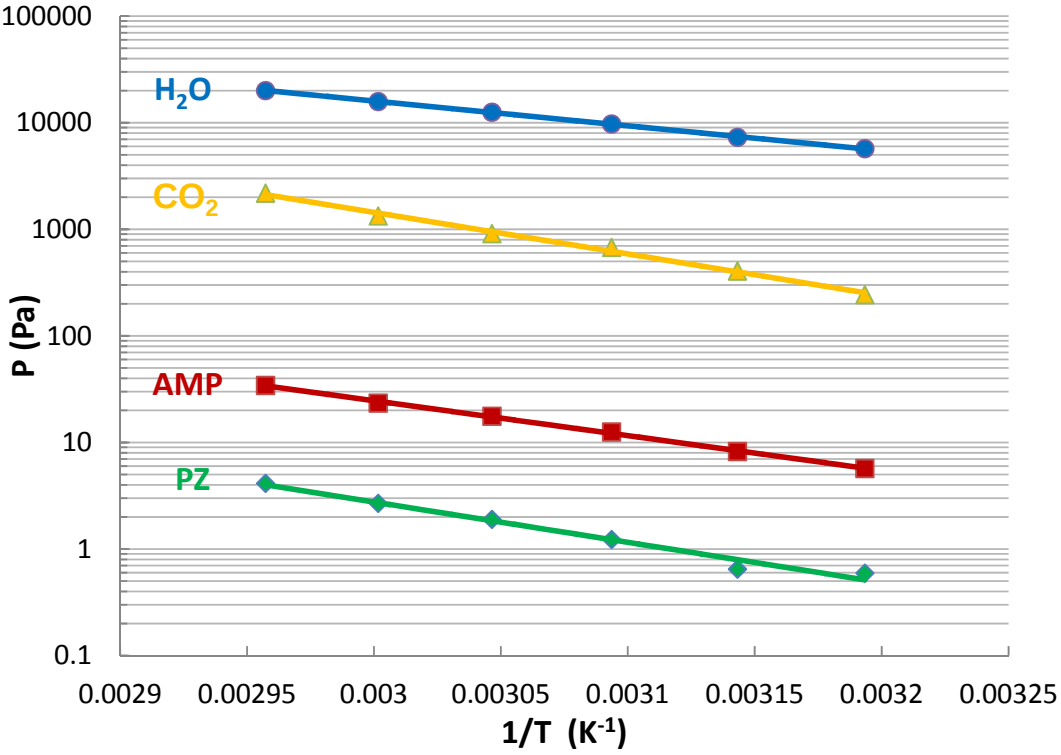

Figure 8: Amine volatility in aqueous 5 m PZ/2.3 m AMP when α = 0.3

Conclusions

1. 6 m PZ/4 m AMP is not an desirable blend owing to its narrow operating window.
2. Even though 6.5 m PZ/3 m AMP has a similar operating window to 8 m PZ, its nearly twice times viscosity, compared with 8 m PZ, limits its application.
3. As for aqueous 5 m PZ/2.3 m AMP, solids are precipitated when the loading is lower than 0.3, but no solids are observed when CO_2 is kept loaded into this blend until the loading reaches 0.5.
4. The performance of aqueous 5 m PZ/2.3 m AMP is similar to 8 m PZ in terms of viscosity, heat of absorption, lean and rich loading departure. Due to lower total alkalinity, the CO_2 capacity is lower.
5. The mass transfer rates in 5 m PZ/2.3 m AMP are higher than those in 8 m PZ when the loading is rich.
6. The disadvantage of this blend is that more solvent will be lost in application because of its high volatility.

Future Work

The heat capacity and NMR speciation for 5 m PZ/2.3 m AMP will be measured next. To gain the knowledge of the degradation products, the thermal degradation experiments will be performed.

The pKa value as a function of temperature will be fitted in Aspen Plus® to generate the AMP/$AMPH^+$ thermodynamic model. Then the AMP/CO_2/H_2O thermodynamic model will be built.

References

Chen X. *Carbon Dioxide Thermodynamics, Kinetics, and Mass Transfer in Aqueous Piperazine Derivatives and Other Amines.* The University of Texas at Austin. Ph.D. Dissertation. 2011.

Chen X, Closmann FB, Rochelle GT. “Accurate screening of amine by the wetted wall column”. *Energy Proc.* 2011;4:101–108.

Chen Y-R, Caparanga AR, Soriano AN, Li M-H. “Liquid heat capacity of the solvent system (piperazine + 2-amino-2-methyl-1-propanol + water)”. *J Chem Thermodynamics*. 2010;42:518–523.

Choi W-J, Cho K-C, Shim J-G, Hwang H-R, Park S-W, Oh K-J. “Removal of carbon dioxide by absorption into blended amines: kinetics of absorption into aqueous AMP/HMDA, AMP/MDEA, AMP/piperazine solutions”. *Green Chem*. 2007;9:594–598.

Dash SK, Samanta AN, Bandyopadhyay SS. “Solubility of carbon dioxide in aqueous solution of 2-amino-2-methyl-1-propanol and piperazine”. *Fluid Phase Equil*. 2011;307:166–174.

Dash SK, Samanta A, Samanta AN, Bandyopadhyay SS. “Absorption of carbon dioxide in piperazine activated concentrated aqueous 2-amino-2-methyl-1-propanol solvent”. *Chem Eng Sci*. 2011;66:3223–3233.

Freeman SA, Dugas RE, Van Wagener DH, Nguyen T, Rochelle GT. "Carbon dioxide capture with concentrated, aqueous piperazine". *IJGGC.* 2010;4:119–124.

Freeman SA. *Thermal Degradation and Oxidation of Aqueous Piperazine for Carbon Dioxide Capture.* The University of Texas at Austin. Ph.D. Dissertation. 2011.

Hilliard MD. *A Predictive Thermodynamic Model for an Aqueous Blend of Potassium Carbonate, Piperazine, and Monoethanolamine for Carbon Dioxide Capture from Flue Gas.* The University of Texas at Austin. Ph.D. Dissertation. 2008.

Murshid G, Shariff AM, Keong LK, Bustam MA. “Physical properties of aqueous solutions of piperazine and (2-amino-2-methyl-1-propanol + piperazine) from (298.15 to 333.15) K”. *J Chem Eng Data*. 2011;56:2660–2663.

Paul S, Mandal B. “Density and viscosity of aqueous solutions of (N-methylkiethanolamine + piperazine) and (2-amino-2-methyl-1-propanol + piperazine) from (288 to 333) K”. *J Chem Eng Data*. 2006;51:1808–1810,

Rochelle GT, et al. "CO_2 Capture by Aqueous Absorption, Second Quarterly Progress Reports 2010." Luminant Carbon Management Program. The University of Texas at Austin. 2010.

Samanta A, Bandyopadhyay SS. “Density and viscosity of aqueous solutions of piperazine and (2-amino-2-methyl-1-propanol + piperazine) from 298 to 333 K”. *J Chem Eng Data*. 2006;51:467–470.

Samanta A, Bandyopadhyay SS. “Absorption of carbon dioxide into aqueous solutions of piperazine activated 2-amino-2-methyl-1-propanol”. *Chem Eng Sci*. 2009;64:1185–1194.

Seo DJ, Hong WH. “Effect of piperazine on the kinetics of carbon dioxide with aqueous solutions of 2-amino-2-methyl-1-propanol”. *Ind Eng Chem Res*. 2000;39:2062–2067.

Sun W-C, Yong C-B, Li M-H. “Kinetics of the absorption of carbon dioxide into mixed aqueous solutions of 2-amino-2-methyl-1-propanol and piperazine”. *Chem Eng Sci*. 2005;60:503–516.

Yang Z-Y, Soriano AN, Caparanga AR, Li M-H. “Equilibrium solubility of carbon dioxide in (2-amino-2-methyl-1-propanol + piperazine + water)”. *J Chem Thermodynamics*. 2010;42:659–665.

Appendix

Table A-1: Detailed Wetted Wall Column Data for 5 m PZ/2.3 m AMP

PZ/AMP		CO_2 ldg	P^*_{CO2}	Temp	Pressure	Gas_{Dry}	Gas_{Wet}	$P_{CO2in, dry}$	$P_{CO2in, wet}$	$P_{CO2out, dry}$	$P_{CO2out, wet}$	CO_2 flux	KG	kg	KG/kg	kg'
m		mol CO_2/mol alk	Pa	C	psig	Std L/min	Std L/min	Pa	Pa	Pa	Pa	mol/s cm^2	mol/s Pa cm^2	mol/s Pa cm^2		mol/s Pa cm2
5	2.3	0.309	325	40	20	5	5.16	0.00	0.00	93.04	90.17	-3.76E-08	1.34E-10	4.57E-10	0.292	1.89E-10
								62.90	60.96	138.01	133.75	-3.03E-08				
								109.31	105.93	170.78	165.51	-2.48E-08				
								475.49	460.82	432.44	419.10	1.74E-08				
								527.40	511.12	477.65	462.91	2.01E-08				
								570.21	552.61	507.07	491.42	2.55E-08				
5	2.3	0.309	2742	60	20	5	5.45	0.00	0.00	755.82	692.83	-3.05E-07	1.27E-10	4.83E-10	0.262	1.71E-10
								557.29	510.85	1131.33	1037.05	-2.32E-07				
								1112.20	1019.51	1604.91	1471.17	-1.99E-07				
								3274.40	3001.53	3233.74	2964.26	1.64E-08				
								3826.91	3508.00	3590.12	3290.94	9.56E-08				
5	2.3	0.309	11146	80	40	5	5.72	0.00	0.00	4098.42	3583.47	-1.05E-06	1.16E-10	3.21E-10	0.361	1.82E-10
								4441.52	3883.47	7065.72	6177.95	-6.72E-07				
								8019.63	7012.00	9490.08	8297.70	-3.76E-07				
								12732.62	11132.83	12921.14	11297.66	-4.83E-08				
								23704.46	20726.12	20575.03	17989.89	8.01E-07				
								27474.85	24022.78	22837.27	19967.89	1.19E-06				
								31132.13	27220.55	24571.65	21484.35	1.68E-06				

Table A-2: Detailed Wetted Wall Column Data for 5 m PZ/2.3 m AMP

PZ/AMP		CO_2 ldg	P^*_{CO2}	Temp	Pressure	Gas_{Dry}	Gas_{Wet}	$P_{CO2in, dry}$	$P_{CO2in, wet}$	$P_{CO2out, dry}$	$P_{CO2out, wet}$	CO_2 flux	KG	kg	KG/kg	kg'
m		mol CO_2/mol alk	Pa	C	psig	Std L/min	Std L/min	Pa	Pa	Pa	Pa	mol/s cm^2	mol/s Pa cm^2	mol/s Pa cm^2		mol/s Pa cm2
5	2.3	0.309	59912	100	60	5	6.22	0.00	0.00	16250.13	13052.47	-3.05E-06	5.23E-11	2.54E-10	0.206	6.59E-11
								25981.67	20869.07	33859.59	27196.79	-1.48E-06				
								50233.30	40348.52	55330.77	44442.92	-9.56E-07				
								89005.00	71490.82	86533.49	69505.65	4.63E-07				
								95492.69	76701.88	91270.54	73310.56	7.92E-07				
								102598.26	82409.24	92403.31	74220.43	1.91E-06				
5	2.3	0.351	93	20	20	5	5.05	0.00	0.00	21.29	21.08	-8.59E-09	1.00E-10	4.46E-10	0.224	1.29E-10
								22.00	21.79	37.55	37.18	-6.27E-09				
								34.44	34.11	47.84	47.37	-5.41E-09				
								59.56	58.97	65.78	65.13	-2.51E-09				
								141.84	140.45	130.83	129.55	4.44E-09				
								191.11	189.24	170.78	169.11	8.21E-09				
5	2.3	0.351	844	40	20	5	5.16	0.00	0.00	186.32	180.57	-7.52E-08	9.85E-11	4.57E-10	0.215	1.26E-10
								202.59	196.34	324.81	314.79	-4.93E-08				
								385.80	373.90	486.50	471.48	-4.06E-08				
								758.21	734.81	793.61	769.12	-1.43E-08				
								1124.63	1089.93	1098.32	1064.43	1.06E-08				
								1486.04	1440.18	1344.92	1303.42	5.70E-08				
								1832.85	1776.29	1619.98	1569.99	8.59E-08				

Table A-3: Detailed Wetted Wall Column Data for 5 m PZ/2.3 m AMP

PZ/AMP		CO_2 ldg	P^*_{CO2}	Temp	Pressure	Gas_{Dry}	Gas_{Wet}	$P_{CO2in, dry}$	$P_{CO2in, wet}$	$P_{CO2out, dry}$	$P_{CO2out, wet}$	CO_2 flux	KG	kg	KG/kg	kg'
m		mol CO_2/mol alk	Pa	C	psig	Std L/min	Std L/min	Pa	Pa	Pa	Pa	mol/s cm^2	mol/s Pa cm^2	mol/s Pa cm^2		mol/s Pa cm2
5	2.3	0.351	5979	60	40	5	5.28	0.00	0.00	1760.77	1667.69	-4.51E-07	9.06E-11	2.98E-10	0.304	1.30E-10
								1474.22	1396.29	2846.65	2696.16	-3.51E-07				
								2933.37	2778.29	3940.06	3731.77	-2.58E-07				
								9033.86	8556.29	8317.49	7877.79	1.83E-07				
								10391.20	9841.88	9184.68	8699.13	3.09E-07				
								11823.95	11198.88	10240.39	9699.03	4.05E-07				
5	2.3	0.351	27778	80	40	5	5.72	0.00	0.00	8095.03	7077.94	-2.07E-06	7.70E-11	3.21E-10	0.240	1.01E-10
								6786.71	5933.99	11903.13	10407.56	-1.31E-06				
								12732.62	11132.83	17143.98	14989.93	-1.13E-06				
								37466.39	32758.94	36222.16	31671.04	3.19E-07				
								49870.99	43604.96	44818.66	39187.43	1.29E-06				
								63142.77	55209.21	56582.29	49473.02	1.68E-06				
5	2.3	0.381	229	20	20	5	5.05	0.00	0.00	43.05	42.63	-1.74E-08	7.85E-11	4.46E-10	0.176	9.53E-11
								59.56	58.97	88.26	87.40	-1.16E-08				
								116.00	114.87	134.90	133.58	-7.63E-09				
								328.40	325.19	308.78	305.77	7.92E-09				
								378.63	374.93	354.23	350.77	9.85E-09				
								429.09	424.90	395.61	391.74	1.35E-08				

Table A-4: Detailed Wetted Wall Column Data for 5 m PZ/2.3 m AMP

PZ/AMP		CO_2 ldg	P^*_{CO2}	Temp	Pressure	Gas_{Dry}	Gas_{Wet}	$P_{CO2in, dry}$	$P_{CO2in, wet}$	$P_{CO2out, dry}$	$P_{CO2out, wet}$	CO_2 flux	KG	kg	KG/kg	kg'
m		mol CO_2/mol alk	Pa	C	psig	Std L/min	Std L/min	Pa	Pa	Pa	Pa	mol/s cm^2	mol/s Pa cm^2	mol/s Pa cm^2		mol/s Pa cm2
5	2.3	0.381	2204	40	20	5	5.16	0.00	0.00	406.61	394.06	-1.64E-07	8.23E-11	4.57E-10	0.180	1.00E-10
								727.11	704.68	1002.17	971.25	-1.11E-07				
								1449.44	1404.71	1583.39	1534.52	-5.41E-08				
								3011.30	2918.38	2906.06	2816.38	4.25E-08				
								3736.03	3620.73	3501.63	3393.57	9.46E-08				
								4470.31	4332.36	4039.79	3915.12	1.74E-07				
5	2.3	0.381	11464	60	40	5	5.28	0.00	0.00	2752.39	2606.88	-7.05E-07	7.01E-11	2.98E-10	0.235	9.16E-11
								2925.82	2771.15	4905.28	4645.97	-5.07E-07				
								6021.32	5703.00	7491.77	7095.72	-3.76E-07				
								17634.13	16701.91	16616.12	15737.72	2.61E-07				
								20537.33	19451.63	18576.73	17594.68	5.02E-07				
								23440.53	22201.36	20688.15	19594.48	7.05E-07				
5	2.3	0.381	49169	80	50	5	5.59	0.00	0.00	11265.15	10068.51	-2.44E-06	4.69E-11	2.67E-10	0.176	5.69E-11
								12915.23	11543.31	19337.17	17283.07	-1.39E-06				
								25268.54	22584.38	29282.25	26171.74	-8.69E-07				
								75796.70	67745.18	72987.10	65234.03	6.08E-07				
								82129.44	73405.23	78338.71	70017.17	8.21E-07				
								88997.35	79543.59	81817.26	73126.21	1.55E-06				

Table A-5: Detailed Wetted Wall Column Data for 5 m PZ/2.3 m AMP

PZ/AMP		CO_2 ldg	P^*_{CO2}	Temp	Pressure	Gas_{Dry}	Gas_{Wet}	$P_{CO2in, dry}$	$P_{CO2in, wet}$	$P_{CO2out, dry}$	$P_{CO2out, wet}$	CO_2 flux	KG	kg	KG/kg	kg'
m		mol CO_2/mol alk	Pa	C	psig	Std L/min	Std L/min	Pa	Pa	Pa	Pa	mol/s cm^2	mol/s Pa cm^2	mol/s Pa cm^2		mol/s Pa cm2
5	2.3	0.420	676	20	20	5	5.05	0.00	0.00	75.58	74.84	-3.05E-08	4.65E-11	4.46E-10	0.104	5.19E-11
								107.39	106.34	168.62	166.98	-2.47E-08				
								200.20	198.24	250.90	248.45	-2.05E-08				
								960.08	950.70	929.94	920.85	1.22E-08				
								1136.35	1125.25	1086.84	1076.22	2.00E-08				
								1314.55	1301.70	1247.57	1235.38	2.70E-08				
5	2.3	0.420	5325	40	20	5	5.16	0.00	0.00	662.53	642.09	-2.67E-07	5.01E-11	4.57E-10	0.109	5.62E-11
								734.29	711.63	1260.49	1221.59	-2.12E-07				
								1475.75	1430.21	1896.71	1838.18	-1.70E-07				
								8911.93	8636.91	8529.24	8266.03	1.54E-07				
								9581.64	9285.95	9127.19	8845.53	1.83E-07				
								10299.18	9981.36	9749.06	9448.21	2.22E-07				
5	2.3	0.420	26451	60	40	5	5.28	0.00	0.00	3989.08	3778.20	-1.02E-06	3.96E-11	2.98E-10	0.133	4.56E-11
								6809.33	6449.36	9448.60	8949.11	-6.76E-07				
								12841.96	12163.07	14727.15	13948.61	-4.83E-07				
								24982.62	23661.93	25397.37	24054.75	-1.06E-07				
								43570.66	41267.32	41836.28	39624.62	4.44E-07				
								50168.85	47516.70	47303.35	44802.68	7.34E-07				
								62988.18	59658.34	57860.45	54801.68	1.31E-06				

Table A-6: Detailed Wetted Wall Column Data for 5 m PZ/2.3 m AMP

PZ/AMP		CO_2 ldg	P^*_{CO2}	Temp	Pressure	Gas_{Dry}	Gas_{Wet}	$P_{CO2in, dry}$	$P_{CO2in, wet}$	$P_{CO2out, dry}$	$P_{CO2out, wet}$	CO_2 flux	KG	kg	KG/kg	kg'
m		mol CO_2/mol alk	Pa	C	psig	Std L/min	Std L/min	Pa	Pa	Pa	Pa	mol/s cm^2	mol/s Pa cm^2	mol/s Pa cm^2		mol/s Pa cm2
5	2.3	0.449	2963	20	20	5	5.05	0.00	0.00	196.13	194.21	-7.92E-08	2.48E-11	4.46E-10	0.056	2.62E-11
								751.03	743.69	875.41	866.85	-5.02E-08				
								1112.20	1101.33	1219.83	1207.91	-4.34E-08				
								2190.91	2169.50	2222.00	2200.29	-1.25E-08				
								5895.84	5838.23	5728.41	5672.44	6.76E-08				
								6709.06	6643.51	6493.80	6430.35	8.69E-08				
								7450.52	7377.73	7187.42	7117.20	1.06E-07				
5	2.3	0.449	17617	40	40	5	5.10	0.00	0.00	1564.71	1534.08	-4.01E-07	2.18E-11	2.87E-10	0.076	2.36E-11
								6692.45	6561.43	7484.23	7337.72	-2.03E-07				
								10085.80	9888.36	10651.36	10442.85	-1.45E-07				
								24828.04	24342.00	24337.89	23861.44	1.25E-07				
								30898.37	30293.50	29842.66	29258.45	2.70E-07				
								37421.15	36688.58	35875.29	35172.99	3.96E-07				

Modeling MDEA/PZ Thermodynamics, Hydraulics, and Kinetics

Quarterly Report for October 1 – December 31, 2011

by Peter Frailie

Supported by the Luminant Carbon Management Program

Department of Chemical Engineering

The University of Texas at Austin

January 31, 2012

Abstract

The goal of this study is to evaluate the performance of an absorber/stripper operation that utilizes MDEA/PZ. A thermodynamic, hydraulic, and kinetic model for 8 m PZ, 7 m MDEA/2 m PZ, and 5 m MDEA/5 m PZ has been regressed in Aspen Plus® (the Fawkes model). This model has already been applied to quantify the potential energy benefits of intercooling and a colder absorber. It has been concluded that intercooling always improves solvent capacity, and a colder absorber has the potential to improve solvent capacity, especially for the 7 m MDEA/2 m PZ blend. Stripper models have been constructed to compare the energy performance of a simple stripper, two-stage flash, and interheated stripper. The Aspen Plus® thermodynamic model has been modified to include recently acquired experimental data and to generate more accurate heat capacity and CO_2 solubility predictions. The goal for the next quarter is to continue to regress the thermodynamics of MDEA/PZ and to incorporate the kinetics for all solvents relevant to this study.

Introduction

The removal of CO_2 from process gases using alkanolamine absorption/stripping has been extensively studied for several solvents and solvent blends. An advantage of using blends is that the addition of certain solvents can enhance the overall performance of the CO_2 removal system. A disadvantage of blends is that they are very complex compared to a single solvent, thus making them much more difficult to model.

This study will focus on a blended amine solvent containing piperazine (PZ) and methyldiethanolamine (MDEA). Previous studies have shown that this particular blend has the potential to combine the high capacity of MDEA with the attractive kinetics of PZ (Bishnoi, 2000). These studies have supplied a rudimentary Aspen Plus®-based model for an absorber with MDEA/PZ. The report also makes the recommendation that more kinetic and thermodynamic data must be acquired for the MDEA/PZ blend before the model can be significantly improved. One of the major goals of this study will be to improve the supplied Aspen Plus® absorber model with up-to-date thermodynamic and kinetic data. Another major goal will be to make improvements to the MDEA and PZ thermodynamic models, which should simplify the construction of the blended amine model.

Methods and Discussion

A thermodynamic, hydraulic, and kinetic model for 8 m PZ, 7 m MDEA/2 m PZ, and 5 m MDEA/5 m PZ has been regressed in Aspen Plus® (the Fawkes model). During the past quarter the MDEA and PZ models were expanded to include experimental data over wider loading and amine concentration ranges.

CO_2 Solubility in MDEA at High Loadings

This study primarily focuses on the removal of CO_2 from the flue gas of coal-fired power plants. Because CO_2 is typically available at 40 °C and 12 kPa in this application, emphasis has been placed on fitting experimental data in this general operating range. However, MDEA is widely used in industry to remove CO_2 from process gases containing much higher partial pressures of CO_2. This quarter the MDEA model developed by Nguyen during Q2 and Q3 of 2011 was expanded to include high pressure CO_2 solubility data for 20 wt %, 25 wt %, and 50 wt % MDEA solutions from 25–120 °C. Figures 1, 2, and 3, respectively, compare experimental data and model predictions for these three solvents.

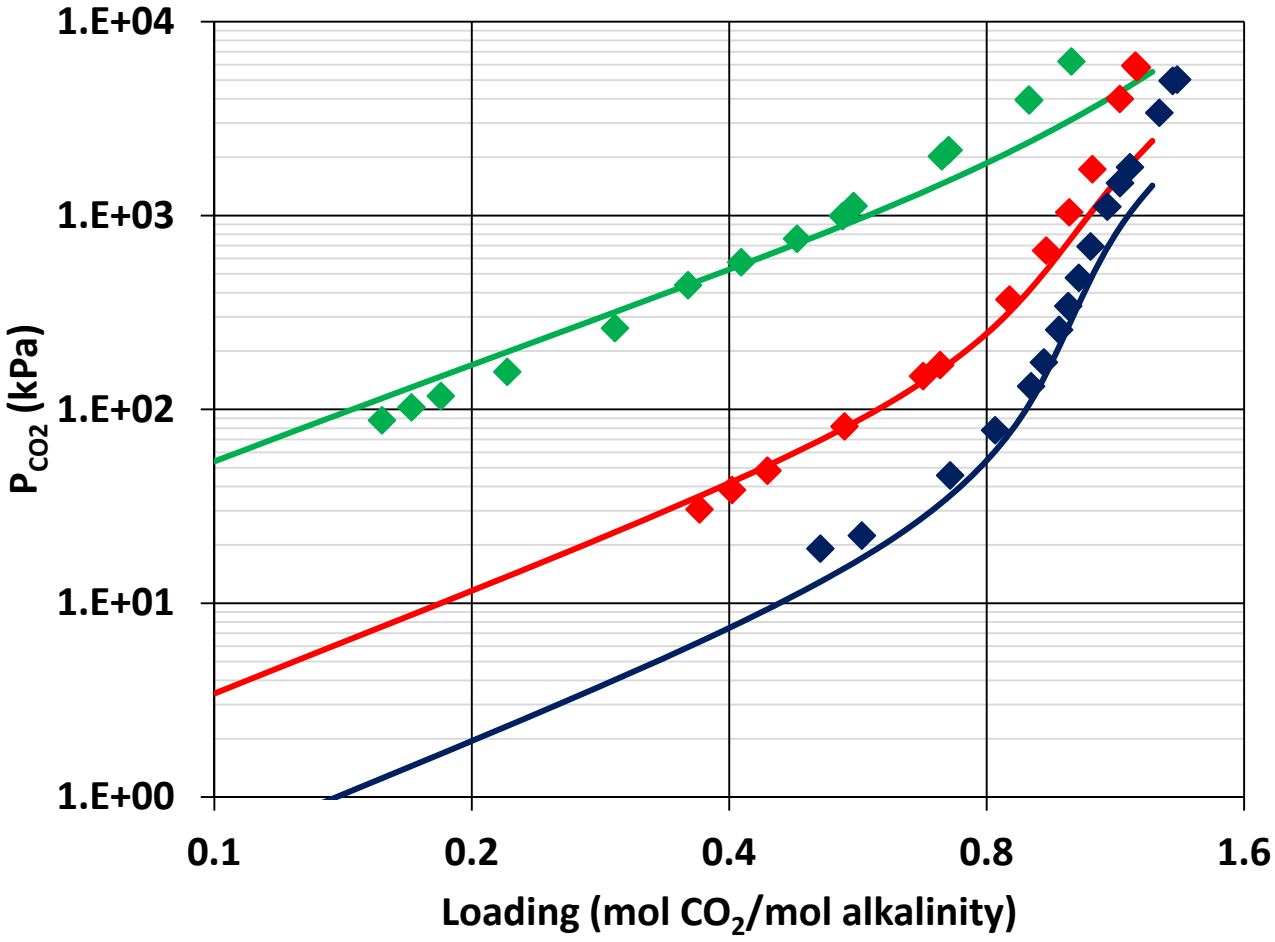

Figure 1: Partial pressure of CO_2 as a function of loading for 20 wt % MDEA (Maddox, 1987) from 38–116 °C.

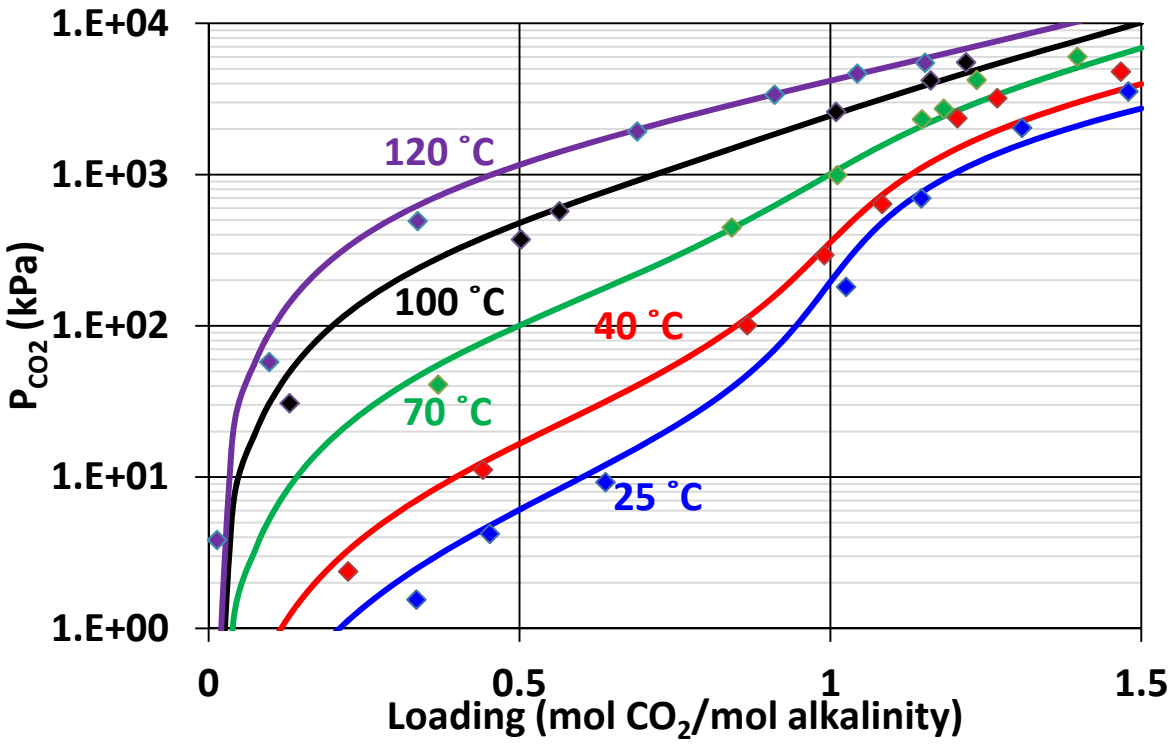

Figure 2: Partial pressure of CO_2 as a function of loading for 25 wt % MDEA (Jou, 1982) from 25–120 ^{o}C.

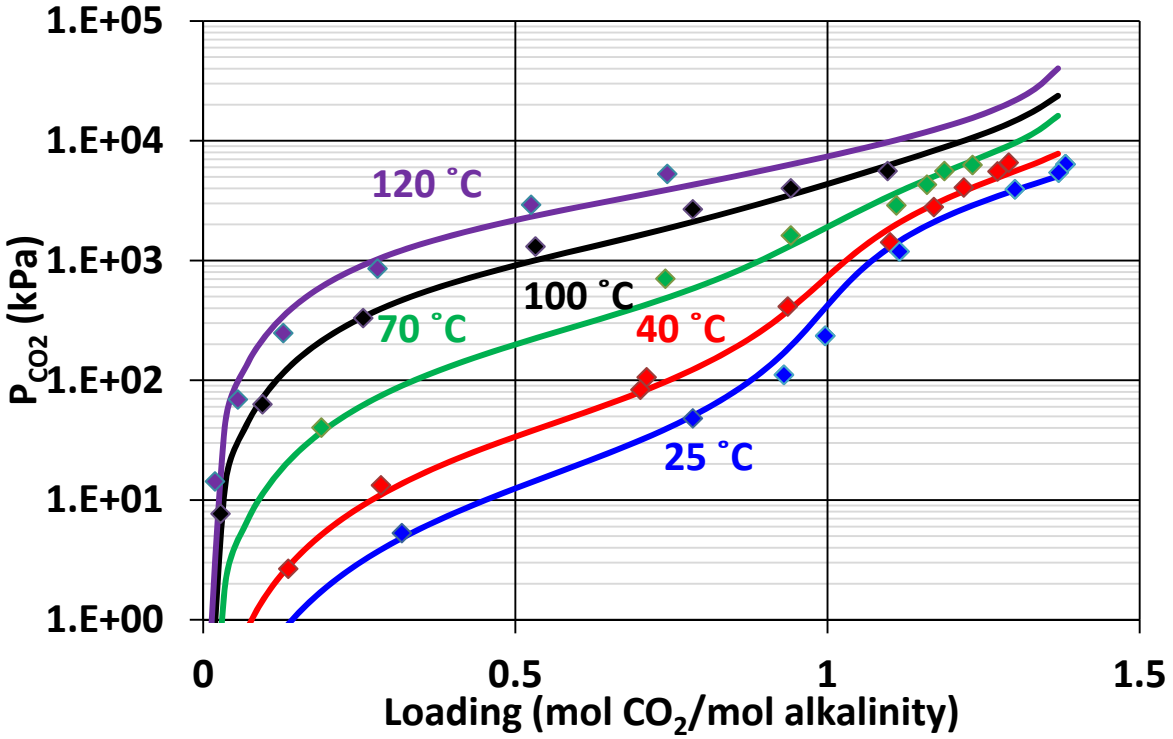

Figure 3: Partial pressure of CO_2 as a function of loading for 50 wt % MDEA (Jou, 1982) from 25–120 ^{o}C.

The parameters used to fit the data in Figures 1–3 are the same as those used to fit the activity coefficient of CO_2. At higher loadings the concentration of free CO_2 is significant enough to influence the solubility of CO_2. Table 1 is a summary of the parameters used to fit the high loading CO_2 solubility data.

Table 1: List of parameters used to fit high loading CO_2 solubility data in Figures 1–3.

Parameter	Species
GMELCC	$CO_2/(MDEAH^+/HCO_3^-)$
GMELCC	$(MDEAH^+/HCO_3^-)/CO_2$
GMELCD	$CO_2/(MDEAH^+/HCO_3^-)$
GMELCD	$(MDEAH^+/HCO_3^-)/CO_2$

The GMELCC and GMELCD parameters correspond to the A and B terms in Equation 1.

$$\tau_{m/ca} = A_{m/ca} + \frac{B_{m/ca}}{T(K)} \quad (1)$$

The τ parameters are used for the calculation of activity coefficients in the electrolyte-NRTL model. The GMELCC and GMELCD parameters for the $CO_2/(MDEAH^+/CO_3^{2-})$ interaction were omitted from the regression because the concentration of CO_3^{2-} at high loading (i.e., low pH) conditions is insignificant.

PZ Thermodynamic Model

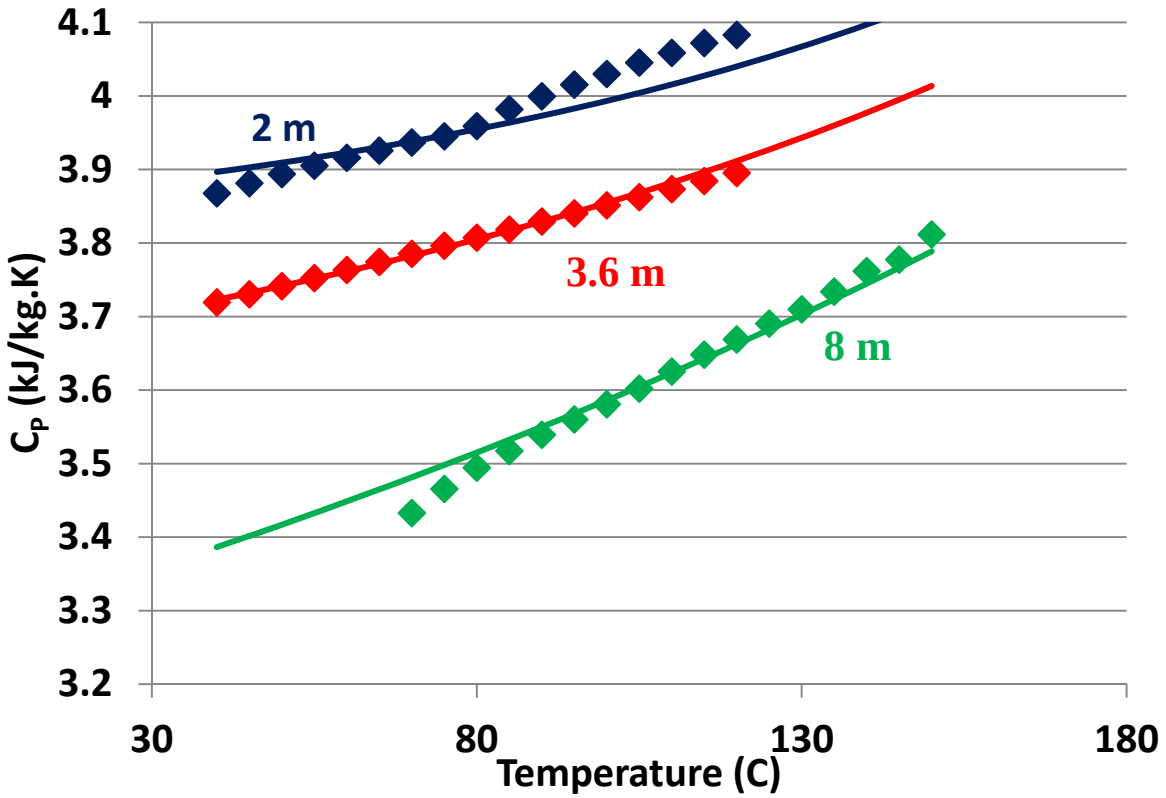

Figure 4: Experimental data (points) and Aspen Plus® predictions (lines) for heat capacity of unloaded 2, 3.6, and 8 m PZ from 40–150 °C.

The Fawkes version of the PZ thermodynamic model was modified to generate more accurate heat capacity and CO_2 solubility predictions. Earlier versions of Aspen Plus® did not calculate the heat capacity of loaded solutions in a thermodynamically consistent way during data regressions. The heat of reaction was omitted when calculating dH/dT. This has been corrected in Aspen Plus® v7.3. Figure 4 compares experimental data and Aspen Plus® predictions of heat capacity as a function of temperature for unloaded 2, 3.6, and 8 m PZ. Figure 5 compares experimental data and model predictions for unloaded amine volatility data for 2, 5, 8, and 10 m PZ from 40–70 °C. A total of 7 parameters were adjusted to regress the PZ/H_2O system.

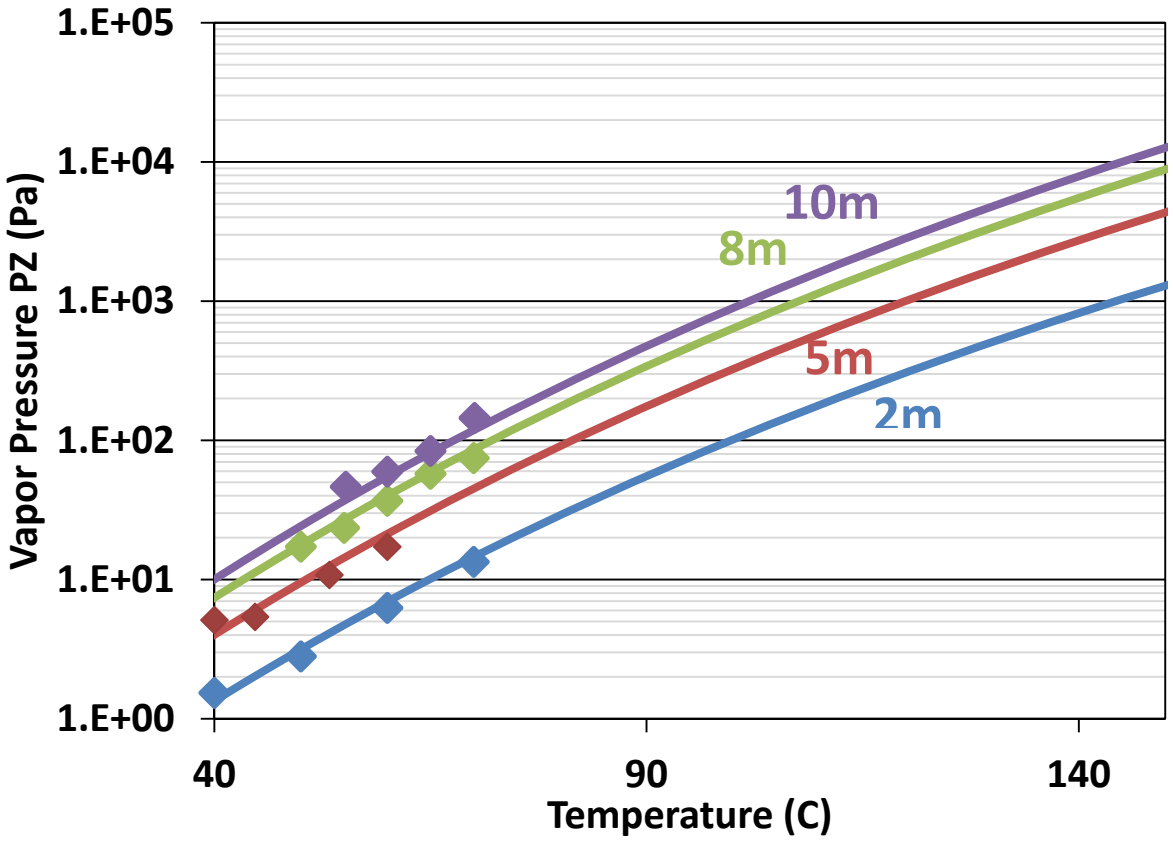

Figure 5: Experimental data (points) and Aspen Plus® predictions (lines) for unloaded amine volatility of unloaded 2, 5, 8, and 10 m PZ from 40–70 °C.

Because the PZ/H_2O system has been modified, the PZ/H_2O/CO_2 system must be re-regressed. Figure 6 compares experimental data and Aspen Plus® predictions of heat capacity as a function of temperature for loaded 8 m PZ solutions containing 0.21, 0.29, and 0.40 mol CO_2/mol alkalinity. Figures 7 and 8 show Aspen Plus® predictions for CO_2 solubility and heat of absorption, respectively, for 8 m PZ from 40—160 °C. In addition to 8 m PZ, heat capacity and CO_2 solubility data for 2, 3.6, 10, and 12 m PZ. A total of 22 parameters were adjusted to regress the PZ/H_2O/CO_2 system, and they are listed in Table 2.

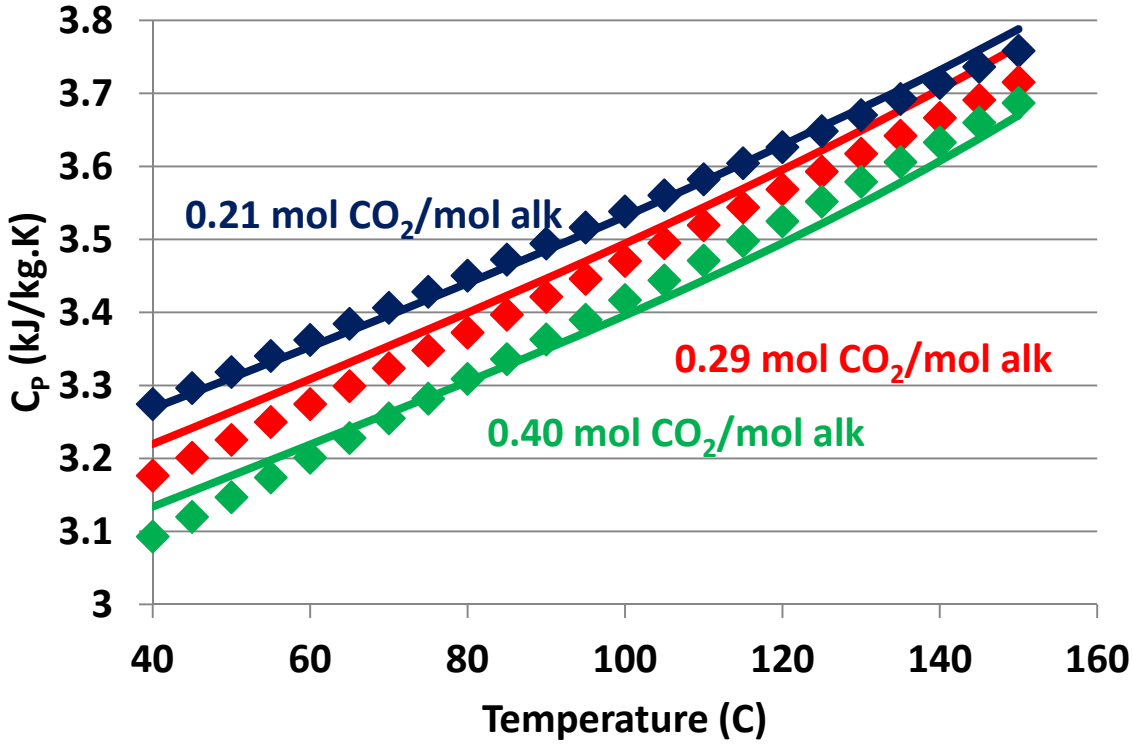

Figure 6: Experimental data (points) and Aspen Plus® predictions (lines) for heat capacity of loaded 8 m PZ from 40–150 °C.

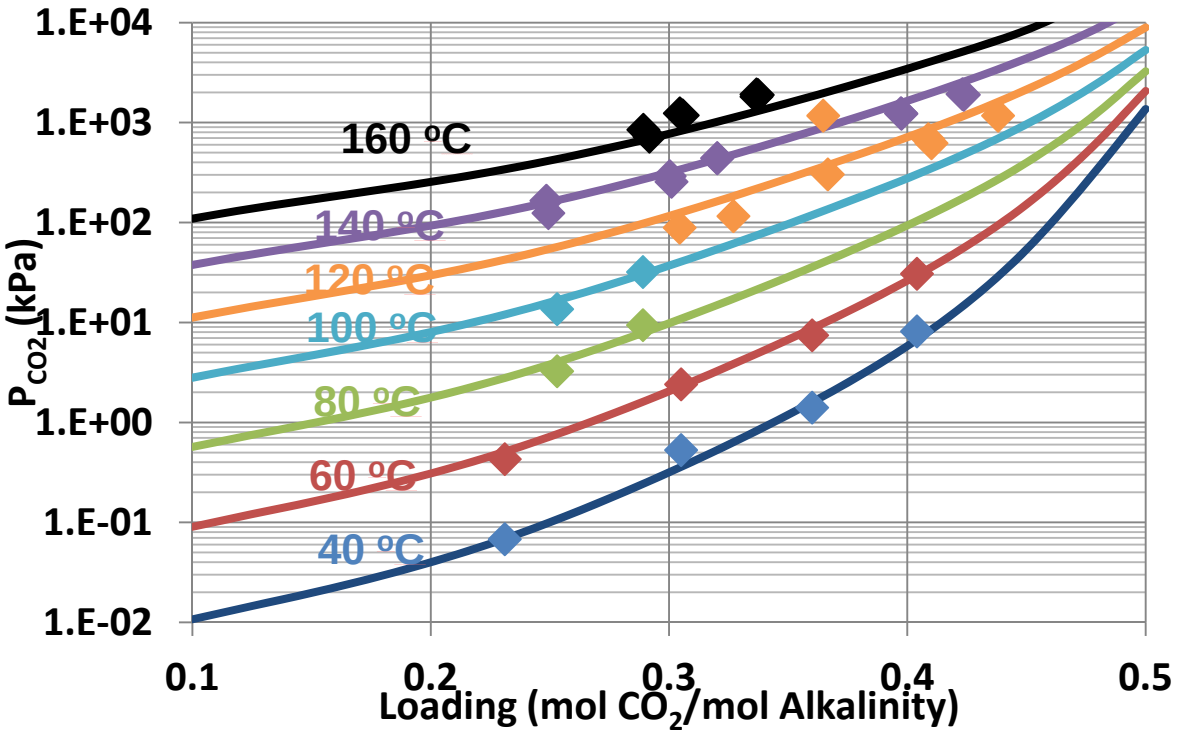

Figure 7: Experimental data (points) and Aspen Plus® predictions (lines) for CO_2 solubility of loaded 8 m PZ from 40–160 °C.

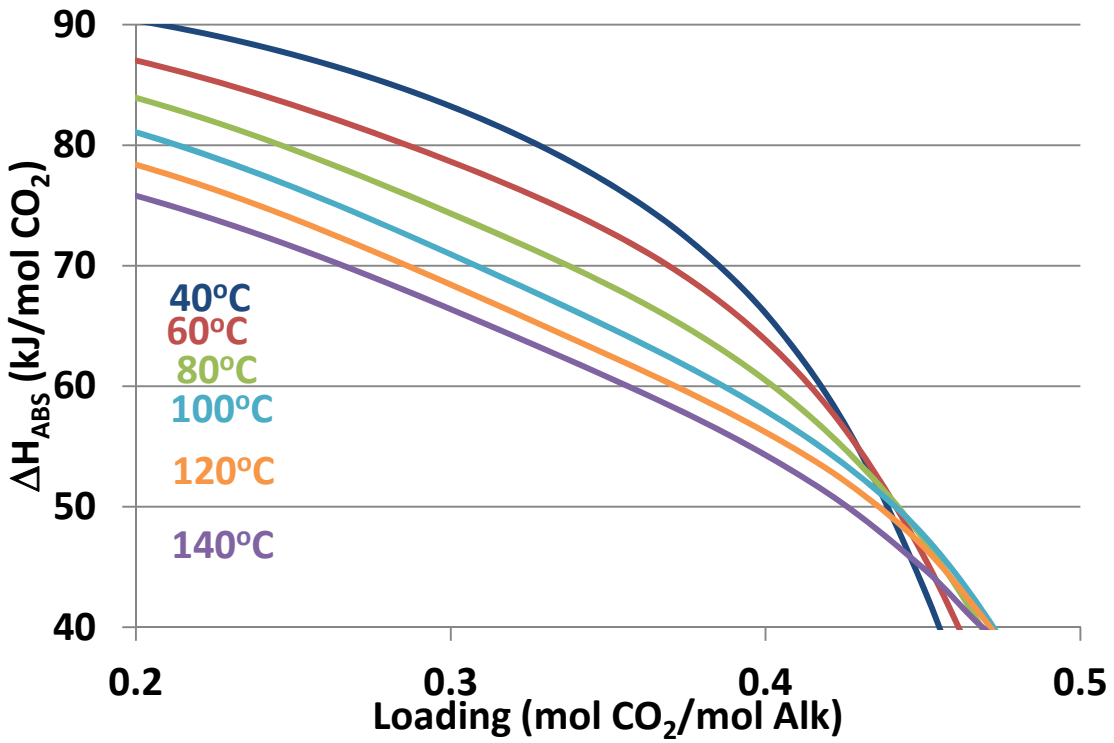

Figure 8: Aspen Plus® predictions for heat of absorption of CO_2 of loaded 8 m PZ from 40–140 °C.

Table 2: List of parameters used to fit $PZ/H_2O/CO_2$.

Parameter	Species
ΔG_{FORM}	$PZCOO^-$, $PZ(COO)_2^{2-}$, H^+PZCOO^-
ΔH_{FORM}	$PZCOO^-$, $PZ(COO)_2^{2-}$, H^+PZCOO^-
$C_P/1$	PZH^+, $PZCOO^-$, $PZ(COO)_2^{2-}$, H^+PZCOO^-
$C_P/2$	PZH^+, $PZCOO^-$, $PZ(COO)_2^{2-}$, H^+PZCOO^-
GMELCC	$H_2O/(PZH^+,PZCOO^-)$, $(PZH^+,PZCOO^-)/H_2O$
GMELCC	$H_2O/(PZH^+,PZ(COO)_2^{2-})$, $(PZH^+,PZ(COO)_2^{2-})/H_2O$
GMELCC	$PZ/(PZH^+,PZCOO^-)$, $(PZH^+,PZCOO^-)/PZ$
GMELCC	$H^+PZCOO^-/(PZH^+,PZCOO^-)$, $(PZH^+,PZCOO^-)/ H^+PZCOO^-$

Conclusions

- High pressure CO_2 solubility data in MDEA can be regressed by adjusting parameters for the activity coefficient of CO_2.
- Simultaneously representing experimental data for the activity coefficient of CO_2 in MDEA and CO_2 solubility at high loadings will require further investigation.
- Experimental data over operationally significant loading, temperature, and amine concentration ranges can be regressed in a thermodynamically consistent manner using parameters from the e-NRTL model.
- Careful regression of CO_2 solubility data and heat capacity data in PZ solution gives a well-behaved, thermodynamically consistent prediction of the heat of CO_2 absorption. At 0.3

mol/equiv PZ, the heat of CO_2 absorption varies from 65 kJ/mol at 40°C to 83 kJ/mol at 140°C.

Future Work

The kinetics for MDEA, PZ, and MDEA/PZ will be regressed into the new thermodynamic model. Novel process configurations will continue to be developed and evaluated using available thermodynamic and kinetic models.

References

Bishnoi S. *Carbon Dioxide Absorption and Solution Equilibrium in Piperazine Activated Methyldiethanolamine*. The University of Texas at Austin. Ph.D. Dissertation. 2000.

Jou FY, Mather AE, Otto FD. "Solubility of hydrogen sulfide and carbon dioxide in aqueous methyldiethanolamine solutions." *Ind Eng Chem Process Des Dev.* 1982;21(4):539–544.

Maddox RN, Bhairi AH, Diers JR, Thomas PA. "Equilibrium Solubility of Carbon Dioxide or Hydrogen Sulfide in Aqueous Solutions of Monoethanolamine, Diglycolamine®, Diethanolamine and Methyldiethanolamine." GPZ Research Report No. 104, 1987.

Plaza JM, Chen E, Rochelle GT. "Absorber Intercooling in CO_2 Absorption by Piperazine-Promoted Potassium Carbonate." *AIChE J*. 2009;56(4):905–914.

Van Wagener DH. *Stripper Modeling for CO_2 Removal Using Monoethanolamine and Piperazine Solvents.* The University of Texas at Austin. Ph.D. Dissertation. 2011.

Absorber Modeling and Pilot Plant Validation

Quarterly Report for October 1 – December 31, 2011

by Darshan Sachde

Supported by the Luminant Carbon Management Program

Department of Chemical Engineering

The University of Texas at Austin

January 31, 2012

Abstract

During the past quarter, Aspen Plus® absorber models were validated using pilot plant data from the J.J. Pickle Research Campus (PRC). The models incorporated heat loss to account for operating conditions at the pilot plant. Independent heat loss calculations by an overall heat transfer coefficient were within approximately 10% of heat loss predicted by data-fitting of pilot plant data in Aspen Plus®. In addition, skin temperature measurements at the pilot plant confirmed the validity of RTD measurements as accurate representations of column inner wall temperatures for modeling and heat loss calculation purposes. Skin temperature measurements also confirmed possible radial temperature profile variation in the pilot plant absorber, highlighting the need for improved measurement and modeling of the column cross-section.

Finally, the validated absorber model was used to develop base case designs for economic evaluation. Part of the base case design included confirmation of a stable operating range for 8 m piperazine (PZ) spanning a lean loading range of 0.27 to 0.3 when operated at 1.1 times the minimum solvent rate.

Introduction

During the past quarter, pilot plant data were used to validate absorber models in Aspen Plus®. An important part of reconciling the energy balance is accounting for heat loss during plant operation. Independent heat loss calculations were performed in conjunction with skin temperature measurements taken during pilot plant operation to develop real heat loss data for pilot plant operation. The field data were then used to validate the heat loss estimations developed via data-fitting in Aspen Plus®.

The newly validated models are being used to develop base case designs for economic evaluation. Designs evaluated to date make use of the identification by Plaza of a stable operating region for packing optimization (Plaza, 2011). The development of base case designs further verifies model performance over a range of design criteria. The economic evaluation and development of design cases identify optimum operating conditions for 8 m PZ and may help develop a method of identifying optimal conditions for any amine based on the amine performance characteristics.

Pilot Plant Data Reconciliation

Data from 8 m PZ pilot plant campaigns (November 2009, September 2010, and December 2010) conducted at PRC were used to validate and improve Aspen Plus® absorber models developed by Plaza (2011). Model validation included closure of heat and material balances and detailed evaluation of operating characteristics such as temperature profiles in the absorber. A data-fitting algorithm in Aspen Plus® was used to reconcile pilot plant data with absorber model predictions via model parameters such as heat loss and packing performance characteristics and by incorporating potential measurement and performance uncertainty into pilot plant data.

To justify and validate the data-fitting procedure, independent verification of performance parameters and uncertainty was required. Some validation, such as uncertainty in loading measurements, is ongoing. However, validation of heat loss parameters was completed within the last quarter and provides a representative case of the model validation procedure.

Column Temperatures and Heat Loss

Column temperatures and heat loss were analyzed in an effort to accurately model temperature variation in the column due to reaction (i.e., match temperature profiles) and to gain information about column performance parameters such as gas-liquid distribution and variation in mass and heat transfer over the cross-section of the column.

Figure 1 compares the pilot plant temperature profiles as measured by RTDs in the column to the gas and liquid temperatures predicted by the Aspen Plus® absorber model. The data in Figure 1 are for a representative run from the December 2010 campaign; the data reflects model to pilot plant comparisons *prior* to adjustments for heat loss.

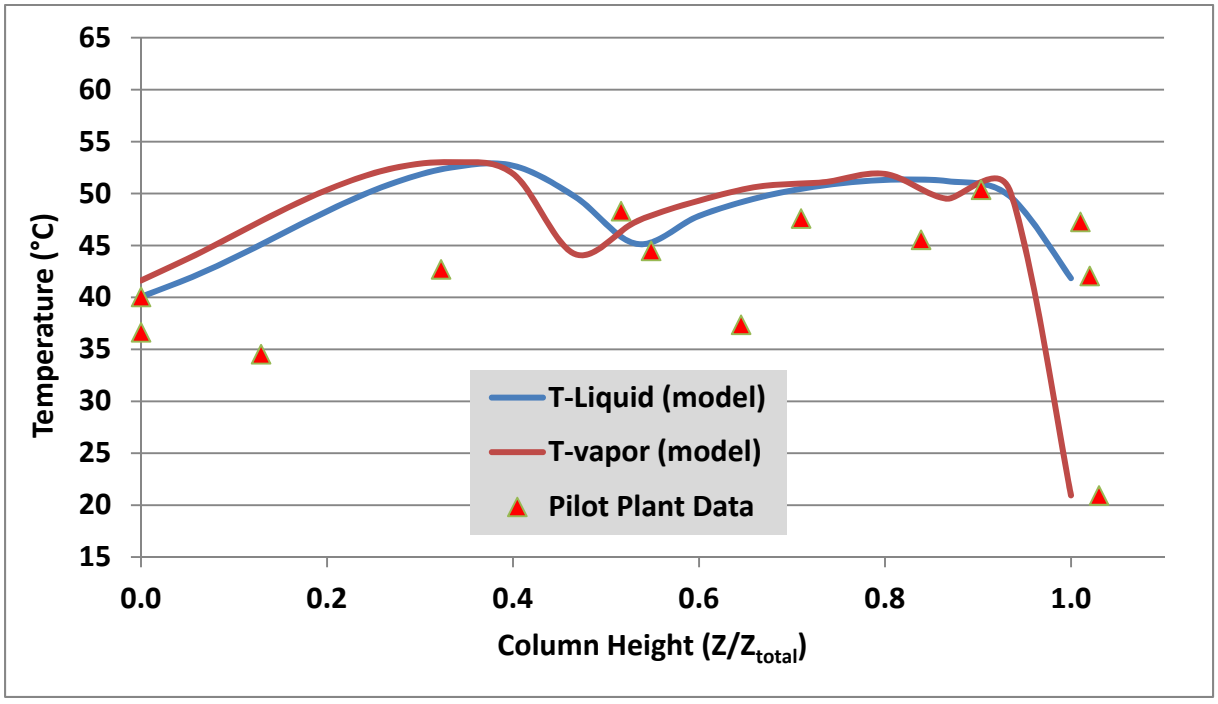

Figure 1: Comparison of RTD temperatures to model predicted gas and liquid temperatures before heat loss corrections (December 2010 campaign)

As seen in Figure 1, the model generally over-predicts the temperature relative to the pilot plant data. The discrepancy in temperature profiles provided the motivation for further investigation of heat loss. The heat loss was incorporated into the pilot plant regression models as follows (Plaza, 2011):

$$Q_f = A_f + B_f T_{amb} \quad (1)$$

Where:

Q_f is the heat loss assigned to phase f (liquid or vapor);
A_f, B_f are variable coefficients used to fit pilot plant data;
and T_{amb} is the ambient temperature during a campaign.

The data reconciliation tool in Aspen Plus® was used to vary the heat loss coefficients based on data from all pilot plant runs across each campaign (i.e., 13 pilot plant runs during the September 2010 campaign) as part of a constrained error minimization routine. The fitted parameters were used to assign an expected heat loss to each pilot plant run.

In order to validate the heat loss predictions from the model, an expected heat loss was calculated for the December 2010 campaign by assuming the RTD temperatures reported from PRC reflected inner wall temperatures of the column, segmenting the full column height into 10 segments (one for each RTD), and calculating an average heat loss over the entire column based on the temperature driving force from the inner wall to the ambient air at each RTD. Table 1 summarizes the column and heat transfer parameters used to perform the heat loss calculation; Table 2 compares the resulting heat loss from the manual calculation to that predicted based on the Aspen Plus® data fit and Equation 1.

Table 1: Heat Loss Estimation Parameters

Parameter	Value	Units
Heat Transfer Coefficient (Air)	50	W/m^2*K
Thermal Conductivity (Steel)	16	W/m*K
Column Inner Radius	0.214	meters
Column Outer Radius	0.229	meters

Table 2: Heat Loss Validation Results (December 2010 Campaign)

Method	Heat Loss (kW)
Manual Calculation	21.6
Aspen Plus® Regressed	19.3

As the table shows, the fitted parameter heat loss data based on pilot plant temperature measurements are in good agreement with the manual heat loss calculation. However, as part of the heat loss calculation, the assumption of the RTD measurement as the inner wall temperature needed to be confirmed; it is unclear what the RTD is actually measuring during operation (e.g., gas temperatures, liquid temperatures, core temperature, well-mixed temperature, etc.). In order to provide more information about the RTD measurements and to provide a second method of validating heat loss at PRC, skin temperature measurements were taken at the location of each RTD penetration during operation of the pilot plant in October 2011. The measurements were made using a Fisher Scientific hand-held infrared thermometer. Figure 2 compares the reported RTD temperatures along the length of the column to the corresponding skin temperature measurement at the same location on the column.

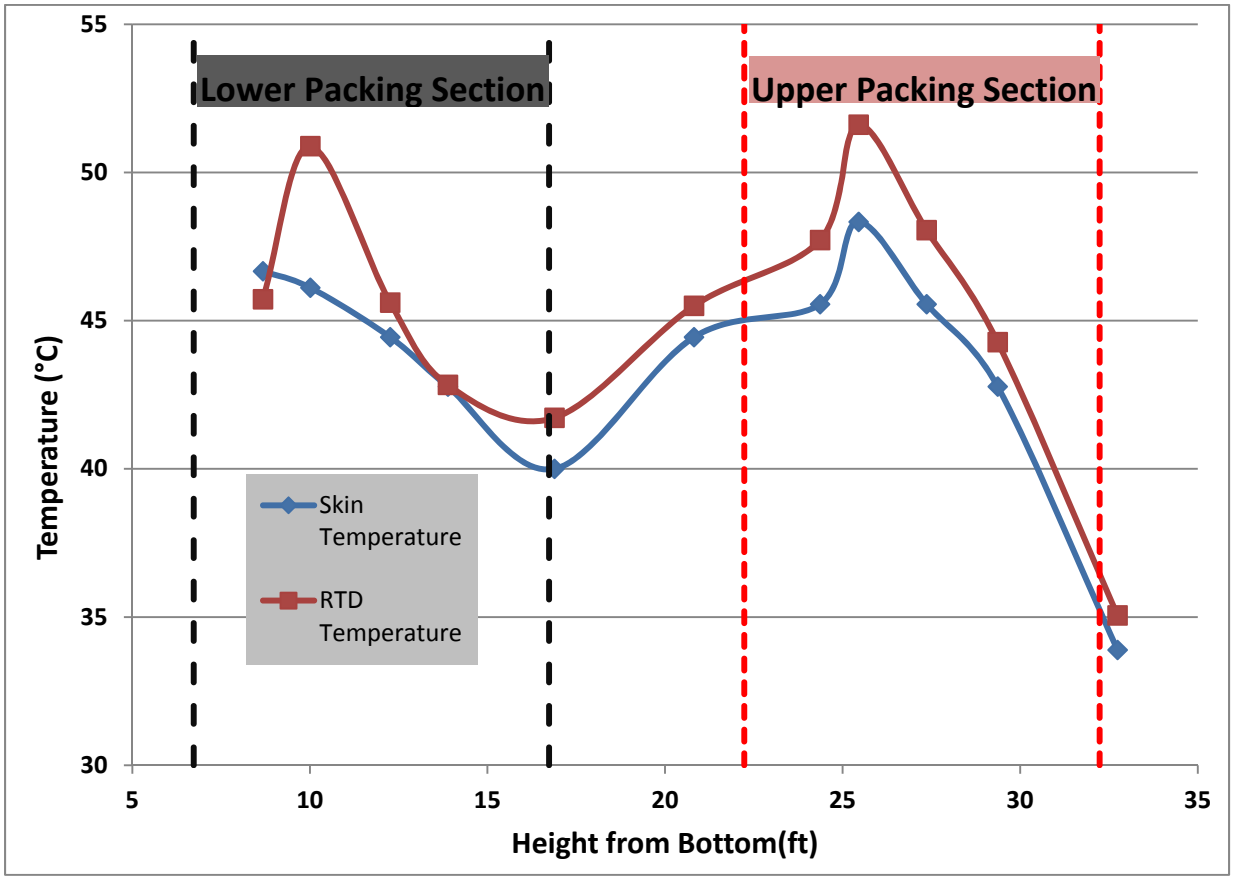

Figure 2: Comparison of RTD temperatures to skin temperature measurements (October 2011 campaign)

Figure 2 shows that the skin temperature measurements closely track the RTD measurements; the average difference between the RTD and skin temperatures was less than 2 °C indicating minimal resistance to heat transfer between the RTD and column surface. Thus, the use of RTD measurements as a proxy for future heat loss predictions is validated by both manual calculations and by verification of temperatures at the column surface.

Finally, in addition to the temperature measurements along the height of the column, several measurements were made radially at fixed column heights to provide an initial confirmation of temperature variations along the cross section of the column. Table 3 summarizes radial

temperature measurements, indicating as much 5 °C variation at a fixed column height. While the skin temperature variation cannot be directly correlated to internal temperature profiles, the initial observation provides motivation to develop techniques to measure temperature profiles along the column cross section in future campaigns at PRC.

Table 3: Radial Variation in Column Skin Temperature (December 2010 Campaign)

RTD	Height from bottom (ft)	Offset from Column Centerline (°)				Max Variation (°C)
		0	90	180	270	
4072	8.68	**116***	114	112	111	5
4076W	25.45	119	**119***	118	121	3
4079	29.36	109	**109***	107	107	2
* Highlighted values correspond to skin temperature at the RTD penetration						

Development of Base Case Models for Economic Analysis

Following pilot plant validation, the Aspen Plus® (5deMayo) absorber model was used to develop several base case scenarios for economic analysis of the absorption stripping process using 8 m PZ. All models were developed on a basis of 90% removal of CO_2 (based on balance around absorber) and used RSP-250 packing.

The lean loading conditions chosen for the economic analysis were derived from the findings of Plaza that identified distinct operating regions for PZ.

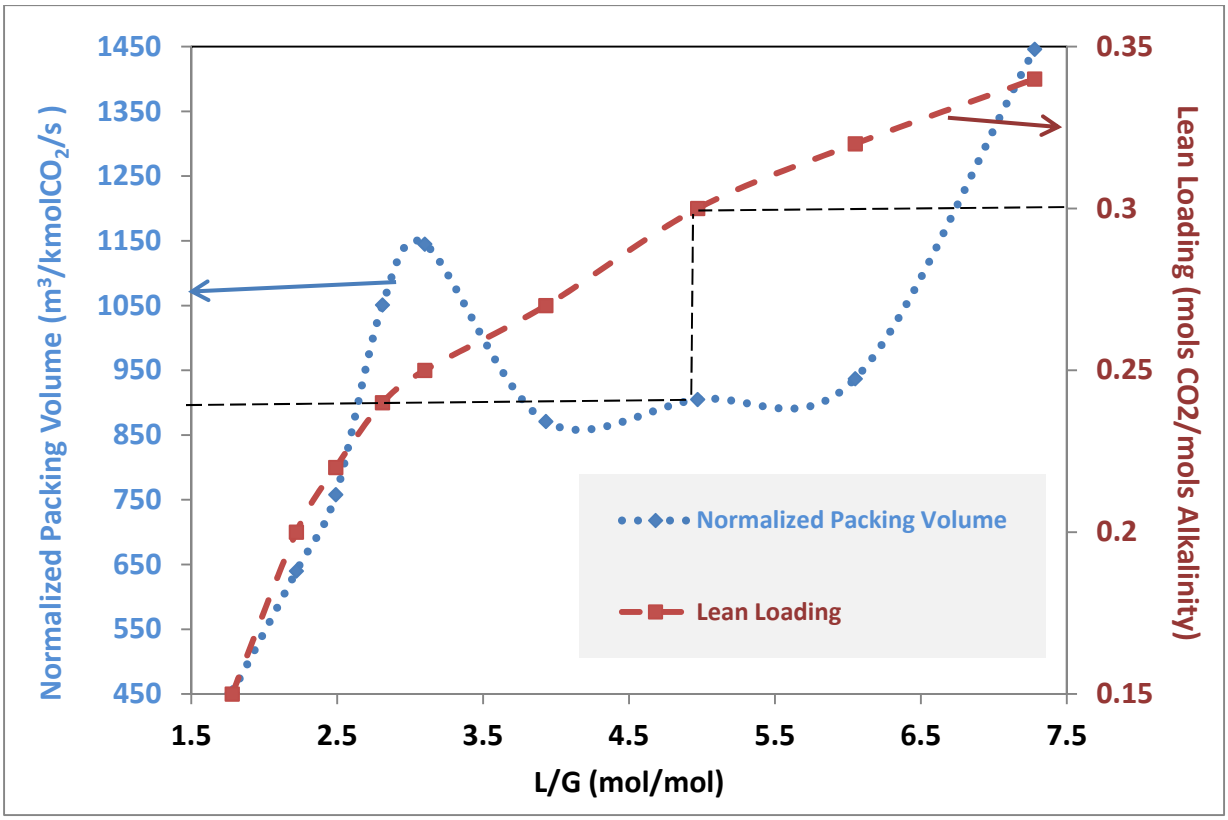

Figure 3: Packing Volume per mol CO_2 removed as a function of L/G and Lean Loading. Fixed Parameters: 90% Removal, RSP-250 packing, 40 °C operating temperature, Intercooling to 40 °C at Z/Z_{total} = 0.5, 1.1*Lmin, and 80% Flood. (Reproduced from Plaza, 2011)

As seen in Figure 3, lean loading choices can minimize packing requirements. However, certain lean loading ranges lead to stable minima, whereas others can lead to large changes in packing requirements as operating conditions are changed. For example, the conditions for 0.3 lean loading are represented in Figure 3 by the black, dashed line. A shift in L/G or lean loading from the condition highlighted for 0.3 lean loading will lead to minimal change in packing volume requirements. This region (represented by the plateau in the normalized packing volume curve) was determined to be most suitable for developing design cases due to the stability. Plaza provides further detail and explanation on the different operating regions (2011).

Table 4 summarizes the conditions for the economic evaluation designs developed to date. Results will be normalized to CO_2 removed to allow for scaling up.

Table 4: Economic Evaluation Design Conditions

	Case 1	Case 2
Lean Amine Feed		
T (°C)	40	40
Mass Flow Rate (kg/s)	1.21	1.53
Volumetric Flow Rate (m^3/s)	1.09E-03	1.37E-03

Loading (mols CO_2/mols alkalinity)	0.27	0.30
Gas Feed		
T(°C)	40	40
Molar Flow Rate (kmol/s)	8.83E-03	8.83E-03
Volumetric Flow Rate (m^3/s)	0.209	0.209
Gas Feed, Mole Fractions		
CO_2	0.149	0.149
H_2O	0.068	0.068
N_2 (includes all inerts)	0.757	0.757
O_2	0.026	0.026

Preliminary Design Case Results

Table 5 provides an overview of key results for the two design cases discussed previously.

Table 5: Overview of Key Results for Base Case Designs

	Lean Loading (mols CO_2/2*mols PZ)	Rich Loading (mols CO_2/2*mols PZ)	L/G (mol/mol)	Operating Temperature (°C)	Intercooling Location (Z/Ztotal)	Volume of Packing per kmol CO_2 removed (m^3/kmol*s^{-1})
Case 1	0.270	0.380	4.83	40	0.5	724
Case 2	0.300	0.390	5.92	40	0.5	898

The gas conditions used in the economic analysis include a higher CO_2 concentration than that evaluated by Plaza in the development of the optimal PZ cases (14.9% vs. 12.7%). To test the validity of the stability of the operating regime chosen (i.e., lean loadings chosen), the temperature and mass transfer profile for each of the economic cases was evaluated.

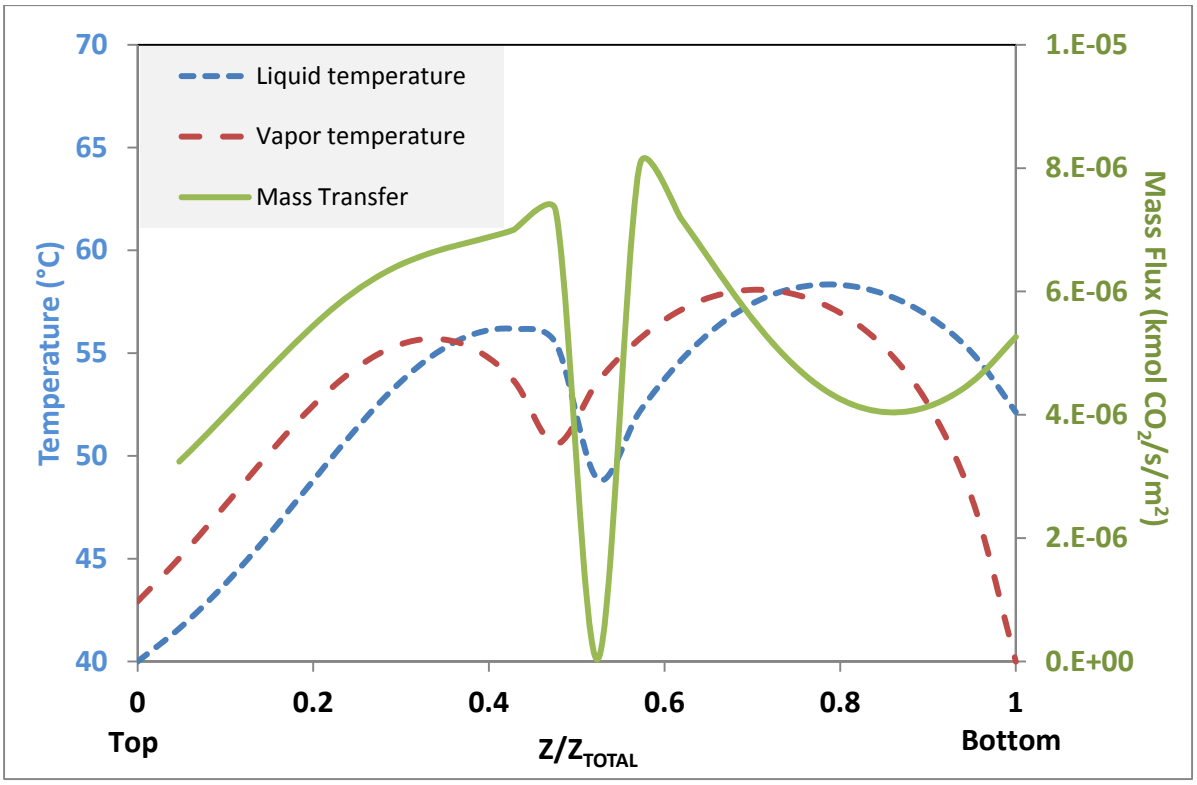

Figure 4: Mass Flux, Liquid, and Gas Temperature Profiles (Case 1, 0.27 Lean Loading)

The key features of Figure 4 are the relatively symmetric temperature and mass transfer profiles throughout the column. The temperature bulge does tend towards the bottom of the column, but the maximum temperature on either side of the intercooling (at Z = 0.5) only differs by approximately 3 °C. The balanced mass transfer and temperature profiles are indicative of the stable L/G and lean loading region highlighted in Figure 3 and discussed at length by Plaza.

Figure 5, for the 0.3 lean loading case, shows similar profiles.

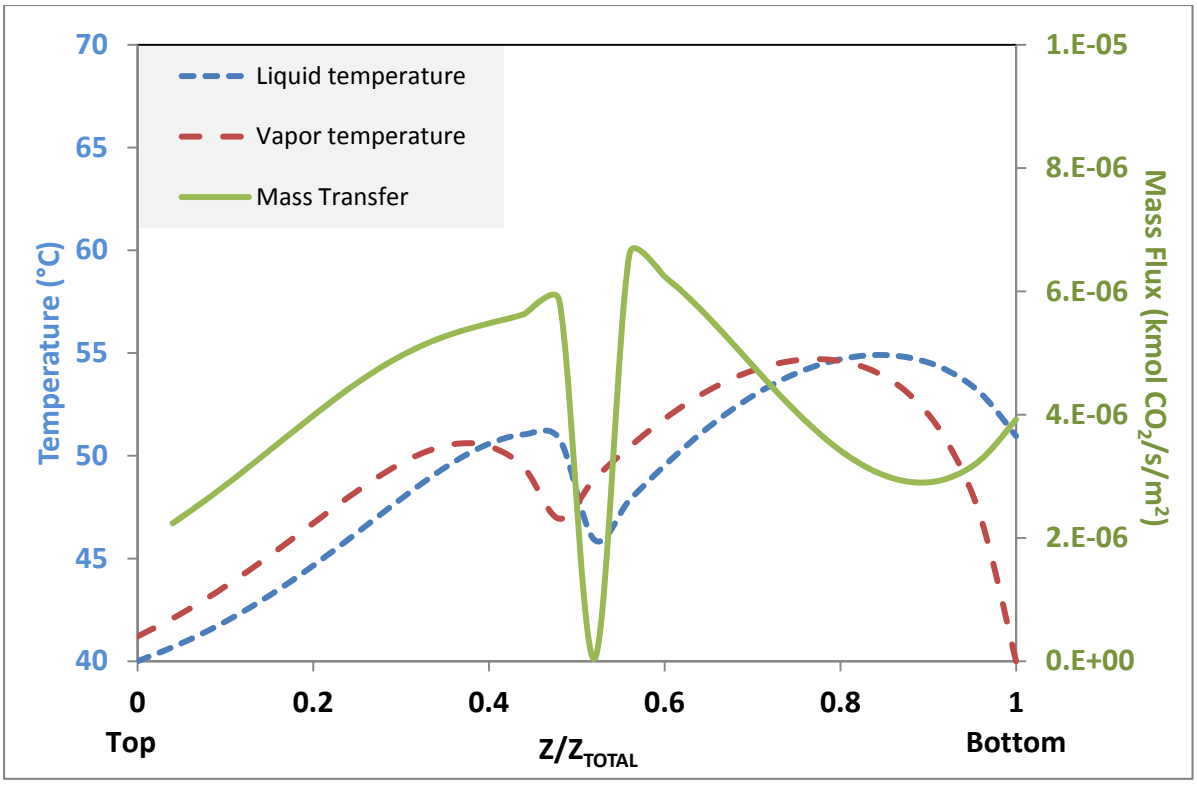

Figure 5: Mass Flux, Liquid, and Gas Temperature Profiles (Case 2, 0.3 Lean Loading)

The bulge shows a distinct shift towards the bottom of the column due to the higher liquid flow rates required to maintain 90% removal. However, the mass transfer profile is still balanced across the column without any pinches.

The initial evaluation indicates that the economic cases conform to the stable process region, but more rigorous analysis is needed to confirm stability across a range of operating conditions and variables.

Conclusions

Work on absorber model validation and development using pilot plant data over the past quarter has yielded the following key findings:

- heat loss measurements predicted in Aspen Plus® via data–fitting of pilot plant data were within 10% of independent calculation using an overall heat transfer coefficient;
- skin temperature measurements at RTD locations on the pilot plant absorber column were, on average, within 2 °C of RTD readings within the column, validating the use of RTD temperatures for heat loss prediction;
- skin temperature measurements indicated as much as 5 °C variation in radial column temperatures at a fixed height;
- preliminary absorber economic design cases indicate the existence of a stable optimum of packing height in the 0.27 to 0.3 lean loading range for 8 m, confirming work by Plaza.

Future Work

Future work related to pilot plant activities includes absorber model validation using data from the October 2011 campaign at PRC, modeling and evaluation of the spray nozzle used in conjunction with intercooling during the October campaign and development of plans for improved temperature measurements in future campaigns.

Further validation of the absorber performance regions developed by Plaza, including economic analysis across a range of operating parameters (e.g., absorber temperature), will be performed. Similar analysis will be developed for MEA with a long range goal of generalizing the identification of stable operating regions based on amine performance properties.

References

Plaza JM. *Modeling of Carbon Dioxide Absorption using Aqueous Monoethanolamine, Piperazine, and Promoted Potassium Carbonate.* The University of Texas at Austin. Ph.D. Dissertation. 2012.

Measurement of Packing Effective Area and Mass Transfer Coefficients

Quarterly Report for October 1 – December 31, 2011

by Chao Wang

Supported by the Luminant Carbon Management Program,

Process Science and Technology Center, and the Separations Research Program

Department of Chemical Engineering

The University of Texas at Austin

January 31, 2012

Abstract

In this quarter, most work has been focused on analysis of previous results. The influence of the superficial gas velocity (u_G) on effective area (a_e) has been explored. For random packing, the influence of gas velocity is as large as liquid velocity. The exponent of effective area on gas velocity is 0.218 for 1" plastic Pall Rings compared with 0.248 on liquid velocity. For Raschig Super Rings #0.5, the exponent is 0.174 for gas velocity and 0.202 for liquid velocity. It is reasonable to include gas velocity influence in the existing area model.

The effective area model has been modified with consideration of gas flow influence for random packings. Gas phase Reynolds number is chosen to represent the gas flow influence. The modified area model is: $\frac{a_e}{a_P} = C[(\frac{\rho_L}{\sigma})g^{1/3}(\frac{Q}{A} * \frac{1}{a_P})^{4/3}]^{0.116}(\frac{u_G \rho_G}{a_P \mu_G})^n$

where:

C is packing constant, and
n is exponent for gas flow rate.

Four data sets of outside sources have been found to compare with data measured by SRP. For 1" plastic Pall Rings, the outside source data is from Pall Ring Product Bulletin 350 by Raschig-Jaeger Products, Inc. The pressure drop measurements for air-water compare fairly well with the SRP data, with an average deviation of 24%. The effective area provided by the Product Bulletin is based on the absorption of 1% CO_2 into 1 gmol/L NaOH. Since the NaOH concentration is large, the gas phase mass transfer resistance cannot be ignored. Their effective area has been corrected by subtracting the gas side resistance and it compares well with the SRP measurements with an average deviation of 18%.

For Raschig Super Rings #0.5 and #0.7, the effective area data are obtained from Kolev (2006), who absorbed 1% CO_2 into 1 gmol/L NaOH. The data are again corrected for gas side resistance and compare well with average deviations of 7.2% and 6% for RSR#0.5 and RSR#0.7 respectively. Film mass transfer coefficient ($k_G a$ and $k_L a$) data are from Product Bulletin 250 by Raschig-Jaeger Products. For $k_G a$, Raschig used the absorption of NH_3 from water into air and

observed a deviation of 40% from the SRP RSR#0.5 data. For k_La, Raschig used the desorption of CO_2 into water from air with a 33% deviation from SRP RSR#0.5 data and 29% from SRP RSR#0.7 data.

For Mellapak 2X, two outside sources of data have been found. One is from Ali Zakeri at NTNU (2011) and the other from Sulzer Chemtech (2011). The system used for pressure drop measurements is air-water for both sources. The average deviation from SRP data is 32% for NTNU data and 16% for Sulzer data. The system used for effective area measurements is the absorption of CO_2 into NaOH. The deviation from SRP data is 9.2% for the NTNU data and 9.4% for the Sulzer data.

Introduction

Packing is widely used in distillation, stripping, and scrubbing processes because of its relatively low pressure drop, good mass transfer efficiency, and ease of installation. Packing is being investigated for post-combustion carbon capture for these reasons. In the CO_2 capture process, absorber performance depends on the effective mass transfer area of the packing (a_e), stripper performance depends on liquid film mass transfer coefficient (k_L), gas cooler and water wash performance depends on gas film mass transfer coefficient (k_G). This research is focused on the measurement of these important fundamental parameters for packing and construction of a mechanistic design model.

Influence of gas flow rate on effective area

Figure 1 shows effective area versus gas flow rate for 1" plastic Pall Rings. According to Figure 1, at the same liquid flow rate, the effective area increases with gas flow rate. From previous research, the exponent of effective area on liquid flow rate for this packing is 0.25. To eliminate the influence of liquid flow rate, $a_e/L^{0.25}$ is chosen as dependent variable and the superficial gas velocity (u_G) is chosen as the independent variable in Figure 2. According to Figure 2, the overall exponent of a_e over u_G is 0.25 for this packing, which is comparable to exponent of a_e over u_L.

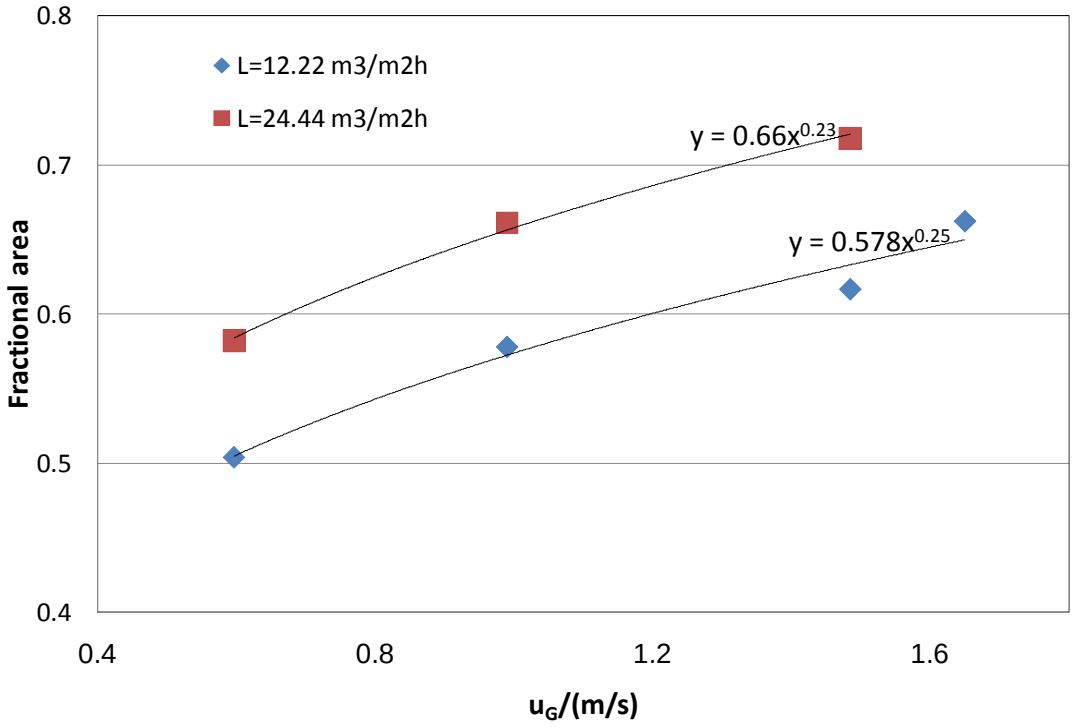

Figure 1: Effective area over gas flow rate for 1" plastic Pall Ring

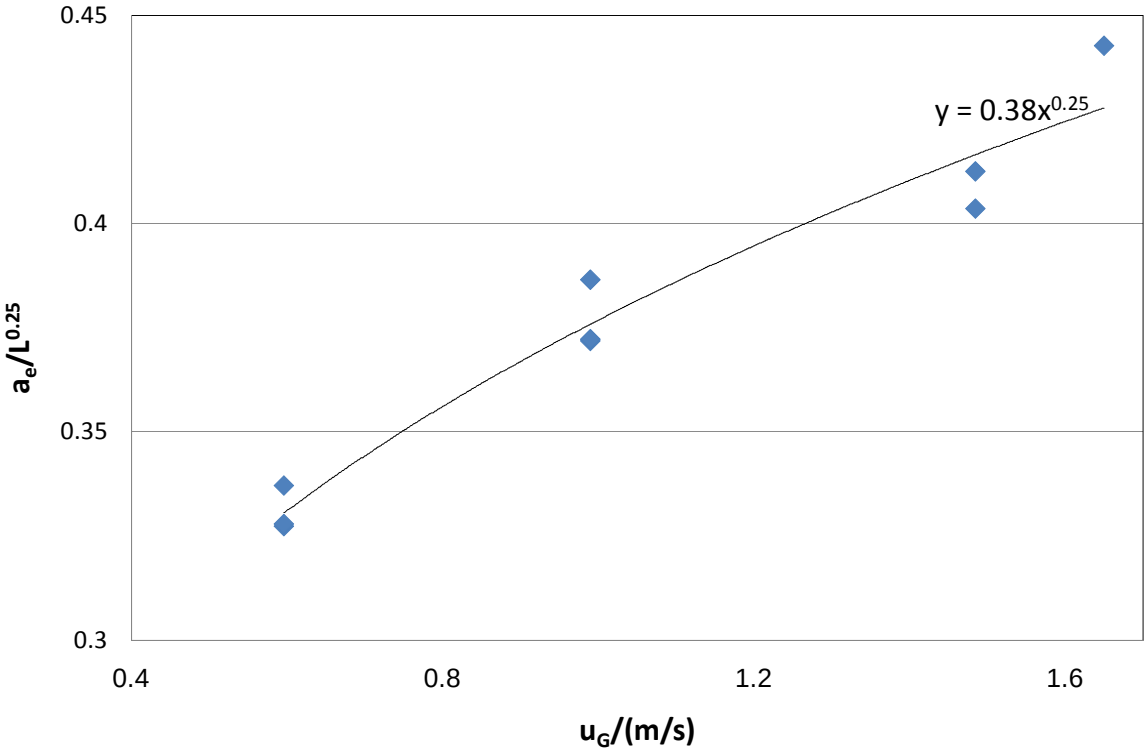

Figure 2: Generalized effective area ($a_e/L^{0.25}$) over gas flow rate for 1" plastic Pall Ring

The relationship between a_e and u_G for other random packings have also been explored. For metal Raschig Super Ring #0.5, the overall exponent of a_e over u_G is 0.18 compared to exponent

of a_e over u_L 0.20. For metal Raschig Super Ring #0.7, the exponent of a_e over u_G is 0.11, compared to exponent of a_e over u_L 0.15. Therefore, for random packings, the influence of gas flow rate on effective area is as large as the effect of liquid flow rate. It is reasonable to add gas flow factor into the existing area model for random packings.

Modified effective area model for random packings

The effective area model has been modified with consideration of gas flow influence for random packings. Gas phase Reynolds number is chosen to represent the gas flow influence. The modified area model is:

$$\frac{a_e}{a_P} = C[(\frac{\rho_L}{\sigma})g^{1/3}(\frac{Q}{A}*\frac{1}{a_P})^{4/3}]^{0.116}(\frac{u_G\rho_G}{a_P\mu_G})^n \qquad (1)$$

where:

C is packing constant;
n is exponent for gas flow rate differs with packings;
Q is volumetric liquid flow rate, m^3/s;
A is area of cross section of the column, m^2.

This model is applied to predict effective area for three random packings. Table 1 lists the values for C, n, and deviation for these three packings: Raschig Super Ring #0.5 and #0.7, 1"plastic Pall Ring).

The modified model can predict effective area for random packings well. Deviation for each packing is below 10%.

Table 1: Constants in the modified area model for random packings

Packing	C	n	Deviation
RSR#0.5	0.524	0.174	3.72%
RSR#0.7	0.913	0.106	1.02%
1" PPR	0.292	0.218	7.78%

Data comparison for 1"plastic Pall Ring

In this quarter, data from outside sources have been compared to data measured by SRP (Separation Research Program). For the 1" plastic Pall Ring, the outside source data is Pall Ring Product Bulletin 350 by Raschig-Jaeger Products, Inc. Both pressure drop data and effective area are compared with SRP data. Figure 3 shows the pressure drop comparison. The system used by Raschig is the same as that used by SRP, which is an air-water system. The deviation between SRP data and Raschig data is 24.7%.

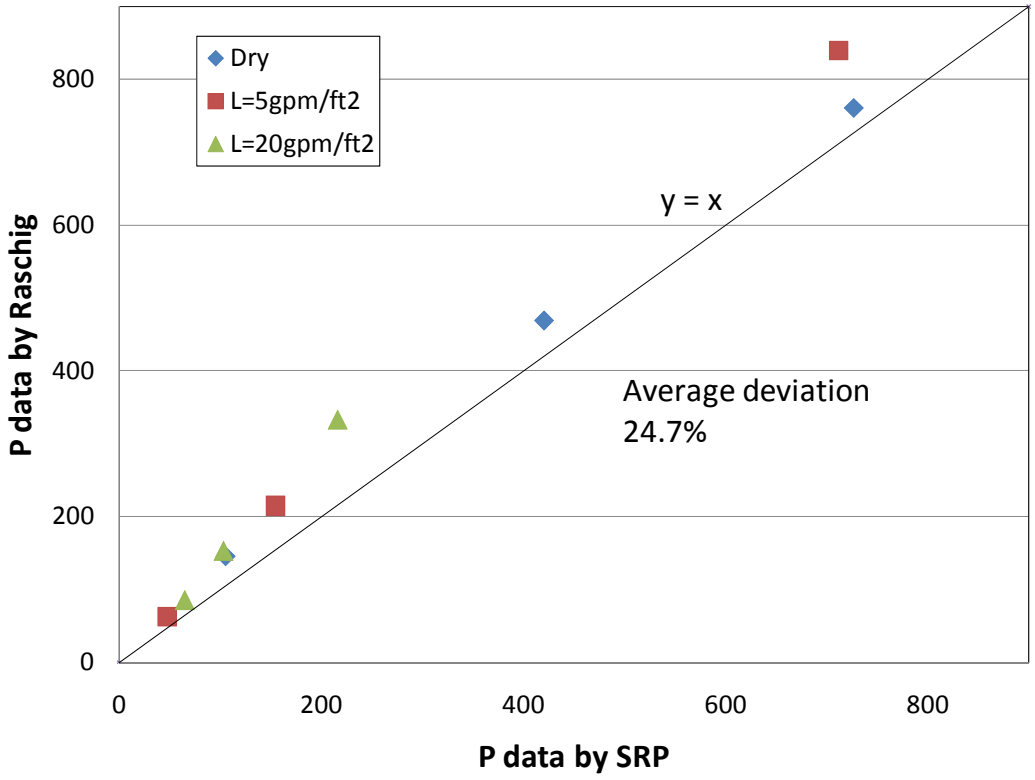

Figure 3: Pressure drop comparison for 1" plastic Pall Ring

The effective area data is compared in Figure 4. The system used by Raschig is absorption of 1% CO_2 into 1 gmol/L NaOH solution, while the system used by SRP is absorption of CO_2 from air (about 400 ppm) into 0.1 gmol/L NaOH. Since the NaOH concentration and CO_2 concentration % is larger, the gas phase resistance cannot be ignored. In the Raschig report, the overall volumetric mass transfer coefficient $K_{OG}a$ is given. The liquid phase mass transfer coefficient k_g' can be calculated by the equation:

$$k_g' = \frac{\sqrt{k_{OH^-}[OH^-]D_{CO2,L}}}{H_{CO2}} \tag{2}$$

Thus, effective area with consideration of gas phase resistance can be calculated:

$$a_e = \frac{1}{k_g'\left(\frac{1}{K_{OG}a} - \frac{1}{k_G a}\right)} \tag{3}$$

Volumetric gas phase mass transfer coefficient k_Ga is from experimental data by SRP. According to calculation, the gas phase resistance accounts for 9.43–12.5% of the overall mass transfer resistance. Including k_Ga correction, effective area is increased by 10% and deviation is reduced from 27.9% to 18.1%. Effective area comparison for 1" PPR is given in Figure 4.

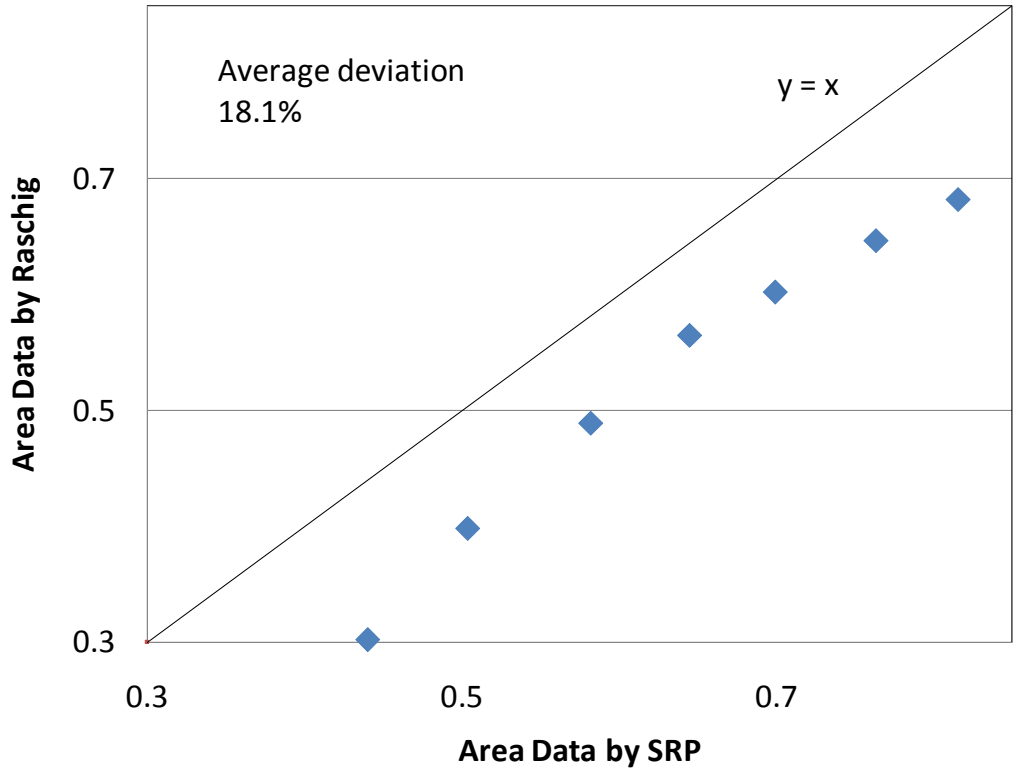

Figure 4: Effective area comparison for 1" plastic Pall Ring

Data comparison for Raschig Super Ring #0.5 and #0.7

Effective area comparison

Similar to 1" plastic Pall Rings, RSR #0.5 and #0.7 data from outside sources are compared with data measured by SRP. The effective area data are from Kolev (2006), and the system used is the absorption of 1% CO_2 into 1 gmol/L NaOH. The effective area data by Kolev are corrected for gas phase resistance. Gas phase resistance for this packing accounts for 6.6–8.7% of overall mass transfer resistance. By including the k_Ga correction, effective area is increased by 7.1–9.5% and overall deviation is reduced from 14.2% to 7.2%. Like RSR#0.5, effective area for RSR#0.7 is corrected using the same method. Gas phase resistance accounts for 11.6–15.7% of overall mass transfer resistance. Effective area comparisons for RSR#0.5 and #0.7 are shown in Figure 5.

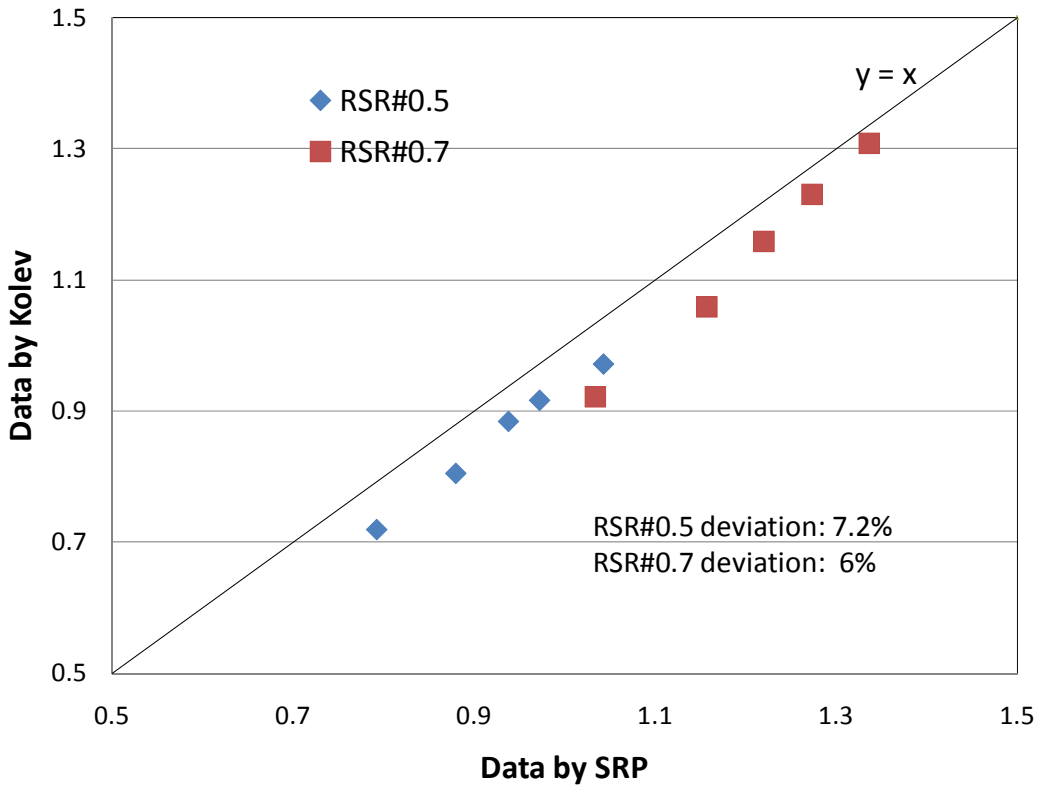

Figure 5: Effective area comparison for RSR#0.5 and #0.7

Mass transfer coefficient comparison

Additional volumetric liquid and gas phase mass transfer coefficients (k_La and k_Ga) are obtained from Product Bulletin 250 by Raschig-Jaeger Products. For k_La, the system used by Raschig is the desorption of CO_2 into water from air. These data are compared with desorption of toluene from water into air used by SRP. Since the system used is different, k_La data has to be transformed from measurement by CO_2/water system into toluene/water system. From previous research, k_L is thought to be a function of diffusivity in liquid phase with a power of 0.5, which is $k_L \sim D_L^{0.5}$. Thus, k_La between different systems can be transformed by using this equation:

$$\frac{(k_L a)_{tol}}{(k_L a)_{CO2}} = \left(\frac{D_{tol.L}}{D_{CO2,L}}\right)^{0.5} = 0.666 \qquad (4)$$

k_La comparison is shown in Figure 6, where k_La data from the outside source are compared with data from SRP at the same gas and liquid flow rate. The deviation for RSR#0.5 is 33.3% and for RSR#0.7 is 28.7%.

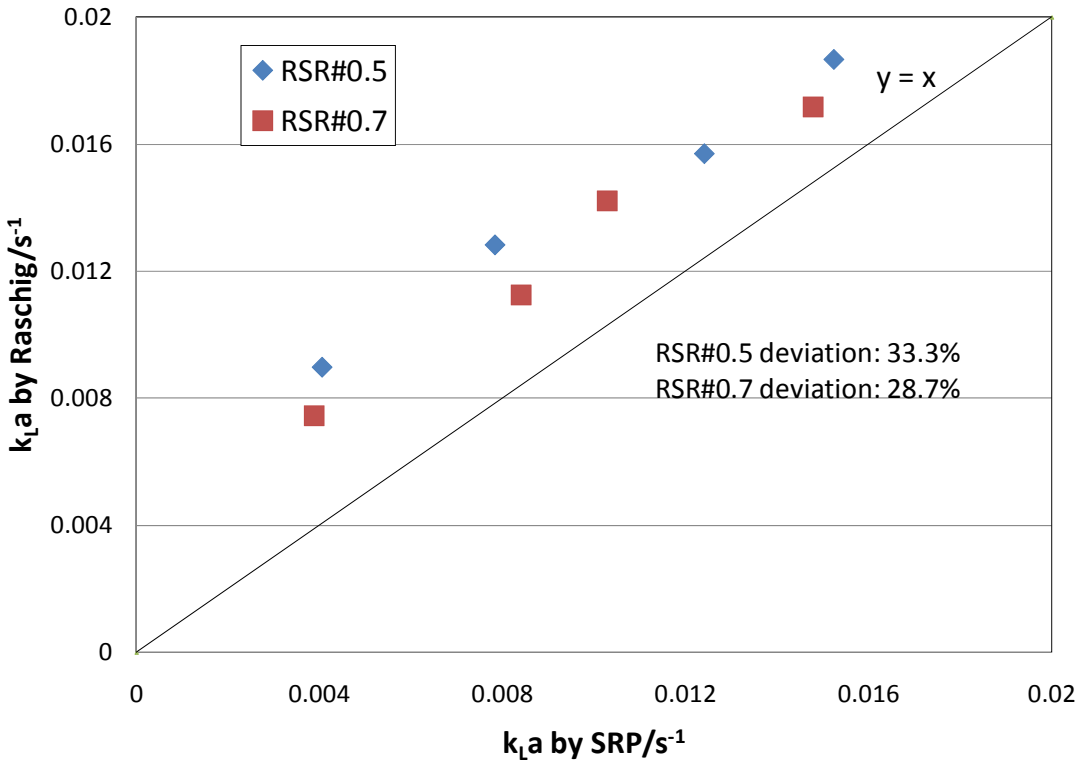

Figure 6: k_La comparison for RSR#0.5 and #0.7

For k_Ga, Raschig used a system of NH_3 absorption from air with water. The Raschig data are compared with the SO_2 absorption into caustic data provided by SRP. Similar to k_La, k_Ga data has to be transformed between different systems. According to previous research (Mehta, 1966; Tamir, 1978; Krebs, 1985), k_Ga is a function of D_G with a power from 0.38–0.68. In this report, the power is thought to be 0.5. Thus, k_Ga between different systems can be transformed by using this equation:

$$\frac{(k_G a)_{SO2}}{(k_G a)_{NH3}} = \left(\frac{D_{SO2}}{D_{NH3}}\right)^{0.5} = 0.756 \qquad (5)$$

k_Ga comparison is shown in Figure 7, where k_Ga data from the outside source is compared with data from SRP at the same gas and liquid flow rate. The deviation for RSR#0.5 is 40.3%.

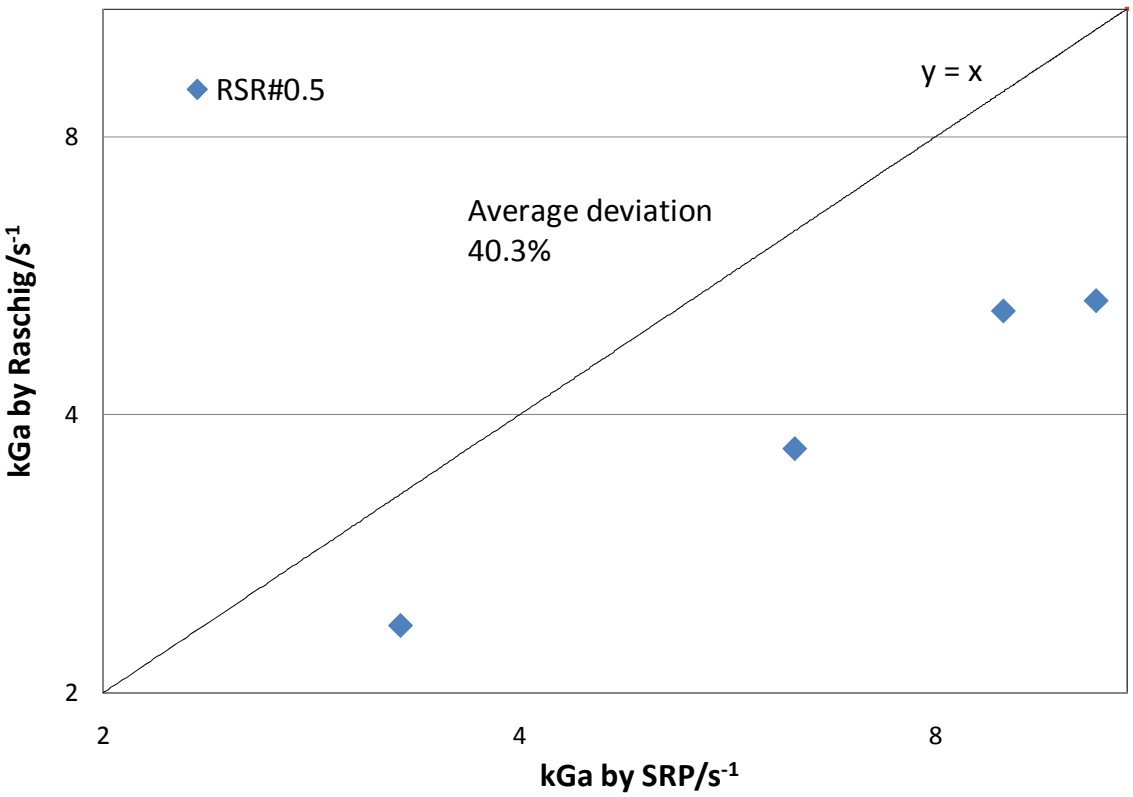

Figure 7: $k_G a$ comparison for RSR#0.5

Data comparison for Mellapak 2X

Pressure drop comparison

For Mellapak 2X, two outside sources of data have been found. One is from Zakeri at NTNU (2011) and the other one is from Sulzer Chemtech (2011). The system used for pressure drop measurement is air-water for both sources. In Figure 8, data from the outside source is compared with data produced by SRP at the same gas and liquid flow rate. Deviation for NTNU data is 32.1% and for Sulzer data is 16.1%.

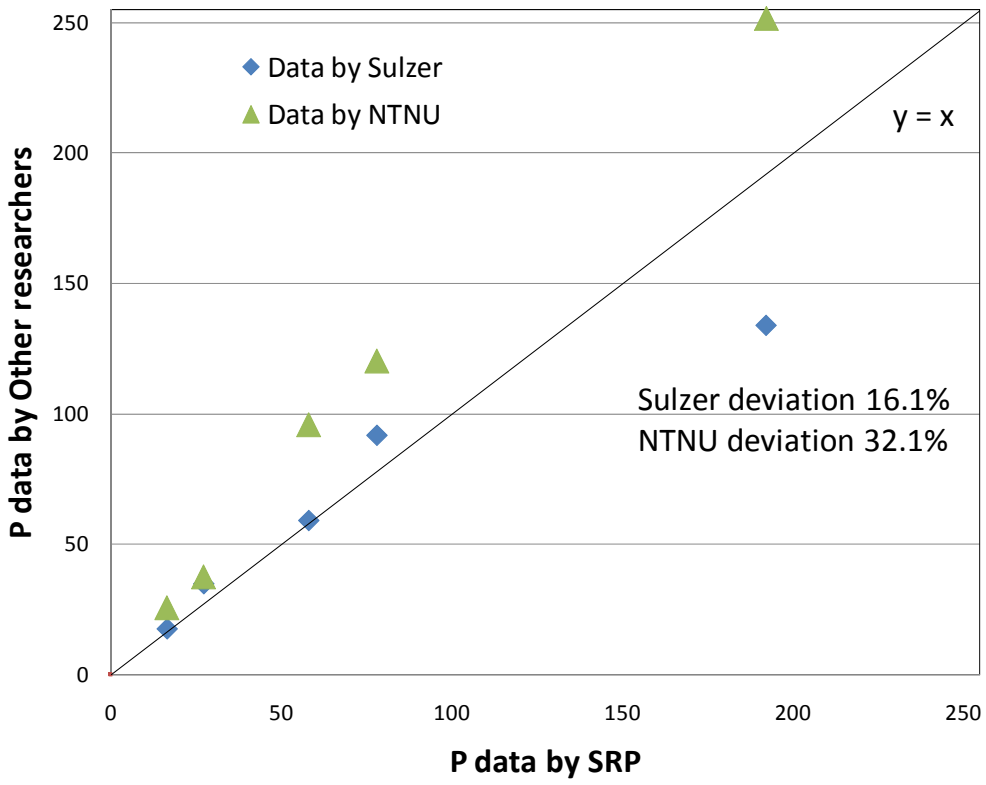

Figure 8: Pressure drop comparison for Mellapak 2X

Effective area comparison

The systems for effective area measurement is absorption of CO_2 into 0.3 gmol/L NaOH solution (by NTNU) and absorption of CO_2 into 1 gmol/L NaOH (by Sulzer). Similar to the effective area of previous packings, k_Ga correction has been made to this packing. Equation 2 is used to calculate k_g' and Equation 3 is used to calculate a_e with consideration of gas phase resistance. Gas phase resistance accounts for 4% of overall mass transfer resistance for the method using 0.3 gmol/L NaOH solution and 10% for the method using 1 gmol/L NaOH. Effective area comparison is shown in Figure 9. Deviation for NTNU data is 9.2%; deviation for Sulzer data is 9.4%.

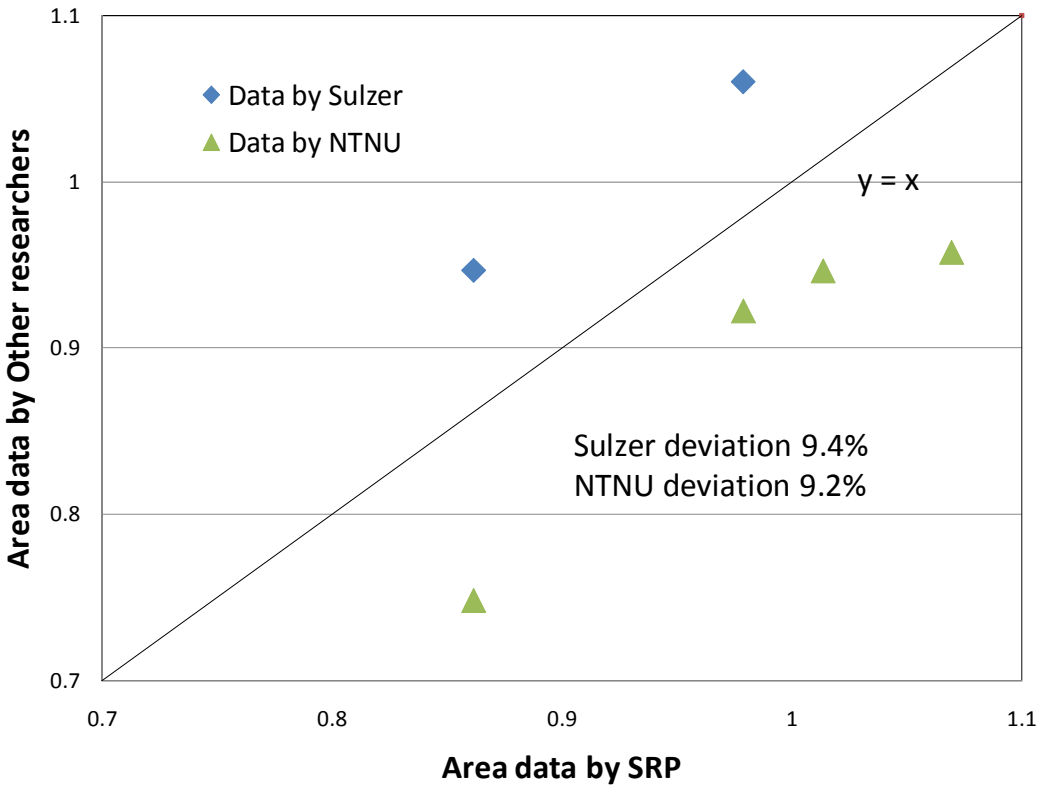

Figure 9: Effective area comparison for Mellapak 2X

Conclusions

1. The effective area model has been modified for random packing to include the gas flow rate influence: $\frac{a_e}{a_P} = C[(\frac{\rho_L}{\sigma})g^{1/3}(\frac{Q}{A} * \frac{1}{a_P})^{4/3}]^{0.116}(\frac{u_G \rho_G}{a_P \mu_G})^n$. The exponent n varies from 0.1 to 0.22 for three random packings. This is comparable to the exponent 0.155 used by Tsai to model the effect of liquid rate in structured packing.
2. Pressure drop for 1" plastic Pall Ring measured by Raschig has been compared with data measured by SRP with an average deviation of 24.7%.
3. The system for effective area measurement for 1"PPR is absorption of 1% CO_2 into 1 gmol/L NaOH by Raschig. Gas phase resistance accounts for 10% of overall mass transfer resistance. Effective area has been corrected by using: $a_e = \frac{1}{k_g^{'}(\frac{1}{K_{OG}a} - \frac{1}{k_G a})}$. Deviation between Raschig data and SRP data is 18.1%.
4. Effective area data for RSR#0.5 and #0.7 by Kolev (2006) is compared with data by SRP. $k_G a$ correction has been made. Deviation is 7.2% for RSR#0.5 and 6% for RSR#0.7.
5. $k_L a$ data by Raschig is compared with data by SRP. The system used by Raschig is desorption of CO_2 from water by air. $k_L a$ data has to be transformed from measurement by

CO_2/water system into toluene/water system using the following equation: $\frac{(k_L a)_{tol}}{(k_L a)_{CO2}} = (\frac{D_{tol.L}}{D_{CO2,L}})^{0.5} = 0.666$. Deviation is 33.3% for RSR#0.5 and 28.7% for RSR#0.7.

6. k_Ga data by Raschig is compared with data by SRP. The system used by Raschig is NH_3 absorption from air by water. k_Ga data has to be transformed from measurement by NH_3/water system into SO_2/NaOH system using the following equation: $\frac{(k_G a)_{SO2}}{(k_G a)_{NH3}} = (\frac{D_{SO2}}{D_{NH3}})^{0.5} = 0.756$. Deviation is 40% for RSR#0.5.
7. Pressure drop for Mellapak 2X measured by Sulzer and NTNU has been compared with data measured by SRP. Deviation for NTNU data is 32% and for Sulzer data is 16%.
8. Effective area data for Mellapak 2X by NTNU and Sulzer are compared with data by SRP. k_Ga correction has been made. Deviation is 9.2% for NTNU data and 9.4% for Sulzer data.

Future Work

Next quarter, a standard 250 m^2/m^3 area structured packing Mellapak 250Y will be measured.

The SO_2 sample conditioner will be installed to eliminate water condensation complications. Once SO_2 sampling troubleshooting is completed, k_G measurement for GT-PAKTM 350Z and Raschig Super Ring #0.7 will be repeated.

References

Kolev N, Nakov S, Ljutzkanov L. “Effective area of a highly efficient random packing.” *Chem Engin Proc.* 2006;45:429–436.

Krebs C. “Gas-side mass transfer in irrigated packed columns. Part II: The effect of diffusion and gas flow non-uniformities on the mass transfer.” *Chem Engin Proc.* 1985;19(3):129–142.

Mehta VD, Sharma MM. “Effect of diffusivity on gas-side mass transfer coefficient.” *Chem Engin Sci* . 1966;21(4):361–365.

Menon A, Duss M. “The New Sulzer MellapakTM CCTM and AYPlusTM DC Structured Packings for Post Combustion Capture.” *Post Combustion Capture Conference 2011.* Abu Dhabi UAE. May 17–19, 2011.

Raschig GMBH Jaeger Products, INC. PALL-RING Product Bulletin 350.

Raschig GMBH Jaeger Products, INC. Raschig Super-Ring Product Bulletin 250.

Tamir A, Merchuk JC. “Effect of diffusivity on gas side mass transfer coefficient.” *Chem Engin Sci.* 1978;33(10):1371–1374.

Zakeri A, Einbu A, Svendson H. “Characterization of packing materials for CO_2 absorption.” *Post Combustion Capture Conference 2011.* Abu Dhabi UAE. May 17–19, 2011.

Pilot Plant Modeling of CO_2 Stripping using Piperazine

Quarterly Report for October 1 – December 31, 2011

by Tarun Madan

Supported by the Luminant Carbon Management Program

Department of Chemical Engineering

The University of Texas at Austin

January 31, 2012

Abstract

Following previous campaigns utilizing the two-stage flash skid for stripping the absorbed CO_2 using concentrated 8 m piperazine (PZ), fresh steady state runs were performed in the pilot plant during October 2011. The results generated from the steady state runs were simulated in Aspen Plus® using the Fawkes model. A Microsoft Excel®-based model was also prepared for equilibrium analysis and quick material balance calculations along with rigorous Aspen Plus® simulation.

The result shows good VLE approach for both the vessels. Also, simulations based on existing model showed a mean deviation of 3% for most values but had much larger inconsistencies for CO_2 stripping rate (deviation of 21%). Both models were updated to consider a shift in loading to take into account the adverse effect of solvent degradation. The resulting models showed significant improvement with a shift in loading of magnitude 0.015–0.03, bringing the CO_2 stripping rate deviation to 3%.

Equivalent work calculations demonstrated better performance than previous trials, giving values as low as 34 kJ/mol CO_2. The simulations will be further analyzed for improvement of model, especially for energy balance.

Introduction

New steady state runs were performed and recorded for CO_2 absorption and stripping using 8 m PZ in a campaign undertaken at the pilot plant at J. J. Pickle Research Campus. The readings, taken over the period of 3 weeks in Oct 2011, utilized the two-stage flash skid for CO_2 stripping from the solvent. Overall, 11 steady state sets at different operating conditions were recorded along with simultaneous sampling for concentration of PZ and CO_2 at various sampling points, and using various methods, as mentioned in the next section.

Previous runs using the same skid earlier in the year were simulated in Aspen Plus® using the 5deMayo model (Plaza, 2011). The results showed large deviation in the overhead flow from HP and LP separator of the flash skids, overhead CO_2 rate, and the hot side temperature of rich solvent (Van Wagener, 2011). Current runs were simulated using the Fawkes model for concentrated PZ (Frailie, 2011). Analysis of vapor-liquid equilibrium in the two flash vessels was performed using Microsoft Excel® and VLE equations developed for loaded PZ (Xu, 2011b).

The heat duty and equivalent work in the earlier runs was also exceptionally high, which was attributed to inefficient operation, especially in the cross exchanger (Van Wagener, 2011). The current runs were analyzed for equivalent work and performance of the cross exchanger.

Methods and Discussion

The flowsheet of the two-stage skid is shown in Figure. Concentration measurements were performed at sampling points, to evaluate the rich (feed entering first stage flash), semi-rich (liquid exiting first stage and entering second stage), and lean (liquid existing second stage) liquid composition and loading. The CO_2 and PZ concentration was measured by manual titration and using an auto-titrator.

Major operating conditions that were varied in the campaign were:

1. Pressure Ratio of HP to LP flash vessel. This was varied from 1.5 to 2 by varying the HP flash pressure from 135 to 195 psig. LP pressure was kept more consistent between 80 and 90 psig.
2. Use of cold rich bypass (5 to 10% flow was bypassed from HP vessel and directly sent to LP vessel in most runs).
3. Use of two intercoolers between inlet rich and outlet lean flow for better heat recovery in some runs.

Major analyses performed using the data are discussed next.

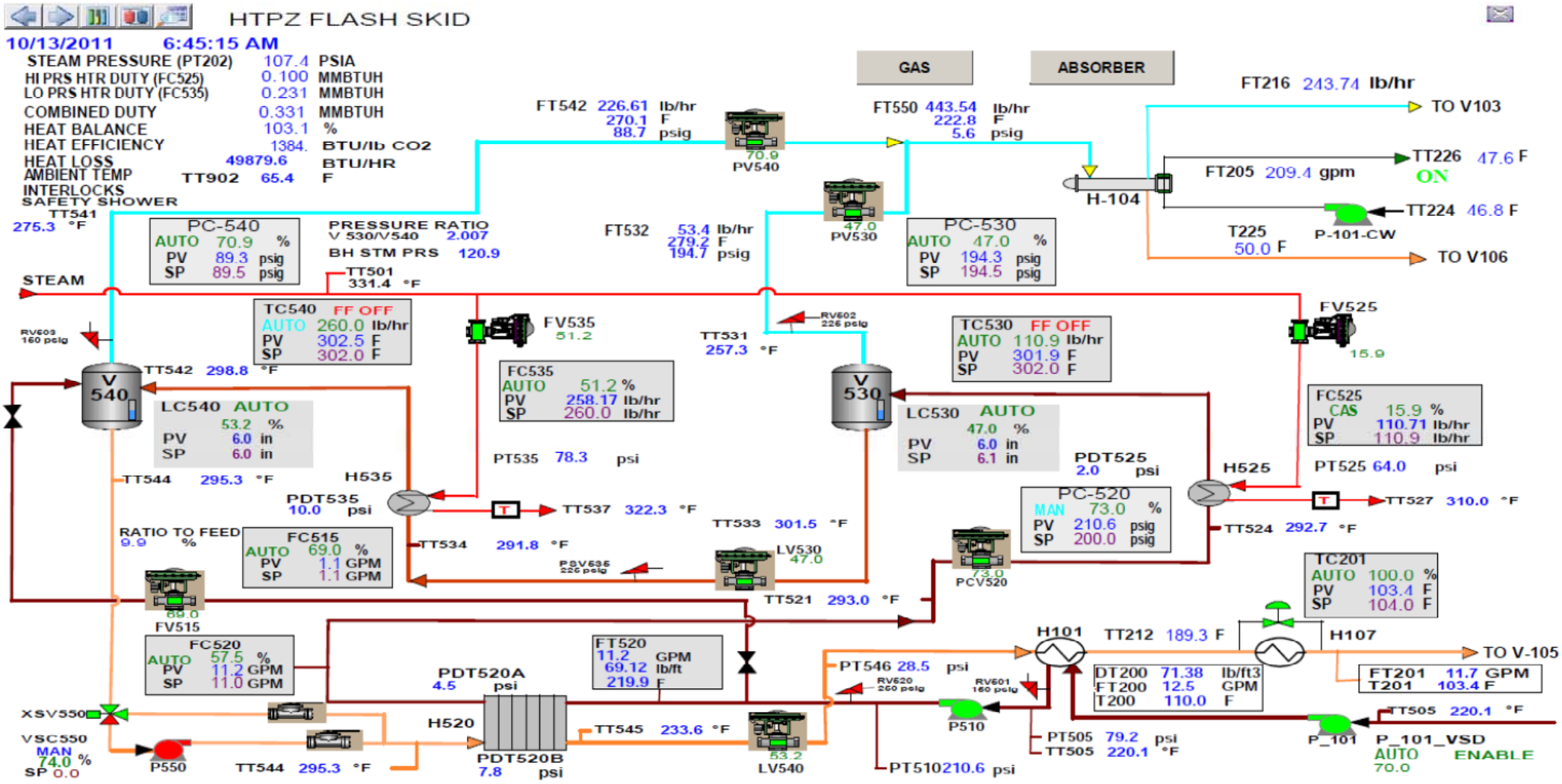

Figure 1: CO_2 Stripping Flowsheet using 2-stage flash

Vapor Liquid Equilibrium

For both HP and LP flash, various temperatures were recorded (inlet to flash, vapor outlet, and liquid outlet). For individual runs, two different loading values were available (one using auto-titrator values, and the other using manual titration values). Equilibrium pressure in any vessel is a function of temperature and loading, with PZ partial pressure calculated using an equation (Equation 1, below) developed in-house for loaded PZ (Xu, 2011a).

$$\ln P_{CO_2}\,(Pa) = 35.3 - 11054\frac{1}{T} - 18.9\alpha^2 + 4958\frac{\alpha}{T} + 10163\frac{\alpha^2}{T} \qquad (1)$$

where, α is the loading of CO_2 in PZ on a mole basis.

Thus,

$$P_{eq} = f(\alpha, T) \qquad (2)$$

Using these equations, we can calculate for any given run various values of pressure based on different values of α and T. Conversely, by fixing T along with P, we can calculate loading required for equilibrium, or by fixing loading along with P, we can calculate equilibrium T.

For the LP vessel, a temperature probe was used for directly measuring the temperature inside the liquid in the LP flash vessel. This temperature was assumed for equilibrium calculations. By fixing P and T, the required loading was calculated for equilibrium. This loading was compared against the measured loading. Results are shown in Figure 2.

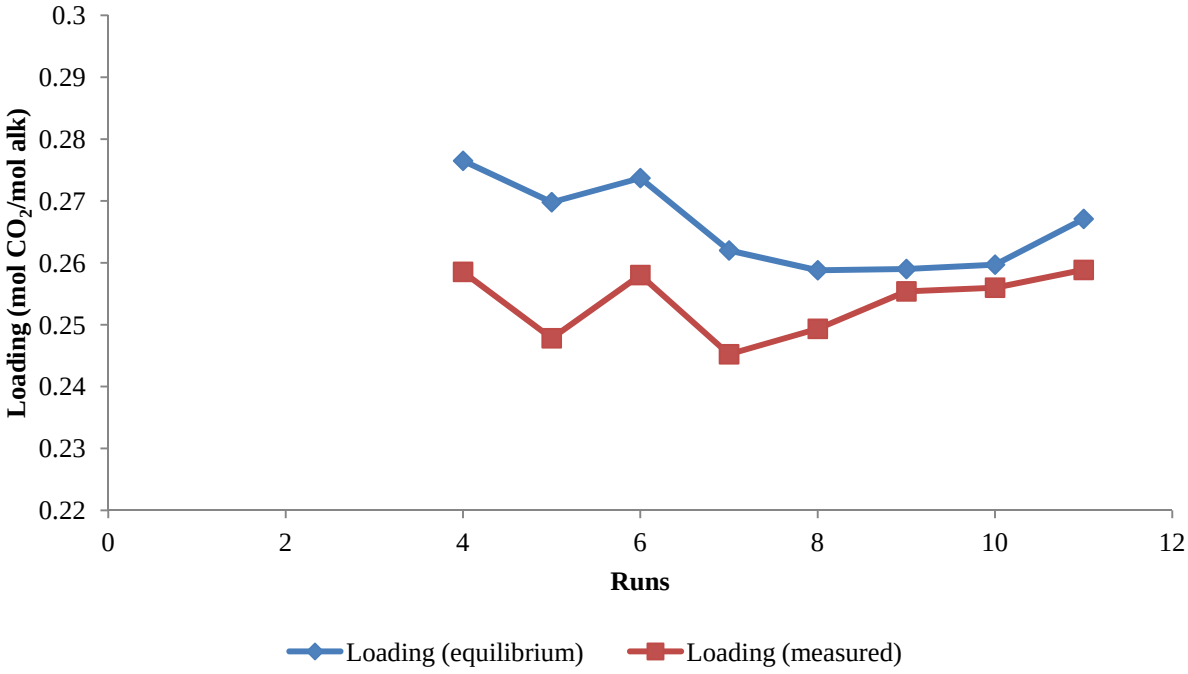

Figure 2: Equilibrium loading compared with measured loading (LP Vessel)

Based on these results, we can see that there is a shift of approximately 0–0.025 between equilibrium loading and measured loading. This can be attributed to solvent degradation which

will effectively decrease the available solvent and thus increase the actual loading. This shift will be further analyzed in simulations.

For the HP vessel, there was no significant difference between inlet temperature and liquid outlet temperature. The inlet temperature was used along with P to calculate loading required for equilibrium. As seen in Figure 3, except for runs 1 and 3, manual values showed better consistency and thus they were used for further analysis.

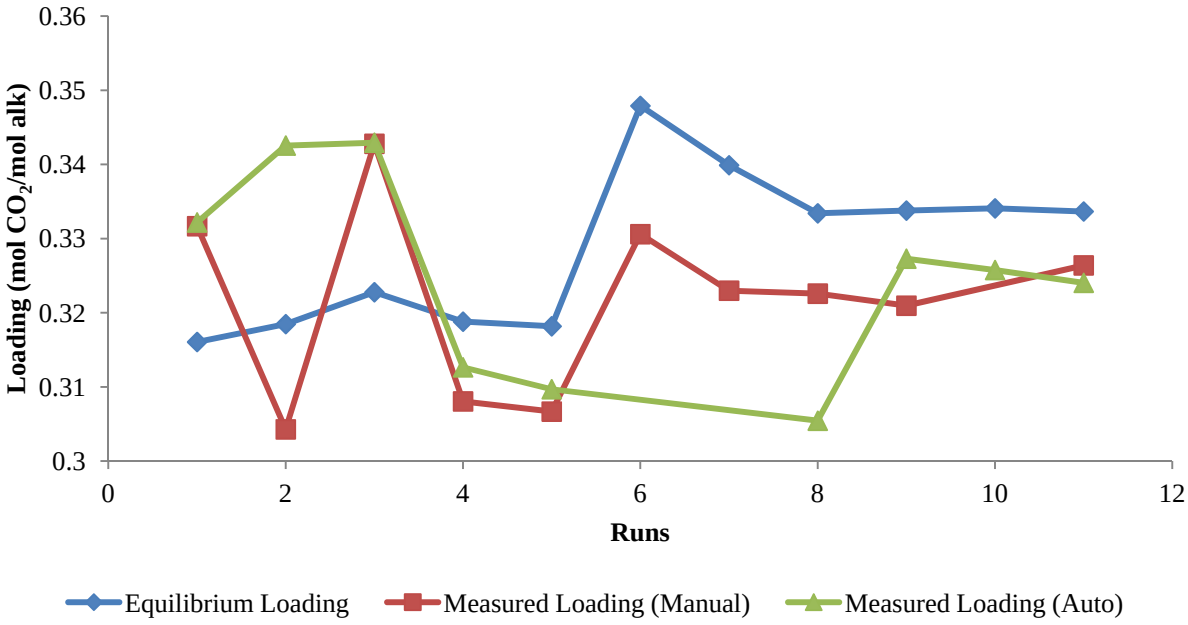

Figure 3: Equilibrium loading compared with measured loading (HP Vessel)

Again, there is a shift of approximately 0–0.02 between equilibrium loading and measured loading which will be analyzed in Aspen Plus® simulations.

CO_2 stripping Analysis

Flash calculations were performed using the above equilibrium conditions and outlet composition and flow estimated in Microsoft Excel®. These runs were rigorously simulated using the Fawkes model in Aspen Plus® to evaluate all the conditions based on inlet conditions. Both the models showed similar results, however, overhead flow and CO_2 rate can be seen as inconsistent with the measured flow. The deviations from the measured quantities are shown in Table 1. The loading shift, introduced in the above analysis, was considered with the simulation, and the resulting simulations showed a better match with the measured results. The mean deviation is shown in Table 2. Figure 4 shows the comparison between measured CO_2 and simulated CO_2 for both cases (with and without loading shift).

Table 1: Deviation between measured and simulated values (no loading shift considered)

Variable	1	2	3	4	5	6	7	8	9	11	MAPE
Lean Flow	1.12%	1.43%	0.42%	0.56%	1.14%	0.12%	0.47%	-0.22%	0.18%	-0.09%	**0.58%**
Semi-rich Loading	6.80%	6.40%	1.92%	6.04%	8.25%	16.89%	17.77%	13.36%	9.54%	13.70%	**10.07%**
Lean Loading	4.74%	6.80%	2.34%	5.79%	8.06%	5.04%	6.53%	2.01%	1.57%	2.32%	**4.52%**
Rich Cold T	-0.73%	-0.60%	-0.72%	-2.33%	-2.30%	-2.02%	-1.03%	-0.68%	-0.34%	-0.59%	**1.13%**
Rich Hot T	-1.33%	-0.99%	-0.37%	-0.69%	-1.27%	-0.92%	-0.11%	-1.62%	-1.83%	-1.83%	**1.10%**
Lean Hot T	1.39%	1.56%	2.16%	1.37%	1.46%	1.21%	3.02%	1.14%	0.87%	0.73%	**1.49%**
HP Overhead T	5.18%	5.69%	5.57%	5.19%	4.94%	8.14%	8.13%	6.56%	7.23%	5.13%	**6.17%**
HP Bottom T	0.11%	0.13%	0.15%	0.10%	0.08%	0.10%	0.11%	0.10%	0.26%	0.04%	**0.12%**
LP Overhead T	-0.03%	0.09%	10.94%	6.26%	0.19%	1.79%	0.51%	6.52%	3.40%	8.25%	**3.80%**
LP Bottom T	1.37%	1.57%	2.17%	1.39%	1.46%	1.20%	3.02%	1.14%	0.87%	0.73%	**1.49%**
MAPE	**2.28%**	**2.53%**	**2.68%**	**2.97%**	**2.92%**	**3.74%**	**4.07%**	**3.33%**	**2.61%**	**3.34%**	**3.05%**
Stripped CO_2	-25.20%	-32.09%	-21.77%	-25.93%	-30.32%	-22.85%	-19.07%	-13.26%	-17.38%	-11.26%	**21.91%**
HP Overhead Flow	-49.65%	-64.39%	-53.26%	-44.59%	-59.55%	-78.99%	-100.00%	-66.51%	-60.84%	-46.17%	**62.40%**
LP Overhead Flow	-13.41%	-11.15%	29.69%	6.64%	-9.77%	5.78%	-0.47%	32.37%	9.90%	25.60%	**14.48%**

*MAPE is Mean Absolute Percentage Error

Table 2: Deviation between measured and simulated values (with loading shift considered)

Variable	1	2	3	4	5	6	7	8	9	11	MAPE
Loading Shift	0.03	0.03	0.03	0.03	0.03	0.03	0.015	0.015	0.015	0.015	
Lean Flow	-0.39%	-0.06%	-0.90%	-0.81%	-0.31%	-1.13%	-0.28%	-0.90%	-0.52%	-0.78%	**0.61%**
Semi-rich Loading	6.12%	5.72%	1.28%	5.03%	7.56%	16.55%	18.12%	13.01%	9.21%	13.70%	**9.63%**
Lean Loading	3.56%	5.20%	0.78%	4.25%	6.45%	3.49%	5.71%	1.20%	0.78%	2.32%	**3.37%**
Rich Cold T	-0.73%	-0.60%	-0.72%	-2.38%	-2.30%	-2.02%	-1.03%	-0.68%	-0.34%	-0.59%	**1.14%**
Rich Hot T	-1.83%	-1.60%	-1.25%	-1.72%	-1.55%	-1.54%	-0.14%	-1.83%	-2.04%	-2.04%	**1.55%**
Lean Hot T	1.39%	1.56%	2.16%	1.37%	1.46%	1.21%	3.02%	1.14%	0.87%	0.73%	**1.49%**
HP Overhead T	5.18%	5.69%	5.57%	5.19%	4.94%	8.14%	8.13%	6.56%	7.23%	5.13%	**6.17%**
HP Bottom T	0.11%	0.13%	0.15%	0.10%	0.08%	0.10%	0.11%	0.10%	0.26%	0.04%	**0.12%**
LP Overhead T	-0.02%	0.08%	9.46%	5.01%	0.13%	1.03%	0.26%	6.17%	3.08%	7.89%	**3.31%**
LP Bottom T	1.37%	1.57%	2.17%	1.39%	1.46%	1.20%	3.02%	1.14%	0.87%	0.73%	**1.49%**
Stripped CO_2	3.66%	-1.21%	6.05%	2.91%	-0.82%	5.90%	-2.76%	2.24%	-2.57%	3.15%	**3.12%**
HP Overhead Flow	2.97%	-1.75%	-1.61%	4.27%	-8.42%	67.15%	-3.79%	-4.71%	-6.06%	-4.78%	**10.55%**
LP Overhead Flow	-13.66%	-11.52%	33.49%	11.22%	-10.11%	6.60%	2.13%	33.13%	9.90%	26.33%	**15.81%**
MAPE	**3.15%**	**2.82%**	**5.04%**	**3.51%**	**3.51%**	**8.93%**	**3.73%**	**5.60%**	**3.36%**	**5.25%**	**4.49%**

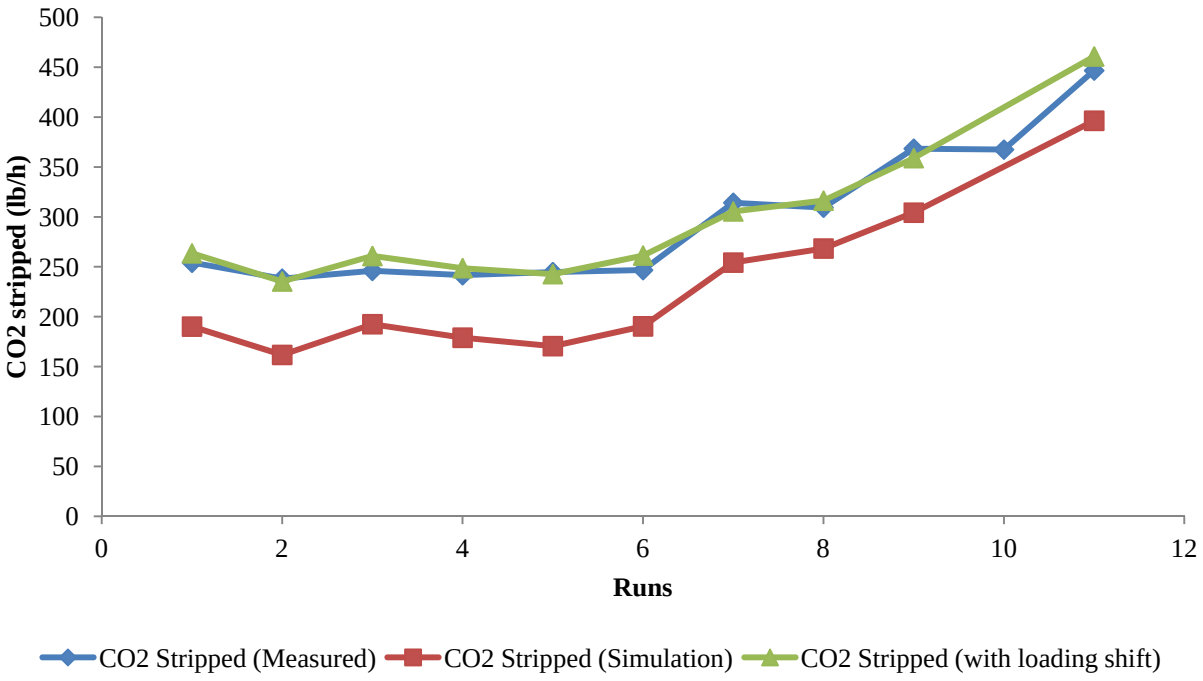

Figure 4: Comparison of CO_2 stripped between measured and simulated quantities

Equivalent Work Analysis

Equivalent work for each run was calculated by using Equation 3.

$$W(eq) = 0.75\left(1 - \frac{T_{sink}}{T_{source}}\right)Q_{reb} + Q_{pump} + Q_{comp} \qquad (3)$$

Equivalent work was calculated for each run based on the heat values and CO_2 stripping rates reported in the pilot plant results. Further, source T of 150 °C and sink T of 40 °C is assumed.

Equilibrium work for the pump is calculated using the simulations for 0.72 efficiency pumps working at conditions specified in the trial results.

Similarly, for compressors, values are based on the equations developed in-house (Van Wagener, 2011) for discharge pressure of 150 bar and assumes a multi-stage compressor with HP and LP CO_2 flow going in corresponding stages. The HP and LP flow split was calculated using the simulations closest to the measured results as obtained above.

$$W_{comp}\left(\frac{kJ}{mol\ CO_2}\right) = \begin{cases} 4.572\ln\left(\frac{150}{P_{in}}\right) - 4.096 & P_{in} \le 4.56\ bar \\ 4.023\ln\left(\frac{150}{P_{in}}\right) - 2.181 & P_{in} > 4.56\ bar \end{cases} \qquad (4)$$

The calculated equivalent work can be compared against the theoretical work based on models and previous trial runs (Van Wagener, 2011). Equivalent work was calculated using the reported heat and using the heat values without the predicted heat loss. Both values are tabulated in Table 3.

Table 3: Equivalent Work

Run	Q (without loss)	W	W (comp)	W (pump)	W (total)	Q (loss)	W (loss)	W (total)
	MMBTU/h	kJ/mol	kJ/mol	kJ/mol	**kJ/mol**	MMBTU/h	kJ/mol	**kJ/mol**
1	0.46	35.97	9.49	1.46	**46.92**	0.049	3.86	**43.06**
2	0.43	36.17	9.45	1.45	**47.08**	0.047	3.93	**43.14**
3	0.41	33.56	9.38	1.47	**44.41**	0.049	3.95	**40.45**
4	0.33	27.54	9.36	1.44	**38.34**	0.050	4.09	**34.25**
5	0.38	30.99	9.43	1.41	**41.83**	0.049	4.02	**37.81**
6	0.33	26.95	9.39	1.97	**38.31**	0.050	4.02	**34.29**
7	0.46	29.12	9.65	1.98	**40.75**	0.046	2.89	**37.86**
8	0.51	32.64	9.62	1.75	**44.01**	0.053	3.41	**40.60**
9	0.60	32.39	9.77	1.63	**43.78**	0.049	2.66	**41.12**
10	0.58	31.68	-	1.63	-	0.048	2.59	-
11	0.69	30.98	9.58	1.74	**42.30**	0.051	2.29	**40.01**

The resulting values, as shown in Table 4, show better performance of this trial compared to the results obtained in a previous trial. This is mainly due to better performance of the cross exchanger in this trial. In some of the trials, where two cross exchangers were used, better performance and less equivalent work is observed.

Figure 5 compares the effect of cross-exchange on equivalent work. In the runs where two intercoolers were used, there was more heat recovery and higher temperature of inlet stream to the main cross exchanger. These cases had considerably less equivalent work due to a lower heat requirement for heating to flash temperatures.

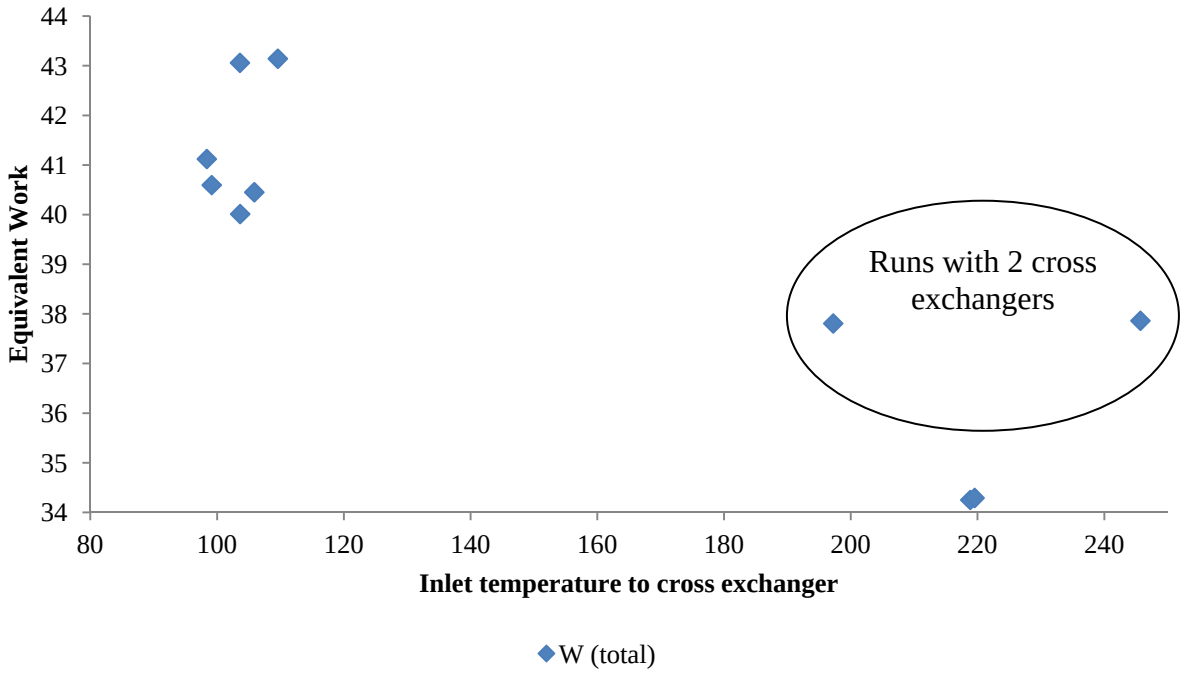

Figure 5: Equivalent work compared with temperature of rich inlet to cross exchanger

Conclusions

1. The flash vessels show good approach to vapor liquid equilibrium. The offset from equilibrium can be attributed to degraded solvent, effectively decreasing the available solvent and increasing the loading.
2. Simulations using the Fawkes model are generally satisfactory, but show larger deviation in CO_2 stripped and heat balance.
3. Adjusted simulations using loading shift due to solvent degradation show much improved performance.
4. Equivalent work calculations show better consistency with modeled values. It is directly correlated with the performance of the cross exchanger, which has shown improved performance in this campaign.
5. With two cross exchangers in series, the pilot plant achieved an equivalent work of 38.3 kJ/mol CO_2 using the two-stage flash with aged 8 m PZ. The heat recovery from the lean stream has increased considerably when two cross exchangers were used instead of only one, thereby decreasing equivalent work.

Future Work

The simulations and data from the steady state runs of the pilot plant will be further analyzed to improve the existing model. The loading shift will be further analyzed to incorporate its effect into the model.

References

Frailie P, Plaza JM, Van Wagener DH, Rochelle GT. "Modeling piperazine thermodynamics." *Energy Proc.* 2011;4:35–42.

Plaza JM. *Modeling of Carbon Dioxide Absorption Using Aqueous Monoethanolamine, Piperazine and Promoted Potassium Carbonate.* The University of Texas at Austin. Ph.D. Dissertation. 2012.

Van Wagener DH. *Stripper Modeling for CO_2 Removal Using Monoethanolamine and Piperazine Solvents.* The University of Texas at Austin. Ph.D. Dissertation. 2011.

Xu Q. *Thermodynamics of CO_2 Loaded Aqueous Amines for CO_2 Capture.* The University of Texas at Austin. Ph.D. Dissertation 2011b.

Xu Q, Rochelle GT. "Total Pressure and CO_2 Solubility at High Temperature in Aqueous Amines." *Energy Proc.* 2011a;4:117–124.

Cold, Rich Bypass to Reduce Stripper Equivalent Work

Quarterly Report for September 1 – December 31, 2011

by Brent Sherman

Supported by the Luminant Carbon Management Program

Department of Chemical Engineering

The University of Texas at Austin

January 31, 2012

Abstract

Cold, rich bypass with two-stage flash was explored to determine the optimal bypass for minimizing equivalent work (W_{eq}). 8 m PZ with a rich/lean loading of 0.386/0.27 was used with a pressure ratio between the flashes of 1.5. The minimum W_{eq} was 30.9 kJ/gmol CO_2 with a 3% bypass to the high-pressure tank and a 5% bypass to the low-pressure tank. This is a 4.9% improvement over the W_{eq} of 32.5 kJ/gmol CO_2 without bypass.

Introduction

The work this quarter focused on using cold, rich bypass to strip a loaded 8 m piperazine (PZ) solution in two flash tanks. The goal of this study was to minimize the equivalent work by varying the amount bypassed to each tank. This builds on previous work done by David Van Wagener. The idea behind cold, rich bypass is to remove a small portion of the loaded amine solution and inject it into the top of each flash tank. This provides for a closer termperature approach on the hot end of the exchanger. It also allows cold liquid to condense the amine and water from the overhead.

Methods and Discussion

The system shown in Figure 1 was modeled in Aspen Plus®. The e-NRTL model is used along with Fawkes (Frailie et al., 2011) to model the PZ solution. What is described in the figure is the removal of two bypass streams from the main stream prior to the heat exchanger. Each bypass is fed into the top of a flash tank to condense the amine and water. The high pressure (HP) flash tank is at a pressure 1.5 times greater than the low pressure (LP) tank. The overhead from the LP tank is sent to a condenser to remove the water and then the remaining vapor is compressed to the HP pressure. This stream and the overhead of the HP tank are mixed in a second condenser, whose overhead goes to the compression train for compression to 150 bar.

In order for the cases to be comparable, the heat exchanger had a 5 °C log-mean temperature difference. Other specifications include the rich/lean loading of 0.386/0.27 and 150 °C reboiler temperature. The HP tank was modeled assuming equilibrium, whereas the LP flash was modeled as rate-based.

The equivalent work (kJ/gmol CO_2) was calculated based on the compressor work (W_{comp}), rich pump work (W_{pump}), and heat work (W_{heat}), which derives from the reboiler duties (Q in kJ/gmol

CO_2), using Equation 1 (Van Wagener, 2011). A 5 K driving force was used for the reboilers (T_i), and T_{sink} was assumed to be 313 K. A lean pump is unnecessary as the pressure in the lean stream is sufficient to move the stream to the top of the absorber. W_{pump} was calculated in Aspen Plus®. W_{comp} was found using the correlation in Equation 2, whose development is detailed in Van Wagener, 2011. It yields the work necessary for compression to 150 bar.

$$W_{eq} = \sum_{i=1}^{n\ reboilers} 0.75\ Q_i \left(\frac{T_i + 5K - T_{sink}}{T_i + 5K}\right) + W_{pump} + W_{comp} \quad (1)$$

$$W_{comps} = \begin{cases} 4.572 \ln\left({}^{150}/_{P_{in}}\right) - 4.0961, & P_{in} \leq 4.56 \text{ bar} \\ 4.023 \ln\left({}^{150}/_{P_{in}}\right) - 2.181, & P_{in} > 4.56 \text{ bar} \end{cases} \quad (2)$$

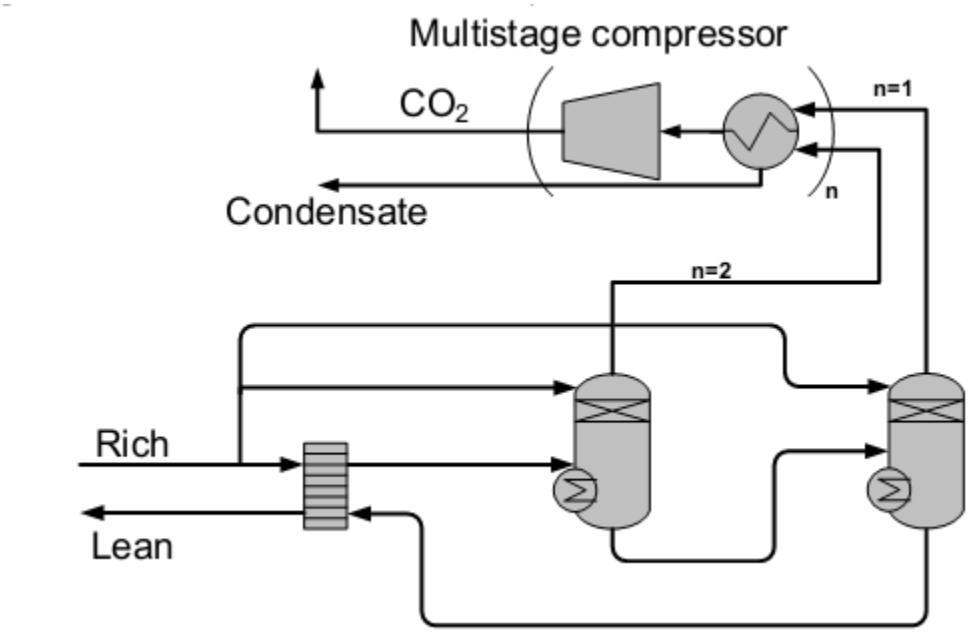

Figure 1: Cold, rich bypass to high pressure and low pressure flashes (Van Wagener, 2011)

Results

By varying the HP and LP bypass, the minimum equivalent work was found. As shown in Figure 2, the optimal bypass of 3% HP with 5% LP resulted in an W_{eq} of 30.90 kJ/gmol CO_2. This is a 4.9% improvement over the no-bypass base case W_{eq} of 32.5 kJ/gmol CO_2 (Van Wagener, 2011). Since there is greater water vapor content in the LP flash, meaning a lower partial pressure of CO_2, in all beneficial cases the LP flash receives more bypass than the HP.

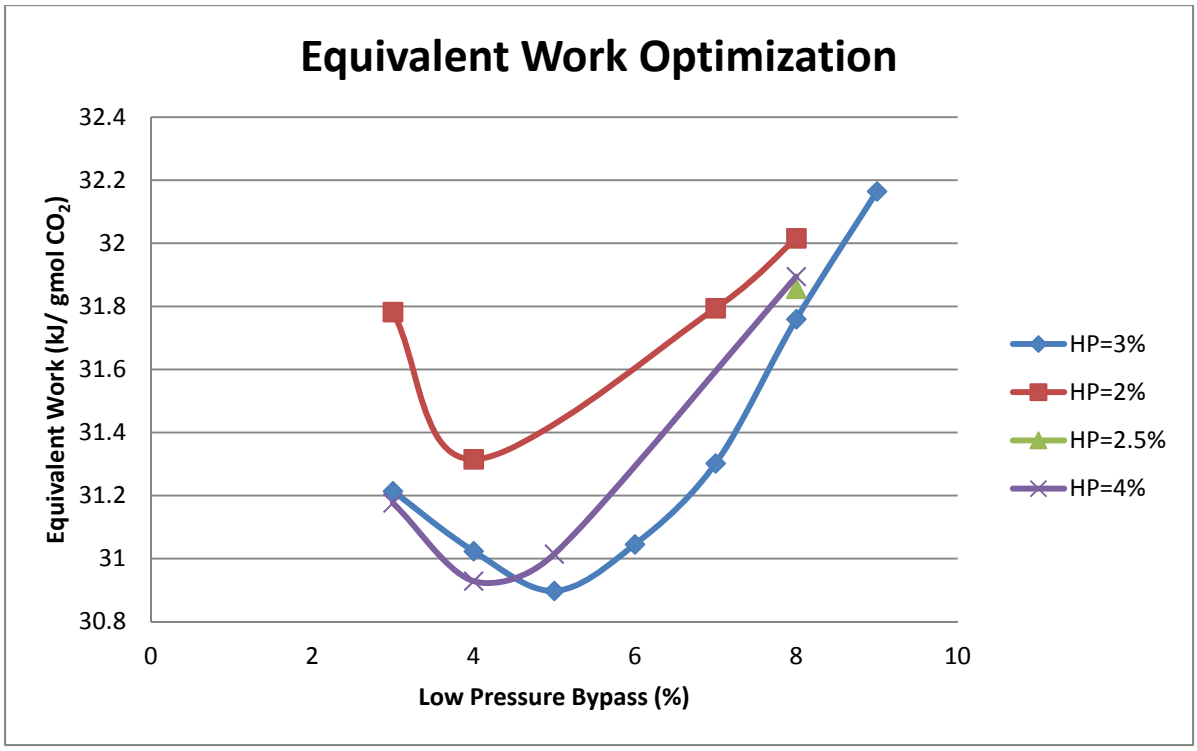

Figure 2: Optimal bypass. Each curve represents a fixed HP bypass. 3% HP bypass with 5% LP bypass yields the minimum W_{eq} of 30.90 kJ/ gmol CO_2.

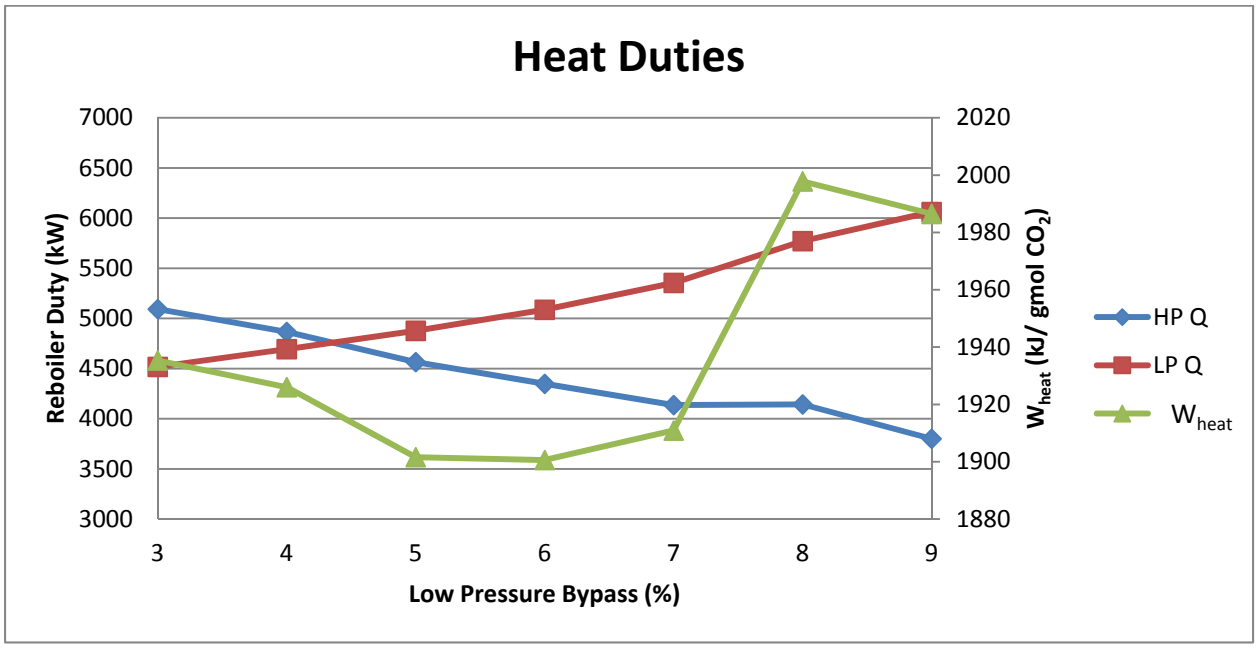

Figure 3: Heat duties for HP bypass of 3%. Near the optimal LP bypass of 5%, the reboiler duty for each flash tank is nearly equal. The W_{heat} curve has a similar shape to the W_{eq} curve.

The compressor and pump work are nearly constant while varying the bypass ratio. However, the reboiler duties of the flash tanks vary substantially, as shown in Figure 3. This variation is the principle reason for the shape of the curve in Figure 2.

For the optimal case, the profile of the two columns is shown **Error! Reference source not found.** and Table 2.

Table 1: LP flash for optimal case. P = 743 kPa, Q_{reb} = 4835 kW.

Stage	Liquid T	Vapor T	Liquid	Vapor	Y	Y
	C	C	kmol/sec	kmol/sec	H2O	CO2
1	76.36	120.68	0.17	0.06	0.27	0.73
2	100.37	132.03	0.18	0.07	0.35	0.65
3	119.42	139.60	0.19	0.08	0.43	0.57
4	131.99	144.49	0.20	0.09	0.49	0.51
5	139.69	147.71	0.20	0.10	0.53	0.46
6	149.92	149.92	3.22	0.10	0.57	0.43

Table 2: HP flash for optimal case. P = 1114.99 kPa, Qreb = 4521.93 kW. This tank is modeled assuming equilibrium.

Stage	T	Liquid	Vapor	Y	Y
	C	kmol/sec	kmol/sec	H_2O	CO_2
1	92.56	0.10	0.05	0.07	0.93
2	121.77	0.11	0.06	0.18	0.82
3	137.74	0.12	0.07	0.29	0.71
4	144.93	0.12	0.07	0.35	0.65
5	147.99	0.12	0.08	0.38	0.62
6	149.90	3.08	0.08	0.39	0.61

Conclusions

1) Compared to no bypass, using cold, rich bypass to a high pressure and a low pressure flash reduces the equivalent work by 4.9% for 8 m PZ.

2) The largest component of equivalent work is the reboiler duty of each flash, and so the optimal amount of bypass occurs when the two duties are nearly equal. This was at a bypass of 3% high pressure and 5% low pressure.

References

Frailie P, Plaza JM, Van Wagener DH, Rochelle GT. "Modeling piperazine thermodynamics." *Energy Proc.* 2011;4:35–42.

Van Wagener DH, Rochelle GT. "Stripper configurations for CO2 capture by aqueous monoethanolamine and piperazine." *Energy Proc.* 2011;4:1323–1330.

Van Wagener DH. *Stripper Modeling for CO_2 Removal Using Monoethanolamine and Piperazine Solvents.* The University of Texas at Austin. Ph.D. Dissertation. 2011.

Sepideh Ziaii – Ph.D. dissertation

Chapter three: Steady State Optimization of Partial Load Operations in CO_2 capture

Absorption/stripping process is a mature technology commonly used for removing CO_2 from flue gases in coal-fired power plants. However, it is an energy intensive process and therefore needs special efforts to be implemented economically in both design and operation.

This chapter is devoted to exploring energy efficient control strategies for a capture plant designed to remove 90% of inlet CO_2 using aqueous MEA solution in response to two load reduction scenarios over a wide range of operation: power plant load reduction and reboiler steam rate reduction.

For this purpose, I integrated the absorption/stripping dynamic model with the steady state model of power cycle steam turbines and general performance curves of the CO_2 compressor to take into account operational interactions. I simulated and analyzed the operational scenarios, and then optimized the operation by implementing solvent circulation rate and compressor speed to minimize total lost work at the new steady state in the presence of operational limitations. Those limitations are related to the thermal degradation of solvent, run off conditions in circulation pumps, and surge conditions of the CO_2 compressor. I explored surge control strategies and compared them for both scenarios and presented an applied guideline for optimally operating the integrated plant during the transitional operations.

3.1. INTRODUCTION

The absorption/stripping process with aqueous amine solution remains one of the commercial post-combustion CO_2 capture technologies in coal-fired power plants, but the drawback of this chemical reaction-based technology is the high energy demand.

There have been many efforts to enhance the energy performance of this process that mainly focused on static analysis of capture when it is operating at full load and consequently numerous publications on this topic exist and several steady state models have been created. Those studies minimized energy consumption or maximized performance of the absorber and stripper at full load operation by investigating different solvent options, operating conditions, and various process configurations. (e.g., Freguia et al., 2003; Oyenekan et al., 2007; Plaza et al., 2010; Van Wagener et al., 2011).

Steady-state analysis does not reflect issues related to transitional behavior and operation of the plant in response to the possible disturbances and potential dynamic operational scenarios. Besides employing appropriate solvent and process configuration, with regard to the operation, the strategy and structure of control play an important role in energy saving and performance enhancement.

According to the paper written Bergerson et al. (2007), CO_2 capture operating at full load could reduce net energy output of a coal-fired power plant by 11–40% from that of an equivalent gross size plant without CO_2 capture. This energy bulk mainly includes the heat required for solvent regeneration and the energy for CO_2 compression. The regeneration heat can be provided by the steam extracted between the intermediate- and low-pressure turbines.

By giving a plant operator the option to choose a desired CO_2 capture operating condition based on current market conditions such as fuel prices, CO_2 prices, and electricity demand, flexible CO_2 capture can be utilized to operate more economically than if capture systems are restricted to continuous, full-load operation (Ziaii et al., 2009).

Transitional conditions that commonly occur in power plants, such as startup, shutdown, and load variation, influence the operation of downstream processes such as CO_2 capture. These operational scenarios, along with the requirement of capture flexibility, are important issues that must be investigated in order to develop efficient control strategies.

Due to the importance of understanding the dynamics of CO_2 capture, there has been growing interest in developing dynamic capture processes over recent years. Kvamsdal et al. (2009) studied the dynamic responses of the absorber to the startup and power plant load variation. Ziaii et al. (2009) presented the dynamic response of the stripper to the step change made in the reboiler steam rate. Lawal et al. (2010) combined the dynamic model of absorber and stripper and observed operation of the plant in response to the disturbances imposed by the upstream power plant. Most previous studies have focused on understanding dynamics of either absorber and stripper or integrated plant and have not performed operation optimization. Schach et al. (2011) wrote about optimizing the operation of CO_2 capture with MEA that used self-optimized control to design a control structure for operating the capture at constant removal with minimal energy demand over 40–100% power plant load change. All previous work that studied the power plant load variation scenario assumed a change only in flue gas inlet condition. However, the variation of total steam rate in the power cycle is a consequence of load variation that seriously influences the operation of capture mainly in stripping and compression parts for the cases that extract required reboiler steam from steam turbines. How to operate the CO_2 compressor during dynamic operations is another important issue that affects the operation of capture and plays an important role in minimizing energy consumption. Previous studies have ignored that effect.

In contrast to previous work, this study integrates the dynamic model of the absorber and stripper, and combines the capture plant with a steady state model of steam turbines and a multi-stage variable speed compressor to take into account all the interactions during power plant load and reboiler steam load reduction scenarios. In addition, by incorporating practical performance models for pumps and the CO_2 compressor, it explores the operational boundaries created by compressor and pump limitations and performs optimization to minimize total lost work at new steady state in the presence of those constraints.

This work is unique in the field since it simulates the operations with a fully integrated model and covers most of the deficiencies found in previous works. It presents a comprehensive analysis and provides new results on control strategies for optimal capture in response to partial load operations.

The following sections detail the plant specifications and the method of simulation of partial load operation, present the results and discussion for both scenarios, and summarize the conclusions.

3.2. METHODOLOGY

The simulation of partial load operation scenarios for CO_2 capture with MEA is initially designed with following specifications:

- Gas rate and composition: 5.48 kmol/s, 13% CO_2

- Electric rate: 100 MW
- Absorber packing height: 15 m.
- Stripper packing height: 10 m.
- CO_2 removal with 30 wt % MEA: 90%.
- Optimum lean loading (or rich solvent rate) that minimizes total equivalent work: 0.233 mole CO_2/mole MEA (solvent rate = 17.462 kmol/sec).
- Reboiler temperature: 120 °C.
- CO_2 discharge pressure compressor: 150 bar.
- Assumed that extracted reboiler steam = 30% total power cycle steam rate
- Steam turbine initial design condition (Lucquiaud, 2010):

P_{HP}^{in}= 290 bar, P_{IP}^{in}= 60 bar, P_{LP}^{in}= 2.65 bar, P_{LP}^{out}= 0.04 bar.

As illustrated in Figure 1, the liquid levels in the sumps and the ratio of liquid levels in storage tanks are controlled via three downstream valves to keep the liquid hold-up in balance. In order to save energy during power plant load reduction, the steam valve is kept wide open during operation while in reboiler steam load reduction it is employed to control the steam rate. The compressor speed and the position of the liquid valve downstream of the rich storage tank are two variables that can be manipulated to maximize the energy performance of the plant in response to both partial load scenarios.

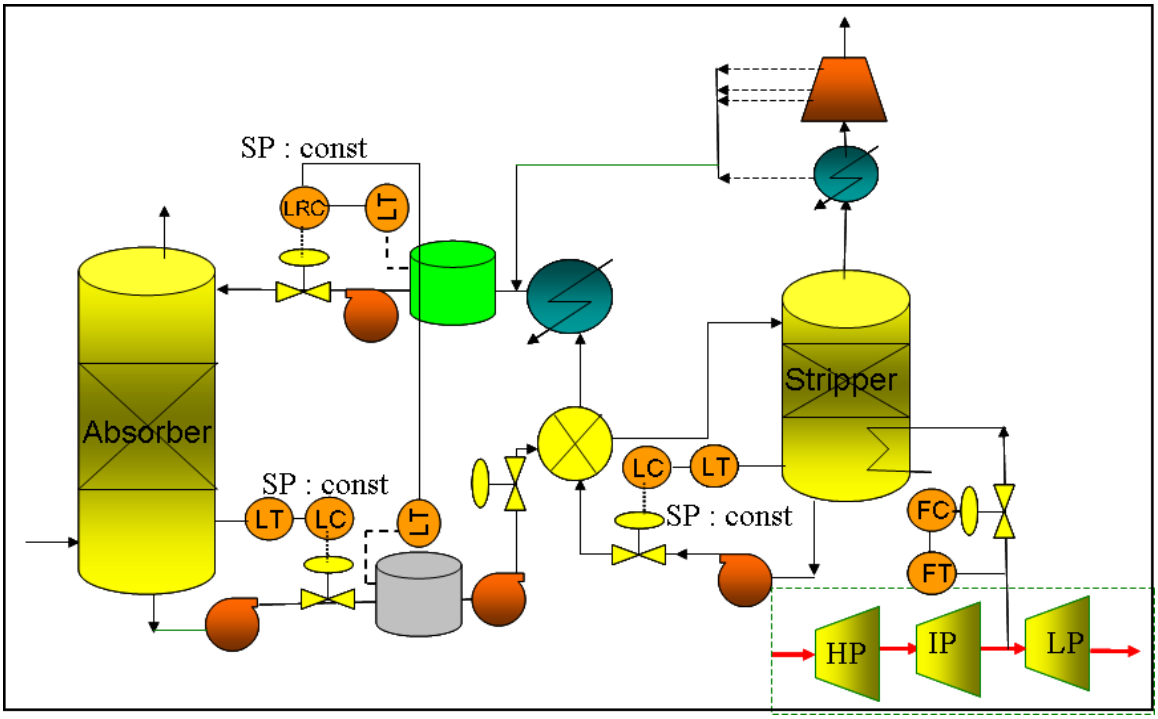

Figure 3.1: Process flow sheet of absorption/stripping process integrated with CO_2 compressor and power cycle steam turbines, used for simulation of dynamic operation. The plant is initially designed to the following specifications: H_{Abs} = 15 m, H_{Stripp} = 10 m, ΔT_{HX} = 5 °C, T_{Reb} = 120 °C, T_{Cooler} = 40 °C P_{HP}^{in} = 290 bar, P_{IP}^{in} = 60 bar, P_{LP}^{in} = 2.65 bar, P_{LP}^{out} = 0.04 bar.

During power plant load variation, some process variables are subject to change. One of the important variables that affects capture plant operation is the property of flue gas entering the absorber. Based on findings by Kvamsdahl et al. (2009) about the effects of power plant load reduction on exhausted gas, the rate of flue gas is reduced accordingly while the composition and temperature are constant. The other issue resulting from boiler load change is related to the steam cycle and further impact on the operation of the stripping section since the reboiler steam is extracted from IP/LP cross point. Accordingly, the total steam rate in steam turbines changes with boiler load and no action is performed to control the pressure at turbine inlet/outlet conditions. This analysis takes into account both effects on the plant at the same time.

The objective of this chapter is to present analysis and optimization of the operating conditions of a capture plant at new steady state in response to those operational scenarios. It will not include results and discussion of the transitional behavior of the MEA plant during operation. For each scenario, the corresponding disturbances are applied, the simulation is run at dynamic mode until the new steady is reached, and the simulation outputs are then recorded. For optimization cases, the dynamic optimization tool of ACM® is used to simulate and ultimately minimize the objective function in the presence of constraints and provide optimum final values for variables.

3.3. RESULTS AND DISCUSSION

This section discusses the results of analyses and optimization of capture plant operation when it is operated in two load reduction scenarios: partial load operation of the power plant, and reboiler steam rate reduction.

3.3.1. POWER PLANT LOAD REDUCTION

As explained in section 3.2, this work simulates partial load operation of a power plant by reducing the inlet flue gas rate of the absorber and inlet total steam rate of the steam turbines at the same time and the same percentage. The simulation outputs are reported when the plant reaches steady state. As power plant load is reduced, the extracted steam pressure decreases due to decreasing inlet flow to the turbines and initially less steam is condensed in the reboiler. In this condition, if the compressor continues to work at its rated speed or higher speed, the stripper and reboiler pressure and temperature tend to decrease initially, which gradually results in condensing more steam at lower pressure and subsequently vaporizing more CO_2 and water and pressurizing the stripper and reboiler. Another potential strategy is to reduce compressor speed, which initially results in pressurizing the stripper. Dynamically, this effect reverses the operation by reducing steam condensation, CO_2 and water vaporization, and finally reducing stripper and reboiler pressure and temperature. The dynamic effects of this operational scenario will be discussed in detail in the next chapter.

The final pressure and temperature primarily depend on the degree of load reduction in the steam cycle of the power plant and the direction and degree of change in the compressor speed, and depends to a much less extent on the solvent circulation rate. As shown in Figure 2, sketched for 90% load operation of the power plant, increasing solvent circulation rate increases the amount of CO_2 absorbed in the absorber and desorbed in the stripper and consequently leads to pressurizing the stripper and reboiler.

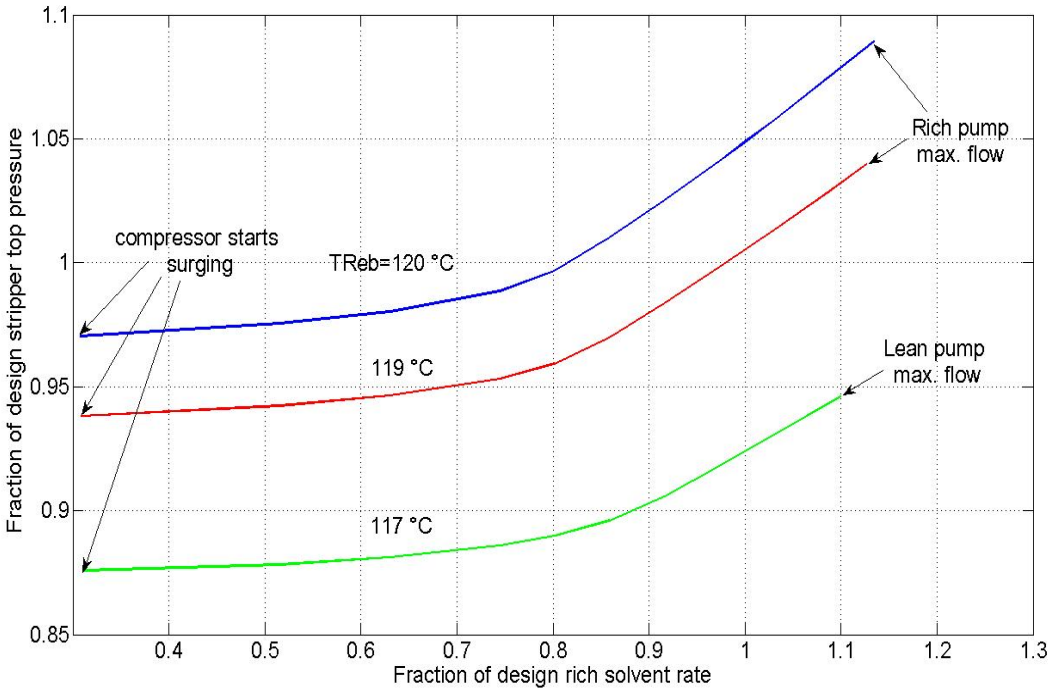

Figure 3.2: Output with boiler load reduction: the effects of rich solvent rate and reboiler temperature (adjusted by compressor speed) on the stripper top pressure at new steady state condition when the plant is operated at 90% boiler load.

The solvent rate may vary over a range set by operational constraints for compressor and pumps. At the minimum solvent rate, which is independent of reboiler temperature, the CO_2 rate entering the compressor is low enough that it causes the compressor to surge. The maximum flow rate is set by one of the pumps that reaches run off (maximum flow) earlier. For the highest temperature, e.g., 120 °C, the pump sending rich solution to the top of the stripper reaches its maximum flow while at lower temperature, 117 °C and 119 °C, the pump handling lean solution reaches maximum flow earlier.

Figure 3.3, representing the operating curves on the multi-stage compressor performance map, indicates how increasing temperature or decreasing solvent rate moves the compressor operating curve to the surge limit curve. For each isothermal curve there is a turning point, which is associated with the turning point on stripper pressure around 80% of design solvent rate (Figure 3.2). At solvent rate less than the turning point, the suction pressure is relatively low and constant such that as the solvent rate increases the compressor volumetric inlet flow increases. At the turning point, the rate of compressor suction pressure becomes greater and consequently, as the solvent rate goes up, inlet gas density increases and volumetric flow decreases.

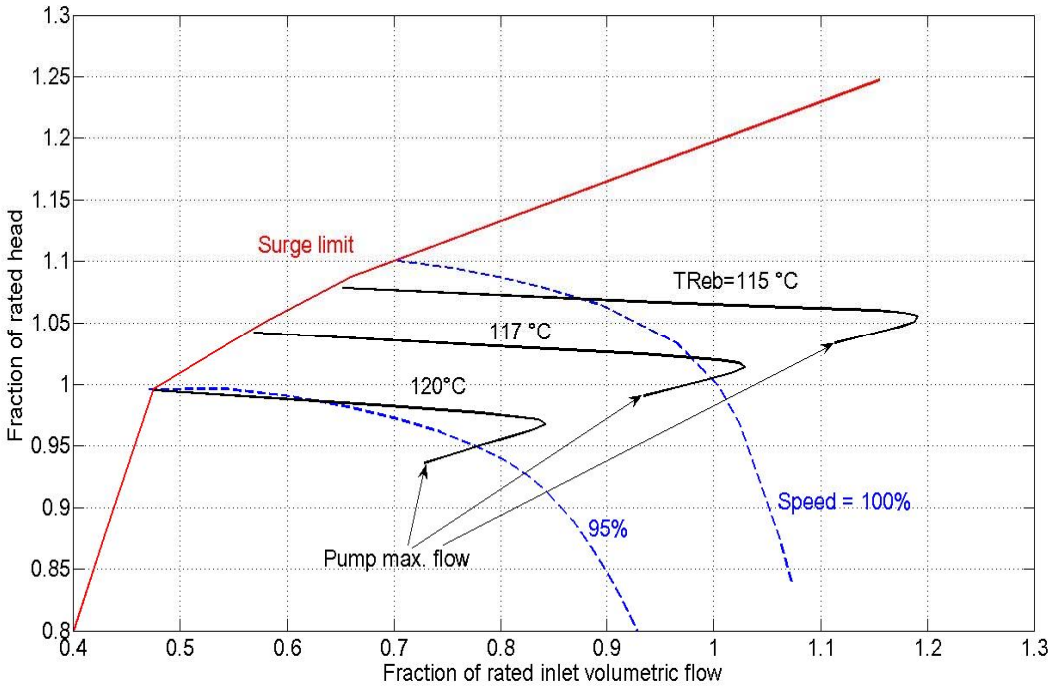

Figure 3.3: The performance map of a multi-stage (5 stages) CO_2 compressor when the power plant is operated at 90% load. The operating curves are associated with different reboiler temperatures (adjusted by compressor speed), while the solvent rate is varied over the range constrained by compressor surge and maximum pump flow.

The results have shown that for every reboiler temperature set by compressor speed there is an optimum solvent rate that minimizes reboiler equivalent work and, consequently, total equivalent work. There is also an optimum solvent rate that maximizes CO_2 removal; however, those optima are not identical (see Figures 3.4 and 3.5).

The maximum reboiler temperature is set at 120 °C, where MEA thermal degradation starts. The minimum temperature for 90% operating load is 115 °C where the compressor speed exceeds 120% of its rated speed. As seen in Figure 3.4, the higher the temperature in the reboiler, the lower the equivalent work. Since the total steam rate in the power cycle is reduced in this scenario, the pressure drops at the extracting point and consequently less steam is condensed in the reboiler and less CO_2 is stripped. Decreasing temperature in the reboiler results in extracting more steam and increasing CO_2 removal.

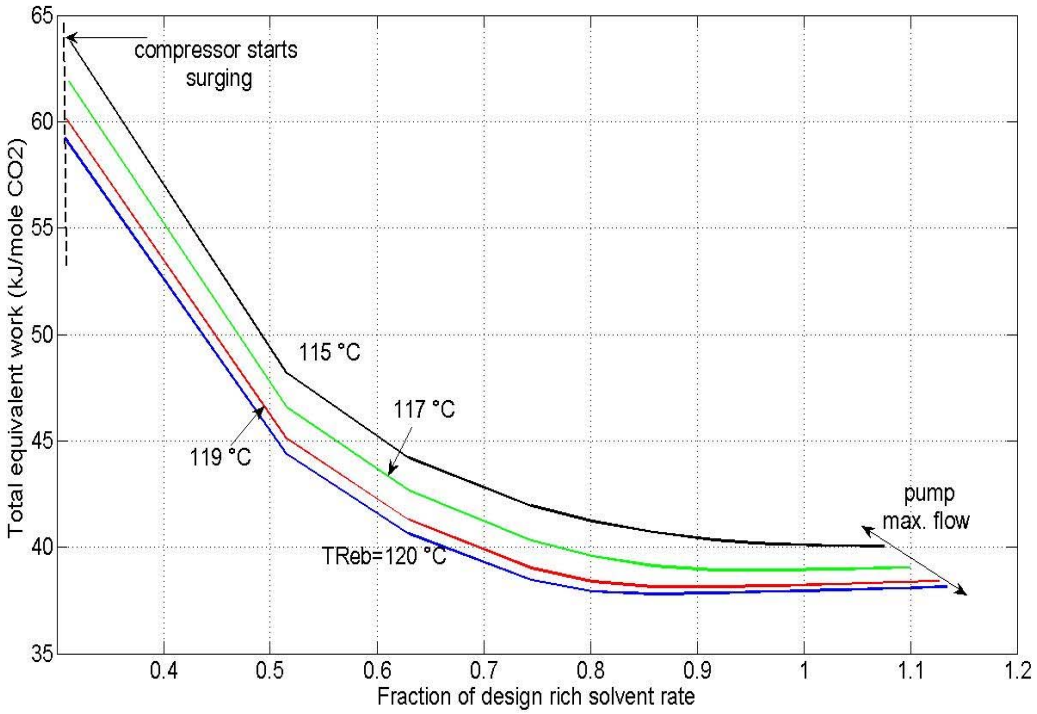

Figure 3.4: The effects of rich solution rate and reboiler temperature (adjusted by compressor speed) on total equivalent work when the power plant is operated at 90% load.

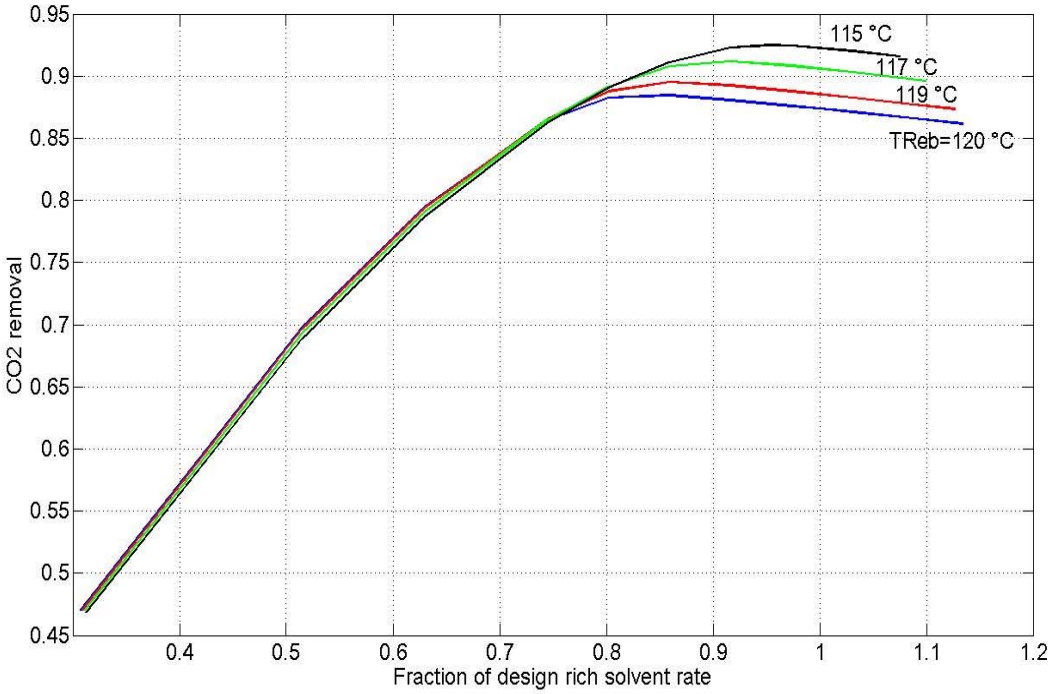

Figure 3.5: The effects of rich solution rate and reboiler temperature (adjusted by compressor speed) on CO_2 removal when the power plant is operated at 90% load.

Operating capture with low liquid circulation rate is not beneficial since the equivalent work is high, CO_2 removal is low, and increasing reboiler temperature does not influence the removal. The solvent rate that maximizes removal is not the same as the one that minimizes equivalent work; however, both optima increase with decreasing reboiler temperature. Figure 3.6 locates optimum solvent rate and reboiler temperature as a function of desired removal when the power plant load is reduced to 90% of full load. These optimum points minimize total equivalent work at a specific removal level. Figure 3.6 also gives a practical and optimum range for reboiler temperature (115–120 °C), fractional solvent rate (0.84–0.96), and removal (88.5–92.5%).

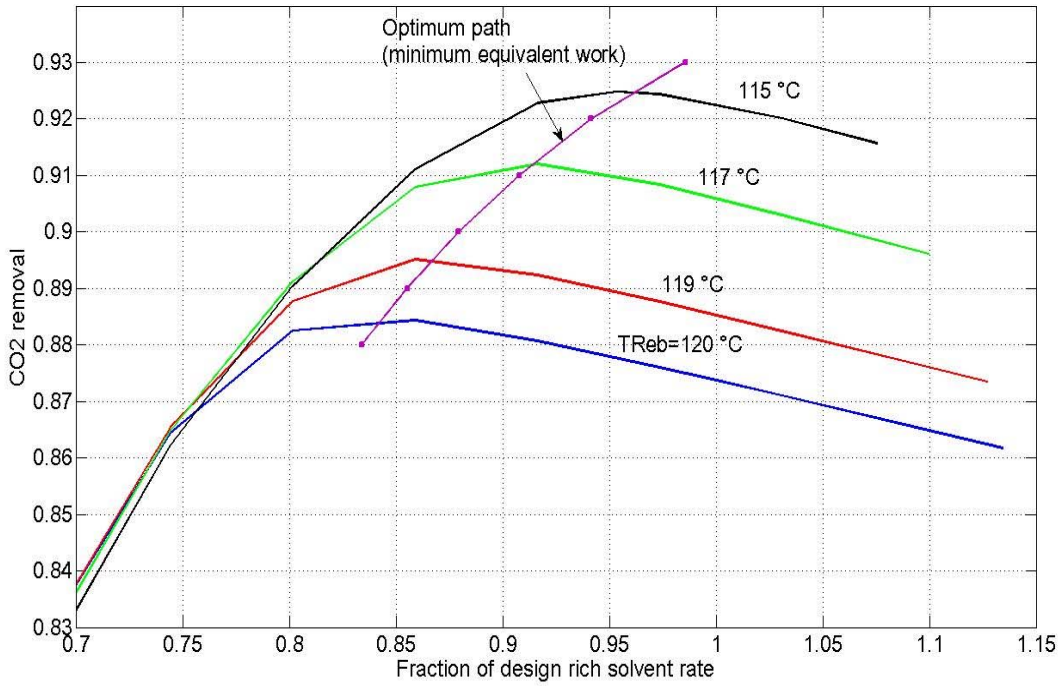

Figure 3.6: Steady state optimization of solvent rate and compressor speed when the power plant is operated at 90% load.

If we assume that there is not an advanced multivariable control system to optimize the set points of control loops in response to the upstream load change, we should find a control strategy that allows the plant to reach an optimum steady state condition with a multi-loop control system, if possible.

One of the strategies commonly used in similar plants is ratio control between two variables, where one process variable is controlled in a manner that varies in proportion to the change in another variable. Mathematically, the variables should move along a line with slope 1 (or diagonal line).

Figure 3.7 shows the normalized optimum solvent rate and the CO_2 rate in the rich and lean solution versus normalized reboiler steam rate for the practical range of CO_2 removal when the power plant is operated at 90% load. The normalization is achieved by dividing the flow rates at new steady state condition by the initial design value. This figure shows that flow rates vary linearly with steam rate, however none of the lines have slope 1. Ratio control between steam rate and CO_2 rate in rich solution seems to keep the plant closer to the optimum path since the line relating them is the closest to the dashed line.

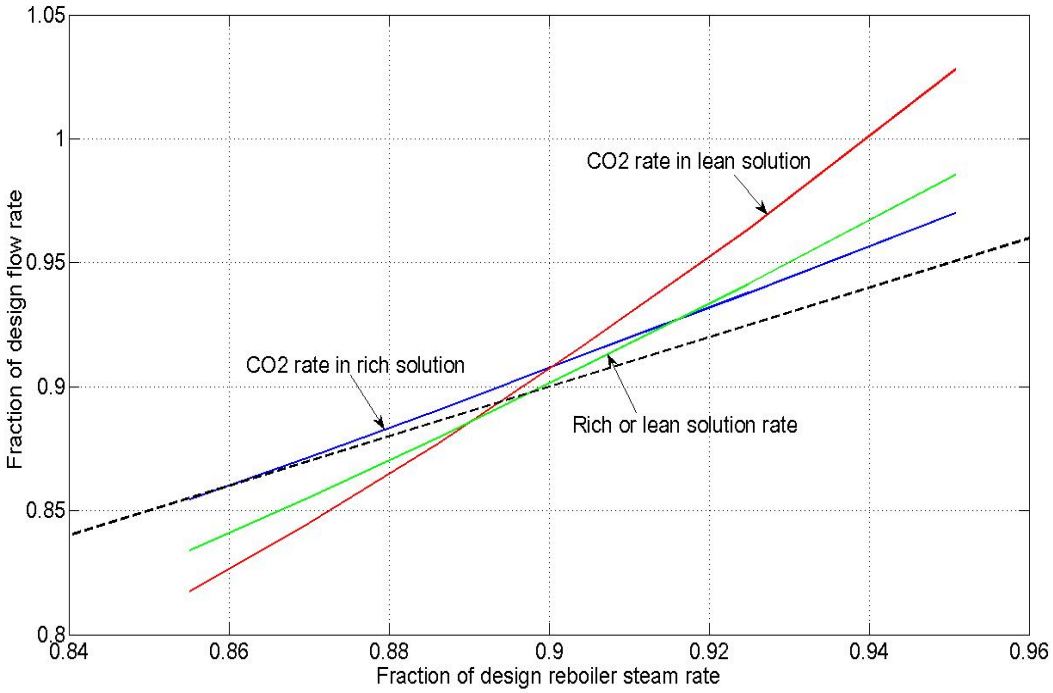

Figure 3.7: Optimum normalized solvent rate, CO_2 rate in lean and rich solution vs. normalized reboiler steam rate when the power plant is operated at 90%

The same analysis has been performed where the plant is operated at 80% load. (Figure 3.8) The shape of curves and distances from the diagonal line vary as load changes from 90% to 80%. Controlling the ratio of total solvent rate and the reboiler steam rate at initial value is the best choice to control the plant close to the optimum path for 80% load. Comparing Figures 3.7 and 3.8, we conclude that no general rule exists for optimum ratio control over a wide range of operation.

Normalized optimum lean loading and normalized removal are found to be another potential pair to match for ratio control. Figures 3.9 and 3.10 show the relation of these variables for 90% and 80% boiler load. For both cases, the curves are close to the diagonal line; however, as load decreases from 90% to 80%, the maximum deviation increases from 2% to 4%. Based on this analysis, if the objective in this case study is to keep the removal at its initial value (90%) while final total equivalent work is minimum in response to the power plant load reduction, the lean loading could be controlled at its initial value.

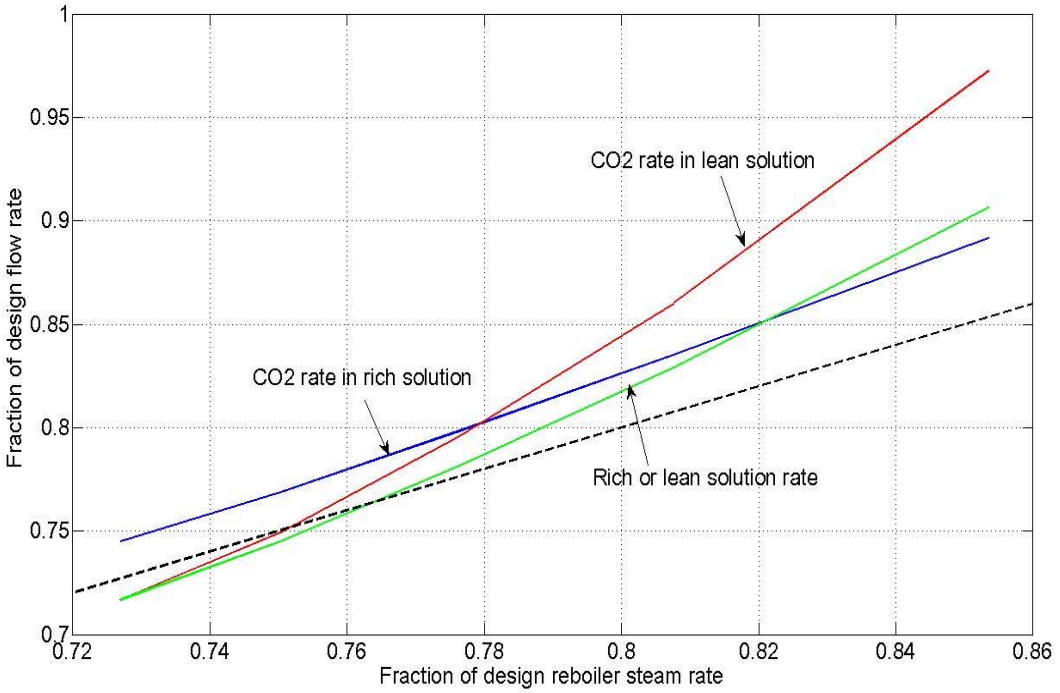

Figure 3.8: Optimum normalized solvent rate, CO_2 rate in lean and rich solution vs. normalized reboiler steam rate when the power plant is operated at 80%.

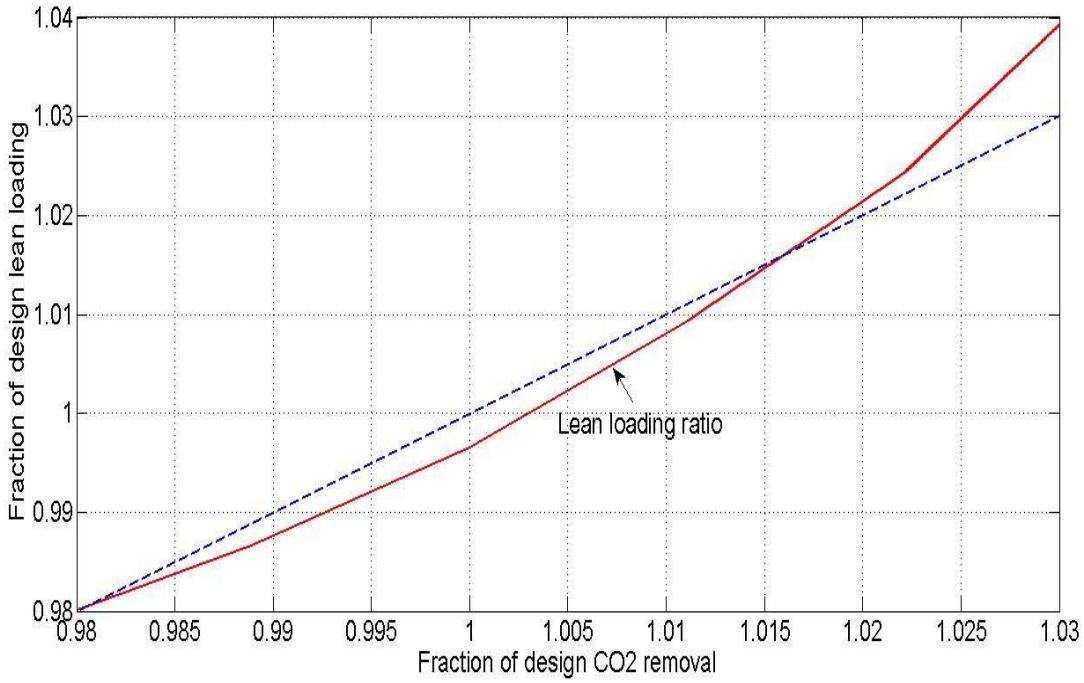

Figure 3.9: Optimum normalized loading of lean solution vs. normalized CO_2 removal when the power plant is operated at 90%.

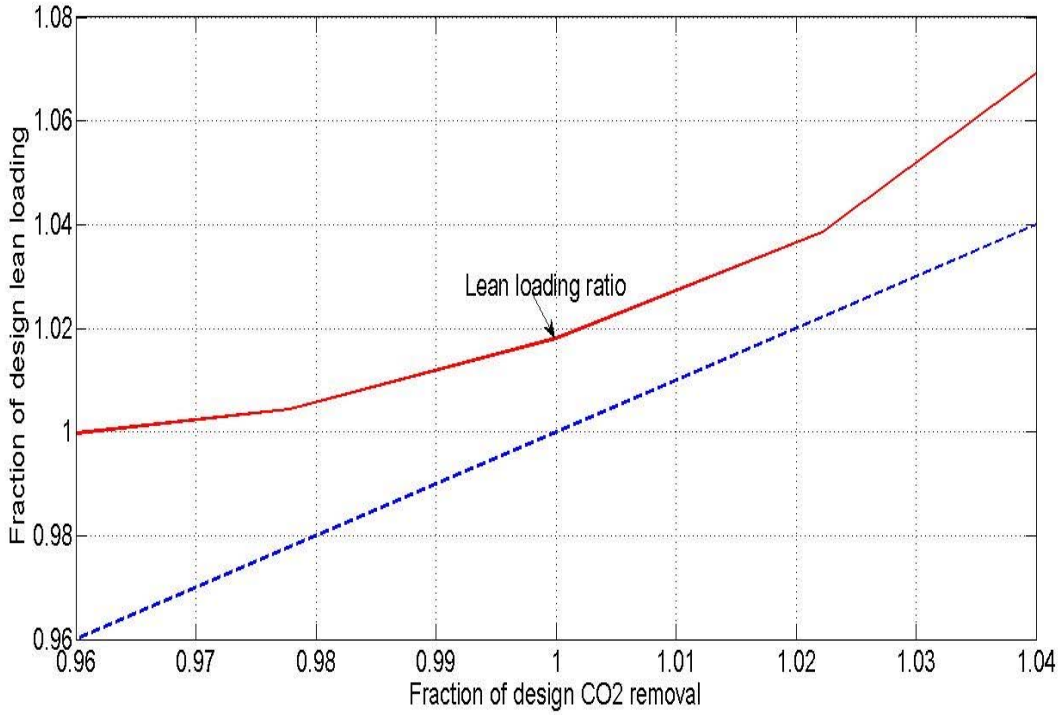

Figure 3.10: Optimum normalized loading of lean solution vs. normalized CO_2 removal when the power plant is operated at 80%.

For 80% load operation, similar to 90% load, the maximum solvent rate is set by maximum flow of rich or lean pumps and minimum flow is set by the compressor surge limit. The maximum and minimum reboiler temperature is set by thermal degradation of MEA and compressor speed limit, respectively. As shown in Figure 3.11, for 80% load operation, the operating range of the fractional solvent rate, reboiler temperature, and removal could be 0.71–0.91, 110–120 °C, and 85.5–94%.

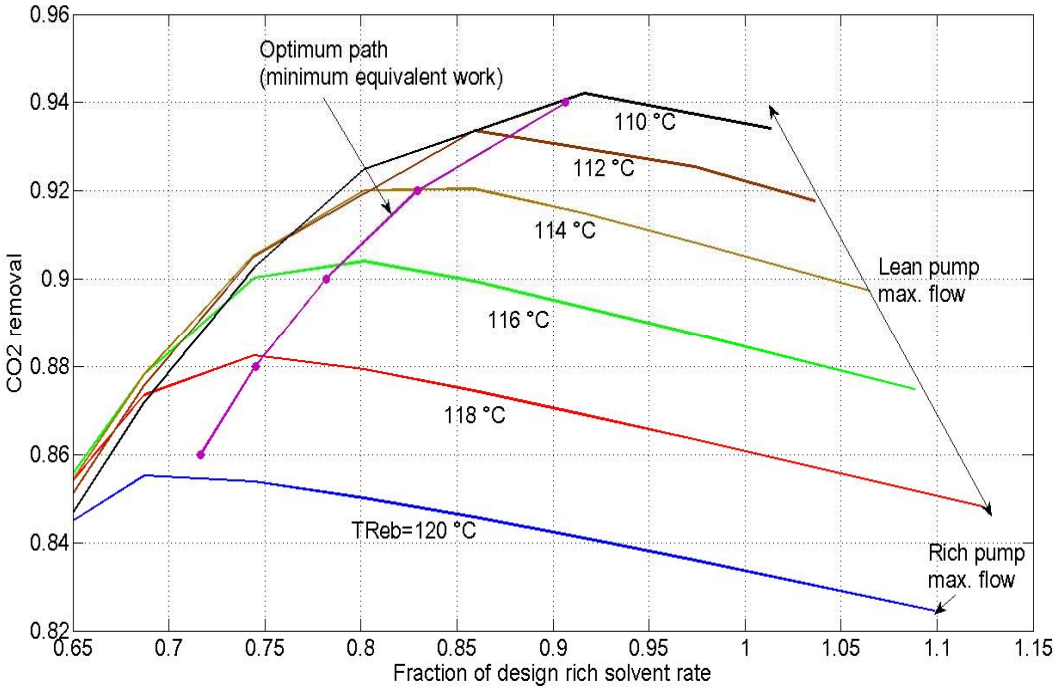

Figure 3.11: Optimum path for reboiler temperature and solvent rate minimizing total equivalent work over an applicable CO_2 removal range when the power plant is operated at 80%.

As shown in Figure 3.12, at 60% boiler load the minimum temperature, which is set by maximum compressor speed, is 106 °C. At low reboiler temperature such as 106 and 112 °C, maximum solvent flow is set by the lean pump run off. However, at higher temperature, 114–118 °C, the first stage of the compressor starts to surge before the pumps reach their maximum flow. At minimum solvent rate, the operating curve intersects the upper part of the surge limit, where the 5th stage is surging. At maximum flow it intersects the lower part of surge limit where the 1st stage is surging. As the reboiler temperature goes up, the operating curve of the compressor gets closer to the surge limit, such that the range of solvent rate that keeps the compressor away from surge is getting smaller and smaller. For 60% boiler load, the solvent rate range is very small for 118 °C and at 120 °C, the compressor curve is always on surge limit and no single value of solvent rate is found to remove compressor from this unwanted condition.

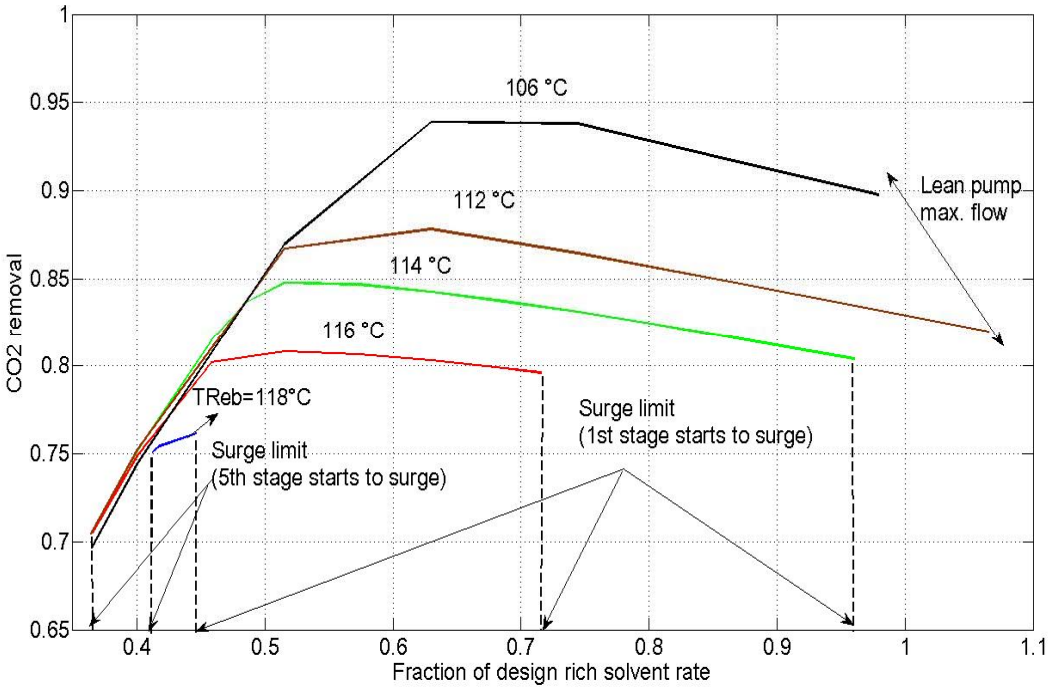

Figure 3.12: Optimum reboiler temperature and solvent rate minimizing total equivalent work over an applicable CO_2 removal range when the power plant is operated at 60% load.

The other factor pushing the compressor to surge condition is decreasing reboiler steam rate, which results from boiler load reduction. Figure 3.13 demonstrates the effect of decreasing boiler load on the operation of the compressor as the reboiler temperature is kept fixed for all 3 loads. For loads less than 58%, both maximum and minimum solvent rates are set by compressor surge conditions. As load decreases, the operating curve gets closer and closer to the surge limit such that, based on simulation results, at 40% load, which is a common minimum load in a power plant, the compressor is always on surge and changing solvent rate and adjusting compressor speed are no longer beneficial to push it away from this condition. The only way to protect the compressor from surging is to activate anti-surge control in which a portion of gas stream is circulating through the stage, which is starting to pass the surge limit.

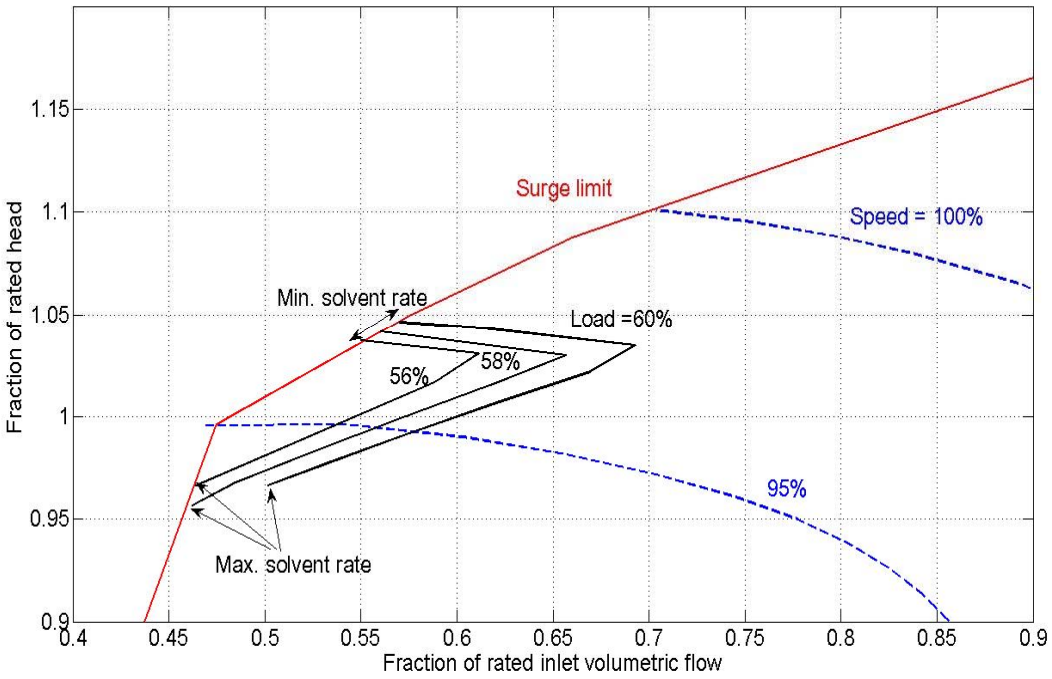

Figure 3.13: The performance map of multi-stage (5 stages) CO_2 compressor at 56% to 60% boiler load, 112 ^{o}C reboiler temperature adjusted by variable compressor speed and solvent rate.

3.3.2. REBOILER STEAM RATE REDUCTION

As explained in section 3.2, partial load operation of reboiler steam is simulated by manipulating the steam valve to achieve the desired steam rate. The simulation is run in dynamic mode and outputs are recorded when the plant reaches the new steady state.

The objective of this work is to find the solvent circulation rate and compressor speed that minimize total equivalent work at a new steady state condition after the steam rate is reduced in the presence of operating constraints. As with boiler partial load, both solvent rate and compressor speed influence the equivalent work and CO_2 removal (Figures 3.14 and 3.15).

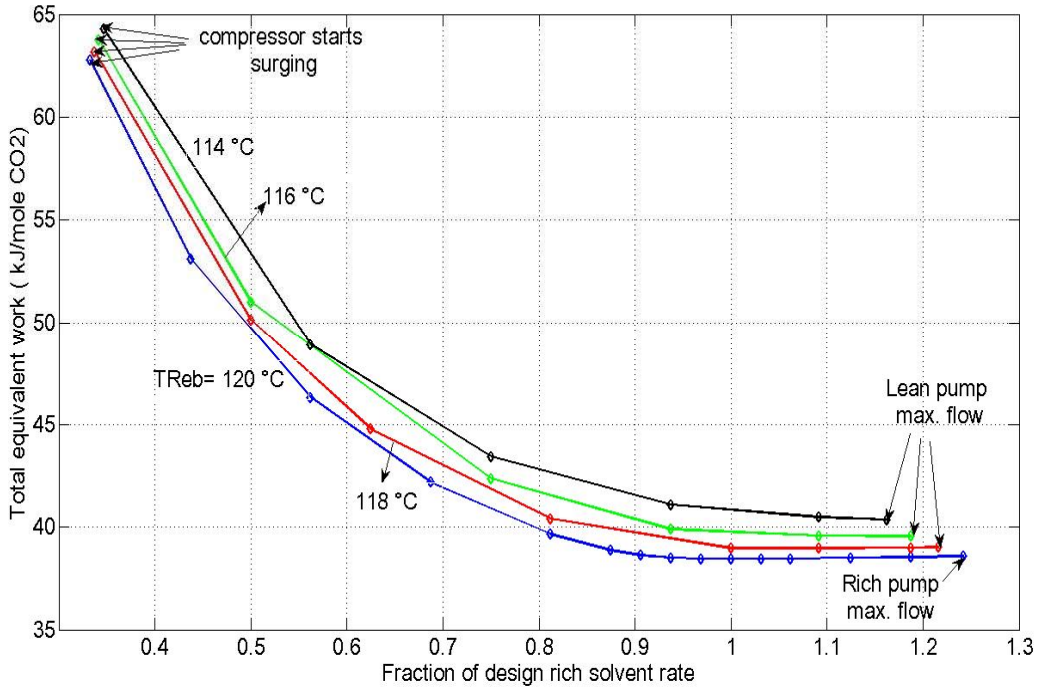

Figure 3.14: Output of simulation of reboiler steam rate reduction scenario: the effects of rich solution rate and reboiler temperature (adjusted by compressor speed) on total equivalent work at new steady state condition when the plant is operated at 90% reboiler load.

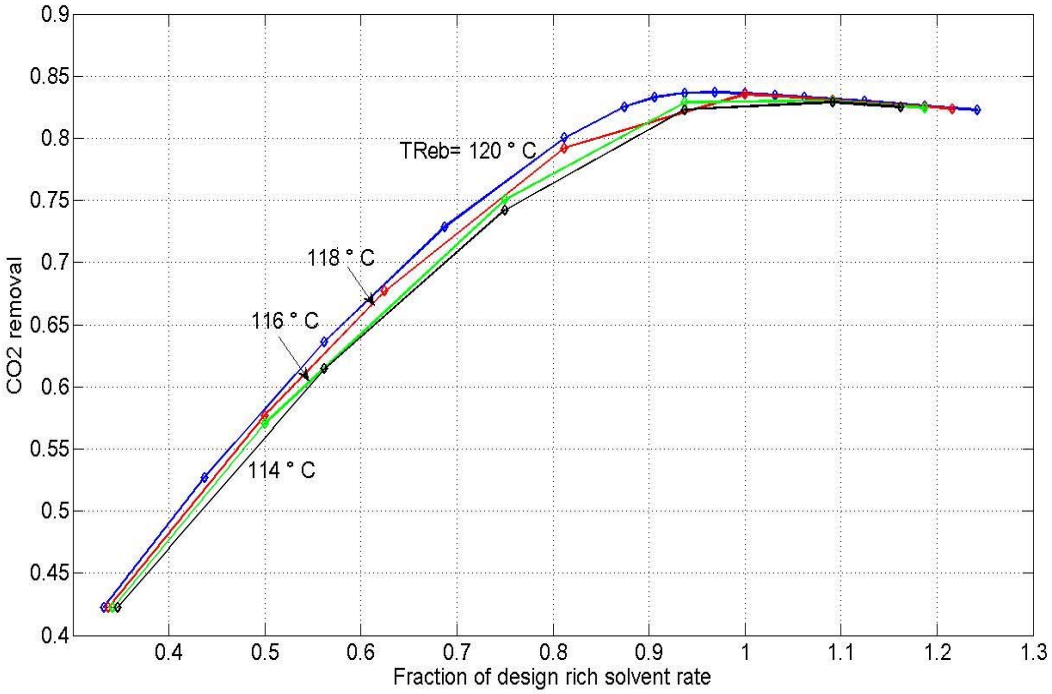

Figure 3.15: reboiler steam rate at 90%: the effects of rich solvent rate and reboiler temperature (adjusted by compressor speed) on CO_2 removal

Reboiler temperature is adjusted by compressor speed and changed in the range between 115 °C and 120 °C to prevent the compressor from over speeding and MEA solution from thermal degradation for 90% load. Solvent rate varies in a range limited by compressor surge and maximum pump flow. There is an optimum solvent rate that minimizes total lost work and maximizes removal, and it increases as the steam rate is reduced such that at 60% load, the optimum solvent rate exceeds the maximum flow of the rich solution pump (Figure 3.16).

Figures 3.14 and 3.15 demonstrate that maximum reboiler temperature provides minimum total equivalent work and maximum removal. As proved by previous studies on steady state lost work minimization in amine plants, higher temperature always provides less equivalent work associated with both reboiler heat duty and CO_2 compression. For this specific operational scenario in which the extracted steam rate is reduced by closing the steam valve, operation at higher temperature is optimum because the steam is available at higher pressure at the extraction point relative to the design condition. In order to keep the reboiler temperature high in response to steam rate reduction, the compressor speed should be reduced.

Regarding CO_2 compressor operation, reducing the steam rate in the reboiler results in pushing the compressor operation to the surge limit. The simulation results show that 60% steam rate is the minimum load where the compressor operates in the non-surge region in the presence of controlling reboiler temperature at 120 °C. Below 60% load, a control strategy should be applied to prevent the compressor from surging. This study proposes and compares two surge control strategies. The first one is activating anti-surge control which is typically installed on the compressor package by manufacturers. In this strategy, a portion of gas exiting of a compressor stage starting to surge is recycled back to the entrance of that stage in order to provide minimum inlet volumetric flow. The disadvantage of this strategy is the addition of energy cost due to gas recycling during surge condition. The second strategy, which is explored in this study, does not implement a built-in compressor anti-surge control system. This strategy controls the compressor speed and solvent rate to keep the operating curve on the surge limit.

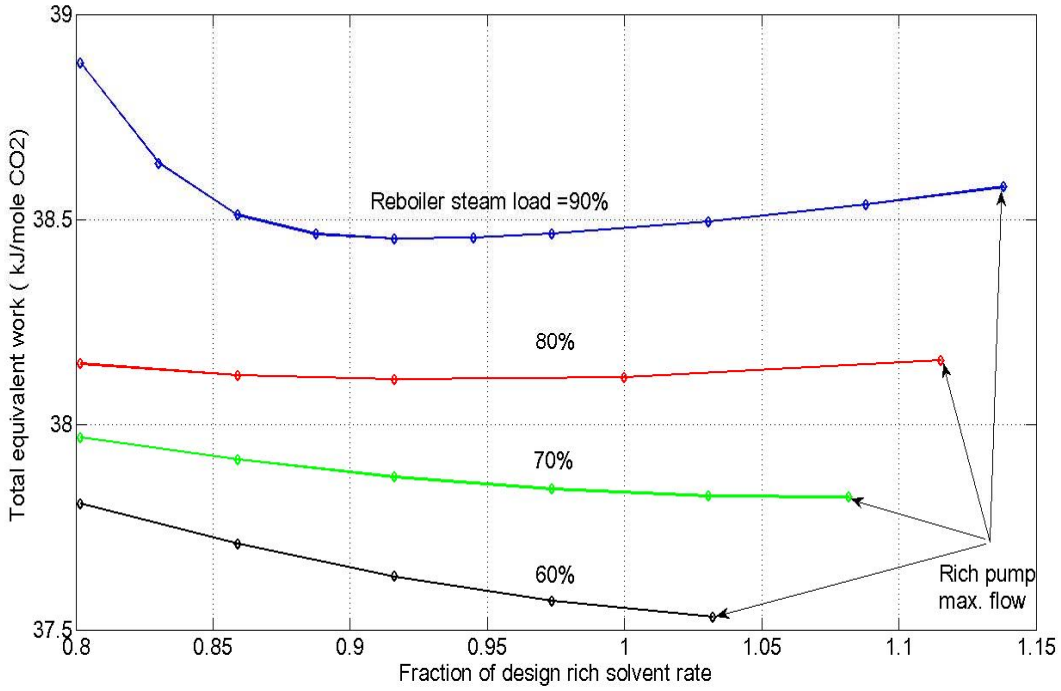

Figure 3.16: Effects of reboiler steam rate reduction on total equivalent work, 120 °C Reboiler, variable compressor speed.

This work optimizes both solvent rate and compressor speed to minimize total lost work at steady state condition for different levels of load reduction. Figure 3.17 presents the obtained optimum path on the 5-stage compressor performance map. As shown in this figure, for loads between 60% and 100%, the compressor is operating normally in non-surge region and as the steam load is reduced, the compressor speed should be reduced. For loads lower than 60%, where the surging onsets, operating curves resulting from the two surge control strategies discussed above are shown. Both optimum curves lie on the surge limit but move in opposite directions.

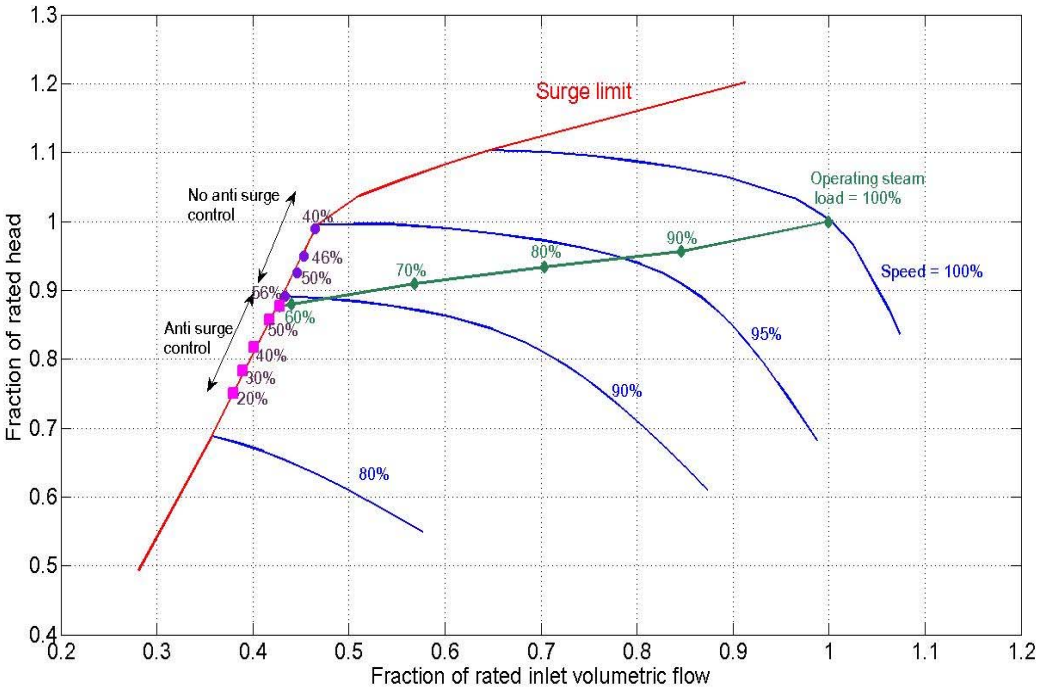

Figure 3.17: The performance map of a multi-stage (5 stages) CO_2 compressor for reduced reboiler steam rate. Operating points are the results of minimization of total equivalent work by optimizing compressor speed and solvent rate. ♦- represents unique optimum points when the plant is operated at 60–100% reboiler steam load. ■- represents optimum points for operating the plant at 20–59% using anti-surge control on the compressor. ●- represents optimum points for operating the plant at 40–59% without using anti-surge control on the compressor.

In anti-surge control strategy, the reboiler temperature (and stripper pressure) remains at maximum value by reducing compressor speed and as load reduces the compressor speed is further reduced. That is why the optimum path associated with this strategy is going down on the surge limit as shown in Figure 3.17. In the second strategy, without anti-surge control on the compressor, the compressor speed should go up, such that at around 40% load, the operating point reaches the turning point of the surge line. After passing the turning point, we need to reduce the stripper pressure and temperature much more than before so that the reboiler downstream pump loses its suction pressure and fails to pump the liquid. One of the interesting results from this analysis is that anti-surge control has the capability to operate the plant at a wider range of steam load (up to 80% reduction) while the second strategy is not applicable when more than 60% steam load reduction is desired unless it employs an oversized pump to handle lean solution coming from the reboiler.

As shown in Figure 3.18, it would be optimum if the reboiler temperature were controlled at 120 °C (the highest allowable temperature) for as long as compressor operation permits. In the non-surge region it is not a problem to run the reboiler at this temperature. In the surge region, the activation of anti-surge control (strategy 1) allows us to operate the reboiler temperature at this optimum value; however, there is additional lost work due to gas recycling in the surging stages. In the second strategy, the reboiler temperature should be reduced to keep the

compressor from surging. This avoids energy cost due to gas recycling, but it increases lost work associated with reboiler heat duty and compression because of reduced pressure and temperature.

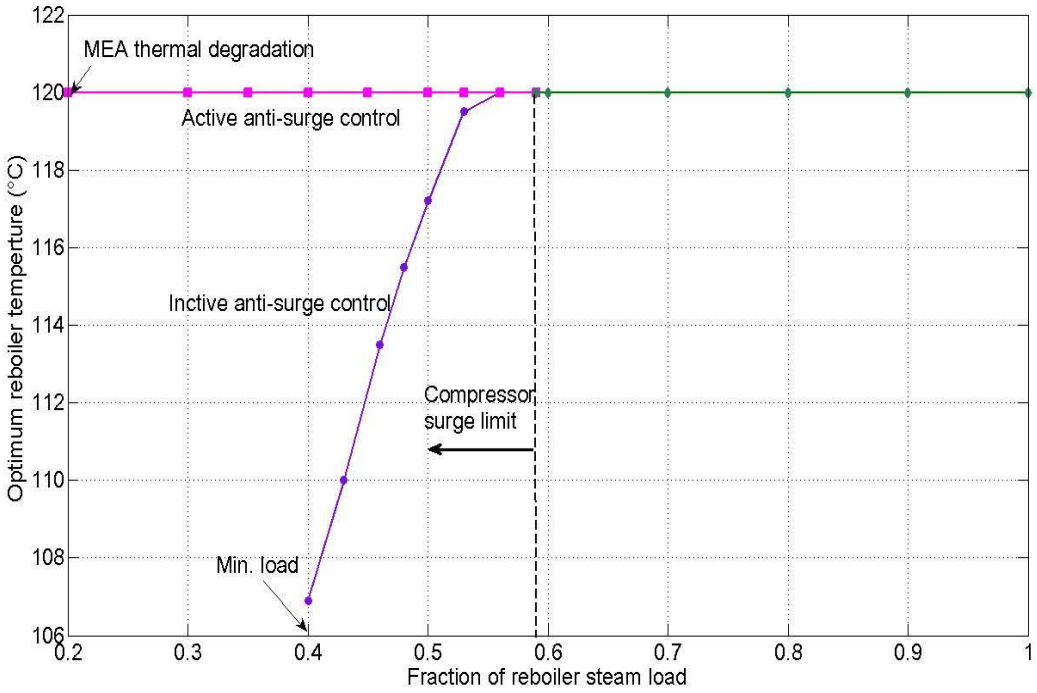

Figure 3.18: Optimization of reboiler steam rate reduction to minimize total equivalent work: optimum reboiler temperature vs. fractional reboiler steam rate by using ♦- compressor non-surge, ■- anti-surge control, and ●-not using anti-surge control.

Figure 3.19 shows how stripper top pressure varies with load reduction in surge and non-surge regions. In the non-surge region, pressure goes up as load decreases, although the reboiler temperature is constant. Anti-surge control on the compressor lets the pressure in the stripper increase with load reduction such that at 20% load, the stripper pressure is about two times greater than its initial design value. Therefore, there is an additional capital cost associated with the stripper column, which must be related for the greater pressure.

As the reboiler steam load is reduced, anti-surge control on the compressor that lets the pressure go up without causing surge leads in increasing the optimum lean loading and decreasing optimum solvent rate (Figures 3.20 and 3.21).

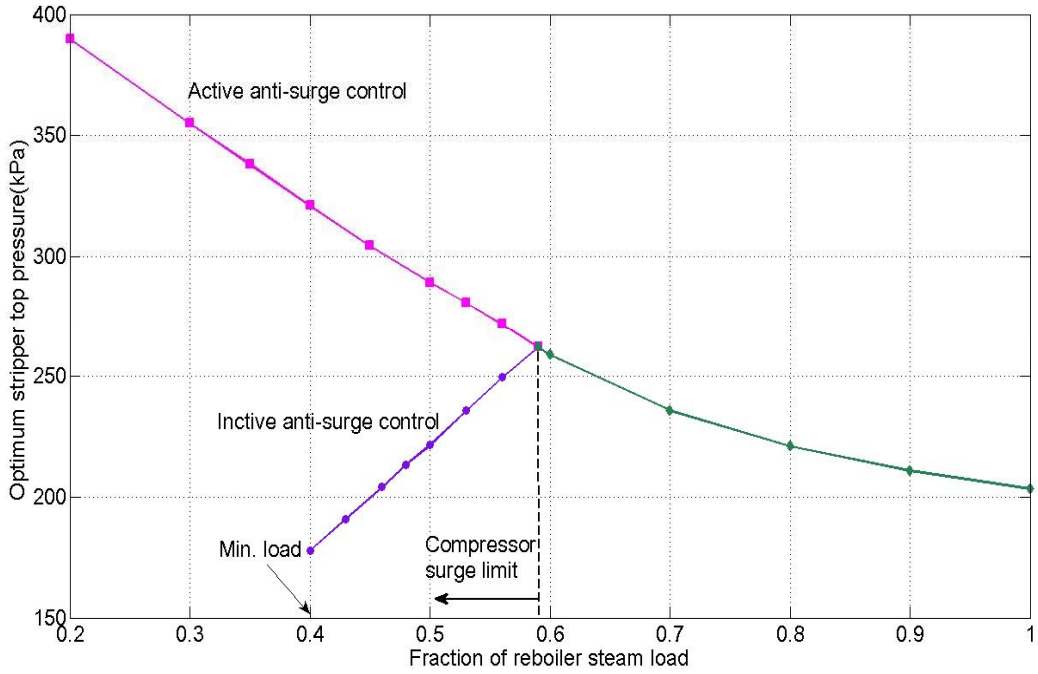

Figure 3.19: Optimization of reboiler steam rate reduction: optimum stripper top pressure vs. reboiler steam rate by using ♦- for compressor non-surge region, ■- for compressor surge region using anti-surge control, and ●- for compressor surge region not using anti-surge control.

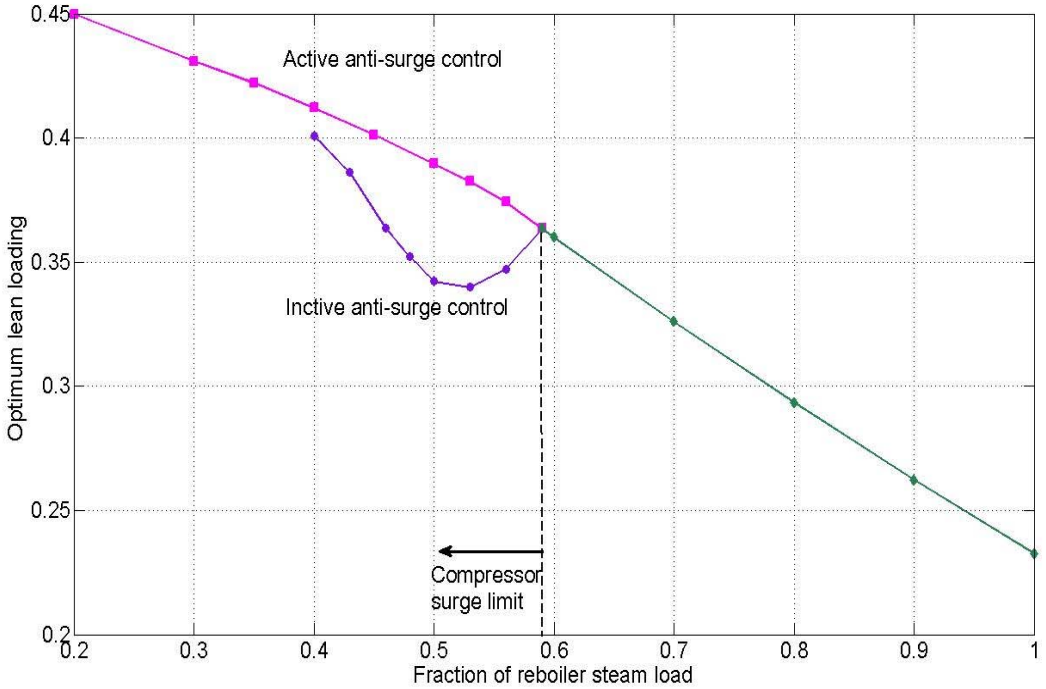

Figure 3.20: Optimization of reboiler steam rate reduction: optimum lean loading vs. fractional reboiler steam rate by using ♦- for compressor non-surge region, ■- for compressor surge region using anti-surge control, and ●- for compressor surge region not using anti-surge control.

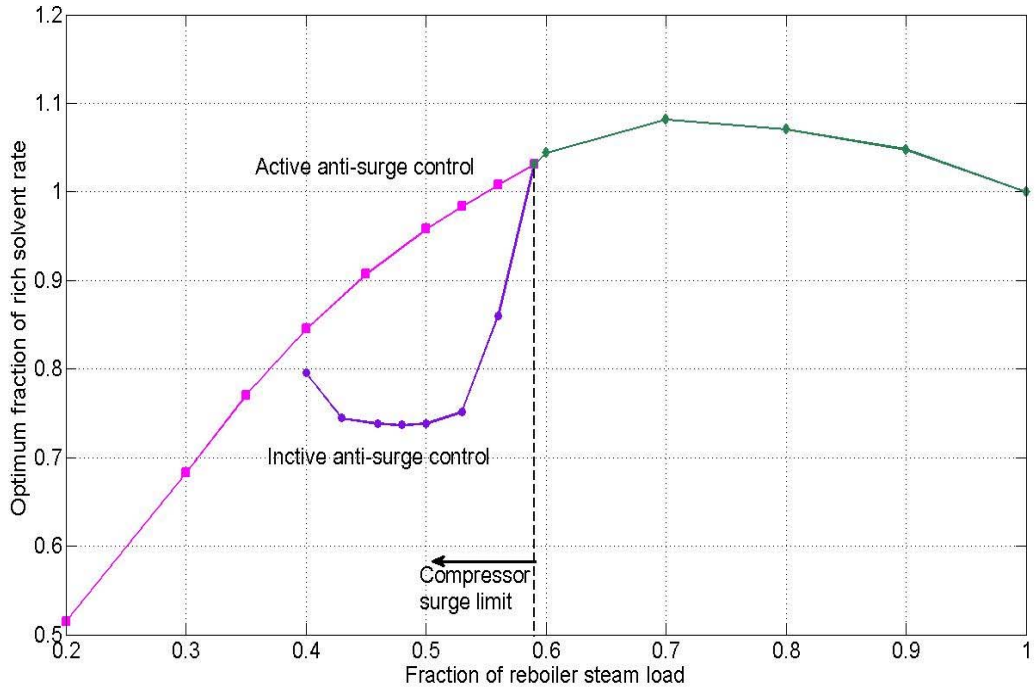

Figure 3.21: Optimization of reboiler steam rate reduction: rich solvent rate vs. reboiler steam rate by using ♦- for compressor non-surge region, ■- for compressor surge region using anti-surge control, and ●- for compressor surge region not using anti-surge control.

As shown in Figure 3.16, optimum solvent rate minimizing total lost work increases with steam rate reduction. However increasing the stripper pressure at the same time does not allow the rich pump (stripper upstream pump) to handle the change of solvent rate desired. For reboiler steam load lower than 70%, the optimum solvent rate is greater than the maximum flow in the rich pump at the specific stripper pressure for each load. Therefore, using the anti-surge control strategy, although the lean loading increases, the optimum solvent rate set by rich pump maximum flow decreases with steam load (Figure 3.21). In conclusion, it is likely to further reduce lost work during partial steam load operation (for 30% or more reduction in steam rate) by initially designing an oversized rich solution pump to handle the liquid while the stripper becomes over-pressurized.

Figure 3.22 shows how the total equivalent work varies at optimum points with steam load reduction in both non-surge and surge regions. In non-surge area it decreases with steam load mainly due to increasing suction pressure of the compressor. It still decreases with load in surge areas when anti-surge control is activated because of increasing stripper pressure. The second surge control strategy that loses the advantage of high reboiler steam pressure leads to increasing equivalent work. CO_2 removal is reduced linearly with steam rate and the surge control strategy chosen does not influence it significantly (Figure 3.23).

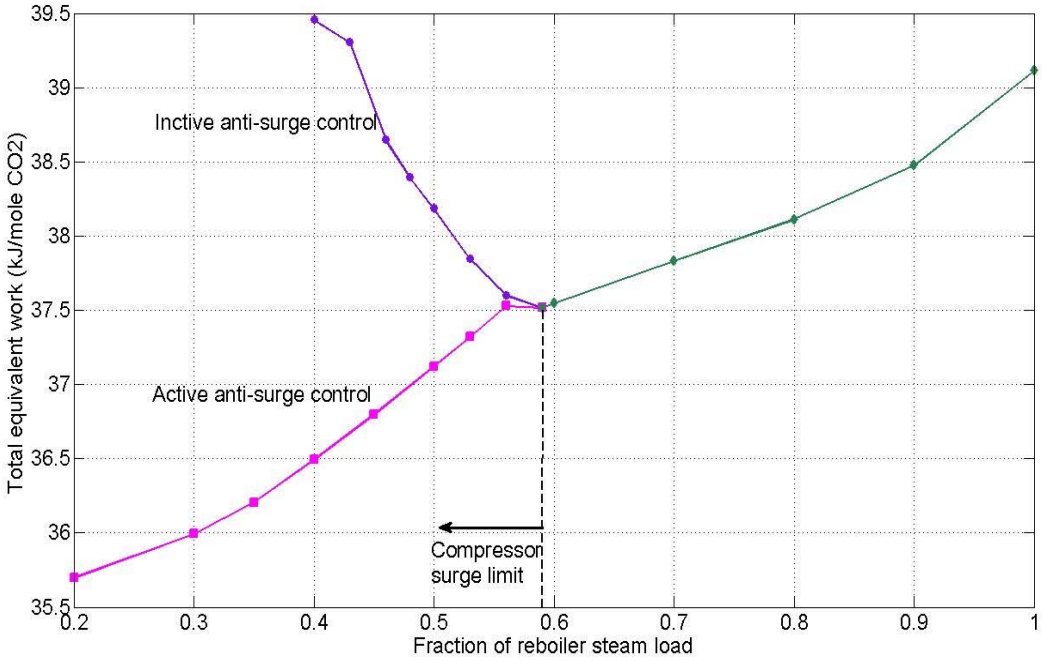

Figure 3.22: Optimization of reboiler steam rate reduction: minimized total equivalent work vs. reboiler steam rate by using ♦- for compressor non-surge region, ■- for compressor surge region using anti-surge control, and ●- for compressor surge region not using anti-surge control.

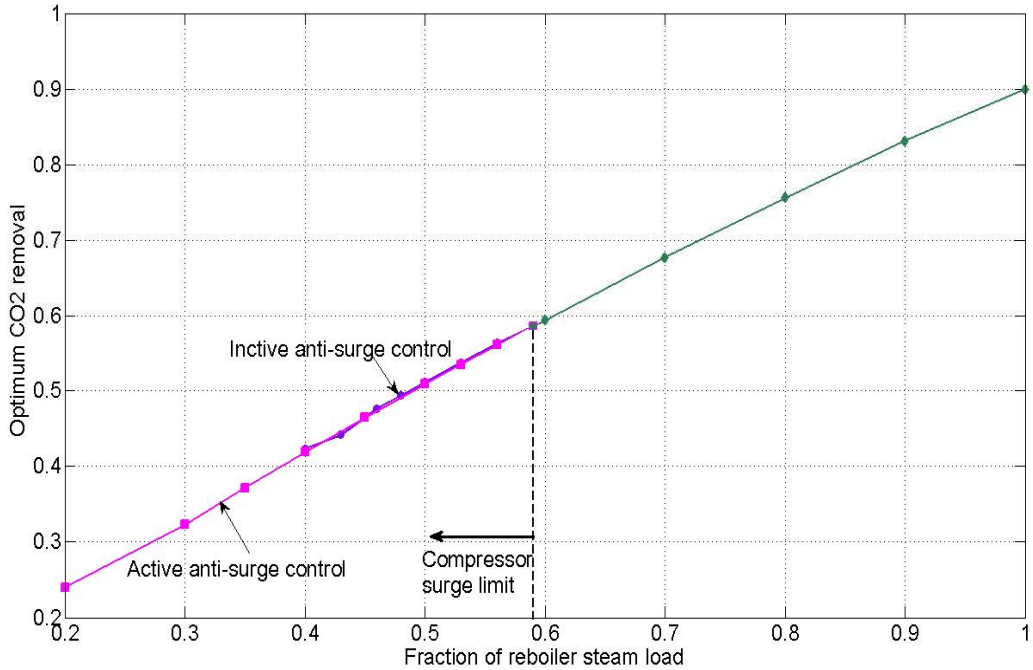

Figure 3.23: Output of simulation and optimization of reboiler steam rate reduction scenario: it demonstrates optimum CO_2 removal vs. fractional reboiler steam rate by ♦- for compressor non-surge region, ■- for compressor surge region using anti-surge control, and ●- for compressor surge region not using anti-surge control.

Comparing these two surge control options with respect to lost work and removal, it is concluded that although anti-surge control introduces additional mechanical energy for recompressing recycled gas during surging, it still causes less lost work relative to the alternative, because it takes advantage of the increased extracted steam pressure that occurs in this operational scenario and operates the reboiler and stripper at optimum temperature and pressure.

3.4. SUMMARY AND CONCLUSIONS

A rigorous dynamic model of MEA absorption/stripping plant integrated with CO_2 compression and power cycle steam turbines is employed to simulate two main operational scenarios occurring in capture plants: power plant load reduction, and partial reboiler steam load operation. The outputs of simulation running in dynamic mode are recorded when the new steady state is reached and are used for operation optimization. The optimization minimizes total lost work at the new operating condition by employing compressor speed and liquid circulation rate as optimization variables.

Changing the compressor speed and liquid rate of the plant identifies operational constraints on the variation of these variables. The compressor speed should not exceed the maximum allowable speed, which is set here at 120% of rated speed. Another constraint is on the reboiler temperature, which should not exceed 120 °C to prevent thermal degradation of the MEA solution. Either the reboiler temperature constraint or the compressor surge limit establishes minimum compressor speed, which varies with the load change for each load reduction scenario. The simulation also indicates that the liquid rate can vary in a feasible range, whose minimum value is set by the compressor surge limit and maximum value is set either by solvent pump (lean or rich pump) maximum flow condition or compressor surge limit.

Partial load operation of the power plant influences the downstream capture by reducing the absorber inlet flue gas rate and reboiler steam pressure. Increasing compressor speed (or decreasing reboiler temperature and pressure) results in extracting more steam for reboiler and consequently removes more CO_2. For each removal, there is a reboiler temperature and a solvent rate that minimizes total equivalent work. Based on equivalent work minimization in the presence of constraints associated with pumps, compressor, and solvent thermal degradation, this work gives a practical CO_2 removal range for an MEA plant operating at 60%, 80%, and 90% load. As the results for these operating loads show, the MEA plant initially designed for 90% removal can remove up to 94% of inlet CO_2 by increasing the compressor speed up to 120% of the rated speed. For low load operation such as 40% load, the compressor-operating curve reaches surge limit and changing speed and solvent rate does not push it away from this undesired region. Recycling gas through surging stages, a practice typically implemented by anti-surge control on the compressor package, is the only way to prevent the compressor from surging during low power plant load operation.

Optimizing MEA plant operation in response to power plant load reduction indicates that optimum total solvent rate and CO_2 rate in rich and lean streams vary linearly with reboiler steam rate. However, the lines are not diagonal; installing ratio control between the CO_2 rate in rich solution and the steam rate could keep the plant close to optimum during partial load operation. More reduction in power plant load results in more deviation of ratio control strategy from the

optimum path, and controlling lean loading at a set point that varies in proportion to the removal is another strategy that controls the plant close to the optimum.

Reboiler steam load reduction would be optimum if the reboiler temperature remained at 120 °C (the maximum temperature to prevent MEA thermal degradation) by adjusting the solvent rate and compressor speed as long as compressor operational limits permit. At steam loads above 60% it is not necessary to run the reboiler at 120 °C. At loads lower than 60%, where the compressor starts to surge, a surge control strategy should be applied. Two surge control strategies are identified and compared:

1. Anti-surge control on the compressor package;
2. Adjusting compressor speed and solvent rate to save compressor from surging.

Comparing the strategies shows that anti-surge control has more advantages with respect to operation and minimum lost work and would be preferable during partial reboiler steam load operation. The following is a summary of reasons for this statement:

1. Although there is an additional energy loss associated with anti-surge control because of recompressing recycled gas, the total lost work is still lower than the second strategy since it lets the reboiler run at 120 °C and the CO_2 compressor compress the gas at higher suction pressure and consequently lower compression ratio.
2. Anti-surge control strategy has the capability of operating the plant at a wider range of steam load (20–100%) while the second strategy could not operate the plant below a 40% load.
3. The disadvantage of anti-surge control is the addition of capital cost for the stripper column. Because it pressurizes the stripper steadily as the steam rate is reduced, at 20% load the stripper pressure is twice the rated pressure.
4. Anti-surge control has the potential for even further reduction in lost work for low steam load cases. By over-sizing the rich pump to enable it to pump rich solution to the pressurized stripper before getting to its maximum flow, it can circulate the liquid at its optimum rate.

References

Bergerson JA, Lave LB. "Baseload Coal Investment Decisions under Uncertain Carbon Legislation." *Environ. Sci. Technol*. 2007;41(10):3431–3436.

Freguia S, Rochelle GT. "Modeling of CO_2 Capture by Aqueous MEA."*AIChE J.* 2003;49(7):1676–1686.

Kvamsdal HM, Jakobsen JP, Hoff KA. "Dynamic Modeling and Simulation of a CO_2 Absorber Column for Post-Combustion CO_2 Capture." *Chem Eng & Proc*. 2009;48:135–144.

Lawal A, Wang M, Stephenson P, Koumpouras G, Yeung H. "Dynamic Modeling and Analysis of Post-Combustion CO_2 Chemical Absorption Process for Coal-fired Power Plants." *Fuel.* 2010; 89(10):2791–2801

Oyenekan BA, Rochelle GT. "Alternative Stripper Configuration for CO_2 Capture by Aqueous Amines." *AIChE J.* 2007;53(12):3144–3154.

Lucquiaud M. *Steam cycle options for capture-ready power plants, retrofits and flexible operation with post combustion CO_2 capture*. Imperial College London. Ph.D. Dissertation. 2010.

Plaza JM, Chen E, Rochelle GT. "Absorber Intercooling in CO_2 Absorption by Piperazine Promoted Potassium Carbonate." *AIChE J.* 2010;56(4):905–914.

Schach MO, Schneider R, Schramm H, Repke JU. "Control structure design for CO_2 absorption processes for large operating ranges." *PCCC1*, Abu Dhabi, 2011.

Ziaii S, Cohen SM, Rochelle GT, Edgar TF, Webber ME. "Dynamic operation of amine scrubbing in response to electricity demand and pricing." *Energy Proc.* 2009;1:4047–4053.

Ziaii S, Rochelle GT, Edgar TF. "Dynamic modeling to minimize energy use for CO_2 capture in power plants by aqueous Monoethanolamine." *Ind Eng Chem Res.* 2009;48(13):6105–6111.

Van Wagener DH, Rochelle GT. "Stripper Configurations for CO_2 Capture by Aqueous MEA and PZ." *Energy Proc.* 2011;4:1323–1330.

A Review of Dynamic Modeling for Post-Combustion Amine Scrubbing

Quarterly Report for October 1 – December 31, 2011

by Matthew Walters

Supported by the Luminant Carbon Management Program

Department of Chemical Engineering

The University of Texas at Austin

January 31, 2012

Abstract

While steady state models for post-combustion amine scrubbing have been extensively studied, there are limited examples of dynamic models that can simulate the process in the presence of disturbances or set point changes. An accurate dynamic model will be necessary to optimally design and operate a process with a minimum energy requirement, maximum economic return, and fast, stable responses to changes in the system. This report presents a review of the dynamic models for carbon capture that have been created and published, and discusses their scope, complexity, and control strategies. The models presented here provide valuable insights into potential variables that can be controlled, measured, and manipulated in order to operate the process optimally. The dynamic models that have been developed to this point provide a solid foundation for work within the field; however none of the models presented here encompass the entire scope of the CO_2 capture and sequestration process and often include simplifying assumptions that decrease model complexity. There is much room for future work in dynamic modeling for post-combustion carbon capture.

Introduction

Dynamic modeling is important for the design and optimization of post-combustion amine scrubbing systems for CO_2 removal. There are three primary objectives in developing a dynamic model: (i) to design a system with stable process operation and control in the presence of disturbances; (ii) to design a system with stable responses to set point changes, including startup and shutdown; and (iii) to predict and optimize steady state operation, especially as system complexity increases. This report presents a literature review of work performed on dynamic modeling for CO_2 capture and discusses how it relates to these three primary objectives. For each publication, the scope, complexity, and control strategies of the model developed will be described.

Model Scope

Post-combustion carbon capture is a complex process with a large solvent recycle rate and interaction with the upstream power plant and downstream compressor. A broad overview of the interactions relevant to the carbon capture system is shown in Figure 1. With this degree of

integration, the optimal design of one unit operation depends on the operation of the entire system. For example, optimal design and operation of the regeneration unit depends on steam load from the power plant, solvent rate and rich loading from the absorber, and the compression work performed on the regenerated gas. Thus, it is critical that a dynamic model has a large enough scope to fully capture all relevant interactions because each unit in the process is highly dependent on the rest of the system. Since it is clear that model scope is directly related to model accuracy, scope will be described for each model reviewed.

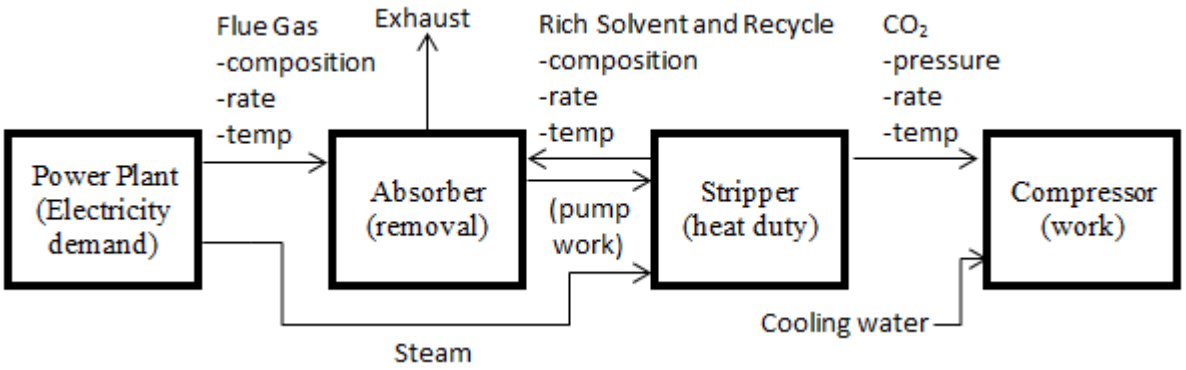

Figure 1: General overview of interactions that exist for the process

Model Complexity

There are varying levels of model complexity for liquid-gas contactors that can be employed when developing a dynamic model for reactive absorption and stripping (Kenig et al., 2001). Mass transfer at each column stage can be modeled as an infinitely fast equilibrium process or as a rate-based process with a boundary layer at the liquid-gas interface. In the simplest form, reactions at each stage can be modeled as being at equilibrium, and complexity can be increased by considering reaction kinetics in the bulk fluid or in both the bulk fluid and the boundary layer. Figure 2 provides a representation of varying levels of model complexity, with complexity increasing from bottom left (equilibrium mass transfer and reactions) to top right (rate-based mass transfer and reaction kinetics in the bulk fluid and boundary layer). In the stripper, it is typically assumed that temperatures are high enough that reactions can be adequately represented as being at equilibrium. In the lower temperature absorber, reaction kinetics becomes more important for predicting actual performance. This report attempts to point out the model complexity of each work reviewed, as this affects the accuracy, scalability, and adaptability of a given model.

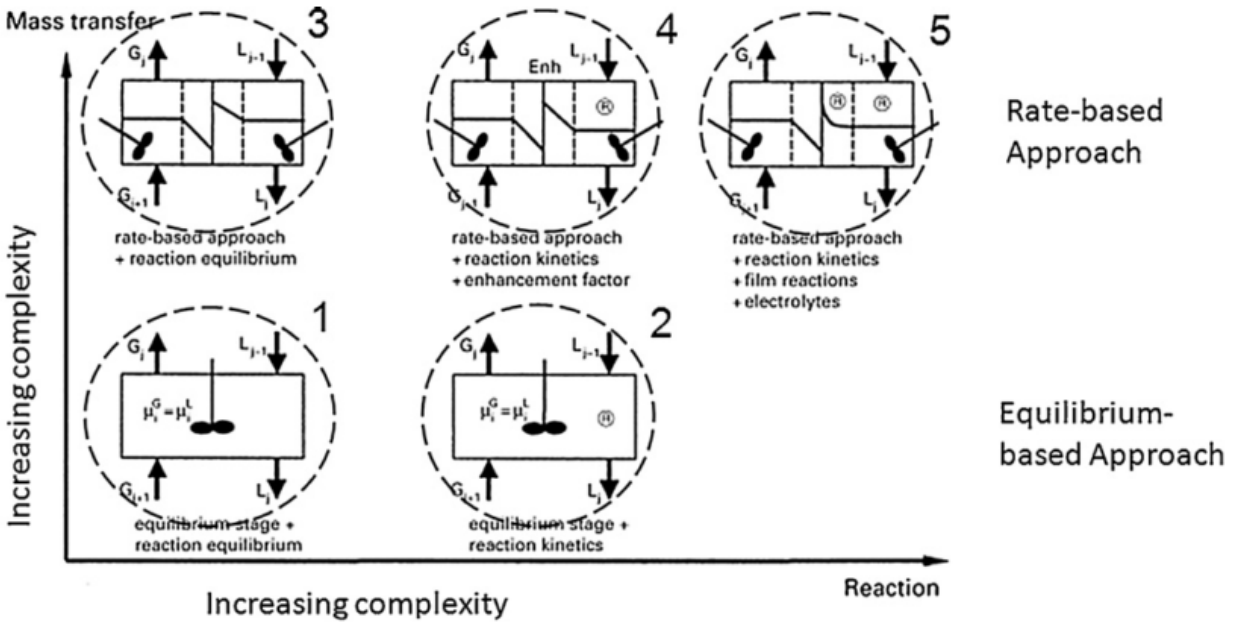

Figure 2: Different Levels of Model Complexity (Kenig et al., 2001)

Model Control Strategies

A dynamic process model can provide insight into possible control techniques to maintain a stable system. Table 1 summarizes control strategies that have been suggested or utilized by researchers modeling carbon capture. It is not meant to be an exhaustive list of possible control scenarios, but rather to give an overview of control strategies that will be encountered later in this review.

Table 1: Overview of Model Control Strategies

	Controlled Variable	Possible Manipulated Variables
CO_2 Capture Rate Controller	Percent removal of CO_2 in absorber	Lean solvent rate Lean loading
Lean Loading Controller	Mol CO_2/mol amine in lean solvent	Rich solvent rate Water makeup rate
Water Makeup Controller	Water mass fraction in lean solvent	Water makeup rate
Reboiler Level Controller	Reboiler level	Reboiler bottoms rate
Reboiler Temperature Controller	Reboiler temperature	Steam rate Rich solvent rate

Condenser Temperature Controller	Condenser temperature	Cooling water rate
Stripper Pressure Controller	Top pressure of stripper	Stripper gas rate
Steam Rate Controller	Steam rate	Steam rate

Literature on Dynamic Modeling for Carbon Capture

This review has been organized by model scope, going from least complex (modeling of an individual unit) to most complex (modeling of multiple interacting units). The final section of the report includes modeling of alternative configurations. Within each section, the literature has been arranged from least model complexity (bottom left of Figure 2) to most model complexity (top right of Figure 2).

Models of Individual Absorption and Stripping Units for Carbon Capture

While it should be emphasized that a model of the entire absorption/stripping system is required to obtain an accurate representation of the process, the work presented in this section on individual units provides a useful qualitative evaluation of operational and design issues related to the system.

Modeling of Stripper by Ziaii et al.

Ziaii et al. (2009) modeled stripper performance in Aspen Custom Modeler® for 7 M MEA solvent using a five-segmented column with Mellapak 250Y structured packing. This model incorporated rate-based mass transfer and equilibrium reactions for CO_2 desorption in the liquid phase (top left of Figure 2). A steady-state energy minimization was performed by calculating the total equivalent work including the reboiler duty and pump work but excluding compression work over a range of packing heights and lean loadings. It was concluded that the optimum conditions were a lean loading of 0.42 mol CO_2/mol amine and a 1.8 m packing height, at a given stripper top pressure, flooding percentage, cross exchanger approach temperature, rich loading, and liquid hold-up time in the reboiler.

The optimized design case was used to carry out dynamic analyses that considered two control strategies in response to reduced steam rate in the reboiler: 1) reduce the rich solvent flowrate proportionally in response to reduced steam rate, and 2) allow lean loading to increase by keeping a constant rich solvent flowrate. In both scenarios, the overhead pressure of the column and liquid level in the reboiler are controlled at a constant value. It was found that the lean loading remained approximately constant when ratio control was used to adjust the rich solvent rate proportionally to steam rate, while lean loading increased by 3% when rich loading remained constant during a 10% decrease in steam rate. The reboiler pressure was simulated for both strategies, and while the final steady state values were approximately equal, strategy 1 reached a steady state value much faster than strategy 2, which could be important for stable system operation. Reboiler temperature was also simulated, and it was found that lean loading is the dominant factor influencing temperature. Since the lean loading is approximately constant

for strategy 1, the reboiler temperature is also approximately constant. Overall, strategy 2 showed a 30 min response time for a step change in flue gas rate, while ratio control in strategy 1 reduced the response time to less than 1 min. Therefore, this study suggests that implementing ratio control for rich solvent rate in response to steam flowrate will lead to a more stable system with faster responses than keeping a constant rich flowrate.

Modeling of Absorber by Lawal et al.

Lawal et al. (2009) modeled the absorber column with MEA solvent in gPROMS® using rate-based mass transfer and equilibrium reactions (top left of Figure 2). A steady state validation of the model was performed using data from the pilot plant at the University of Texas at Austin. The validation showed that the model was more accurate at a low value for L/G, which corresponds to a lower CO_2 absorption level. However, even at a low L/G, the model under predicted values for rich loading and temperature profile in the column. For a high L/G, the model was not a good fit for the pilot plant data, which could be a result of modeling the reactions as equilibrium rather than rate based.

Two dynamic analyses were performed on the absorber: 1) reducing flue gas rate with and without changing the lean flowrate of MEA, and 2) increasing the MEA lean loading. From the first scenario, it was concluded that the performance of the absorber is more sensitive to the ratio L/G than it is to the absolute flowrates themselves. Therefore the steam load and overall energy requirement of the regeneration system can be reduced by maintaining a constant L/G ratio if the flue gas rate is reduced, demonstrating the need for a control strategy for lean solvent flowrate and reboiler duty. The second scenario showed that the CO_2 absorption rate is significantly reduced by increases in lean loading. The authors suggest the absorption rate can be controlled by increasing the rate of lean solvent or decreasing the loading through increased reboiler duty or a makeup solvent stream. However, it is unclear that maintaining a constant percentage of CO_2 removal through these control strategies will lead to optimal system performance.

Modeling of Absorber by Kvamsdal et al.

Kvamsdal et al. (2009) also modeled an absorber column in gPROMS® for MEA solvent with rate-based mass transfer like the previous work, but accounted for reaction kinetics in the liquid phase through an enhancement factor (top middle of Figure 2). Again, University of Texas at Austin pilot plant data were used to validate the model in the steady state with two cases of high and low L/G ratio. The gPROMS® model was more accurate at predicting the temperature profile in the pilot plant absorber column for the low L/G ratio case. The overall model accuracy is improved from the previous work, which may reflect the use of reaction kinetics instead of assuming equilibrium reactions.

Dynamic simulations were performed to demonstrate: 1) plant startup, and 2) load reduction without (case 1) and with (case 2) changing liquid flowrate to maintain constant CO_2 removal. Several assumptions were used to simulate startup, including a 3.5 mol/s ramp rate of liquid at constant lean loading and a 0.5 mol/s ramp rate of flue gas once the desired liquid rate was achieved. Using these assumptions, a column filled with ambient air was simulated for 7 min, the liquid rate was ramped up from 7 min to 20 min, and after one additional minute the flue gas rate was ramped up to the 45 min mark. It was noted that the temperature bulge moved from the bottom to the top of the column as the flue gas rate was increased and that at 27 min the amount of CO_2 exceeded liquid capacity. The authors point out several aspects of the model which are

usually valid assumptions for steady state operation but which need to be further investigated for their validity in the dynamic simulation of startup. These assumptions include: plug flow regime; constant pressure drop in the column; thermal equilibrium between liquid and solid column internals; and constant effective interfacial area. The authors also say that further study needs to be performed to ensure that column operability limits such as flooding, adequate wetting of the packing, and pressure drop are observed during the dynamics of the process.

In considering load reduction from the upstream power plant, the cooling tower and blower were also modeled in a very simplified form with the absorber. For case 1 of load reduction (constant liquid rate), the removal rate increased, the rich loading decreased, and the temperature bulge moved towards the bottom of the column as gas rate decreased. For case 2 of load reduction (varying liquid rate for constant removal), the removal rate initially increased but then decreased to its initial value, rich loading increased, and the temperature bulge moved upwards as gas rate decreased. A higher value for rich loading uses less energy by creating a larger driving force for solvent regeneration. In both cases, liquid temperature was decreased which may influence stripper performance. It is unclear that either control strategy in case 1 or 2 will lead to an economic optimum. Qualitatively, it can be concluded that case 1 will use more energy in the stripper because of an unnecessarily high liquid rate. Case 2 uses less energy, but it is possible that there are more optimal control strategies than maintaining a constant CO_2 removal rate.

Plantwide Models for Carbon Capture

The previous dynamic models discussed consider only the operation of either the absorber or stripper. However, the absorber and stripper are complex unit operations and optimal performance of one unit interferes with the other, which demonstrates the need for a plantwide dynamic model. There are limited examples of dynamic models for plantwide control, and none of these models are capable of accurately predicting plant performance due to their low level of model complexity.

Plantwide Modeling by Lin et al.

Lin et al. (2011) used an equilibrium stage model with equilibrium reactions (bottom left of Figure 2) in Aspen Dynamics® to investigate the impact of solvent recycle on control structure design. The model used 30 wt % MEA and column dimensions that correspond to a pilot plant that will be completed at the China Steel Corporation in Kaohsiung, Taiwan. While an equilibrium model fails to capture the actual performance of the system, this work does provide some insights on strategies for plantwide control. A steady state optimization of an absorber, stripper, reboiler, cross exchanger, trim cooler, and condenser was performed in Aspen Plus®, and it was found at a 90% removal rate that the optimum lean loading was 0.38 mol CO_2/mol amine which corresponds to an L/G ratio of 7.7. This optimum steady state case was exported to Aspen Dynamics® for dynamic simulation.

Four control techniques were examined in dynamic operation of the plant: 1) control water makeup to maintain liquid level in the reboiler and in response to changes in water composition in the flue gas; 2) control lean solvent rate in response to changes in flue gas rate and CO_2 composition in the flue gas; 3) control lean solvent rate and reboiler duty in response to changes in CO_2 removal set point; and 4) control reboiler temperature to optimize energy efficiency. Water makeup was shown to be an important design parameter to maintain a system water balance, because water was accumulated or depleted when level control was relinquished and the

water makeup rate was changed. Thus, level control through water makeup is a necessary component of the system, although it is unclear that adding the makeup water to the bottom of the stripper as done in this work will lead to optimal system design. Lean solvent rate was also shown to be an important design parameter to maintain a constant CO_2 removal set point, as expected. By controlling lean solvent rate, flexible capture can be achieved which could lead to economic benefits through reduction of reboiler duty at peak electricity generation times. Reboiler temperature, which the authors state is the only operating degree of freedom in their system, was varied to optimize energy consumption by the system. However, the scope of this system does not include the compressor, and constant stripper top pressure was assumed by controlling the stripper gas flow rate. If compressor work was considered, it is possible that this optimization would have yielded different results.

Plantwide Modeling by Lawal et al.

Lawal et al. expanded the scope of their 2009 model by integrating the absorber with a stripper, as well as pumps, heat exchangers, and a cold lean solvent storage tank, to more accurately represent the dynamics of the carbon capture plant (Lawal et al., 2010a). The model complexity remains in the top left of Figure 2. This new model was again validated with steady state pilot plant data from the University of Texas at Austin, and the results showed that the integrated system was more accurate than the stand-alone columns by themselves.

Four dynamic analyses were performed for this absorber/stripper system: 1) switching off water balance control; 2) increasing flue gas flowrate; 3) increasing CO_2 concentration in the flue gas; and 4) reducing reboiler heat duty. When there is no water makeup, it was shown that the lean loading and thus the CO_2 removal rate vary significantly because there was a net water loss via evaporation in the absorber. Failure to maintain a water balance can lead to corrosion of the system due to increased concentration or operational issues, so there is a clear need for water control in the system. However, adding the water makeup directly to the solvent storage tank as Lawal et al. did is probably not the optimum process design.

Flue gas rate was increased by 10% with capture control turned off to simulate a 10% increase in power plant load. When the lean solvent rate was kept constant, it was found that both the capture rate and energy requirement per mass CO_2 decreased. When the lean solvent rate was also increased by 10% to maintain a constant L/G ratio, it was found that both the capture rate and the energy requirement per mass CO_2 remained approximately constant. Additionally, flue gas composition was increased to 50% CO_2 and the mass flow of CO_2 to the absorber was kept constant to simulate partial oxy-fuel mode operation. In this scenario, the lean solvent rate and system heat requirement both decreased when CO_2 removal rate was kept constant due to the greater driving force in the absorber. Lawal et al. (2011) provides a more detailed analysis on combining O_2 enhancement with post-combustion capture, showing that higher partial pressures of CO_2 led to a decreased overall energy requirement even with energy intense air separation.

A 10% step change decrease in reboiler duty was introduced to the system with capture rate and reboiler duty control turned off. The dynamic response showed that lean loading increased and the removal rate decreased with constant solvent rate, as expected. The time constant for this response was estimated at 57 min. This time constant accounted for the hold-up in the absorber and regenerator sumps, reboiler, and lean solvent storage tank, but excluded transport delay. It should be noted that the single largest contributor to the time constant was the MEA storage

tank, which has a hold-up of 23 min. The authors suggest that a rich solvent storage tank could be investigated to allow for a constant removal rate even when steam load is reduced.

Lawal et al. (2010b) further expanded the scope of their combined absorber/stripper model by linking it to a 500 MWe supercritical coal-fired power plant. There were three main interactions between the capture plant and the power plant: 1) flue gas stream to be processed; 2) steam draw-off from the intermediate pressure/low pressure turbine crossover in the power plant for reboiler duty; and 3) reboiler condensate return to the power plant. Steam draw-off is controlled by measuring the lean solvent temperature from the reboiler and using a control valve to adjust the steam rate accordingly. Dynamic analyses were performed where power plant output was decreased and capture rate was increased. The results showed that the carbon capture plant has slower response times than the power generation plant. It was also revealed that the control loops of capture rate and power plant output have interactions with each other.

Plantwide Modeling by Ziaii et al.

Ziaii et al. (2011) expanded the scope of their 2009 ACM® stripper model to a plantwide system that included the absorber, compressor, pumps, heat exchangers, and high, intermediate, and low pressure power plant turbines for a 100 MWe capacity plant. The model was optimized both in the steady state and dynamically with power plant profit as the objective function. A range of ratios of cost per ton of CO_2 emitted to price of electricity generated per kWh was used in the profit optimizations. The FEASOPT method in ACM® was connected to the steady state model and profit was maximized by adjusting lean loading and CO_2 removal simultaneously. The same method was used for dynamic scenarios to optimize set point paths of steam rate, solvent rate, and stripper pressure simultaneously.

The two dynamic scenarios explored were: 1) partial steam load operation in flexible capture, and 2) partial boiler load operation leading to a simultaneous decrease in flue gas rate and power cycle steam rate. The results from both scenarios showed that it was most profitable to keep the pressure valve wide open and allow the stripper pressure to swing. This is an important result because other works that did not include the compressor in the scope of their model came to different conclusions about controlling stripper pressure. For the first scenario, a linear relationship was found to exist between optimum solvent rate and reboiler steam rate with a slope near 1. For the second scenario, another linear relationship was found between the optimum solvent rate and reboiler steam rate with the boiler load (which is directly proportional to flue gas rate), and again the slope was near 1. This implies that ratio control between solvent rate and steam rate in scenario 1 and ratio control among solvent rate, steam rate, and flue gas rate in scenario 2 will lead to optimum operation in response to disturbances.

Models of Alternative Configurations for Post-Combustion Carbon Capture

It is possible that alternative process configurations could minimize capital or operating costs for carbon capture. To the knowledge of this author, there is only one example of a dynamic model that was developed for an alternative process configuration to the basic absorber/stripper post-combustion amine scrubbing process.

Two-Stage Flash Modeling by Rochelle et al.

Rochelle et al. (2011) designed a two-stage flash using piperazine solvent in MATLAB® as an alternative to a stripper for CO_2 regeneration. A two-stage flash system complicates control

strategies because there are now two pressures, two temperatures, and two heat duties to account for rather than one pressure, one temperature, and one heat duty for a simple stripper. This model assumed equilibrium reactions and mass transfer (bottom left of Figure 2). Both flashes were maintained at 150 °C, and the pressure ratio between the first high pressure flash to the second low pressure flash was maintained at 1.5–2. In both flashes, temperature, pressure, and level were controlled. The scope and complexity of this model is being increased, and it has not yet been validated with pilot plant data. A two-stage flash system offers advantages over a conventional stripper due to its reduced capital cost and ability to feed CO_2 at different pressures to different stages of the compressor.

Conclusions

Literature on dynamic modeling for post-combustion carbon capture has been reviewed. The following conclusions can be drawn based on the results of the dynamic models that have been developed:

1. Models that incorporate reaction kinetics tend to better predict pilot plant data than models that assume equilibrium reactions.
2. It is more important to control the ratio L/G to maintain a stable system than the absolute flowrates themselves.
3. Ratio control between rich solvent rate and steam rate will lead to stable and potentially optimal system control.
4. A model that included the compressor in the model scope came to different conclusions about optimal system operation than models that did not include the compressor.
5. Total system hold-up is an important factor for response times to set point changes.
6. A control strategy for water makeup must be developed to maintain the system water balance.
7. Combining post-combustion capture with partial oxy-combustion operation could potentially reduce the energy requirement of carbon capture.

Future Work

There are limited examples of dynamic models for post-combustion amine scrubbing plants. While the publications presented in this review have provided a valuable basis for future modeling work, many of them lacked the scope and complexity needed to accurately create a scalable and adaptable model for a carbon capture plant. Recommendations for future work in dynamic modeling include:

1. Validate dynamic models with dynamic rather than steady state pilot plant data.
2. Expand model scope to include a rigorous design of the downstream compressor and upstream power plant.
3. Increase model complexity and examine the effects of model assumptions that reduce complexity.
4. Determine plantwide optimal control strategies to maximize power plant profit.
5. Explore alternative and more complex process configurations that could lead to more optimal operation, such as a two-stage flash regeneration system.

References

Kenig EY, Schneider R, Górak A. “Reactive absorption: optimal process design via optimal modeling.” *Chem Eng Sci.* 2001;56:343–350.

Kvamsdal HM, Jakobsen JP, Hoff KA. “Dynamic modeling and simulation of a CO_2 absorber column for post-combustion CO_2 capture.” *Chem Eng Proc: Process Intensif.* 2009;48:135–144.

Lawal A, Wang M, Stephenson P, Koumpouras G, Yeung H. “Dynamic modeling of CO_2 absorption for post combustion capture in coal-fired power plants.” *Fuel*. 2009;88:2455–2462.

Lawal A, Wang M, Stephenson P, Koumpouras G, Yeung H. "Dynamic modeling and analysis of post-combustion CO_2 chemical absorption process for coal-fired power plants." *Fuel*. 2010a;89:2791–2801.

Lawal A, Wang M, Stephenson P, Koumpouras G, Yeung H. “Demonstrating full-scale post-combustion CO_2 capture for coal-fired power plants through dynamic modeling and simulation.” *Fuel*. 2010b; Corrected proof in press.

Lawal A, Wang M, Stephenson P. “Investigating the dynamic response of CO_2 chemical absorption process in enhanced-O_2 coal power plant with post-combustion CO_2 capture.” *Energy Proc*. 2011;4:1035–1042.

Lin Y-J, Pan T-H, Wong DS-H, Jang S-S, Chi Y-W, Yeh C-H. “Plantwide control of CO_2 capture by absorption and stripping using monoethanolamine solution.” *Ind Eng Chem Res.* 2011;50:1338–1345.

Rochelle GT et al. "CO_2 Capture by Aqueous Absorption, Third Quarterly Progress Report 2011." Luminant Carbon Management Program. The University of Texas at Austin. 2011.

Ziaii S, Rochelle GT, Edgar TF. “Dynamic modeling to minimize energy use for CO_2 capture in power plants by aqueous monoethanolamine.” *Ind Eng Chem Res.* 2009;48:6105–6111.

Ziaii S, Rochelle GT, Edgar, TF. “Optimum design and control of amine scrubbing in response to electricity and CO_2 prices.” *Energy Proc*. 2011;4:1683–1690.

Electric Grid-Level Implications of Flexible CO_2 Capture Operation

Quarterly Report for October 1 – December 31, 2011

by Stuart Cohen

Supported by the EPA STAR Fellowship Program and the

Luminant Carbon Management Program

Department of Chemical Engineering

The University of Texas at Austin

January 31, 2012

Abstract

Flexible post-combustion absorption/stripping that vents carbon dioxide (CO_2) or stores rich solvent at partial or zero load could add value to facilities with CO_2 capture, with one reason being an increased ability to perform grid reliability services (ancillary services, or AS). The Electric Reliability Council of Texas (ERCOT) electric grid operates four AS markets, and these markets could become more lucrative as the already substantial ERCOT wind capacity increases. The new grid-level electricity dispatch model introduced in the third quarterly report of 2011 has now been tested with flexible CO_2 capture facilities and with up to 144 individually represented facilities. The model uses performance parameters for each generation facility, electricity demand, wind-based electricity production, and AS requirements to determine the power plant operation that minimizes total dispatch costs. It is intended to determine whether flexible CO_2 capture increases AS revenues and improves grid reliability.

Major conclusions from this quarter include the following.

- The grid-level dispatch model successfully demonstrates venting-only flexible CO_2 capture, but ensuring functionality of solvent storage systems requires further testing.
- Under appropriate market conditions, flexible CO_2 capture can reduce electricity dispatch costs and improve the ability of a facility to earn revenue from ancillary service procurements.
- The grid-level model functions properly and has reasonable computation time with up to 144 individually represented power generation facilities.
- Minimum load requirements on power systems can cause over-procurement of high-value AS such as regulation up and a corresponding under-procurement of lower-value AS such as responsive reserves.
- Despite relatively high plant-level resolution and generous ramp rates, electricity prices can still spike to the $3,000 per megawatt-hour offer cap when online units cannot ramp up or down fast enough to respond to changes in demand.

Introduction to Flexible CO_2 Capture

Flexible operation of a post-combustion amine absorption and stripping system entails varying the liquid and vapor flow rates in the stripping and/or absorption systems in order to choose the most economical CO_2 capture operating point for current electricity market conditions. During partial- or zero-load CO_2 capture, some or all of the steam being used for solvent regeneration is redirected back to the low pressure turbine in the power cycle to increase electrical output. The resulting decrease in CO_2 flow exiting the stripper also reduces energy requirements for CO_2 compression. Solvent flow to the absorber and stripper and flue gas flow to the absorber could also be modulated for efficient system operation.

Flexible CO_2 capture could allow the plant operator to increase power output when electricity prices are high if additional electricity sales offset any increase in CO_2 emissions costs under a CO_2 regulatory framework (Ziaii et al., 2008). In addition, operating CO_2 capture at zero load during annual peak electricity demand can eliminate the need to spend billions of dollars to replace generation capacity lost when CO_2 capture operates at full load (Cohen et al., 2010). If the load on energy-intensive CO_2 capture components can be reduced quickly, CO_2 capture energy requirements could be offered as reserve capacity in ancillary service (AS) markets for grid reliability services. AS markets can be quite lucrative, and the demand for AS might grow with greater penetration of intermittent renewable electricity sources such as wind (Chalmers et al., 2009). At the grid level, flexible CO_2 capture provides another method to control power output and respond to expected or unexpected changes to electricity supply and demand.

There are two basic concepts for flexible CO_2 capture using amine scrubbing. One reduces the energy requirements of solvent stripping and CO_2 compression while allowing the CO_2 removal rate to fall. Figure 1 displays one way to implement such a configuration, where steam and rich solvent flow rates to the stripper are reduced equally and simultaneously during partial- or zero-load operation (Ziaii et al., 2008). At partial load, rich solvent diverted from the stripper is recycled to the absorber, so CO_2 removal rates in the absorber will decrease as solvent becomes saturated with CO_2. Zero load could involve recirculating all solvent through the absorber, or the CO_2 capture system could be bypassed completely. Assuming a retrofit application where the low pressure turbine and generator has been sized to operate without CO_2 capture, this design has negligible capital cost, but its primary disadvantage is any cost and environmental impact of increased CO_2 emissions.

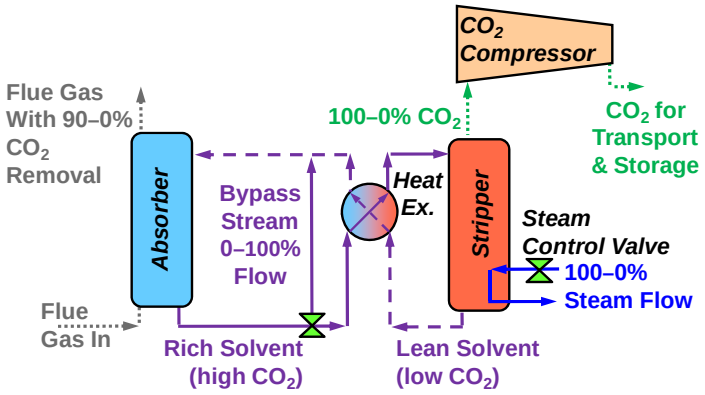

Figure 1: Simultaneously reducing steam and rich solvent flow to the stripper allows increased output but at the expense of additional CO_2 emissions.

Another flexible CO_2 capture concept uses auxiliary solvent storage tanks to maintain high CO_2 removal when stripping and compression systems operate at partial or zero load (Figure 2) (Chalmers and Gibbins, 2007; Rochelle et al., 2009). When electricity prices are high, the plant can reduce stripper and compressor load while maintaining full-load CO_2 absorption by feeding the absorber from a lean solvent storage tank and depositing rich solvent into another tank. When electricity prices are low, stripping and compression systems return to a higher load to treat the current process stream and the stored rich solvent. To treat both the current stream and stored solvent, stripping and compression systems must be larger and require more total energy than a CO_2 capture system without solvent storage. Maintaining high CO_2 removal keeps operating costs down while storing rich solvent, but any operating profit improvement must be weighed against the capital cost of solvent inventory, storage tanks, and larger stripping and compression equipment. A facility with solvent storage would likely also maintain the ability to vent CO_2 when economically desirable or necessary for maintenance.

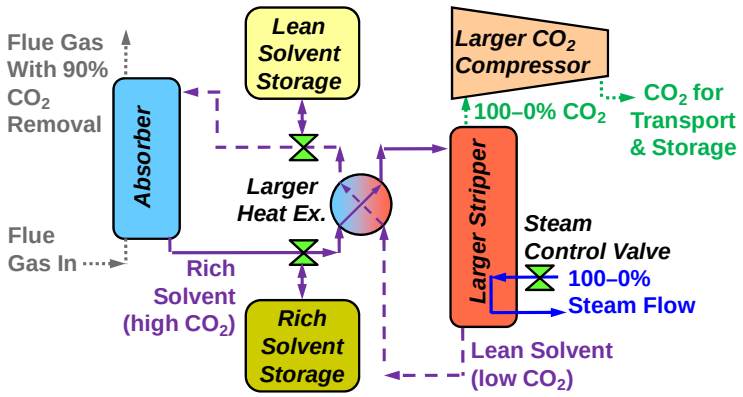

Figure 2: Including solvent storage incurs significant capital costs but allows continued high CO_2 removal at partial and zero load.

Grid-Level Least-Cost Dispatch Model

Primary activities this quarter were continued testing and development of the grid-level least-cost dispatch model described previously (Rochelle et al., 2011). Most model characteristics were discussed in the previous report, so this report will briefly summarize that content while focusing primarily on new developments.

Activities since the last quarter include the following.

- Functionality testing has been performed for the inflexible and flexible CO_2 capture configurations.
- Ancillary service constraints have been modified for flexible CO_2 capture.
- The model has been tested for functionality and computational expense with 42- and 144-facility databases.
- The ability to model several new power plant types has been added: oil-based units, natural gas-based steam boiler units, natural gas internal combustion (IC) engines, and biomass-based units.
- The model has been modified to treat combined heat and power (CHP) facilities as "must-run" at their maximum output.

- A MATLAB data analysis code has been created to expedite data processing and visualization.
- A unit-specific performance specification database is nearly complete.

Description of the ERCOT Market

Before discussing the model, the ERCOT market will be described in brief. ERCOT comprises ~550 generating units across ~200 power generation facilities that supply 85% of electricity demand in Texas (ERCOT, 2010a; USEPA, 2010). Its total installed capacity at the end of 2010 was 84.2 gigawatts (GW) with an available capacity of 75.8 GW after derating the 9.3 GW of wind capacity to its average availability (ERCOT, 2010a).

ERCOT operates markets for electricity to meet consumer demand as well as ancillary services to ensure grid reliability. Based on electricity and ancillary service offers submitted to ERCOT, forecast electricity demand, and ERCOT AS requirements, ERCOT co-optimizes electricity supply and ancillary service procurements for each hour in a day-ahead market. The day-ahead market determines which units will be online (committed) in each hour, then the real-time market determines electricity prices every 15 minutes by averaging shadow prices for electricity over each three successive 5-minute intervals.

There are four ancillary service markets in ERCOT, each with its own purpose and requirements. Regulation Up (RU) and Regulation Down (RD) services are procured to respond within 5 minutes to discrepancies between expected and actual load (ERCOT, 2011a). The RU and RD requirement varies by hour and month depending on current load uncertainty, historical Regulation deployments, and installed wind capacity (ERCOT, 2011a). Responsive Reserve Service (RRS), commonly called spinning reserves, must be supplied by online units capable of responding within 10 minutes (ERCOT, 2011a). Total RRS procurements must be able to alleviate the largest single outage possible within ERCOT, currently 2300 megawatts (MW), the maximum output of the South Texas Project nuclear facility (ERCOT, 2011a). Up to half of the RRS requirement can be met by interruptible load facilities that are contracted to reduce demand if necessary to maintain grid reliability (ERCOT, 2011a). Non-Spinning Reserve Service (NSRS) can be provided by online or offline units as well as interruptible load and must be able to respond within 30 minutes. The quantity of NSRS required in each hour depends on the Regulation Up procurement and net load uncertainty (ERCOT, 2011a).

Model Description and Formulation

The model employs a two-stage optimization procedure for each day to mimic ERCOT operating procedures. A day-ahead optimization minimizes the cost of meeting electricity demand and AS requirements in each hour, and the optimal solution determines the commitment status (online or offline) of each facility as well as ancillary service procurements. Commitment status and AS procurements are then fixed, and electrical output in 15-minute intervals is determined in a real-time market optimization. If the grid is assumed to contain energy storage systems, the quantity of stored energy in each time period is also determined by the real-time optimization. The solution from the current day then informs initial conditions for the following day, and the process repeats for the desired number of days.

The model does not perform AS deployments, which are executed in ERCOT in response to discrepancies between planned and actual electricity demand, wind generation, and unplanned transmission and generation outages. Modeling the manner in which AS are deployed is outside

the scope of this work. Instead, the model assesses a large cost penalty for any imbalances between electricity supply and demand, and the existence of these penalties indicates when AS deployments would likely be required.

The model can consider several power plant types: coal-fired, natural gas-fired combined-cycle (NGCC), open-cycle gas turbines (OCGT), gas-fired steam boilers (NGBLR), natural gas internal combustion (NGIC), oil-fired, nuclear, hydroelectric, wind, and biomass. Thermal generation facilities can also be designated as CHP facilities. CHP facilities are typically designed to meet constant heat loads, so these systems are assumed to operate continuously at their maximum output regardless of operating costs. Interruptible load is also included in the model. The framework to study grid-scale energy storage is included, as energy storage could be a primary competitor with flexible CO_2 capture in electricity price arbitrage and ancillary service provision. Inflexible and flexible CO_2 capture facilities at coal-fired power plants can also be modeled.

The model is implemented as a mixed-integer linear program and was created using GAMS software. It is a mixed-integer model because there are both integer (binary) variables (online/offline status and startup/shutdown status of power and CO_2 capture systems) and continuous variables (electrical output, electrical input to storage, stored energy level, CO_2 capture load, CO_2 capture solvent storage level). The objective function and all constraint equations are all linear functions of the variables, which improves solvability and reduces computation time.

Objective Function

The objective function sums all operating costs over all plants and time periods in the day being optimized. Power plant operating costs include startup costs, shutdown costs, and operating costs not attributed to fuel or CO_2 emissions. All fossil-fueled facilities have fuel costs as well as CO_2 emissions costs that are assessed if a CO_2 price is assumed to exist due to an emissions reduction policy. If an energy storage system uses compressed air energy storage with a natural gas turbine to produce power, it also has fuel costs. Interruptible load can be assigned operating costs if appropriate. There are usually no direct costs for procuring AS, but costs on the order of 10^{-5} \$/MW are assessed to help prevent the model from over-procuring AS.

For facilities with CO_2 capture, additional costs are assessed for the following: solvent makeup to offset degradation and volatility losses, caustic sodium hydroxide (NaOH) for thermal solvent reclaiming, reclaimer waste disposal, additional water use for CO_2 capture, CO_2 transport and storage, and ramping the capture system components up and down. CO_2 capture ramping costs are a proxy for costs associated with efficiency losses during transient CO_2 capture operation.

The model also assesses cost penalties for any electricity supply-demand imbalance using the same penalties as ERCOT. The real-time market penalty for oversupply is \$250 per megawatt-hour (MWh), and the penalty for undersupply increases with the supply deficiency until reaching the market maximum electricity price of \$3,000/MWh above 50 MW undersupply (ERCOT, 2010b).

Constraints

Most constraints have not changed since the formulation discussed in the last report (Rochelle et al., 2011). Table 1 lists the constraint types included in the model formulation and the systems to which they apply.

Table 1: The model contains the following constraints on the systems indicated.

Constraint type	Systems applicable
Minimum and maximum load	Power output, absorber, stripper, power input (storage)
Ramp rate	Power output, absorber, stripper, power input (storage)
Minimum time online after startup and offline after shutdown	Power output, absorber, stripper, power input (storage)
Combined energy and AS must be within output limits	Power output
AS offer limitations by ramp rate and capacity fraction	Power output
Maximum storage capacity	Energy storage, CO_2 capture solvent storage
Stored energy flow balance	Energy storage
CO_2 flow balance	Solvent storage
Electricity supply-demand balance	Electric grid
AS requirements	Electric grid

In addition, interruptible load facilities may only provide RRS and NSRS and can only be procured for up to 50% of the RRS requirement. Interruptible load would act as additional electricity supply output if deployed, but AS deployments are not included in the model.

Ancillary service offers are limited by how much a facility can ramp its net power output up and down within a specified time frame. For typical facilities, the limitation is the product of its ramp rate and the required response time for the AS (5 min. for RU/RD, 10 min. for RRS, 30 min. for NSRS in ERCOT). However, facilities with flexible CO_2 capture have a larger "net" ramp rate because power systems could be ramped up while CO_2 capture systems are ramped down and vice versa. Thus, AS limitations have been modified to reflect the net ramping capabilities if flexible CO_2 capture is available.

In addition, constraints that ensure that combined electricity output and AS procurements fall within output limits must also account for limitations on flexible CO_2 capture systems. For a typical facility without flexible CO_2 capture (or energy storage), procured RD must not exceed the difference between current and minimum power output, and the sum of procured RU, RRS, and NSRS must not exceed the difference between maximum and current power output. Modifications for energy storage were discussed in the last quarterly report (Rochelle et al., 2011). With flexible CO_2 capture, RD could be provided by the ability to ramp power output

down or ramp CO_2 capture load up, so the appropriate constraint must include terms for the maximum net power output reduction if CO_2 capture load was increased. Similarly, RU, RRS, and NSRS could be provided by the ability to ramp CO_2 capture systems down, so procurements of these services must be limited by the difference between current and minimum CO_2 capture load in addition to available power output capacity.

Data Analysis

In earlier model testing with a set of 10 plants optimized over two days, data were manipulated and plotted in Excel to verify successful model operation. However, using Excel in this manner is very time consuming for larger plant data sets optimized over longer time periods. To make data analysis faster and more versatile, a MATLAB script was created to automatically read output from the GAMS grid-level optimization model, perform desired data manipulations, and plot results. The script automatically detects the number of facilities modeled and the total time being optimized. It then performs necessary data operations and plots electrical output and AS procured from each facility and facility type. If energy storage systems are included in input data, energy storage levels over time are plotted along with the total energy stored if there are multiple storage facilities. Shadow prices for energy and AS are plotted to display the time-varying price of each commodity. Absorber load, stripper load, and stored CO_2 level are also plotted for CO_2 capture facilities, and average quantities of these variables are also plotted to demonstrate typical CO_2 capture system behavior.

Input Database Creation

The last quarterly report described a 10-facility power plant data set used for preliminary model testing (Rochelle et al., 2011). This data set comprised a wide variety of generation types, but its level of plant aggregation limits its accuracy in representing the actual ERCOT electricity system. To examine model functionality and computation time for power plant data sets that better approximate actual ERCOT facilities, more resolved plant data sets were created.

Semi-Aggregated 42-Plant Data Set

A 42-plant data set was created to serve as a first step toward representing all plants or units in ERCOT. In this database, some facilities are represented individually while others are aggregated by plant type and performance. The primary data source is the U.S. Environmental Protection Agency (EPA) eGRID 2010 v1.1 database, which uses 2007 plant-level data (USEPA, 2010). EPA eGRID data include heat rate, CO_2 emissions rate, nameplate capacity, annual net generation, and CHP status. The following plant types are represented, with the option for designating thermal plants as CHP facilities:

- Coal
- Oil
- Nuclear
- Hydroelectric
- Biomass
- Natural gas combined-cycle
- Natural gas boiler
- Open-cycle natural gas
- Internal Combustion

All hydroelectric and biomass-based facilities are aggregated because their total capacity in ERCOT is small, and their low marginal costs should allow near-continuous operation at

maximum output. The two nuclear facilities in ERCOT are also aggregated, as they are likely to operate in a similar manner. Coal- and oil-fired facilities are represented separately by plant because there are relatively few (14 coal, 5 oil), and they have disparate performance characteristics.

Gas-fired facilities are numerous and have widely varying performance characteristics, so they were aggregated using three dimensions: 1) unit type (combined-cycle, steam boiler, open-cycle, internal combustion); 2) status as a combined heat and power unit (yes or no); and 3) heat rate. Twenty was then chosen as a reasonable number of gas-fired facilities for this stage of testing. An Excel Solver optimization is used to determine the number of facilities of each unit type-CHP combination by finding with integer values that sum to 20 and most closely approximate the 20 multiplied by the fraction of each unit type-CHP combination among the ERCOT gas-fired facilities in eGRID.

Table 2: An Excel Solver optimization is used to find the number of gas-fired facilities with each unit type-CHP status combination in the 42-plant data set.

Natural gas unit type	CHP status	# Facilities in eGRID	# Facilities in 42-plant data set
Combined-cycle	Yes	26	4
Combined-cycle	No	27	4
Gas boiler	Yes	3	1
Gas boiler	No	33	5
Open-cycle	Yes	19	3
Open-cycle	No	6	1
Internal combustion	Yes	2	1
Internal combustion	No	5	1
Total		**121**	**20**

Performance specifications of each unit-CHP type must then be specified. To do so, eGRID facilities of the same unit-CHP combination are put into groups separated by heat rate percentile rank within the category. For instance, if there are to be 4 facilities of a given unit-CHP combination, facilities of the same category in eGRID will be split into 4 bins of heat rates (HR) in the following percentile ranges: $0\% \leq HR \leq 25\%$, $25\% < HR \leq 50\%$, $50\% < HR \leq 75\%$, $75\% < HR \leq 100\%$. Then, the heat rate of each aggregated facility representing a heat rate bin is equal to the annual generation-weighted average heat rate of all facilities in the bin. CO_2 emissions rates are calculated using the annual generation-weighted average CO_2 emissions rate of all facilities in the heat rate bin, and maximum power output capacity is the total capacity of all facilities in the bin.

Other plant characteristics required by the model are not contained in eGRID. These include startup costs, non-fuel/CO_2 variable operation and maintenance (VOM) cost at the base plant, minimum output, ramp rate, and minimum up and down time. The 42-plant data set is solely for testing purposes, so generic values are used for each plant type (Table 3). A range of startup

costs is used so that no two facilities have the same startup costs. This strategy is intended to prevent the model from having difficulty deciding between facilities to utilize, though differentiated heat rates are probably sufficient to mitigate this issue. Hydroelectric facilities are assumed able to ramp from 0–100% within the smallest time interval in the model, 15 minutes.

Table 3: The following generic plant characteristics are used in the 42-plant data set.

Plant type	Startup cost ($/startup)	Base plant VOM cost ($/MWh)	Minimum output (%cap)	Ramp rate up & down (%cap/min)	Minimum up/down time (hr)
Hydro	0	24.3	0	100	0.5
Biomass	100	5	30	2	6
Nuclear	15,000	17.15	30	1	168
Coal	12,000–13,700	5	30	2	24
NG combined-cycle	8,000–8,240	5	25	4	6
NG boiler	4,000–4,160	5	30	6	6
Open-cycle NG	500–515	5	10	10	0.5
NG internal combustion	500	5	10	10	0.5
Oil	500–520	5	10	10	0.5

Wind turbines are not represented in the plant data set. The model optimizes facility operation in response to net load: consumer electricity demand minus wind generation. Therefore, input net load data will account for wind-based electricity.

Plant-Specific 144-Plant Data Set

After testing model efficacy with the 42-plant data set, a 144-plant ERCOT data set with very little aggregation by plant type was created for further testing. This data set was also derived from the eGRID 2010 v1.1 database and uses the same generic characteristics by plant type as shown in Table 3 (USEPA, 2010). Hydroelectric and biomass units remain aggregated, but nuclear-, coal-, oil-, and gas-based facilities are represented individually.

Unit-Specific Data Set

Representing each generating unit would be the greatest level of resolution for power plant input data. To test model effectiveness at this level, a unit-specific data set is being created. This data set is intended for final results production, so greater care is being taken to ensure its accuracy.

A more recent list of ERCOT generating units has been provided by ERCOT representatives, so this list will be used in future analysis (ERCOT, 2011b). Unit-specific performance data are proprietary, but ERCOT representatives have provided unit-specific maximum capacity as well

as generic plant-type specific values for minimum capacity fraction, ramp rate, minimum up/down time, startup cost, heat rate, CO_2 emissions rate, and non-fuel/CO_2 VOM cost (ERCOT, 2011b). These data are publicly available as part of a contract between ERCOT and the U.S. Department of Energy.

ERCOT-provided values for minimum capacity fraction, minimum up/down time, startup cost, and non-fuel/CO_2 VOM cost will be used for all units of each plant type. ERCOT does not provide a minimum capacity fraction for nuclear facilities because its studies assume constant full-load operation, but the present work will relax this assumption so that nuclear facilities have the option to reduce output or provide regulation down service. Currently, minimum capacity for nuclear facilities is assumed to be 30% of the maximum. ERCOT-provided ramp rates are very conservative because they are intended to reproduce average actual operation, but other sources of ramp rate data are being explored to allow study of a more idealized system.

Generic values for each plant type are sufficient for many parameters. However, if generic heat rates and CO_2 emissions rates are used for each plant type, all facilities of each type will have the same operating cost, which is unrealistic and will lead to inaccurate dispatch and electricity pricing. The eGRID database provides plant-specific heat rates and CO_2 emissions rates for many of the facilities listed by ERCOT; however, it lacks enough unit-specific data to calculate unit-specific performance parameters (USEPA, 2010). Furthermore, eGRID values are averaged over a calendar year, so for plants with multiple units, heat rates and CO_2 emissions rates depend on the relative utilization of each unit, which is unknown. When all units are the same type, assuming equivalent performance is often reasonable, but for plants with multiple unit types, there is greater uncertainty as to which units have the greatest influence on average performance parameters. To maximize the utilization of the plant-specific information in eGRID while creating a unit-specific database, the following procedures are proposed.

- Case 1: Performance specifications for the plant appear in both the eGRID and ERCOT databases
    - If all units are the same type, use the eGRID heat rate and CO_2 emissions rate for all units.
    - If the plant has units of multiple types, use the following procedures.
        - If the ERCOT specifications are within 10% of the eGRID specifications for one of the unit types, use the eGRID value for that unit type and the ERCOT value for all other unit types.
        - If the ERCOT specifications are not within 10% of the eGRID specifications, use ERCOT values.
        - Heat rate only: If the ERCOT specifications are not within 10% of the eGRID specifications for any unit type and some units are NG internal combustion engines, use the eGRID values for non-NGIC units and use the ERCOT values for NGIC units (eGRID does not indicate any NGIC units in its ERCOT plant database)
- Case 2: Performance specifications for the plant appear in the ERCOT database but not in eGRID
    - Use the generic unit-type ERCOT values for heat rate and CO_2 emissions rate.
- Case 3: Performance specifications for the plant appear in neither database

- Use generic ERCOT values. If there are a few generic values for the unit type, choose based on the age of the facility (e.g., if unit is new, use the low-end heat rate and CO_2 emissions rate). If age is unknown, use median generic values.

The above procedure helps minimize the number of facilities with the same performance characteristics. If additional differentiation is desired, parameters might be randomized or ordered such that larger units are slightly more efficient than smaller ones.

Preliminary Results

All testing is performed using a near-sinusoidal electricity demand curve for a two-day period. Volatile wind production is not implemented in these input data. To include some temporal AS variability, regulation up and down requirements are adjusted from 500 MW for 10,000 MW installed wind capacity using factors recommended in a General Electric study commissioned by ERCOT (ERCOT, 2011a). For testing purposes, net load uncertainty, which is used to determine non-spinning reserve requirements, is randomized between 1,000 MW and 1,500 MW. Responsive reserve requirements are always 2,300 MW as specified by ERCOT.

CO_2 capture performance parameters are identical to those used in previous work (Cohen et. al., 2010). When testing with interruptible load, a maximum load reduction of 2,000 MW and a ramp rate of 200 MW/min is assumed. If energy storage is tested, input/output ranges from -1,000 MW to +1,000 MW, output/input efficiency is 90%, ramp rate is 500 MW/min, and minimum up/down time is 0.5 hr. Storage systems are given 10,000 MWh storage capacity, and the stored energy level must return to 5,000 MWh each day. An energy storage system of this size and efficiency is unlikely to be feasible; these characteristics are primarily used to ensure storage system utilization during model functionality testing.

All studies assume a $1.54 per million British thermal unit (MMBTU) coal price and a $4/MMBTU natural gas price.

CO_2 Capture Functionality Testing with 10 Plants

CO_2 capture functionality was tested by running the model with a CO_2 price of $35 per metric ton of CO_2 (tCO_2), where previous work has indicated flexible CO_2 capture is valuable (Cohen et al., 2010). Figure 3 shows electricity dispatch for each facility when there are two coal-fired facilities with venting-only flexible CO_2 capture (Figure 1). Hydroelectric and nuclear facilities operate continuously at maximum output. At this CO_2 price, coal-based capacity without CO_2 capture remains base load along with the *ngcc 1* facility. The *ocgt 1* facility is marginal except during demand troughs where *ngcc 2* is marginal. There is little use of energy storage at these conditions.

Both facilities with flexible CO_2 capture reduce CO_2 capture load when electricity demand is high to limit the use of the open-cycle gas turbine facility. When the open-cycle turbine is offline, dispatch is less expensive with the CO_2 capture system at full load.

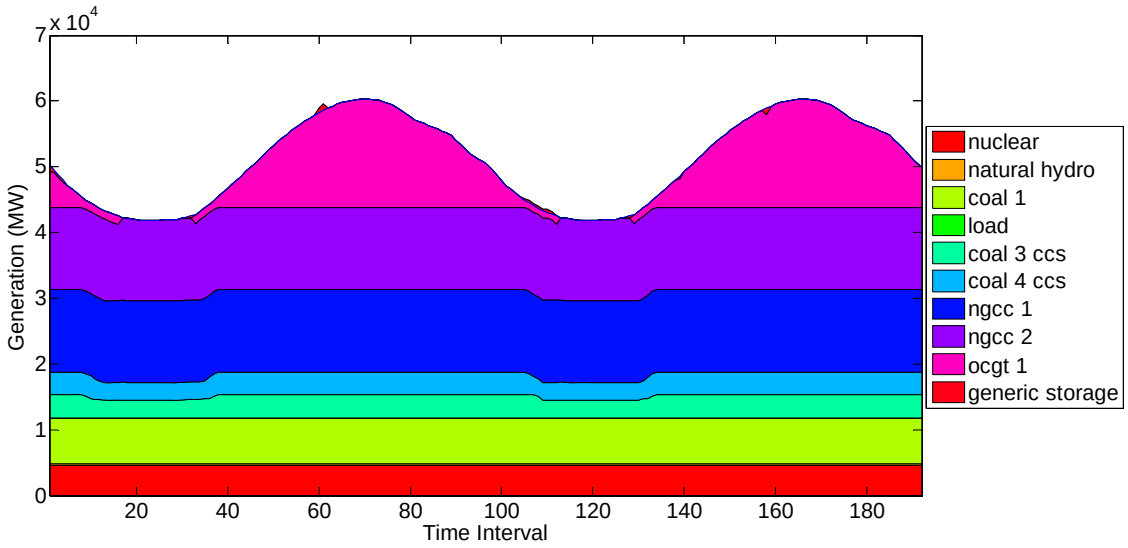

Figure 3: Real-time market electricity dispatch demonstrates flexible CO_2 capture systems being online at low demand but offline at high demand.[1]

Figure 4 plots responsive reserve service procurements from each facility. Most RRS is provided by interruptible load (limited to 50% of the total RRS requirement) and the open-cycle turbine when it is online. Energy storage systems also provide some RRS. However, during demand troughs, RRS is procured from flexible CO_2 capture facilities. RRS provision is possible because these facilities are operating CO_2 capture at full load, giving them the option to reduce CO_2 capture load if additional electricity supply is needed. Without flexible CO_2 capture, these facilities would not be able to supply RRS without withholding power output capacity.

[1] Note: In all area plots, colors in the figure are stacked in the opposite order of the colors in the legend.

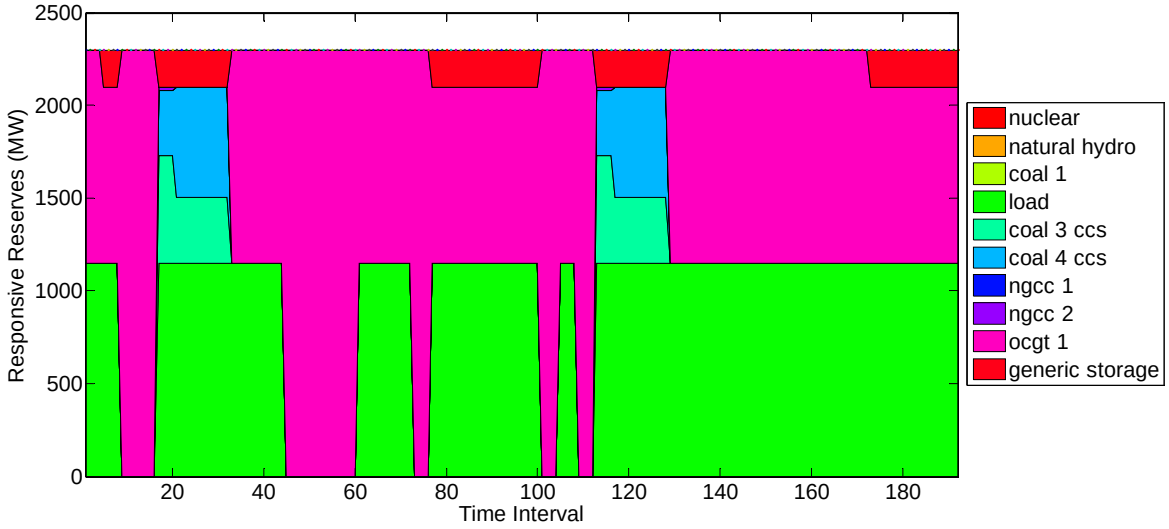

Figure 4: Responsive reserve service requirements are primarily met by interruptible load and the marginal open-cycle gas turbine, but they are also partially satisfied by energy storage and facilities with flexible CO_2 capture.

Figure 5 demonstrates the full impact of flexible CO_2 capture on AS offer capability. This figure plots gross and net power output along with CO_2 capture load, responsive reserve procurement, and regulation down procurement from the *coal 3 ccs* facility in the first 12 hours (48 intervals) of the demand data. This time period encompasses one of the electricity demand troughs where CO_2 capture systems are turned on. An inflexible CO_2 capture facility would require the fractional load on power and CO_2 capture systems to be equal, so the only opportunity for AS provision would be a regulation down offer if the facility is willing to reduce load on power systems to keep capacity available for RD. However, flexible CO_2 capture allows the facility to offer both regulation down and responsive reserve while maintaining constant load on power systems. When CO_2 capture load is low, the facility can offer regulation down because it has the ability to increase CO_2 capture load and reduce net output. When CO_2 capture load is high, the facility can offer responsive reserve (as well as regulation up and non-spinning reserve) because the facility has the ability to reduce CO_2 capture load and increase net power output. These results are a proof-of-concept that there are market conditions where flexible CO_2 capture improves the ability to offer into AS markets; however, future research must examine the range of conditions where this situation is true.

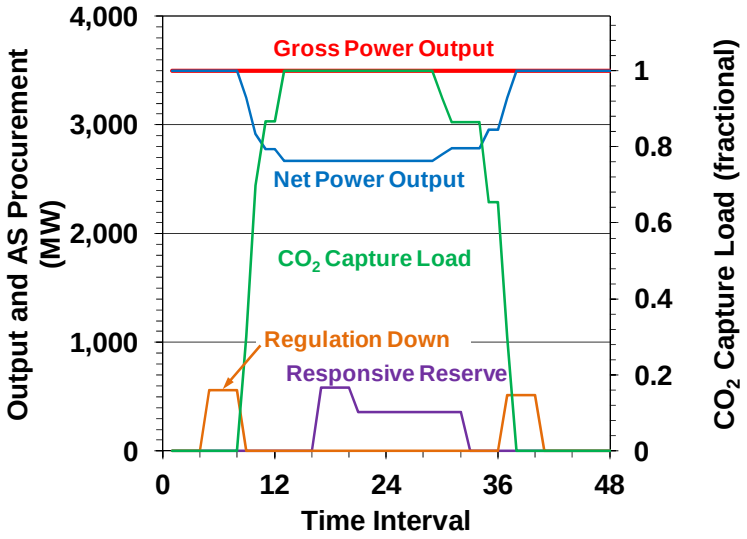

Figure 5: Electrical output and AS procurements from the *coal 3 ccs* facility demonstrate that, depending on electricity market conditions, flexible CO_2 capture could be used for both up- and down-ramping ancillary services.

In initial testing with solvent storage, the model appeared to function properly, but solvent storage systems were not utilized. Results were essentially identical to those with venting-only flexible CO_2 capture. Additional testing will examine a wider range of market conditions to determine if there is a problem with model functionality or if utilizing storage is simply not optimal at these market conditions.

Computational Efficiency and Functionality with 42 and 144 Plants

One objective with the grid-level model is to use the finest plant- or unit-level resolution with reasonable computation time, so testing has been conducted on successively less aggregated data sets. Table 4 contains the computation time with 10-, 42-, and 144-facility data sets when optimized over the two-day test period; each row contains results for one of the four CO_2 capture scenarios. For the 42- and 144-plant data sets, 8 of the 14 coal-fired facilities are considered with CO_2 capture (54% of the total coal-based capacity), and there are no interruptible load or energy storage facilities. All studies assume \$1.54/MMBTU coal, \$4/MMBTU natural gas, and \$35/tCO_2. The model was run on a 32-bit Dell Latitude D830 laptop with 2 GB RAM and a 2.40 GHz Intel Core 2 Duo processor. Computation times are expected to vary widely with market conditions and plant specifications, so the entries in Table 4 are meant primarily to confirm or deny the ability to run the model in a reasonable amount of time with a given number of facilities. The model will ultimately be run on high performance computers owned by the UT Mechanical Engineering department, which should have significantly shorter runtimes.

Computation time increases with the number of facilities being modeled, but times remain on the order of 5–15 minutes for the 144-plant data set, which is considered reasonable. The inflexible CO_2 capture case has the most solution difficulty, likely because constraining power and CO_2 capture systems to the same fractional load makes them difficult to operate in a least-cost manner. Generally, these results indicate that a plant- or unit-specific data set can be used without exorbitant computation times.

Table 4: Computation time (h:mm:ss.#) increases with the size of the input plant data set but remains reasonable in all cases.

Scenario	Computation time for 10-plant data set	Computation time for 42- plant data set	Computation time for 144-plant data set
No CO_2 capture	0:00:10.6	0:00:35.1	0:04:48.0
Inflexible CO_2 capture	0:00:15.6	0:09:42.6	0:16:34.0
Venting-only flexible capture	0:00:28.9	0:00:45.5	0:05:33.4
Flexible capture with solvent storage	0:00:22.5	0:00:49.5	0:05:10.6

Figures 6 and 7 display electrical output by plant type with the 42- and 144-plant data sets. Based on eGRID information, ERCOT has a very large amount of CHP capacity, so forcing these units to operate at maximum load has a significant effect on dispatch. CHP facilities along with nuclear, hydroelectric, and biomass-based generators supply a large portion of base-load demand. Since there is no CO_2 capture and a \$35/tCO_2 price, coal-fired facilities are marginal except at peak load, when gas-fired boiler units are needed to meet peak demand. Dispatch is qualitatively similar between both data sets, with slightly smoother data when 144 plants are used due to fewer abrupt output reductions at some facilities to satisfy minimum load constraints of others during startup or shutdown.

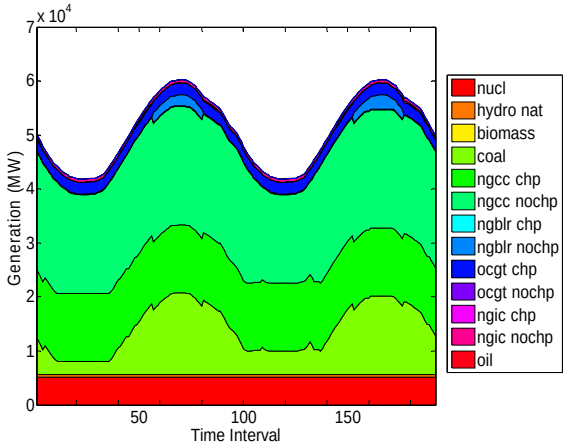

Figure 6: At \$35/tCO_2, electricity dispatch with 42 plants displays the large quantity of CHP generation and use of coal as marginal generation.

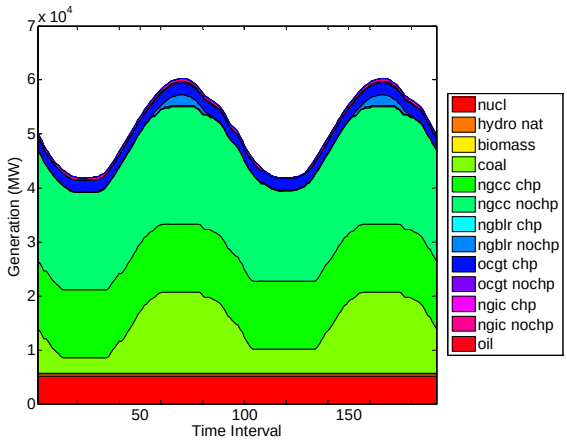

Figure 7: Dispatch patterns are similar with the greater plant-level resolution of the 144-plant data set.

Figures 8 and 9 display regulation up procurements by plant type for each data set, and results are qualitatively similar. Regulation up is provided by marginal or near-marginal facilities, which are coal, combined-cycle gas, open-cycle gas, or gas-based boilers, depending on the time. For the 144-plant data set, there are also some periods where gas-fired internal combustion

engines provide some RU service. RU is grossly over-procured during peak demand periods in order to satisfy minimum load constraints on open-cycle gas turbines and gas-fired boilers.

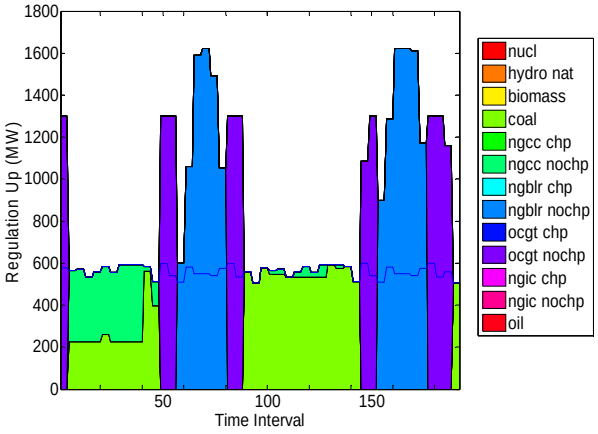

Figure 8: With 42 plants, regulation up is over-procured due to minimum load constraints on gas-based facilities that must be turned on to meet peak demand.

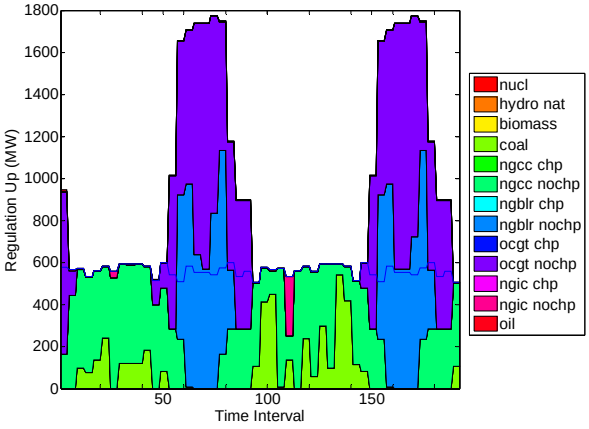

Figure 9: With 144 plants, there is similar over-procurement of regulation up from marginal gas-fired facilities.

Figures 10 and 11 display the corresponding responsive reserve procurements by plant type. RRS is also supplied by marginal or near-marginal facilities. In contrast to RU, RRS is grossly under-procured during peak demand times. This occurs because the model allows higher value services to be procured for lower value services, so the over-procurement of RU shown in Figures 8 and 9 is used to meet RRS requirements.

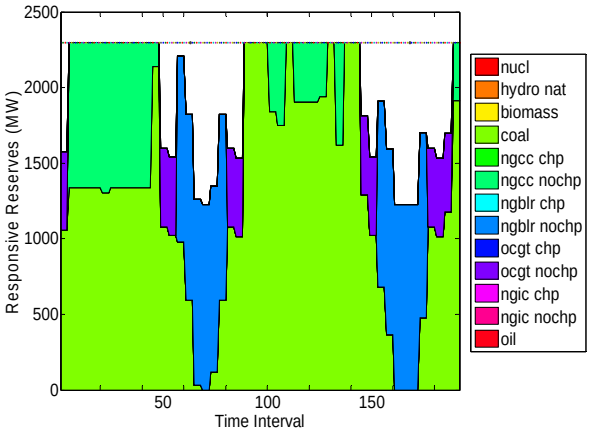

Figure 10: With 42 plants, over-procured regulation up allows under-procurement of responsive reserves.

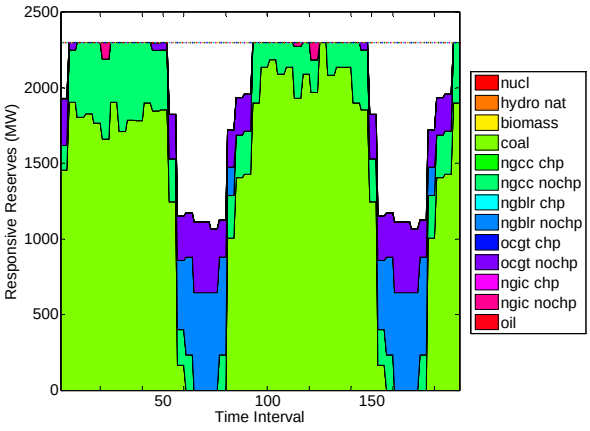

Figure 11: With 144 plants, responsive reserve is again under-procured due to regulation up over-procurement.

Figures 12 and 13 plot shadow prices of electricity in the real-time market alongside net load. Most often, electricity price equals the marginal generating costs of the most expensive facility

required to meet demand, so prices generally trend with electricity demand. Prices can also be influenced by startup costs in time periods where a unit turns on. With 42 plants, there are three instances where prices spike to the $3,000/MWh offer cap when online units cannot ramp fast enough to meet the change in net load. There are more frequent price spikes at peak load with 144 facilities, but greater plant-level resolution allows for enough online units to avoid a supply-demand imbalance and the resulting high cost penalty.

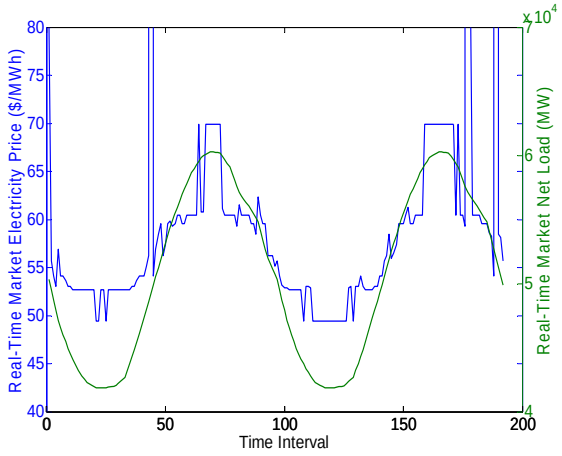

Figure 12: With 42 plants, electricity prices follow marginal unit costs except for price spikes when ramping capability is insufficient.

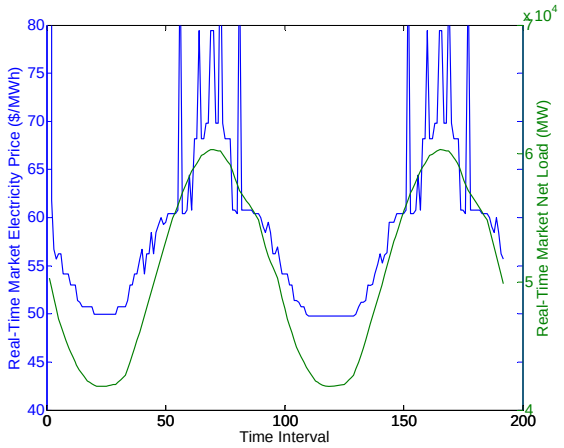

Figure 13: Electricity price patterns are similar with 144 facilities, but greater plant-level resolution eliminates most of the extreme price spikes.

Conclusions

The following conclusions can be drawn about the grid-level dispatch model and model testing conducted this quarter.

- The grid-level dispatch model successfully demonstrates venting-only flexible CO_2 capture, but ensuring functionality of solvent storage systems requires further testing.
- Under appropriate market conditions, flexible CO_2 capture can reduce electricity dispatch costs and improve the ability of a facility to earn revenue from ancillary service procurements.
- The grid-level model functions properly and has reasonable computation time with up to 144 individually represented power generation facilities.
- Minimum load requirements on power systems can cause over-procurement of high-value AS such as regulation up and a corresponding under-procurement of lower-value AS such as responsive reserves.
- Despite relatively high plant-level resolution and generous ramp rates, electricity prices can still spike to the $3,000/MWh offer cap when online units cannot ramp up or down fast enough to respond to changes in demand.

Future Work

The unit-specific data set will be finalized, and the grid-level model will be tested to ensure proper functionality and reasonable computation time. Flexible capture systems with solvent storage will be explored at other market conditions to better understand its usefulness in an electricity system. After deciding on appropriate data for net load and AS requirements, the model will be used to explore the impact of flexible CO_2 capture on AS provision for a wide range of market conditions and CO_2 capture performance specifications.

The single-plant optimization model described in previous work will be used to study the sensitivity of results to market conditions such as fuel and electricity prices. The model will then be used for a detailed study of the solvent storage configuration that compares solvents and design operating points to test tradeoffs among solvent price, solvent capacity, and energy performance. Sensitivity to the capital cost of stripping and compression equipment will be explored, as well as the degree to which equipment is oversized for treating stored rich solvent.

Once analysis with the single-plant and grid-level models is complete, results from both models will be used to inform investment analysis using traditional net present value calculations and more rigorous approaches to decision making under uncertainty.

References

Chalmers H, Gibbins J. "Initial evaluation of the impact of post-combustion capture of carbon dioxide on supercritical pulverised coal power plant part load performance." *Fuel.* 2007;86:2109–2123.

Chalmers H, Lucquiaud M, Gibbins J, Leach M. "Flexible Operation of Coal Fired Power Plants with Postcombustion Capture of Carbon Dioxide." *J Environ Engin*. 2009.

Cohen SM, Rochelle GT, Webber ME. "Turning CO_2 Capture On & Off in Response to Electric Grid Demand: A Baseline Analysis of Emissions and Economics." *ASME J Energy Res Tech.* 2010;132:021003-1–8.

Cohen SM, Rochelle GT, Webber ME. "Optimal operation of flexible post-combustion CO_2 capture in response to volatile electricity prices." Presented at *GHGT-10*. Amsterdam, The Netherlands, 2010.

ERCOT. "2009 Annual Report." 2010a.

ERCOT. "Setting the Shadow Price Caps and Power Balance Penalties in Security Constrained Economic Dispatch." Taylor, TX, 2010b.

ERCOT. "ERCOT Methodologies for Determining Ancillary Service Requirements." 2011a.

ERCOT. *Generic_Database_Characteristics_REV_1.xls.* 2011b.

Rochelle GT, et al. "CO_2 Capture by Aqueous Absorption, Second Quarterly Progress Report 2009." Luminant Carbon Management Program. The University of Texas at Austin. 2009.

Rochelle GT, et al. "CO_2 Capture by Aqueous Absorption, Third Quarterly Progress Report 2010." Luminant Carbon Management Program. The University of Texas at Austin. 2010.

Rochelle GT, et al. "CO_2 Capture by Aqueous Absorption, Third Quarterly Progress Report 2011." Luminant Carbon Management Program. The University of Texas at Austin. 2011.

USEPA. Emissions & Generation Resource Integrated Database (eGRID). *eGRID2010_Version_1_1*. 2010.

Ziaii S, Cohen SM, Rochelle GT, Webber ME. "Dynamic operation of amine scrubbing in response to electricity demand and pricing." Presented at *GHGT-9*. Washington, DC. 2008.

Nitrosamine Formation in CO_2 Capture by Piperazine

Quarterly Report for October 1 – December 31, 2011

by Mandana Ashouripashaki

Supported by the Luminant Carbon Management Program

Department of Chemical Engineering

The University of Texas at Austin

January 31, 2012

Abstract

Nitrosamines are formed from the reaction between secondary amines and nitrite and they are thought to be carcinogenic. Piperazine (PZ) is an amine of interest in our study and nitrosation products of PZ are N-nitrosopiperazine (MNPZ) and N,N'-dinitrosopiperazine (DNPZ).

The available methods for detecting nitrosamines are not applicable for DNPZ because of its lack of volatility. Hence, a method has been developed for quantifying DNPZ using liquid chromatography followed by mass spectrometry (LC-MS). Results show that the amount of DNPZ produced is negligible, and as the temperature of the reaction increases, DNPZ will disappear.

A new method for quantifying MNPZ has been developed using HPLC with a standard reverse phase column using 5% to 50% acetonitrile in water buffered with ammonium carbonate. A calibration curve has been established for MNPZ.

Kinetic study of the reaction between nitrite and PZ has been performed from of 20 to 150 °C. Nitrite consumption is modeled as a first order reaction in nitrite. MNPZ is produced at temperature greater than 75 ^{o}C and then decomposes at 100 to 150 ^{o}C.

Methods and Experiments

This research developed a method to quantify mononitrosopiperazine (MNPZ) and N,N'-dinitrosopiperazine (DNPZ) using a combination of mass spectrometry and/or HPLC in non-biological conditions. The kinetics of nitrosamine formation and decomposition was measured at conditions of CO_2 capture using aqueous piperazine (PZ).

DNPZ was synthesized by USP method 24 (USP, 2000) from piperazine citrate and from PZ, and then a quantitative comparison has been done on the DNPZ production efficiency.

The USP 24 procedure uses nitrosation under acidic conditions. Attempts were also made to prepare DNPZ in the presence of formaldehyde because studies showed that formaldehyde can catalyze the nitrosation under alkaline conditions (Keefer and Roller, 1973; Kunisaiki and Hayashi, 1978). Experiments have been conducted over the range of CO_2 capture absorber temperature.

Experimental Methods

Standard sample of Dinitrosopiperazine

The fundamental procedure for both experiments in acidic and alkaline conditions is the same and follows USP 24.

1. Nitrosation reaction in the presence of hydrochloric acid

The USP 24 method consists of the following steps:

1. Make a solution of 2 g PZ citrate and 50 ml hydrochloric acid 3N and filter it.
2. Add 10 ml of sodium nitrite solution (1 part sodium nitrite and 2 parts water).
3. Chill the solution in an ice bath for 15 minutes while stirring.
4. Filter solution to separate precipitate.
5. Wash filtrate with cold water.
6. Dry the product (N,N'-dinitrosopiperazine).

The above steps were followed and, after drying the filtrate, yellow pale crystals of DNPZ were obtained. During the reaction a significant amount of brown gas was released, which is nitrogen dioxide.

DNPZ was synthesized over a range of pH. Results are shown Tables 1 and 2 and Figure 1.

To see the difference between nitrosation yield of PZ citrate and PZ, the experiments were done with PZ as well.

Table 1 shows the conditions of reaction between PZ citrate and sodium nitrite ($NaNO_3$) in the presence of HCl. At low pH, amine will be protonated and NO^-, which is a nitrosating regent, will be released. The nitrite ion reacts with the PZ ion and makes MNPZ and DNPZ. Experiments show a greater yield of DNPZ at pH 2 and 3 than at other pH values. This pH range is almost the same for reactions which use PZ instead of PZ citrate (2.11–3.11).

PZ citrate (2 g) + $NaNO_2$ (10 ml) + HCl → DNPZ + C

Table 1: The effect of HCl on DNPZ yield by USP 24 method

Piperazine citrate (g)	Sodium nitrite (1 to 2) (ml)	Hydrochloric acid (3N) (ml)	pH of the Solution	N,N'-Dinitrosopiperazine (g)
2	10	0	8.20	0
2	10	10	4.00	1.06
2	10	20	2.98	1.72
2	10	30	2.40	1.10
2	10	40	2.00	1.21
2	10	50	1.76	0.90
2	10	60	1.57	0.88
2	10	70	1.40	0.60

Table 2: The effect of HCl on DNPZ production using PZ in USP 24 method

Piperazine (g)	Sodium nitrite (1 to 2) (ml)	Hydrochloric acid (3N) (ml)	pH of the Solution	N,N'-Dinitrosopiperazine (g)
2	10	0	6.90	0
2	10	10	4.21	1.09
2	10	20	3.11	3.73
2	10	30	2.50	2.77
2	10	40	2.11	3.3
2	10	50	1.83	3.1
2	10	60	1.62	3.00
2	10	70	1.45	2.49

Figure 1 shows a comparison between DNPZ formation when PZ citrate and PZ have been used in the presence of different quantities of HCl, at different pH values. These observations have been demonstrated before for some secondary amines and amino acids, (Mirvish, 1972, 1975; Zeibarth, 1975; Lijinsky and Keefer, 1970; Bonnett and Nicolaidou, 1977), and this research shows the same behavior for both PZ and PZ citrate nitrosation. DNPZ that has been synthesized at a pH of 1.76 will be used as a standard to develop a preferred method for DNPZ detection in LC-MS.

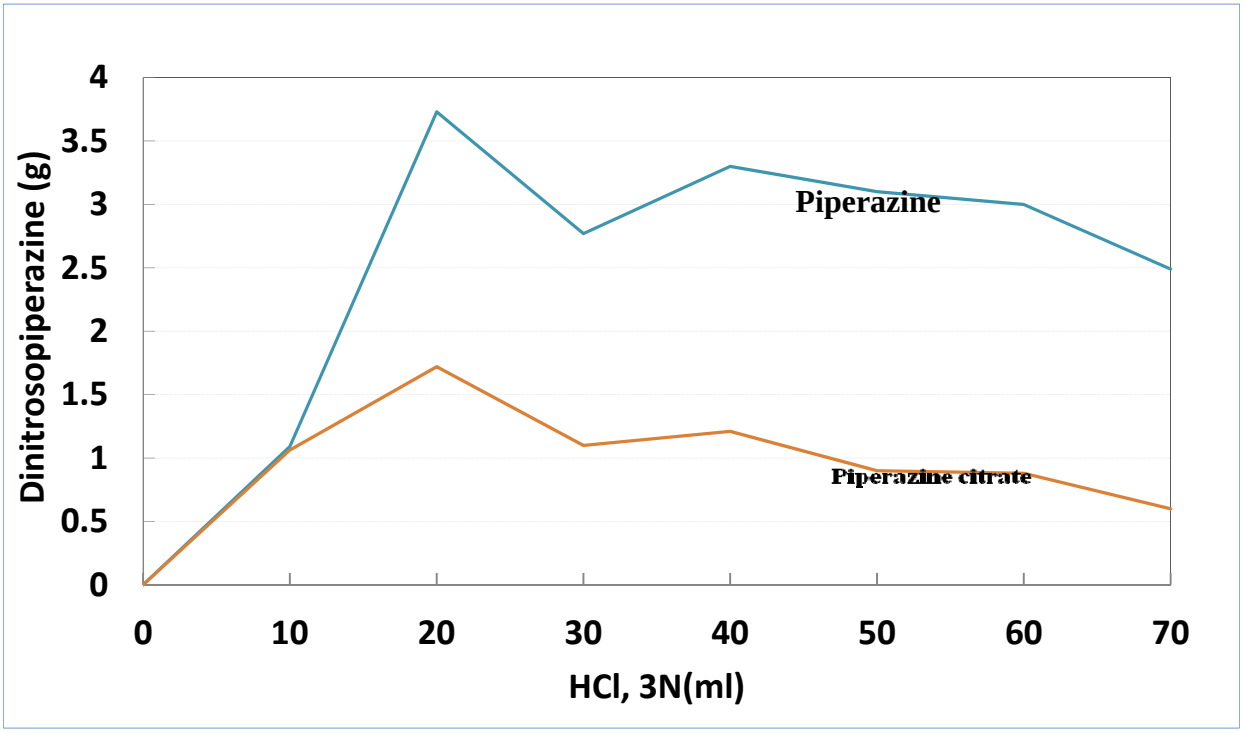

Figure 1: DNPZ production versus hydrochloric acid by the reaction between PZ citrate and PZ with sodium nitrite

2. Nitrosation reaction of piperazine citrate and in presence of formaldehyde

In an alkaline solution, there is no nitrosation reaction, so when experimental work was done with a mixture of PZ citrate and sodium nitrite with a pH of 8.2, there was no evidence of the production of DNPZ. When formaldehyde was added to the process, however, DNPZ precipitation was observed. Experiments have been performed using different concentrations of formaldehyde, and under the range of temperature conditions found in the absorber. Results are shown in Table 3 and Figure 2.

Table 3: The effect of formaldehyde on DNPZ production by the reaction between PZ citrate and sodium nitrite in the range of absorber temperatures

Piperazine citrate (g)	Sodium nitrite (1 to 2) (ml)	Formaldehyde (37%) (ml)	pH of the Solution	N,N'-Dinitrosopiperazine *(mole DNPZ/mole PZ)*			
				20 °C	40 °C	50 °C	60 °C
2	10	0	8.20	***0***	***0***	***0***	***0***
2	10	1	6.18	***0.56***	***0.59***	***0.45***	***0.4***
2	10	2	5.91	***0.76***	***0.77***	***0.62***	***0.52***
2	10	3	5.69	***0.57***	***0.53***	***0.44***	***0.42***
2	10	5	5.33	***0.93***	***0.66***	***0.52***	***0.49***
2	10	10	4.75	***0***	***0***	***0***	***0***
2	10	15	4.40	***0.56***	***0.59***	***0.45***	***0.4***
2	10	20	***4.0***	***0.0***	***0.0***	***0.47***	***0.0***

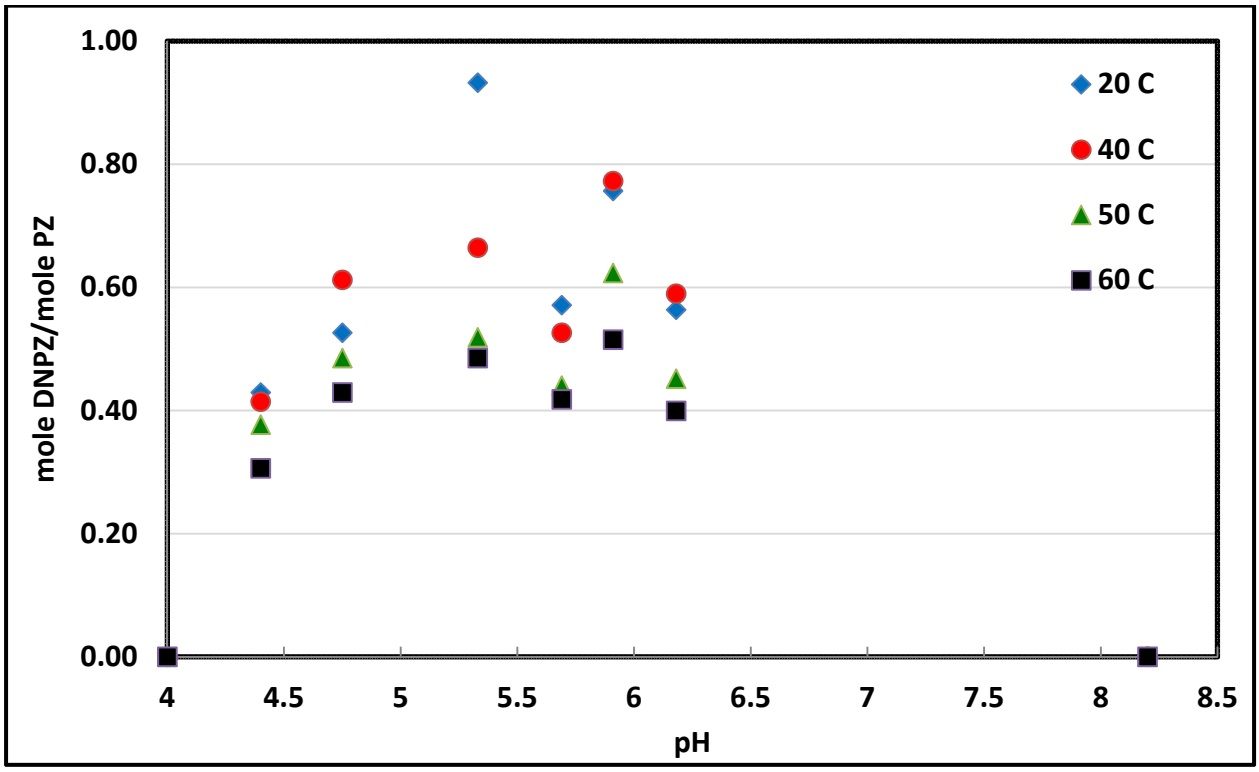

Figure 2: Nitrosation reaction of PZ citrate according to formaldehyde concentration in absorber temperature range

Previous research shows that there is no evidence of PZ citrate nitrosation at a pH greater than 4. This new result shows that formaldehyde has a catalytic effect on the reaction and nitrosation does occur at a pH greater than 4.

Figure 2 shows a comparison between nitrosation reaction products when PZ citrate has been used in the presence of different quantities of formaldehyde (different pH).

The temperature effect on nitrosation reaction has been investigated and the result has been demonstrated in Figure 2. At low temperature (20 °C) the reaction efficiency is greater than at other temperatures, and when the temperature increases the efficiency of the nitrosation reaction decreases. It was also observed that at higher temperatures more time is required for starting the reaction.

3. Nitrosation reaction of piperazine in the presence of formaldehyde

A solution of 2 g PZ and 10 ml sodium nitrite (1/2 V) was prepared with a measured pH of 10.45. Under the defined conditions there was no evidence of any reaction between these reagents, but adding formaldehyde and changing the pH initiated a nitrosation reaction. Experiments have been conducted with different concentrations of formaldehyde and at various pH levels in the temperature range of 20–98 °C; results are shown in Table 4 and Figure 3. These reactions have been investigated because there is some evidence of aldehyde in amine degradation products, and aldehyde can be an intermediate product of the reaction between CO_2 and monoethanolamine (MEA).

Table 4 shows conditions of reaction between PZ and sodium nitrite ($NaNO_2$) in the presence of formaldehyde. As noted in the introduction, nitrosation at alkaline conditions is unlikely, but catalysts such as formaldehyde can accelerate the nitrosating reaction.

Reactions at high pH have been started by PZ citrate and sodium nitrite and, as expected, there is no evidence of DNPZ. Adding formaldehyde and decreasing the pH, however, causes DNPZ to appear in reaction (precipitation). Figure 3 shows the effect of increasing the formaldehyde value in reactions, and using different temperatures in the range of absorber temperature.

PZ (2 g) + $NaNO_2$ (10 ml) + Formaldehyde → DNPZ + Other products

Nitrosation of PZ did not occur at a pH greater than 8, an alkaline environment, but the new results show that at a high pH and in very strong basic medium, formaldehyde can catalyze a nitrosation reaction of PZ.

Figure 3 shows a comparison between nitrosation reaction products when PZ has been used in the presence of different quantities of formaldehyde (different pH). These observations have been demonstrated before for some secondary amines and amino acids (Mirvish, 1970, 1975; Lijinsky and Keefer, 1970), and this research shows the same behavior for PZ nitrosation.

The temperature effect on nitrosation reaction has been investigated and the results are shown in Figure 2. At low temperature (20 °C) the reaction efficiency is greater than at other temperatures and increasing the temperature decreases the efficiency of the nitrosation reaction. It is also observed that at a higher temperature it takes longer for the reaction to start.

Table 4: The effect of formaldehyde concentration on nitrosation reaction between PZ and sodium nitrite at different temperatures

Piperazine (g)	Sodium nitrite (1 to 2) (ml)	Formaldehyde (37%) (ml)	pH of the Solution	Nitrosation reaction products (g)				
				20 °C	40 °C	60 °C	80 °C	98 °C
2	10	0	10.45	***0***	***0***	***0***	***0***	***0***
2	10	1	10.21	***0.6***	***0.81***	***0.64***	***0.6***	***0.62***
2	10	2	10.17	***0.9***	***0.94***	***0.94***	***0.94***	***0.94***
2	10	3	10.06	***0.7***	***0.68***	***0.81***	***0.62***	***0.77***
2	10	4	9.98	***0.7***	***0.62***	***0.56***	***0.43***	***0.85***
2	10	5	9.65	***0.8***	***0.72***	***0.62***	***0.31***	***0.53***
2	10	6	9.51	***0.7***	***0.6***	***0.36***	***0.34***	***0.25***
2	10	7	9.33	***0.5***	***0.58***	***0.47***	***0.24***	***0.28***
2	10	8	9.12	***0.6***	***0.36***	***0.45***	***0.39***	***0.25***
2	10	10	8.96	***0.6***	***0.31***	***0.23***	***0.26***	***0.21***
2	10	12	8.8	***0.5***	***0.35***	***0.25***	***0.17***	***0.12***
2	10	15	8.71	***0.4***	***0.21***	***0.13***	***0.13***	***0.12***
2	10	20	8.55	***0.3***	***0.21***	***0.11***	***0.08***	***0.05***
2	10	30	8.00	***0.0***	***0.0***	***0.0***	***0.0***	***0.0***

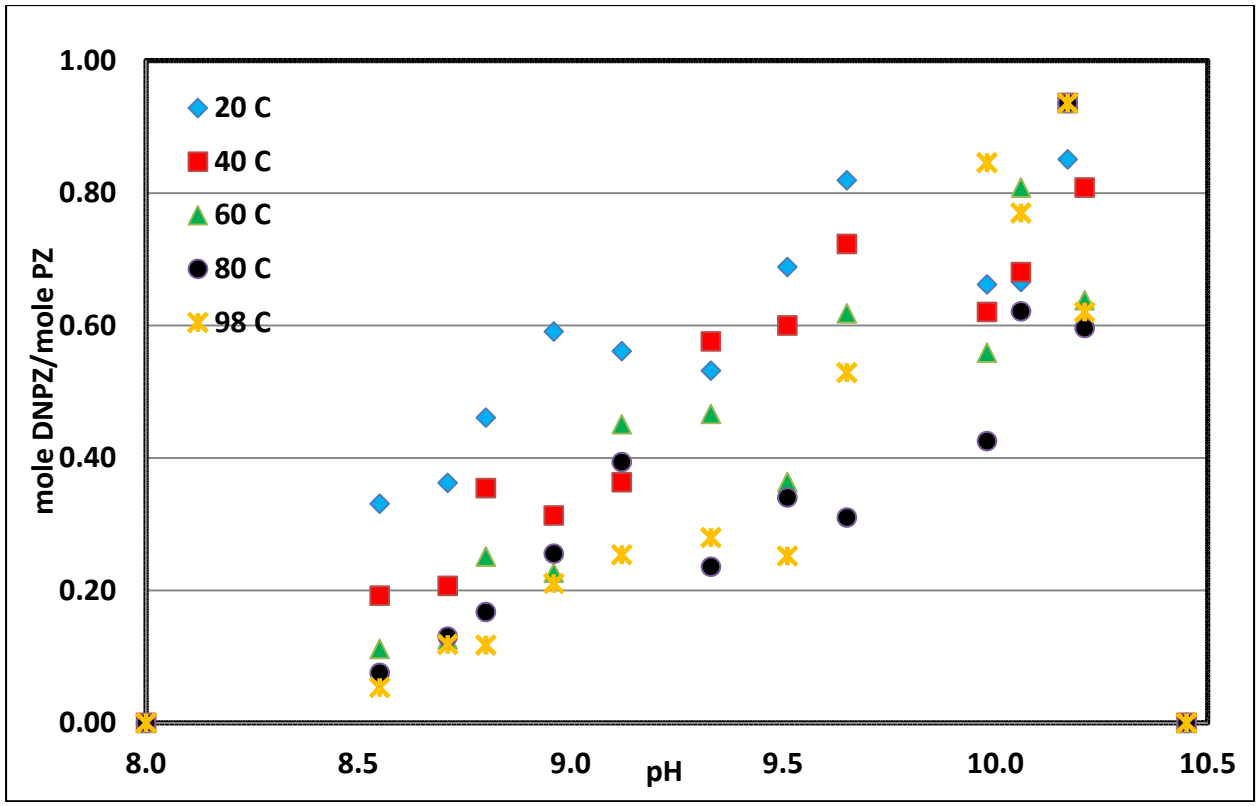

Figure 3: Nitrosation reaction of PZ in different concentrations of formaldehyde as indicated by pH

4. Quantifying MNPZ by HPLC

Detection method has been applied to standard solutions of MNPZ using HPLC. To perform a calibration curve for measuring MNPZ the best method is to use standard reverse phase 5% Acetonitrile 20% Acetonitrile in water buffered with ammonium carbonate to detecting standard MNPZ solution of methanol with a dilution factor of 20. Figure 4 shows the calibration curve of MNPZ.

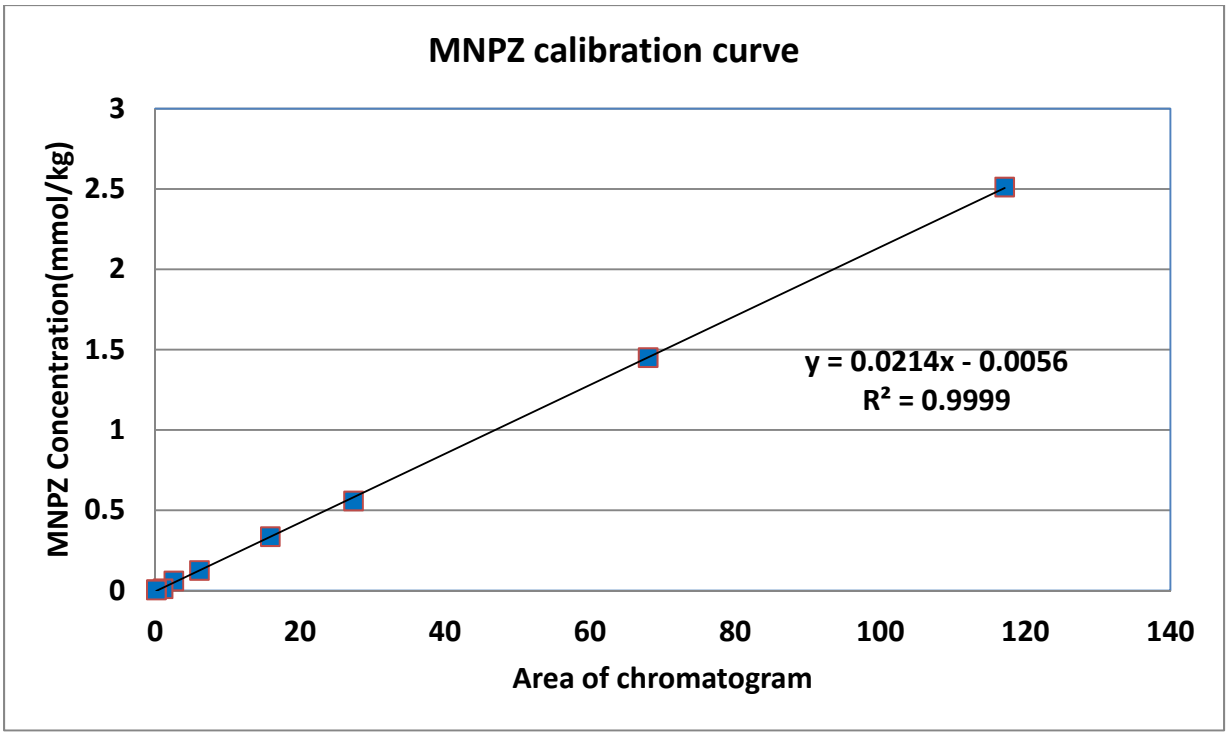

Figure 4: Calibration curve for standard MNPZ, with a detection limit of $4x10^{-4}$ mmol/kg

A planned kinetic study of nitrosation will focus on MNPZ detection rather than DNPZ because previous studies showed that DNPZ will be produced at low temperature while CO_2 capture plants operate at a minimum temperature of 40 °C. Further, formation of DNPZ follows the formation of MNPZ so if the process does not make any MNPZ it will not produce DNPZ either.

5. PZ Nitrosation

5-1. Effect of Nitrite concentration

The loss of nitrite in 8 molal loaded PZ was measured with three starting concentrations of sodium nitrite, 5, 20, and 50 mmolal. Eight samples were taken over 7 days and analyzed by IC to monitor the concentration of nitrite. Results show that lower concentrations of nitrite react more slowly with 8 m loaded PZ (Figure 5), and nitrite loss is pseudo linear. Therefore a concentration of 50 mmolal of nitrite was chosen for later experiments.

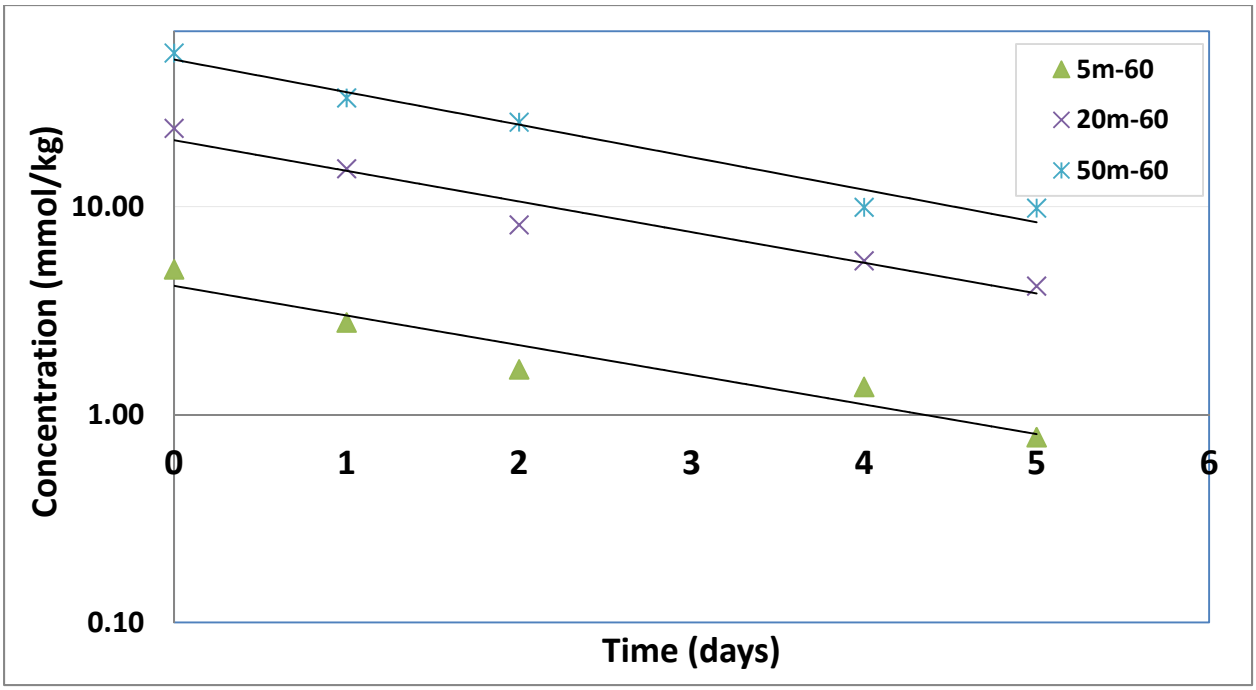

Figure 5: Nitrite concentration change in the reaction at 60 ^{o}C and different initial nitrite concentration.

5-2. Effect of Temperature

Additional experiments were carried out to determine the activation energy of reaction, using 8 m loaded PZ and 50 mmolal of $NaNO_2$ at three different temperatures, 21, 60, and 75 °C for 6 days. Results show that at 75 °C, nitrite concentration decreases faster than at the other two temperatures (Figure 6).

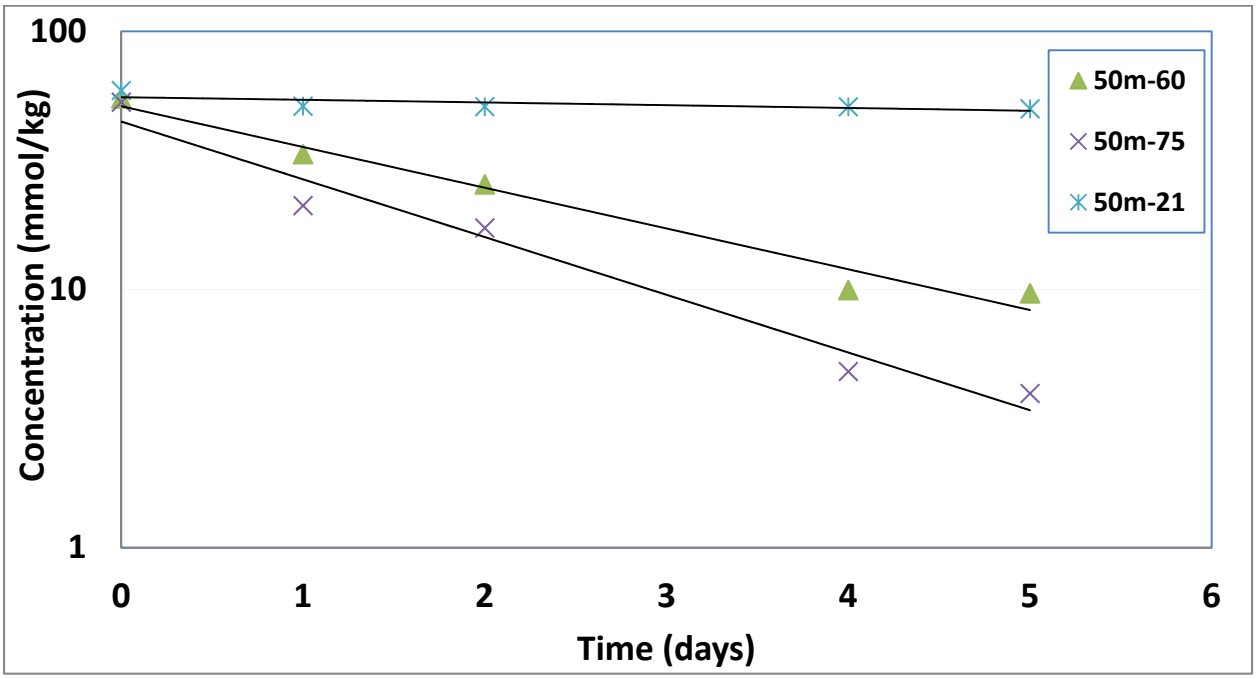

Figure 6: Nitrite concentration changes in different temperature at 5 days reaction time

5-3. Effect of PZ concentration

To assess the effect of PZ concentration on nitrite loss, instead of 8 m loaded PZ, the nitrite reaction of 2 m loaded PZ and 50 mmolal of nitrite at 60 °C was examined. Results show that a lower concentration of PZ causes lower nitrite consumption (Figure 7), but reaction to the PZ concentration is first order (Figure 7).

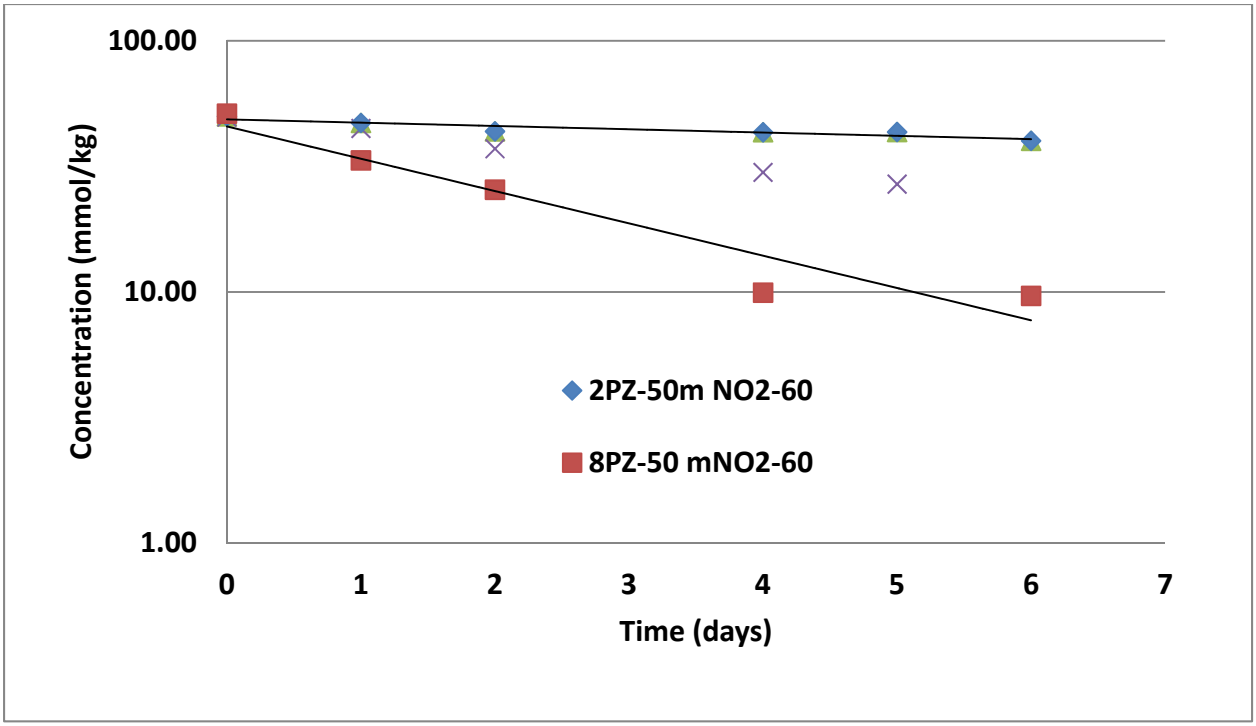

Figure 7: Nitrite concentration changes in different PZ concentrations at 6 days reaction time

5-4. Effect of pH

Unloaded PZ reacts very slowly with nitrite compared to loaded PZ. H_2SO_4 was used to adjust the pH of the solution in order to confirm the effect of loading. Sulfuric acid was shown to catalyze the reaction but to a lesser degree than CO_2 in loaded PZ (Figure 8).

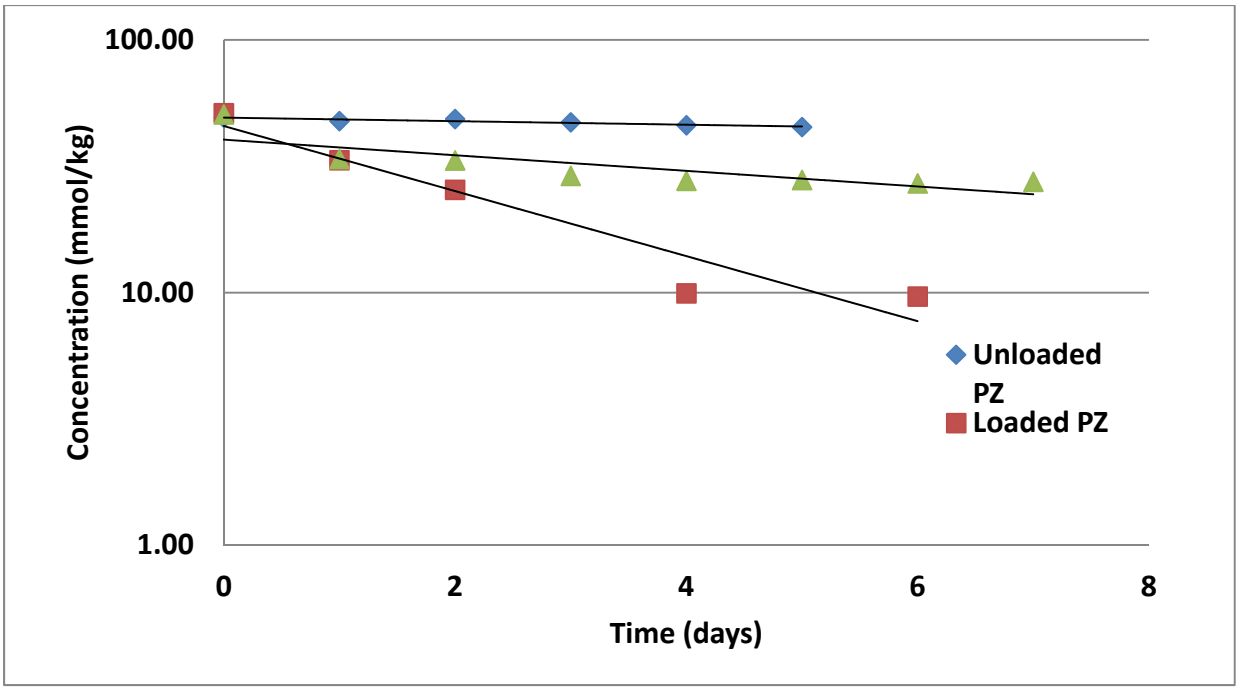

Figure 8: Effect of Acidity (pH) on nitrite consumption during the reaction with 8 m PZ

5-5. Effect of Formaldehyde

Since formaldehyde is known as a catalyst for nitrosation in alkaline solution, nitrite loss in 8 m loaded PZ in the presence of 50 mmol/kg formaldehyde has been studied. Formaldehyde increases the rate of reaction slightly, with more nitrite consumption after the same period compared to the reaction without formaldehyde (Figure 9).

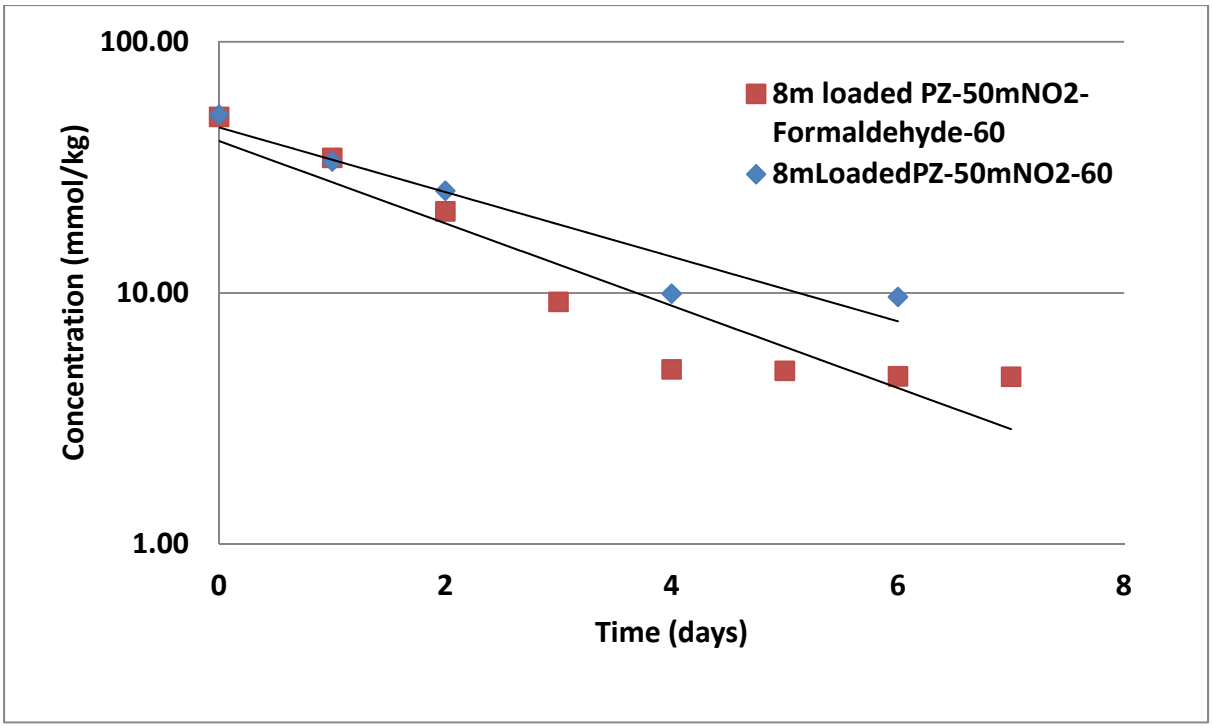

Figure 9: Effect of formaldehyde on nitrite consumption during the reaction with 8 m PZ

6. Kinetics of nitrite reaction with loaded piperazine

The results for the disappearance of nitrite suggest that nitrite reacts with PZ by a first order reaction in both total PZ and total nitrite:

$$\text{Rate (mol/day-kg}_{\text{solution}}) = k_2 [PZ]_T[NO_2^-]$$

where the concentrations are given in mol/kg$_{\text{solution}}$.

In a given experiment, the total piperazine $[PZ]_T$ is assumed to be constant and the loss of nitrite follows first order behavior, so the rate constant, k_2, is determined from the fit of data given by:

$$Ln[NO_2^-] = Ln\,[NO_2^-]_0 - bt$$

or

$$Ln[NO_2^-] = Ln\,[NO_2^-]_0 - k_2[PZ]_T t$$

where $k_2 = b/[PZ]_T$

The rate constant, k_2, is further correlated as a function of temperature using the Arrhenius expression:

$$k_2 = (k_2)_{ref}\, e^{(-E/RT)}$$

$$Ln(k_2) = \ln(k_2)_{60°C} + (E/R)(1/T - 1/333)$$

Figure 10 shows that all three reactions (at 21, 60, and 75 °C) follow a linear path on a log/linear plot so the slope of each line is the first order reaction rate constant at each temperature (K_r). The reaction activation energy is obtained from the slope of $\ln(k_2)$ versus reciprocal temperature as in Figure 10.

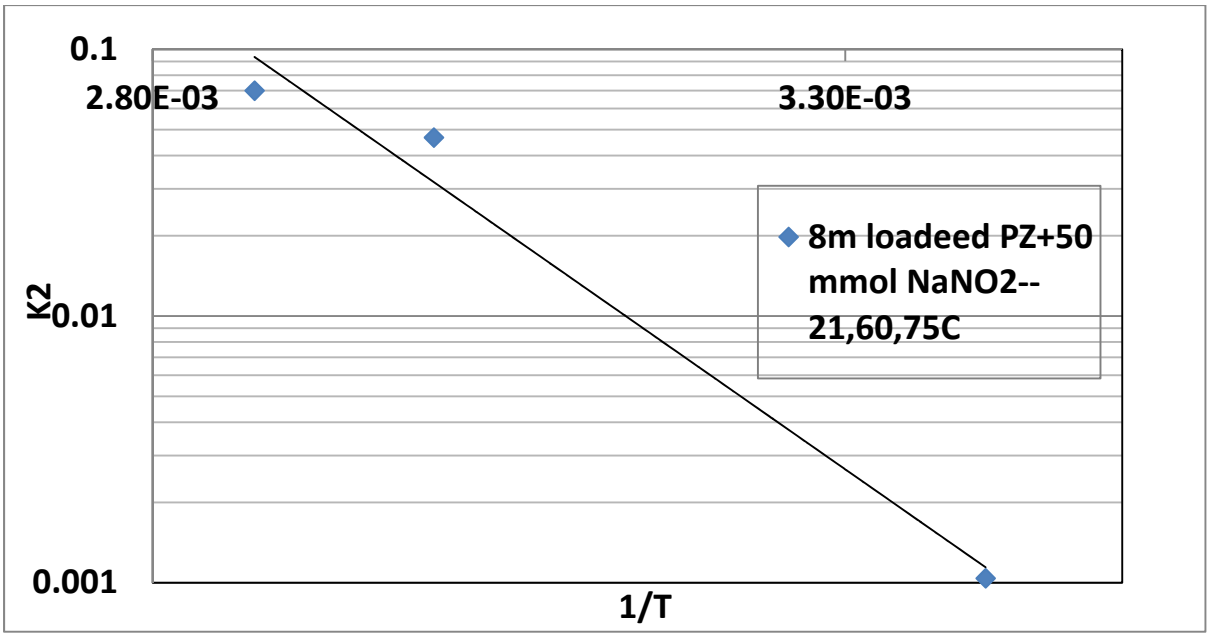

Figure 10: Natural log of reaction rate constant in terms of 1/T to calculate the activation energy of reaction

$k_{2(60\ ^\circ C)} = 0.0463$

R = 8.314 J/K.mole

Ea/R = 8346

Ea = 69.4 Kj/mole

Based on previous results and calculations, the following equation represents a general reaction rate of loaded PZ and nitrite:

$$R = k_2[PZ]_T[NO_2^-]$$

From this, the equation for calculating the reaction rate constant for PZ and nitrite will be as follows:

$$Ln\ (k_2) = 0.0463+(8346)(1/T-1/333)$$

Formaldehyde is a well-known catalyst in nitrosation reactions, but results show that the reaction rate of 8 m loaded PZ and 50 mmol/kg nitrite in the presence of formaldehyde is slightly higher than without catalyst. Loaded PZ is more reactive with nitrite, which might be related to the acidic behavior of CO_2 and water in solution, but results of the reaction of unloaded 8 m PZ and 50 mmol $NaNO_2$ when we adjust the pH of reaction to the pH of loaded solution by H_2SO_4 show that pH is not the acceleration factor for loaded PZ reaction and this might be because of producing piperazine carbamate which react with nitrite ion faster and easier. Figure 11 summarizes all the results for the reaction between PZ and nitrite.

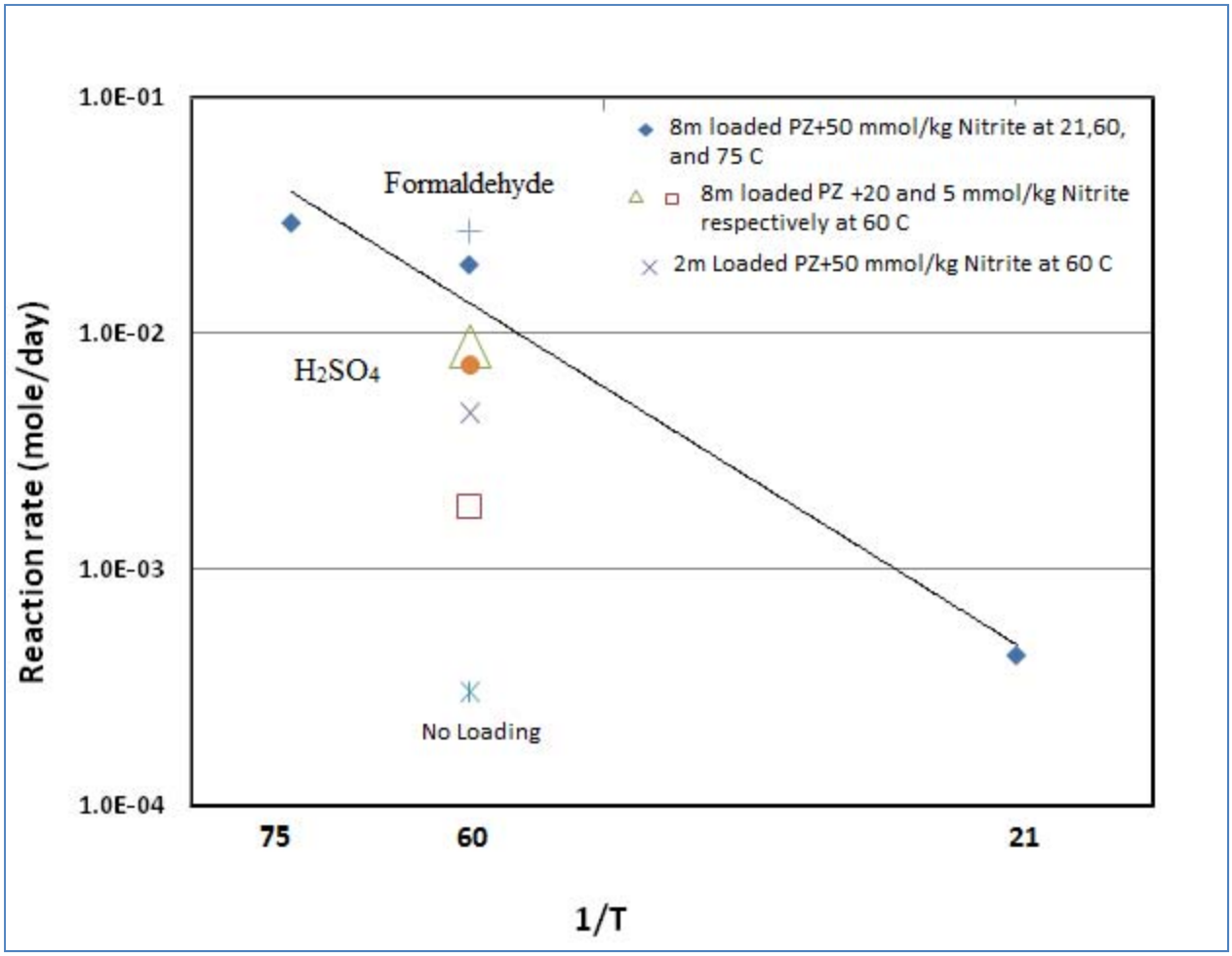

Figure 11: Reaction rate of PZ and nitrite under different conditions with respect to temperature (1/T)

Average DNPZ production in the above experiments was $4x10^{-4}$ mmol/kg (0.058 ppm) with 50 mmol/kg nitrite; therefore the nitrosation of loaded PZ under the experimental conditions does not lead to significant production of DNPZ.

In the presence of Stainless Steel metals (0.4 mM Fe^{2+}, 0.1 mM Ni^{+}, and 0.05 mM Cr^{+2}) the loss rate of nitrite is a first order function of nitrite somewhat lower than without the metals.

Reaction of NO_2 and nitrite with loaded piperazine at the presence of gas

In the process of absorbing CO_2 by amine solution, flue gas, which contains mainly air and CO_2 with small amounts of NO_2 and other gasses, contacts the amine solution. Three experiments were conducted to simulate this process using about 350 ml 8 m loaded PZ in contact with:

- Low gas flow (100 ml/min) containing 97% O_2, 2% CO_2, and 1% NO_2 for 2 weeks;
- High gas flow (7 l/min) containing 97% O_2, 2% CO_2, and 1% NO_2 for 5 days;
- Low gas flow (100 ml/min) containing 98% O_2, 2% CO_2, and 50 mmol $NaNO_2$ for 7 days.

In these continuous experiments the rate of nitrite loss is slight slower than when the process is done at batch conditions (Figure 12).

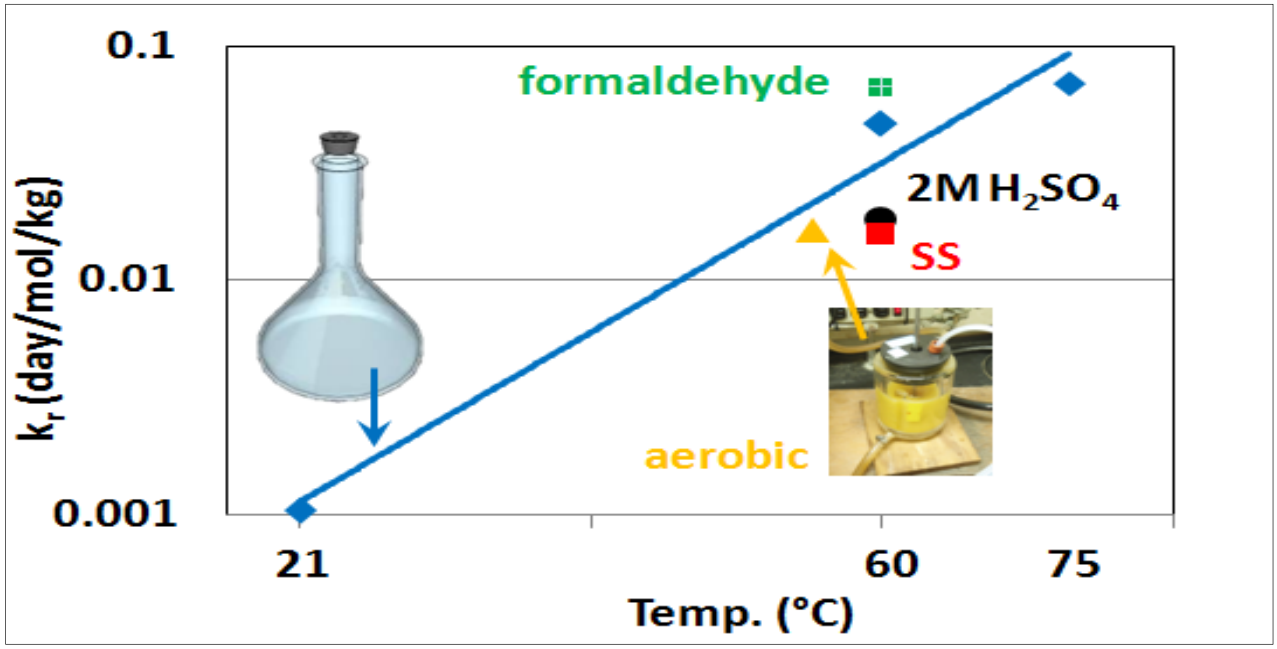

Figure 12: Nitrite disappearance rate in an aerated reactor from the reaction of 8 m PZ and 50 mmolal/kg nitrite at 55 C during 7 days. Line shows results without oxygen.

In the low gas flow experiment, the flow rate was 100 ml/min of gas containing 97% O_2, 2% CO_2, and 1% NO_2. 4.8 mmole of nitrite entered the reactor during the experiment and 3.2 mmole of total nitrite ion remained in the reactor at the end, which means that 1.6 mmole (33%) was lost either by reaction or by exiting with the gas.

The reaction of both low and high flow rate gas containing NO_2 shows an accumulation of nitrite in solution, but analysis shows that some of the entering nitrite reacted with the amine solution or exited the system in the low flow rate experiment (Figure 13). The yield of MNPZ is 1.3% of the concentration of nitrite.

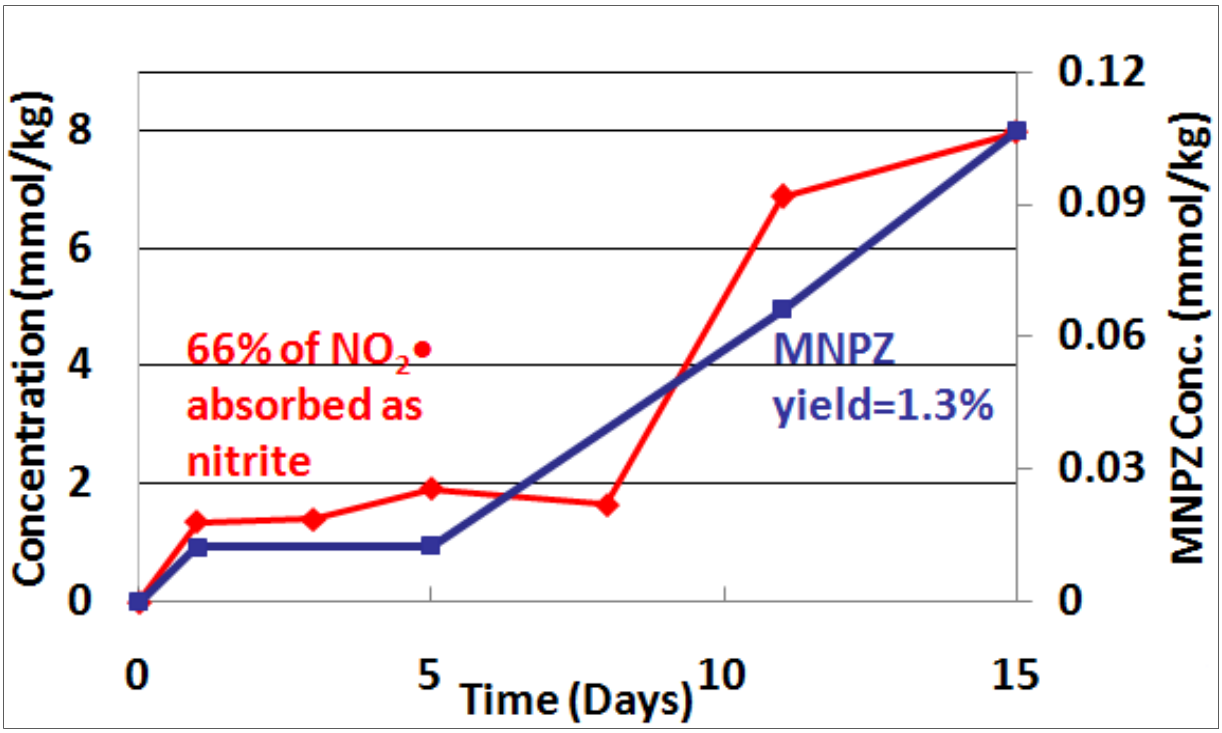

Figure 13: Nitrite accumulation and MNPZ production from the reaction of 8 m loaded PZ and 50 ppm NO_2 in a low gas flow experiment.

In the high gas flow experiment, the flow rate of gas is 7.7 l/min which contains 97% O_2, 2% CO_2, and 1% NO_2. 99 mmole of NO_2 entered the reactor during the experiment and 29.9 mmole of total nitrite ion remained at the end of experiment, which means that 70 mmol (80%) was lost either by reaction or leaving the reactor with exiting gas.

The rate of nitrite accumulation in the high gas flow experiment is considerably greater than with low gas flow. 20% of inlet NO_2 is absorbed as nitrite and there is a greater rate of nitrite accumulation in the system, but the yield of MNPZ is lower than with low gas flow (Figure 14).

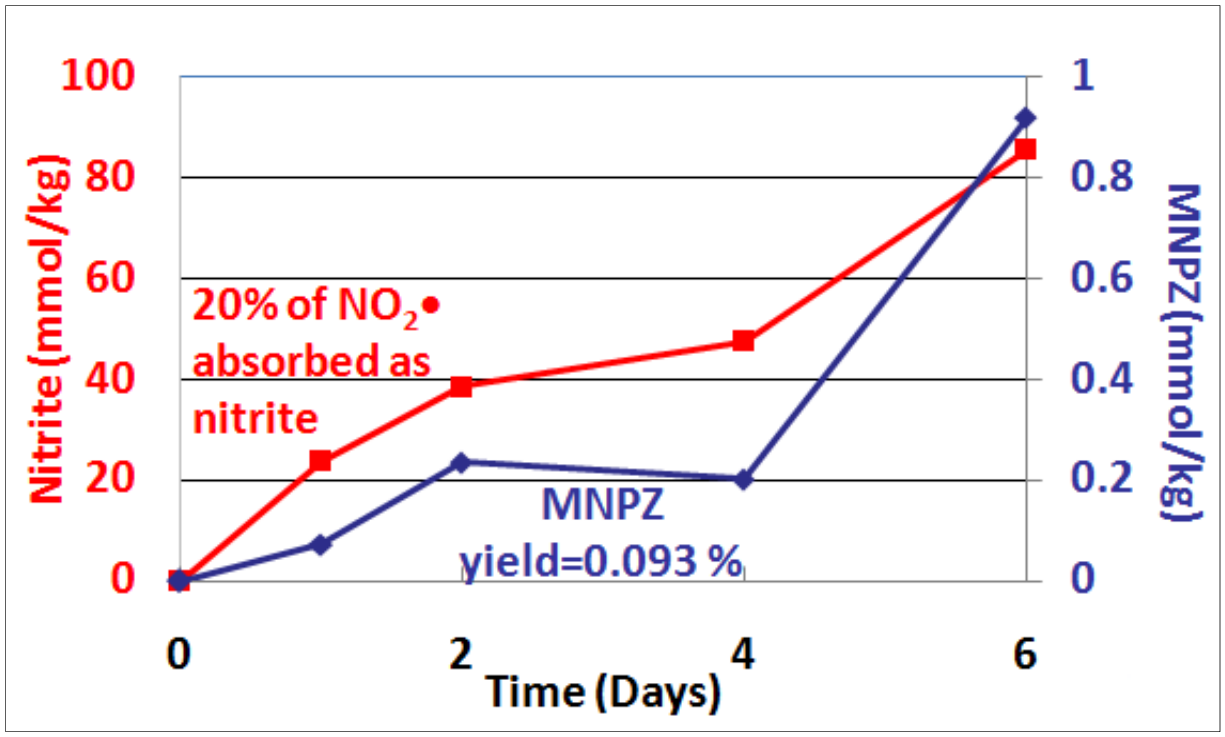

Figure 14: The reaction of 8 m loaded PZ and 50 ppm NO_2 in high gas flow experiment, In a semi-batch experiment with low gas flow rate of CO_2 and O_2, using 50 mmol/kg nitrite instead of NO_2, at 55 °C, as expected the rate of nitrite consumption follows first order reaction rate and the yield of MNPZ production is greater, at 6% (Figure 15).

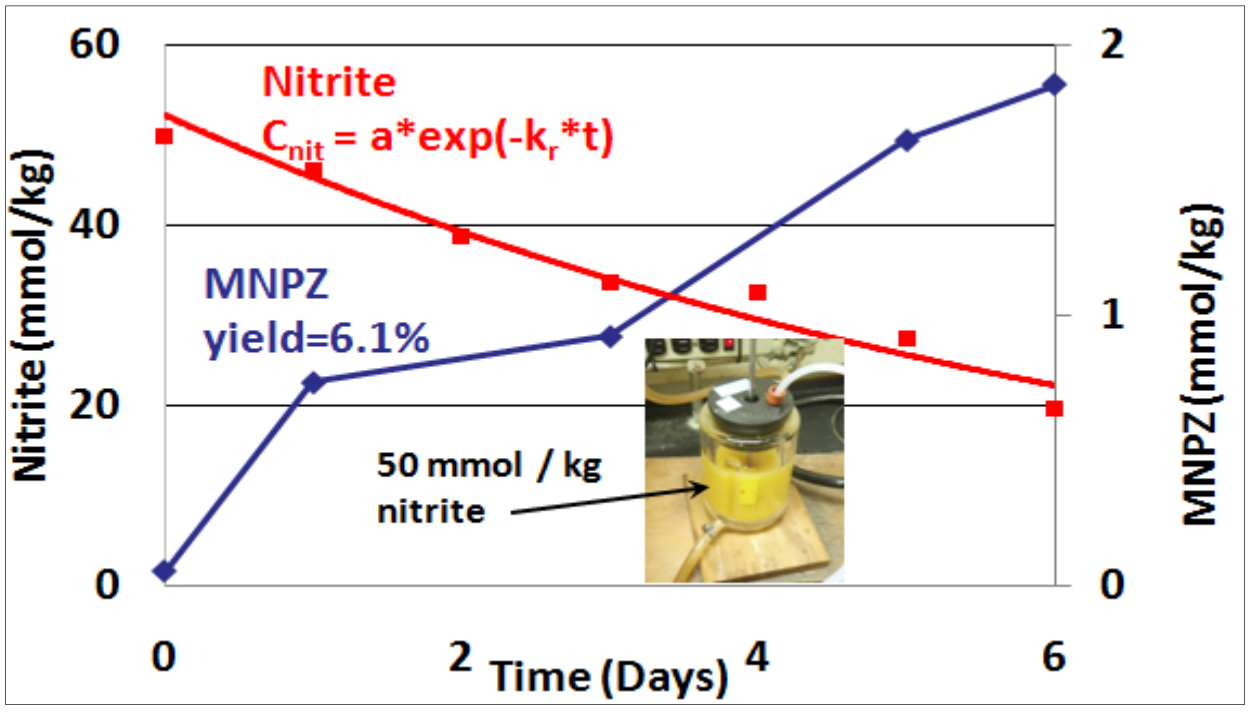

Figure 15: Nitrite consumption and MNPZ production from the reaction of 8 m loaded PZ and 50 mmol/kg nitrite in a low gas flow experiment , 100 ml/min of 98% O_2, 2% CO_2

7. Reaction of nitrite with loaded piperazine at high temperature

High temperature experiments using 8 m loaded PZ and 50 mmol/kg nitrite were performed using thermal cylinders at 100, 135, and 150 °C. At 100 °C nitrite concentration decreases following first order reaction rate as observed at lower T. At 135 °C 150°C the nitrite disappears in less than 3 hours and it is not possible to extract a reaction order (Figure 16).

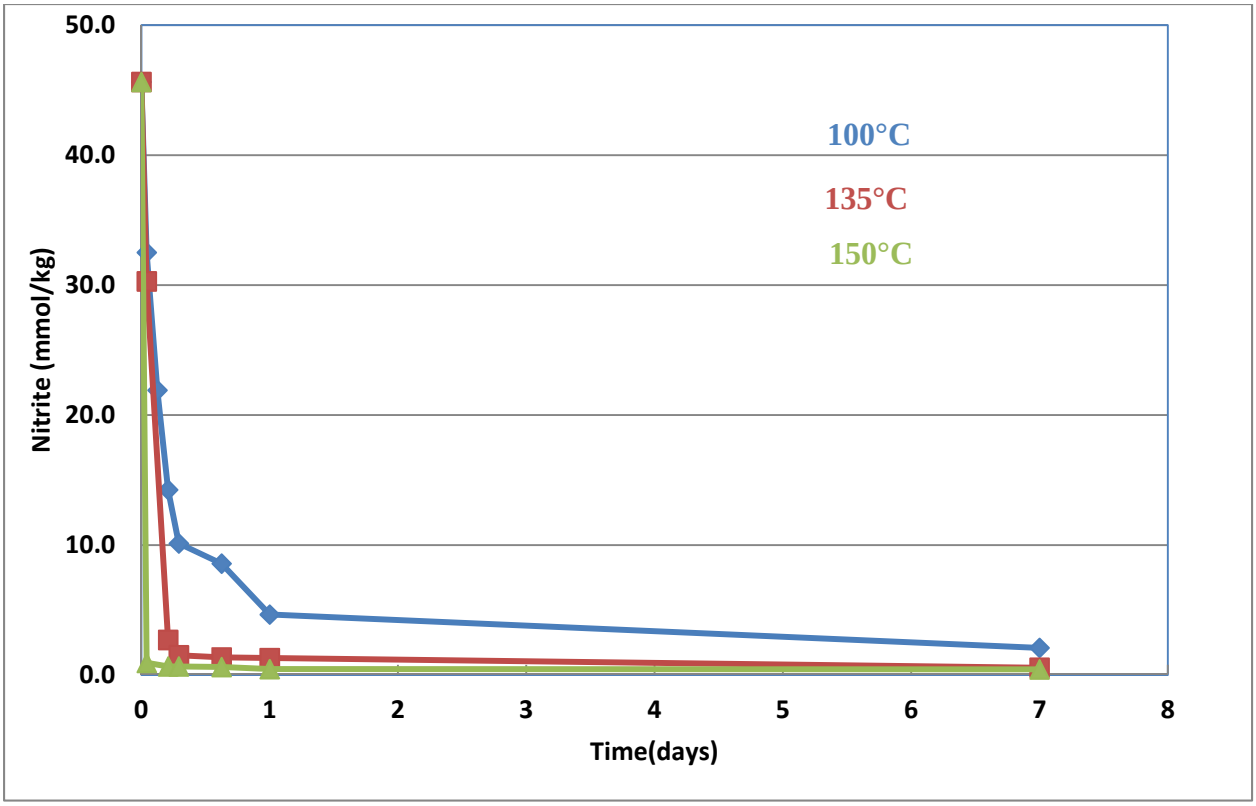

Figure 16: Nitrite consumption from the reaction of 8 m PZ, 0.3 mol CO_2/equiv N, and 50 mmol/kg of nitrite at high temperature

Appendix B contains all detailed data of high temperature experiments.

The results of high temperature experiments examined through HPLC show that at 100 °C MNPZ increases during first 15 hrs but after that decreases gradually. The same happens at 135 °C, but the maximum concentration of MNPZ occurs in the first 7 hrs, after which it seems MNPZ decomposes and disappears rapidly. At 150 °C, MNPZ is produced in just1 hr and then it disappears rapidly; after 24 hrs no trace of MNPZ remains (Figure 17).

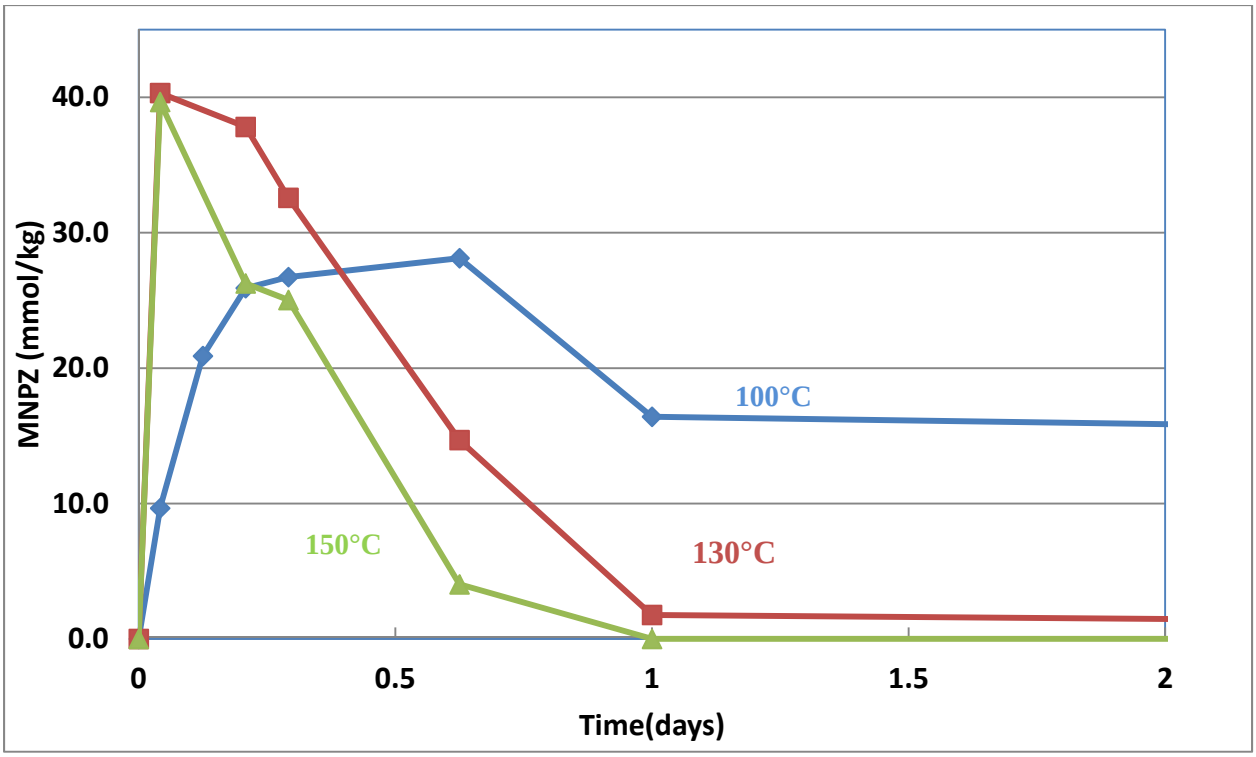

Figure 17: MNPZ production from the reaction of 8 mPZ, 0.3 mol CO_2/equiv N, and 50 mmol/kg nitrite at high temperature

Experiments have also been conducted using 2 m loaded PZ and 50 mmol/kg of nitrite at the above temperatures. The trends of nitrite consumption and MNPZ production are given in Figures 18 and 19, respectively. Figures 16 and 18 show that the rate of nitrite disappearance in nitrosation of 8 m PZ is faster than in 2 m PZ.

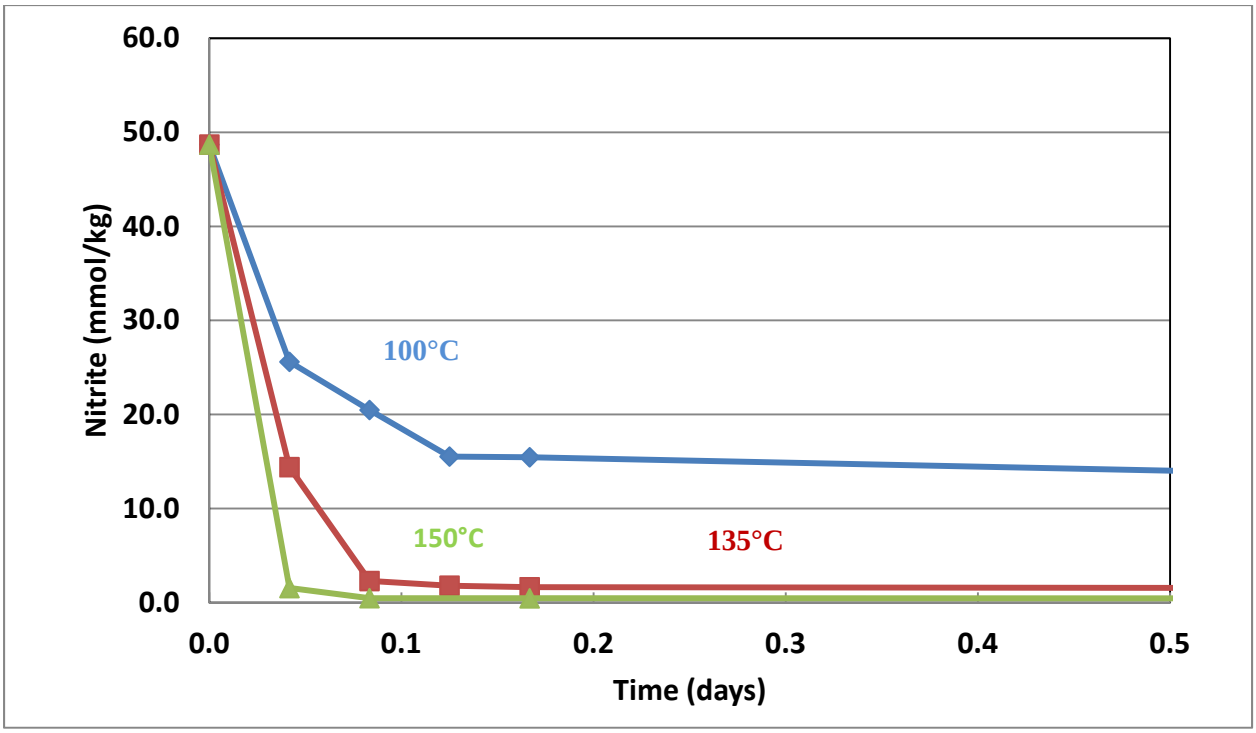

Figure 18: Nitrite consumption from the reaction of 2 m PZ, 0.3 mol CO_2/equiv N and 50 mmol/kg nitrite at high temperature

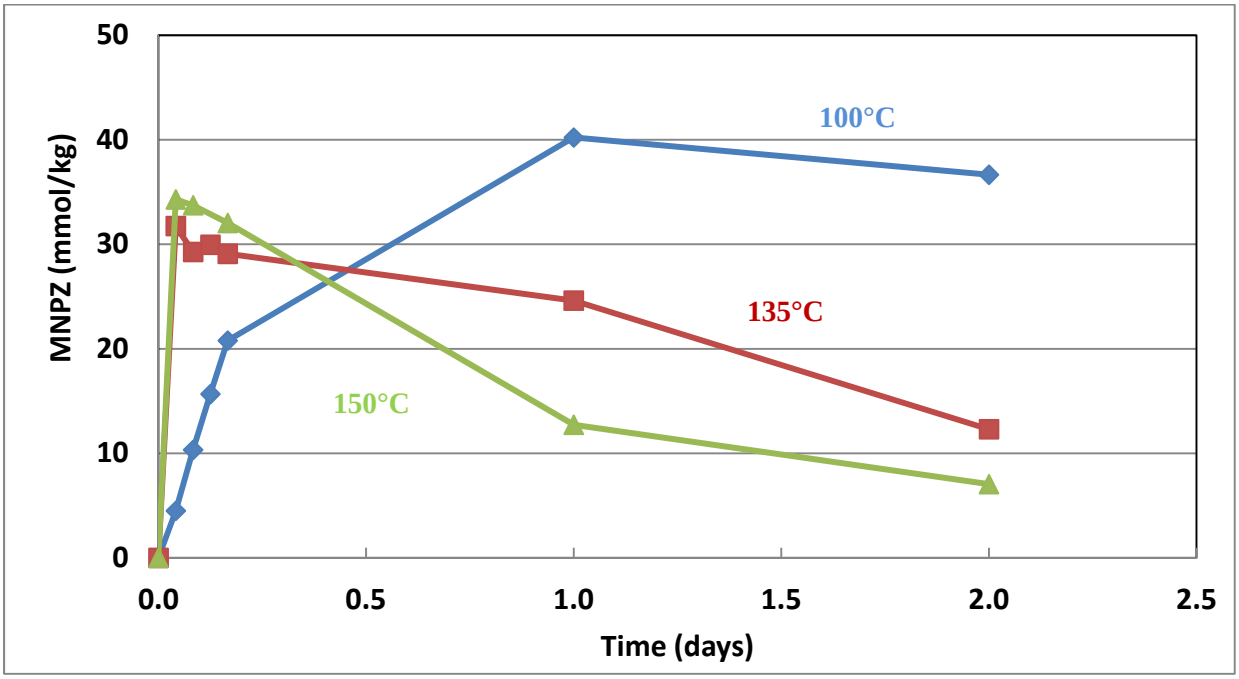

Figure 19: MNPZ production from the reaction of 2 mPZ, 0.3 mol CO_2/equiv N, and 50 mmol/kg of nitrite at high temperature

For a better understanding of the process of MNPZ production and decomposition at high temperature and stripper conditions, loading has been selected as one factor in modeling the behavior of MNPZ. Figures 20 and 21 present the nitrite consumption and MNPZ production at a loading of 0.1.

Figures 22 and 23 show the same results but for loading 0.2.

Nitrite consumption rate is not a strong function of loading but the rate of MNPZ production increases at higher loading while the rate of MNPZ decomposition at lower loading is more than that at higher loading.

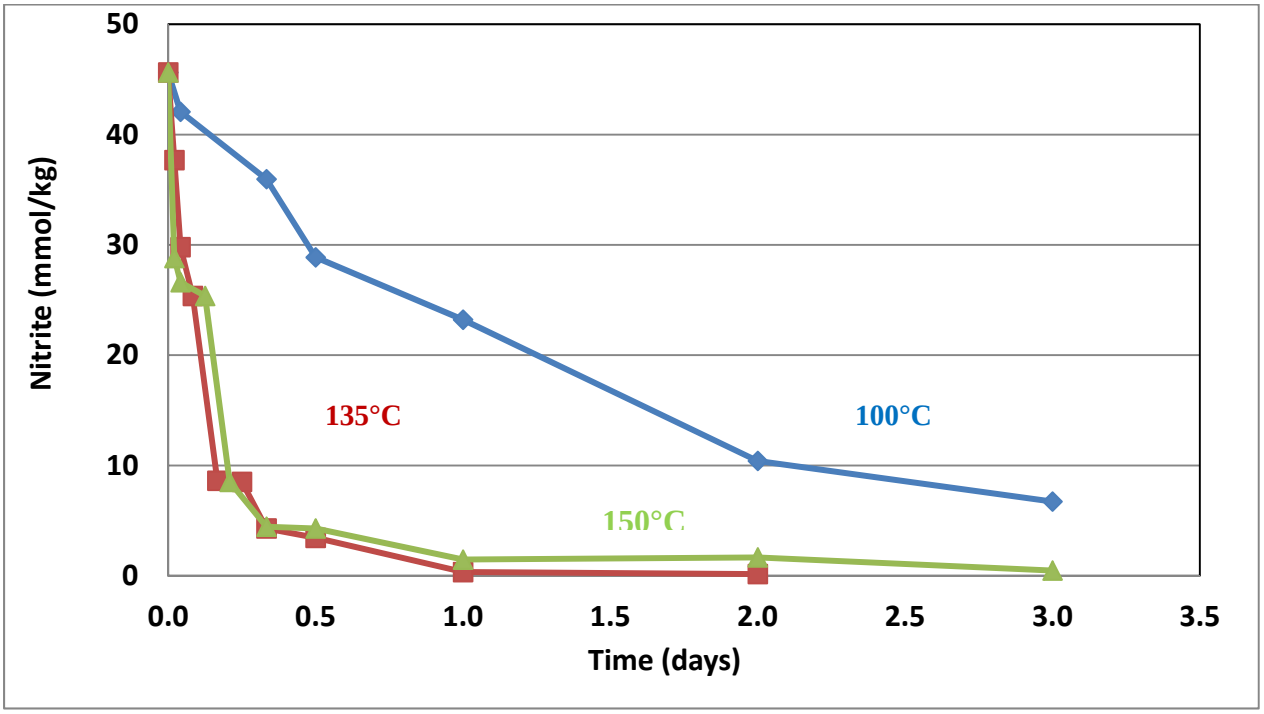

Figure 20: Nitrite consumption from the reaction of 8 m loaded PZ, 0.1 mol CO_2/equiv N, and 50 mmol/kg nitrite at high temperature

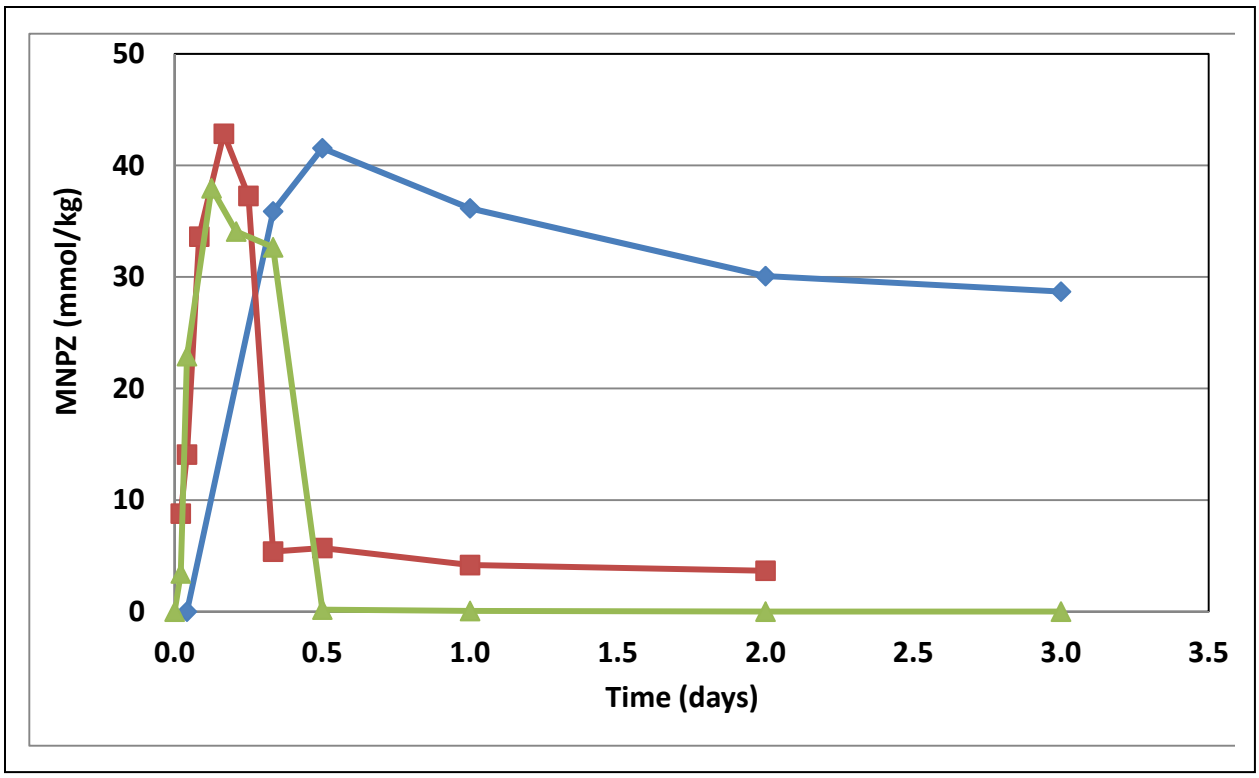

Figure 21: MNPZ production from the reaction of 8 m loaded PZ, 0.1 mol CO_2/equiv N, and 50 mmol/kg nitrite at high temperature

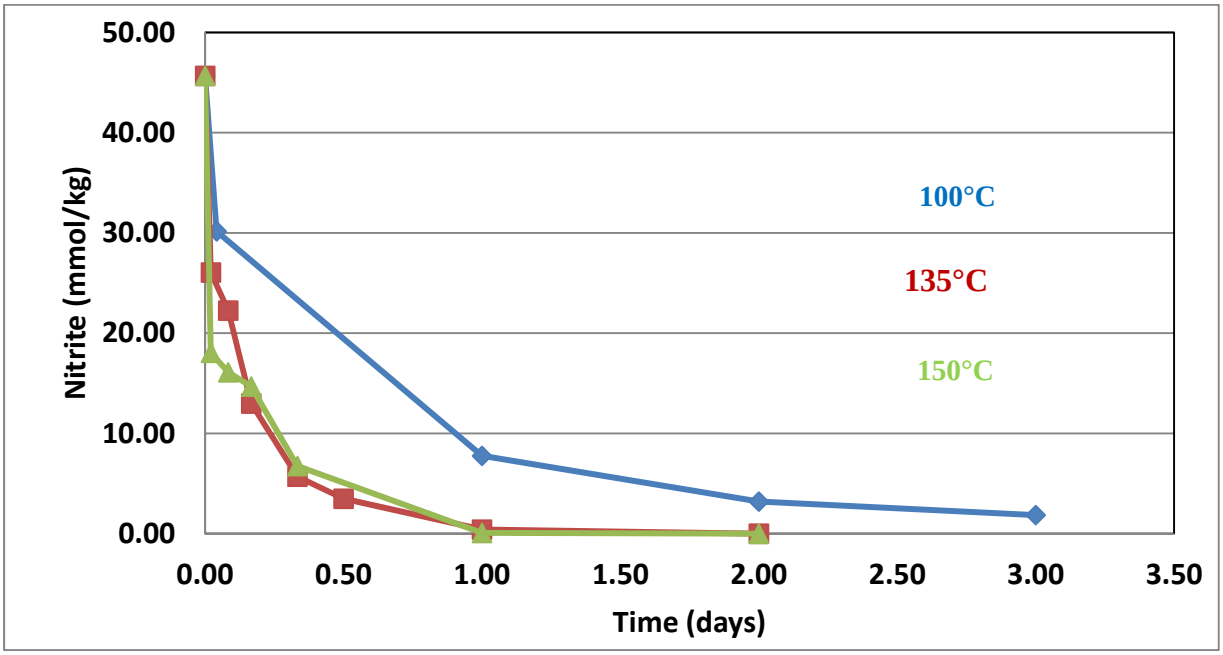

Figure 22: Nitrite consumption from the reaction of 8 m loaded PZ, 0.2 mol CO_2/equiv N, and 50 mmol/kg nitrite at high temperature

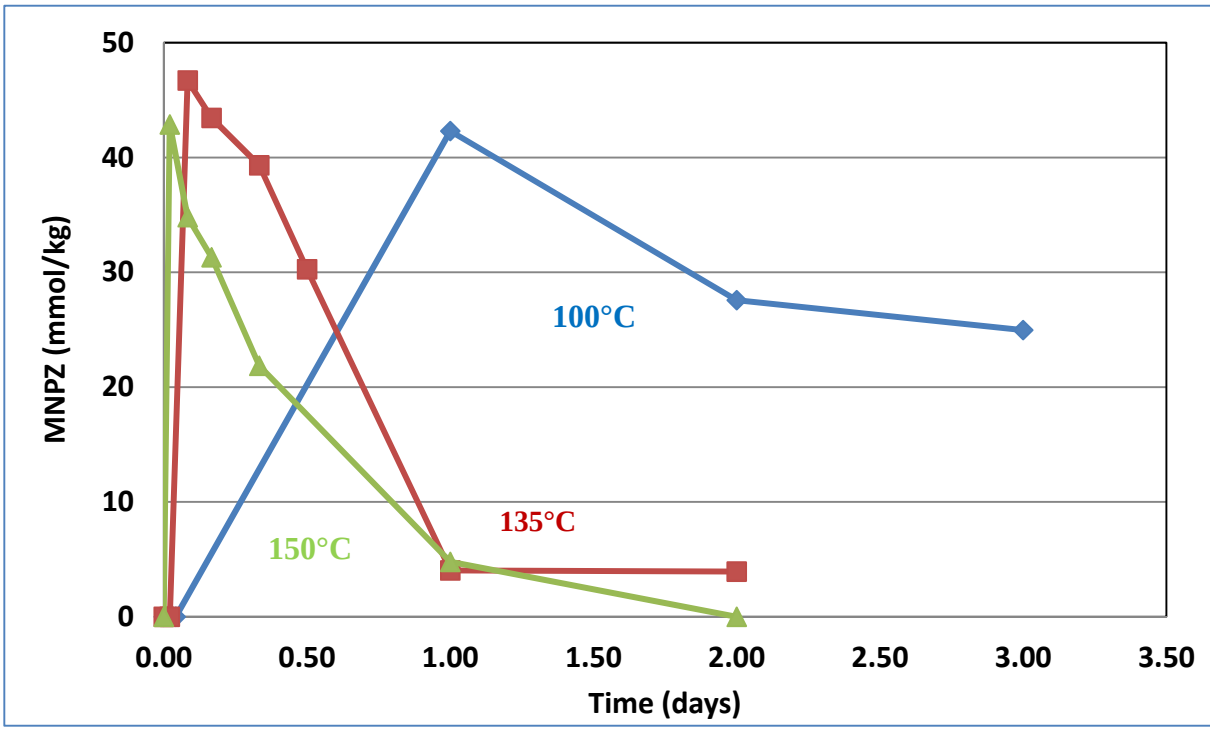

Figure 23: MNPZ production from the reaction of 8 m loaded PZ, 0.2 mol CO_2/equiv N, and 50 mmol/kg nitrite at high temperature

Conclusions

A reaction rate equation for MNPZ production has not been established, but at low temperature there is little MNPZ production and at high temperature, in spite of initial production of MNPZ it decomposes rapidly. Based on the residence time of the stripper and also reclaimer conditions in the CO_2 capture process, it is clear that MNPZ is not a major product of the reaction between PZ and nitrite and the reaction products include components that need to be identified.

Future Work

Experimental work will be finished and M.S. thesis completed.

Appendix A

Method development for detecting and measuring DNPZ and MNPZ

Direct injection of dinitrosopiperazine (DNPZ) to Mass Spectrometry

Mass Spectrometry (MS) is an analytical technique used to determine the elemental composition of a sample or molecule. The instrument consists of three main sections:

1. Ion source, which converts gas phase sample molecules into ions;
2. Mass analyzer, which sorts the ions by their masses by applying electromagnetic fields;
3. Detector, which measures the value of an indicator quantity and provides data for calculating the quantities of each ion present.

Here is a short explanation of the keywords that appear later in this report:

Direct Injection: Using the syringe pump that can be connected directly to the ion source to provide a steady state introduction of sample or tuning and calibrating solution.

Fragmentation: Breaking molecules into specific ions. Fragmentation pattern has led to mass spectra being used as "fingerprints" for identifying compounds.

According to the suggested method (Atalla et al., 2010) for detection, samples of 0.00007–0.7 mmol of DNPZ per ml of methanol have been injected directly to MS to see if MS can detect it. The mass spectrum diagram is shown in Figure1.

When the process outlined above showed no evidence of DNPZ, water was added to the solution and in this case DNPZ could be detected by MS. To obtain more accurate results, the fragmentation method has been run with results shown in Figures 2– 5.

For quantifying DNPZ, an LC-MS system has been used; the method of measurement was developed by employing a reverse phase column.

Solutions of 500 ppm PZ), DNPZ, and DNPZ + PZ in 80% methanol (MeOH) and 20% water have been injected to the LC-MS, and primary results are shown in Figures 6–14.

Mass spectrometry shows the mass per charge of molecules and their relative abundance. For DNPZ we are looking for m/z = 145 because the molecular weight of DNPZ is 144 and by protonating with one hydrogen atom, the mass of ion will be 145.

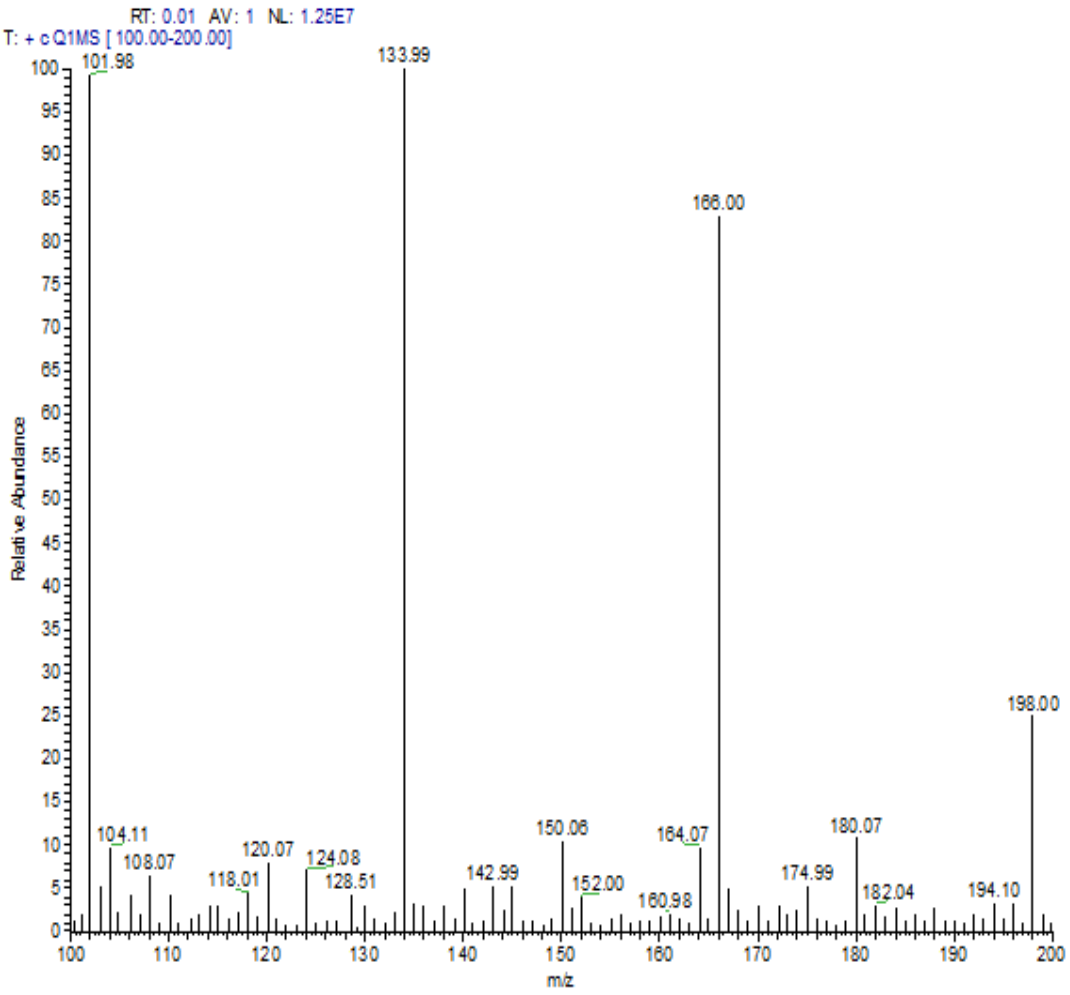

Figure 1: Mass spectrum of a sample of DNPZ and methanol (relative abundance in terms of m/z)

Figure 1 shows the typical mass spectrum of samples that have been injected into the MS. All sample results were almost the same and in this report just one of them that was a common spectrum in most of the runs, has been described. There is no evidence of m/z = 145.

By adding water to the solutions (2 parts methanol and 1 part water) and then injecting new samples to the MS, surprisingly, mass spectrum showed a peak at m/z of 145 which is DNPZ (Figure 2).

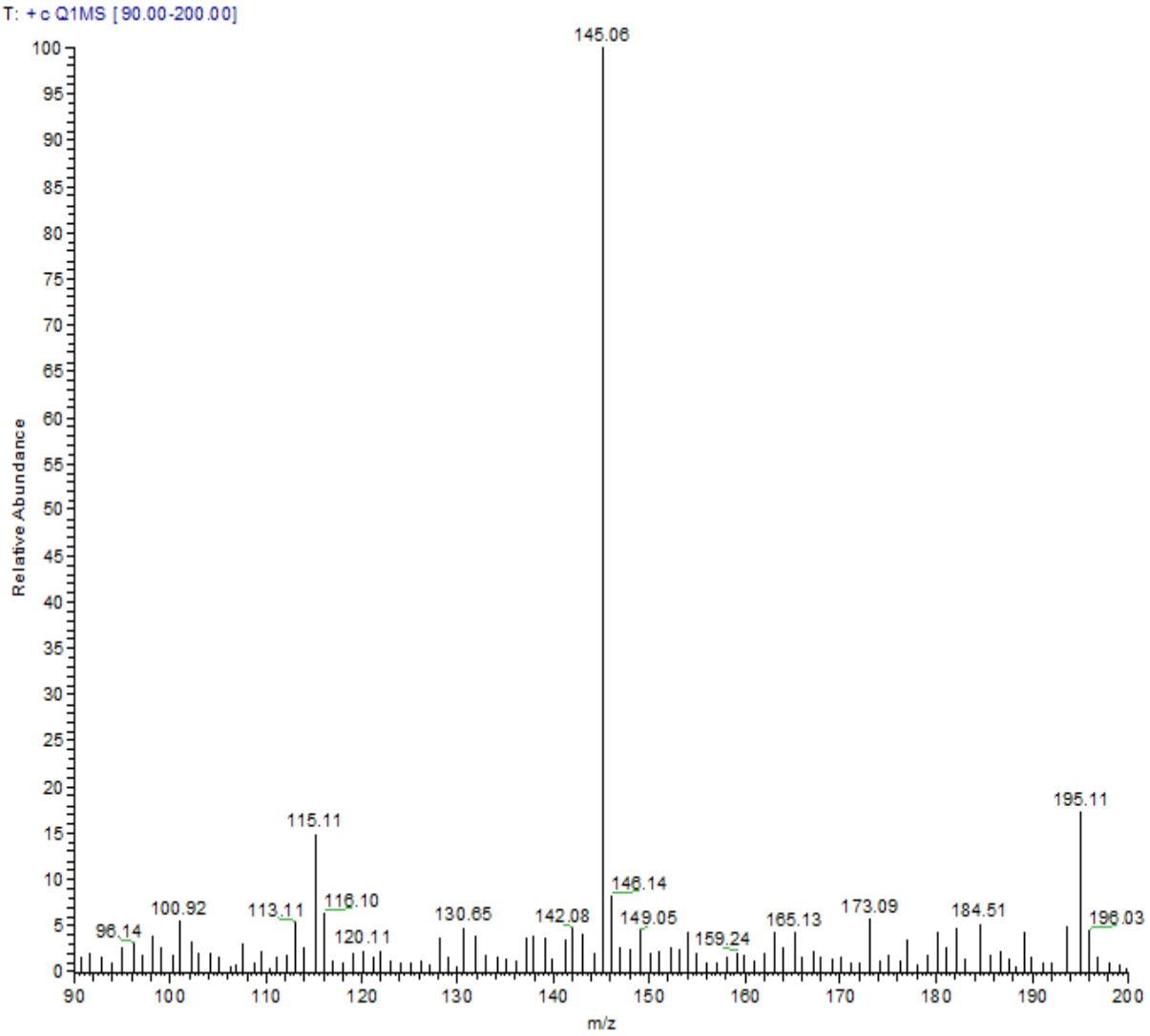

Figure 2: Mass spectrum of a sample of DNPZ in methanol and water

(Relative abundance in terms of m/z)

Rather than a big peak of DNPZ, there is a small amount of MNPZ in the injected sample as shown in Figure 2. m/z of 116.1 represents the molecular weight of MNPZ which is 115.

When there is a very small amount of a molecule in a sample, or when more than one molecule with the same molecular weight may exist, the fragmentation method has been used to confirm the detection of a specific molecule. By using fragmentation, an extremely small quantity of a component is recognizable.

Figures 3– 5 show the fragmentation steps of DNPZ to 2 ions with m/z of 85.1 and 56.15.

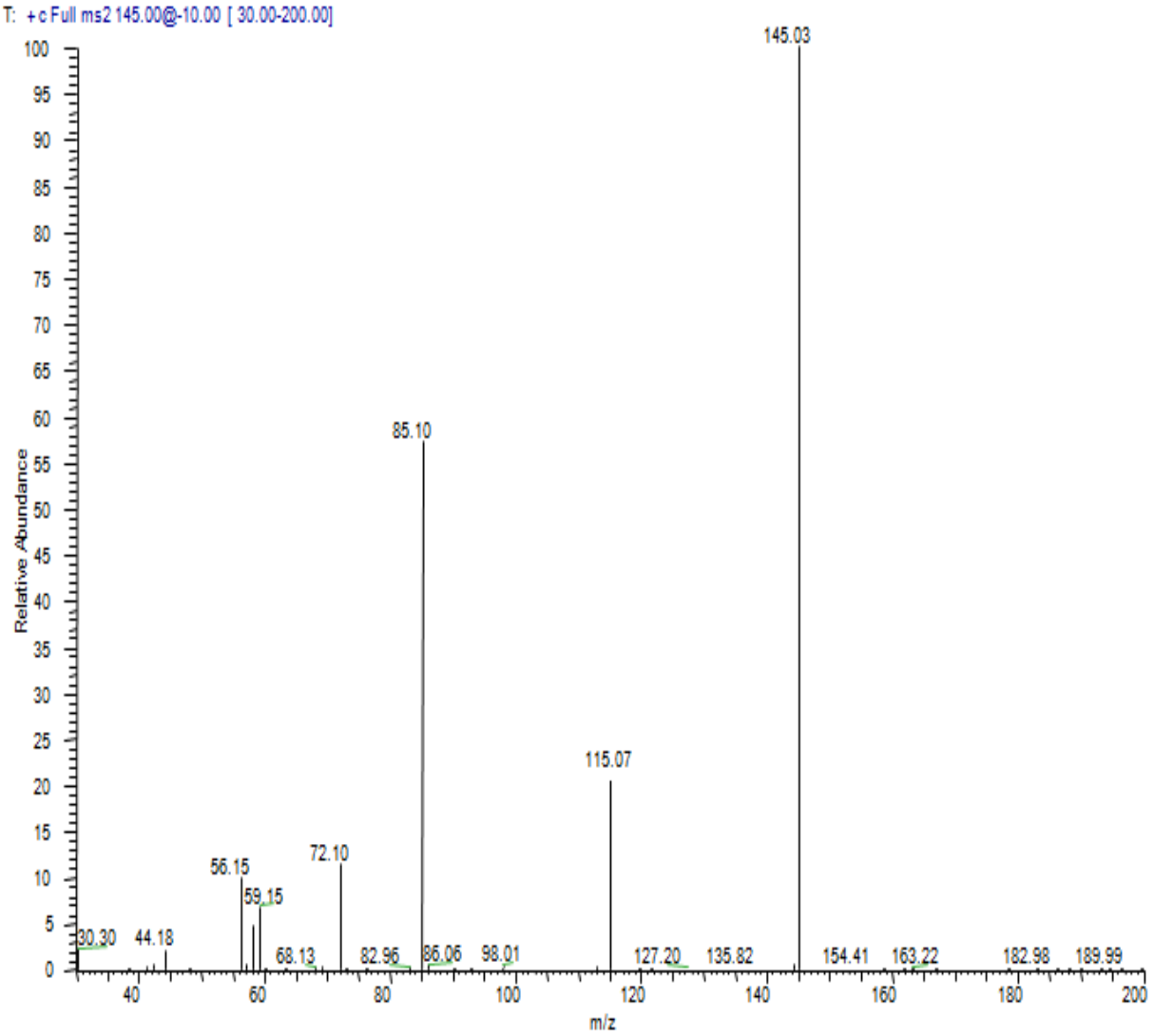

Figure 3: Mass spectrum of fragmentation of a sample of DNPZ in methanol and water by collision energy of 10. (Relative abundance in terms of m/z)

Figure 3 shows that collision energy of 10 does not break DNPZ very well and just one ion with m/z of 85.1 appears. By increasing collision energy to 20, DNPZ breaks and rather than decreasing in its relative abundance ions, with m/z of 85.1 and 56.15 it showed up very well, as seen in Figure 3.

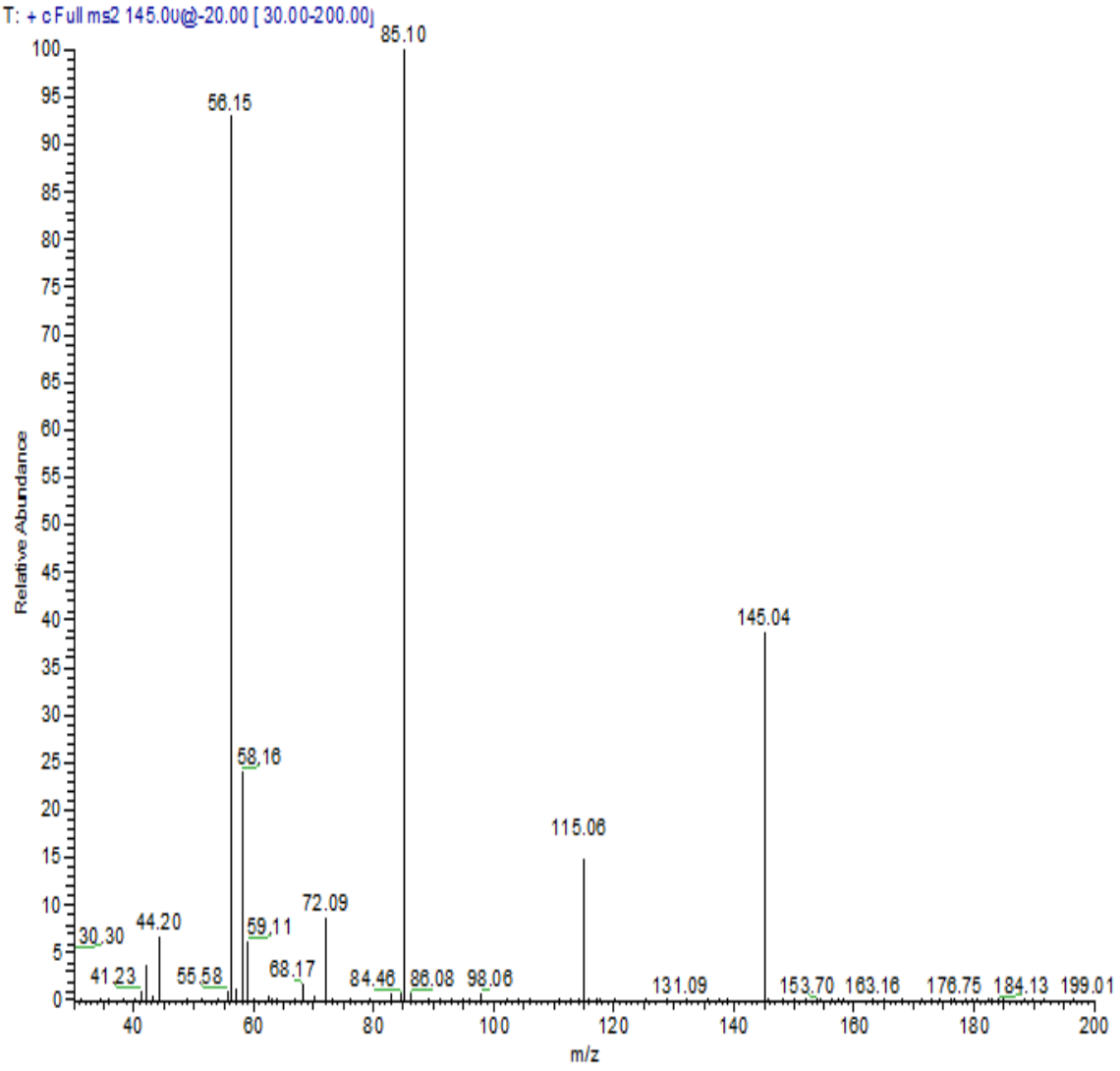

Figure 4: Mass spectrum of fragmentation of a sample of DNPZ in methanol and water by collision energy of 20. (Relative abundance in terms of m/z)

Collision energy of 20 breaks almost 40% of the DNPZ, so the collision energy has been increased one more step to 30. Figure 8 shows that with collision energy of 30 almost all DNPZ is broken into ions with m/z of 85.1 and 58.15.

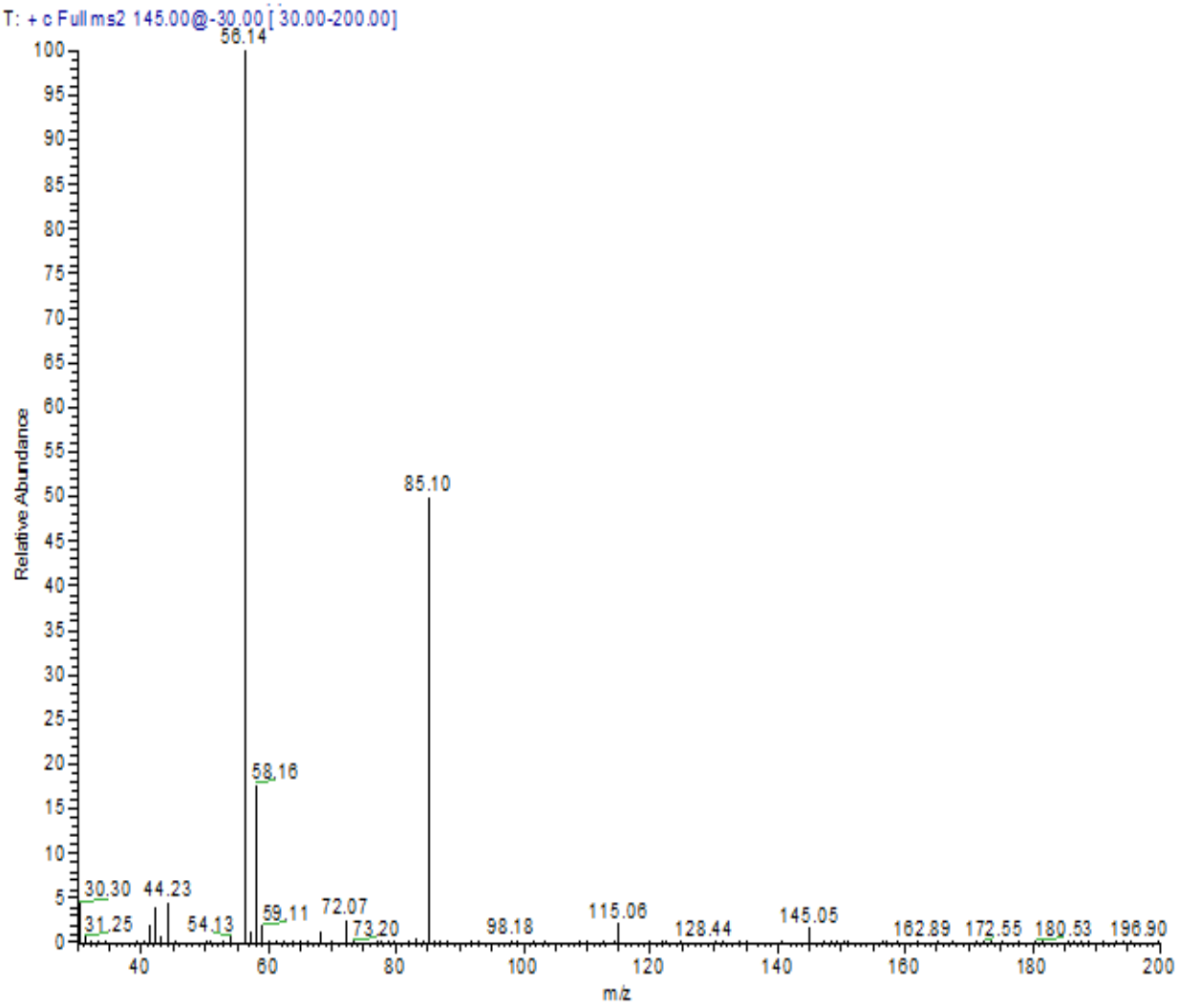

Figure 5: Mass spectrum of fragmentation of a sample of DNPZ in methanol and water by collision energy of 30. (Relative abundance in terms of m/z)

Quantifying DNPZ by Liquid chromatography and Mass Spectrometry (LC-MS)

After DNPZ has been detected by MS, its concentration in different solutions was quantified using a LC-MS system. Samples of DNPZ, PZ, and DNPZ+PZ in 80% methanol and 20% were separated with LC-MS using a reverse phase column.

The chromatograms were divided in three parts of mass ranges, 145–145.2 for DNPZ, 116–116.2 for MNPZ, and 87–87.2 for PZ. Figures 6–14 show the respective results.

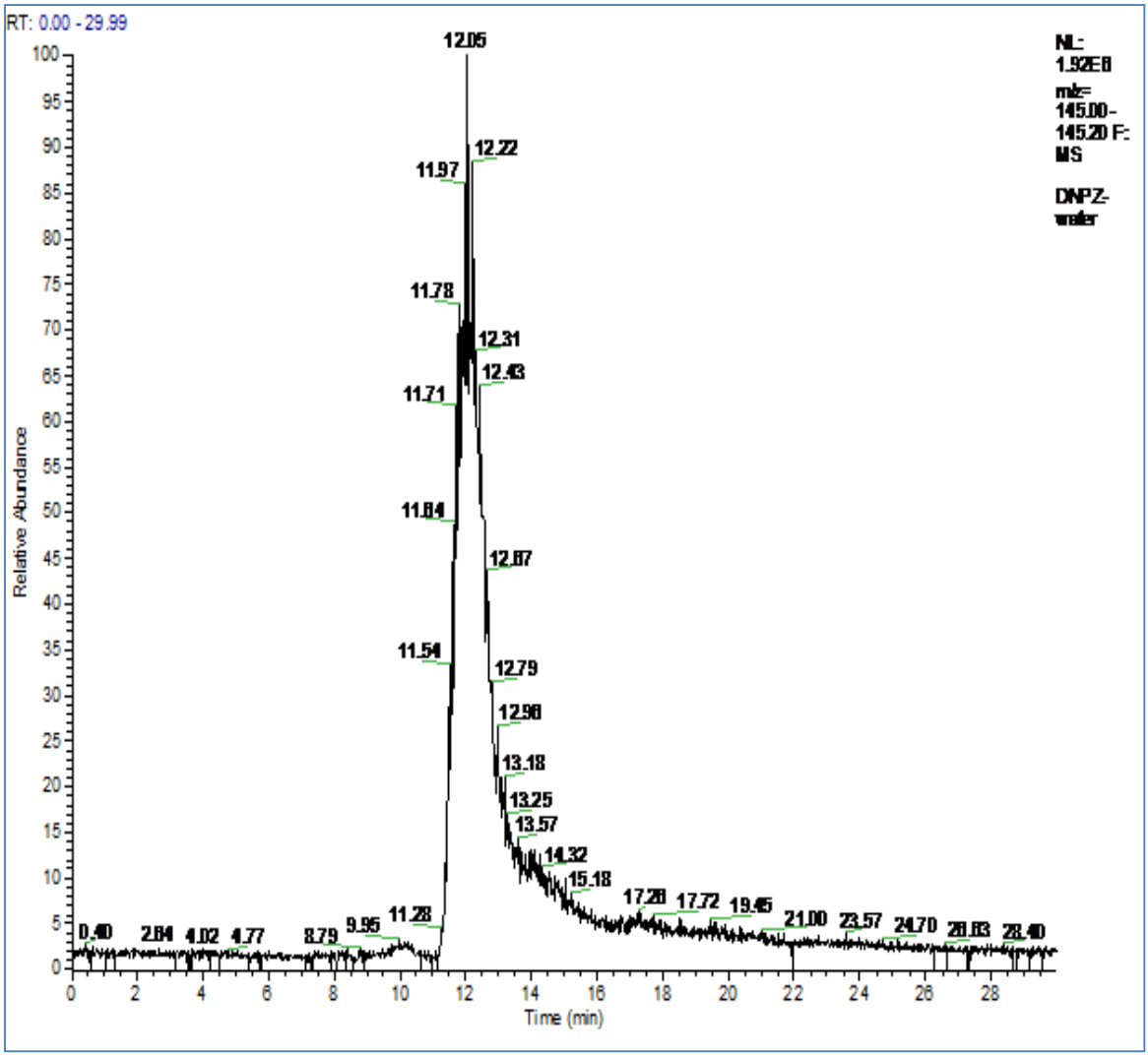

Figure 6: Chromatogram of a sample of DNPZ in methanol and water analyzed by LC-MS

Figure 5 shows the chromatogram of DNPZ analysis by LC-MS when the mass range of detection is between 145 and 145.2. The vertical axis presents relative abundance and the horizontal axis shows retention time.

DNPZ comes out at 12.05 minutes with a high relative abundance while there are other components with mass close to DNPZ, and considerably lower relative abundance, around it.

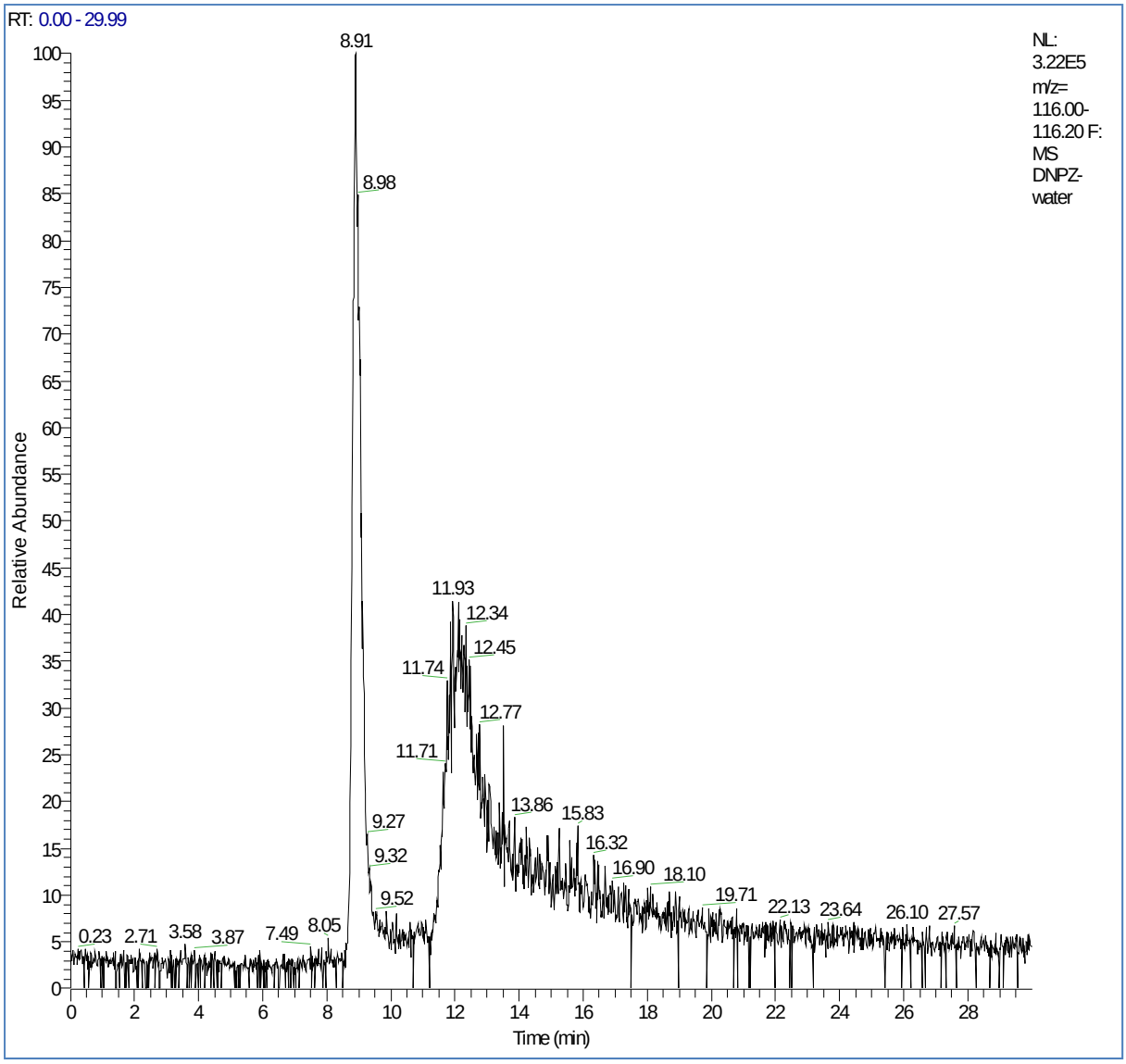

Figure 7: Chromatogram of a sample of DNPZ in methanol and water analyzed by LC-MS in mass range of MNPZ (116)

Figure 7 shows that MNPZ can be produced when DNPZ is dissolved in methanol and water. Its retention time is 8.9 minutes.

Figure 8 shows that there is very little PZ in a DNPZ sample, showing that LC-MS is a good method to quantify DNPZ, although more work must be done to obtain calibration curves and measurement sensitivity.

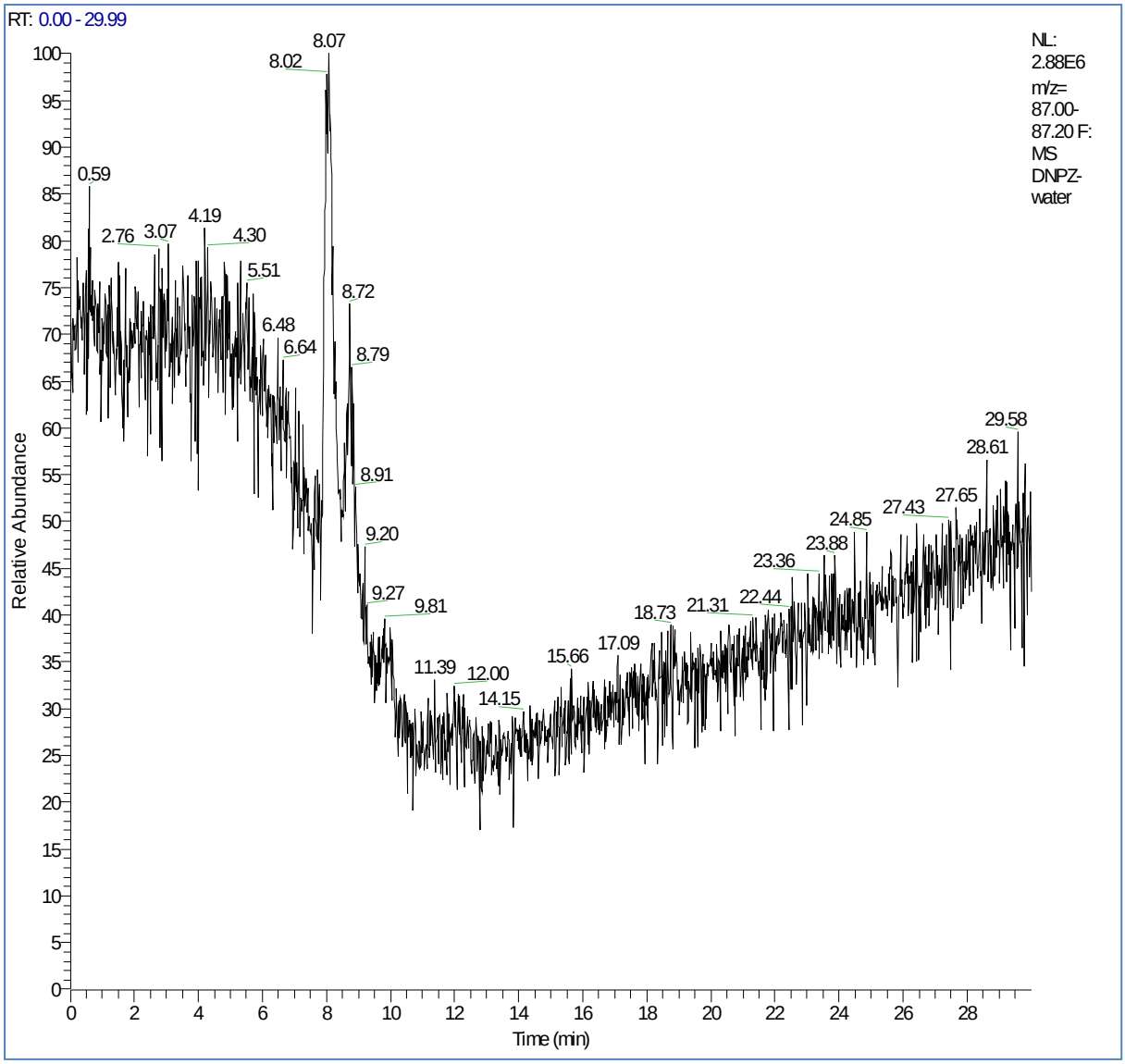

Figure 8: Chromatogram of a sample of DNPZ in methanol and water analyzed by LC-MS in mass range of PZ (87)

The following two chromatograms show the response of LC-MS to a solution of PZ in methanol and water.

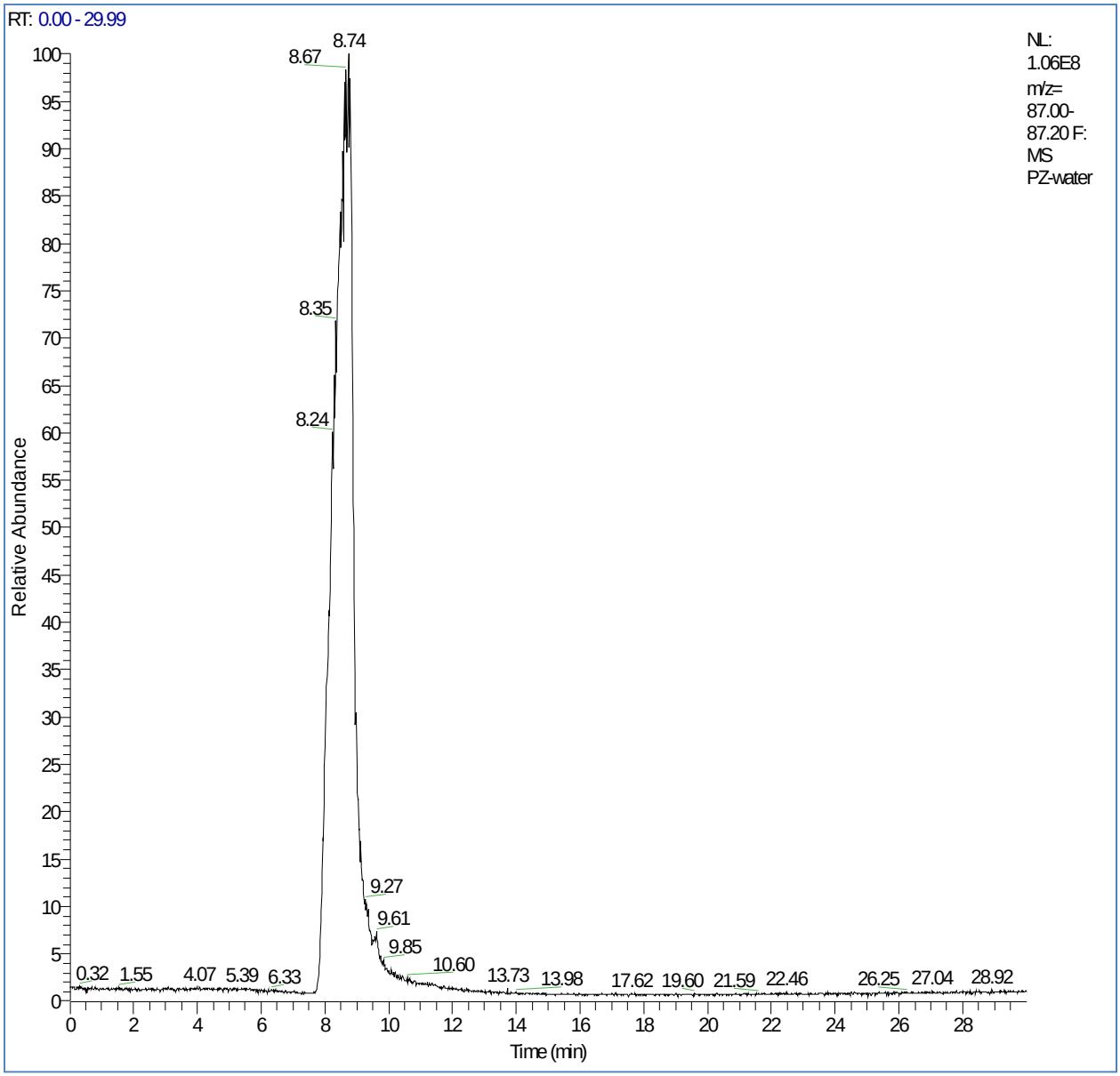

Figure 9: Chromatogram of a sample of PZ in methanol and water analyzed by LC-MS in mass range of PZ (87)

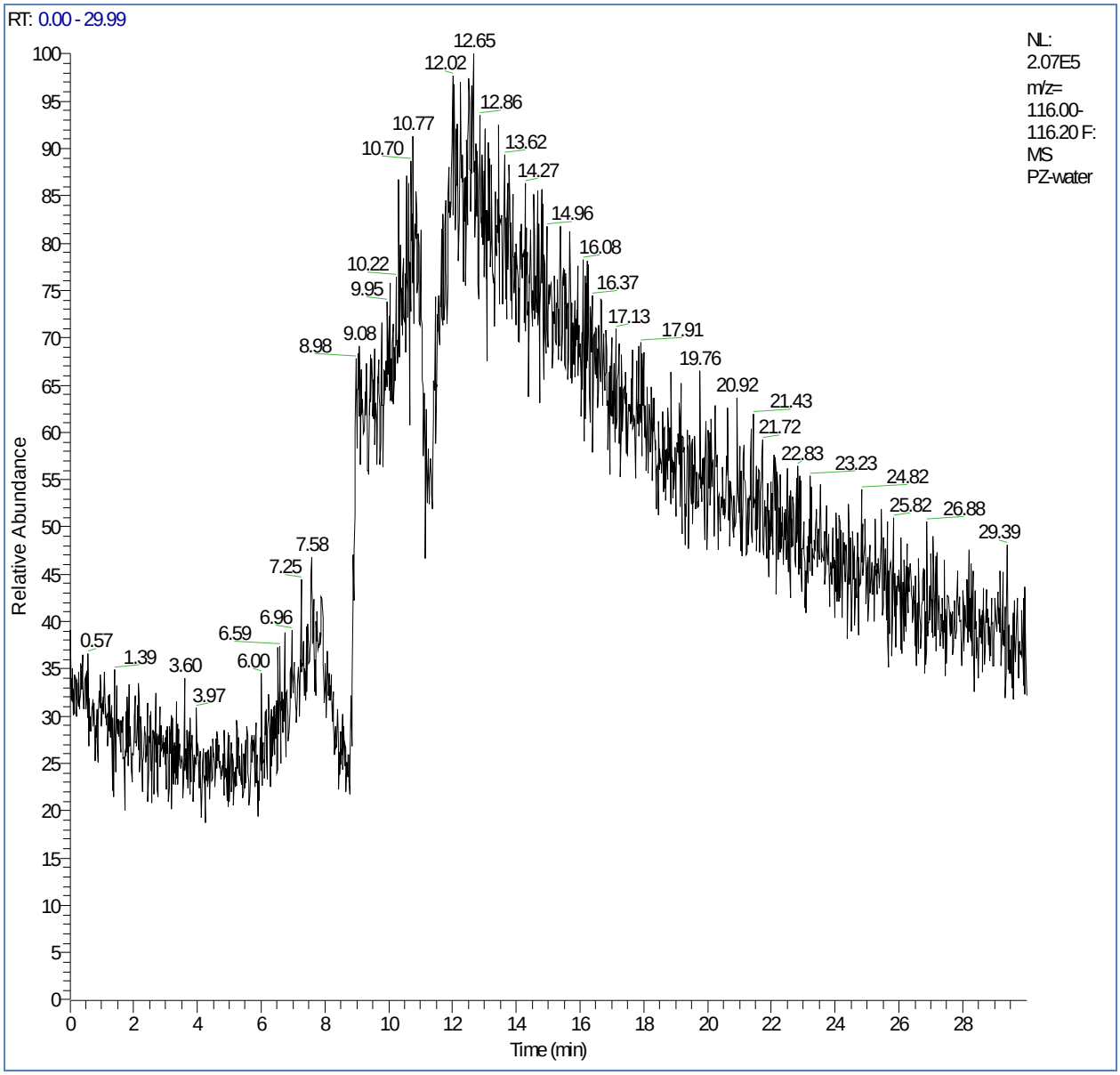

Figure 10: Chromatogram of a sample of PZ in methanol and water analyzed by LC-MS in mass range of MNPZ (116)

The following three chromatograms show the analysis of equal concentrations of DNPZ and PZ in methanol and water by LC-MS. As noted there is some MNPZ rather than PZ and DNPZ in LC-MS analysis.

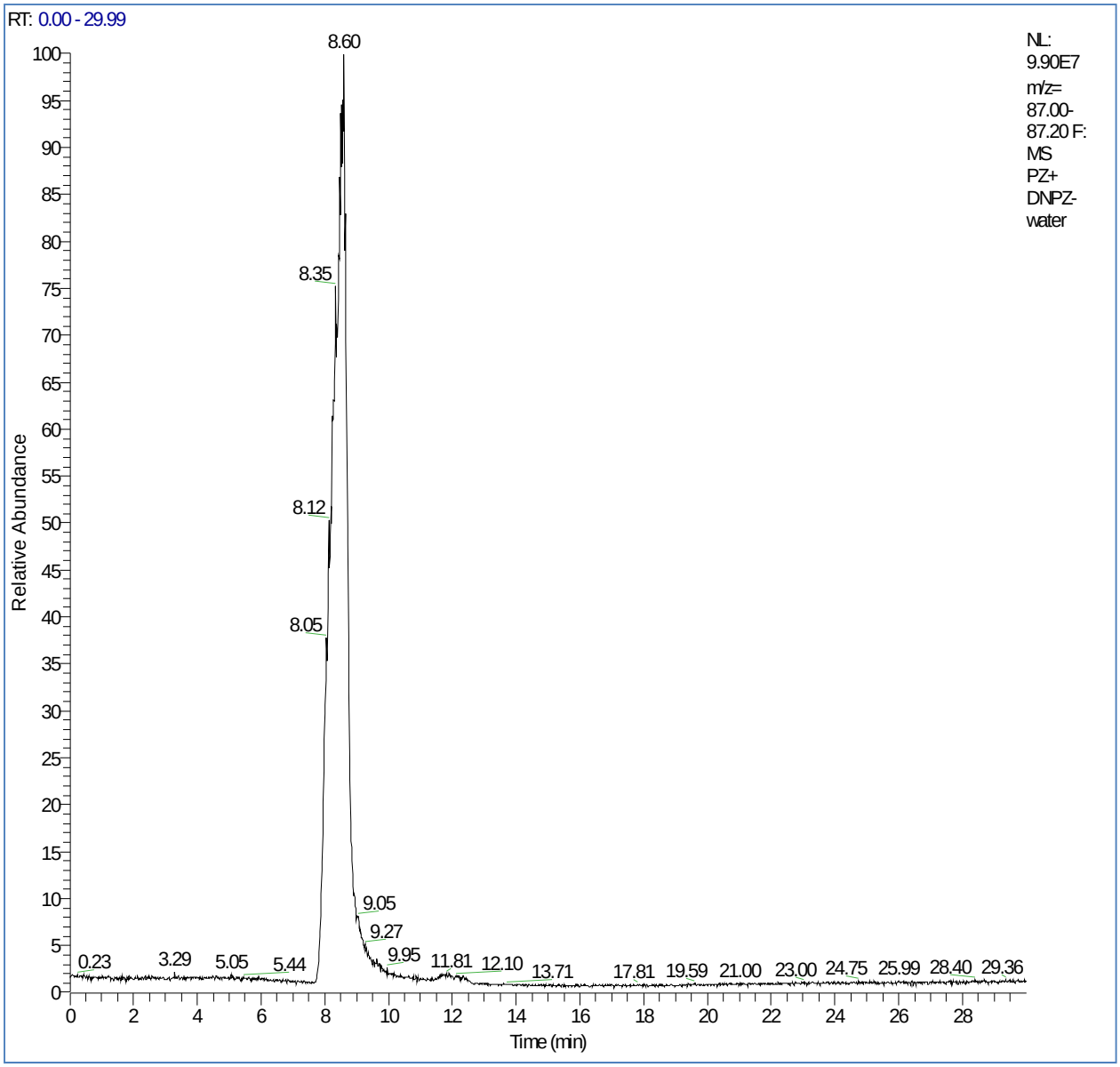

Figure 11: Chromatogram of a sample of PZ and DNPZ in methanol and water analyzed by LC-MS in mass range of PZ (87)

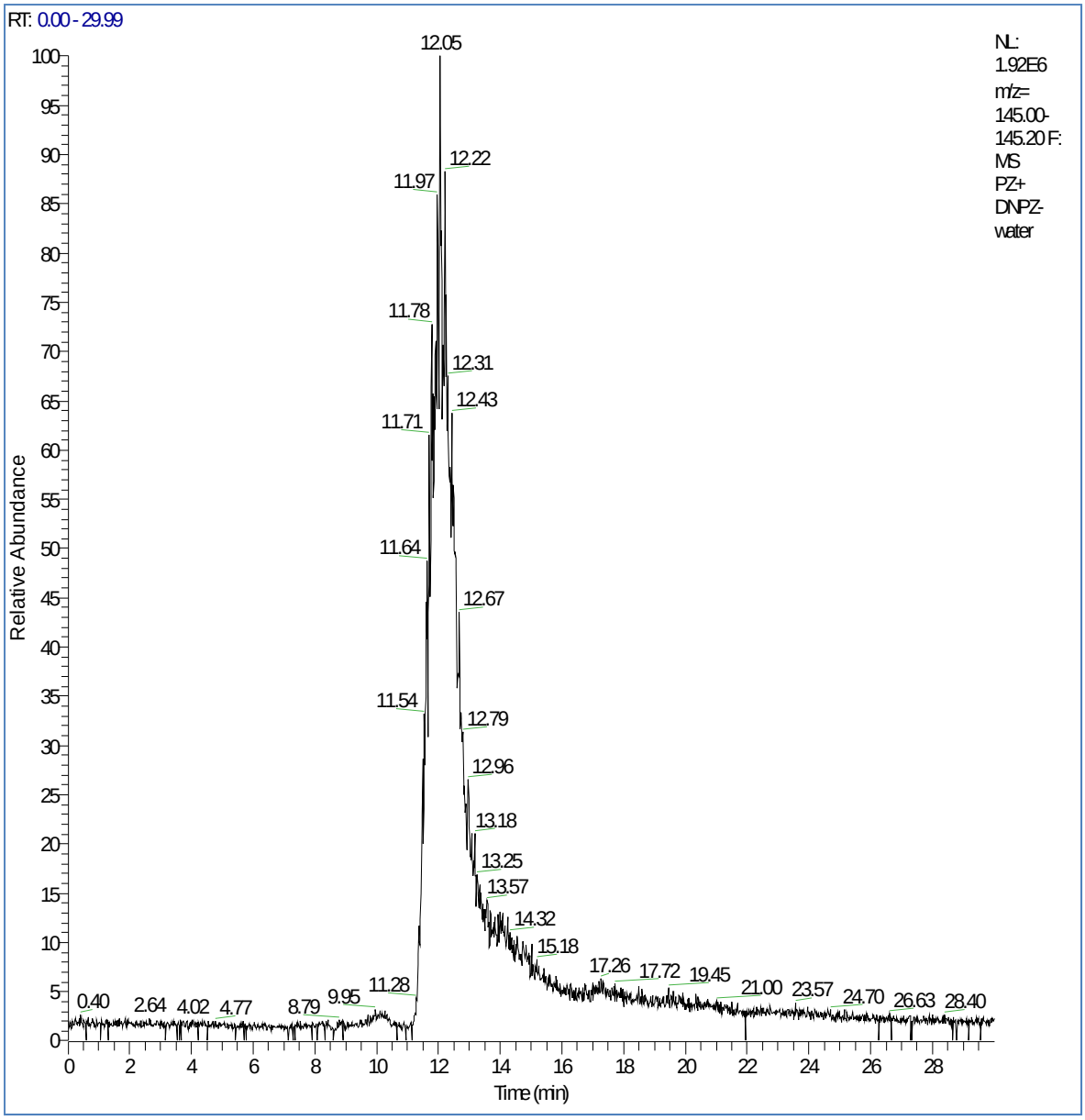

Figure 12: Chromatogram of a sample of PZ in methanol and water analyzed by LC-MS in mass range of DNPZ (145)

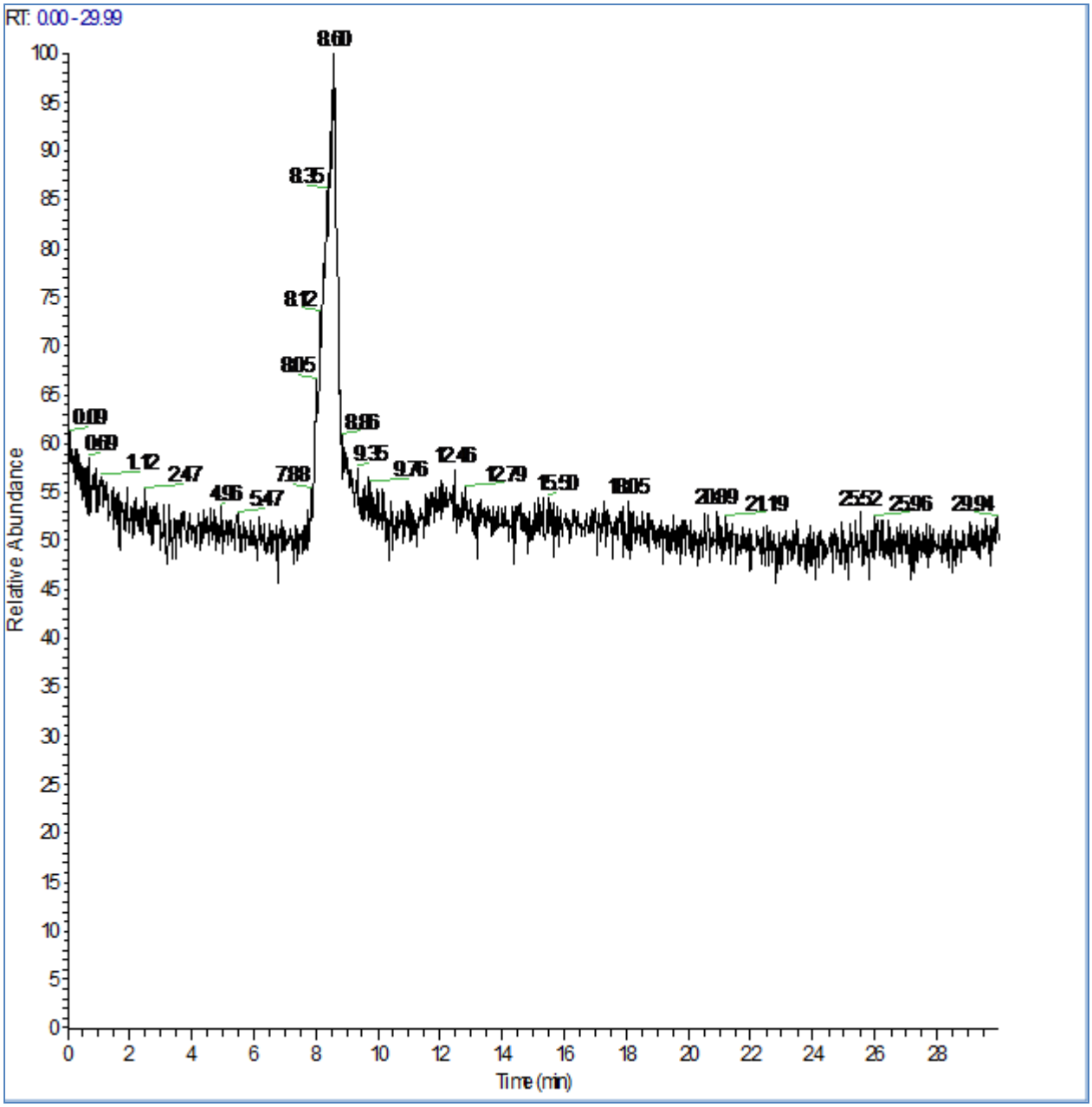

Figure 13: Chromatogram of a sample of PZ in methanol and water analyzed by LC-MS in mass range of MNPZ (116)

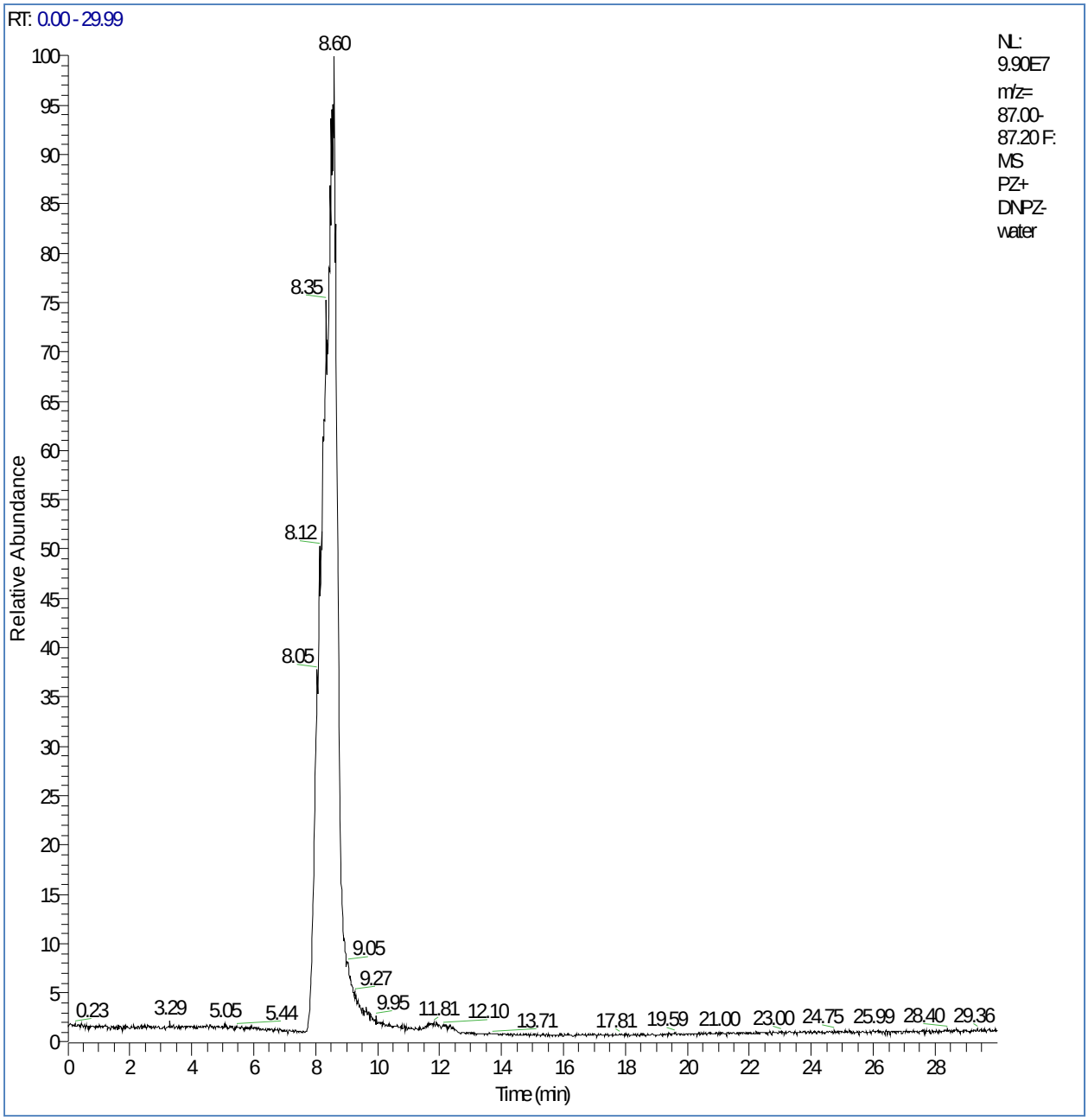

Figure 14: Chromatogram of a sample of piperazine in methanol and water analyzed by LC-MS in mass range of PZ (87)

Quantifying Dinitrosopiperazine by Liquid chromatography and Mass Spectrometry (LC-MS)

After detection of DNPZ by MS, for quantifying the concentration of DNPZ in different solutions, a LC-MS system was used. Different concentrations of standard DNPZ in 80% methanol and 20% water have been applied to LC-MS using a reverse phase column. The areas under the peaks in the chromatograms are related to the concentration of each standard, so a calibration curve has been established with a sensitivity of $5x10^{-5}$ (Figure 15).

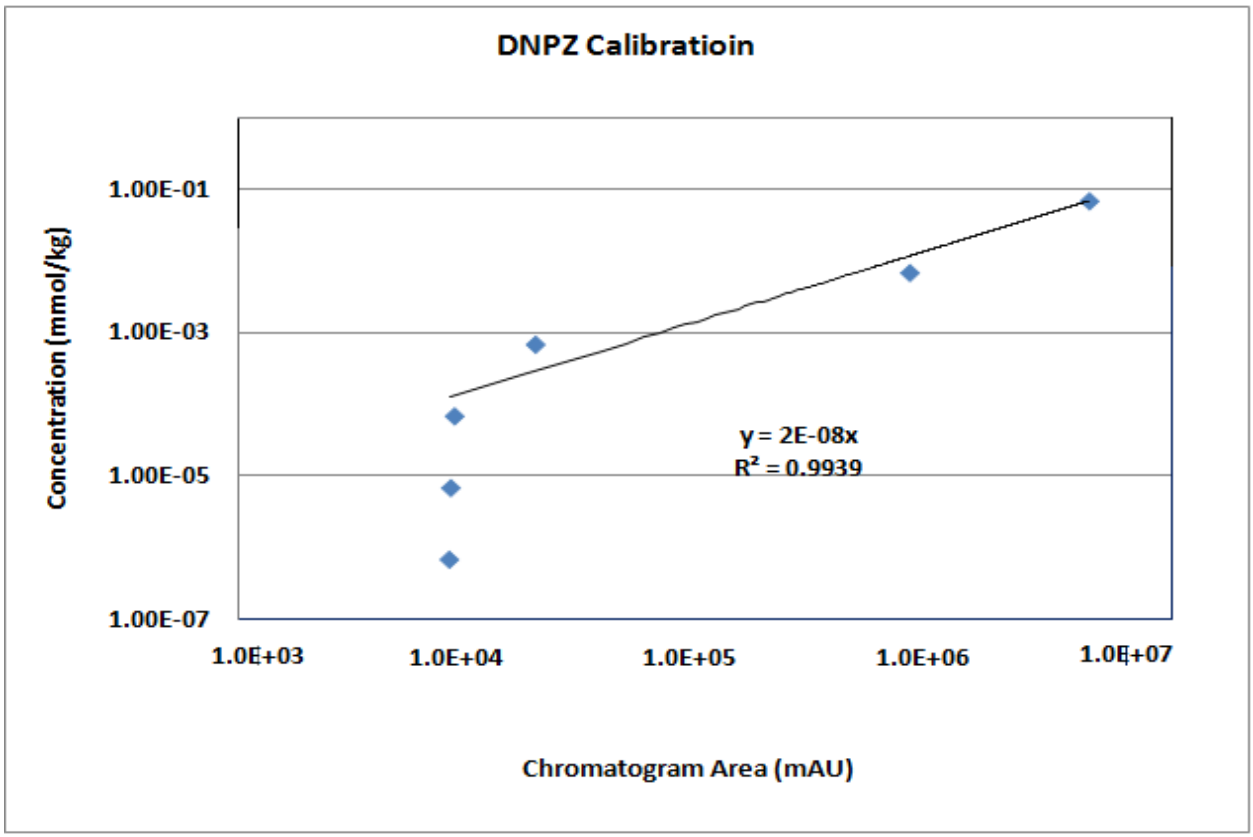

Figure 15: Calibration curve for standard DNPZ, with a detection limit of $9x10^{-5}$ mmol/kg

Figure 15 shows the chromatogram area by the mass spec detector related to the different concentrations of DNPZ, and the relevant calibration curve. This will be used when a sample with an unknown concentration of DNPZ is injected into the LC-MS.

Detecting MNPZ and DNPZ in a solution of PZ

The DNPZ detection method has been used for purchased standard MNPZ, but results show that the method should be refined; therefore we have established a new method, in which the mobile phase contains 10% methanol and 90% water with the rate of 200 µl/min over 30 minutes. This method gives better separation of PZ, MNPZ, and DNPZ.

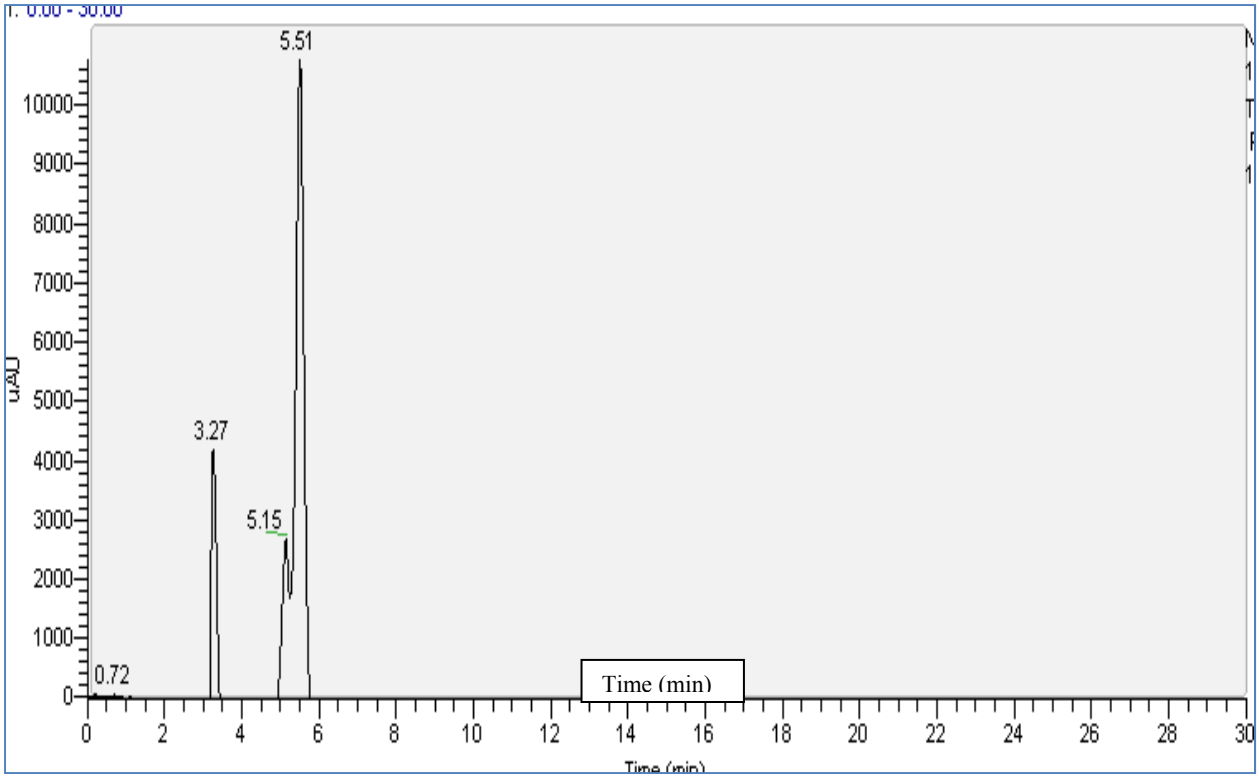

Figure 16: Chromatogram of MNPZ, DNPZ, and PZ when the mobile phase contains 50% methanol and 50% water

Figure 16 shows the response of LC-MS to a sample which contains 8 m loaded PZ, MNPZ, and DNPZ, where the mobile phase contains 50% methanol and 50% water at a rate of 350 µl/min. As seen in the figure, there is not a good separation between component peaks so the mobile phase composition has been changed. When the rate of methanol was increased peaks were combined and there was no specific peak for species in solution. The method has been developed by decreasing the portion of methanol in the mobile phase and the results are shown in the following figures. Decreasing the flow rate of the mobile phase to 200 µl/min improves results.

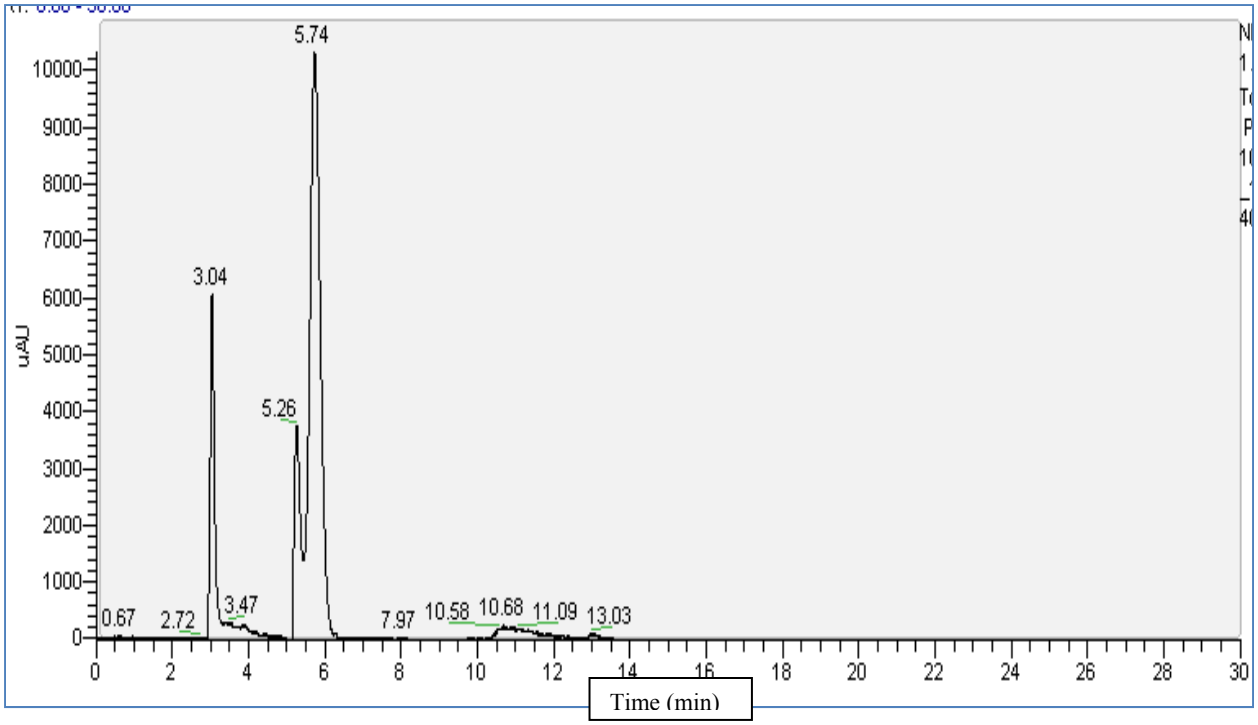

Figure 17: Chromatogram of MNPZ, DNPZ, and PZ when the mobile phase contains 40% methanol and 60% water

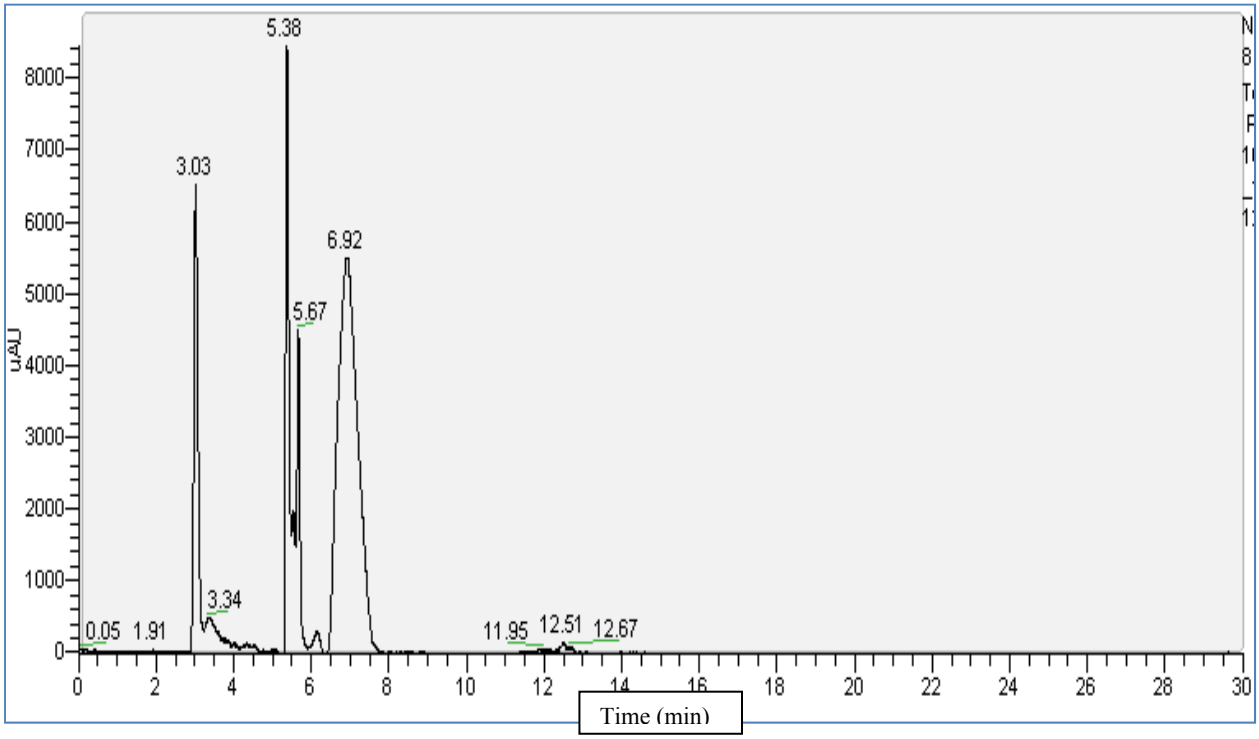

Figure 18: Chromatogram of MNPZ, DNPZ, and PZ when the mobile phase contains 20% methanol and 80% water

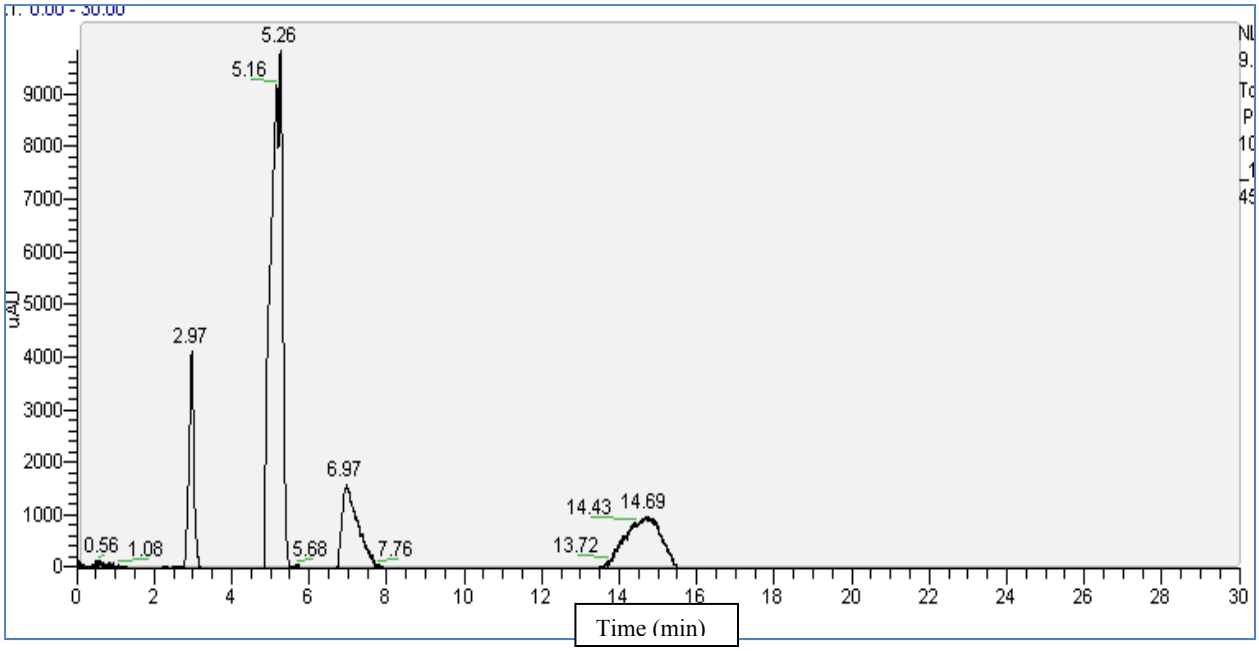

Figure 19: Chromatogram of MNPZ, DNPZ, and PZ when the mobile phase contains 10% methanol and 90% water

When experimental samples from the kinetic study of nitrosation were analyzed, many components other than MNPZ and DNPZ were found in the reaction products, for example m/z of 87.19 represents PZ, and m/z of 65 indicates methanol, but m/z of 74.17, 97.21, 106.21, and 128.19 are unidentified (Figure 13). However MS analysis shows that MNPZ and DNPZ are the least common products from nitrosation of 8 m loaded PZ (Figure 21).

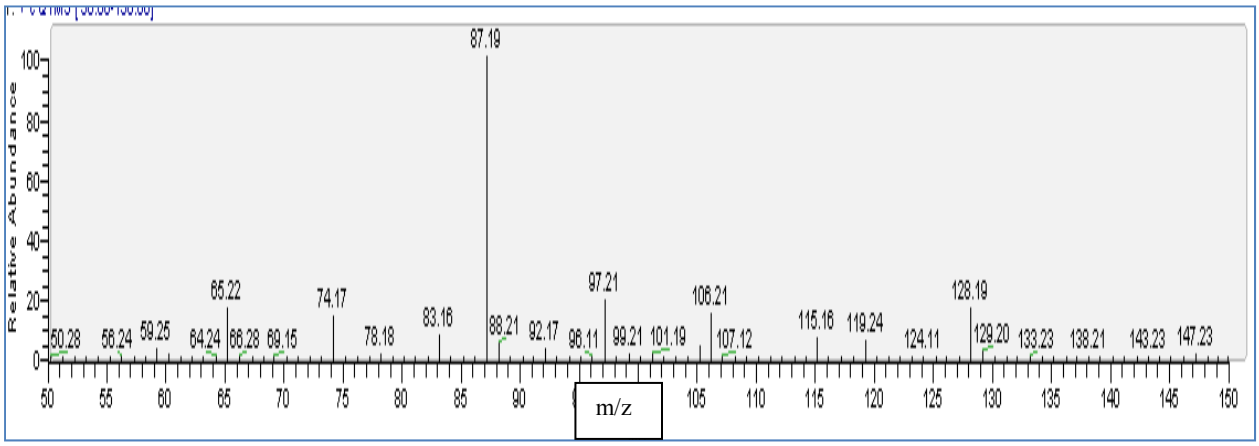

Figure 20: Chromatogram of the reaction product of 8 m loaded PZ and 50 mmol/kg $NaNO_2$ at 60 °C

Analysis of the MS chromatogram of specific samples shows that the concentration of MNPZ and DNPZ is very low (Figure 21).

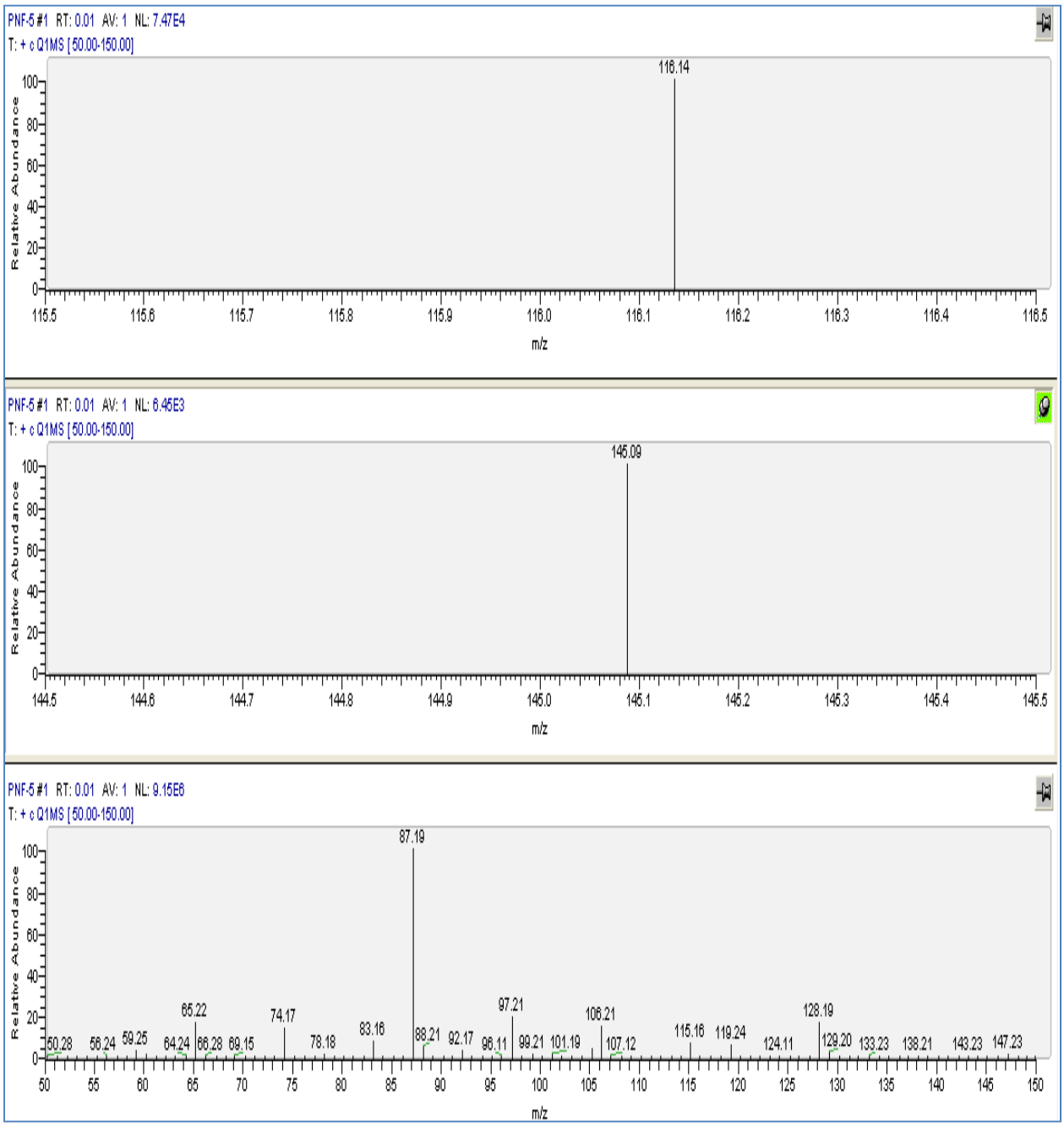

Figure 21: Concentrations of MNPZ and DNPZ in reaction products of 8 m loaded PZ and 50 mmol/kg nitrite at 60 °C

The total ion content of the original sample is 9.15E6. By calculating the ratio of MNPZ and DNPZ ion content to the total ion content of the sample, the concentration of MNPZ and DNPZ can be obtained, which for this sample, is 0.05 ppm (4.35E-4 mM)MNPZ and 0.004 ppm (2.77E-5 mM) DNPZ.

Further studies are being done to obtain a calibration curve that will show the concentration of different species in an unknown sample using the MS data.

Note that the amount of MNPZ and DNPZ in the sample of the reaction products of 8 m loaded PZ and 50 mmol/kg $NaNO_2$, is related to the reaction between PZ and a high concentration of nitrite.

Detecting MNPZ and DNPZ in aqueous PZ using HPLC with UV detection

A new detection method has been applied to standard solutions of MNPZ, DNPZ, and a solution of PZ containing MNPZ and DNPZ using HPLC. The best method is to use standard reverse phase 5% Acetonitrile - 50% Acetonitrile in water buffered with ammonium carbonate to detect standard MNPZ and DNPZ in a solution of methanol. Studies are under development to build calibration curve for detecting MNPZ and DNPZ in unknown samples.

Primary results show that MNPZ and DNPZ are detectable with this HPLC method but PZ is not. Figure 25 shows a chromatogram of a sample containing MNPZ, DNPZ, and PZ. MNPZ gives a better detection peak while DNPZ has a wider peak, which might be because of some impurities in DNPZ standards.

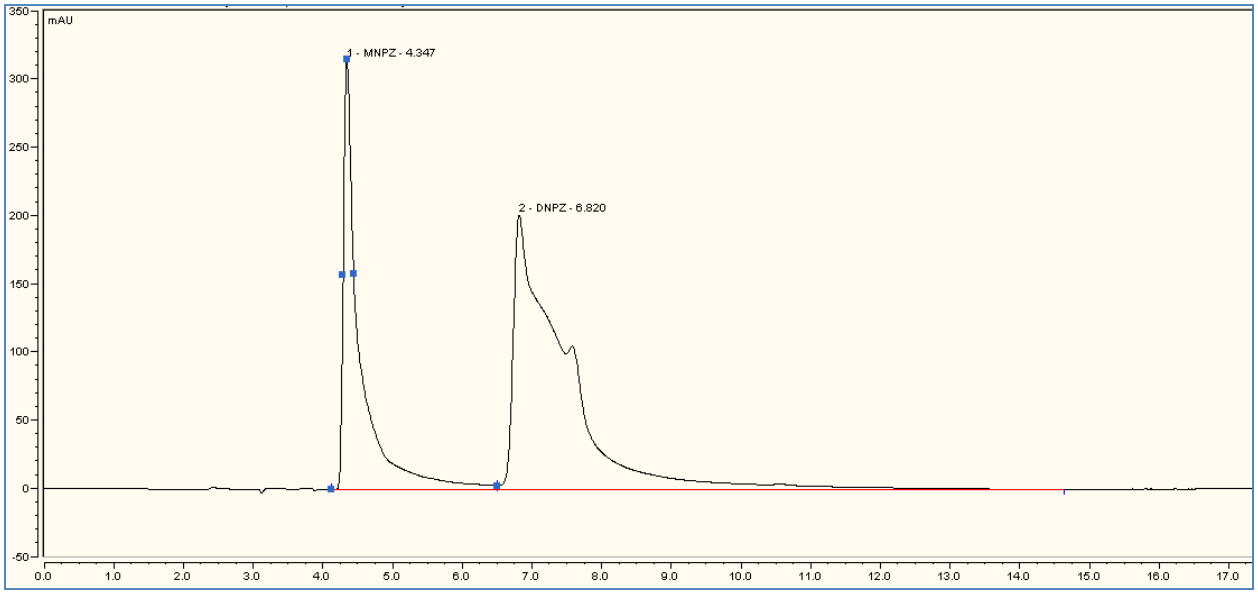

Figure 22: Chromatogram of 500 ppm of MNPZ, DNPZ, and PZ, using HPLC

Comparing the results of LC-MS and HPLC for unknown samples

Samples were injected into both LC-MS and HPLC to compare the analysis and select the more accurate way to detect and measure nitrosopiperazine.

Figure 26 shows the results of samples from high gas flow experiments at the beginning, middle, and end of the course of experiments. There are three clear peaks that show PZ, MNPZ, and DNPZ. Chromatograms show evidence of MNPZ and DNPZ, but by developing the reaction, MNPZ and DNPZ disappear. Applying the peak area of these results and the calibration curves show that the concentration of MNPZ and DNPZ is very low and less than 6x10-5 mmol/kg at the beginning.

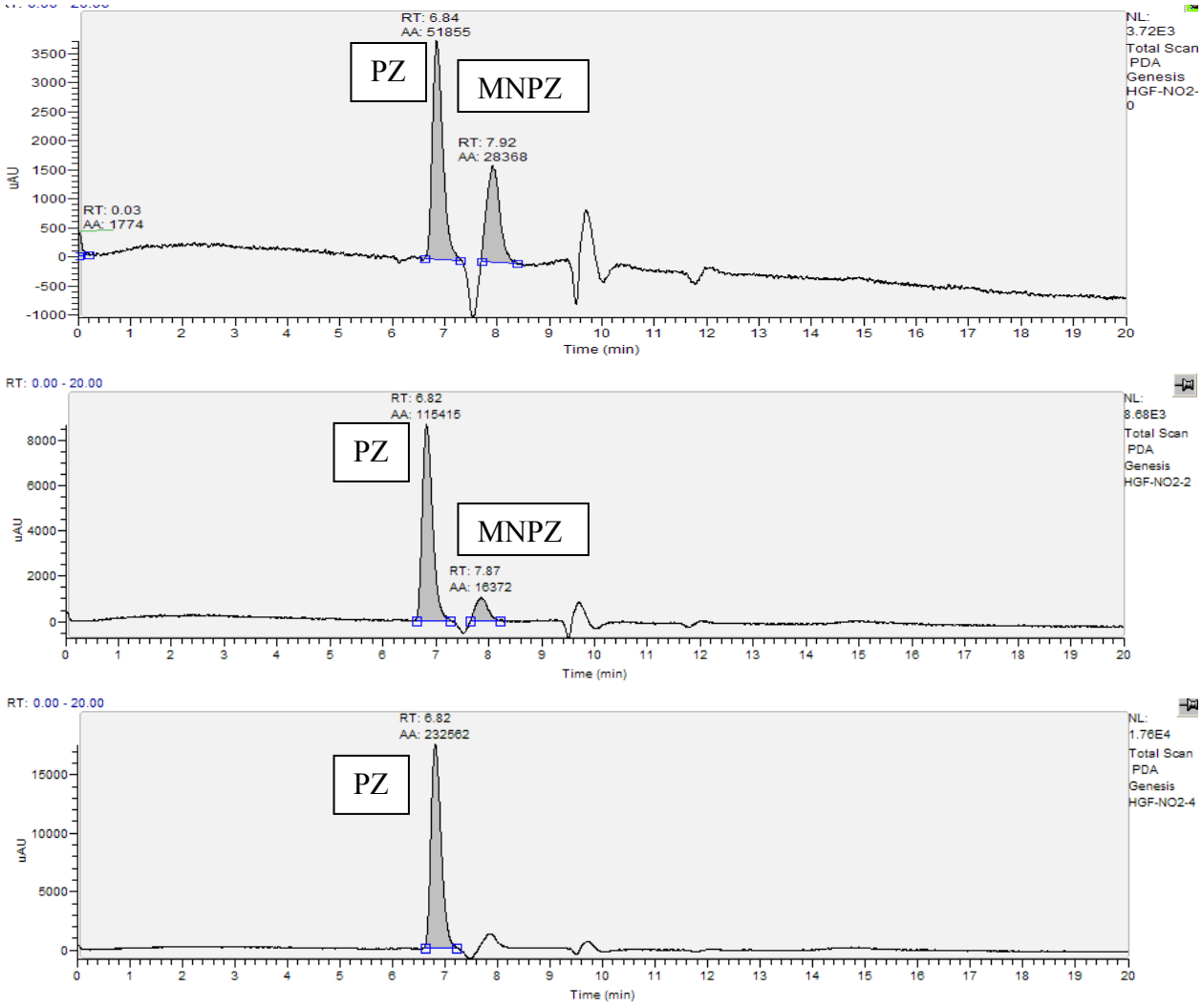

Figure 23: Chromatogram of reaction products of HGF experiments at the t = 0, 3, and 5 days of the reaction, analyzed by LC-MS

Figure 24 shows the same samples as Figure 5 but analyzed by HPLC. HPLC shows good response to standard MNPZ, but as shown in Figure 8, it does not have the accuracy of LC-MS.

HPLC does show the production of an unknown component during the reaction which has a retention time close to that of MNPZ and DNPZ. Since this could be something other than MNPZ or DNPZ, another analytical method (MS) should be used to identify the new product.

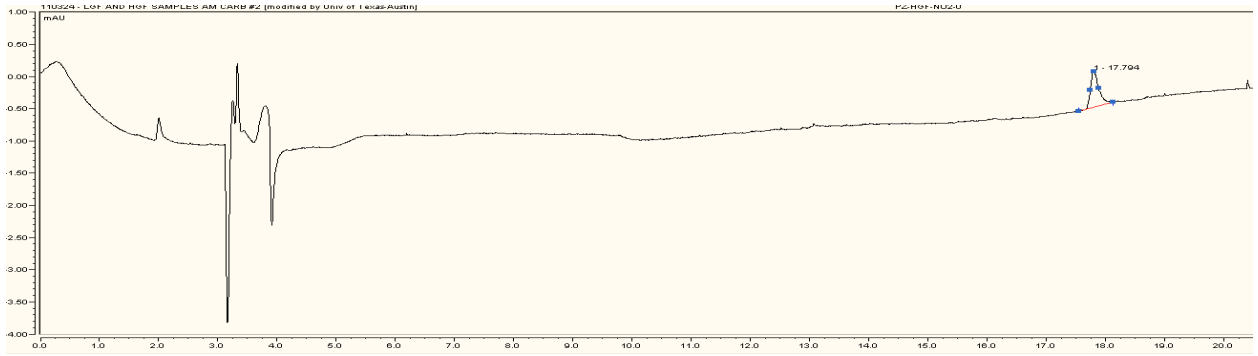

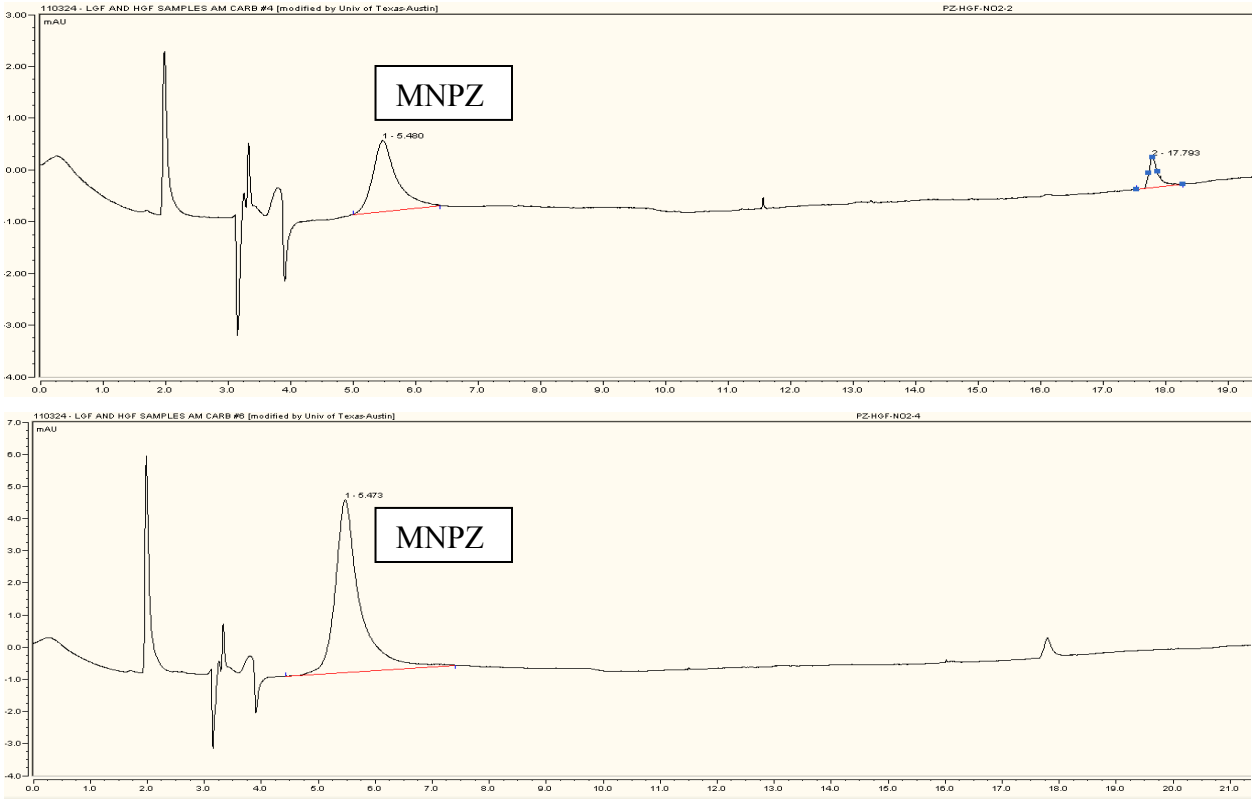

Figure 24: Chromatogram of reaction products of HGF experiments at t = 0, 3, and 5 days, analyzed by HPLC/UV

The same analysis has been done for the low gas flow experiment (Figures 25, 26).

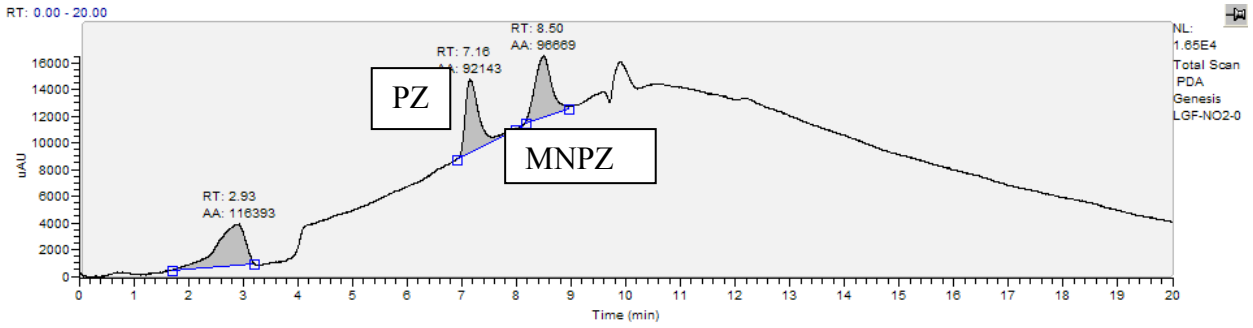

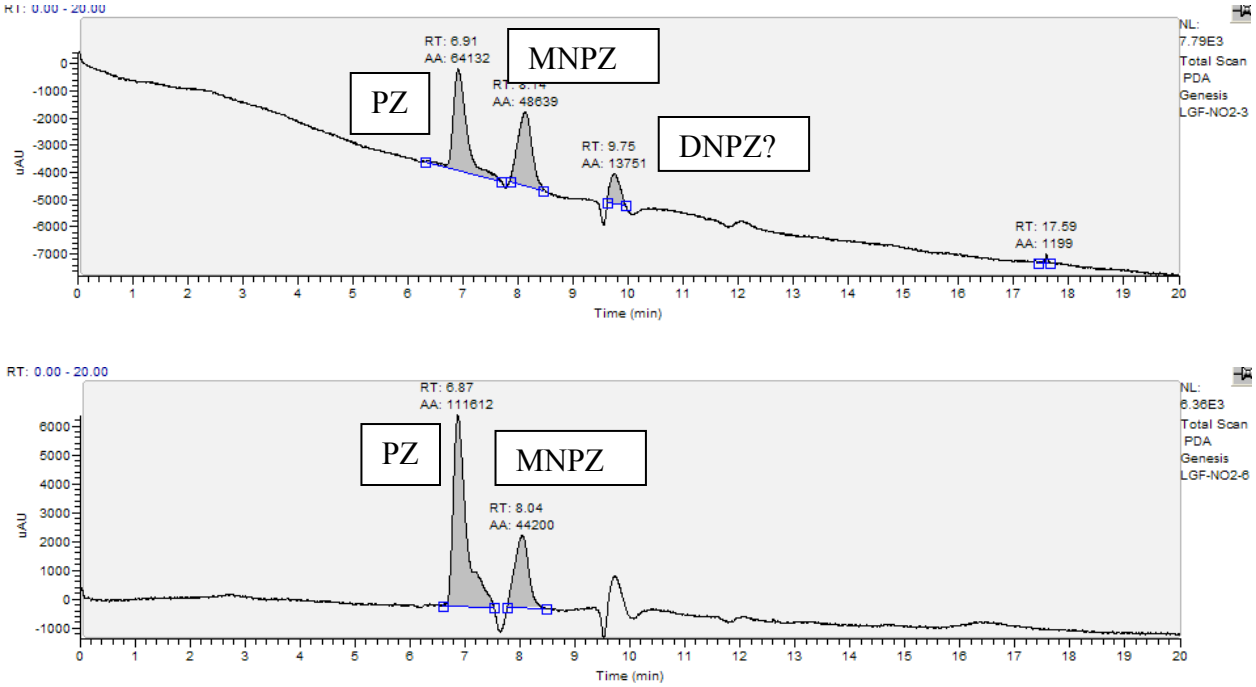

Figure 25: Chromatogram of reaction products of LGF experiments at the t = 0, 3, and 15 days of reaction, analyzed by LC-MS. as before, show the times

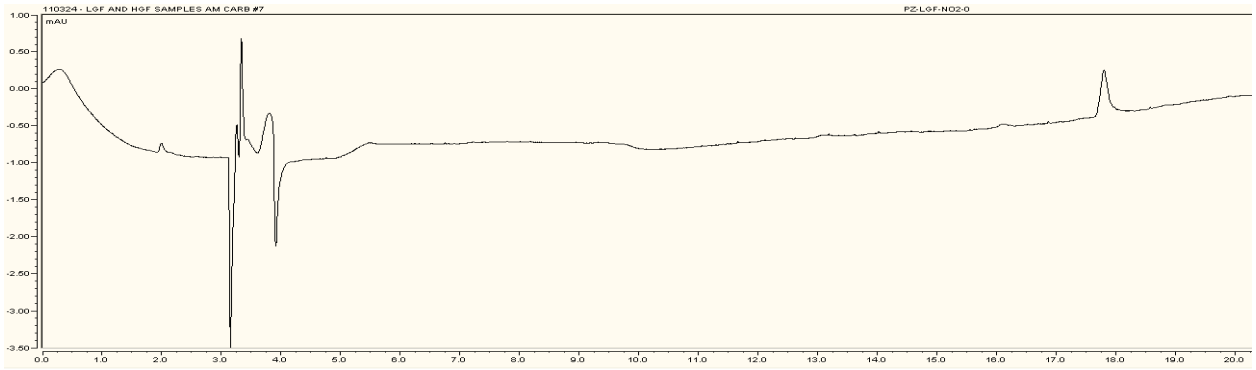

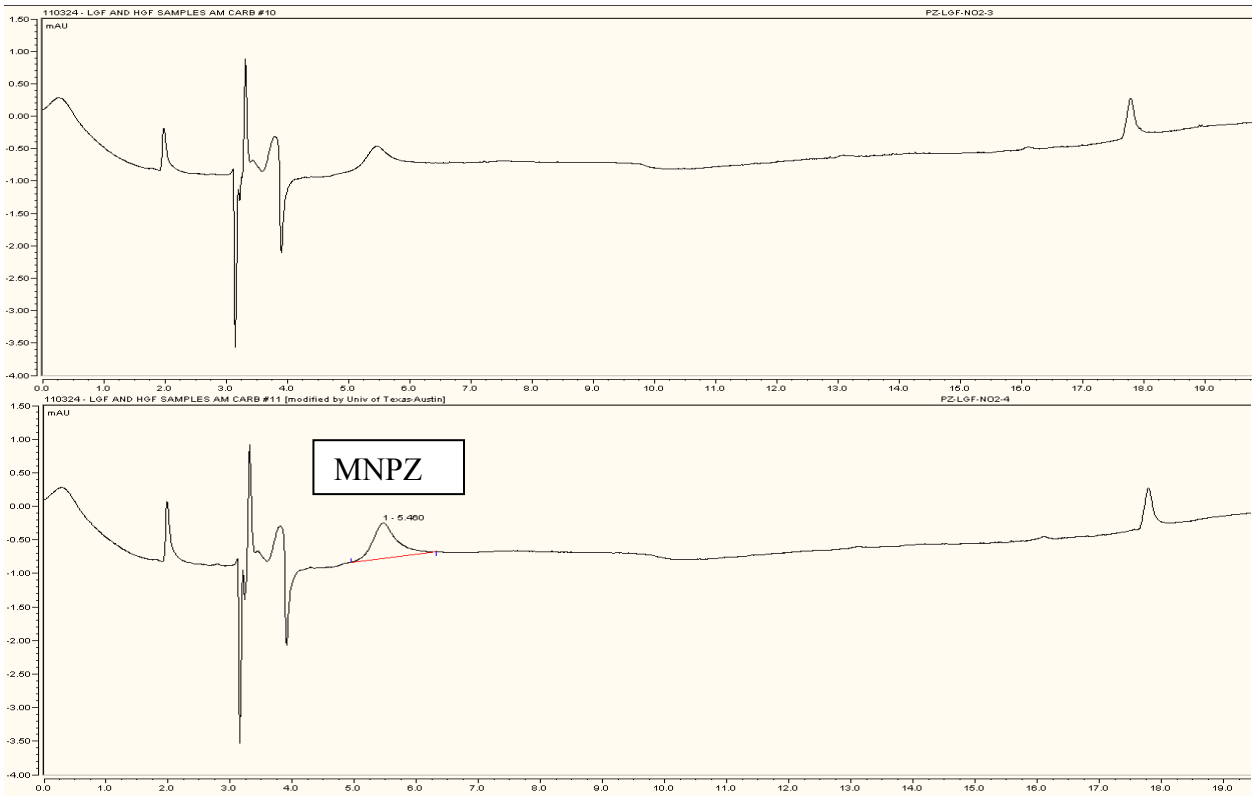

Figure 26: Chromatogram of reaction products of LGF experiments at the t = 0, 3, and 15 days of reaction, analyzed by HPLC

Appendix B

High temperature Data

8 m PZ+50 mmol/kg Nitrite + 0.3 mole CO_2/Equiv N T = 100 °C		
Time (days)	**Nitrite (mmol/kg)**	**MNPZ (mmol/kg)**
0.00	45.63	0.00

0.04	32.51	9.65
0.13	21.91	20.90
0.21	14.25	25.91
0.29	10.12	26.73
0.63	8.58	28.12
1.00	4.66	16.41
7.00	2.09	13.13
15.75	0.54	11.64

8 m PZ+50 mmol/kg Nitrite + 0.3 mole CO_2/Equiv N T = 135 °C		
Time (days)	**Nitrite (mmol/kg)**	**MNPZ (mmol/kg)**
0.00	45.63	0.00
0.04	30.29	40.32
0.21	2.70	37.82
0.29	1.53	32.58
0.63	1.36	14.69
1.00	1.31	1.77
7.00	0.56	0.00
15.75	0.35	0.00

8 m PZ+50 mmol/kg Nitrite + 0.3 mole CO_2/Equiv N T = 150 °C		
Time (days)	**Nitrite (mmol/kg)**	**MNPZ (mmol/kg)**
0	45.63	0.00
0.04	0.94	39.66
0.21	0.66	26.26
0.29	0.66	25.04
0.63	0.62	4.03
1	0.46	0.00
7	0.44	0.00
15.8	0.29	0.00

8 m PZ+50 mmol/kg Nitrite + 0.2 mole CO_2/Equiv N T = 100 °C		
Time (days)	**Nitrite (mmol/kg)**	**MNPZ (mmol/kg)**
0.00	45.68	0.00
0.04	30.17	0.00
0.63	NA	42.30
1	7.77	27.58
2	3.2	24.97
3	1.86	22.74

8 m PZ+50 mmol/kg Nitrite + 0.2 mole CO_2/Equiv N T = 135 °C		
Time (days)	**Nitrite (mmol/kg)**	**MNPZ (mmol/kg)**
0.00	45.68	0.00
0.02	26.06	0.00
0.08	22.26	46.71
0.17	12.98	43.45
0.33	5.69	39.32
0.50	3.49	30.27
1	0.41	4.03
2	NA	3.93
3	0.09	3.16

8 m PZ+50 mmol/kg Nitrite + 0.2 mole CO_2/Equiv N T = 150 °C		
Time (days)	**Nitrite (mmol/kg)**	**MNPZ (mmol/kg)**
0.00	45.68	0.00

0.02	18.05	42.88
0.08	16.1	34.81
0.17	14.68	31.31
0.33	6.75	21.86
1	0.08	4.78
2	NA	0.00
3	0.02	0.00

8 m PZ+50 mmol/kg Nitrite + 0.1 mole CO_2/Equiv N T = 100 °C		
Time (days)	**Nitrite (mmol/kg)**	**MNPZ (mmol/kg)**
0.00	45.63	0.00
0.04	42.07	0.00
0.33	35.96	NA
0.50	28.87	35.87
1	23.22	41.55
2	10.42	36.15
3	6.73	30.07
3.5	1.8	27.68

8 m PZ+50 mmol/kg Nitrite + 0.1 mole CO_2/Equiv N T = 135 °C		
Time (days)	**Nitrite (mmol/kg)**	**MNPZ (mmol/kg)**
0.00	45.63	0.00
0.02	37.69	8.78
0.04	29.79	14.08
0.08	25.38	33.61

0.17	8.62	42.84
0.25	8.52	37.26
0.33	4.29	5.38
0.50	3.44	5.70
1	0.34	4.17
2	0.16	3.66

8 m PZ+50 mmol/kg Nitrite + 0.1 mole CO_2/Equiv N T = 150 °C		
Time (days)	**Nitrite (mmol/kg)**	**MNPZ (mmol/kg)**
0.00	45.63	0.00
0.02	28.81	3.41
0.04	26.62	22.89
0.13	25.38	37.95
0.21	8.52	34.07
0.33	4.45	32.66
0.50	4.29	0.18
1.00	1.47	0.06
2.00	1.67	0.00
3.00	0.47	0.00

2 m PZ+50 mmol/kg Nitrite + 0.3 mole CO_2/Equiv N T = 100 °C		
Time (days)	**Nitrite (mmol/kg)**	**MNPZ (mmol/kg)**
0.00	48.70	0.00
0.04	25.60	4.50
0.08	20.48	10.33
0.13	15.53	15.67
0.17	15.46	20.79
1.00	11.87	40.22

2.00	8.63	36.66

2 m PZ+50 mmol/kg Nitrite + 0.3 mole CO_2/Equiv N T = 135 °C		
Time (days)	**Nitrite (mmol/kg)**	**MNPZ (mmol/kg)**
0.00	48.70	0.00
0.04	14.40	31.75
0.08	2.30	29.27
0.13	1.80	29.96
0.17	1.63	29.09
1.00	1.43	24.61
2.00	1.22	12.31

2 m PZ+50 mmol/kg Nitrite + 0.3 mole CO_2/Equiv N T = 150 °C		
Time (days)	**Nitrite (mmol/kg)**	**MNPZ (mmol/kg)**
0.00	48.70	0.00
0.04	1.55	34.29
0.08	0.47	33.74
0.13	NA	NA
0.17	0.46	32.04
1.00	0.44	12.73

2.00	0.42	7.05

References

Bonnet R, Nicolaidou P. "Nitrite and the environment, the nitrosation of a-amino acid derivatives." *Heterocyles*. 1977;7:637–659.

Keefer LK, Roller PP. "N-Nitrosation by Nitrite Ion in Neutral and Basic Medium." *Science*. 1973;181:1245–1247.

Kunisaki N, Hayashi M. "Formation of N-Nitrosamines from Secondary Amines and Nitrite by Resting Cells of Escherichia coli B." *Appl Envir Microbio*. 1978;37(2):279–282.

Lijinsky W, Keefer L, Loo J. "The preparation and properties of some nitrosamino acids." *Tetrahedron*. 1970;26:5137.

Mirvish S, Wallcave L, Eagen M. "Ascorbate-Nitrite Reaction: Possible Means of Blocking the Formation of Carcinogenic N-Nitroso Compounds." *Science*. 1972;177(4043):65–68.

Mirvish S. "Formation of N-nitroso compounds chemistry kinetics and in-vivo occurrence." *Toxical Appl Pharmacol*. 1975;3(1):325.

Roller PP, Keefer LK, Slavin BW. "N-Nitroso compounds: Analysis, Formation and Occurance." IRAC Publication 31, Lyon, 1980;119.

United States Pharmacopeia XXIV. National Formulary 19, Rockville, USP Convention, Washington; 2000;1341 & 2235.

Ziebarth D, Bogovski P, Walker AE. "N–nitroso Compounds in the Environment." IARC, 1975;137.

Thermal Degradation of Piperazine Blends

Quarterly Report for October 1 – December 31, 2011

By Omkar Namjoshi

Supported by the Luminant Carbon Management Program

Department of Chemical Engineering

The University of Texas at Austin

January 31, 2012

Abstract

Thermal degradation of 8 m 1,4-diaminobutane (DAB, previously referred to as Amine Y) and 8 m 3-oxapentane-1,5-diamine (ODA) previously referred to as Amine Z) at a CO_2 loading of 0.4 mol CO_2/mol alkalinity was studied at 175 ^oC.

The degradation rate of loaded 8 m ODA is fairly close that of loaded 6 m PZ/2 m ODA. This confirms that blend synergism (enhancement of degradation rates) is not taking place with ODA. On the other hand, the degradation rate of loaded 8 m DAB is about half that of 6 m PZ/2 m DAB.

The primary degradation pathway of DAB appears to be ring closing. The ring closing mechanism does not appear to be the dominant degradation pathway for ODA.

Background and Motivation

PZ is currently considered to be a state-of-the-art solvent for use in CO_2 capture from flue gas, with high absorption rate, high working capacity, and negligible oxidative and thermal degradation compared to other solvents. However, it has a limited solid solubility window somewhat close to its operating range and can cause precipitation issues and problems for plant operators. Because of this limitation it is desirable to develop blends of other amines with PZ that eliminate the solid solubility limitations without negatively impacting other solvent properties.

In the previous quarter, the degradation of 6 m PZ/2 m 1,4-diaminobutane (Amine Y) and 6 m PZ/2 m 3-oxapentane-1,5-diamine (Amine Z) at 175 ^oC was analyzed. Blend synergism from a degradation standpoint was not observed in either of the blends. In this quarter the degradation of 8 m 1,4-diaminobutane (DAB) and 8 m 3-oxapentane-1,5-diamine (ODA) was analyzed to better understand why blend synergism is not observed.

Experimental

Experimental techniques are the same as described in the third quarterly report.

Piperazine (99%) was supplied by Sigma-Aldrich. 1,4-diaminobutane (99%) was supplied by Acros Organics. 3-oxapentane-1,5-diamine (95.2%) was provided by an amine supplier.

Results and Discussion

Thermal Degradation – 8 m 1,4-diaminobutane

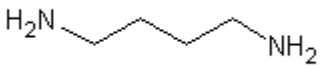

Figure 1: Structure of 1,4-diaminobutane

8 m 1,4-diaminobutane was degraded at 175 °C over 69 days. Concentration of the amine as a function of time is plotted below. The degradation rate was approximated using first order kinetics.

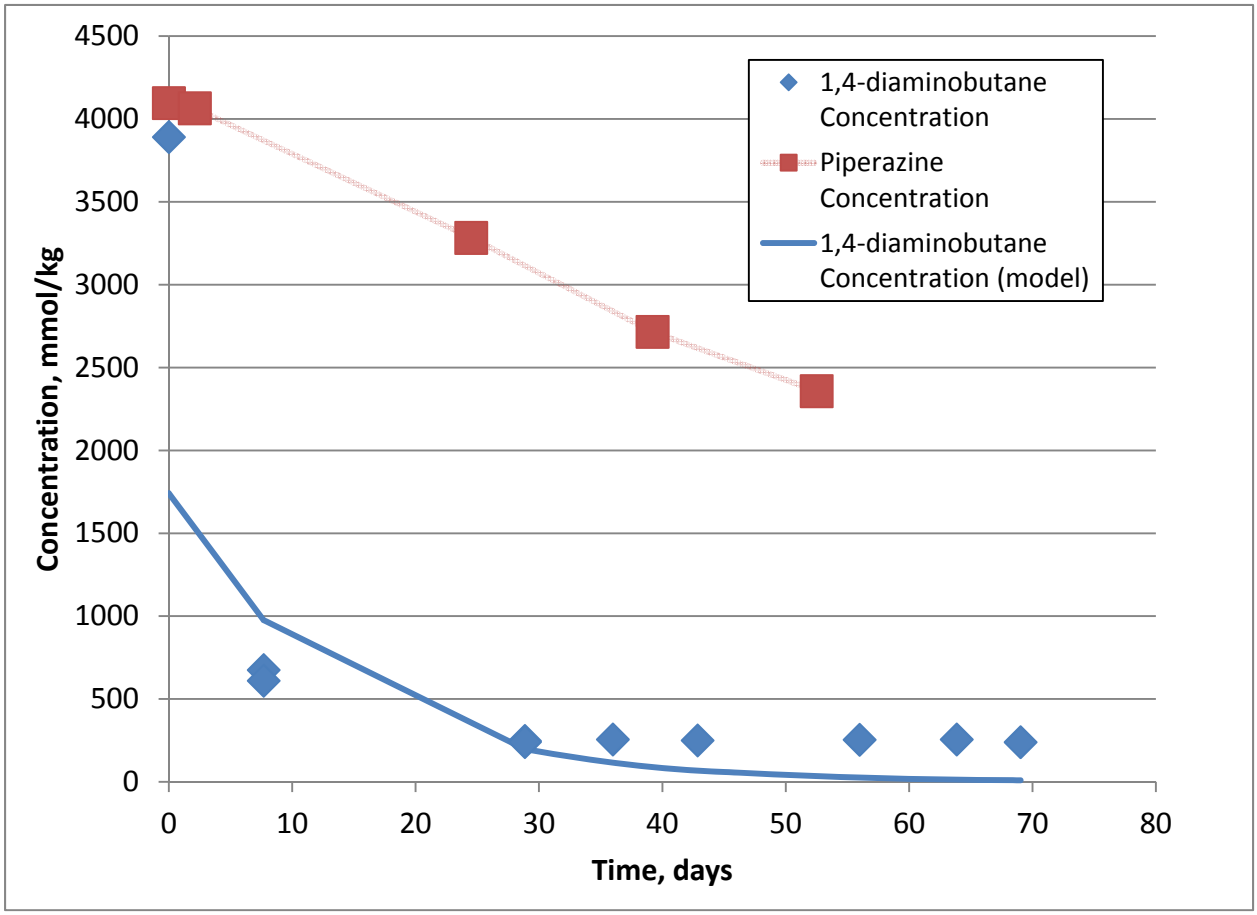

Figure 2: Degradation of 8 m 1,4-diaminobutane at 175 °C. The degradation of 8 m PZ is from Freeman (2011) and at a loading of 0.3 mol CO_2/mol alkalinity.

Unlike PZ, the degradation of DAB is fairly rapid; using first order kinetics, it has a degradation rate constant of $750*10^{-9}$ 1/sec, compared to $130*10^{-9}$ 1/sec for PZ. Only the data for the first two weeks are considered for the degradation analysis as the concentration of DAB appears to reach a constant value after two weeks at 175 °C. This behavior was not seen when 1,4-diaminobutane was blended with PZ; all of the DAB degraded after two weeks when blended with piperazine.

The chromatogram of a sample after 1 week at 175 ^{o}C is included below.

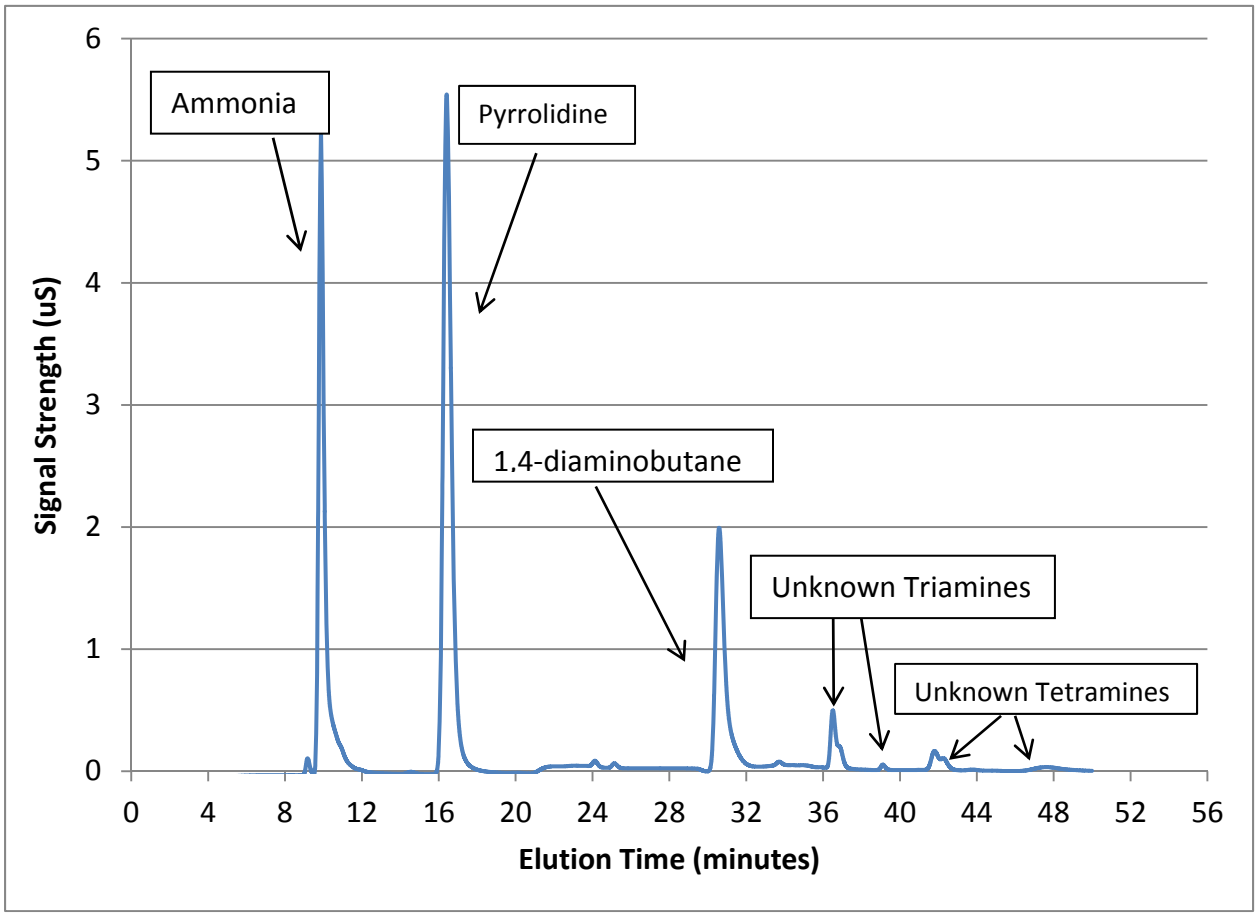

Figure 3: Chromatogram showing degradation products of 1,4-diaminobutane after one week. Temperature was held at 175 ^{o}C with initial loading equal to 0.4 mol CO_2 / mol alkalinity.

The primary degradation products appear to be pyrrolidine and ammonia. Minor degradation products include unknown triamines and tetramines; these are probably degradation products between DAB and itself, pyrrolidine and itself, or DAB and pyrrolidine.

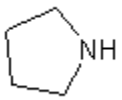

Figure 4: structure of pyrrolidine

A proposed degradation pathway is given in the figure below, in which the nitrogen on one end of the molecule attacks the alpha carbon of the amino group on the other end of the molecule, creating a cyclic amine and forming ammonia in the process.

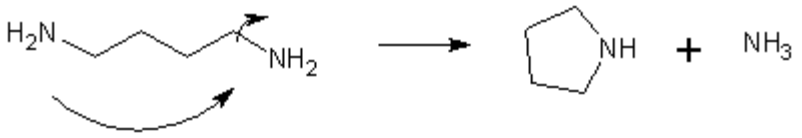

Figure 5: Proposed degradation pathway of 1,4-diaminobutane to pyrrolidine and ammonia

Figure 6 shows a plot of the concentration of pyrrolidine over time and concentration of 1,4-diaminobutane over time. It appears that after about two weeks the concentrations of 1,4-diaminobutane and pyrrolidine stabilize and approach an equilibrium.

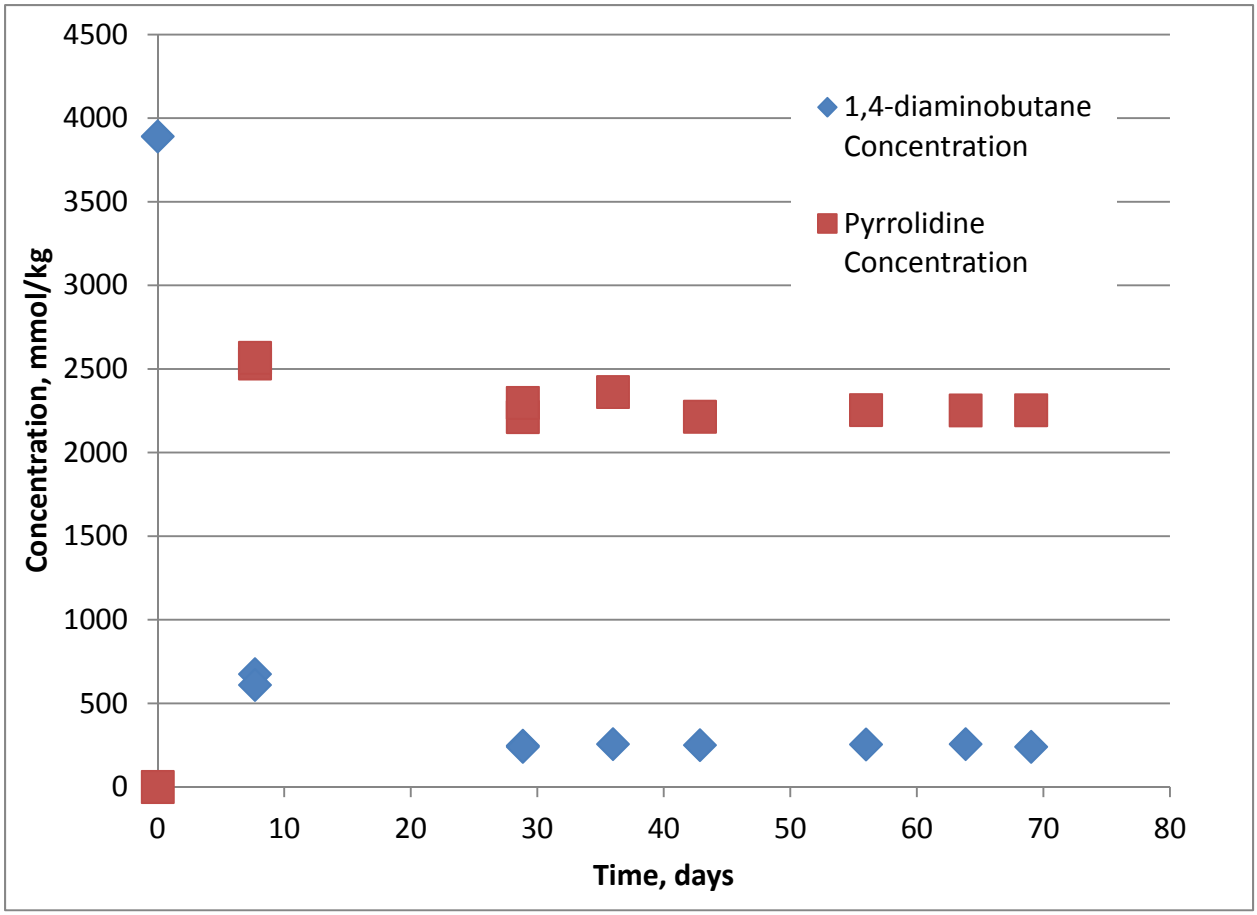

Figure 6: Degradation of 8 m DAB at 175 °C

Figure 7 shows the concentration of formate salts over time. Other salts (oxalates, nitrates) were present but below the detection range of the instrument. The samples were not hydrolyzed with sodium hydroxide prior to analysis. There is scatter in the data, but the free formate seems to increase steadily with time. At a maximum value of 12 mmol/kg solution, it does not represent a significant fraction of the degraded DAB, 3500 mmol/kg.

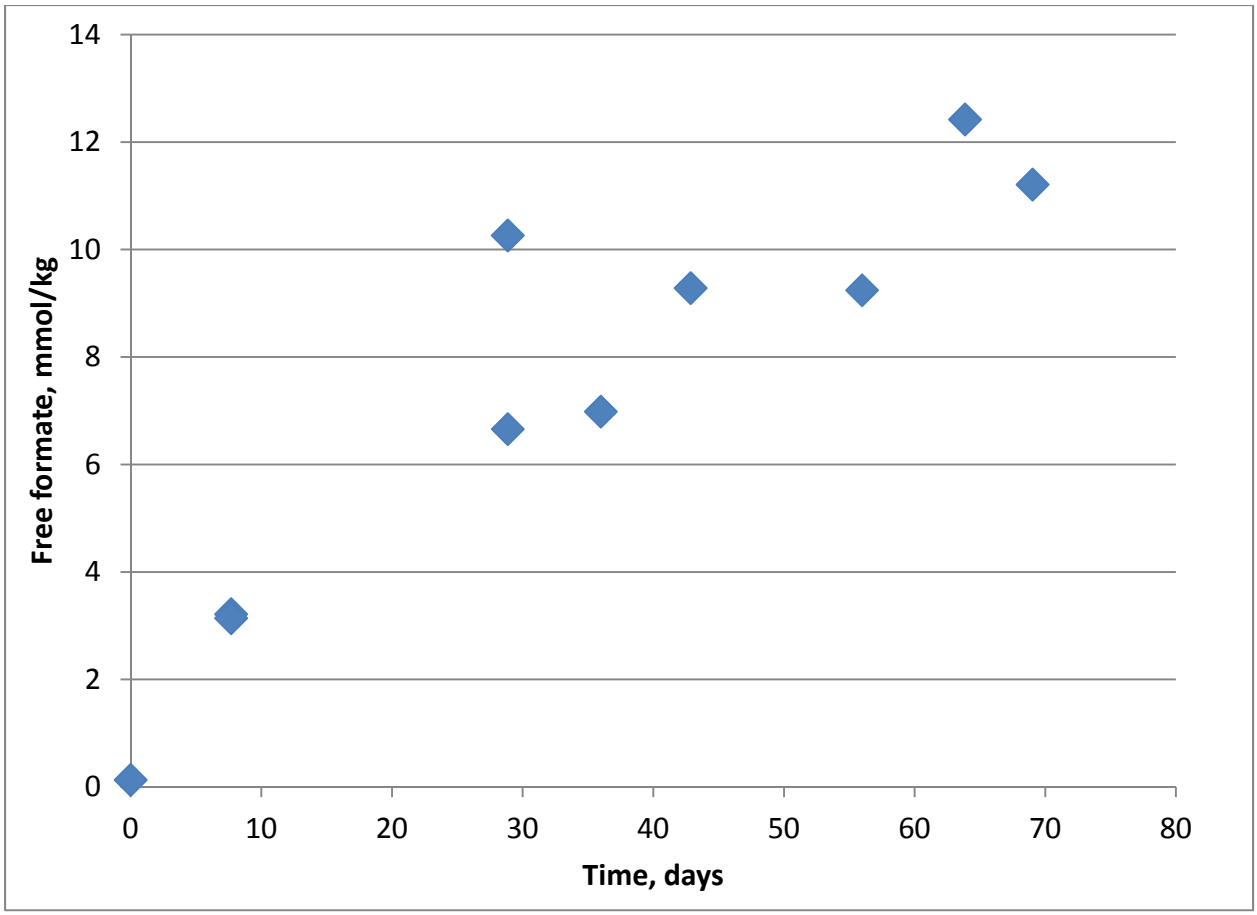

Figure 7: Formation of free formate over time in 8 m DAB at 175 °C. Samples were not hydrolyzed.

Thermal Degradation – 8 m 3-oxapentane-1,5-diamine

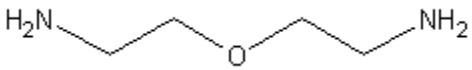

Figure 8: Structure of 3-oxapentane-1,5-diamine

8 m ODA was degraded at 175 °C over 51 days. The concentration of the amine as a function of time is plotted below.

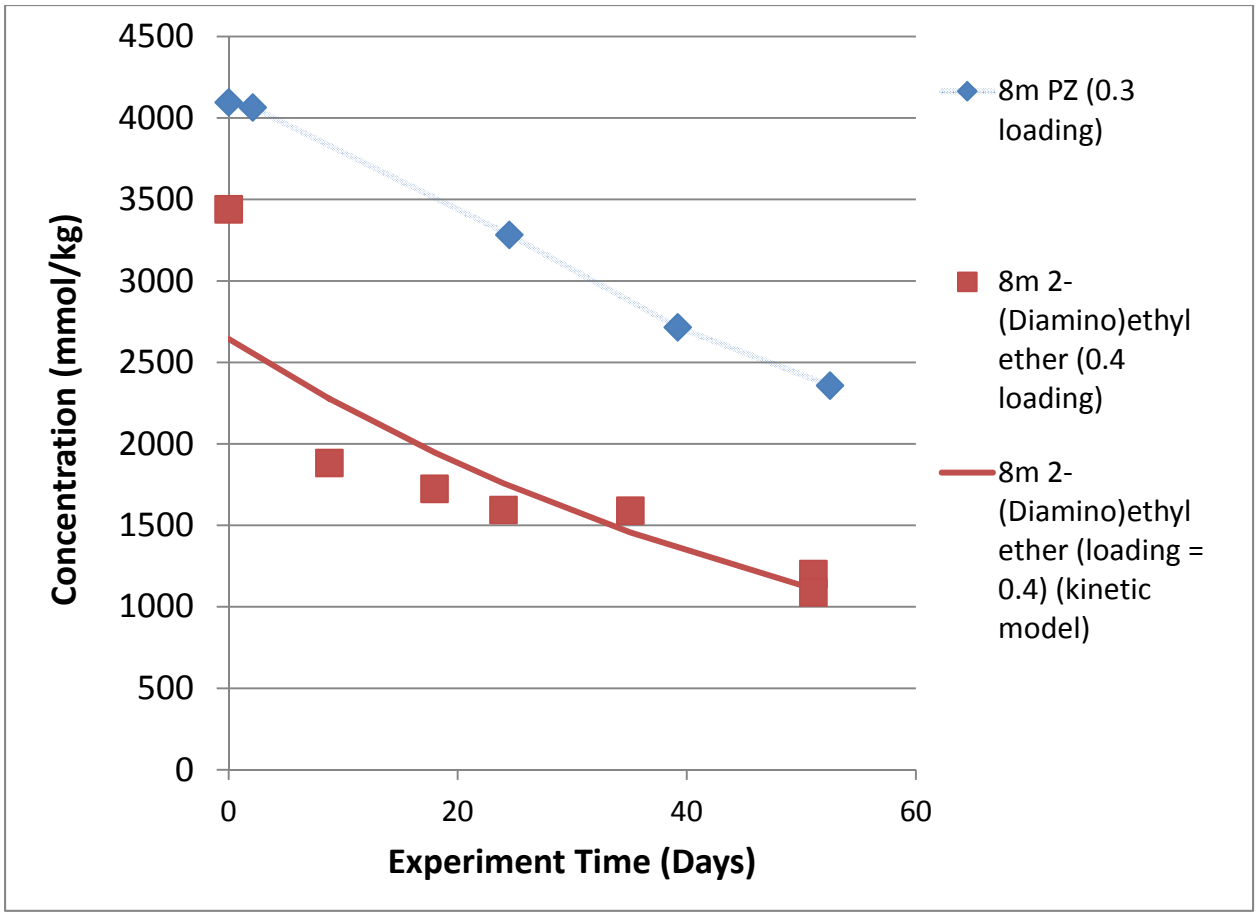

Figure 9: Degradation of 8 m 3-oxapentane-1,5-diamine at 175 ^{o}C. The degradation of 8 m PZ is from Freeman (2011).

Like PZ, ODA is resistant to thermal degradation with a first order degradation rate constant of about $200*10^{-9}$ 1/sec. For comparison, the first order degradation rate constant of 8 m PZ is about $130*10^{-9}$ 1/sec. The first order degradation rates of PZ and ODA when in a 6 m PZ/2 m ODA blend were about $130*10^{-9}$ 1/sec and $130*10^{-9}$ 1/sec respectively, which suggests that blend synergism is not taking place.

Key degradation products likely consist of morpholine, ammonia, an unknown triamine, and an unknown tetramine. Like 1,4-diaminobutane, these degradation products might be between ODA and itself, ODA and morpholine, or morpholine and itself. The elution times of these products are presented in the chromatogram in Figure 3.

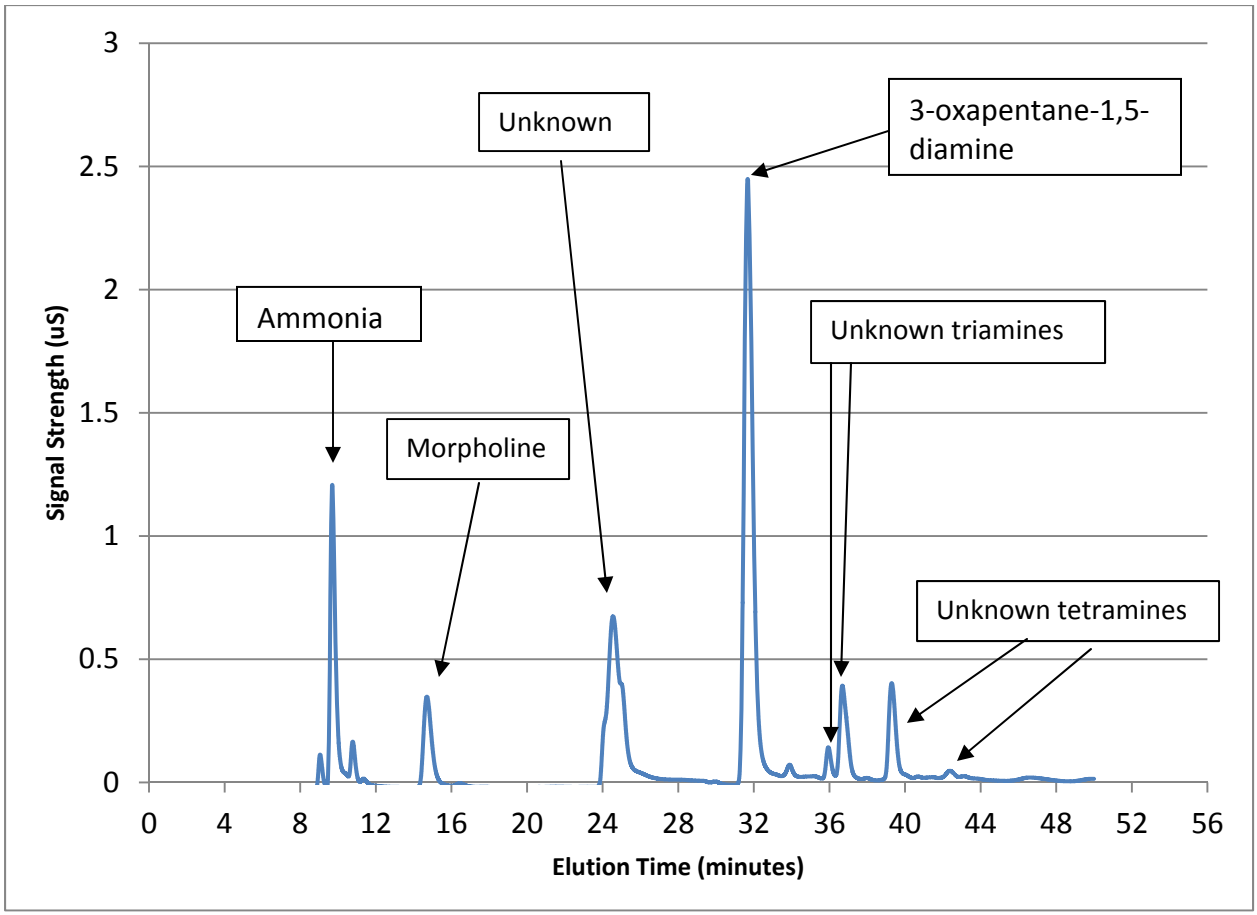

Figure 10: Chromatogram showing degradation products of 3-oxapentane-1,5-diamine after one week. Temperature was held at 175 ^{o}C with initial loading equal to 0.4 mol CO_2 / mol alkalinity.

Morpholine might be formed from the ring closing of ODA in a manner similar to how 1,4-diaminobutane ring closes to form pyrrolidine:

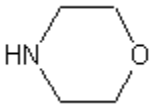

Figure 11: Morpholine

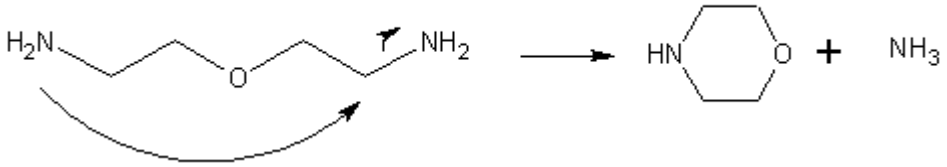

Figure 12: Proposed degradation pathway of 3-oxapentane-1,5-diamine to morpholine and ammonia

Future Work

Additional work will consist of completing the anion analysis for both DAB and ODA, and identifying unknown degradation products using either IC/MS or LC/MS methods. Degradation pathways will be proposed when unknown degradation products are determined. Additional amines will be studied to determine what properties of the amine promote degradation via the ring closing mechanism.

Conclusions

- 8 m 1,4-diaminobutane at a loading of 0.4 mol CO_2/mol alkalinity has a degradation rate of around $750*10^{-9}$ 1/sec at 175 ^{o}C.
- 1,4-diaminobutane degrades twice as fast when blended with PZ.
- The principal degradation products of 1,4-diaminobutane are ammonia and pyrrolidine.
- Concentrations of 1,4-diaminobutane appear to reach equilibrium with pyrrolidine after two weeks. This behavior was not seen when 1,4-diaminobutane was blended with PZ.
- A ring closing mechanism is likely the principal degradation pathway in which 1,4-diaminobutane thermally degrades.
- 8 m 3-oxapentane-1,5-diamine at a loading of 0.4 mol CO_2/mol alkalinity has a degradation rate of around $200*10^{-9}$ 1/sec at 175 ^{o}C.
- Degradation rates of 3-oxapentane-1,5-diamine are not enhanced when blended with PZ.
- The ring closing mechanism does not appear to be the principal degradation pathway in which 3-oxapentane-1,5-diamine thermally degrades.

References

Freeman SA. *Thermal Degradation and Oxidation of Aqueous Piperazine for Carbon Dioxide Capture*. The University of Texas at Austin. Ph.D. Dissertation. 2011.

A Piperazine-based Blend as a Solvent for CO_2 Capture

Quarterly Report for October 1 – December 31, 2011

by Yang Du

Supported by the Luminant Carbon Management Program

Department of Chemical Engineering

The University of Texas at Austin

January 31, 2012

Abstract

The novel piperazine-based blended amine solvent PZ/W is being investigated as a possible alternative to the standard 30 wt % MEA for CO_2 capture from coal-fired flue gas. The solid solubility of PZ/W with variable amine concentration (5/2, 4/2.67, 3/3.33) and 0–3 mol CO_2/mol alkalinity was measured. The viscosity of loaded 5 m PZ/2 m Y blends was measured from 20 to 60 °C. A long-term thermal degradation experiment for 5 m PZ/2 m Y with 0.3 mol CO_2/mol alkalinity is being conducted at 150 °C and 175 °C.

PZ/W has a greater solid solubility than pure PZ with equal total alkalinity. The highest CO_2 loading at room temperature and 1 atm is 0.39 mol/mol alkalinity for 5 m PZ/2 m Y, 0.38 mol/mol alkalinity for 4 m PZ/2.67 m Y, and 0.38 mol/mol alkalinity for 3 m PZ/3.33 m Y. No precipitates were observed at high CO_2 loading. The viscosity of 5 m PZ/2 m Y blend is comparable to that of8 m PZ. No data are yet available for thermal degradation.

Introduction

Concentrated piperazine (PZ) was proposed as a possible alternative to the standard 30 wt % MEA for CO_2 capture from coal-fired flue gas (Freeman, 2011). While PZ has a higher CO_2 absorption rate, higher CO_2 capacity, and higher resistance to degradation than 30 wt % MEA, the application of concentrated PZ in industry may be limited by solid precipitation at both lean and rich CO_2 loading as well as by high viscosity (Freeman, 2011).

Blending solvents already in use is one approach to combine desirable characteristics (Appl et al., 1982). PZ with low concentration (below 2.0 or 2.5 molality) has been used in blended systems as a promoter to enhance the rate of CO_2 absorption in systems with advantageous solution characteristics but low absorption rates (Bishnoi, 2000; Cullinane et al., 2007).

A novel PZ-based blend (PZ/W) is being investigated this quarter to remediate the precipitation of pure concentrated PZ without sacrificing its CO_2 capacity and absorption rate as well as resistance to degradation.

Experimental Methods

Solid solubility of PZ/W

Solid solubility measurements were based on visual observations and the method has been described in detail by Freeman (2011). Transition temperatures of PZ/W blends with variable concentration (5/2, 4/2.67, 3/3.33) and CO_2 loading of 0–3 mol/mol alkalinity were measured.

Viscosity

Viscosity measurements were done with 5 m PZ/2 m Y. The method has also been described by Freeman. Viscosity under shear rate from 100 s^{-1} to 1000 s^{-1} was measured and the average value and standard deviation calculated from the 10 individual measurements will be reported.

Thermal degradation

Thermal degradation experiments are being conducted for 5 m PZ/2 m Y. Experimental apparatus, procedure, and analytical methods were described in detail by Davis (2009). 5 m PZ/2 m Y was sealed in 10 mL stainless steel cylinders. The cylinders were placed in forced convection ovens at 150 °C and 175 °C for extended periods and removed for analysis.

Results and discussion

Solid solubility of PZ/W

The transition temperatures of PZ/W blends with variable concentration (5/2, 4/2.67, 3/3.33) over a range of CO_2 loading from 0 to 3 mol/mol alkalinity are shown in Table 1 and Figure 1. The transition temperature for pure 8 m PZ from Freeman (2011) is also shown in Figure 1 for comparison.

The shapes of the transition temperature curves for the three PZ/W blends are all similar to that of pure 8 m PZ. However, as PZ concentration in a blend decreases, the transition temperature decreases. For 5 m PZ/2 m Y and 4 m PZ/2.67 m Y, a CO_2 loading of approximately 0.20 mol/mol alkalinity is required to maintain a liquid solution without precipitation at room temperature (22 °C), which is lower than 0.25 mol/mol alkalinity required for 8 m PZ. For 3 m PZ/3.33 m Y, a CO_2 loading of 0.15 mol/mol alkalinity is enough to keep the blend in liquid form. Unlike 8 m PZ (Freeman, 2011), no precipitates were observed at rich CO_2 loading for the three blends. The maximum rich loading obtained at room temperature and 1 atm was 0.39 mol/mol alkalinity for 5 PZ/2 Y, 0.38 mol/mol alkalinity for 4 PZ/2.67 Y, and 0.38 mol/mol alkalinity for 3 PZ/3.33 Y.

Table 1: Transition temperatures for PZ/W blend

PZ/W (m)	CO_2 (mol/mol alk)	Crystal T (°C)	Melting T (°C)
5/2	0	38.0	40.0
5/2	0.05	36.5	37.0
5/2	0.10	33.0	34.0
5/2	0.15	26.5	31.0
5/2	0.20	19.0	21.5
5/2	0.23	18.0	19.0
5/2	0.25	2.5	4

5/2	0.30	≤0	——
4/(2.67)	0	35.5	36.5
4/(2.67)	0.05	32.0	33.0
4/(2.67)	0.10	28.5	31.0
4/(2.67)	0.15	24.0	25.0
4/(2.67)	0.20	17.5	20.0
4/(2.67)	0.23	8.0	12.0
4/(2.67)	0.25	≤0	——
3/(3.33)	0	33.0	34.0
3/(3.33)	0.05	27.0	31.0
3/(3.33)	0.10	24.0	25.0
3/(3.33)	0.15	18.0	19.0
3/(3.33)	0.20	16.0	16.0
3/(3.33)	0.23	2.5	4.0
3/(3.33)	0.25	≤0	——

——: not measured

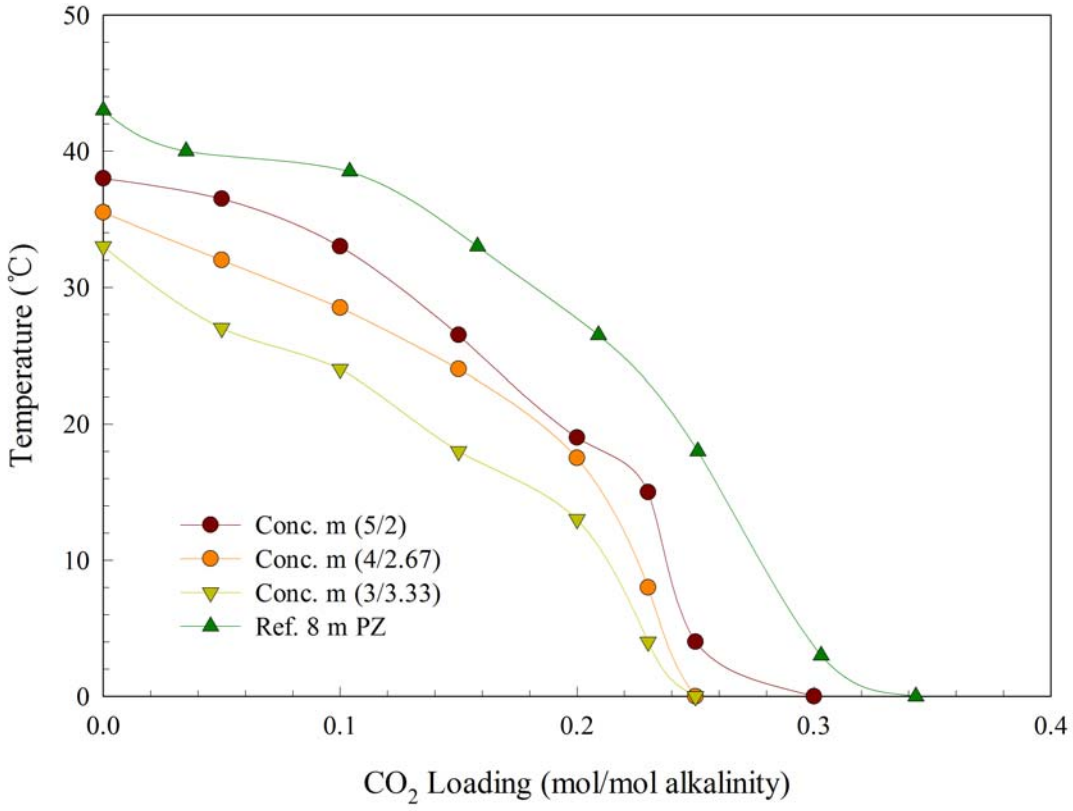

Figure 1: Crystal transition temperatures for PZ/W blend

Viscosity Measurements

Viscosity measurements of 5 m PZ/2 m Y with CO_2 loading of 0.2 and 0.3 mol/mol alkalinity were conducted at 20 °C, 40 °C and 60 °C (Table 2). The primary result suggests that the viscosity of the blend is comparable to that of pure 8 m PZ (i.e., 11.96 cP for 5 PZ/2 Y vs. 9.99 cP for 8 m PZ at 0.3 loading and 40 °C). The data also demonstrate the expected trend that viscosity increases with increasing CO_2 concentration and decreasing temperature.

Table 2: Viscosity of 5 m PZ/2 m Y from 20 to 60 °C

CO_2 Loading (mol/mol alk)	Viscosity (cP)		
	20 °C	40 °C	60 °C
0.20	21.92 ± 0.068	9.843 ± 0.082	5.88 ± 0.162
0.30	24.75 ± 0.090	11.96 ± 0.108	7.78 ± 0.720

Thermal Degradation

The experiment tested the degradation of 5 m PZ/2 m Y with a CO_2 loading of 0.3 mol/mol alkalinity at 150 °C and 175 °C. This experiment is slated to continue for 30 weeks at 150 °C and 5 weeks at 175 °C, and is currently in week 2. The results of this experiment will be included in the next quarterly progress report.

Conclusions

PZ/W has a greater solid solubility than PZ. At 20°C, solids form at a CO_2 loading of 0.24 in 8 m PZ, 0.19 in 5 m PZ/2 m Y, and 0.13 in 3 m PZ/3.33 m Y.

No precipitates were observed at greatest CO_2 loading provided by the loader at 1 atm CO_2.

The viscosity of loaded 5 m PZ/2 m Y is comparable to that of loaded 8 m PZ.

Future Work

The thermal degradation experiment that is ongoing will be completed and analyzed in the next quarter. Thermal equilibrium and oxidative degradation experiments will also be performed. A separate effort will be made to conduct a high temperature vapor-liquid equilibrium experiment for PZ/W.

References

Appl M, Wagner U, Henrici HJ, Kuessner K, Volkamer K, Fuerst E. "Removal of CO_2 and/or H_2S and/or COS from Gases Containing These Constituents." BASF GmbH, Germany. US Patent 4,336,233. 1982.

Bishnoi S. *Carbon Dioxide Absorption and Solution Equilibrium in Piperazine Activated Methyldiethanolamine.* The University of Texas at Austin. Ph.D. Dissertation. 2000.

Cullinane JT, Rochelle GT. "Kinetics of carbon dioxide absorption into aqueous potassium carbonate and piperazine." *Ind Eng Chem Res.* 2007;45(8):2531–2545.

Davis JD. *Thermal Degradation of Aqueous Amines Used for Carbon Dioxide Capture.* The University of Texas at Austin. Ph.D. Dissertation. 2009.

Freeman SA. *Thermal Degradation and Oxidation of Aqueous Piperazine for Carbon Dioxide Capture.* The University of Texas at Austin. Ph.D. Dissertation. 2011.

Degradation and Contamination in Amine Solutions for CO_2 Capture

Quarterly Report for October 1 – December 31, 2011

by Alexander Voice

Supported by the Luminant Carbon Management Program

and the Netherlands Organisation for Applied Scientific Research

Department of Chemical Engineering

The University of Texas at Austin

January 31, 2012

Summary of Work

Miniplant with MEA

The degradation of monoethanolamine (MEA) was studied in a miniature CO_2 capture plant (miniplant). Ammonia was produced at a rate of 8.5–23 mmol/hr. Some inhibitors identified in previous work, including 1,2dimercapto-1,3,4-thiadiazole (DMcT), diethylenetriamine pentaacetic acid (DTPA), hydroxyethilidene diphosphonic acid (HEDP), and Inhibitor A (Inh A) were ineffective at reducing ammonia production.

Ammonia production rates from MEA were assessed under various conditions. Ammonia was not produced in the absence of oxygen. The introduction of metals into the system (by blending a used MEA solution with the fresh solution) increased ammonia production in the presence of air and CO_2. Reducing the absorber temperature reduced the rate of ammonia production; the activation energy of this process was 33 kJ/mol.

Miniplant with PZ

Formation and degradation of mono-nitrosopiperazine (MNPZ) in 10 wt % piperazine (PZ) was also studied in the miniplant. Reaction of 10 wt % PZ with 8.6 mMol/kg potassium nitrite produced MNPZ at an initial rate of 0.56 mMol/kg/hr. Thermal degradation of MNPZ occurred at a rate of 0.027 mMol/kg/hr at 120 °C; in the presence of oxygen, the rate was only 0.014 mMol/kg/hr. The rate was zero order in MNPZ concentration. The Addition of 0.5 wt % ascorbic acid to the system had little impact on the yield of MNPZ from addition of potassium nitrite; however it resulted in an ammonia production rate of 5.6 mmol/hr from the solution and visibly changed the solution color from pale yellow to brown.

MNPZ was also measured in the condensate from the miniplant; the relative volatility of MNPZ was determined to be 1.02 times the volatility of PZ. No significant amount of potassium was found in the condensate, indicating that the MNPZ was in the gas phase, and not the result of mechanical entrainment.

UV Degradation of Nitrosamines

Destruction of MNPZ in 40 wt % PZ by ultraviolet (UV) light was studied in a circulating batch system with 15% hold-up in an 11 W lamp. The rate of UV degradation of MNPZ in PZ was -0.34 to -0.45 mol/kg/hr in this system, which is equivalent to 28–36 J/mol CO_2 for flue gas containing 5 ppm_v NO_2 and 12% CO_2, and a UV light with 1% hold-up. The degradation rate was zero order in MNPZ concentration, and it did not vary significantly with the CO_2 loading, the presence of oxygen, or the presence of dissolved metals. The rate of PZ degradation was 3.3 mmol/kg/hr in this system.

Destruction of NDELA in water and MEA with UV light was also studied in the same system. The rate of destruction in water and amine solutions at basic conditions was between -0.13 and -0.83 mmol/kg/hr and was not obviously affected by the pH. The rate was zero order in NDELA from 1000 ug/g to below 0.1 ug/g. The presence of degradation products that competed for UV light significantly reduced the rate of destruction.

Thermal Degradation of Nitrosamines

MNPZ in 40 wt % PZ was thermally degraded in a once-through reactor at high temperatures (160–180 °C) and pressure (200 bar). The results from this work indicate that the activation energy of thermal degradation is 78–90 kJ/mol. However, the rates observed at high pressure did not agree with measurements at low pressure, indicating that pressure may be a variable of interest in thermal degradation of nitrosamines.

Background

Oxidation is a well-known problem affecting amine solvents, particularly MEA, for CO_2 capture. One solution is the use of chemical oxidation inhibitors to slow or stop the reaction. Although free radicals can initially be produced by reaction of ferrous with oxygen or MEA, the dominant reaction in MEA oxidation is likely the production of free radicals by peroxide homolysis (Figure 1). This reaction is catalyzed by transition metals (such as iron), and therefore can be inhibited by the introduction of chelating agents into the solution. Because MEA can also complex the metal, the chelating agent must be strong enough or present in sufficiently high concentration to break the MEA-metal complex.

$$\text{MEAOOH} \xrightarrow{Fe^{3+}\rightarrow Fe^{2+}} \text{MEAOO}\bullet + H^+$$

$$\text{MEAOOH} \xrightarrow{Fe^{2+}\rightarrow Fe^{3+}} \text{MEAO}\bullet + {}^-OH$$

$$\text{MEA} + \text{R}\bullet \rightarrow \text{MEA}\bullet + \text{RH}$$

$$\text{MEA}\bullet + O_2 \rightarrow \text{MEAOO}\bullet$$

$$\text{MEAOO}\bullet + \text{MEA} \rightarrow \text{MEAOOH} + \text{MEA}\bullet$$

Figure 1: Iron-catalyzed homolysis of MEA peroxide

Other types of inhibitors have also been proposed. Inh A acts by scavenging free radicals. Methyldiethanolamine and sulfite sacrificially scavenge reactive oxygen species; MDEA forms a stable peroxide product quenching the source of free radicals. Of these inhibitors, sulfite is rapidly consumed and MDEA requires high concentrations (5 wt % or greater) to be effective.

Inh A, DTPA, and HEDP have been shown to be effective at low to moderate concentrations (0.1–1.5 wt %). These inhibitors are summarized in Table 1.

Table 1: Summary of some known MEA oxidation inhibitors

Inhibitor	*Name*	*Type*
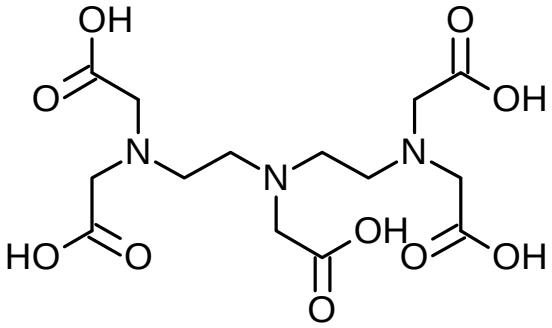	Diethylenetriamine penta(acetic acid) (DTPA)	Chelating agent
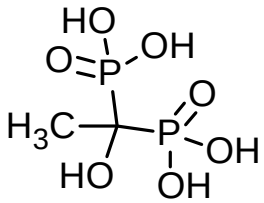	Hydroxy ethylidene diphoshponic acid (HEDP)	Chelating agent
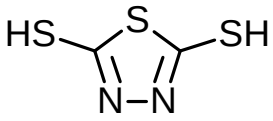	2,5-dimercapto-1,3,4-thiadiazole (DMcT)*	Chelating agent
	Inhibitor A**	Free-radical scavenger
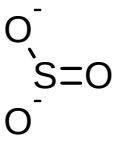	Sulfite***	Oxygen scavenger
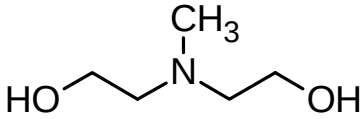	MDEA****	Oxygen scavenger

*Carette, 2009; **Goff, 2005; ***Hakka, 2009; ****McCullough, 1990.

Mitigation of nitrosamines is an important area of solvent management in CO_2 capture. Nitrosamines are potentially harmful to human health and the environment; furthermore, they are likely to exist in any CO_2 capture plant treating flue gas containing nitrogen oxides. Nitrosamines can be destroyed by application of heat or ultraviolet light. Nitrosamines can be chemically inhibited by scavenging nitrite and preventing it from reacting with an amine. Several methods of nitrosamine mitigation in CO_2 capture were examined in this study.

Experimental Methods

Miniplant

The mini-plant was used for replicating the conditions of a real CO_2 capture plant on a smaller scale (Figure 2). The plant was modified by removing the membrane contactor and adding a

glass column with structured packing. A peristaltic pump was used to pump liquid and gas from the bottom of the absorber to the absorber sump (constructed from an empty glass column). An electronic level indicator on the absorber sump was used to control the rich pump rate. Water and CO_2 exiting the condenser were fed back to the absorber sump to eliminate water loss from the stripper. The sump was open to the atmosphere, allowing CO_2 to exit the system.

Dry nitrogen or air with 12% CO_2 was fed to the absorber at a rate of 2.37 sm^3/hr. The liquid was recirculated at 50.0 L/hr. The stripper was operated at 120 °C and 2.1 bar. The CO_2 capture rate in the absorber was 75–95% for all experiments. The absorber temperature was 32 °C with the trim cooler on, and 48 °C when it was bypassed. The absorber sump was 35 °C with the trim cooler and 48 °C without it. The approach temperature in the cross exchanger was 7 °C on the hot side and 2 °C on the cold side. The total solvent inventory was approximately 50 L. The absorber hold-up was 330 mL (0.66% of the whole system); the absorber sump hold-up fluctuated between approximately 500 mL and 1 L. The reboiler hold-up was approximately 40 L (80%).

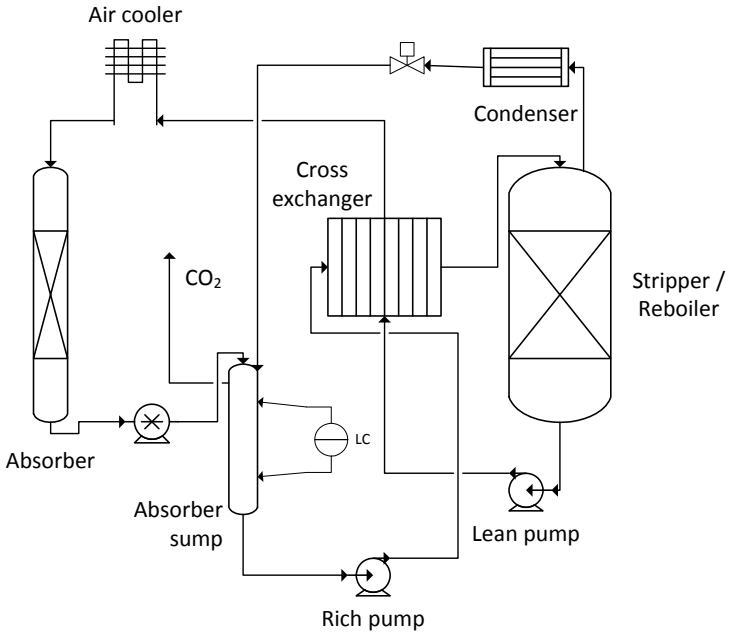

Figure 2: Process flow diagram of the miniplant

Single-Pass Thermal Degradation

Thermal degradation of MNPZ was conducted at 200 bar and at three temperatures: 160 °C, 180 °C, and 200 °C (Figure 3). Variations of up to ±10 °C from the set point were observed at the inlet and outlet over the course of the experiment. The reactor consisted of 3 m of ¼" stainless steel tubing in a convection oven held at a constant temperature. The solvent was pumped through the reactor at 3 mL/min. The residence time in the reactor was 16.4 minutes. After one hour of pumping the solution, samples were collected at the exit of the reactor. Samples were diluted and analyzed immediately after being collected. The average rate of degradation was calculated from the difference in MNPZ concentration in the solution entering and leaving the reactor.

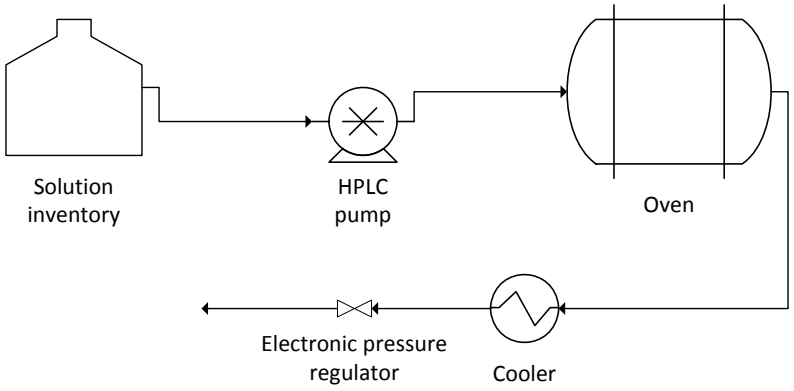

Figure 3: Process flow diagram of the single-pass thermal degradation apparatus

Batch UV Degradation

Ultra-violet (UV) degradation of nitrosamines was carried out in a batch reactor with an 11 W UV-C light (Figure 4). The total inventory of the system was 2 L with 300 mL hold-up (15%) in the UV light. The reservoir was stirred at 900 RPM. The pump rate was 120 mL/min, which was sufficiently fast relative to the rate of degradation to keep the system well-mixed. Liquid samples (1 mL) were taken via the sampling point periodically.

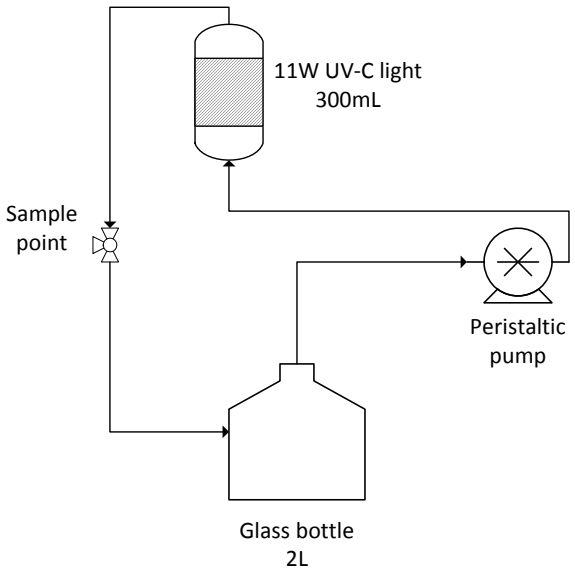

Figure 4: Process flow diagram of the circulating batch UV degradation system

Analytical Methods

Acid Titration

Total alkalinity of the solution (at pH = 2.0) and CO_2 loading were determined by titrating a small aliquot of the sample (typically 100–300 mg) with 0.1 N HCl. Fresh, loaded amine solutions exhibit two distinct end points (Figure 5): the moles of acid to reach the first end point corresponds to the moles of dissolved CO_2 (present as $CO_{2,l}$, CO_3^{2-}, HCO_3^-, and N-CO_2^-); the second corresponds to the number of nitrogen equivalents in the solution. Titration of used

amine solutions may exhibit interference in the first end point by heat-stable salts, resulting in an error in the loading calculation. The second end point includes all basic nitrogen, which may include some N-containing degradation productions. The software uses the second-derivative analysis to interpolate the exact position of each end point from the data (Figure 5).

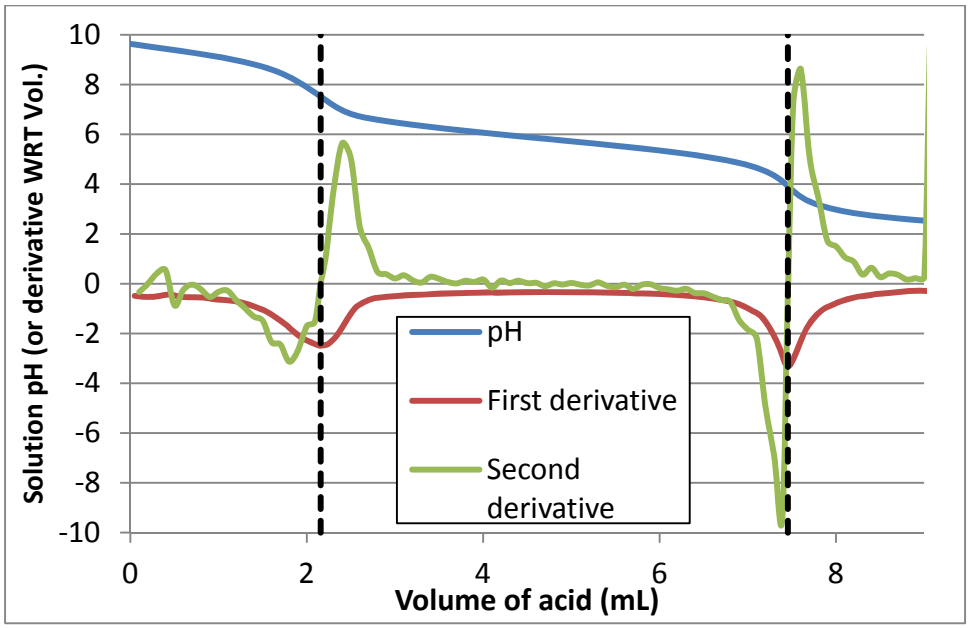

Figure 5: Titration of loaded amine solutions with hydrochloric acid for determining number of N equivalents and CO_2 loading

High-Pressure Liquid Chromatography (HPLC)

Nitrosamines were analyzed by HPLC with UV detection at 245 nm (UV max for MNPZ) or 234 nm (UV max for NDELA). The column was an Acclaim PolarAdvantage II, C18, 5 µm, 120Å, 4.6 x 250 mm. The column was chosen due to its high hydrolytic stability and extended lifetime under 100% aqueous conditions at pH 9.0. These conditions allow better peak shape and retention of very hydrophilic, alkaline components by buffering the eluent at or above their pKa. Mononitrosopiperazine (MNPZ) and nitrosodiethanolamine (NDELA) were easily detected at concentrations below 0.1. The retention times were 3.77 minutes for NDELA and 4.74 minutes for MNPZ. The instrument response was linear over four orders of magnitude (Figure 6). The eluent composition for the method is shown in Table 2. Simple amines (such as MEA and PZ) do not show up on this method because they do not contain a double bond.

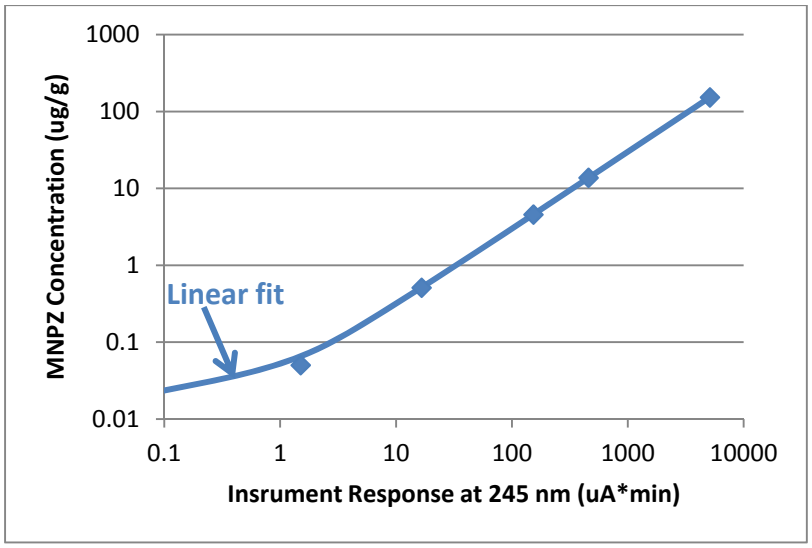

Figure 6: Log-log calibration curve of MNPZ analysis on the HPLC at 245 nm

Table 2: Eluent ramp for nitrosamine analysis on the HPLC

Time	*10 mM aqueous $NH_4^+CO_3^-$*	*Acetonitrile*
0	95	5
5	95	5
5.1	50	50
10	50	50
10.1	95	5
12	95	5

Fourier-Transform Infrared Spectroscopy (FTIR)

A method was implemented to analyze gas leaving the absorber by FTIR for water, CO_2, MEA, and ammonia. NO_2 was also initially included, however no NO_2 was observed and therefore the component was removed from the method. The analysis method was developed with TQ Analyst computer program. This method can be used as-is, or modified to include additional components such as NO_2 and SO_2. The method specifies the IR regions used for quantification of each component. The experimental method (used for collecting a series of data over several hours or days) is accessed using the Omnic computer program.

Gas exiting the absorber was sampled by a heated pump at approximately 10 LPM. The gas first passed through a liquid knockout. The liquid knockout was essential for reducing liquid entrainment to the heated lines and the FTIR. After the knockout, the gas passed through a metal mesh filter before being pulled through the first heated line by the heated pump, followed by the second heated line, and then the analyzer.

Table 3 shows the regions used for quantification of MEA, NH_3, water, and CO_2 in the absorber gas. Figure 7 shows how a clean background scan should look; Figure 8 shows a typical gas sample from the absorber. Figures 9–12 show the calibration curves for the four components in the TQ analyst software.

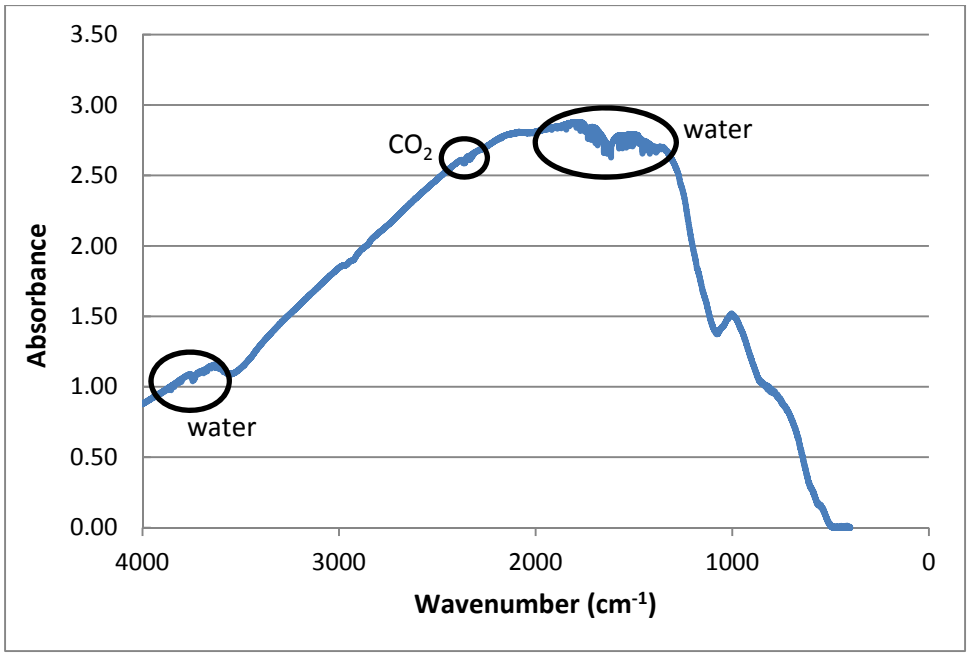

Figure 7: Clean background scan on the FTIR

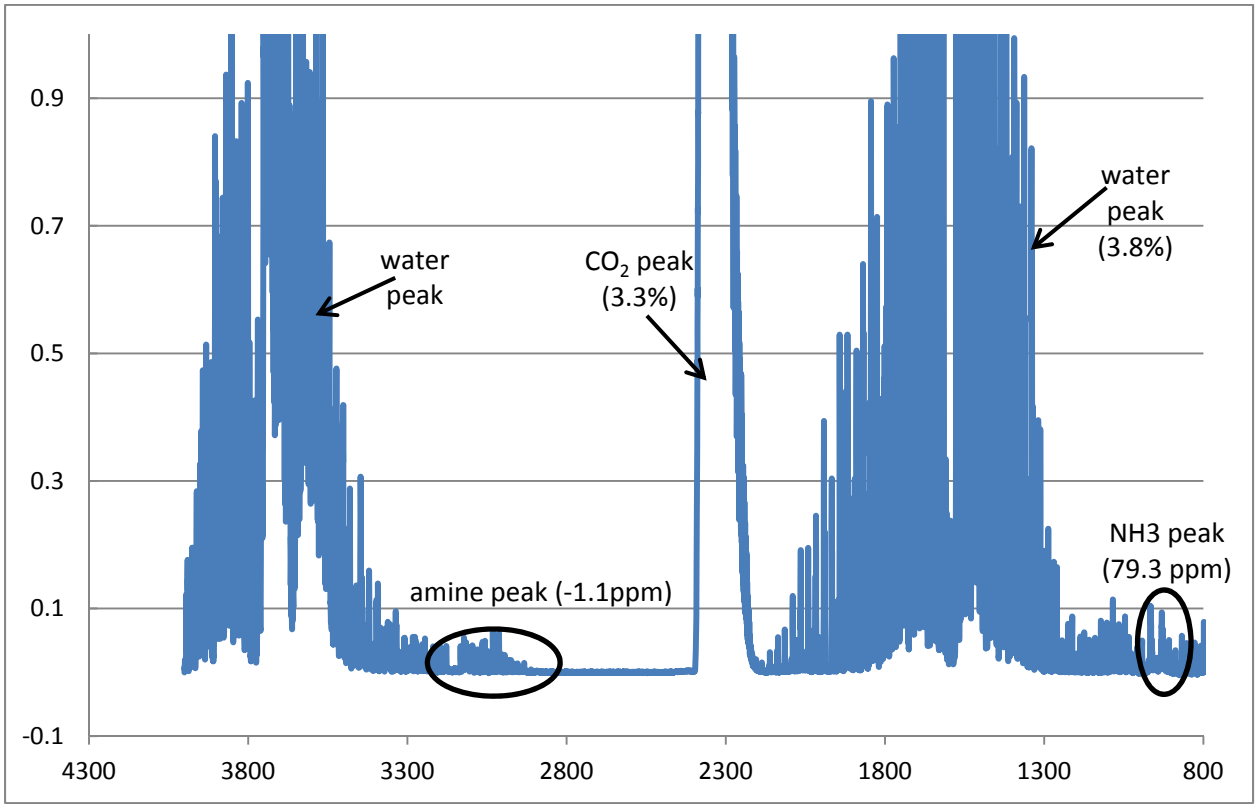

Figure 9: Typical FTIR spectrum of absorber gas from the miniplant with 24 wt % MEA

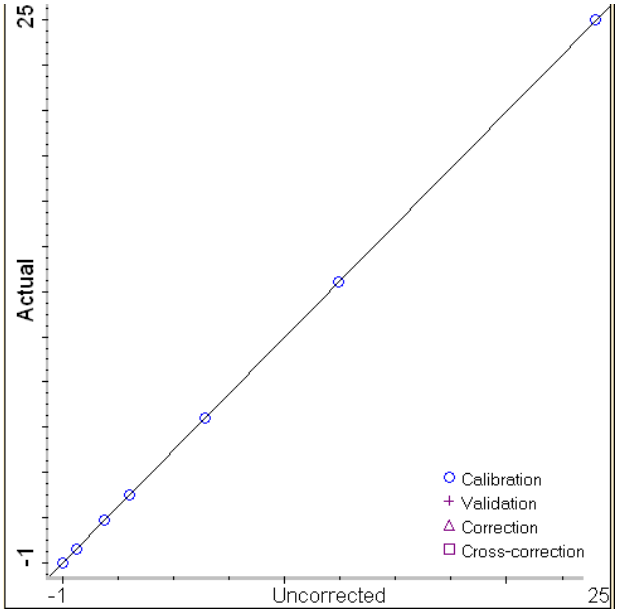

Figure 10: Calibration curve for carbon dioxide analysis in the FTIR

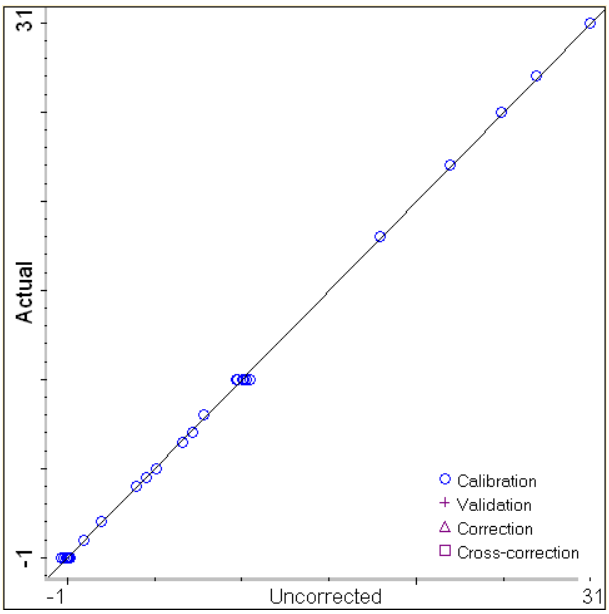

Figure 11: Calibration curve for water analysis in the FTIR

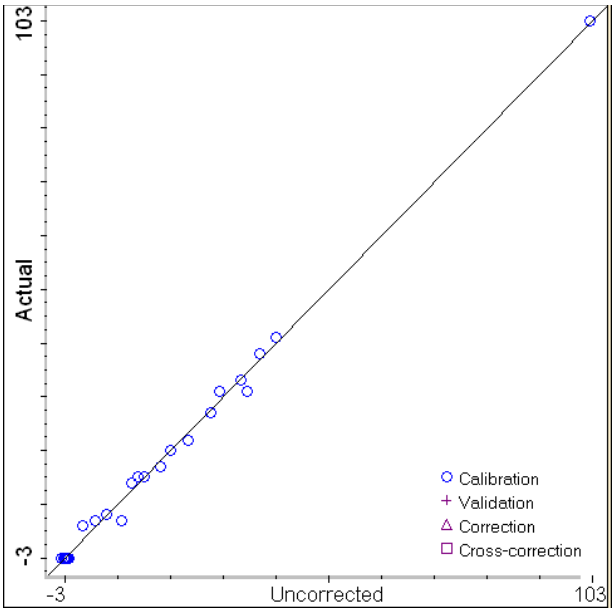

Figure 12: Calibration curve for monoethanolamine in the FTIR

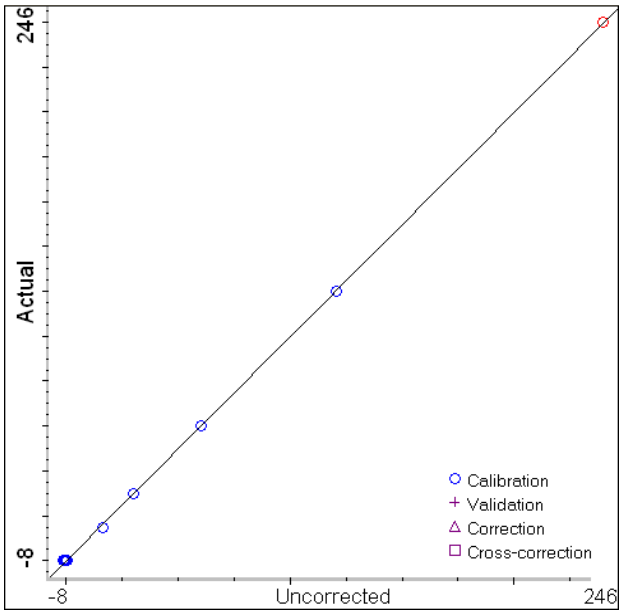

Figure 13: Calibration curve for ammonia in the FTIR

Table 3: Analysis regions for components in absorber gas in the FTIR

	NH3	MEA	H_2O	CO_2
3157 – 3425	YES	NO	YES	NO
910 – 1003	YES	YES	YES	YES
2165 – 2251	NO	NO	YES	YES
2500 – 3100	NO	YES	YES	NO

Results

Results were produced using the three experimental apparatuses described above: the mini CO_2 capture plant (miniplant); the single-pass thermal degradation setup; and the batch UV degradation system.

The mini-plant was used for studying oxidation of MEA and PZ by observing ammonia production from the solution using an FTIR. The thermal degradation and UV degradation systems were used for demonstrating nitrosamine countermeasures for CO_2 capture.

Miniplant Experiments

Oxidative Degradation of CATO MEA (11.1 wt %)

MEA used at the CATO pilot plant with flue gas for several months was used for oxidation studies in the miniplant. The solution was used as-received; acid-titration showed that it contained 11.1 wt % MEA. Prior to use, the solution was analyzed for metals by ICP-OES (Table 4). Iron was the most prevalent metal found at 10.6 µg/g (0.19 mMol/kg). This concentration is sufficient to catalyze oxidation of MEA (Goff, 2005).

Table 4: Elemental analysis of CATO pilot-plant MEA sample (values in µg/g)

Elements from Corrosion	
Fe	10.6
Cr	2.35
Ni	4.85
Mn*	0.43

*below LOQ=1µg/g

Other Elements	
Ca	4.76
Cl	261
K	3.06
Mg	2.03
Na	26.9
Zn	2.15
C	5.87e4
PO_4	3.96
SO_4	343

The solution was contacted with nitrogen in the absorber of the miniplant. Ammonia was initially produced from the solution at a rate of nearly 20 mmol/hr, however the rate decreased over the course of the day (Figure 14).

A UV-C light (11 W) with 300 mL hold-up (0.6%) was installed in the plant; powering the light on did not visibly increase ammonia production in the presence of nitrogen.

Addition of makeup MEA solution to the miniplant (identical to the initial solution) briefly increased ammonia production in the presence of nitrogen as dissolved ammonia was stripped out of the solution.

After two days, the absorber gas was switched from nitrogen to air; this change resulted in a visible increase in ammonia production from the solution. After several days, the ammonia rate reached a steady state at 23 mMol/hr

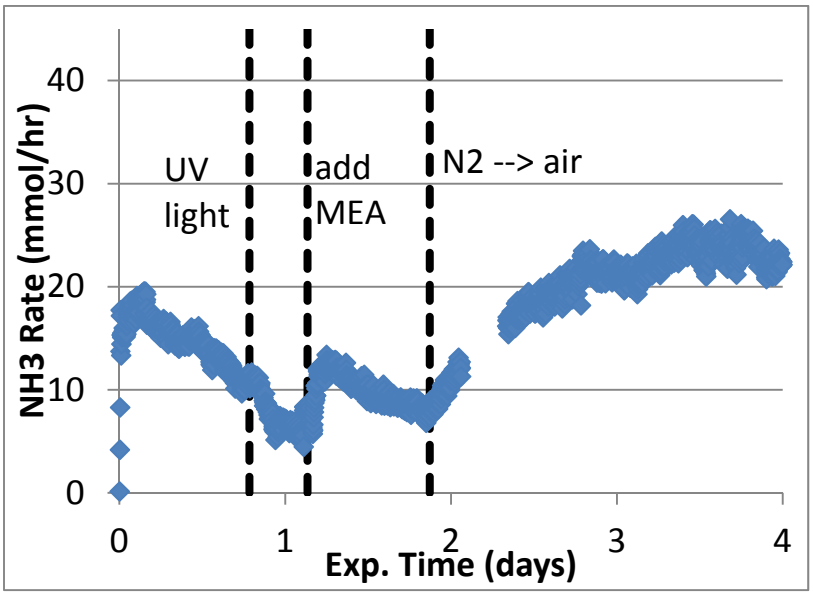

Figure 14: Ammonia production from CATO pilot plant MEA solution (11.1 wt % MEA). Reboiler: 120 °C, 2.1 bar. Absorber: 32 °C, 50 L/hr, 2.37 SCMH, 330 mL hold-up in absorber packing. Total inventory 50 L. Iron content: 10.6 ppm

Oxidative Degradation of 24% (neat) MEA in the Miniplant

Neat MEA from Sigma Aldrich was oxidized in the miniplant with air and CO_2. Oxidation of the solvent was monitored by quantifying ammonia production from the solution. The initial rate of oxidation was 3–5 mmol/hr with the fresh solution (Figure 15).

Addition of 10 kg of degraded MEA from the CATO pilot plant (to a total inventory of 50 kg) increased ammonia production to 9 mMol/hr. This solution contained 0.19 mMol/kg of iron resulting in 0.04 mMol/kg of iron in the total solution. Rust and scale were observed in the final solution indicating that additional metals were likely picked up from corrosion of the plant. The final solution was not analyzed for iron or other metals.

Inhibitors diethylenetriamine penta(acetic acid) (DTPA), hydroxyethylidene diphosphonic acid (HEDP), dimercapto thiadiazole (DMcT), and Inh A were tested in the miniplant. These structures are shown below. DTPA, HEDP, and DMcT act as chelating agents, whereas Inh A is a free-radical scavenger. Acids were neutralized with sodium hydroxide to pH 10 prior to addition to the miniplant; all substances were dissolved in water and pumped into the stripper.

Inh A is a proprietary inhibitor developed at the University of Texas. The effectiveness of this substance as an inhibitor of MEA oxidation was demonstrated by Goff (2005).

HEDP and DTPA were mildly effective at reducing the oxidation rate. The rate decreased slightly from 9 mMol/hr to 7.6 mMol/hr with addition of 0.1 wt % (2.54 mMol/kg) DTPA and 0.05 wt % (2.43 mMol/kg) HEDP. Addition of a further 0.5 wt % (12.7 mMol/kg) DTPA decreased the ammonia rate to 6.7 mmol/hr (Figure 15).

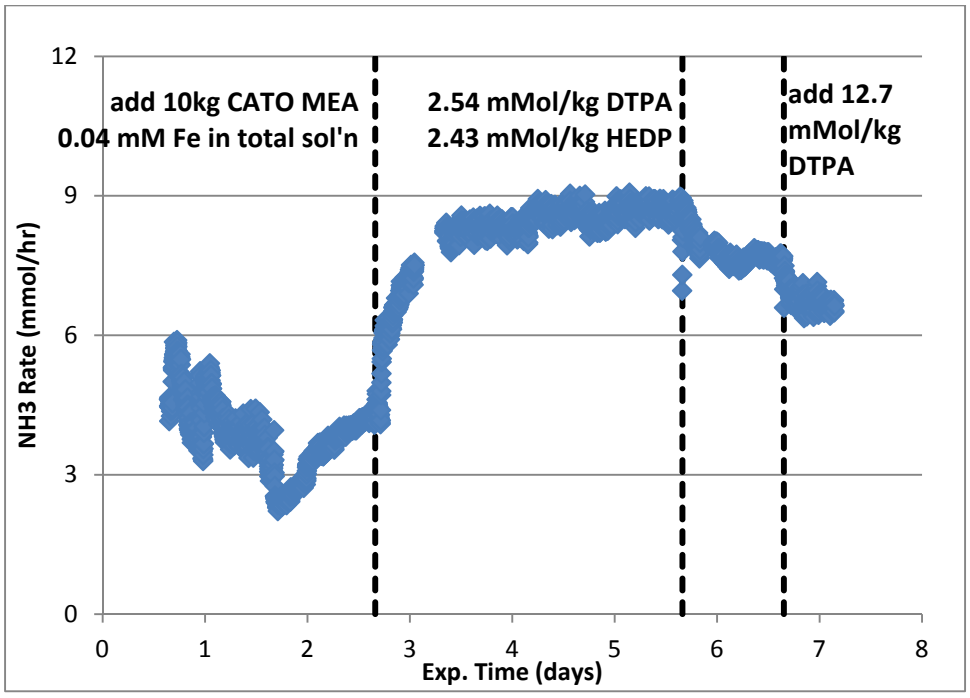

Figure 15: Effect of HEDP and DTPA on ammonia production from MEA in the miniplant. Conditions: Reboiler = 120 °C, 2.1 bar; absorber = 32 °C, liquid rate = 50 L/hr, gas rate = 2.37 SCMH, absorber packing hold-up = 330 mL. Total inventory 50 kg.

Several days after adding DTPA and HEDP to the solution, the absorber gas was switched from air to nitrogen to determine the response time of the system (Figure 16). The ammonia rate decreased dramatically in the first 24 hours, although the system required 4.5 days for the ammonia rate to decrease by 90%. The steady-state concentration of ammonia was calculated as 7.3 mMol/kg by integrating the ammonia rate curve after the air was switched to nitrogen.

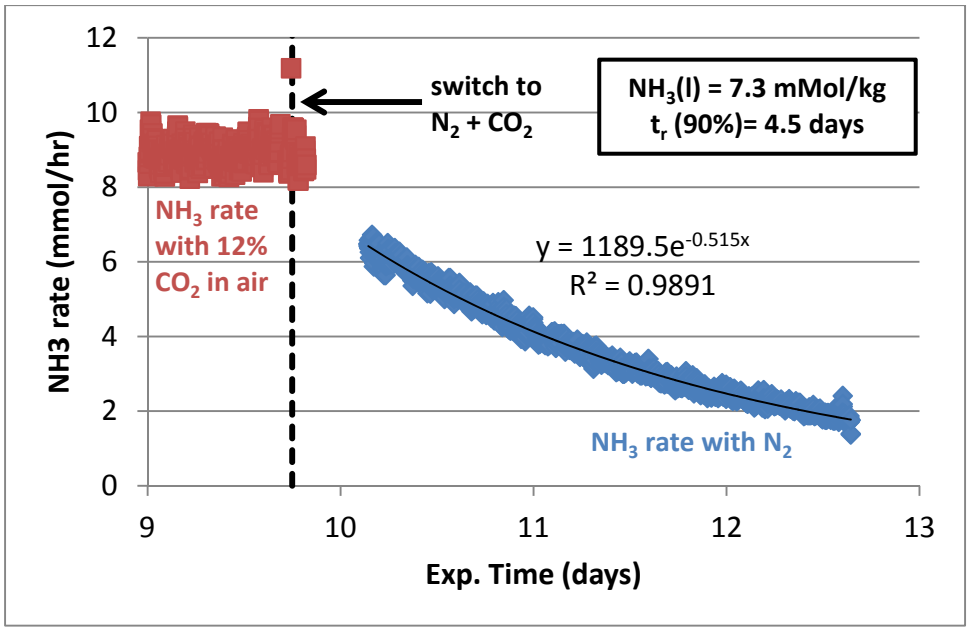

Figure 16: System response time and effect of switching absorber gas from air to nitrogen on ammonia production from MEA in the miniplant. Conditions: Reboiler = 120 °C, 2.1 bar; absorber = 32 °C, liquid rate = 50 L/hr, gas rate = 2.37 SCMH, absorber packing hold-up = 330 mL. Total inventory 50 L. Iron added: 0.04 mMol/kg.

The absorber gas was switched back to air and CO_2, which resulted in a gradual increase in ammonia production to 21 mMol/hr (Figure 17). This was exactly the same behavior that was observed in the previous experiment with 11.1 wt % MEA and no inhibitors. In this case the system took roughly 5 days to reach steady state.

Inhibitors DMcT (at 0.4 wt %; 26.6 mMol/kg) and Inh. A (at 66.7 mMol/kg) had no effect on the steady-state rate of ammonia production. A bulge is observed in the ammonia trend where DMcT was added; this was likely caused by some air being accidentally pumped into the stripper when the DMcT was added.

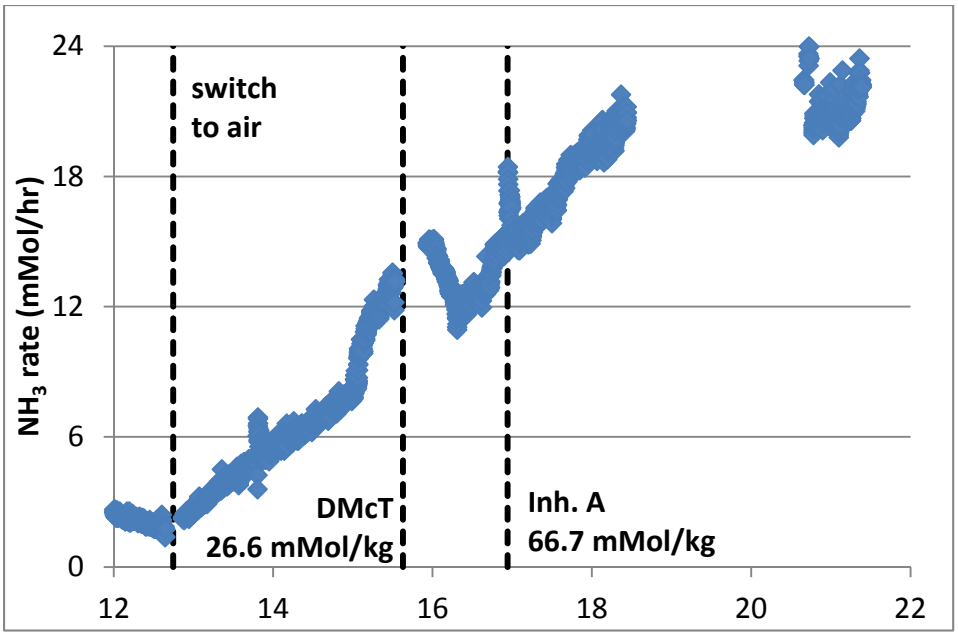

Figure 17: Effect of switching absorber gas from air to nitrogen and effect of DMcT and Inh A on ammonia production from MEA in the miniplant. Conditions: Reboiler = 120 °C, 2.1 bar; absorber = 32 °C, liquid rate = 50 L/hr, gas rate = 2.37 SCMH, absorber packing hold-up = 330 mL. Total inventory 50 L. Iron added: 0.04 mMol/kg.

Finally, the effect of the absorber temperature on ammonia production was studied by de-activating the air trim cooler in front of the absorber. Under normal operation the trim cooler was used to keep water losses from the absorber to a manageable level. When the trim cooler was bypassed, the absorber inlet temperature rose from 32 °C to 48 °C, resulting in an increased rate of ammonia production. The change in ammonia production from the solution suggests an activation energy of 29 kJ/mol for this process (Figure 18). This is significantly different than the activation energy of 68–70 kJ/mol that has been reported for the rate of ammonia production and the rate of MEA loss in other work for low-temperature oxidation of MEA (Voice, 2011).

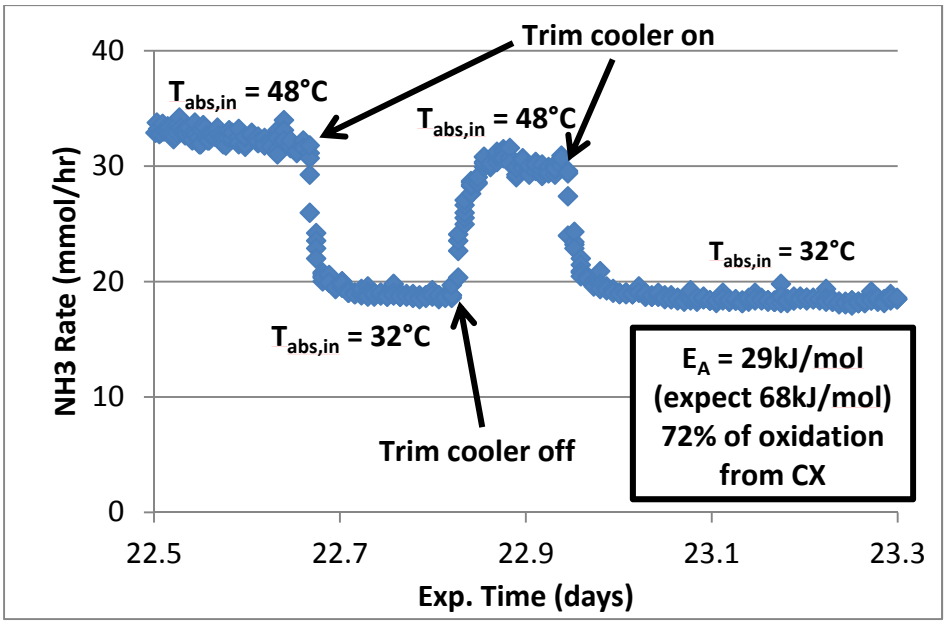

Figure 18: Effect of absorber temperature on ammonia production from MEA in the miniplant. Conditions: Reboiler = 120 °C, 2.1 bar; liquid rate = 50 L/hr, gas rate = 2.37 SCMH, absorber packing hold-up = 330 mL. Total inventory 50 L. Iron added: 0.04 mMol/kg.

The lower activation energy of ammonia production in the miniplant is one indication that oxidation is not only taking place in the absorber; namely, oxidation of the solution by dissolved oxygen and entrained air-bubbles in the stripper. This hypothesis is supported by two other observations: the failure of inhibitors known to work at low temperatures to inhibit oxidation in the miniplant, and the observation of entrained bubbles in the absorber sump (Figure 19). The sump was filled with dumped packing in an attempt to force the bubbles to nucleate (Figure 20), a strategy that has been shown to eliminate bubble entrainment (Closmann, 2011). However, this change also did not affect ammonia production so the hypothesis that entrained bubbles are a main cause of MEA oxidation in this system could not be confirmed

Figure 19: Presence of entrained bubbles in the absorber sump

Figure 20: Dumped packing used to eliminate bubbles in the absorber sump

MNPZ Formation and Destruction in the Miniplant

Formation and destruction of MNPZ in 10 wt % PZ solution was studied in the miniplant. MNPZ was synthesized in the miniplant by adding a potassium nitrite solution to the stripper, which contained aqueous PZ solution.

The initial rate of nitrosation was 0.56 mmol/kg/hr for an addition of 8.6 mmol/kg of nitrite. The yield of MNPZ from nitrite was calculated as 59.3% by extrapolation (Figure 21).

The zero order rate of thermal degradation of MNPZ was 0.027 mmol/kg/hr with nitrogen and CO_2 in the absorber, whereas it was 0.014 mmol/kg/hr with air and CO_2 in the absorber (Figure 21). This difference suggests that the presence of oxygen in the stripper somehow slows degradation of MNPZ.

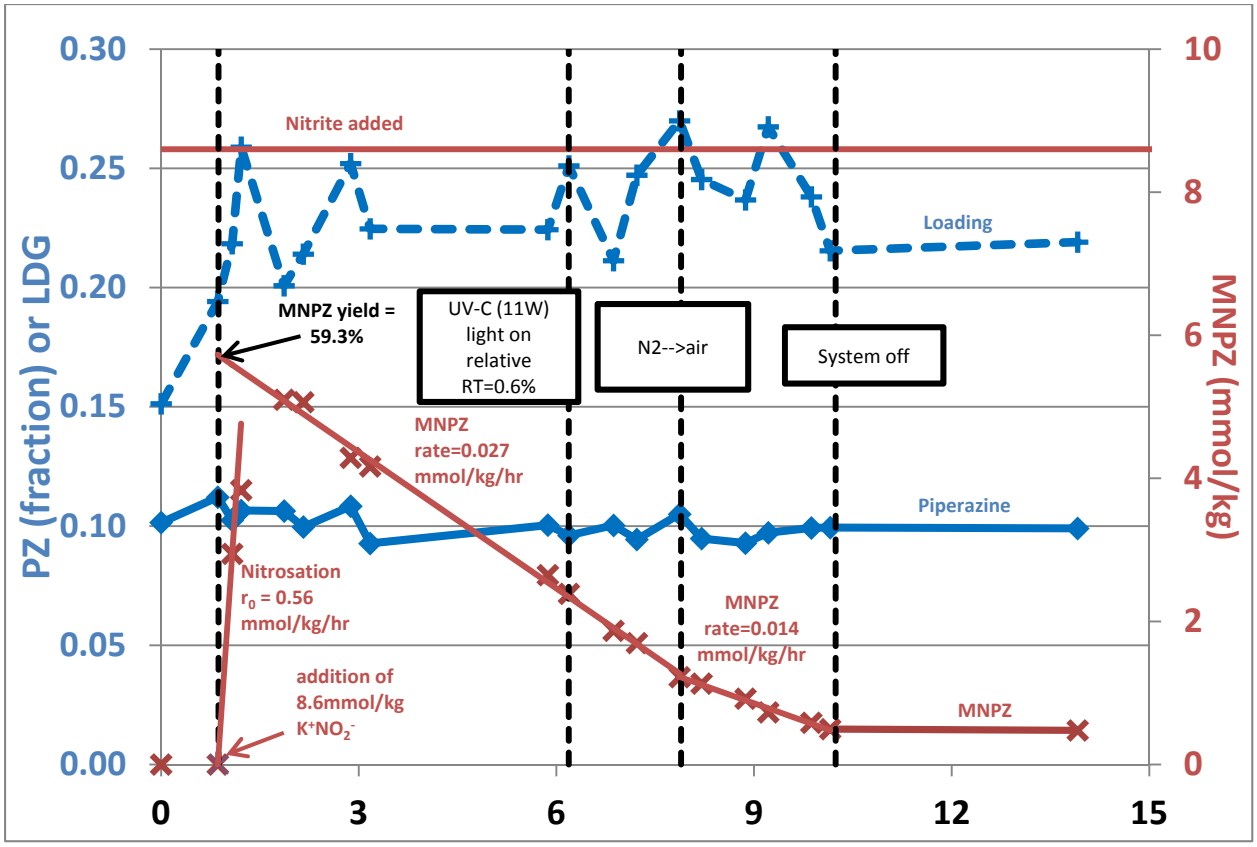

Figure 21: MNPZ formation and thermal decomposition in the miniplant with 10 wt % PZ. Conditions: Reboiler = 120 °C, 2.1 bar; absorbe r = 32 °C, liquid rate = 50 L/hr, gas rate = 2.37 SCMH, absorber packing hold-up = 330 mL. Total inventory 50 L, reboiler inventory = 40 L.

Ascorbic acid was investigated as a chemical inhibitor of MNPZ formation. Ascorbic acid is designed to act as a competitive inhibitor of PZ nitrosation by reacting with nitrite before it can react with PZ to form the nitrosamine.

Potassium nitrite solution was added to the miniplant at 7.4 mMol/kg concentration in the presence of 0.5 wt % (28.4 mMol/kg) ascorbic acid. Under these conditions, the nitrosamine

yield was 45.5% as compared with 59.3% without ascorbic acid, indicating that ascorbic acid did not significantly inhibit nitrosamine formation (Figure 22).

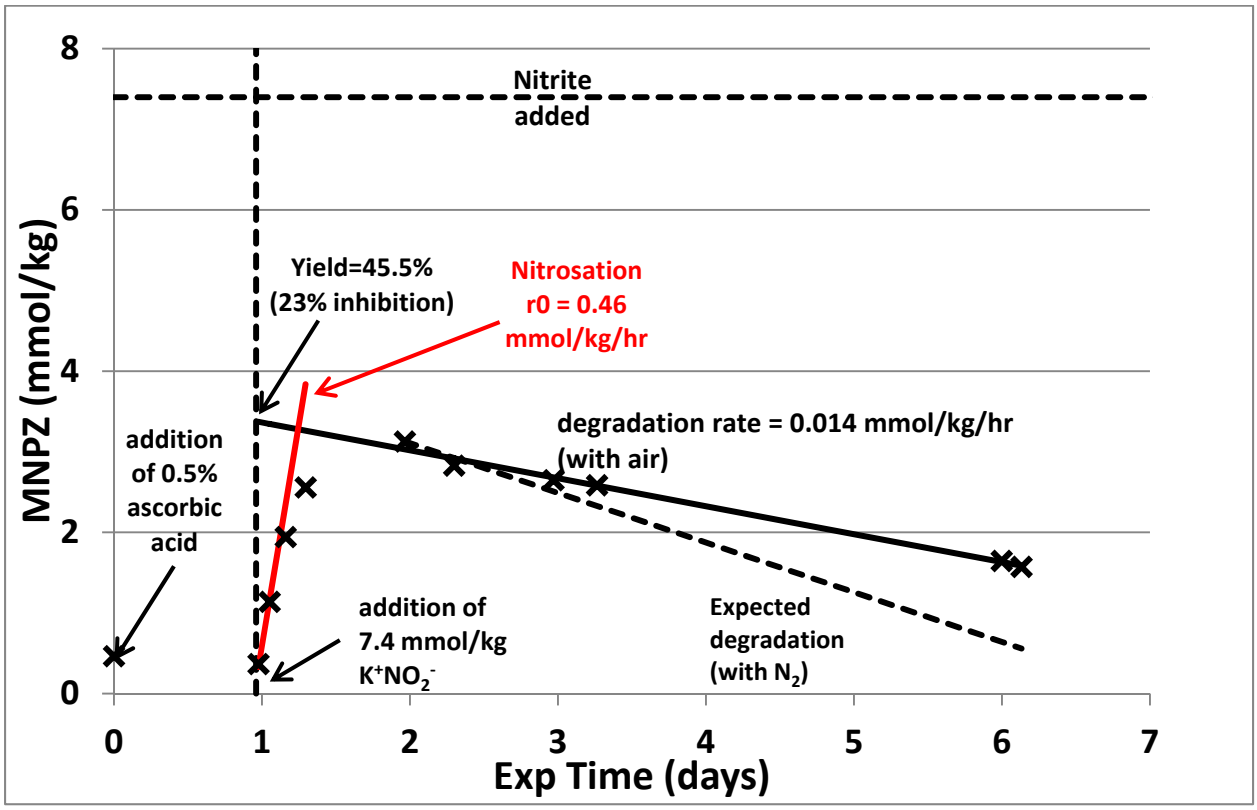

Figure 22: MNPZ formation and thermal decomposition in the miniplant with 10 wt % PZ and 28.4 mMol/kg ascorbic acid. Conditions: Reboiler = 120 °C, 2.1 bar; absorber = 32 °C, liquid rate = 50 L/hr, gas rate = 2.37 SCMH, absorber packing hold-up = 330 mL. Total inventory 50 L, reboiler inventory = 40 L.

The rate of nitrosation of PZ with nitrite was 0.46 mmol/kg/hr with addition of 7.4 mmol/kg potassium nitrite, compared with 0.56 mmol/kg/hr from addition of 8.6 mMol/kg of potassium nitrite in the previous experiment. This result confirms previous findings that the rate of nitrosation is first order in nitrite concentration (Rochelle, 2011).

The rate of thermal degradation with air, CO_2, and ascorbic acid was 0.014 mmol/kg/hr and was observed to be zero order in MNPZ concentration. The rates of thermal degradation of MNPZ in the miniplant are summarized in Table 5.

Addition of ascorbic acid to the PZ solution resulted in ammonia production from the solution at a rate of 6 mMol/hr decreasing to 2 mMol/hr after several days (Figure 23). Ascorbic acid has been shown to catalyze low temperature oxidation of MEA in previous experiments (Goff, 2005).

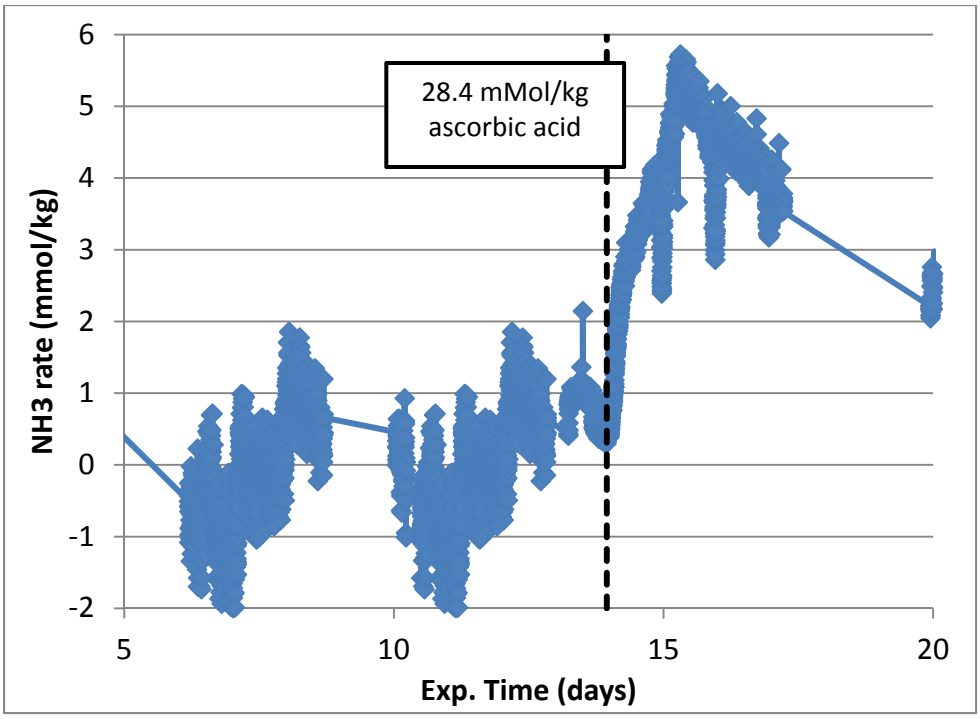

Figure 23: MNPZ formation and thermal decomposition in the miniplant with 10 wt % PZ and 28.4 mMol/kg ascorbic acid. Conditions: Reboiler = 120 °C, 2.1 bar; absorber = 32 °C, liquid rate = 50 L/hr, gas rate = 2.37 SCMH, absorber packing hold-up = 330 mL. Total inventory 50 L, reboiler inventory = 40 L.

Table 5: Summary of MNPZ thermal degradation rates in the miniplant

Solution	*$K^+NO_2^-$ added (mmol/kg)*	*MNPZ yield (%) (extrapolated)*	*MNPZ initial formation rate (mmol/kg/hr)*	*Thermal degradation rate (mmol/kg/hr) (with air)*
10 wt % PZ	8.6	59.3	0.56	0.027 (0.014)
10 wt % PZ + 0.5 wt % ascorbic acid	7.4	45.5	0.46	(0.014)

Relative Volatility of MNPZ

The volatility of MNPZ from the absorber was determined to be 1.02 times the volatility of PZ. The relative volatility of MNPZ was determined by measuring the concentration of PZ, MNPZ, and K^+ in the rich solution and the absorber condensate. PZ was measured by acid titration, MNPZ was measured by HPLC with UV detection, and K^+ was measured with ICP-OES (Table 6).

The results show that the ratio of PZ to MNPZ in the rich solution and the absorber condensate is almost identical. Potassium was not found in the condensate, indicating that the MNPZ detected is not the result of mechanical entrainment. This volatility is significantly higher than the predicted volatility in recent modeling work (Fulk, 2011; Rochelle, 2011).

Table 6: Relative amounts of PZ, MNPZ, and K^+ in the absorber liquid and condensate

Species	*Rich solution*	*Absorber condensate*	*Ratio*

PZ (mmol/kg)	1157	12.52	**92.45**
MNPZ (mmol/kg)	4.973	0.0528	**94.20**
K+ (ppm)	150.5	0.04*	**3761.5**
PZ/MNPZ Ratio	232.7	237.1	

*LOD = 0.1ppm

Continuous Thermal Degradation of MNPZ

Thermal degradation of MNPZ was studied in a once through continuous plug-flow reactor. MNPZ was first synthesized by reacting nitrite with 40 wt % PZ and 0.36 CO_2 loading at 90 °C for several days. This mimics the formation of nitrosamines in an industrial CO_2 capture system, where nitrite formed from NO_2 in the absorber reacts to form nitrosamines in the stripper. 10.7 mmol/kg of sodium nitrite yielded an equimolar quantity of MNPZ after heating.

The MNPZ was then degraded from an initial concentration of 10.7 mmol/kg using the continuous thermal degradation apparatus described above at a temperature of 160–200 °C and 200 bar. The temperature of the reactor was not tightly controlled and drifted by up to 10 °C above or below the set point, introducing significant error into the temperature measurement (Figure 24).

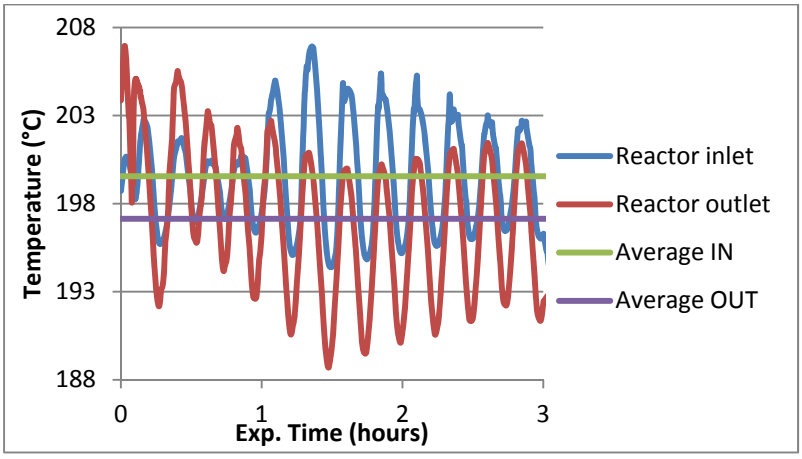

Figure 24: Temperature fluctuations in thermal degradation system

The Arrhenius plot for thermal degradation of MNPZ at high temperature is shown in Figure 25. The activation energy for the temperature range of 160–200 °C was 78 kJ/mol. This result is compared in Figure 25 with the reaction rates observed in two other experimental apparatuses. Data from a batch reactor (sealed stainless steel tube with variable pressure) showed a reaction rate comparable to those observed in the flow-through system (Fine, 2011). However, the rate of thermal degradation of MNPZ in the miniplant (described above) was significantly lower than expected.

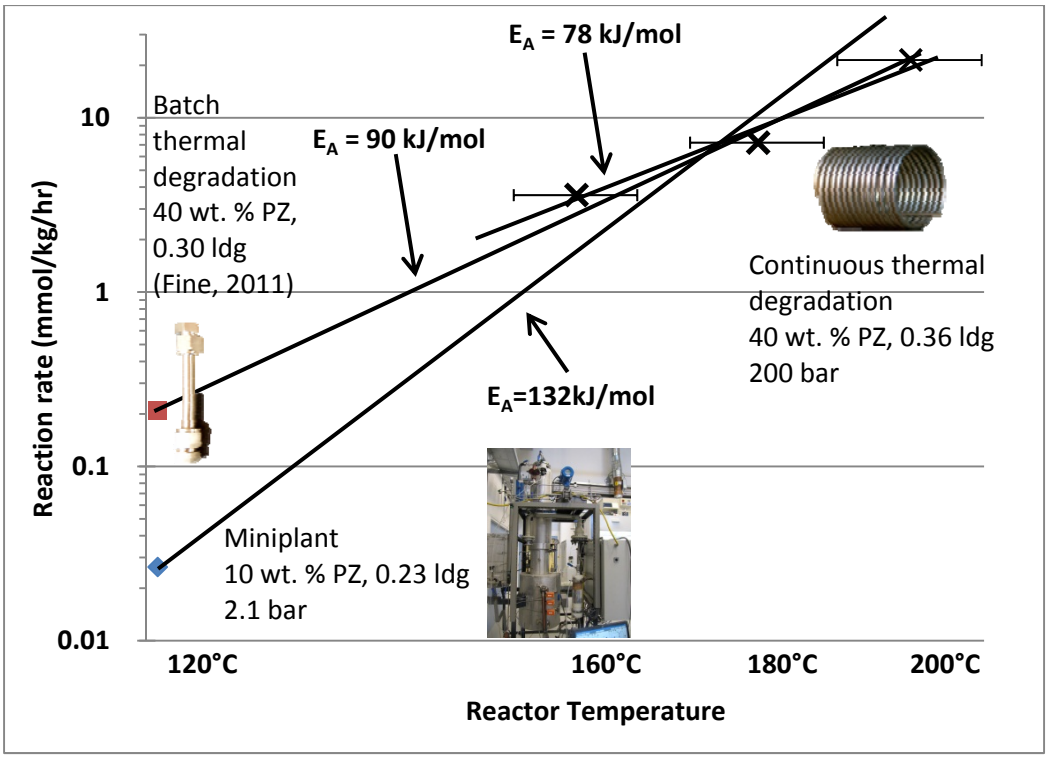

Figure 25: Thermal degradation of MNPZ comparison in different systems

One hypothesis is that thermal degradation of MNPZ produces a gas-phase product (such as NO•) that degrades a second MNPZ molecule. At low pressures (as in the miniplant), some of this product flashes out before it can react, slowing the rate of thermal degradation. This degradation pathway (shown below in Figure 26) was proposed by Williams (1994). The rates of thermal degradation of MNPZ are summarized in Table 7.

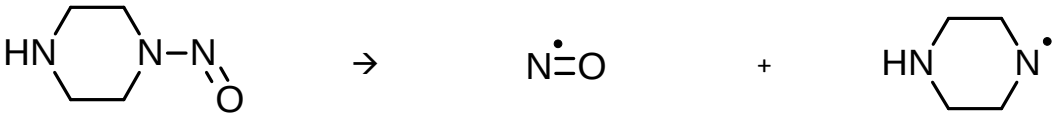

Figure 26: Thermal degradation of MNPZ

Table 7: Rates of thermal decomposition of MNPZ in loaded PZ solution

Apparatus	*Temperature (°C)*	*Pressure (bar)*	*Rate (mmol/kg/hr)*
Single-pass	200	200	21
Single-pass	180	200	7.2
Single-pass	160	200	3.6
Batch reactor	120	Unknown	0.21
Miniplant	120	2.1	0.023

Batch UV Degradation of Nitrosamines

MNPZ and NDELA were degraded in a batch-system by UV light. The rates are believed to be zero order because the reaction does not involve any collisions. Observed deviations from zero order rate are attributed to the production of other compounds resulting from degradation of the solution that compete with the nitrosamines for ultraviolet light. With amine solutions (MEA and PZ) a visible change in the color of the solution (from clear or pale yellow to light orange) was observed after 12 to 24 hours.

Degradation of MNPZ

MNPZ in 40 wt % PZ at 0.27 loading was degraded rapidly by UV light. The reaction is believed to be zero order in MNPZ concentration. Deviation from the zero order rate is believed to be attributed to the production of other UV-absorbing compounds during the course of the experiment. The solution was observed to change color from pale yellow to light orange after exposure to UV light for 24 hours.

Nitrogen was sparged into the reservoir for the first six hours of the experiment. At this point, the nitrogen was switched to air, introducing dissolved oxygen into the solution. The degradation rate was not affected by the presence of dissolved oxygen. No degradation was observed prior to turning on the UV light (Figure 26).

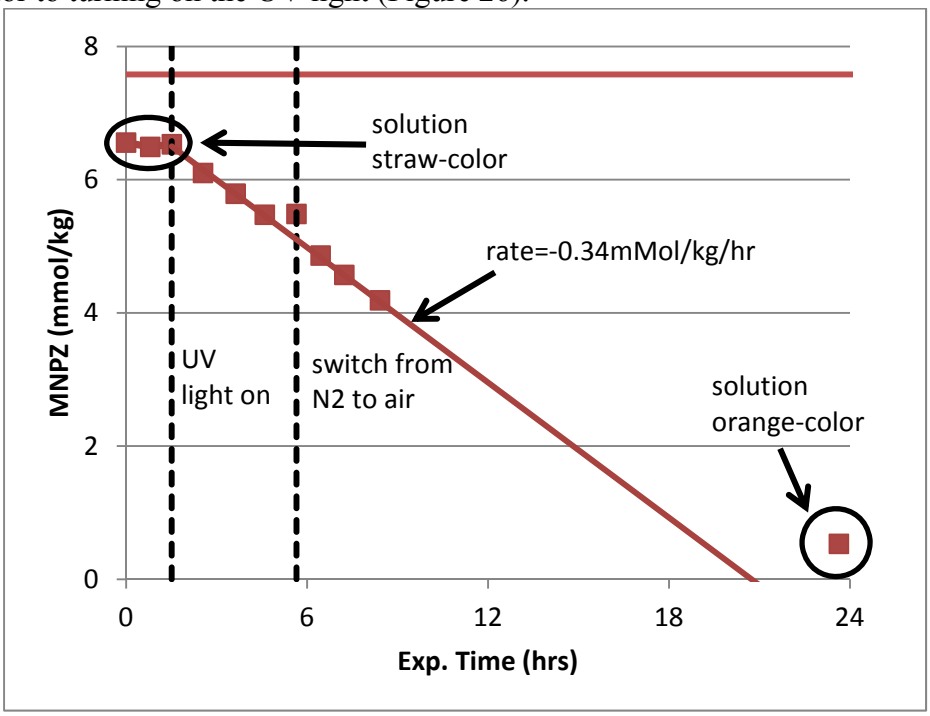

Figure 26: Degradation of MNPZ in 40 wt % PZ at 0.27 loading with UV-light. Conditions: room temperature, 15% hold-up in 11 W UV-C lamp, pH = 10.10, 2 L inventory, 900 RPM agitation in liquid reservoir.

MNPZ was also degraded in 0.36 loaded 40 wt % PZ. The loading did not have a large effect on the initial rate of MNPZ degradation. However, the data deviated more severely from the expected zero order rate law than at the lower loading (Figure 27). It is believed that UV degradation of the solution was faster at the higher loading, producing higher quantities of products that competed for UV light, which slowed the rate of MNPZ degradation.

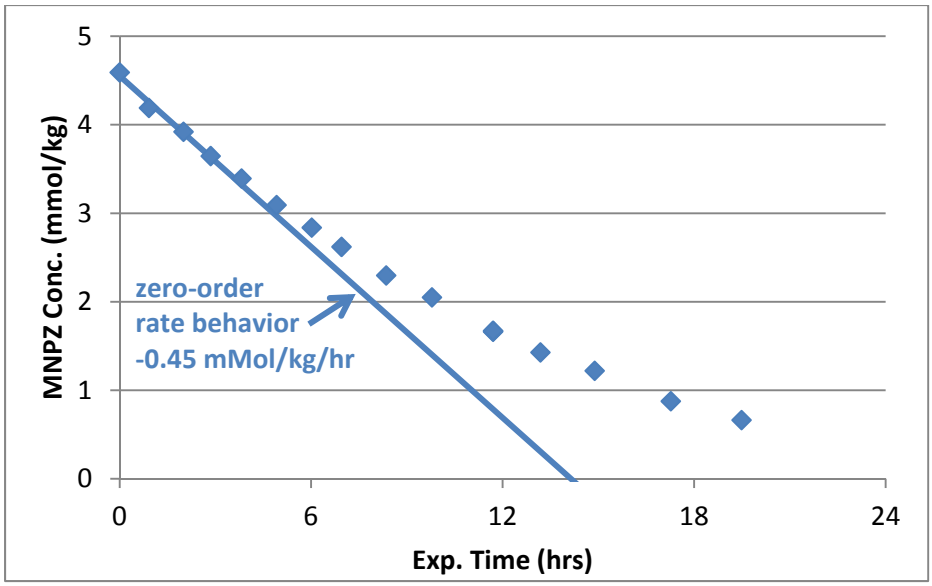

Figure 27: Degradation of MNPZ in 40 wt % PZ at 0.36 loading with UV-light. Conditions: room temperature, 15% hold-up in 11 W UV-C lamp, pH = 8.95, 2 L inventory, 900 RPM agitation in liquid reservoir.

Degradation of PZ in the batch UV system was determined by measuring the rate of alkalinity loss of the solution over a period of several days (Figure 28). The rate was 3.3 mMol/kg/hr; this rate is considerably higher than the rate of degradation in the presence of oxygen at 55 °C with no UV light (<0.5 mMol/kg/hr) (Freeman, 2011).

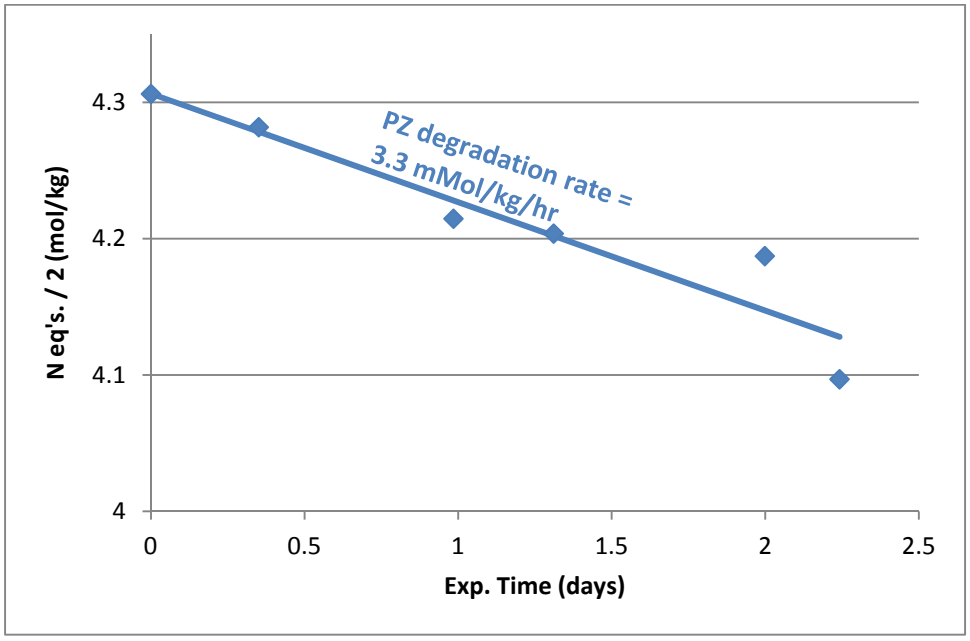

Figure 28: Degradation of PZ by UV light in the presence of air. Conditions: 40 wt % PZ, 0.27 loading, room temperature, 15% hold-up in 11 W UV-C lamp, 2 L inventory, 900 RPM agitation in liquid reservoir.

Batch UV Degradation of NDELA

Degradation of NDELA by UV light in water and MEA solutions was carried out in the same batch system with 15% hold-up in an 11 W UV-C lamp.

Degradation rates with UV light, which were generally observed to be zero order in NDELA concentration over more than three orders of magnitude, are reported in Table 8. For clear solutions with NDELA, the rates ranged from -0.52 to -0.86 mmol/kg/hr.

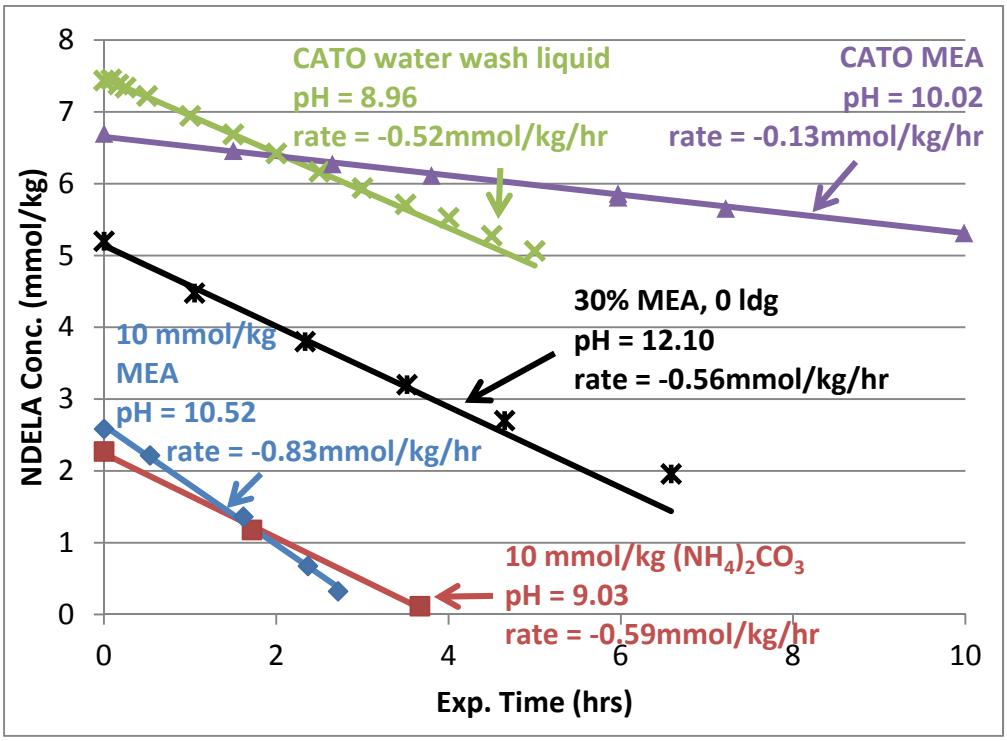

Figure 29: Comparison of NDELA destruction rates by UV light. Conditions: room temperature, 15% hold-up in 11 W UV-C lamp, 2 L inventory, 900 RPM agitation in liquid reservoir.

Table 8: Summary of UV degradation rates of NDELA and MNPZ. Conditions: room temperature, 15% hold-up in 11 W UV-C lamp, 2 L inventory, 900 RPM agitation in liquid reservoir

Nitrosamine	*Solution*	*pH*	*Initial rate*
NDELA	Water + 10 mMol/kg MEA	10.52	-0.83
NDELA	Water + 10 mMol/kg $(NH_4^+)_2CO_3^{2-}$	9.03	-0.59
NDELA	CATO water wash liquid	8.96	-0.52
NDELA	30 wt % MEA	12.10	-0.56
NDELA	CATO absorption liquid (11.1 wt % MEA)	10.02	-0.13
MNPZ	40 wt % PZ, 0.27 ldg	10.10	-0.34
MNPZ	40 wt % PZ, 0.36 ldg	8.95	-0.45

Rates of destruction of NDELA in water were sufficiently rapid that the NDELA concentration was reduced to below 0.75 µmol/kg (the detection limit of the HPLC) in several hours. The pH of the solution did not have a large impact on the degradation rate, however the rate in an amber-colored degraded MEA solution was significantly slower (at -0.13 mMol/kg/hr) than in the clear solutions (neat MEA or CATO water wash liquid). This is attributed to the presence of UV-light absorbing compounds in the solution. The UV absorbance spectrums of clean MEA and the CATO MEA solution are shown in Figure 30. UV degradation in an industrial system would be most effective employed on the water wash solution rather than the absorption liquid.

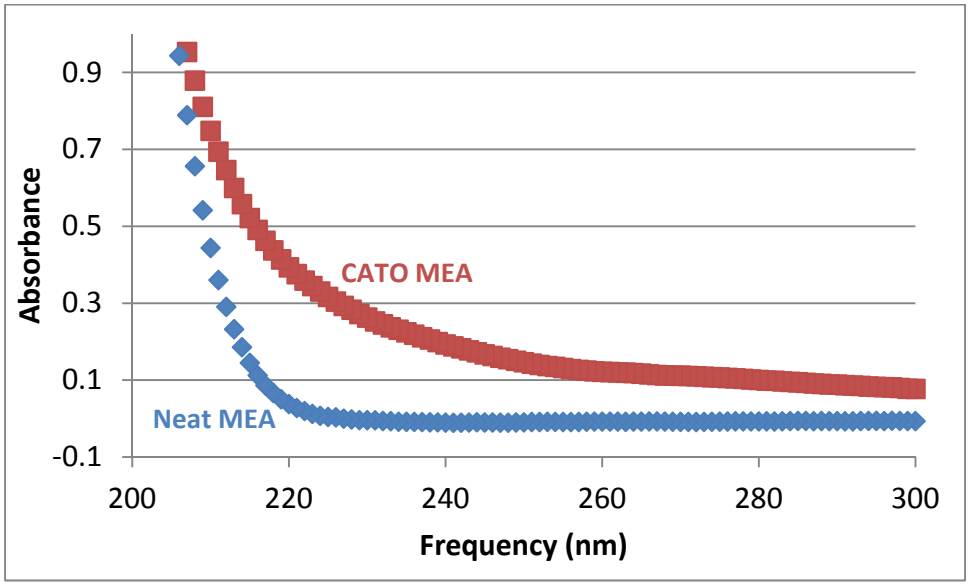

Figure 30: UV absorption spectrums of neat MEA and CATO pilot plant MEA. 1000x dilution.

Conclusions

- Ammonia was produced at 3–4 mMol/hr in the miniplant with clean MEA; for used MEA the rate was 20–24 mMol/hr. No chemical inhibitors of MEA oxidation were able to significantly reduce ammonia production in a mini CO_2 capture plant (tested DTPA, HEDP, DMcT, Inh A).
- The activation energy of ammonia production from the absorber in the miniplant was 29 kJ/mol, indicating that air bubble entrainment may be responsible for 72% of oxidation
- UV degradation of NDELA was four times faster in the CATO water-wash solution (-0.52 mMol/kg/hr) than in the absorption liquid (-0.13 mMol/kg/hr). The rate of UV degradation of NDELA and MNPZ in water was zero-order in nitrosamine over several orders of magnitude. The presence of impurities reduced the degradation rate by a factor of 4.3x; pH and amine concentration did not significantly affect the degradation rate.
- Thermal degradation of nitrosamines occurred at rates from 3.6 to 21.4 mMol/kg/hr at high temperatures (160–200 °C). The rate was lower than expected at lower pressure and in the presence of oxygen
- The volatility of MNPZ from the absorber in the miniplant was roughly the same (1.02 x) the volatility of PZ at the absorber conditions. The MNPZ emissions were not the result of mechanical entrainment.

References

Carrette P-L. World patent no. WO 2009/156619 A2. 30 December 2009.

Closmann F. *Oxidation and thermal degradation of methyldiethanolamine/piperazine in CO_2 capture*. The University of Texas at Austin. Ph.D. Dissertation. 2011.

Fine N. Personal communication. 8 Dec 2011.

Freeman SA. *Thermal degradation and oxidation of aqueous piperazine for CO_2 capture*. The University of Texas at Austin. Ph.D. Dissertation. 2011.

Fulk S. "Contaminant control in amine-based CO_2 capture." Presentation at The University of Texas at Austin. Austin, TX. 8 Nov 2011.

Goff GS. *Oxidative Degradation of Aqueous Monoethanolamine in CO_2 Capture Processes: Iron and Copper Catalysis, Inhibition, and O_2 Mass Transfer*. Ph.D. Dissertation. The University of Texas at Austin. 2005.

Hakka LE. US patent no. 7056482 B2. 6 Jun 2006.

McCullough JG. US patent no. 4971718. 20 Nov 1990

Rochelle GT et al. "CO_2 Capture by Aqueous Absorption, Third Quarterly Progress Report 2011." Luminant Carbon Management Program. The University of Texas at Austin. 2011.

Voice AK. "MEA oxidation in CO_2 capture." Presented at the 6th Trondheim CCS conference (TCCS-6). Trondheim, Norway. 15 Jun 2011.

Williams DLH. *Quantitative aspects of nitrosamine denitrosation*. In: *Nitrosamines and related N-nitroso compounds;* Leoppky RN, Michejda CJ, Ed.; ACS Symposium Series. 1994.

Volatile Emission Control in CO_2 Capture

Quarterly Report for October 1 – December 31, 2011

by Steven Fulk

Supported by the Luminant Carbon Management Program

Department of Chemical Engineering

The University of Texas at Austin

January 31, 2012

Abstract

In this quarter, an Ultraviolet-Visible (UV-VIS) absorption spectroscopy method was developed to locate characteristic absorption bands for pure compounds and aqueous solutions. Mononitrosopiperazine (MNPZ) and N-Nitrosodiethanolamine (NDELA) absorption spectra were measured to determine the efficacy of UV techniques for nitrosamine destruction. MNPZ showed two strong absorption peaks at wavelengths of 237 and 341 nm. NDELA showed two strong absorption peaks at wavelengths of 232 and 345 nm. Amber vials will prevent UV degradation of nitrosamines in samples because nitrosamines absorb only in the UV region.

CO_2 solubility was measured for 8 and 0.15 m PZ solutions between 40–70 °C. Measured CO_2 partial pressures agree closely with predictions using the Fawkes model, further validating speciation predictions and steady-state loading estimations from previous water wash modeling work.

A combined water wash/absorber column was designed in Aspen Plus® using the Fawkes thermodynamic and kinetic framework. The water wash and absorber column were combined to prevent the gas exiting the absorber from flashing prior to entering the water wash packed section.

Goals for next quarter include sensitivity analysis of the combined absorber/water wash column to determine the effects of process variables on column physical dimensions and temperature profiles/aerosol formation driving forces. Degradation compound absorption spectra will be measured using UV-VIS spectroscopy to locate absorption spectral overlap with nitrosamine compounds.

Introduction

Volatile emissions are a primary concern for CO_2 capture plants using amine scrubbers. Emissions constitute increased economic expense through solvent loss as well as a source of potentially hazardous environmental pollutants. Compounds found in treated flue gas include contaminants from thermal degradation and oxidation as well as combustion byproducts. Degradation and reaction products have a wide range of toxicity and biodegradation characteristics which potentially represent unacceptable emissions; as a result, recent work has focused on estimating volatile losses and assessing their toxicological impact.

Volatile emissions can be reduced through the use of an absorber column using recycled water as a solvent, called a water wash. Last quarter, a water wash column was simulated in Aspen Plus® with input conditions specified from a separate absorber column. In this quarter, the water wash and absorber columns were combined into one column with separate packing sections to prevent preflashing of the vapor from the absorber into the water wash.

A notable risk for amine scrubbers is the production and emission of nitrosamines created through reaction of nitrogen oxides present in flue gas with secondary amines. Nitrosamines are of particular concern due to their carcinogenic, mutagenic, and teratogenic characteristics. Primary and tertiary amines do not react directly to produce nitrosamines, but production of secondary amines by degradation can create pathways to nitrosamine formation.

One possible way to control nitrosamine emission in CO_2 capture plants is to use UV light sources to selectively degrade nitroso compounds. Every chemical compound has a characteristic absorption spectrum; therefore, photo-degradation can be applied with specificity by filtering light sources to narrow sets of wavelengths.

UV treating systems must be designed to degrade nitrosamines while minimizing photo-oxidation of the capture solvent. UV-VIS spectra can be measured to determine possible spectral overlaps between nitrosamines and other preferentially degradable compounds and aqueous amine solvents.

Experimental Methods

Ultraviolet – Visible Spectroscopy

Absorption spectroscopy was used to locate characteristic absorption bands for pure compounds and solutions in water. A Cary 5000 UV-VIS NIR Spectrometer was used to measure absorption between wavelengths of 200–800 nm. Solutions were placed into Suprasil Quartz cuvettes with 10 mm path lengths and sealed with PTFE caps.

A background absorption spectrum was taken with a cuvette filled with DDI water. Absorption spectra were then measured for aqueous solutions. The background spectrum was subtracted from the aqueous solution spectra revealing absorption peaks of all dissolved solutes.

Amine Volatility Apparatus

Low temperature CO_2 solubility was measured using a recirculated vapor, vapor-liquid equilibrium apparatus. 500 mL of solution was loaded into an insulated 1 L glass-jacketed reactor with motorized agitation at 300 rpm. The reactor temperature was regulated by circulating di-methyl silicone oil from an external heated bath. Vapor from the head space was sampled by a sample pump at 5 L/min and sent through a heated Teflon line at 180 °C to a hot-gas FTIR analyzer (Temet Gasmet Dx-4000). The vapor from the analyzer was sparged into the bottom of the reactor at 55 °C below the reactor temperature.

For a more detailed description of the amine volatility procedure, see section 2.3.4 of Hilliard (2008).

Analytical Methods

Total Inorganic Carbon Analysis (TIC)

The Total Inorganic Carbon analysis was used to quantify CO_2 loading in samples. Generally, a sample of known mass is injected into a port containing 30 wt % H_3PO_4 where the sample is acidified and CO_2 is given off according to the following equilibrium equations:

$$HCO_3^- + H_2O \leftrightarrow H_3O^+ + CO_3^{2-} \quad (1)$$

$$CO_2 + 2H_2O \leftrightarrow H_3O^+ + HCO_3^- \quad (2)$$

The CO_2 is then carried by a nitrogen stream to a Horiba PIR 2000 CO_2 analyzer where voltage response versus time data is sent to a computer for tabulation. A plot of voltage versus time for a given experimental run reveals a series of peaks corresponding to sample injections. The area of a given injection peak provides a means of calculating the amount of CO_2 contained in a sample when compared to injections of a carbon standard. The carbon standard used for this analysis technique was a buffered K_2CO_3/$KHCO_3$ 1000 ppm by mass standard.

Injection volume depends on the concentration of CO_2 in the sample; consequently, the dilution factor of the sample plays a role in fine-tuning injection volumes to fall in the appropriate voltage range of the CO_2 analyzer. Once the solutions were diluted properly, the injection volumes were adjusted to achieve a voltage response of approximately 0.5 V. The injection volume of samples ranged from 25–-45 μL. After all of the samples were injected in triplicate, five different volumes of the 1000 ppm by mass carbon standard were injected with a voltage response range encompassing all of the sample responses to create a calibration curve. The calibration curve was then used to calculate the moles of CO_2 contained in a sample. CO_2 concentration information given by TIC used in conjunction with amine concentration information from cation chromatography allows calculation of loading (moles CO_2/mol alkalinity) of the samples.

For a more detailed description of the TIC procedure, see Appendix B.2–B.7 of Hilliard (2008).

Results

Amine Volatility/CO_2 Solubility

In the previous quarter, water wash modeling showed that steady-state loadings in the recirculating water in the water wash were higher than loadings found in the absorber; therefore, validation of the thermodynamic predictions was necessary prior to further water wash modeling.

CO_2 solubility measurements for 0.15 m PZ solutions agreed closely with predictions from the Fawkes thermodynamic model. Equilibrium CO_2 partial pressure predictions and measurements at 40 °C for 0.15 and 8 m PZ solutions are shown in Figure 1 below. Measured loadings are shown in Table 1. Measurements above 50 °C for 0.15 m PZ solutions became erratic due to strong spectral interference of water.

CO_2 solubility depends on amine concentration when bicarbonate formation represents a significant portion of loading. Speciation predictions from the Fawkes model show that when the PZ concentration drops below 0.5 m, the majority of dissolved CO_2 exists as bicarbonate. Since the heat of absorption is lower for bicarbonate formation than for carbamate species, the equilibrium partial pressure of CO_2 will be lower for a given temperature.

Table 1: Solution loading and CO_2 equilibrium partial pressure at 40 °C

Piperazine (m)	Loading (mol CO_2/mol alk.)	P^*_{CO2} (kPa)
8	0.294	0.295
	0.349	1.035
	0.399	5.227
0.15	0.314	0.235
	0.349	0.419
	0.357	0.519
	0.409	0.757

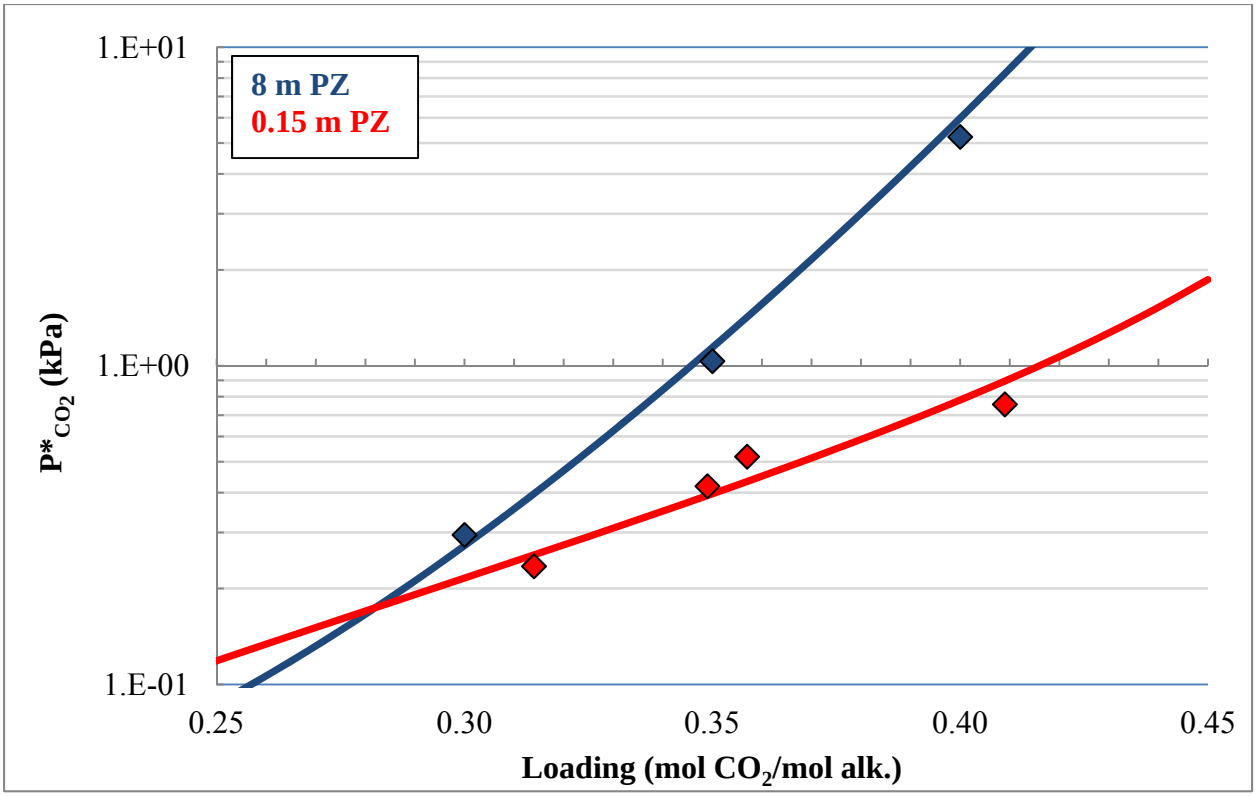

Figure 1: CO_2 solubility for 8 and 0.15 m PZ solutions at 40 °C. (Lines – Fawkes Predictions, Points – Measured Values.)

The Fawkes model accurately predicts CO_2 solubility at PZ concentrations as low as 0.15 m. Consistency between CO_2 solubility measurements and model predictions indicate accurate speciation. Correct speciation predictions lead to more accurate amine volatility estimation. Over this wide range of PZ the equilibrium CO_2 partial pressure is a function of CO_2 loading and amine concentration.

UV-VIS Spectroscopy

Figures 2 and 3 show pure compound UV-VIS spectra for MNPZ and NDELA, respectively. Absorption peaks correspond to electronic transitions in molecular orbitals. Larger wavelengths correspond to lower energy transitions. Absorption peaks at 340 nm correspond to non-bonded

pair electrons transitioning to anti-bonded pi orbitals, and absorption peaks at 235 correspond to bonded pi orbital electrons transitioning to anti-bonding pi orbitals. Since the peak positions for MNPZ and NDELA are very similar, the electronic configuration of the nitrosamine bond is not appreciably affected by the rest of the molecular structure.

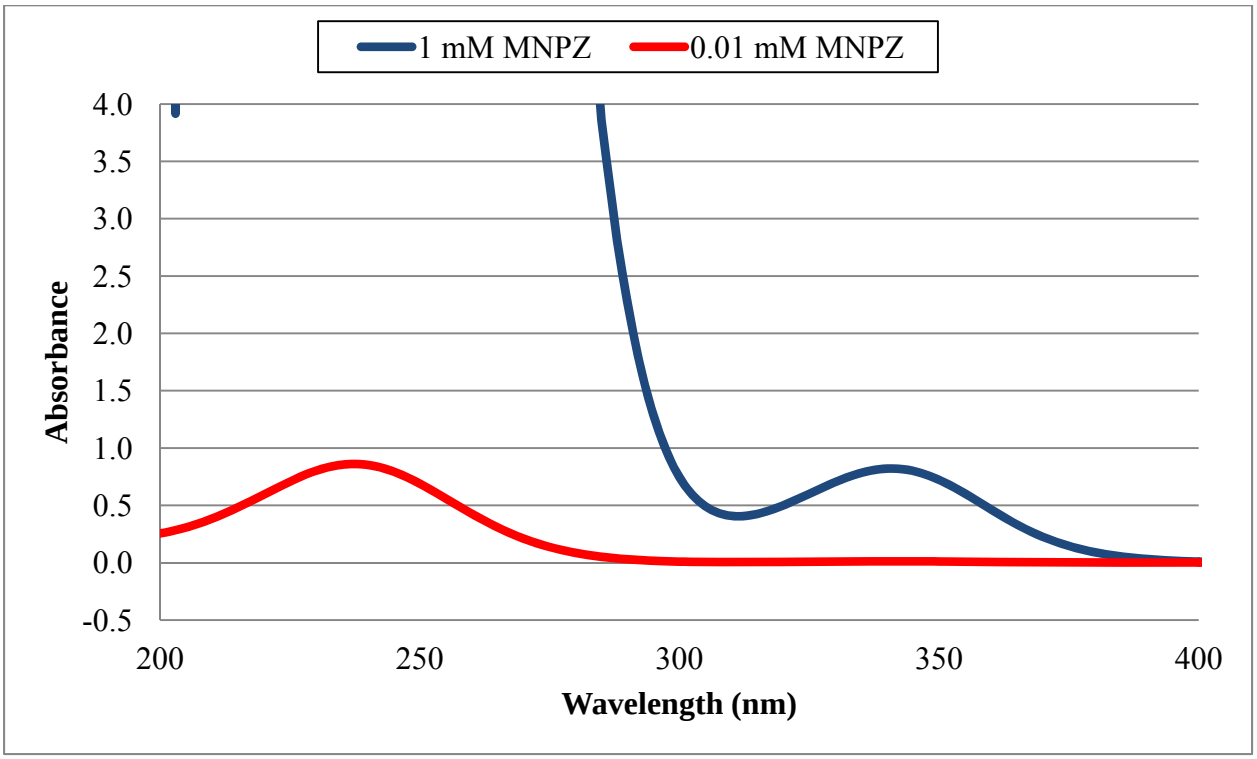

Figure 2: MNPZ UV-VIS absorption spectra

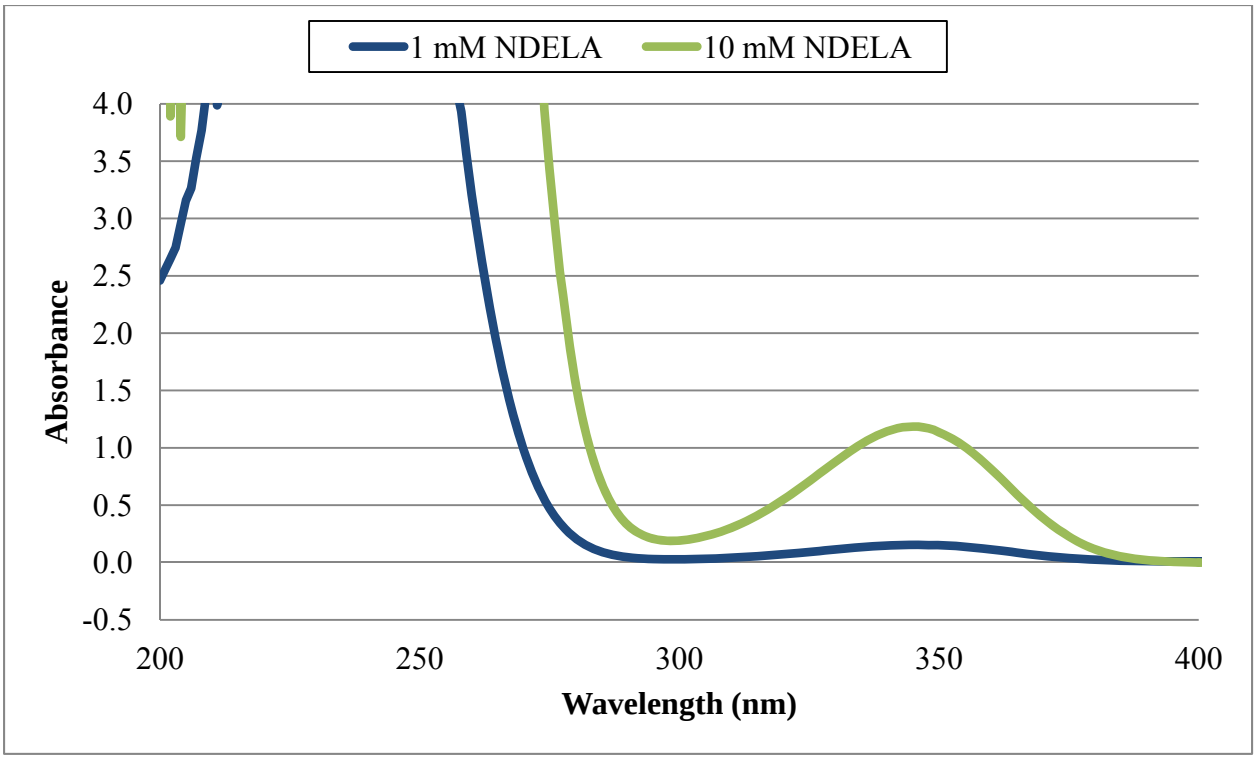

Figure 3: NDELA UV-VIS absorption spectra

The measured UV spectra show that MNPZ is a much stronger absorber than NDELA at equivalent concentrations.

Water Wash Modeling

In this quarter a combined water wash/absorber column (Figure 4) was modeled in Aspen Plus® using the Fawkes model developed by the Rochelle group. The Jones-Dole viscosity model was used instead of correlations developed by the Rochelle group due to inaccurate predictions at low amine concentrations.

In the transfer section from the absorber to the water wash, the recirculating water wash solution exits the column and the lean CO_2 capture solution enters. A small purge stream, which contains the total amount of amine absorbed per pass in the water wash section, is transferred into the absorber section. The vapor from the absorber passes directly into the water wash, preventing flashing prior to water wash mass transfer calculations.

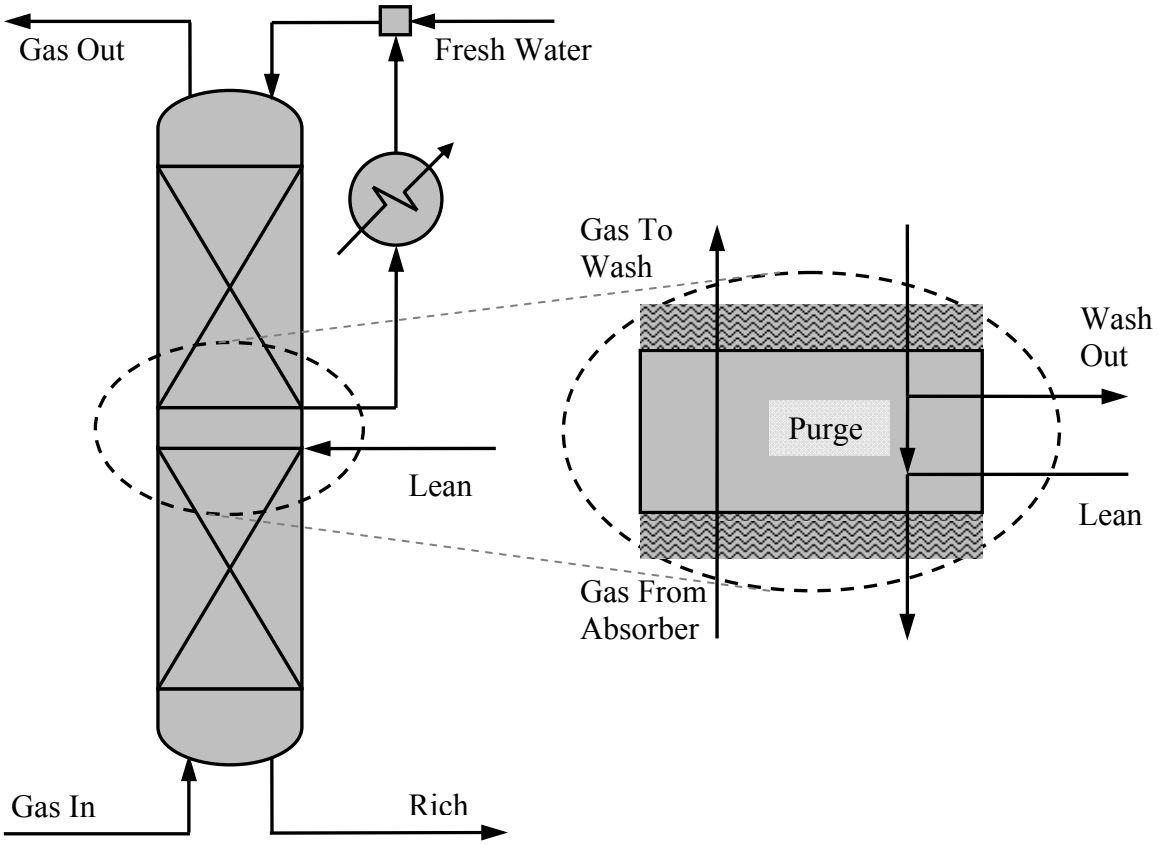

Figure 4: Combined absorber/water wash column with magnified transfer section.

In the next quarter, sensitivity analyses will determine the effects of process variables on column physical dimensions and temperature profiles/aerosol formation driving forces

Conclusions

- MNPZ has maximum absorption peaks at 237 and 341 nm.
- NDELA has maximum absorption peaks at 232 and 345 nm.
- MNPZ is a much stronger UV absorber than NDELA.
- Amber vials prevent photo-oxidation of nitrosamines in samples.
- The Fawkes model accurately predicts CO_2 solubility of solutions at low amine concentrations.
- At water wash conditions, 1 kPa CO_2, 40 ^oC, and 0.15 m PZ, the equilibrium CO_2 solubility is 0.42 mol CO_2/equiv PZ.

Future Work

Goals for next quarter include sensitivity analysis of the combined absorber/water wash column to determine the effects of process variables on column physical dimensions and temperature profiles/aerosol formation driving forces. Degradation compound absorption spectra will be measured using UV-VIS spectroscopy to locate absorption overlap with nitrosamine compounds.

References

Hilliard MD. *A Predictive Thermodynamic Model for an Aqueous Blend of Potassium Carbonate, Piperazine, and Monoethanolamine for Carbon Dioxide Capture from Flue Gas.* The University of Texas at Austin. Ph.D. Dissertation. 2008.

Rochelle GT et al. "CO_2 Capture by Aqueous Absorption, Third Quarterly Progress Report 2009." Luminant Carbon Management Program. The University of Texas at Austin. 2009.

Rochelle GT et al. "CO_2 Capture by Aqueous Absorption, Fourth Quarterly Progress Report 2010." Luminant Carbon Management Program. The University of Texas at Austin. 2011.

Sandler SI. *Chemical, Biochemical, and Engineering Thermodynamics*. 4th ed. Hoboken, NJ: John Wiley & Sons, Inc.; 2006.

Piperazine Degradation in Pilot Plants

Quarterly Report for October 1 – December 31, 2011

by Paul T. Nielsen, III

Supported by the Luminant Carbon Management Program

Department of Chemical Engineering

The University of Texas at Austin

January 31, 2012

Abstract

This progress report discusses the findings made in solvent degradation characterization at the pilot-plant scale. In the fall of 2011, pilot plant campaigns were run at the Pickle Research Campus using 8 m piperazine (PZ). Also, a second campaign was run at "Pilot Plant 2" using the same solvent. Data from these campaigns can be used to determine the degradation rate of PZ and the formation of harmful byproducts, including N-nitrosopiperazine (MNPZ), a known carcinogen. MNPZ was shown to form in both pilot plants, but at a very small concentration in the solvent of no more than 8 ppm at the Pickle Research Campus and 324 ppm at Pilot Plant 2. After an initial spike within the first month of startup at Pilot Plant 2, MNPZ concentration settled at a steady state of approximately 100 ppm for the following 6 weeks.

Goals for next quarter include a more complete determination of the degradation products and rates from the pilot plant samples.

Introduction

PZ has shown promise as a solvent for carbon dioxide capture, with greater capacity, adsorption rate, and stability than the baseline monoethanolamine solvent. PZ degradation has been extensively studied in a laboratory setting (Freeman, 2011), but less data has been collected from pilot plant studies. It is vitally important to compare laboratory and pilot plant data in order to ensure the validity of the theories and models developed and to determine the scalability of PZ-based carbon capture facilities.

PZ can degrade into a wide variety of products, including N-nitrosopiperazine (MNPZ) and N,N-nitrosopiperazine (DNPZ), which have shown carcinogenic properties in laboratory tests. PZ can react with NO_2^- absorbed from the flue gas to form MNPZ, which can then react with more NO_2^- to form DNPZ. PZ may also degrade into a wide variety of other products through either thermal or oxidative degradation reactions. (Closmann, 2011; Freeman, 2011).

Samples of PZ solvent were collected from pilot plants at the Separations Research Program (SRP) at the Pickle Research Campus (PRC) in Austin, Texas, and from "Pilot Plant 2." PRC ran a campaign using 8 m PZ with a two-stage flash stripping system in September and October 2011. A large sample of PZ was collected at the end of the run for extensive testing. Pilot Plant 2 included a test of a solvent reclaiming process and a water wash system to capture volatile degradation products. Samples of solvent were collected at least once a week from Pilot Plant 2

to explore the changes over time. Also, samples of water were collected from the water wash system installed on Pilot Plant 2.

Experimental Methods

HPLC

HPLC (Dionex ICS3000) was used to measure MNPZ and several other nonpolar degradation products in the solvent and wash samples. PZ solvent samples were diluted to a factor of 20X by weight and water wash samples were diluted to 5X. A 0.01 M aqueous ammonium carbonate solution, acetonitrile, and methanol were used as eluents. The ramp time for these solvents is shown below in Figure 1. The column was used with a UV wavelength of 240 nm (Voice, 2011).

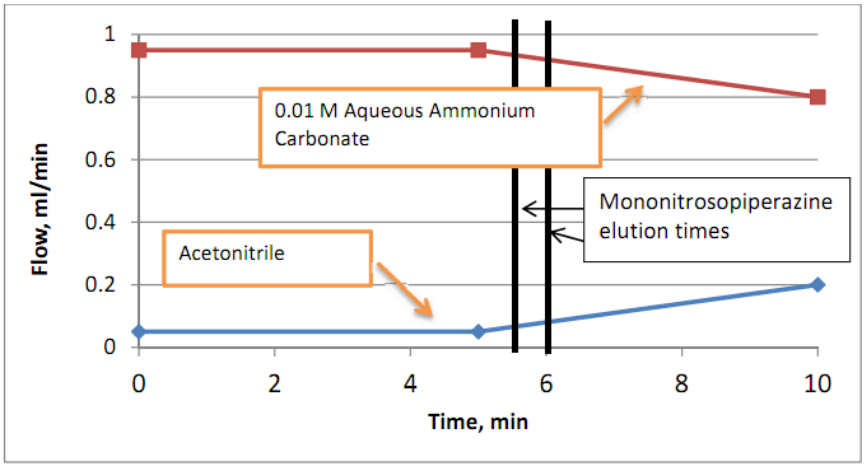

Figure 1: HPLC eluent flow as a function of time, adapted from Voice, 2011

MNPZ eluted at around 6 minutes. A calibration curve for MNPZ was developed from data collected by Fine in November 2011. The data were fit with the following quadratic regression, which had an r^2 value of 0.99994. "x" is the peak area (mAU*min), DF is the dilution factor, and "y" is the actual MNPZ concentration (ppm):

$$y = DF\times[4.7790\times10^{-5}(x)^2 + 1.7134(x) - 0.16449] \quad (1)$$

Cation IC

The concentration of PZ and other degradation products was measured using cation chromatography (Dionex ICS2100) at a dilution factor of 10000X. Cation IC measures the concentration of positively charged cations. The eluent consisted of methanesulfonic acid (MSA) in deionized water. The method uses an eluent ramp starting at 5.5 mM MSA and increasing in concentration over the course of the run to 38.5 mM MSA. The run time per sample was 50 minutes. Flowing the sample and eluent between a cathode and anode separated by two membranes, the anions were removed from the sample, leaving only cations, as shown in figure 2. The separation occurred in an IonPac GC 17 guard column and an IonPac CS 17 analytical column. Both columns contained ethylvinylbenzene cross-linked with 55% divinylbenzene resin as the primary separation medium. Changes in solution conductivity were then measured over time using a conductivity detector to create a chromatogram (Freeman, 2011).

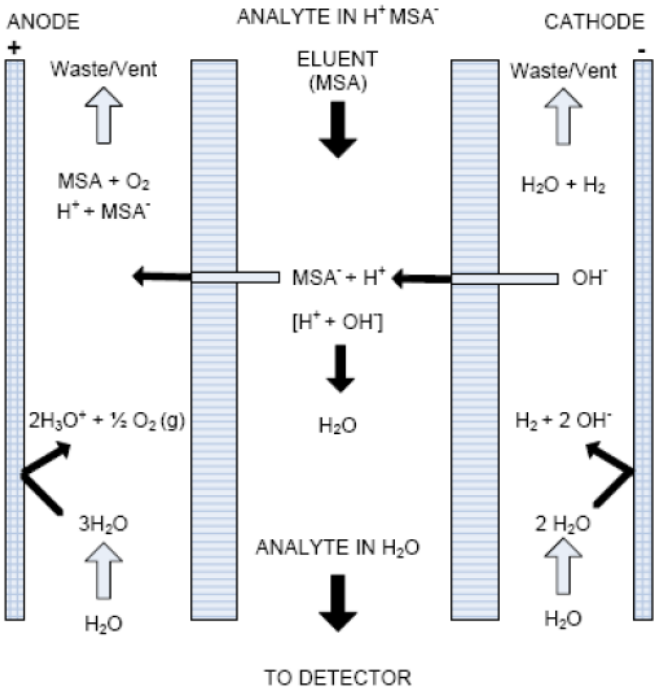

Figure 2: Schematic of CSRS 3000 anion suppressor, adapted from Freeman (2011)

PZ eluted at approximately 33 minutes.

TIC

The Total Inorganic Carbon (TIC) method was used to determine CO_2 loading of the solvent samples. At a dilution of 100X, the samples were treated with 30 wt % phosphoric acid, which reacted with the PZ and released all the CO_2 as a vapor. The CO_2 could then be measured with an infrared CO_2 detector.

Results

Production of MNPZ and Other Degradation Products

For the Pilot Plant 2 and PRC solvent, the concentration of MNPZ and other degradation products was measured using HPLC. A typical absorption spectrum for a more-degraded lean sample from Pilot Plant 2 is shown below in

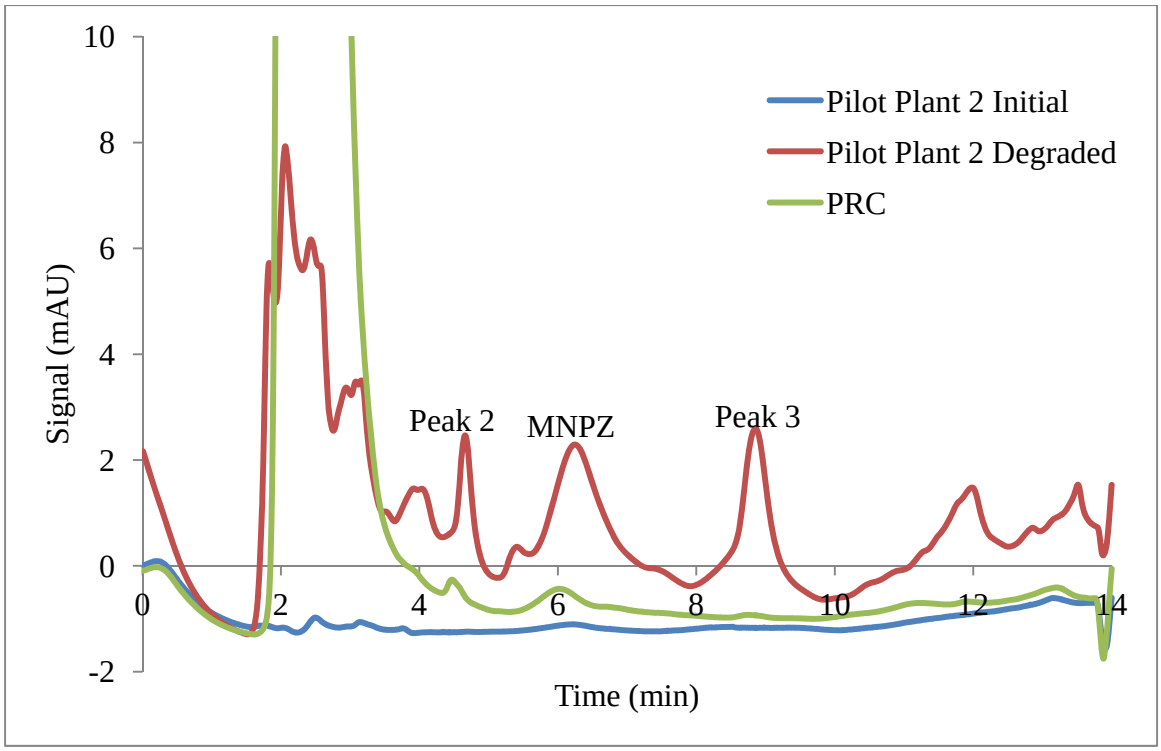

Figure 3, overlaid with the PRC solvent spectrum. MNPZ eluted at around 6 minutes. For the Pilot Plant 2 solvent, two other peaks were studied in detail, labeled on

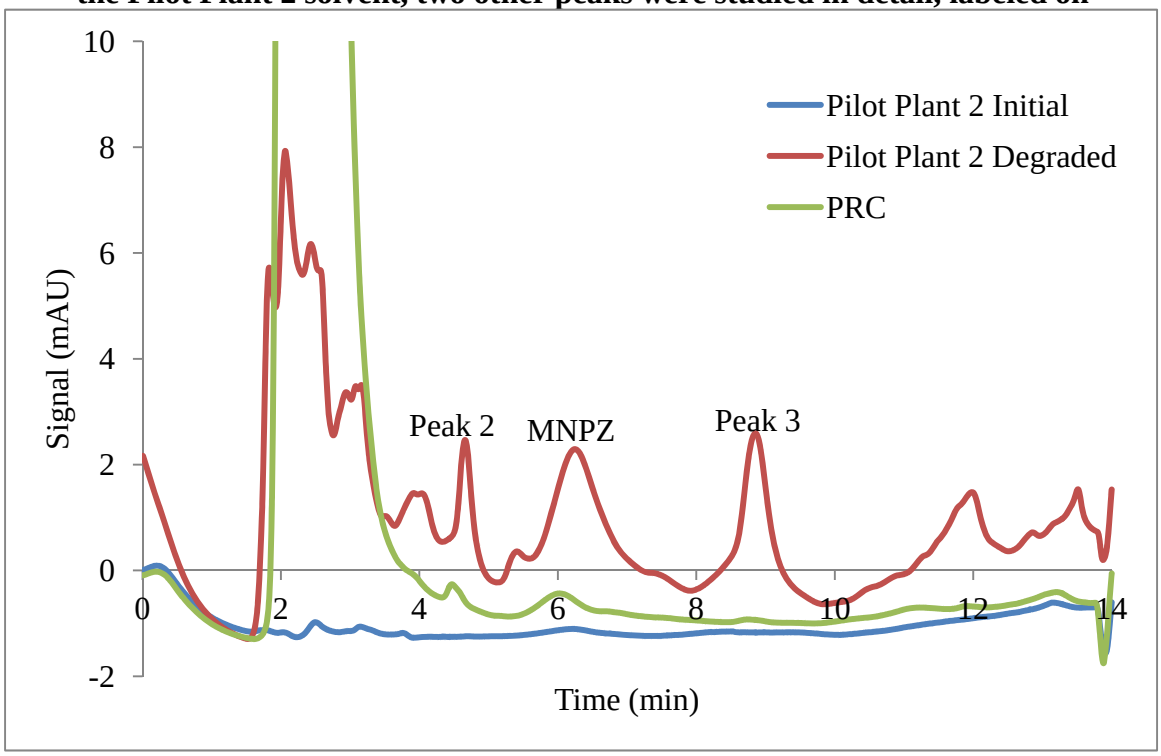

Figure 3 as "Peak 2" (4.5 minutes) and "Peak 3" (8 minutes). Positive identification of these peaks has not yet been made, but it is possible that "Peak 2" may be 2-imidazolidone (2-Imid), which has been observed to elute at around 5 minutes in previous work (Freeman, 2011). 2-Imid

is a secondary degradation product formed from ethylenediamine (EDA). "Peak 3" may be DNPZ, which has been observed to follow MNPZ by approximately 2 minutes. However, the observed peak does not have the characteristic shape normally associated with DNPZ.

The Pilot Plant 2 spectrum also contains a cluttered mass of peaks in the 2–4 minute time range. These peaks do not appear in the earliest solvent samples and build up over time, indicating that they are also degradation products.

Based on peak area, the PRC sample has an MNPZ concentration of approximately 7.6 ppm while the Pilot Plant 2 solvent contains 78 ppm MNPZ after 60 days. The PRC solvent also showed far less formation of other degradation products, although some products may be occluded by the injection peak at 2.5 minutes.

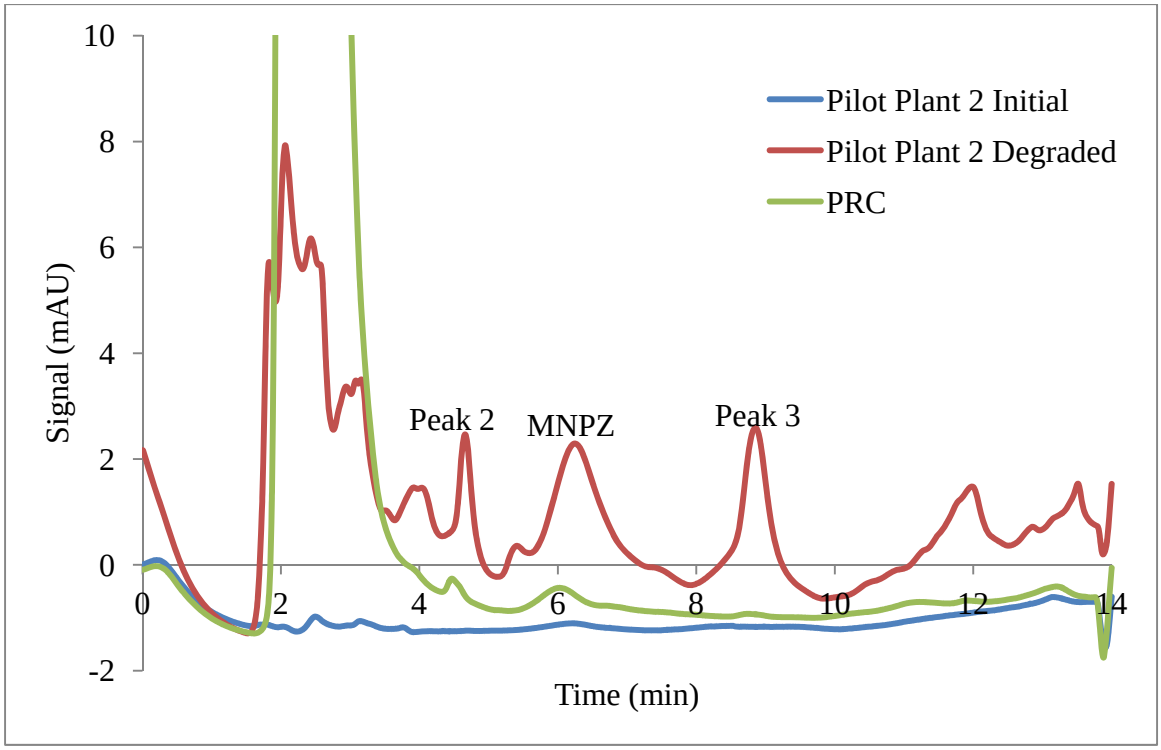

Figure 3: HPLC spectra for degraded PZ solvent from Pilot Plant 2 (lean, day 1 and degraded) and Pickle Research Campus (end of run)

In Figure 4, the concentration of MNPZ in the lean and rich Pilot Plant 2 solvents is plotted over time. MNPZ initially spiked to 320 ppm early before dropping off substantially between. After this, the MNPZ concentration stayed at roughly 100 ppm throughout the rest of the campaign. Reclaiming was run near the end of the campaign. This may have temporarily slowed the formation of MNPZ but did not eliminate the carcinogenic compound. MNPZ concentration did not differ significantly between the lean and rich solvents.

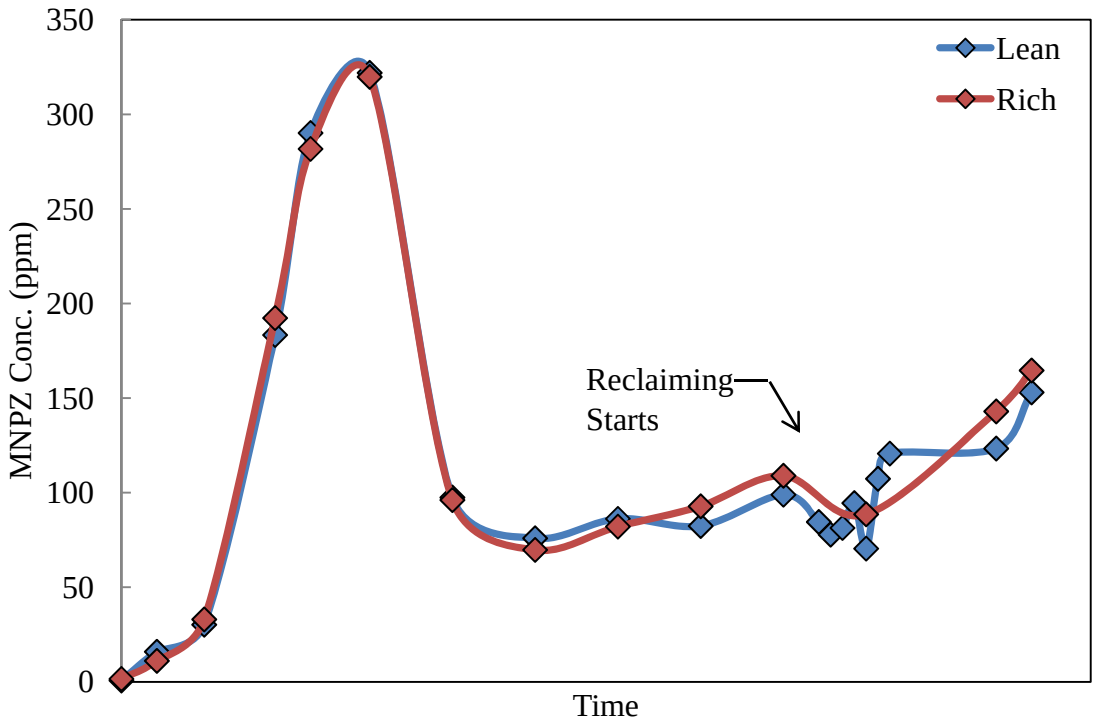

Figure 4: MNPZ formation in PZ solvent of Pilot Plant 2

Two other degradation peak areas were analyzed to illustrate degradation over time. "Peak 2," possibly 2-Imid, is shown in Figure 5. "Peak 3," possibly DNPZ, is shown in Figure 6. Both show a steady increase in the concentration of the degradation products, especially after week 4. However, both reached equilibrium when the reclaiming process was started. The concentration of the compound represented by Peak 2 seems to be higher in lean solvent than rich solvent, although the same effect is not observed in Peak 3, where the compound concentration seems to be the same regardless of whether the solvent is lean or rich.

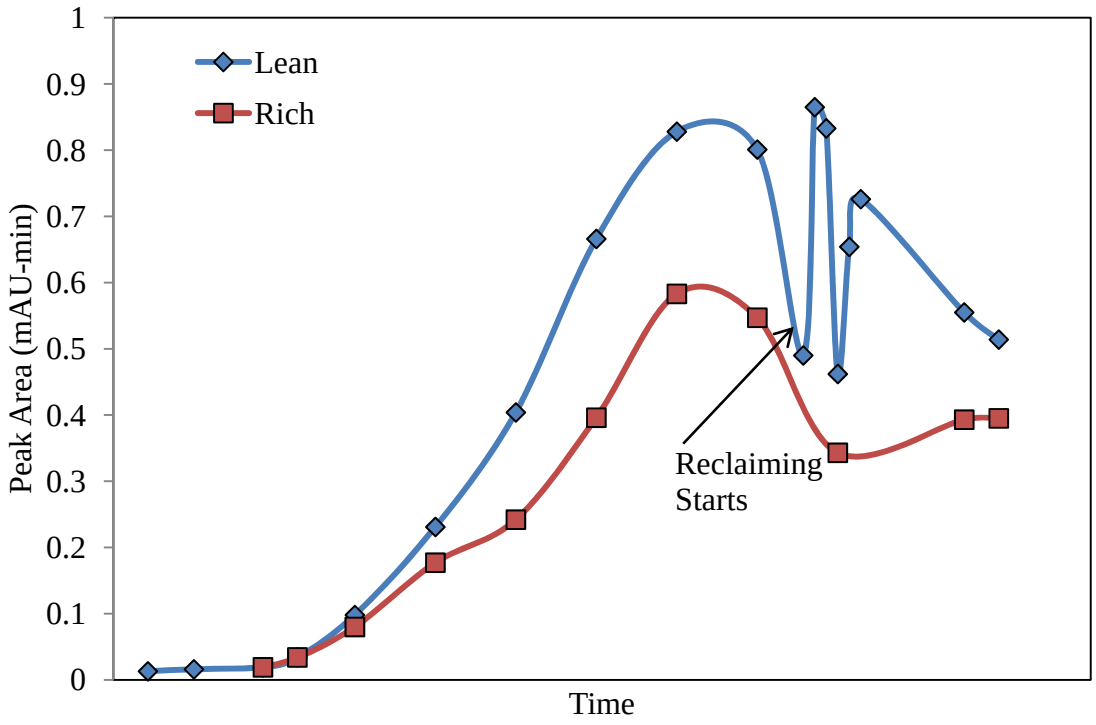

Figure 5: Pilot Plant 2 area of "Peak 2" from HPLC data

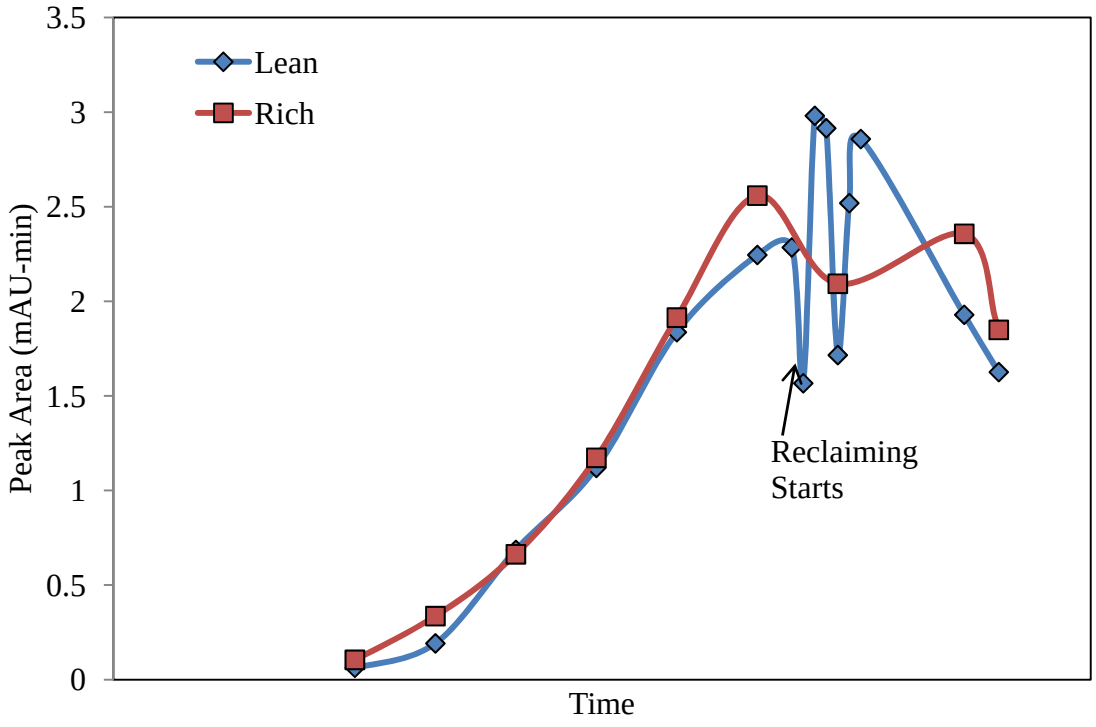

Figure 6: Pilot Plant 2 area of "Peak 3" from HPLC data

Water wash samples were collected from Pilot Plant 2 and tested for MNPZ. The results are shown below in Figure 7. At the beginning of the run, MNPZ concentration was nearly 8 ppm in the wash water. Later in the run the concentration fell to around 2 to 4 ppm. This drop is consistent with the decrease in MNPZ observed in the solvent samples after week 4.

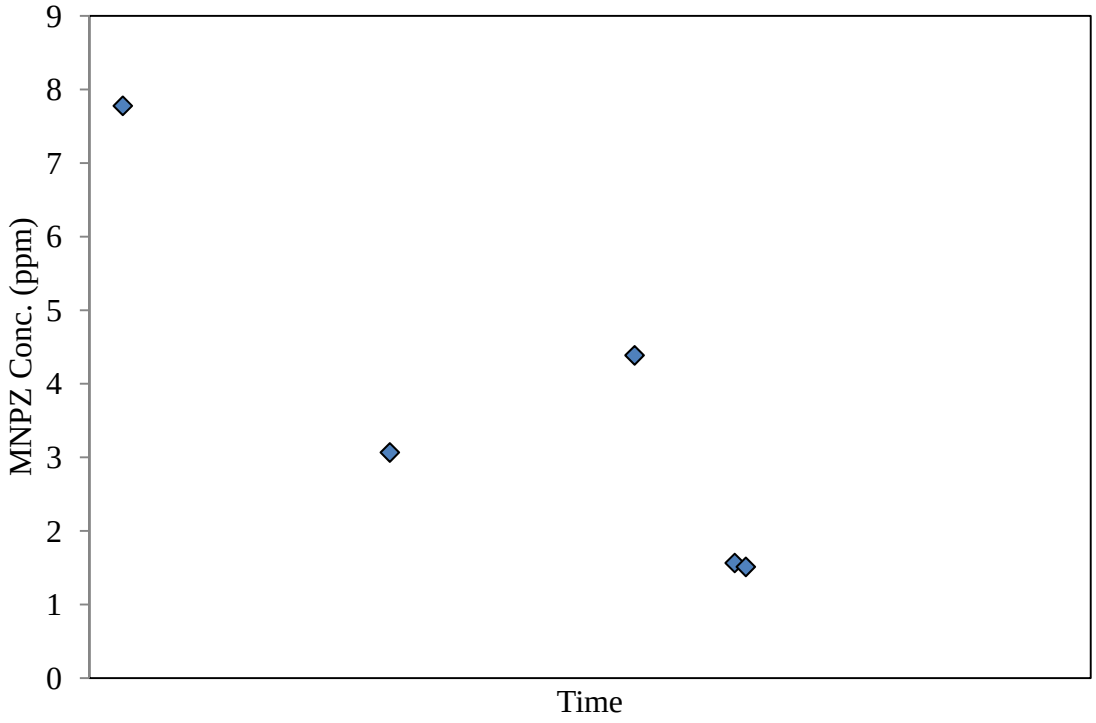

Figure 7: MNPZ concentration in Pilot Plant 2 water wash

CO_2 Loading of Solvent Samples

CO_2 loading was measured using TIC. The PRC lean solvent had a loading of 0.304 mol CO_2/mol alkalinity at the end of its run.

Conclusions

The Pickle Research Campus pilot plant campaign solvent contained 7.6 ppm MNPZ at the end of the run, a relatively small amount. The PRC pilot plant uses air with the addition of CO2 to simulate flue gas. There should be no significant concentration of NO_x in the ambient air. There may be production of NO_x or nitrosamine from oxidation of the piperazine by oxygen in the air.

Pilot Plant 2 had a significantly higher concentration of MNPZ, around 100 ppm for most of its run and as high as 324 ppm. However, the concentration of MNPZ in the water wash system of Pilot Plant 2 was much lower, never higher than 10 ppm. Pilot Plant Plant 2 uses coal-fired flue gas from a commercial unit using SCR for NO_x control. It is significant that the MNPZ reaches a steady-state concentration around 100 ppm and that the water wash is only 10 ppm with no express attempt to control the MNPZ. It is probable that the MNPZ is decomposing at the T and residence time of the stripper.

Based on this preliminary data, the reclaiming system used in Pilot Plant 2 had the effect of halting the formation of new degradation products, but did not reduce the concentration of degradation products already present in the system. MNPZ concentration was not significantly affected by reclaiming.

Future Work

A great deal more work needs to be done on the solvent and wash samples. All solvent samples were run in the Cation IC to determine PZ concentration and the formation of other positively-charged degradation products such as EDA and FPZ. However, the data had not been analyzed before the holiday break. PZ standards will also be run to create a calibration curve.

Anion IC has not yet been run due to issues with the column. This would allow for the measurement of formate production, one of the most important measurements of PZ degradation. The anion IC should be back online in early January.

The HPLC spectra will be further analyzed to determine the unidentified peaks. This will be done by running standards of suspected degradation products and by using LC-MS.

Some solvent samples were treated with 5 N NaOH to determine amide formation using the AA-LC method. These samples will be run through HPLC and anion and cation IC.

A major goal of the next quarter will be to determine methods to qualitatively measure degradation products that have been previously hypothesized but not positively identified in previous works, including 1-piperazineacetic acid (1-PA) and N-(2-aminoethyl)glycine (AEP). AEP is believed to form from 2-piperazinone and is likely a major product of oxidative degradation of PZ (Freeman, 2011). It will be determined whether these compounds will show up on HPLC if the buffer concentration (and thus pH) is changed. It has been hypothesized that AEP may be charge-balanced at a pH of between 7 and 8 and thus may be detectable with HPLC.

Once all the data from the solvent samples have been fully analyzed, a comparison will be made with the laboratory-scale work done previously by Freeman and Closmann to compare results. Eventually, an accurate model for PZ degradation may be constructed.

References

Closmann FB. *Oxidation and thermal degradation of methydiethanolamin/piperazine in CO_2 capture*. The University of Texas at Austin. Ph.D. Dissertation. 2011.

Freeman SA. *Thermal Degradation and Oxidation of Aqueous Piperazine for Carbon Dioxide Capture*. The University of Texas at Austin. Ph.D. Dissertation. 2011.

Voice AK. *Production of MNPZ from reaction of aqueous nitrite with piperazine in 4 m 2-AMP + 6 m PZ for CO2 Capture*. Unpublished Manuscript. 2011.

Formation and Decomposition of N-Nitrosopiperazine in CO_2 Capture

Quarterly Report for October 1 – December 31, 2011

by Nathan Fine

Supported by the Luminant Carbon Management Program

Department of Chemical Engineering

The University of Texas at Austin

January 31, 2012

Abstract

Nitrosamines are a harmful degradation product formed by the nitrosation of amines used in CO_2 capture. A large majority of nitrosamines are carcinogenic, producing alkylating agents that react with the guanine amine in DNA. The DNA mutation has been shown to cause tumor growth in target organs of humans.

N-Nitrosopiperazine (MNPZ) is a nitrosamine formed by the nitrosation of piperazine (PZ), a promising amine for carbon capture. The rates of MNPZ formation and subsequent decomposition were measured for 8 m PZ at 120 ^{o}C using $NaNO_2$ as the nitrite source. MNPZ formation was two orders of magnitude faster than MNPZ decomposition. Both rates were found to be first order with respect to the reactants, and irreversible at these conditions.

The rate constants were then used to calculate a first order approximation of the steady state MNPZ concentration in a carbon capture absorption-stripping unit. The steady state concentration can be lowered by increasing the residence time in the stripping sump, decreasing available nitrite from the flue gas, or increasing the temperature in the sump.

Background and Motivation

PZ is currently considered a promising solvent for CO_2 capture in coal-fired power plants due to its high absorption rate, high working capacity, and resistance to thermal degradation. However, PZ has two active secondary amines with no steric hindrance, so it readily undergoes nitrosation to form MNPZ and DNPZ, two relatively stable nitrosamines (Mitch, 2011). Both MNPZ and DNPZ are known carcinogens with a TD of 8.7 and 2.0 mg/kg/day respectively (Garcia, 1970; Pai, 1981). Therefore it is important to characterize and then minimize the steady state concentrations of MNPZ and DNPZ in the absorption-stripping unit.

Experimental Methods

Solvent Preparation

An 8 m PZ solvent was prepared gravimetrically and then loaded with CO_2 at $\alpha = 0.3$. Iron, nickel, and chromium ions were also added volumetrically at concentrations of 0.4 mM, 0.1 mM,

and 0.05 mM, respectively, to match the stainless steel conditions found in the absorption-stripper unit.

Sample Preparation

The solution was spiked volumetrically with 50 mM sodium nitrite. 8 mL samples were then pipetted into 10 mL stainless steel thermal cylinders and placed in a convection oven operating at 120 ^{o}C. The 2 mL of headspace in the cylinder reduced the chance of cylinder failure due to overpressure. Samples were removed from the oven over a period of eight days with longer periods between samples towards the end of the experiment. Samples which leaked more than one gram were considered failures and not reported.

Concentration Measurement

After 15 minutes of cooling, the thermal cylinders were opened and the samples were diluted to 20x in water. The diluted samples were then analyzed using HPLC (Dionex UltiMate 3000) to measure the concentration of MNPZ as a function of time. The concentration was obtained by fitting the absorption curve results to the calibration curve prepared by Namjoshi (Figure 1).

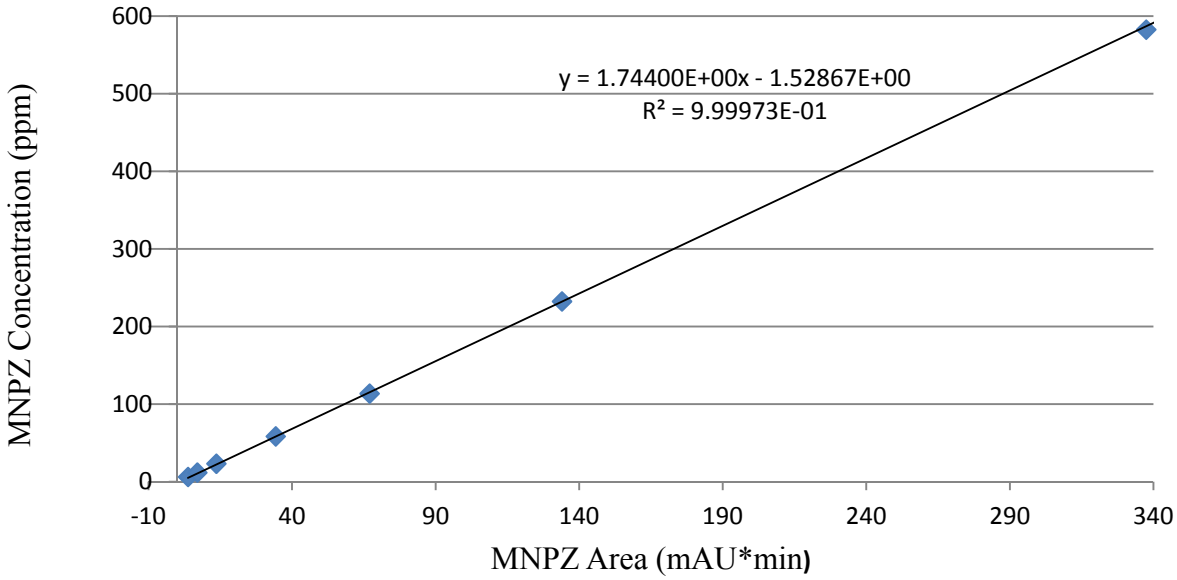

Figure 1: MNPZ Calibration Curve Prepared 7/21/2011

Materials

Piperazine (99 wt % purity)	supplied by Sigma-Aldrich
Sodium Nitrite (98.5 wt % purity)	supplied by Acros organics
Carbon Dioxide (99.99% purity)	supplied by Matheson Tri-Gas
Nickel Sulfate (0.2 M)	Prepared by Stefanie Freeman
Chromium Sulfate (0.2 M)	Prepared by Stefanie Freeman
Iron Sulfate (0.2 M)	Prepared by Stefanie Freeman

Results and Discussions

Experimental Data

Table 1: Experimental Results

Time (day)	Absorption (maU*min)	Dilution Factor (g total/g solvent)	Concentration (mMol MNPZ/kg solvent)
0.00	0.00	20.09	0.00
0.06	111.61	23.48	52.65
0.06	106.95	23.67	50.84
0.13	123.59	22.85	56.78
0.13	128.61	21.69	56.10
0.19	121.86	21.37	52.34
0.19	138.02	19.45	54.02
0.26	141.91	19.22	54.90
0.26	146.67	18.91	55.83
0.31	119.21	22.39	53.65
0.31	130.83	21.31	56.06
1.00	103.10	21.10	43.68
1.00	111.98	19.59	44.07
1.11	106.86	19.05	40.87
1.11	98.14	20.59	40.54
1.28	89.26	21.39	38.28
2.00	76.72	20.11	30.88
2.00	76.05	21.22	32.29
2.15	63.86	21.12	26.93
2.15	78.74	19.38	30.56
2.30	64.64	21.28	27.47
2.71	63.88	20.84	26.58
3.00	60.05	20.77	24.88
3.73	49.30	19.80	19.41
4.00	42.52	19.02	16.03
8.25	9.89	20.67	3.77

Parameter Fitting

Work by Ashouripashaki has suggested that the kinetics for MNPZ formation and decomposition are as follows:

$$NO_2^- \underset{k2}{\overset{k1}{\rightleftarrows}} MNPZ \xrightarrow[k3]{} Byproducts \quad (1)$$

$$\frac{dC_{NO_2}}{dt} = -k_1 C_{NO_2} C_{PZ} ldg^z + k_2 C_{MNPZ} ldg^n \quad (2)$$

$$\frac{dC_{MNPZ}}{dt} = k_1 C_{NO_2} C_{PZ} ldg^z - k_2 C_{MNPZ} ldg^n - k_3 C_{MNPZ} C_{PZ}{}^{\alpha} ldg^m \quad (3)$$

Since the loading and PZ concentration do not change throughout the batch process, they can be rolled into the rate constants, simplifying the governing rate equations to the following:

$$\frac{dC_{NO_2}}{dt} = -k_1 C_{NO_2} + k_2 C_{MNPZ} \quad (4)$$

$$\frac{dC_{MNPZ}}{dt} = k_1 C_{NO_2} - k_2 C_{MNPZ} - k_3 C_{MNPZ} \quad (5)$$

The rate equations were numerically integrated with a time step of 0.001 days. The parameters k_1, k_2, k_3, and starting nitrite concentration were fitted to the data using a simple least squares approach.

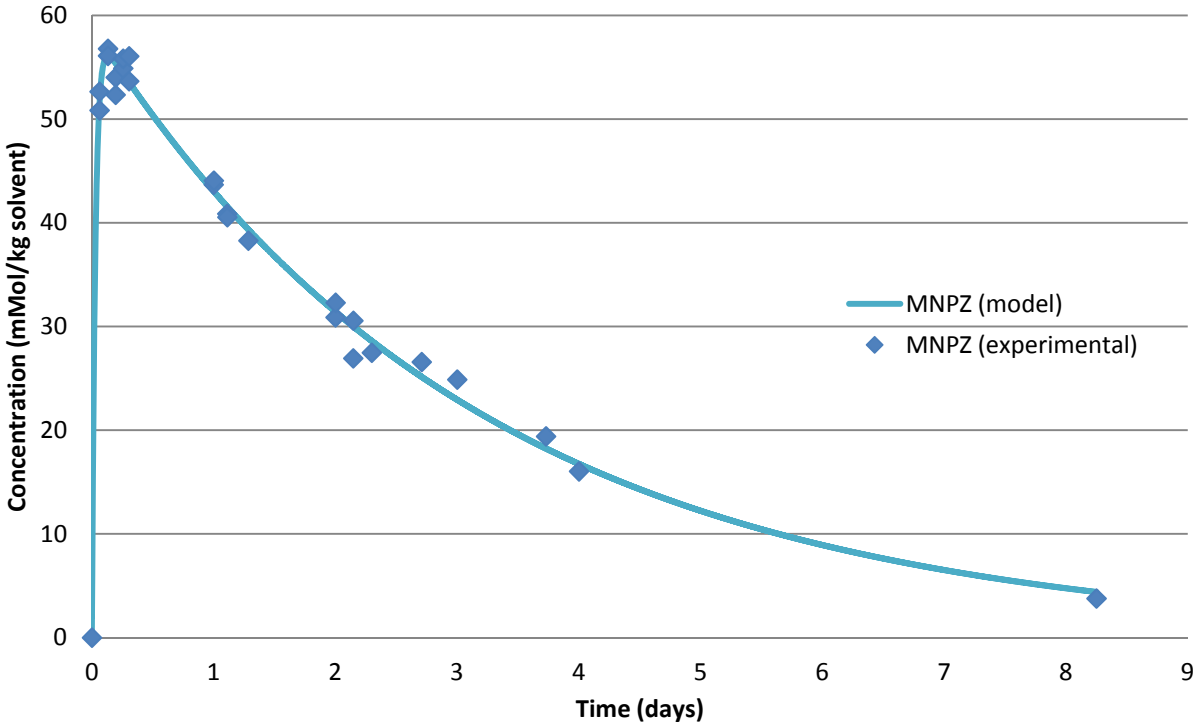

Figure 2: Kinetics of MNPZ Formation and Decomposition
Conditions: 8 m PZ, α = 0.3, 120 °C

The R^2 value is 0.993 and the residuals appear to be normally distributed. Thus the model is a good fit for the data. Furthermore, using the 68/95/99.7 rule, the residual plot suggests that each individual measurement has a standard deviation of around 1 mmol/kg solvent.

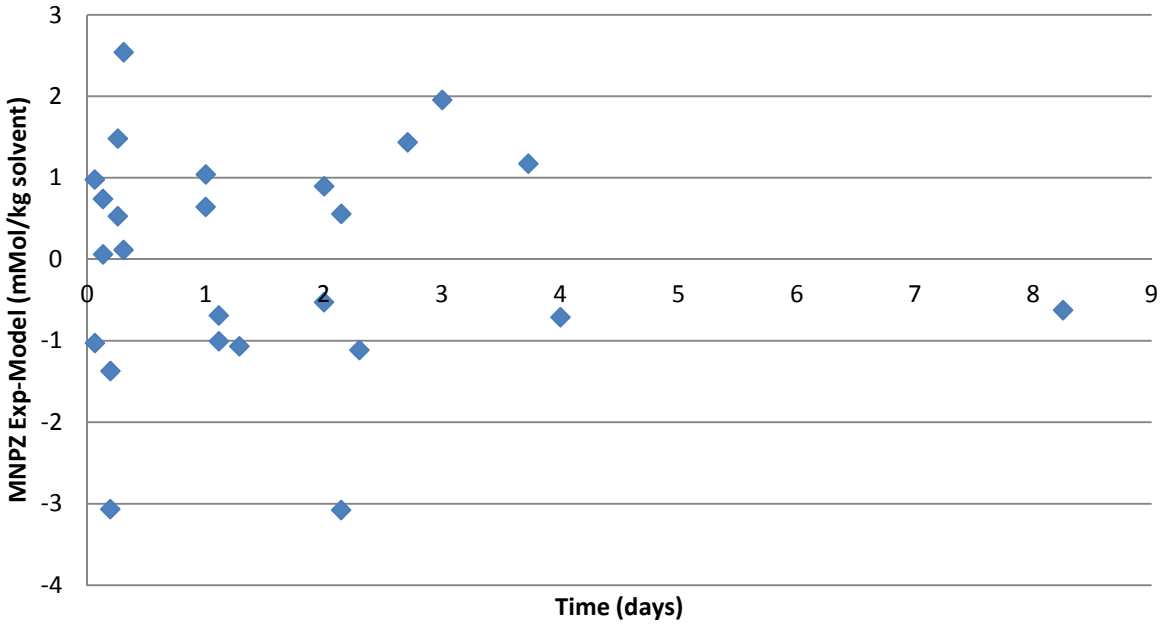

Figure 3: Residuals between the Experimental Data and the Model

The values of the four parameters are listed below with a 95% confidence interval. The covariance between parameters has not yet been determined.

Table 2: Fitted Parameters

Parameters	Values
k_1*10^6 (s^{-1})	409±29
k_2*10^6 (s^{-1})	0+2.7
k_3*10^6 (s^{-1})	3.6±0.1
NO^-_2 (mmol/kg)	58.4±0.3

Determining Steady State Concentration of MNPZ

A first order approximation of the MNPZ steady state concentration was made from the following assumptions:

1. There is no nitrosation or MNPZ decomposition outside of the stripping sump.
2. The stripping sump is an ideal continuously stirred tank reactor (CSTR).
3. The sump operates at 120 ^oC.
4. The nitrite feed comes from the flue gas, and there is negligible solvent loss from the system.
5. There is no equilibrium between nitrite and MNPZ in the sump ($K_2 = 0$).

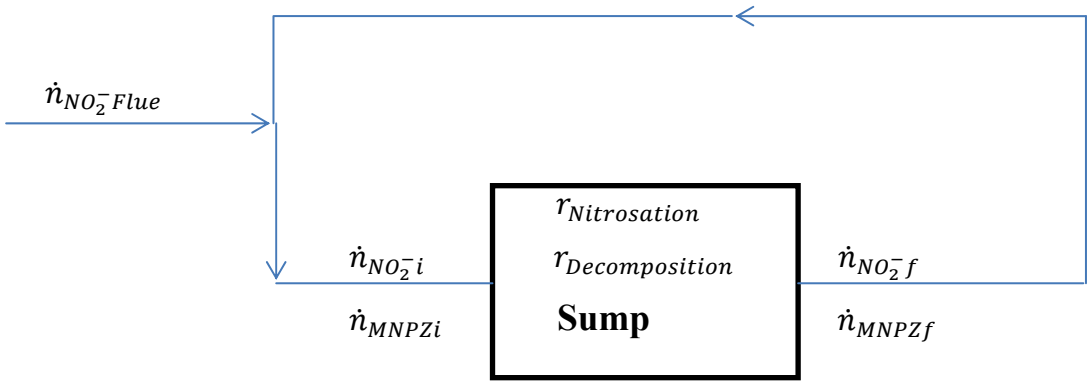

Figure 3: Schematic of Steady State Molar Flow Rates

From these assumptions, the following four material balances can be derived:

$$Overall\ Nitrite: \quad \dot{n}_{NO_2^- i} = \dot{n}_{NO_2^- f} + \dot{n}_{NO_2^- FL} \tag{6}$$

$$Nitrite\ Reacted\ In\ Sump: \quad \dot{n}_{NO_2^- f} - \dot{n}_{NO_2^- i} = -k_1 \dot{n}_{NO_2^- F} \tau_{sump} \tag{7}$$

$$Overall\ MNPZ: \quad \dot{n}_{MNPZi} = \dot{n}_{MNPZf} \tag{8}$$

$$MNPZ\ Formed\ and\ Decomposed: \quad \dot{n}_{MNPAf} - \dot{n}_{MNPZi} = k_1 \dot{n}_{NO_2^- f} \tau_{sump} - k_3 \dot{n}_{MNPZf} \tag{9}$$

Solving the four equations simultaneously leads to the steady state inlet and outlet molar flow rates of nitrite and MNPZ for the sump.

$$\dot{n}_{NO_2^- i} = \frac{(1+k_1\tau_{sump})\dot{n}_{NO_2^- Fl}}{k_1\tau_{sump}} \tag{10}$$

$$\dot{n}_{NO_2^- f} = \frac{\dot{n}_{NO_2^- Fl}}{k_1\tau_{sump}} \tag{11}$$

$$\dot{n}_{MNPZi} = \dot{n}_{MNPZf} = \frac{\dot{n}_{NO_2^- Fl}}{k_3\tau_{sump}} \tag{12}$$

For the stripper/absorber system at the Pickle Research Campus, the approximate steady state concentration of MNPZ will be 5 mM with a nitrite feed of 0.01 millimols/mol CO_2 removed.

The concentration can be lowered by increasing the MNPZ decomposition rate constant, increasing the stripper sump volume, or decreasing the inlet nitrite concentration.

Conclusions

- The first order rate constant for nitrosation of 8 m PZ at 120 ^oC and a CO_2 loading of 0.3 is approximately $4*10^{-4}$ s^{-1}
- The first order rate constant for MNPZ decomposition under the same conditions is approximately $3.6*10^{-6}$ s^{-1}, which is 100 times slower than PZ nitrosation.
- Under the same conditions, the nitrosation reaction is irreversible ($k_2 = 0$).

- The MNPZ steady state concentration would be 5 mM -with a sump operating at 120 ^{o}C, a sump residence time of 10 minutes, and a flue gas NO_2 concentration of 0.01 millimols/mol CO_2 removed.

Future Work

- Current samples will be analyzed for nitrite concentration using anionic chromatography, and the data will be used to refine the current rate constants.
- Rate constants for nitrosation and MNPZ decomposition will be determined for different amine blends over a range of temperatures.
- Rate constants will be determined for solvent samples from pilot plants.
- The steady state concentration approximation will be refined by taking into account solvent loss due to reclaiming.
- A temperature dependent model will be developed for MNPZ concentration at possible sump conditions.

References

Garcia H, Keefer L, Lijinsky W, Wenyon CEM. "Carcinogenicity of nitrosothiomorpholine and 1-nitrosopiperazine in rats." *Cancer Res Clin Oncol.* 1970;74;179–184.

Mitch W. "Critical Literature Review of Nitrosation/Nitration Pathways." Results from the First Studies of the Health and Environment Issues of Amines Used in CO_2 Capture. Gassnova 2011.

Pai SR, Shirke AJ, Gothoskar SV. "Long-term feeding study in C17 mice administered saccharin coated betel nut and 1,4-dinitrosopiperazine in combination." *Carcinogenesis.* 1981;2:175–177.

The Dissertation Committee for Qing Xu Certifies that this is the approved version of the following dissertation:

Thermodynamics of CO_2 Loaded Aqueous Amines

Committee:

Gary T. Rochelle, Supervisor

Keith Johnston

Isaac Sanchez

Frank Seibert

Steven Bryant

Thermodynamics of CO_2 Loaded Aqueous Amines

by

Qing Xu, B.E.; M.S.E.

Dissertation

Presented to the Faculty of the Graduate School of

The University of Texas at Austin

in Partial Fulfillment

of the Requirements

for the Degree of

Doctor of Philosophy

The University of Texas at Austin

December 2011

Dedication

To my family

Acknowledgements

Firstly I would like to thank my advisor, Dr. Gary Rochelle. His guidance, encouragement, and insights for the research have inspired and helped me the most through my projects, which sometimes were not that smooth. His passion and dedication to work was very impressive to me. He was always willing to offer help and discuss the projects. Looking into my drawer, there are almost four inches of notes written by him from the weekly meeting on my specific research since year 2006 when I joined the group. Besides work, I also learned a lot from his attitude to life and to people. I feel lucky to have had him as my supervisor and I will carry the influence from him into my career in chemical engineering and into my life.

I would also like to thank the 30+ sponsors of the Luminant Carbon Management Program and the Industrial Associates Program for CO_2 Capture by Aqueous Absorption. I would have no chance to perform this research without their financial support. Thanks to their dedication to reducing the carbon dioxide emission. Specifically, thanks to Dr. Chau-Chyun Chen in Aspen Technology Inc. for his help with Aspen Plus®.

I am also grateful to the Chemical Engineering staff that has kindly supported me. Our administrative coordinator Maeve Cooney was always helpful, quick, precise, and patient. It was nice and relaxing to talk with her after spending a long time in research. I was not as good in either oral or written English in my earlier years in the US but she was very patient with that. I also want to thank Dr. Friedman for letting me use the equipment for pressure calibration, Dr. Freeman for the use of DSC, and Dr. Johnston for the use of the equilibrium cells with windows. I would like to acknowledge the help from T Stockman, Eddie Ibarra, Jim Smitherman, Butch Cunningham, Randy Rife, Patrick Danielewski, and Kevin Haynes. Their assistance in administration, processing

lab supply and equipment orders, repairing lab equipment, fixing computer problems, etc. was very effective and made my Ph.D. life easier.

I also want to express the appreciation to my excellent colleagues in the group. Marcus Hilliard, Ross Dugas, Bob Tsai, Eric Chen, Andrew Sexton, and Jason Davis joined the group before me and helped me a lot as I started. I still remember my first day in the lab when Marcus showed me how to load CO_2 into solution. And those who joined the group in similar years with me or later than me: Jorge Plaza, David Van Wagener, Sepidah Ziaii, Stephanie Freeman, Fred Closman, Xi Chen, Thu Nguyen, Stuart Cohen, Alex Voice, Peter Frailie, Chao Wang, Lynn Li, Steven Fulk, Shan Zhou, Humera Rafique, Mandana Ashouripashaki, and Omkar Namjoshi. Thank you all for the time, assistance, and companion in these years. Special thanks for the help from Peter, Jorge, and David with Aspen Plus® modeling, and experimental assistance from Steven, Alex, and Xi. I would also like to thank my undergraduate research assistants who helped me a lot with the experiments: Martin Metzner, Mychal Zipper, and Jeffrey Giordanelli. I wish you all the best in both career and life.

I am also very grateful to my friends who came into my life in Austin and shared lots of time with me: Wei X., Tuo W., Xinyu G.; my roommates Ji Z., Shao, Li J.; and many of other friends. I really appreciate the time we spent together and your understanding and support for me. I wish you all have a bright future while fulfilling your dreams.

Last but not least, I would like to thank my parents for their love and support throughout my study. I would not have come to this point without your earlier education and continuous encouragement.

Thermodynamics of CO_2 Loaded Aqueous Amines

Qing Xu, Ph.D.

The University of Texas at Austin, 2011

Supervisor: Gary T. Rochelle

Thermodynamics is important for the design of amine scrubbing CO_2 capture processes. CO_2 solubility and amine volatility in aqueous amines were measured at high temperature and pressure. A rigorous thermodynamic model was developed for MEA-CO_2-H_2O in Aspen Plus®.

CO_2 solubility at 80-190°C was obtained from total pressure measurements. Empirical models as a function of temperature and loading were developed for CO_2 solubility from 40 to 160°C in aqueous monoethanolamine (MEA), piperazine (PZ), 1-methylpiperazine (1MPZ), 2-methylpiperazine (2MPZ), PZ/2MPZ, diglycolamine® (DGA®), PZ/1MPZ/1,4-dimethylpiperazine (1,4-DMPZ), and PZ/methyldiethanolamine (MDEA). The high temperature CO_2 solubility data for MEA is comparable to literature and compatible with previous low temperature data. For MEA and PZ, amine concentration does not have obvious effects on the CO_2 solubility. The heat of CO_2 absorption derived from these models varies from 66 kJ/mol for 4 m (molal) PZ/4 m 2MPZ and to 72, 72, and 73 kJ/mol for MEA, 7 m MDEA/2 m PZ, and DGA. The heat of absorption estimated from the total pressure data does not vary significantly with temperature.

At 0-0.5 loading (α), 313-413 K, 3.5-11 m MEA (mol fraction x is 0.059-0.165), the empirical model of MEA volatility is $\ln(P_{MEA}/x_{MEA}) = 30.0-8153/T-2594\alpha^2/T$. In 7

m MEA with 0.2 and 0.5 loading, P_{MEA} is 920 and 230 Pa at 120 ℃. At 0.3-0.5 loading, the enthalpy of MEA vaporization, $-\Delta H_{vap,MEA}$, is about 70-73 kJ/mol MEA. At 0.25-0.4 loading, 313-423 K, 4.7-11.3 m PZ (x is 0.078-0.169), the empirical model of PZ volatility is $\ln(P_{PZ}/x_{PZ}) = -123+21.6\ln T+20.2\alpha-18174\alpha^2/T$. In 8 m PZ with 0.3 and 0.4 loading, P_{PZ} is 400 and 120 Pa at 120 ℃, and 2620 and 980 Pa at 150 ℃. At 0.25-0.4 loading, $-\Delta H_{vap,PZ}$ is about 85-100 kJ/mol PZ at 150 ℃ and 66-80 kJ/mol PZ at 40 ℃. $\Delta H_{vap,PZ}$ has a larger dependence on CO_2 loading than $\Delta H_{vap,MEA}$ in rich solution because of the more complex speciation/reactions in PZ at rich loading. Specific heat capacity of 8 m PZ is 3.43-3.81 J/(g·K) at 70-150°C.

Two new thermodynamic models of MEA-CO_2-H_2O were developed in Aspen Plus® starting with the Hilliard (2008) MEA model. One (Model B) includes a new species MEACOOH and it gets a better prediction than the other (Model A) for CO_2 solubility, MEA volatility, heat of absorption, and other thermodynamic results. The Model B prediction matches the experimental pK_a of MEACOOH, and the measured concentration of $MEACOO^-$/MEACOOH by NMR. In the prediction the concentration of MEACOOH is 0.1-3% in 7 m MEA at high temperature or high loading, where the heat of formation of MEACOOH has effects on P_{CO2} and CO_2 heat of absorption. Model B solved the problems of Model A by adding MEACOOH and matched the experimental data of pK_a and speciation, therefore MEACOOH may be considered an important species at high temperature or high loading. Although mostly developed from 7 m MEA data, Model B also gives a good profile for 11 m (40 wt%) MEA.

Table of Contents

List of Tables

List of Figures

Chapter 1: Introduction

This chapter introduces the application and objectives of this research. Amine based CO_2 capture is the most promising approach to reduce CO_2 emissions from coal-fired power plants. However it uses about one third of the output electricity from a power plant. New solvents and configurations have been investigated to improve the process. High temperature stripping at elevated pressure may reduce the energy cost when thermally resistant amine solvents are used. Thermodynamics is essential in the process design. Prior research in thermodynamics of CO_2 loaded amines was limited in amine types, temperature, or pressure. To better design the high temperature and pressure processes, new experiments need to be conducted to expand the temperature range to selected novel solvents, especially thermally resistant amines like piperazine and piperazine derivatives. The new data will be used in model development in Aspen Plus®.

1.1 Climate Change and CO_2 Emissions

Fossil fuel burning has increased CO_2 concentration in atmosphere over the past 200 years. The 2005 concentration of CO_2 was about 35% higher than 150 years ago. According to the US National Oceanic and Atmospheric Administration (NOAA) and the US National Aeronautics and Space Administration (NASA) data, the Earth's surface temperature has increased 1.2 to 1.4 ℉ in the past 100 years (EPA, 2007). Other aspects of climate, such as rainfall patterns, are also changing and causing weather disasters. IPCC Fourth Assessment Report – Climate Change 2007 concluded that "Most of the observed increase in global average temperature since the mid-20th century is very likely to due to the observed increase in anthropogenic greenhouse gas

generations." Researchers over the world have been investigating effective methods to manage CO_2 emissions.

Figure 1-1 shows the world CO_2 emissions in year 2007 from different sectors. The largest emission source is electricity and heat and occupies 41% of the total. The second largest source is transport, but CO_2 emission from this sector is much harder to control.

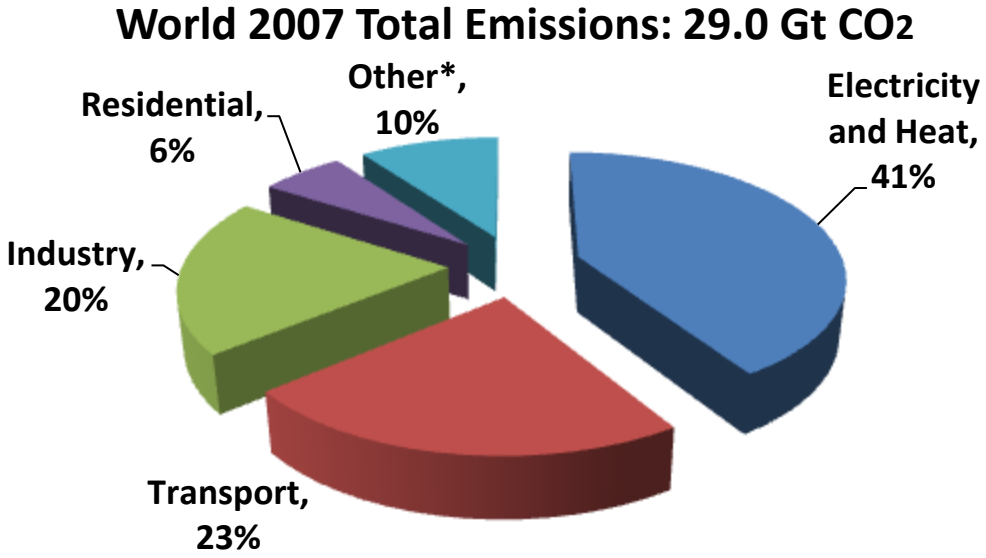

Figure 1-1: 2007 World CO_2 Emissions by Sector. **Re-plotted from Figure 11 in CO_2 emissions from fuel combustion highlights (2009 edition), International Energy Agency, 2009. *: Other includes commercial/public services, agriculture/forestry, fishing, energy industry other than electricity and heat generation, and other emissions not specified elsewhere.**

1.2 Amine Based Post Combustion CO_2 Capture

One direct approach to reduce CO_2 emissions from large stationary sources is to capture the CO_2 and store it away from atmosphere, like underground or submarine. The captured CO_2 can also be used for chemicals production as well as enhanced oil recovery (EOR). Non-biological CO_2 capture from coal fired power plants and other industry includes generally three types: pre-combustion, oxy-combustion and amine

based post combustion. Amine scrubbing has been investigated in acid gas treating processes for decades and is among the closest technology to commercialization for CO_2 capture. Aqueous monoethanolamine (MEA) solution serves as the baseline solvent to capture CO_2 from flue gas. New solvents like aqueous concentrated piperazine (PZ) are being investigated.

Figure 1-2 shows a typical amine based CO_2 capture process. The cooled flue gas at 40 ℃ with about 12% CO_2 enters the bottom of the absorber and counter-currently contacts the lean amine stream. After absorbing CO_2, aqueous amine becomes rich in CO_2 and flows out from the bottom. The temperature in the absorber is 40-70 ºC. In the cross heat exchanger the cool rich stream is heated by the hot lean stream from the stripper to above 100ºC and then the hot rich solution enters the top of the stripper. Steam is used to heat the reboiler up to 100-150 ºC to release CO_2 from the hot rich solution, and the pressure in the stripper can be elevated to 1.6-10 bar. CO_2 exits from the top of the stripper and is compressed to 150 bar for sequestration. After releasing CO_2, the hot lean solution flows out of the bottom of the stripper, cooled by the cross heat exchanger and a trim cooler, and enters the absorber. A slip stream is withdrawn from the reboiler and enters a reclaimer to remove degradation products, and the reclaimer temperature can be up to 150-180ºC.

In this process, amine solution is recycled between the absorber and stripper, the main energy input is to the reboiler and compressors.

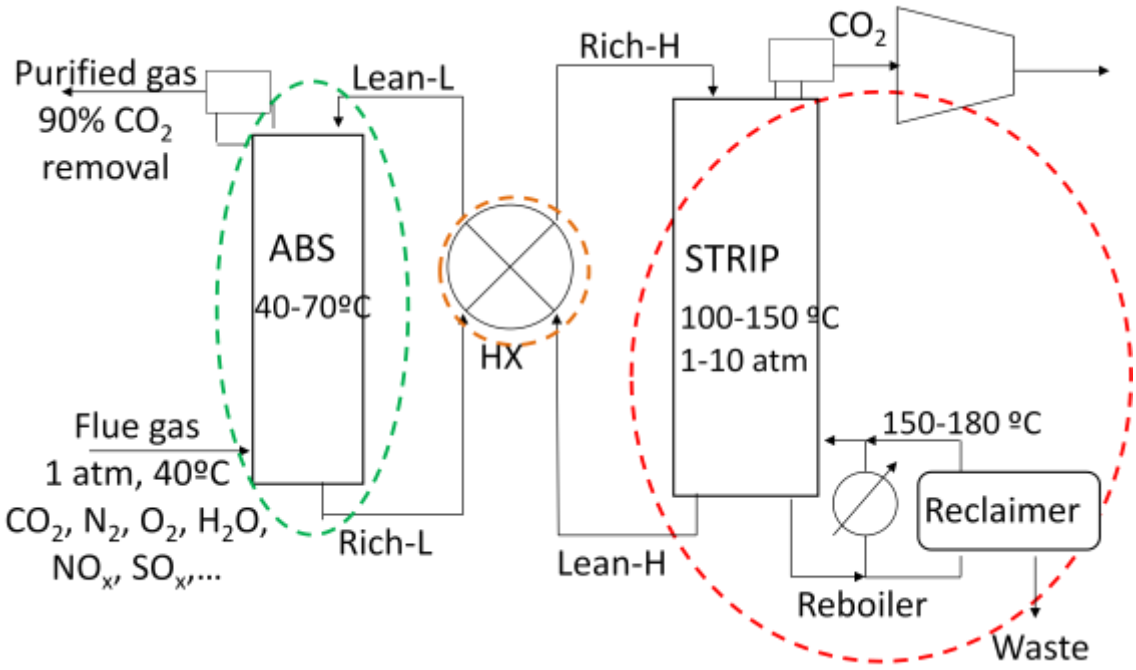

Figure 1-2: A Typical Amine Based CO_2 Capture Process

1.3 Needs for Thermodynamics and High Temperature Data

Thermodynamics is essential in the design of CO_2 capture process and researchers have been working on measuring thermal properties and building thermodynamic models of CO_2 loaded aqueous amines.

Better energy performance can be achieved by elevating the stripper temperature and pressure (Van Wagener, 2011). High temperature stripping thermally compresses CO_2 vapor before it enters the compressors. Thermal compression has a higher efficiency than mechanical compression; and less heat will be put into the heating for water vaporization because the CO_2/H_2O ratio in vapor increases as temperature increases. Some amines like MEA and ethylenediamine (EDA) are not thermally resistant and the stripper temperature cannot exceed 120ºC; but for thermally resistant amines like PZ and PZ derivatives the temperature in the stripper can be elevated to 150

ºC. For both cases high temperature thermodynamics is helpful in understanding the high temperature processes, which are in the red circle in Figure 1-2. Mid-temperature thermodynamics can be interpolated from the high temperature and low temperature data, for the design of heat exchangers in the orange circle in Figure 1-2.

Thermodynamics at greater temperature and pressure is needed for other high temperature processes. Figure 1-3 gives an example for the application in a novel stripping configuration. It was developed by Van Wagener (Rochelle et al., 2010) and shows the two stage flash stripping process. This is to replace the simple stripper configuration. After heat exchanging, the hot rich PZ solution enters the two flashes in sequence at 150 ℃. The pressure is reduced in the flashes and CO_2 is released. Then CO_2 enters different stages of the multi-stage compressor. The hot lean solution exiting the second flash goes to the heat exchanger and then goes back to the absorber. More flash stages may save more energy but the capital cost will increase. According to Van Wagener's research, 0.3 to 0.5 kJ/mol CO_2 of energy can be saved by using 2 and 3 stage flash, respectively, when 9 m MEA is used as the solvent. There are also other stripping configurations with elevated temperature and pressure saving more energy than a simple stripper, e.g., interheated column (Van Wagener, 2011).

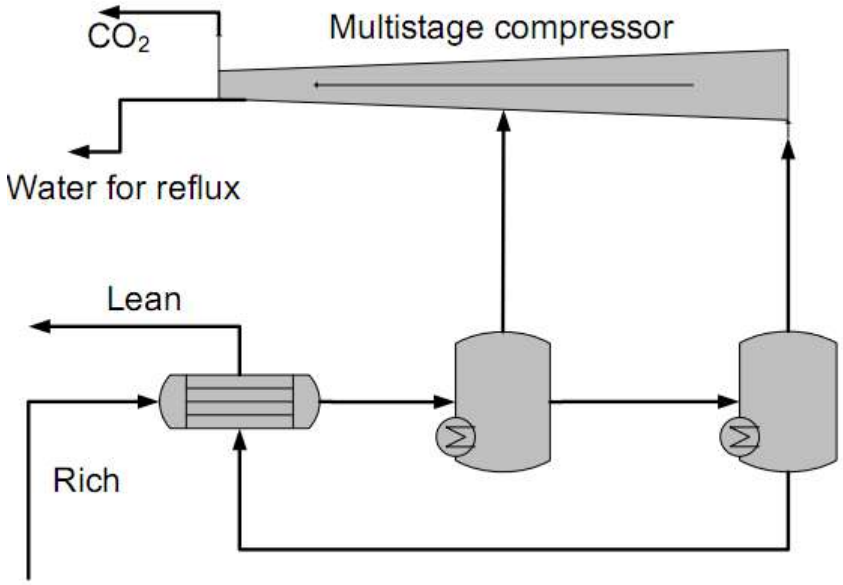

Figure 1-3: Two Stage Flash (Van Wagener, 2010[1])

Prior research in thermodynamics of CO_2 loaded amines is limited in amine types, temperature, or pressure. To better understand vapor-liquid equilibrium, heat capacity, and heat of absorption and their dependence on temperature, new experiments were conducted to expand the temperature range to selected novel solvents, especially thermally resistant amines including piperazine and piperazine derivatives.

1.4 PRIOR WORK

1.4.1 Amine Solvents

MEA has been used in acid gas treating since 1960's and is a baseline amine for CO_2 capture. It has relatively high heat of absorption, moderate reaction rate and capacity, low viscosity, low price, moderate environmentally degradability, and intensive operating experiences in industry. However it reacts with O_2 in the absorber and thermally degrades at greater than 120 ℃.

[1] Rochelle et al., 2010.

PZ has been used as a promoter for some slow amines like methyl-diethanolamine (MDEA) and 2-amino-2-methyl-1-propanol (AMP) because it accelerates the CO_2 reactions. However PZ in blends degrades faster than in aqueous PZ. Concentrated PZ is a very promising solvent because of its high capacity, fast reaction rate, negligible oxidative and thermal degradation up to 150 ℃ and moderate to high heat of absorption. The tolerance of high temperature gives the possibility of elevating regeneration temperature and pressure for better energy performance.

PZ derivatives, which include 1-methylpiperazine (1MPZ) and 2-methylpiperazine (2MPZ), are a new set of amines recently studied in Rochelle group. Preliminary results showed that PZ derivatives are also thermally resistant and react fast with CO_2 (Freeman 2011, Chen et al. 2011).

Diglycolamine (DGA®) has been used in absorbing CO_2 and H_2S from natural gas for decades. Similar to PZ, it is relatively thermally stable.

Figure 1-4 shows the structures of commonly used amines in CO_2 absorption.

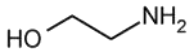

Monoethanolamine (MEA)

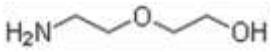

Diglycolamine® (DGA®)

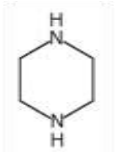

Piperazine (PZ)

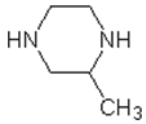

2-methylpiperazine (2MPZ)

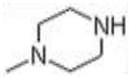

1-methylpiperazine (1MPZ)

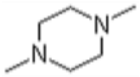

1,4-dimethylpiperazine (1,4-DMPZ)

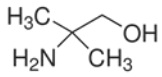

2-amino-2-methyl-1-propanol (AMP)

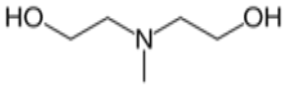

Methyldiethanolamine (MDEA)

Figure 1-4: Structure of Commonly Used Amines in CO_2 Capture

1.4.2 Vapor-liquid Equilibrium

Table 1-1 through 1-5 give a brief literature review of VLE data for unloaded and loaded aqueous amines.

Table 1-1: Summary of Literature VLE Data for MEA-H_2O

Author	Data	Pressure (kPa)	MEA (mol frac)	T (^oC)
Touhara et al. (1982)	P, T, x	0.065-5.623	0.03-0.89	25, 35
Nath and Bender (1983)	P, T, x	1.3-75	0-0.93	60, 78, 91.7
Cai et al. (1996)	P,T, x, y	66.7, 101.3	0.05-0.93	90-159
Park and Lee (1997)	P,T, x, y	101.3	0.03-0.98	100-170
Tochigi et al. (1999)	P,T, x, y	4.02-70.07	0.03-0.89	90
Hilliard (2008)	P,T, x, y	5-21	0.06-0.30	39.8-72.7
Kim et al. (2008)	P,T, x, y	6-100	0-0.56	40, 60, 80, 100

Table 1-2: Summary of Literature CO_2 Solubility in Aqueous MEA at High T/P

Author	MEA (wt%)	T (℃)	P_{CO2} (kPa)
Reed and Wood (1941)	15	100, 120, 140	138-1724
Lyudkovskaya and Leibush (1949)	3, 12, 30	25, 50, 75	254-4054
Goldman and Leibush (1959)	6, 12, 15, 30	75, 100, 120, 140	0.3-467
Jones et al. (1959)	15	40, 60, 80, 100, 120, 140	<931
Lawson and Garst (1976)	15	40, 60, 80, 100, 120, 134, 140	2.9-2786
Lee et al. (1976)	6, 15, 23, 30	25, 40, 60, 80, 100, 120	0.2-6616
Sartori et al. (1983)	3 M	40, 120	~0.3-336
Shen and Lee (1992)	15, 30	40, 60, 80, 100	1.1-2550
Murrieta-Guevara et al. (1993)	15, 30	30, 50, 100	1.5-2210
Robinson (1993)	20, 30	40, 70, 100, 120	0.003-6293
Jou et al. (1995)	30	0, 25, 40, 60, 80, 100, 120, 150	0.0012-19954
Ma'mun et al. (2005)	30	120	7-191
Aronu et al. (2011)	15,30,45,60	60, 80, 100, 120	<1060

Table 1-3: Summary of Literature VLE Data for PZ-H_2O

Author	Data	PZ (m)	T (℃)
Wilson and Wilding (1994)	P_t	0-1 (mole frac)	113, 199
Xia et al. (2003)	P_t	1.99, 3.97	120
Hilliard (2008)	T, P, x, y	0.9, 2, 2.5, 3.6, 5	40-60
Nguyen et al. (2010)	T, P, x, y	2, 5, 8, 10	40-70

Table 1-4: Summary of Literature CO_2 Solubility in Aqueous PZ

Author	PZ (m)	T (℃)	P_{CO2} (kPa)
Bishnoi et al. (2000)	0.6	40, 70	0.032-40
Perez-Salado Kamps et al. (2003)	2, 4	40-120	13.3-9560 (P_t)
Derks et al. (2005)	0.2 M, 0.6 M	25, 40, 70	0.27-111
Ermatchkov et al. (2006)	2-4.2	80, 100	0.111-77.63
Hilliard (2008)	0.9-5	40, 60	0.029-51.4
Dugas et al. (2009)	2-12	40, 60, 80, 100	0.065-39.29
Nguyen et al. (2010)	8, 10	40, 60	0.1-28.3
Kadiwala et al. (2010)	0.3 M, 1.2 M	40, 70	<7400

Table 1-5: CO_2 Solubility in DGA® in Literature

Author	DGA® (wt%)	P_{CO2} (kPa)	T (℃)
Martin et al. (1978)	60	1.6-5980	50, 100
Maddox et al. (1987)	20-60	6.8-6523	25, 40, 50, 60
Dingman et al. (1983)	65	<181	37.8, 60, 82.2

1.4.3 Specific Heat Capacity (C_p)

The specific heat capacity can be used in calculating temperature dependence of CO_2 heat of absorption and in thermodynamic modeling of the CO_2-H_2O-amine systems. Differential Scanning Calorimetry (DSC) has been used in previous research by Hilliard (2008) and Nguyen (Rochelle et al., 2009) for C_p measurement of CO_2 unloaded and loaded amine at 40-120 ℃. Tables 1-6 and 1-7 give the relative previous work on specific heat capacity measurements.

Table 1-6: Literature Summary of Specific Heat Capacity for Aqueous MEA

Author	T (°C)	Data Type	Method
Page et al. (1993)	10,25,40	unloaded	Flow microcalorimeter
Weiland et al. (1997)	25	pure, loaded, unloaded	Batch calorimeter
Chiu et al. (1999a and 1999b)	30-80	pure, unloaded	DSC
Hilliard (2008)	40-120	Pure, loaded, unloaded	DSC

Table 1-7: Literature Summary of Specific Heat Capacity for Aqueous PZ*

Author	T(°C)	Data type
Hilliard (2008)	40-120	2 m and 3.6m, unloaded
Y-R Chen et al. (2010)	30-80	x_{PZ}=0.05, 0.1, 0.15, 0.2, unloaded
Nguyen (Rochelle at al., 2009)	40-120	8-12 m, 0.21, 0.29, 0.31, 0.4 CO_2 loading

*: All used DSC method.

1.4.4 Heat of Absorption ($-\Delta H_{abs}$)

It is important to know the heat of absorption of CO_2 in aqueous amines because it effects the energy input in the reboiler, and reflects the temperature dependence of CO_2 partial pressure. In the absorber the CO_2 absorption into amine is exothermic, and in the

stripper the releasing of CO_2 is endothermic. According to the research by Kim et al. (2007), heat of absorption of CO_2 in 7m MEA increases with temperature.

There are two types of $-\Delta H_{abs}$: integral and differential. Heat of absorption obtained from CO_2 partial pressure data are referred to as differential heat of absorption. This method was used by Jou et al. (1994) for MEA solution. This method requires very accurate CO_2 partial pressure measurement and cannot get temperature dependence of ΔH_{abs}. Integral heat of absorption could be obtained from direct measurement by a calorimeter. However ΔH_{abs} from this method also has big deviations. Table 1-8 lists the summary of previous CO_2 heat of absorption measurements for aqueous MEA.

Table 1-8: Summary of CO_2 Heat of Absorption into Aqueous MEA in Literature

Author	Amine Concentration	T (°C)	P (kPa) / Loading
Mathonat et al. (1995)	30 wt% MEA	40, 80, 120	2000, 5000, 10000 kPa
Carson et al. (2000)	10, 20, 30 wt% MEA	25	Unloaded aqueous MEA
Kim et al. (2007)	30 wt% MEA	40, 80, 120	0.04-0.72 loading

1.4.5 Electrolyte-NRTL Models for MEA

The electrolyte-Nonrandom Two-Liquid (ENRTL) theory was developed by Chen et al. (1979 and 1982), then improved by Chen and Evans (1986) and Mock et al. (1986). Aspen Plus® has a built-in ENRTL model to deal with the liquid phase non-ideality, especially for aqueous or mixed solvent electrolyte systems. The model contains a Debye-Huckel term, Born-correction for mixed solvents, and the local interaction term.

In the Rochelle group, Austgen (1989) was the first to apply the ENRTL model in Aspen Plus® to the amine-H_2O-H_2S-CO_2 system. The data regression system (DRS) of Aspen Plus® was used in the rigorous thermodynamic model. After that, Posey (1996), Bishnoi (2000), Dang (2001), Freguia (2002) and Cullinane (2005) all made some contributions to the rigorous thermodynamic equilibrium/rate models. The more recent

MEA-H_2O-CO_2 model was by Hilliard (2008), and Plaza recently modified the Hilliard MEA model. The Hilliard PZ model (2008) has been modified and developed by Van Wagener, Plaza, and Frailie. The latest version is the Fawkes PZ model (Frailie et al., 2010). For amine-H_2O-CO_2 system, vapor phase non-ideality was modeled by the SRK equation of state.

With the rigorous thermodynamic models, reasonable accurate predictions should be made for the thermodynamic properties. Also the important parameters help interpreting and understanding thermal behaviors. Since the current MEA model includes limited high temperature data, the temperature dependences and the high temperature predictions are not perfect and need improvement.

1.5 RESEARCH OBJECTIVES

Thermodynamics serves as the base knowledge in the design of amine scrubbing process. CO_2 solubility, heat of CO_2 absorption, specific heat capacity and amine volatility are key thermal components to the process design. CO_2 solubility and total pressure determine how much CO_2 could be removed under certain conditions. On the other hand the heat of absorption plays an important role in the prediction of stripper energy and is critical for the process design. Specific heat capacity helps to understand the temperature dependence of heat of absorption. Amine volatility mostly involves environmental impact as well as the design of the water wash and the condenser. Investigations in amine-water systems can help to understand the more complex amine-water-CO_2 system.

There are internal connections among these factors. CO_2 partial pressure over aqueous amine is mostly determined by temperature, amine type and the CO_2 loading (mole CO_2/mol alkalinity). For a specific amine, P_{CO2} is a function of temperature and

loading. Amine volatility depends on amine structure, concentration, temperature and CO_2 loading. By taking derivatives to logarithm of the partial pressure of CO_2 or amine, more thermo parameters can be obtained:

According to Equation XVIII.9 in Lewis and Randall (1923) and Equation IV.109 in Dodge (1944), the CO_2 heat of absorption $\Delta H_{abs} = -R\frac{\partial lnP_{CO2}}{\partial(\frac{1}{T})}$. In the amine-$H_2O$ system $\Delta H_{vap,amine} = -R\frac{\partial lnP_{amine}}{\partial(\frac{1}{T})}$. R is the gas constant.

By definition, the specific heat capacity $C_p = (\frac{\partial H}{\partial T})_P$ and C_p=A+BT+CT^2+…. For the amine-water-CO_2 system, on a molar lean solution base, $\Delta H_{abs}(120℃) = \Delta H_{abs}(40℃) + \int_{120℃}^{40℃}[Cp(lean) + Cp_{CO2(g)}m_{CO2(g)}]dT + \int_{40℃}^{120℃} Cp(rich)\cdot(1 + \frac{m_{CO2(g)}}{44.01})dT$.

The primary target of this project is to quantify in aqueous MEA and PZ, how the CO_2 solubility, amine volatility and heat of absorption depend on temperature, and give theoretical explanations for these behaviors. Therefore the specific objectives of this project include:

1. Develop experimental methods for high temperature/pressure CO_2 solubility and amine volatility measurements and validate the methods by comparing with previous vapor-liquid equilibrium data of aqueous MEA.
2. Measure CO_2 solubility and amine volatility at 100-160 ℃ for aqueous MEA and PZ, and specific heat capacity up to 150 ℃ for concentrated PZ for high temperature stripping design.
3. Identify and explain the temperature dependence of CO_2 solubility and amine volatility for aqueous MEA and PZ systems.

4. Based on the vapor-liquid equilibrium and specific heat capacity data, obtain CO_2 ΔH_{abs} in aqueous MEA and PZ, as well as $\Delta H_{vap,amine}$ in aqueous MEA and PZ. Identify and explain the temperature dependence of the ΔH.
5. Improve Hilliard MEA Aspen Plus® thermodynamic model for CO_2-H_2O-MEA and test the Fawkes PZ Aspen Plus® model.
6. Screen new thermally resistant solvents by measuring CO_2 solubility at high temperature.

Chapter 2: Total Pressure and CO_2 Solubility at High Temperature and Pressure

This Chapter presents a total pressure experimental method and the measured vapor-liquid equilibrium data at 80-191 ℃. Nine amine solvents that could be used for CO_2 capture from coal-fired power plants were screened by this method: monoethanolamine (MEA), piperazine (PZ), 1-methyl-piperazine (1MPZ), 2-methyl-piperazine (2MPZ), PZ/2MPZ, PZ/1MPZ/1,4-dimethylpiperazine (1,4-DMPZ), diglycolamine® (DGA®), and two blends of PZ/methyl-diethanolamine (MDEA). CO_2 solubility was derived from the total pressure data. An empirical model was developed for each solvent to predict CO_2 partial pressure at 40-160 ℃.

The high temperature CO_2 solubility data for MEA is comparable to literature and is compatible with the previous low temperature data. For MEA and PZ, amine concentration does not have obvious effects on the CO_2 solubility. The heat of CO_2 absorption derived from these empirical models varies from 66 kJ/mol for 4 m PZ/4 m 2MPZ and to 72, 72, and 73 kJ/mol for MEA, 7 m MDEA/2 m PZ, and DGA and does not vary significantly with temperature. The measured CO_2 heat of absorption in MEA from literature is not consistent with the partial pressure CO_2 data, or with the previous measured specific heat capacity.

2.1 Review of Acid Gas Solubility Measurement at High Temperature and/or Pressure

The solubility of acid gas, such as CO_2 and H_2S, in alkanolamine solvents has been measured at high temperature and/or pressure by previous researchers. The apparatus can be sorted as static and dynamic, with or without analysis for vapor and liquid composition. In a static method the system is closed without phase circulation;

mixing is obtained by agitation or rocking. Samples of vapor and liquid can be withdrawn and analyzed after the system reaches equilibrium. If no sample is collected, mass balance and certain equations of state is needed to calculate partial pressure data. The total pressure method in this work belongs to this category.

In a dynamic method for acid gas solubility measurement, usually the vapor phase is circulated to accelerate the process to equilibrium. Therefore it is easier to collect a vapor sample in a dynamic method than in a static method.

In the acid gas-water-amine vapor-liquid equilibrium, the partial pressure of amines is very small compared with acid gas and water, and is usually ignored. At high temperature and/or pressure, the acid gas partial pressure is the main part of the total pressure. In most apparatus with sampling and analysis, the vapor stream is condensed to get rid of water and amine, and then enters the analytical instrument.

2.1.1 Static Methods without Vapor Sampling

The static method without sampling is easy to perform and requires mass balance calculation to get the solubility data. If adequate mixing can be achieved, this method can be highly productive to generate CO_2 solubility data.

Maddox et al. (1987) measured the solubility of CO_2 and H_2S in aqueous MEA, DGA®, DEA, and MDEA at 25-60 ℃. An equilibrium cell with liquid and gas charging systems was used, no sample was collected, and mixing was obtained by a shaker. The measured P_{CO2} was 4-6789 kPa.

Murrieta-Guevara et al. (1988, 1992, 1993, 1998) measured the solubility of CO_2 and H_2S in various amines at 298-373 K from 2-2730 kPa partial pressure. Gas was circulated by a magnetic pump for mixing.

Shen et al. (1992), Xu et al. (1998) and Liu et al. (1999) measured CO_2 solubility in various MEA, MDEA, MEA/MDEA, and MDEA/PZ solutions at 30-100 ℃ with P_{CO2} from 1 to 2000 kPa with an autoclave. Raoult's law was used to calculate water partial pressure, and amine partial pressure was ignored.

Derks et al. (2005) measured CO_2 solubility in 0.2 and 0.6 M PZ at 25, 40, and 70 ℃, P_{CO2} at 0.27-111.37 kPa. The equilibrium cell was agitated and sometimes liquid samples were taken.

Jenab et al. (2005, 2006) measured CO_2 solubility in the mixtures of DIPA+PZ, DIPA+MDEA, and MDEA+PZ+ Sulfolane at 30-70 ℃, 30-5000 kPa.

CO_2 solubility in a range of new solvents was measured in a double wall glass reactor by Puxty et al. (2009) at 40 ℃, 0.3-900 kPa.

Recently Aronu et al. (2011) measured the total pressure in 2.9-24.5 m CO_2 loaded aqueous MEA at 60-120 ℃ and pressure up to 1060 kPa.

Another special static method was by observation of the CO_2 releasing point from the solution through the sapphire windows. Anoufrikov et al. (2002), Kamps et al. (2003), Xia et al. (2003), and Bottger et al. (2009) used this method for P_{CO2} in aqueous PZ, MDEA, and PZ/MDEA at 313-393 K with up to 10 MPa total pressure.

2.1.2 Static Methods with Sampling and Analysis

Jones et al. (1959) measured the solubility of H_2S and CO_2 in aqueous MEA at 40-140 ℃, up to 6983 P_{CO2}. The equilibrium cell was rocked for at least 16 hr before sampling. The vapor sample was collected and analyzed by MS.

With a similar apparatus Lawson et al. (1976) measured solubility of H_2S and CO_2 in aqueous MEA and DEA at 100-300 ℉, up to 32800 mmHg P_{CO2}.

Dingman et al. (1983) measured the solubility of H_2S and CO_2 in aqueous DGA®. Total pressure was maintained at 1500 mm Hg by methane and mixing was obtained by rocking. Vapor and liquid were sampled and gas chromatography (GC) was used in analysis.

Addicks et al. (2001, 2002) measured CO_2 and methane solubility in aqueous MDEA up to 200 bar at 313 and 353 K. The vapor composition was analyzed by GC and liquid was analyzed by titration.

Huttenhuis et al. (2007) measured the solubility of H_2S and CO_2 in aqueous MDEA at 10-25℃ at 6.9-69 kPa. An equilibrium cell with agitation was used and methane used as make-up gas. After the system reached equilibrium, a small sweep stream of methane (~200 Nml/min) was routed through the reactor and the outlet was analyzed by GC.

2.1.3 Dynamic Methods

In dynamic methods for CO_2 solubility measurement, gas chromatography, infrared analyzer, and mass spectrometer have been used to analyze CO_2. Water partial pressure is usually calculated, and amine partial pressure is neglected. To maintain a relative high pressure in the system, N_2, methane, or He is usually used as the inert gas.

One series of studies used a closed system with circulation of the gas of interest by a magnetically driven piston pump. This method expanded the acid gas partial pressure to 0.001-20000 kPa and temperature can be 0-150℃. N_2 was used to maintain the total pressure P_t when P_t was less than 200 kPa. Vapor was analyzed by GC. Liquid samples were injected into NaOH solution and analyzed. Using this method, Lee et al. (1976) measured the CO_2 and H_2S solubility in aqueous MEA. Martin et al. (1978) measured the CO_2 and H_2S solubility in aqueous DGA®. Teng et al. (1989,

1990) measured the solubility of H_2S and CO_2 in aqueous AMP. Jou et al. (1982, 1994, 1995) measured solubility of H_2S and CO_2 in MDEA and CO_2 solubility in MEA and MDEA/MEA.

With a similar experimental setup, Kadiwala et al. (2010) measured CO_2 solubility in 0.3 and 1.2 M PZ at 313 and 343 K up to 7400 kPa. Liquid samples were injected into 50 wt% MEA instead of NaOH solution and then analyzed by GC. The method and experimental set-up were first standardized by comparing CO_2–water–MEA equilibrium data obtained on this set-up versus data reported in the literature by Jou et al. (1995).

Sartori et al. (1983) measured CO_2 solubility in MEA and AMP at 40-120 ℃, 0.08-300 psia P_{CO2}. An autoclave with agitation was used, and the gas mixture of CO_2 and He was sparged into the liquid and entered GC for analysis. Water balance was maintained by a pre-saturator and a condenser.

Li et al. (1994, 1995) used a similar setup as Sartori and measured CO_2 and H_2S solubility in MEA/AMP at 40-100 ℃, with acid gas partial pressure 1-200 kPa.

Mass spectrometer (MS) has been used in analyzing the vapor samples. Muhlbauer et al. (1957) measured CO_2 and H_2S solubility in aqueous MEA. Gas was analyzed by MS for CO_2, N_2, Ar, and H_2S. The sum of P_{water} and P_{amine} were measured separately and subtracted from the measured P_t. Tontiwachwuthikul et al. (1991) used similar apparatus and procedure to measure CO_2 solubility in AMP at 20-80 ℃, 1-100 kPa P_{CO2}.

Ma'mun et al. (2005) used three equilibrium cells in series, with gas circulating, and measured CO_2 solubility in aqueous MEA and MDEA. Gas phase was analyzed by Infrared analyzer for CO_2 concentration.

The total pressure method in this work is basically a static method without vapor sampling. The mixing of vapor and liquid phases was obtained by a hollow shaft with two impellers and the agitation rate can be as high as 2500 rpm. Thus adequate mixing was achieved, mass transfer was accelerated, and time to equilibrium is reduced. It is shown that this method is highly productive to generate equilibrium data for high temperature pressure CO_2-amine-water systems. The measured total pressure and calculated partial pressure of CO_2 were comparable with literature data.

2.1.4 Basic Chemistry

Figure 2-1 shows the structures of amines used in this work. Primary amines have two hydrogen atoms attached to a nitrogen atom and are generally the most alkaline. MEA and DGA are primary amines. Secondary amines have one hydrogen atom attached to a nitrogen atom, such as PZ and 2MPZ. Tertiary amines have no hydrogen atom attached to a nitrogen atom, such as MDEA and 1,4-DMPZ.

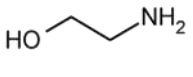

Monoethanolamine (MEA)

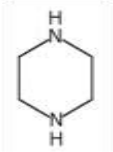

Piperazine (PZ)

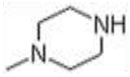

1-methylpiperazine (1MPZ)

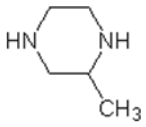

2-methylpiperazine (2MPZ)

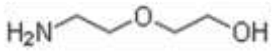

Diglycolamine® (DGA®)

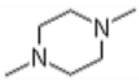

1,4-dimethylpiperazine (1,4-DMPZ)

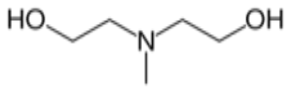

Methyldiethanolamine (MDEA)

Figure 2-1: Structure of Amines Used in This Work

The reactions between CO_2 and different types of amines are:

For primary amines:

$2RNH_2+CO_2 \leftrightarrow RNH_3^+ + RNHCOO^-$

$RNH_2+CO_2+H_2O \leftrightarrow RNH_3^+ + HCO_3^-$

For secondary amines:

$2R_2NH+CO_2 \leftrightarrow R_2NH_2^+ + R_2NCOO^-$

$R_2NH+CO_2+H_2O \leftrightarrow R_2NH_2^+ + HCO_3^-$

For tertiary amines:

$R_3N+CO_2+H_2O \leftrightarrow HCO_3^- + R_3NH^+$

R is a substituent other than a hydrogen atom.

2.2 EXPERIMENTAL METHODS

2.2.1 Apparatus

One run with aqueous MEA and three runs with aqueous PZ were conducted in the calorimeter. The autoclave was used in all the other experiments. The results do not show obvious differences between the two apparatuses.

2.2.1.1 Calorimeter

The first measurements of total pressure were performed using a 400 mL stainless steel calorimeter (by Parr Instrument) as the equilibrium cell (Figure 2-2). Pressure was measured with a Validyne® DP15 transducer (±15 kPa accuracy), calibrated by heating water and correlating the readings with known water vapor pressures from DIPPR (BYU, 1998- Provo, version 13.0). The calibration can be found in Appendix A. The voltage of the heating tape was manually controlled by a power controller to maintain selected temperature. An Omega® K type thermocouple (±1.5 ℃ accuracy) was installed inside the thermal well and an Omega® 4001A temperature controller was used as the

temperature indicator. There is an extra opening with a valve on the top of the calorimeter for venting. The calorimeter was not agitated.

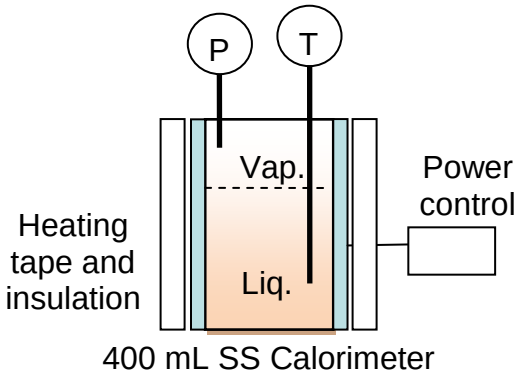

Figure 2-2: Total Pressure Measurement with a Calorimeter

2.2.1.2 Autoclave

As shown in Figure 2-3, a 500 mL stainless steel autoclave (ZipperClave®, by Autoclave Engineers) was used as the equilibrium cell for most of the measurements. Closure was effected by a resilient spring member inserted through a circumferential groove in the body and cover (Autoclave Engineers, 2009). A magnetic hollow shaft agitator (~4.60'' in length, adjustable, MAG075, MagneDrive II Series, by Autoclave Engineers) was used to get equilibrium without leaking to the atmosphere. A compressed air motor (2AM-NCC-16, by Gast®) provided agitation from 100 to 2500 rpm. The agitator circulates liquid and vapor phases. As shown in Figure 2-4, vapor entered from the top holes of the shaft and was sparged from the bottom holes of the shaft, which were under the bottom impeller (1 ¼ inch diameter). The top impeller is at about the interface of vapor and liquid to improve mixing. In some experiments, two baffle bars were placed in the autoclave for better mixing. Temperature was controlled by a Fuji Electric PXZ-4 PID temperature controller, with connection to a K-type thermocouple (±1.5 ℃ accuracy) placed inside the thermal well of the autoclave. A

pressure transducer (Druck® PTX 611, 0-30 bar absolute, ±2.4 kPa precision) was connected to a signal converter and a NI USB-6009 data logger to record data. The pressure indicator was calibrated by a dead weight pressure tester (S/N 19189/278, by Budenberg Volumetrics, INC.). The calibration can be found in Appendix A. There are extra openings with valves on the top of the autoclave for venting.

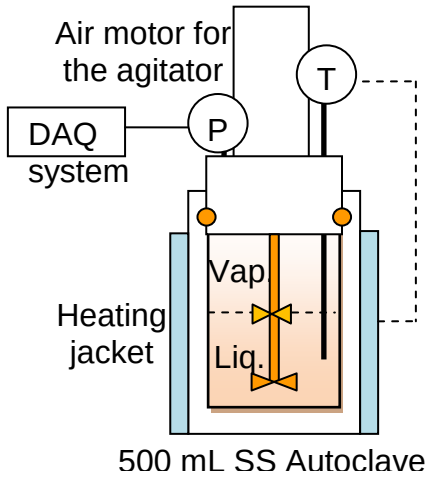

Figure 2-3: Total Pressure Measurement with an Autoclave

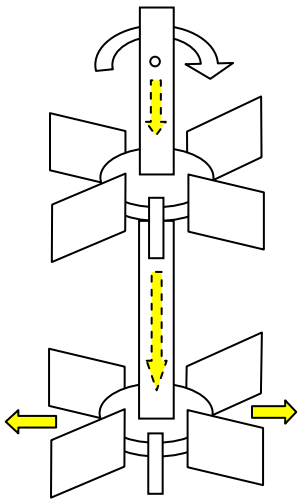

Figure 2-4: Autoclave Engineers' Patented Dispersimax™ Turbine Type Impeller with Modification. Reproduced from Autoclave Engineers Bulletin for Agitator/Mixers and modified as in the experiments. Yellow arrows are vapor flow; dashed arrows are inside the hollow shaft.

2.2.2 Solution Preparation

About 330 to 380 mL solution was prepared for each experiment. Certain amounts of amine and DDI water were weighed and combined to achieve the target molality (m). Then the mixture was stirred by a magnetic stir bar. For PZ and PZ derivatives, the mixture was heated and stirred on a hot plate to make the solid dissolve. After the solution was clear and well mixed, it was transferred into a glass gas sparging column (for PZ and PZ derivatives the column was pre-heated) on a scale. CO_2 was sparged into the solution, and the absorbed CO_2 weight was recorded. Details can be found in the Dissertations by Hilliard (2008) and Freeman (2011).

2.2.3 Procedure

Before each run, 300 to 330 mL of CO_2 loaded aqueous amine was prepared and added into the equilibrium cell. To avoid the effects of O_2, N_2 was used to purge air and then the cell was sealed. The initial pressure of N_2 and temperature were recorded. Then the cell was heated and recording of both temperatures and pressures started at around 100 ℃. After holding at temperature for at least 30 min or until the pressure did not change for 10 min, the system was assumed to be at equilibrium. The solution was heated to about 160 ℃ (or higher in selected runs) and then cooled down to 100 ℃. Data were taken during both heating and cooling processes to make the interval 10 ℃ in general. After each run the system was left overnight to cool down. Liquid samples were collected before and after each experiment at room temperature and analyzed for total inorganic carbon (CO_2) and total alkalinity (amine).

2.2.4 Analytical Methods

2.2.4.1 Total Inorganic Carbon (TIC)

The concentration of total CO_2 in solution was determined by Total Inorganic Carbon (TIC) analysis. The liquid samples collected through each run were gravimetrically diluted by a factor of 50-100, depending on the expected CO_2 concentration. About 20–30 μL diluted sample was injected into 30 wt% H_3PO_4 to release CO_2, and a continuous N_2 flow carried the CO_2 into an IR analyzer (Model 525, Horiba PIR 2000). PicoLog® software was used to record the voltage signal from the IR analyzer. In order to get a correlation curve between the voltage peak areas and carbon mass fraction, a series of calibration points were carried out at the end of each analysis by injecting known amounts of inorganic carbon standard (1000 ppm carbon, Ricca Chemical Company, Arlington, TX). Details can be found in Hilliard (2008) and Freeman (2011). The measurement precision is about 0.5-1%.

2.2.4.2 Acid Titration

The total alkalinity of each liquid sample was determined by titration using a Metrohm-Peak 835 Titrando equipped with an automatic dispenser, Metrohm-Peak 801 stirrer, and 3M KCl pH probe. 120-300X dilution of the sample was titrated with 0.1 N H_2SO_4 to pH 2.4. Details are available in Appendix A.3 of Hilliard (2008) and Appendix F of Sexton (2008). The measurement precision is about 0.5%.

2.2.5 Chemicals

Reagent chemicals were used: CO_2 (Clinical Purity, 99.5%, Matheson Tri Gas), MEA (99%, Acros Organics), anhydrous PZ (99%, Sigma-Aldrich and Acros Organics), 1-methyl-piperazine (1MPZ, 99+%, Acros Organics), 2-methyl-piperazine (2MPZ, 99%, AK Scientific), diglycolamine® (DGA®, 99%, Huntsman), Methyl-diethanolamine

(MDEA, 99%, Acros Organics), 1,4-dimethylpiperazine (1,4-DMPZ, 98.5% Acros Organics). DDI water was used for solution preparation.

2.3 CO_2 SOLUBILITY IN AMINES

The measured total pressure includes the pressure of the amine-H_2O-CO_2 system and N_2. Thus the total pressure of amine-H_2O-CO_2 is $P_t=P_{meas}-P_{N2}$, where P_{meas} is the measured pressure and P_{N2} is the N_2 partial pressure; N_2 was assumed to be an ideal gas so $P_{N_2} = P_{N_2,0} \cdot \frac{T(K)}{T_0(K)}$. 0 stands for the initial condition.

The partial pressure of CO_2 was estimated by subtracting an estimate of the water partial pressure from the total pressure.

$$P_{CO_2} = P_t - P_{H_2O} - P_{amine} = P_t - P^*_{H_2O} \cdot x_{H_2O} - P^*_{amine} \cdot x_{amine} \quad (2\text{-}1)$$

P_{H2O} and P_{amine}: partial pressure of water and amine.

P^*_{H2O} and P^*_{amine}: pressure of pure water and pure amine at T.

The mole fractions in solution were represented as $x_{H2O}+x_{amine}=1$, assuming there is water and total amine but no free CO_2. P_{amine} was assumed to be negligible except for MEA. Pure H_2O and MEA pressure was obtained from DIPPR (1998-Provo, BYU).

Liquid analysis gives the total CO_2 loading at room temperature. At low to medium temperature, CO_2 loading $\alpha = \frac{n_{T,CO_2}}{n_{T,alkalinity}}$. At temperature above 100°C, liquid loadings were corrected by the estimated amount of CO_2 in the vapor.

$$\alpha = \frac{n_{T,CO_2} - n_{V,CO_2}}{n_{T,alkalinity}}$$
$$n_{V,CO_2} = \frac{P_{CO_2} V_{vap}}{RT} \quad (2\text{-}2)$$

Where $n_{T,\ CO2}$ and $n_{V,\ CO2}$ are the total CO_2 (mol) and CO_2 in vapor (mol), respectively. $n_{T,\ alkalinity}$ is the total alkalinity (mol).

2.3.1 Benchmark – CO_2 Solubility in MEA

Figure 2-5 shows a favorable comparison of the MEA data in this work with data by Jou et al. (1995), Dugas et al. (2009), and Ma'mun et al. (2005). The lines are predicted by the empirical model from this work, which will be presented in the next section. Figure 2-6 shows a comparison of total pressure data in this work with data by Aronu et al. (2011).

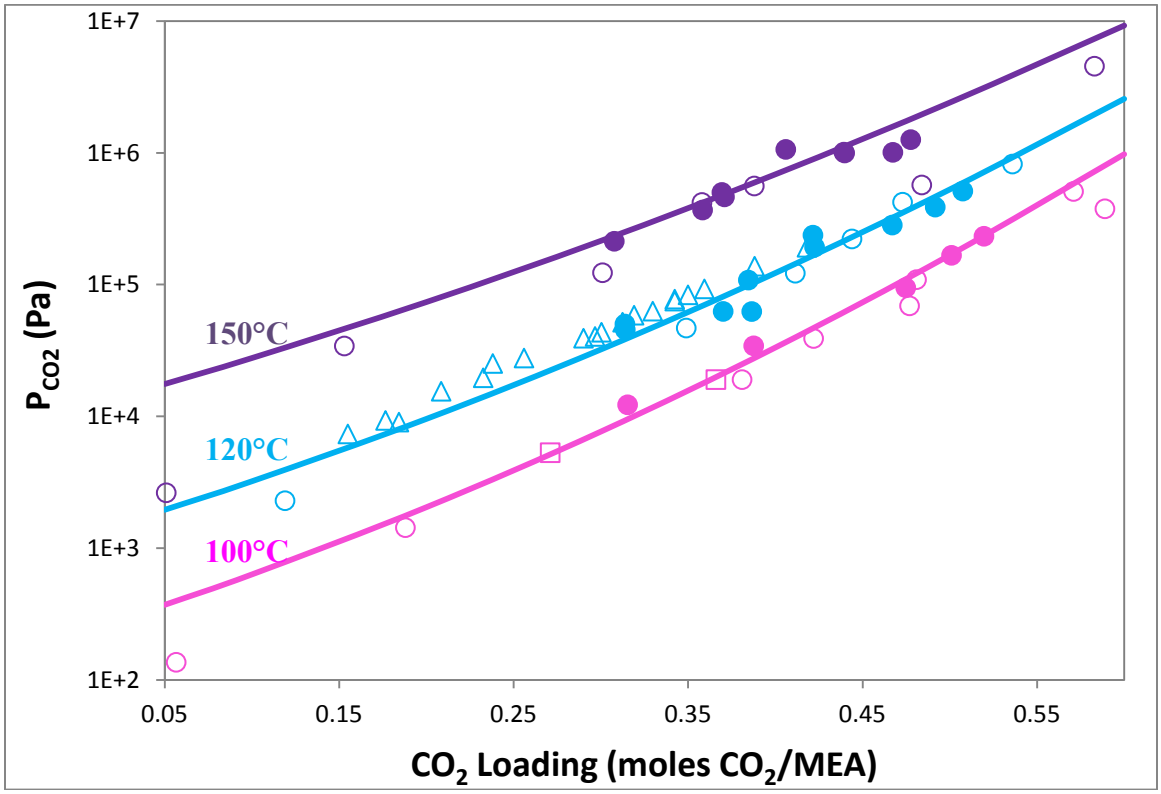

Figure 2-5: Comparison of CO_2 Solubility in 7 m MEA at 100, 120 and 150°C. ●: This work; ○: Jou et al. (1995); □: Dugas et al. (2009); Δ: Ma'mun et al. (2005); Lines: empirical model, 7 m MEA.

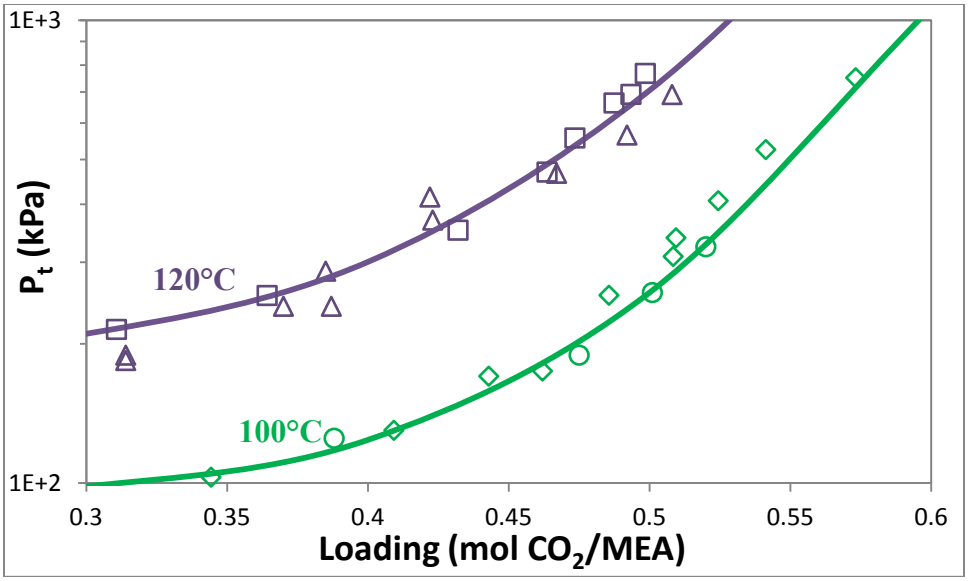

Figure 2-6: Comparison of Total Pressure in 7 m MEA. **○: 100°C this work; ◊: 100°C Aronu et al. (2011); Δ: 120°C this work; □: 120°C Aronu et al. (2011); lines: empirical model.**

2.3.2 CO_2 Solubility in Amines

Tables 2-1 to 2-9 present all the data from this work for MEA, PZ, 1MPZ, 2MPZ, PZ/2MPZ, DGA, PZ/1MPZ/1,4-2MPZ, 7 m/2 m MDEA/PZ, and 5 m/5 m MDEA/PZ. Loading is reported as mol CO_2/equivalent alkalinity. Amine concentration is given as molality (m, gmol/kg water).

Table 2-1: Measured Total Pressure and Calculated CO_2 Solubility in MEA

MEA	T	Loading	P_{CO2}	P_t	MEA	T	Loading	P_{CO2}	P_t
m	℃		kPa	kPa	m	℃		kPa	kPa
6.97*	110	0.424	138	266	6.86	120.4	0.314	50	189
6.97*	110	0.424	123	251	6.86	121.8	0.314	45	184
6.97*	120	0.422	237	415	6.86	129.9	0.313	77	220
6.97*	120	0.423	192	370	6.86	131.9	0.313	73	217
6.97*	130	0.419	352	594	6.86	141.4	0.311	131	279
6.97*	130	0.421	292	535	6.86	142.3	0.31	145	293
6.97*	140	0.414	613	937	6.86	150.2	0.308	213	366
6.97*	140	0.417	464	788	6.86	152	0.307	236	390

MEA	T	Loading	P_{CO2}	P_t	MEA	T	Loading	P_{CO2}	P_t
m	℃		kPa	kPa	m	℃		kPa	kPa
6.97*	150	0.406	1062	1490	6.86	159	0.303	332	490
6.86	101	0.475	95	189	6.87	100	0.501	167	258
6.86	111	0.472	171	303	6.87	120	0.492	387	565
6.86	121	0.467	283	467	6.87	140	0.477	764	1089
6.86	130	0.461	448	691	6.87	150	0.467	1008	1437
6.86	139	0.45	716	1032	6.85	100	0.52	233	324
6.86	140	0.452	683	1008	6.85	120	0.508	512	691
6.86	149	0.44	997	1414	6.85	140	0.489	964	1289
6.86	150	0.439	1012	1440	6.85	150	0.478	1259	1688
6.86	160	0.424	1427	1984	6.85	160	0.464	1626	2184
6.86	161	0.424	1442	2013	6.87	120	0.37	63	241
6.86	166	0.42	1568	2216	6.87	140	0.364	217	542
6.82	100	0.388	34	125	6.87	150	0.358	368	797
6.82	110	0.387	61	190	6.87	160	0.351	569	1126
6.82	120	0.387	62	241	10.39	100	0.411	40	127
6.82	120	0.385	108	287	10.39	110	0.410	98	220
6.82	129	0.382	176	412	10.39	120	0.407	176	346
6.82	131	0.383	153	403	10.39	130	0.403	316	547
6.82	140	0.378	289	614	10.39	140	0.397	515	825
6.82	140	0.377	308	633	10.39	150	0.389	801	1210
6.82	150	0.371	463	892	10.39	160	0.379	1189	1720
6.82	150	0.369	500	929	10.60	100	0.520	321	407
6.82	160	0.361	724	1281	10.60	110	0.516	477	599
6.82	160	0.361	732	1289	10.60	120	0.509	703	872
6.82	170	0.348	1090	1805	10.60	130	0.501	996	1226
6.82	170	0.35	1051	1766	10.60	140	0.489	1417	1726
6.86	109	0.314	36	169	10.60	150	0.477	1859	2267
6.86	111.3	0.315	22	157	10.60	160	0.462	2435	2964
6.86	101.1	0.315	12	143					

*: conducted with the calorimeter apparatus.

Table 2-2: Measured Total Pressure and Calculated CO_2 Solubility in PZ

PZ	T	Loading	P_{CO2}	P_t	PZ	T	Loading	P_{CO2}	P_t
m	℃		kPa	kPa	m	℃		kPa	kPa
7.78*	110	0.312	125	251	7.93	161	0.337	1816	2369
7.78*	110	0.312	125	251	7.93	163	0.334	1934	2516
7.78*	120	0.311	211	385	7.86	110.1	0.252	14	140
7.78*	120	0.311	211	385	7.86	118.5	0.251	28	193
7.78*	130	0.311	268	505	7.86	129.9	0.251	59	295
7.78*	130	0.310	343	579	7.86	131.1	0.250	100	344
7.78*	140	0.308	517	833	7.86	140.9	0.249	124	449
7.78*	140	0.308	546	863	7.86	141.1	0.248	166	492
7.78*	150	0.304	894	1311	7.86	149.5	0.247	252	663
7.78*	150	0.305	864	1281	7.86	151.5	0.247	237	670
7.78*	160	0.301	1247	1788	7.86	159.8	0.244	417	955
7.43*	100	0.311	79	168	7.86	163.4	0.243	447	1036
7.43*	110	0.311	41	167	7.86	171.9	0.239	664	1388
7.43*	110	0.310	115	242	7.86	173.2	0.237	749	1497
7.43*	119	0.310	146	315	7.86	180.5	0.234	957	1844
7.43*	120	0.310	95	270	7.86	182.9	0.231	1093	2030
7.43*	130	0.308	285	522	7.86	191.8	0.224	1482	2623
7.43*	130	0.309	195	433	8.00	100	0.448	711	800
7.43*	140	0.306	531	849	8.00	100.6	0.451	596	686
7.43*	140	0.307	427	745	8.00	110	0.444	881	1006
7.43*	150	0.302	877	1296	8.00	112.2	0.444	891	1026
7.43*	150	0.304	653	1072	8.00	117.8	0.440	1067	1228
7.43*	160	0.298	1317	1861	8.00	120	0.438	1175	1348
7.43*	160	0.301	974	1518	8.00	128.3	0.433	1423	1647
7.43*	169	0.297	1374	2054	8.00	129.4	0.431	1507	1738
7.43*	170	0.291	1954	2651	8.00	140.5	0.424	1901	2221
7.43*	180	0.281	3006	3888	8.00	140.6	0.423	1928	2248
7.93*	120	0.328	116	290	8.00	146.7	0.418	2203	2583
7.93*	125	0.328	124	327	4.93	100.6	0.292	20	115
7.93*	130	0.327	229	465	4.93	108.9	0.291	31	157
7.93*	139	0.325	441	748	4.93	110.6	0.291	40	174
7.93*	140	0.325	440	756	4.93	120	0.290	60	242
7.93*	149	0.321	780	1184	4.93	130	0.289	105	353
7.93*	150	0.321	777	1193	4.93	138.9	0.287	152	473
7.93*	160	0.317	1238	1778	4.93	140	0.286	176	507

PZ	T	Loading	P_{CO2}	P_t	PZ	T	Loading	P_{CO2}	P_t
m	℃		kPa	kPa	m	℃		kPa	kPa
7.93*	161	0.318	1181	1737	4.93	150	0.283	273	709
7.93*	167	0.311	1831	2473	4.93	150	0.283	295	732
7.92	100	0.306	20	109	4.93	159.4	0.278	447	1005
7.92	110	0.306	37	162	4.93	160.6	0.277	457	1032
7.92	120	0.304	89	262	4.93	169.4	0.271	665	1381
7.92	130	0.303	135	371	4.93	170	0.269	711	1436
7.92	130	0.303	156	392	4.93	180	0.261	991	1909
7.92	140	0.301	256	571	4.93	180.6	0.260	1035	1967
7.92	140	0.300	291	607	4.93	191.1	0.248	1436	2615
7.92	150	0.297	460	876	4.96	100	0.372	76	169
7.92	150	0.296	510	926	4.96	100.6	0.371	103	198
7.92	160	0.292	723	1263	4.96	109.4	0.370	140	268
7.92	160	0.289	849	1389	4.96	110	0.369	170	301
7.92	170	0.283	1160	1852	4.96	120	0.367	243	425
7.92	170	0.282	1251	1943	4.96	120.6	0.366	272	458
7.92	174	0.278	1421	2183	4.96	130	0.363	388	636
7.94	81	0.422	94	137	4.96	130.6	0.362	415	667
7.94	82	0.421	126	171	4.96	140	0.358	578	909
7.94	89	0.421	151	210	4.96	140	0.357	607	938
7.94	90	0.419	197	258	4.96	148.3	0.352	823	1240
7.94	94	0.419	200	271	4.96	150	0.351	835	1271
7.94	100	0.417	322	410	4.96	160	0.344	1149	1715
7.94	101	0.418	277	369	4.96	160.6	0.342	1194	1769
7.94	110	0.413	478	604	4.96	170	0.334	1538	2264
7.94	111	0.414	447	576	4.96	170.6	0.333	1580	2317
7.94	120	0.410	623	797	4.96	175	0.329	1775	2593
7.94	120	0.409	682	856	7.92	100	0.416	301	390
7.94	130	0.404	898	1134	7.92	110	0.413	471	597
7.94	130	0.403	945	1181	7.92	120	0.408	679	853
7.94	139	0.398	1228	1534	7.92	130	0.402	971	1207
7.94	140	0.397	1243	1558	7.92	140	0.395	1302	1618
7.94	146	0.393	1452	1825	7.92	150	0.387	1709	2125
7.94	150	0.389	1646	2062	7.92	160	0.378	2192	2732
7.94	150	0.389	1639	2055	7.80	120	0.300	64	238
7.94	157	0.384	1911	2411	7.80	140	0.297	220	537
7.75	100	0.373	174	263	7.80	150	0.294	374	791

PZ	T	Loading	P_{CO2}	P_t	PZ	T	Loading	P_{CO2}	P_t
m	℃		kPa	kPa	m	℃		kPa	kPa
7.75	110	0.371	281	407	7.80	160	0.289	602	1142
7.75	110	0.367	419	545	7.93	100	0.357	86	174
7.75	120	0.367	444	618	7.93	120	0.352	270	443
7.75	120	0.364	577	751	7.93	130	0.349	433	669
7.75	130	0.359	798	1034	7.93	140	0.344	668	984
7.75	134	0.361	723	989	7.93	150	0.338	980	1396
7.75	140	0.357	913	1229	7.93	160	0.330	1358	1898
7.75	140	0.353	1085	1401	9.69	100	0.302	25	111
7.75	150	0.345	1505	1922	9.69	110	0.301	59	181
7.75	151	0.347	1415	1844	9.69	120	0.300	112	280
7.75	160	0.337	1919	2460	9.69	130	0.299	203	432
7.75	160	0.337	1892	2433	9.69	140	0.296	354	661
7.93	110	0.368	223	348	9.69	150	0.292	585	989
7.93	119	0.365	390	558	9.69	160	0.287	918	1443
7.93	121	0.367	304	483	9.92	100	0.379	209	297
7.93	129	0.360	609	838	9.92	110	0.376	367	492
7.93	137	0.357	760	1050	9.92	120	0.372	567	741
7.93	139	0.354	901	1208	9.92	130	0.367	840	1075
7.93	146	0.350	1106	1479	9.92	140	0.362	1167	1482
7.93	150	0.346	1316	1731	9.92	150	0.355	1588	2003
7.93	152	0.345	1369	1807	9.92	160	0.347	2065	2603

*: conducted with the calorimeter apparatus.

Table 2-3: Measured Total Pressure and Calculated CO_2 Solubility in 1MPZ

1MPZ	T	Loading	P_{CO2}	P_t	1MPZ	T	Loading	P_{CO2}	P_t
m	℃		kPa	kPa	m	℃		kPa	kPa
7.76	120	0.192	225	399	7.66	100	0.246	244	333
7.76	130	0.188	381	617	7.66	120	0.238	630	804
7.76	140	0.183	616	932	7.66	130	0.232	917	1154
7.76	150	0.178	903	1320	7.66	140	0.224	1289	1606
7.76	160	0.170	1282	1823	7.66	150	0.215	1744	2161
					7.66	160	0.205	2272	2814

Table 2-4: Measured Total Pressure and Calculated CO_2 Solubility in 2MPZ

2MPZ	T	Loading	P_{CO2}	P_t	2MPZ	T	Loading	P_{CO2}	P_t
m	℃		kPa	kPa	m	℃		kPa	kPa
7.61	120	0.279	145	319	6.69	160	0.340	2269	2819
7.61	130	0.276	262	499	7.41	100	0.392	306	398
7.61	140	0.272	449	766	7.41	110	0.387	519	648
7.61	150	0.266	715	1133	7.41	120	0.380	792	971
7.61	160	0.258	1126	1668	7.41	130	0.372	1129	1372
6.69	120	0.379	571	748	7.41	140	0.362	1594	1919
6.69	130	0.372	859	1100	7.41	150	0.350	2118	2547
6.69	140	0.363	1247	1569	7.41	160	0.337	2751	3307
6.69	150	0.353	1709	2133					

Table 2-5: Measured Total Pressure and Calculated CO_2 Solubility in PZ/2MPZ*

PZ+2MPZ	T	Loading	P_{CO2}	P_t	PZ+2MPZ	T	Loading	P_{CO2}	P_t
m	℃		kPa	kPa	m	℃		kPa	kPa
7.63	120	0.306	142	316	7.86	100	0.397	227	315
7.63	130	0.303	252	489	7.86	120	0.389	576	750
7.63	140	0.300	427	744	7.86	130	0.384	837	1073
7.63	150	0.295	673	1091	7.86	140	0.376	1201	1517
7.63	160	0.288	1011	1554	7.86	150	0.369	1585	2001
					7.86	160	0.359	2084	2624

*: PZ/2MPZ mol ratio ≈ 1:1.

Table 2-6: Measured Total Pressure and Calculated CO_2 Solubility in DGA

DGA	T	Loading	P_{CO2}	P_t	DGA	T	Loading	P_{CO2}	P_t
m	℃		kPa	kPa	m	℃		kPa	kPa
9.55	120	0.402	252	421	9.6	100	0.488	356	442
9.55	130	0.396	417	647	9.6	120	0.473	732	901
9.55	140	0.387	662	970	9.6	130	0.463	990	1220
9.55	150	0.375	975	1380	9.6	140	0.450	1329	1637
9.55	160	0.361	1359	1885	9.6	150	0.437	1699	2104
					9.6	160	0.421	2150	2676

Table 2-7: Measured Total Pressure and Calculated CO_2 Solubility in PZ/1MPZ/1,4-DMPZ

Amine*	T	Loading	P_{CO2}	P_t	Amine*	T	Loading	P_{CO2}	P_t
m	℃		kPa	kPa	m	℃		kPa	kPa
7.57	100	0.320	276	365	7.57	160	0.269	2771	3314
7.57	110	0.316	455	581	7.92	120	0.240	165	338
7.57	120	0.310	702	876	7.92	130	0.237	276	513
7.57	130	0.303	1036	1274	7.92	140	0.234	466	782
7.57	140	0.294	1497	1814	7.92	150	0.228	742	1158
7.57	150	0.283	2052	2470	7.92	160	0.221	1129	1669

*: Amine concentration is the total of PZ, 1MPZ, and 1,4-DMPZ and the mol ratio is about 3.75:3.75:0.5.

Table 2-8: Measured Total Pressure and Calculated CO_2 Solubility in 7 m MDEA / 2 m PZ

Amine*	T	Loading	P_{CO2}	P_t	Amine*	T	Loading	P_{CO2}	P_t
m	℃		kPa	kPa	m	℃		kPa	kPa
10.51	110	0.133	78	202	10.49	140	0.205	1376	1688
10.51	120	0.132	136	307	10.49	150	0.193	1866	2278
10.51	130	0.129	226	460	10.49	160	0.177	2477	3011
10.51	140	0.125	355	668	10.71	100	0.234	189	276
10.51	150	0.119	553	964	10.71	110	0.229	346	470
10.51	160	0.113	787	1321	10.71	120	0.223	527	698
10.49	100	0.236	253	341	10.71	130	0.214	827	1060
10.49	110	0.232	411	535	10.71	140	0.203	1181	1492
10.49	120	0.225	634	806	10.71	150	0.191	1609	2019
10.49	130	0.216	962	1196	10.71	160	0.178	2054	2587

*: Amine concentration is the total alkalinity of MDEA and PZ and the mol ratio of MDEA/PZ is about 7:2.

Table 2-9: Measured Total Pressure and Calculated CO_2 Solubility in 5 m MDEA / 5 m PZ

Amine*	T	Loading	P_{CO2}	P_t	Amine*	T	Loading	P_{CO2}	P_t
m	℃		kPa	kPa	m	℃		kPa	kPa
14.43	110	0.221	98	220	14.61	100	0.277	111	197
14.43	120	0.219	173	342	14.61	110	0.275	204	326
14.43	130	0.216	298	528	14.61	120	0.271	350	519
14.43	140	0.212	489	796	14.61	130	0.266	567	797
14.43	150	0.206	760	1165	14.61	140	0.259	901	1208
14.43	160	0.197	1144	1670	14.61	150	0.250	1289	1693
					14.61	160	0.240	1776	2301

*: Amine concentration is the total alkalinity of MDEA and PZ and the mol ratio of MDEA/PZ is about 5:5.

Empirical models were regressed based on the data in this work and selected literature for each amine. The models for MEA, PZ, 1MPZ, 2MPZ, DGA have been reported (Xu et al., 2011) and some of them are updated in this paper, and new models for the rest of the amines are regressed from the new data.

Table 2-10 lists the correlated parameters, coefficient of determination (R^2) for the empirical models, and the literature that provided additional data for the regression.

Table 2-10: Empirical Correlation of CO_2 Partial Pressure (P_{CO2}, Pa) with Loading (α, gmol CO_2/equiv. alkalinity) and T (K). $\ln P_{CO_2}(\mathrm{Pa}) = a + b\frac{1}{T} + c\alpha + d\alpha^2 + e\frac{\alpha}{T} + f\frac{\alpha^2}{T}$

	MEA	PZ	1MPZ	2MPZ	PZ/2MPZ
a	38.6±0.4	35.3±0.3	34.0±0.1	39.9±0.8	40.1±0.8
b	-12379±139	-11054±120	-9923±50	-12469±267	-12807±266
c	NF**	NF**	NF**	-21.6±2.6	-21.3±2.4
d	-16.0±2.5	-18.9±2.7	NF**	NF**	NF**
e	3556±231	4958±347	7555±107	13990±905	14114±837
f	8702±932	10163±1085	NF**	NF**	NF**
R^2	0.994	0.993	0.999	0.999	0.999
Literature*	Jou et al. 1995; Hilliard 2008; Dugas 2008; Ma'mun 2005; Aronu 2011.	Hilliard 2008; Dugas 2008; Ermatchkov 2006; Nguyen 2010; Kamps 2003.	Chen 2011	Chen 2011	Chen 2011

	DGA	PZ/1MPZ/1,4-DMPZ	7 m MDEA/2 m PZ	5 m MDEA/5 m PZ	
a	49.2 ±2.3	34.5 ±0.1	31.2 ±0.2	36.1 ±0.2	
b	-15066 ±761	-10629 ±54	-8701 ±58	-11199 ±173	
c	-42.8 ±6.2	NF**	23.0 ±1.1	NF**	
d	26.0 ±4.2	NF**	-18.8 ±3.5	-29.1 ±4.3	
e	14174 ±1814	7578 ±120	NF**	10551 ±772	
f	NF**	NF**	NF**	NF**	
R^2	0.998	1.000	0.999	1.000	
Literature*	Chen 2010	Rochelle 2010	Chen 2010	Chen 2010	

*: "et al." is neglected to save space in this table.

**: NF – not fit. It means the coefficient was not important in improving the regression, so it was excluded in the final regression and its value is 0.

Figures 2-7 through 2-15 show the temperature and loading dependence of CO_2 solubility in the screened solvents, respectively.

In Figure 2-7 the MEA data is compared with Aspen® model prediction by Hilliard (2008). The Hilliard model is good for 60-120 ℃ within 0.2-0.5 loading. At higher than 140 ℃, it over predicts the CO_2 partial pressure.

In Figure 2-8 the PZ data is compared with the PZ Aspen® Fawkes model prediction by Frailie et al. (2010). The Fawkes model predicts well for 40-160 ℃ with 0.2-0.45 loading. At higher than 0.45 loading, there is no experimental data and the model prediction is higher than the empirical correlation.

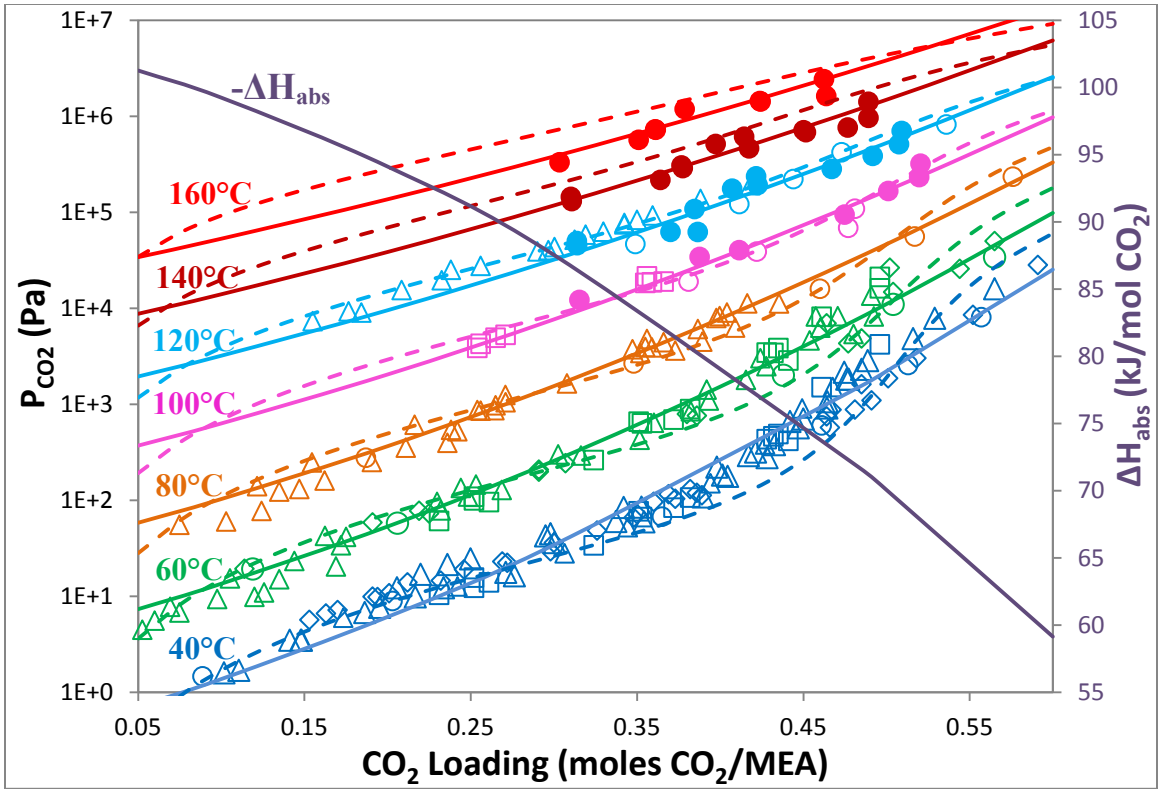

Figure 2-7: CO_2 Solubility in 2.9-24.6 m MEA. ●: this work; ○: Jou et al. (1995); □: Dugas et al. (2008); ◊: Hilliard (2008); Δ: Ma'mun et al. (2005); solid lines: empirical model; dashed lines: Aspen® Hilliard Model (2008) for 7 m MEA.

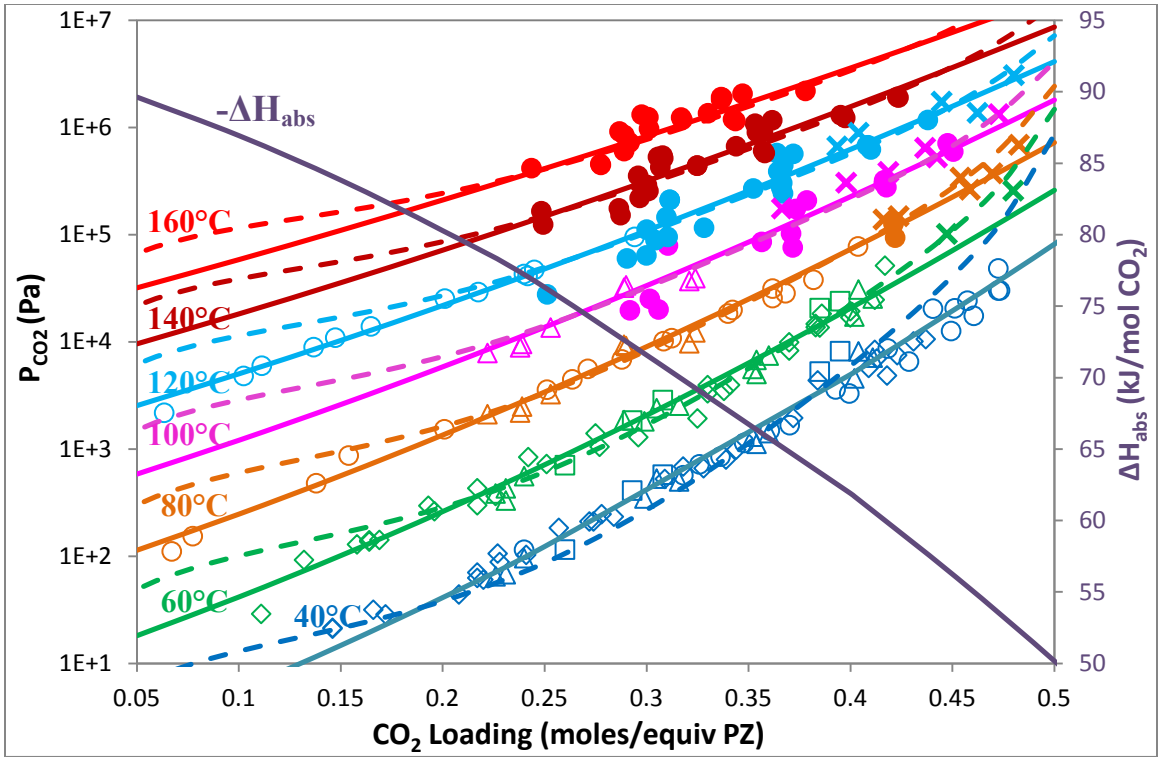

Figure 2-8: CO_2 Solubility in 0.9-12 m PZ. **●: this work; ○: Ermatchkov et al. (2006); □: Nguyen et al. (2010); ◊: Hilliard (2008); Δ: Dugas et al. (2008); X: Kamps et al. (2003); solid lines: empirical model; dashed lines: Aspen® Fawkes Model (Frailie et al., 2010) for 8 m PZ**

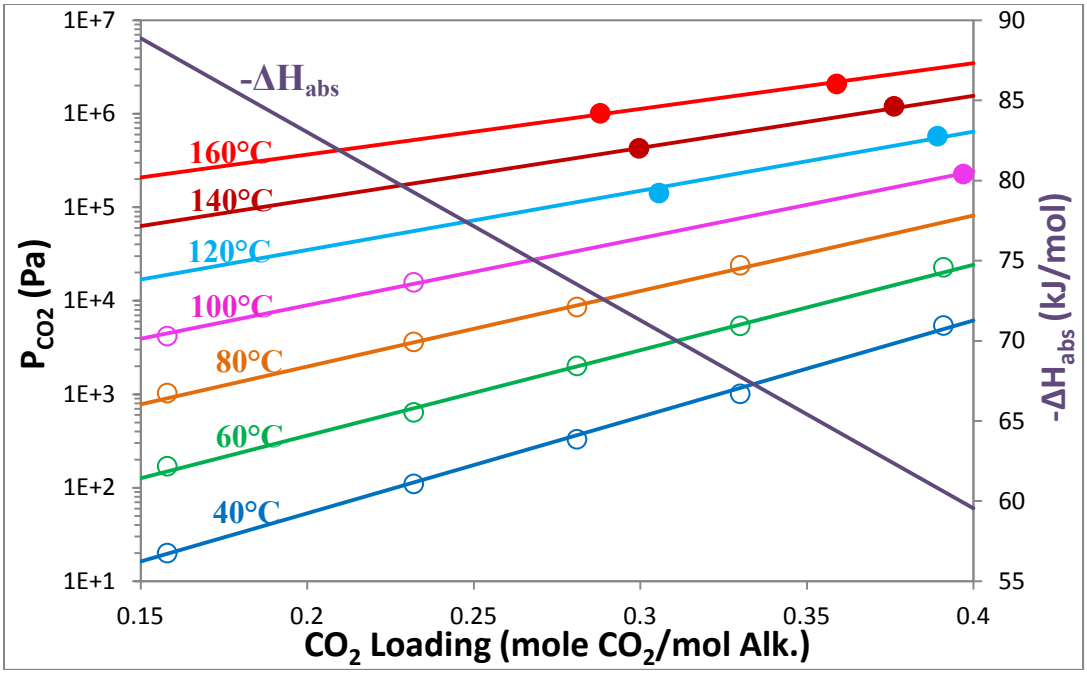

Figure 2-9: CO_2 Solubility in 4 m PZ/4 m 2MPZ. ●: this work; ○: Chen et al., 2011; solid lines: empirical model.

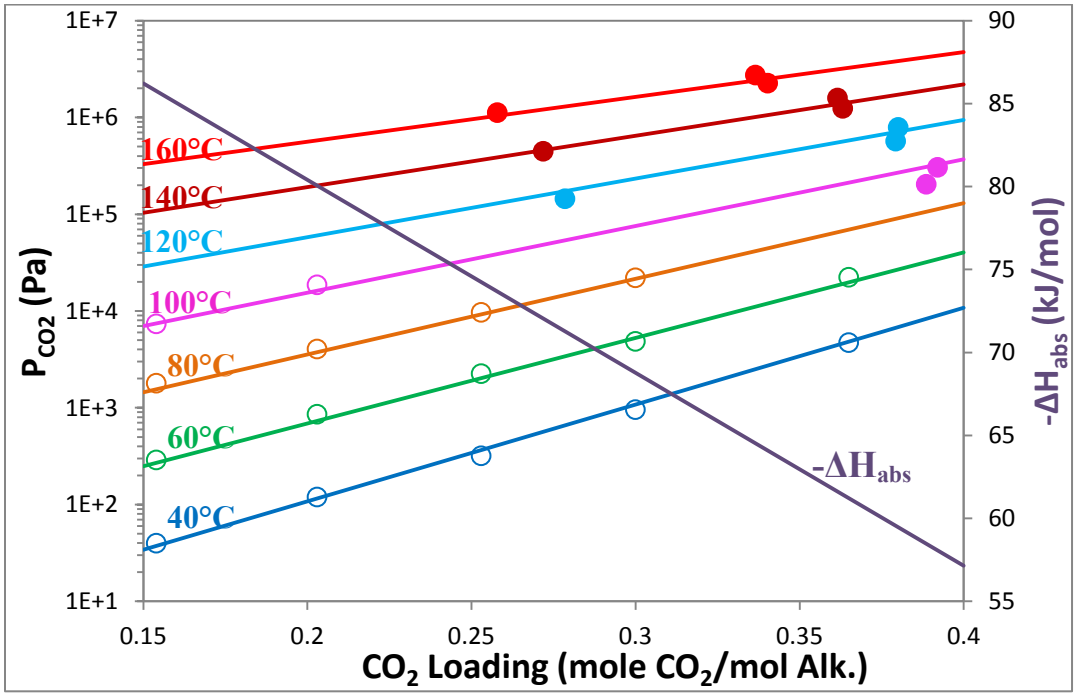

Figure 2-10: CO_2 Solubility in 8 m 2MPZ. ●: this work; ○: Chen et al., 2011; solid lines: empirical model.

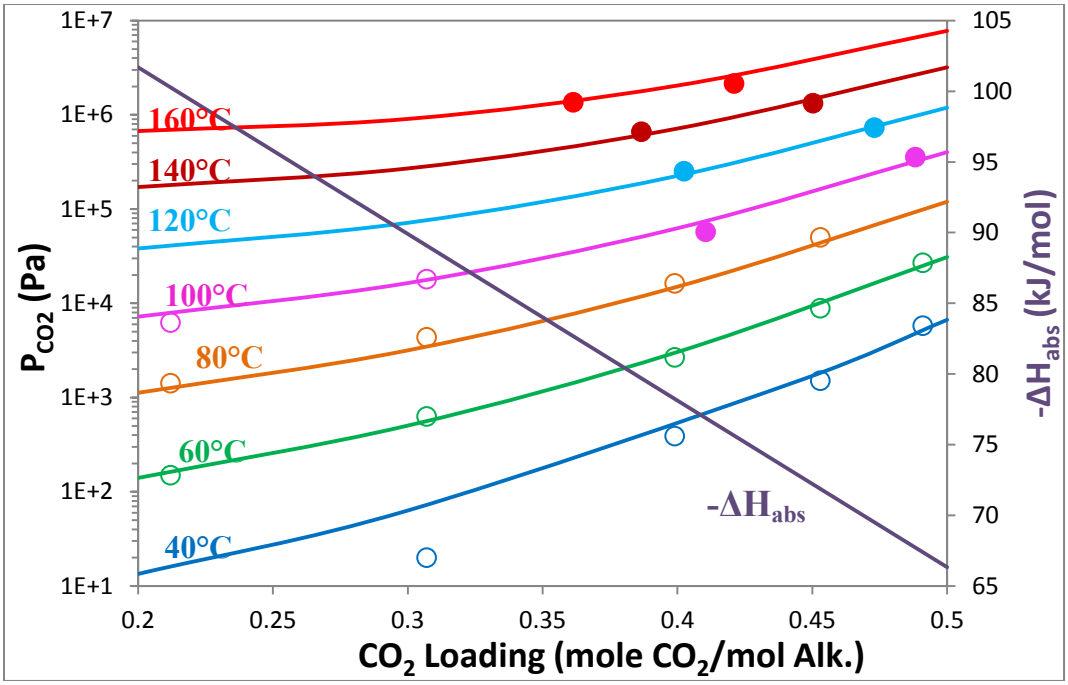

Figure 2-11: CO_2 Solubility in 10 m DGA. **●: this work; ○: Chen et al., 2010; solid lines: empirical model.**

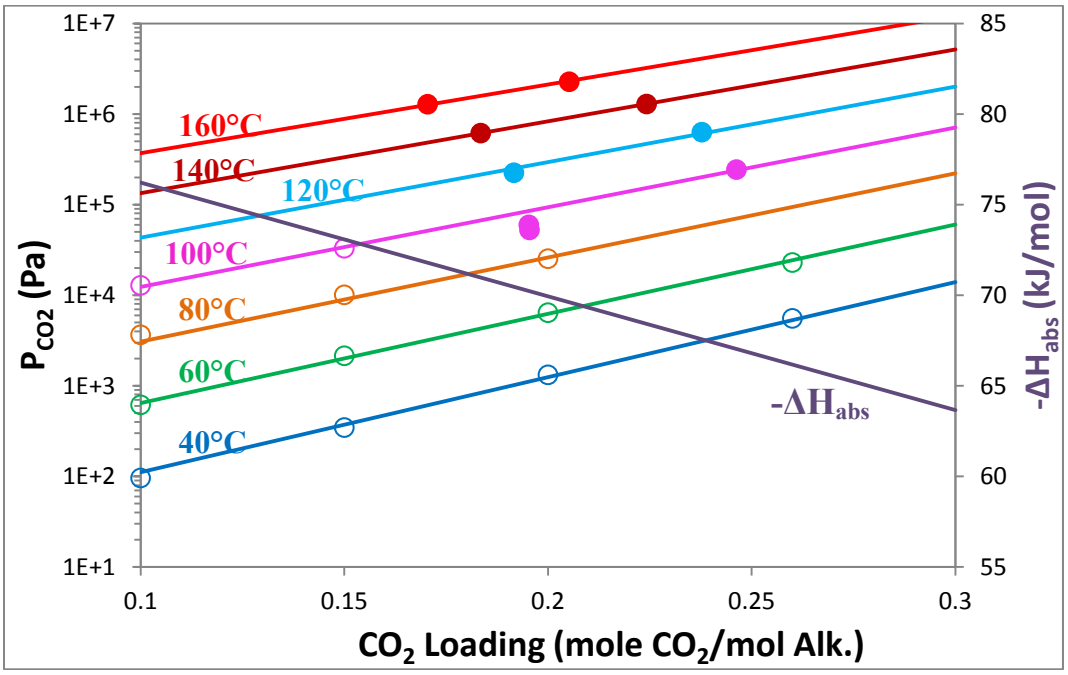

Figure 2-12: CO_2 Solubility in 8 m 1MPZ. **●: this work; ○: Chen et al., 2011; solid lines: empirical model.**

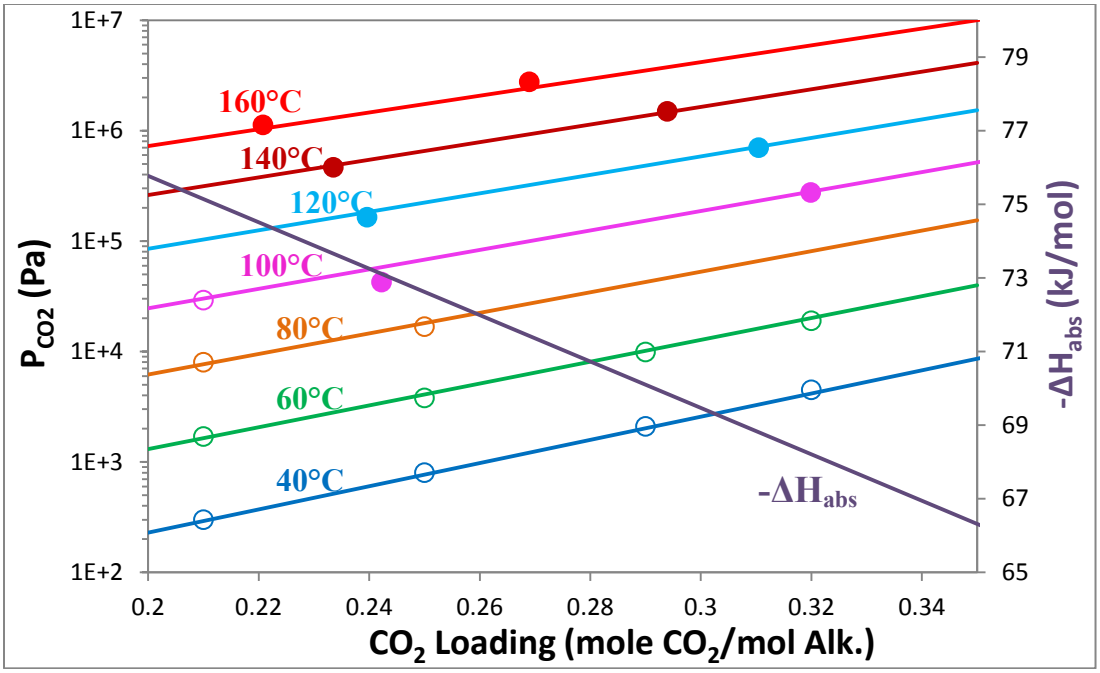

Figure 2-13: CO_2 Solubility in 3.75/3.75/0.5 m PZ/1MPZ/1,4-DMPZ. ●: this work; ○: Rochelle et al., 2010; solid lines: empirical model.

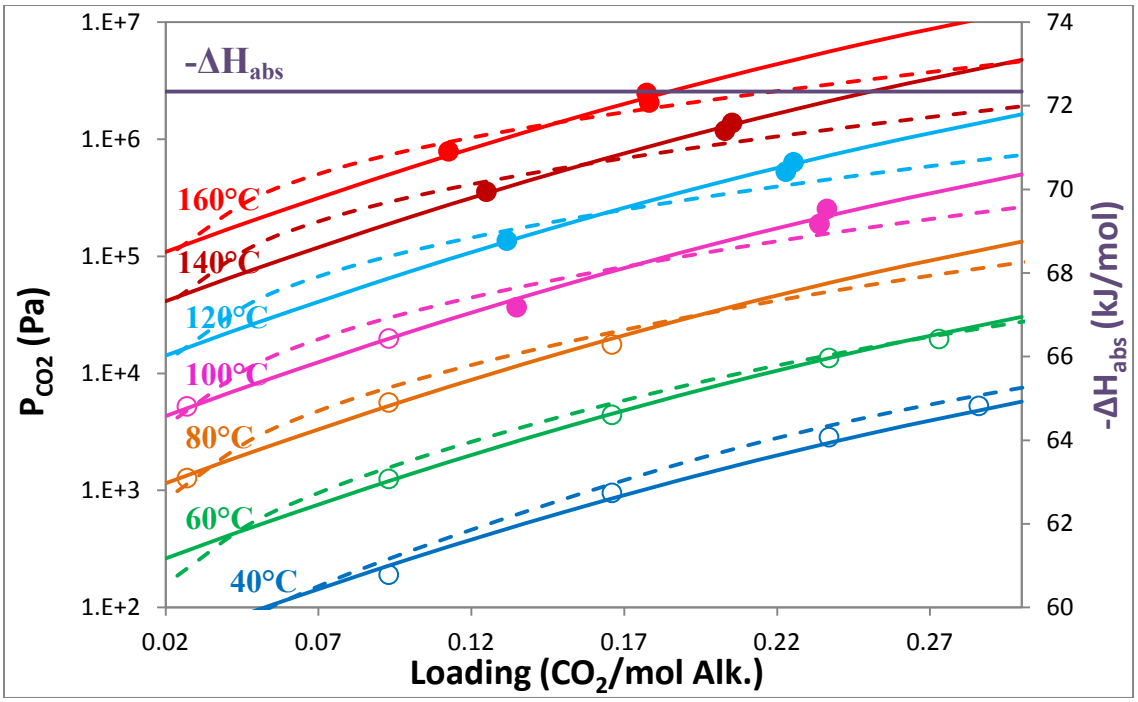

Figure 2-14: CO_2 Solubility in 7 m MDEA/2 m PZ. ●: this work; ○: Chen et al. 2010; solid lines: empirical model; dashed lines: Aspen® Fawkes Model (Frailie et al., 2010)

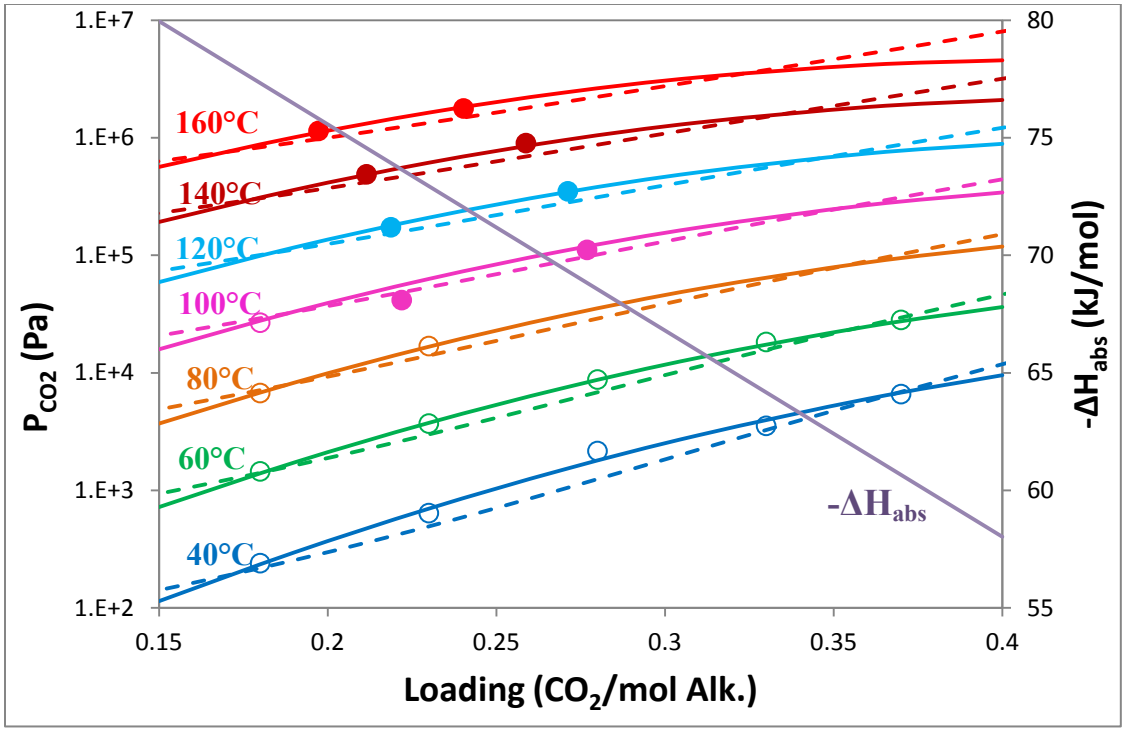

Figure 2-15: CO_2 Solubility in 5 m MDEA/5 m PZ. **●: this work; ○: Chen et al., 2010; solid lines: empirical model; dashed lines: Aspen® Fawkes Model (Frailie et al., 2010)**

2.3.3 Error Analysis

Errors generally came from the measurements of temperature, pressure, liquid analysis of CO_2 and amine, CO_2 partial pressure calculation, and the correction of the CO_2 loading in liquid. Table 2-11 lists the estimated error from the experiment.

Table 2-11: Estimated Error from the Total Pressure Experiments

Error Source	Value range	Estimated Error
Measured pressure: P_{meas}	200-3,000 kPa	2.4 kPa
$P_t = P_{meas}-P_{N2}$	200-3,000 kPa	4.8 kPa
T measurement	80-190 °C	1 °F (0.6 °C)
Alkalinity from titration	5-10 mol/kg sol.	1%

Error Source	Value range	Estimated Error
CO_2 wt% from TIC	6-15 wt%	2%
P_{CO2} calculation	100-2,500 kPa	10%
Correction of CO_2 loading in liquid	0.25-0.55	0.005
Total error in P_{CO2}	-	15%
Total error in CO_2 loading	-	0.01

Figure 2-16 gives an example in aqueous PZ that most of P_{CO2} data fall within the ±25% deviation curves from the empirical model prediction.

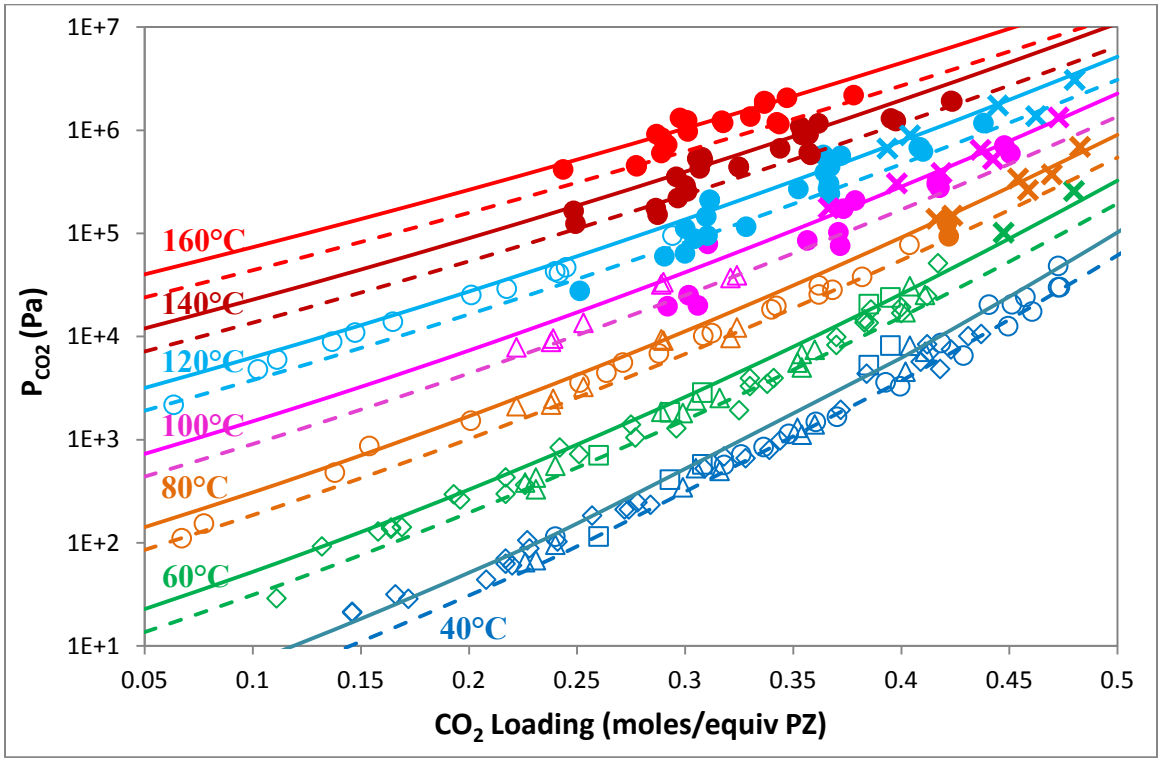

Figure 2-16: CO_2 Solubility in 0.9-12 m PZ – Deviation from the Empirical Model.
●: this work; ○: Ermatchkov et al. (2006); □: Nguyen et al. (2010); ◊: Hilliard (2008); Δ: Dugas et al. (2008); X: Kamps et al. (2003); solid lines: +25% from empirical model – 8 m PZ; dashed lines: -25% from empirical model - 8 m PZ

2.3.4 Total Pressure in CO_2 Loaded Aqueous Amines

Total pressure can be calculated using the empirical models of P_{CO2}. From DIPPR (1998-Provo, BYU), pure water vapor pressure can be expressed as:

$$P^*_{H2O}(Pa) = \exp\left(A + \frac{B}{T(K)} + ClnT(K) + DT(K)^E\right) \quad (2\text{-}3)$$

Where A=73.649, B= -7258.2, C= -7.3037, D=4.1653E-6, E=2.

Pure amine pressure P^*_{amine} is neglected except for MEA.

$$P^*_{MEA}(Pa) = \exp\left(A' + \frac{B'}{T(K)} + C'lnT(K) + D'T(K)^{E'}\right) \quad (2\text{-}4)$$

Where A'=92.624, B'= -10367, C'= -9.4699, D'=1.9E-18, E'=6.

$$x_{H2O} = \frac{\text{mol of } H_2O}{\text{mol of amine} + \text{mol of } H_2O} \quad (2\text{-}5)$$

$$x_{amine} = \frac{\text{mol of amine}}{\text{mol of amine} + \text{mol of } H_2O} \quad (2\text{-}6)$$

Therefore

$$P_t = P_{CO2} + P_{H2O} + P_{amine} = P_{CO2} + P^*_{H_2O} \cdot x_{H_2O} + P^*_{amine} \cdot x_{amine} \quad (2\text{-}7)$$

Substitute the empirical model of P_{CO2} and Equation (2-3) through (2-6) into Equation (2-7) and yield the total pressure P_t.

Figures 2-17 and 2-18(a) are the total pressure in 7 m MEA and 8 m PZ, respectively. The model prediction fits the data well. For the reading convenience in practice, Figure 2-18(a) is enlarged in Figure 2-18(b).

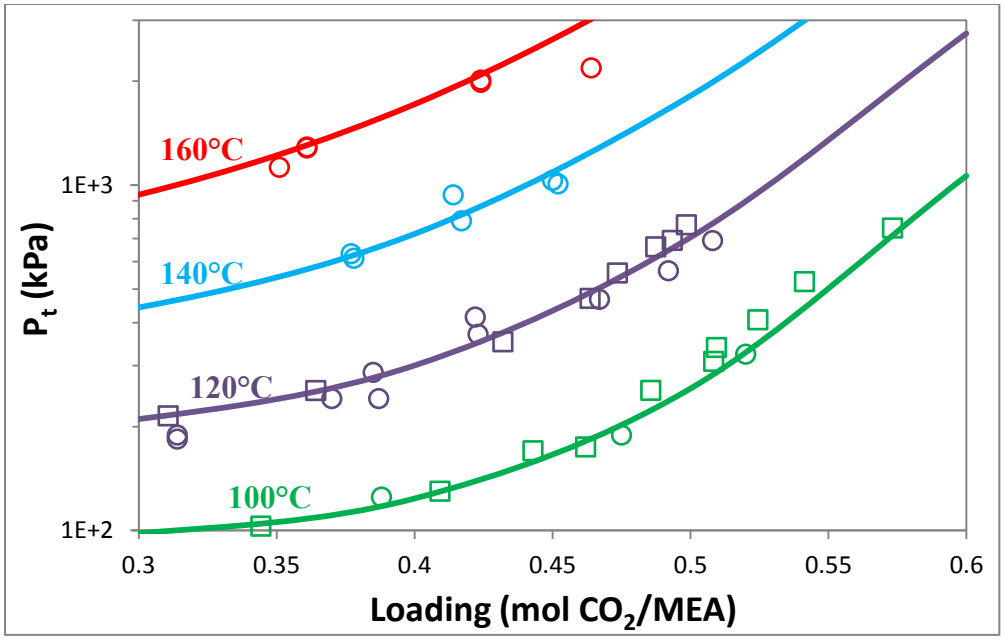

Figure 2-17: Comparison of Total Pressure in 7 m MEA. ○: this work; □: Aronu et al. (2011); lines: Equation (2-7).

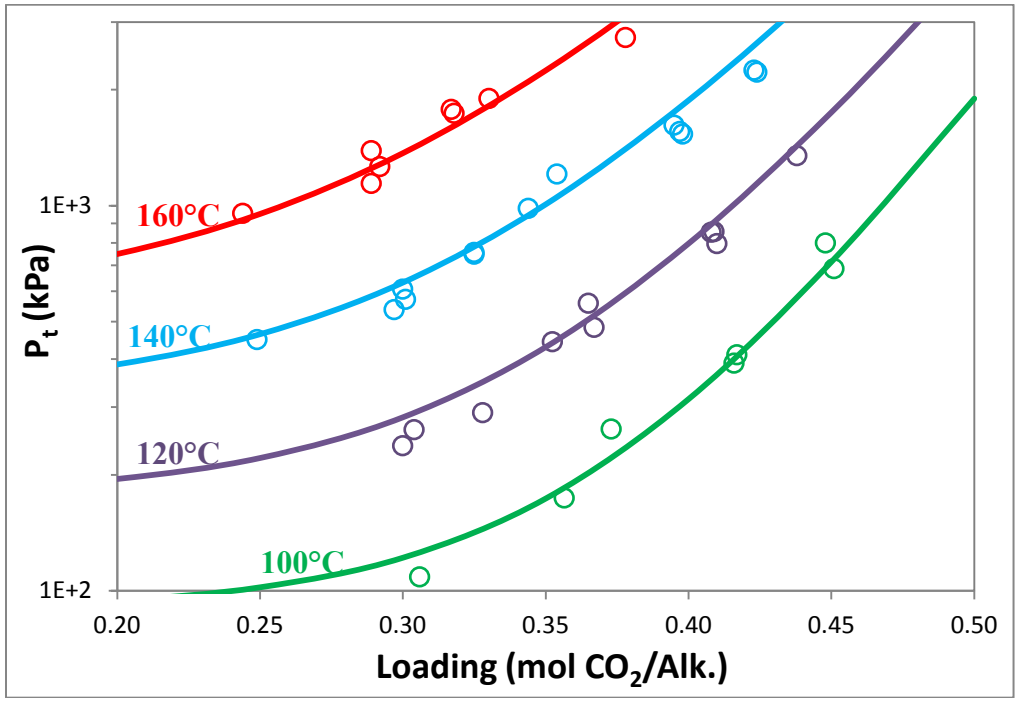

Figure 2-18 (a): Comparison of Total Pressure in 8 m PZ. ○: this work, experimental data; lines: Equation (2-7).

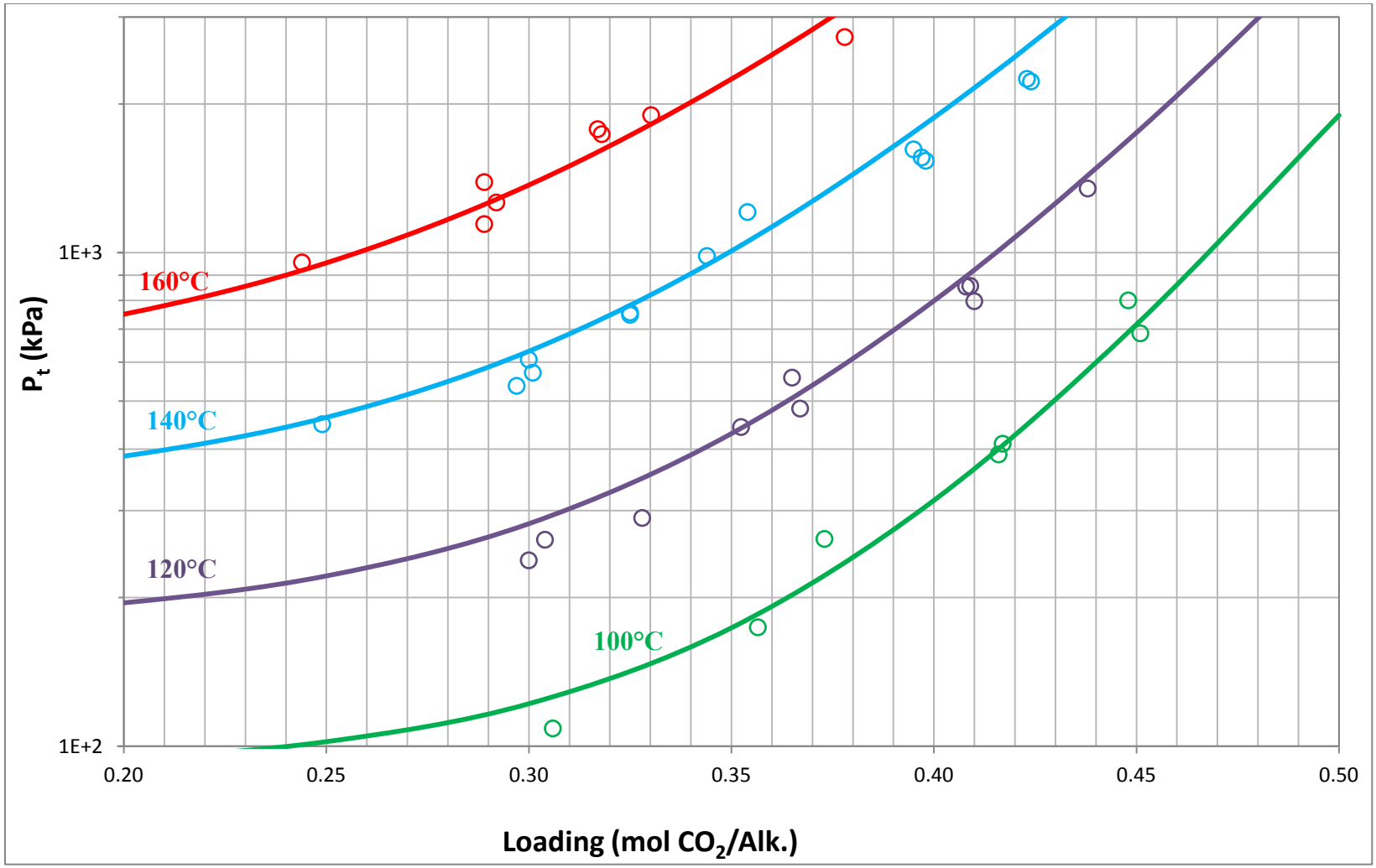

Figure 2-18 (b): Comparison of Total Pressure in 8 m PZ. ○: this work, experimental data; lines: Equation (2-7).

2.3.5 Heat of Absorption of CO_2 in Aqueous Amines

2.3.5.1 Apparent Differential Heat of Absorption

Equation XVIII.9 in Lewis and Randall (1923) and Equation IV.109 in Dodge (1944) relate the fugacity with the heat of absorption of a solution constituent.

$$\left(\frac{\partial ln f_1}{\partial T}\right)_{P,N} = \frac{H_1^* - \bar{H}_1}{RT^2}$$ Equation (XVIII.9), Lewis and Randall (1923)

Where f_1 is the fugacity of the constituent 1, $H_1^* - \bar{H}_1$ is the heat absorbed per mol when a small quantity of the constituent X_1 evaporates from the solution into a vacuum.

$$\frac{\partial ln \bar{f}_i}{\partial T} = -\frac{\bar{H}_i - \bar{H}_i^o}{RT^2}$$ Equation (IV.109), Dodge (1944)

Where $\bar{f}_i$ is the fugacity of the constituent i, $-(\bar{H}_i - \bar{H}_i^o)$ is the heat absorbed per mol when a small quantity of the constituent X_i evaporates from the solution into a vacuum.

Applying the derivation to CO_2 loaded aqueous amines, the equilibrium is $CO_2(g) \leftrightarrow CO_2(aq)$. i refers to CO_2 and:

$\bar{G}_i$: partial molar Gibbs free energy; G_i^o: Gibbs free energy at standard state; $\bar{f}_i$: fugacity; f_i^o: fugacity at standard state; S_i^o: entropy at standard state; $\bar{S}_i$: partial molar entropy; $\bar{H}_i$: partial molar enthalpy; H_i^o: enthalpy at standard state.

By the definition of fugacity, between the two states CO_2(g) and CO_2(aq),

$$\bar{G}_i - G_i^o = RTln\frac{\bar{f}_i}{f_i^o} \quad (2\text{-}8)$$

Take derivatives on both sides with respect to T,

$$\left(\frac{\partial \bar{G}_i}{\partial T}\right)_{p,x} - \left(\frac{\partial G_i^o}{\partial T}\right)_{p,x} = Rln\frac{\bar{f}_i}{f_i^o} + RT\left(\frac{\partial ln\bar{f}_i}{\partial T}\right)_{p,x} - RT\left(\frac{\partial ln f_i^o}{\partial T}\right)_{p,x} \quad (2\text{-}9)$$

f_i^o does not change with T, and from (2-8), $Rln\frac{\bar{f}_i}{f_i^o} = \frac{\bar{G}_i - G_i^o}{T}$, thus

$$\left(\frac{\partial \bar{G}_i}{\partial T}\right)_{p,x} - \left(\frac{\partial G_i^o}{\partial T}\right)_{p,x} = \frac{\bar{G}_i}{T} - \frac{G_i^o}{T} + RT\left(\frac{\partial ln\bar{f}_i}{\partial T}\right)_{p,x} \quad (2\text{-}10)$$

Then apply $\left(\frac{\partial G_i^o}{\partial T}\right)_{p,x} = -S_i^o = -\frac{H_i^o - G_i^o}{T}$, $\left(\frac{\partial \bar{G}_i}{\partial T}\right)_{p,x} = -\bar{S}_i = -\frac{\bar{H}_i - \bar{G}_i}{T}$ to (2-10)

and get

$$\left(\frac{\partial ln\bar{f}_i}{\partial T}\right)_{p,x} = -\frac{\bar{H}_i - \bar{H}_i^o}{RT^2} \quad (2\text{-}11)$$

Assume $\bar{f}_i = P_i$, then $\left(\frac{\partial lnP_i}{\partial T}\right)_{p,x} = -\frac{\bar{H}_i - \bar{H}_i^o}{RT^2} = -\frac{-\Delta H_{abs}}{RT^2}$,

$$-\Delta H_{abs} = R\left(\frac{\partial lnP_{CO_2(g)}}{\partial \frac{1}{T}}\right)_{P,x} \quad (2\text{-}12)$$

This should be used under constant total pressure and loading. According to Figure 2 in De Koeijer et al. (2004), at constant loading and temperature, P_{CO2} increases 2-3% when the total P increases from 1 to 25 bar. In this work P_t and P_{CO2} are within 0-30 bar range, so the effect of P_t on P_{CO2} was neglected.

For CO_2, the critical pressure P_c = 7.38 MPa and the critical temperature T_c = 304.3 K, therefore at 160 ℃ and 25 bar, the compressibility factor of CO_2: $Z_{CO2} \approx 0.98$. Thus for most experimental data points $Z_{CO2} \geq 0.98$. The assumption $f_{CO2} \approx P_{CO2}$ can be made in this work.

According to Equation (2-12), correlations of $-\Delta H_{abs}$ were derived from the empirical models of P_{CO2}. Table 2-12 gives $-\Delta H_{abs}$, lean and rich CO_2 loading, and CO_2 capacity derived from the empirical models. Within the precision of these measurements and estimates, the heat of CO_2 absorption is independent of temperature and amine concentration, but varies with CO_2 loading. The statistics of the empirical regression suggest that the heat of absorption is determined with a confidence interval of 0.5 to 9 kJ/mol.

Table 2-12: Heat of CO_2 Absorption and CO_2 Capacity

Solvent (m)	ΔH_{abs} (J/mol CO_2)	$-\Delta H_{abs}$ kJ/mol CO_2 [1]	CO_2 loading [2] (mol/mol alkalinity)			CO_2 Capacity [3] (mol/kg amine+H_2O)
			Lean	Mid	rich	
2.9–24.6 MEA	$-R(-12379+3556\alpha+8702\alpha^2)$	72±2	0.434	0.483	0.535	0.50 [4]
0.9–12 PZ	$-R(-11054+4958\alpha+10163\alpha^2)$	67±2	0.310	0.354	0.400	0.85 [5]
7.7–8 1MPZ	$-R(-9923+7555\alpha)$	69.4±0.5	0.162	0.208	0.258	0.85
6.7–8 2MPZ	$-R(-12469+13990\alpha)$	67±3	0.267	0.314	0.367	0.89
4/4 PZ/2MPZ	$-R(-12998+14684\alpha)$	66±3	0.294	0.341	0.391	0.89
9.6–10 DGA	$-R(-15066+14174\alpha)$	73±9	0.400	0.445	0.490	0.44
3.75/3.75/0.5 PZ/1MPZ/1,4-DMPZ	$-R(-10629+7578\alpha)$	70.9±0.5	0.232	0.278	0.328	0.87
7/2 MDEA/PZ	72.3	72.3±0.5	0.135	0.201	0.288	0.84
5/5 MDEA/PZ	$-R(-11199+10551\alpha)$	69±2	0.214	0.270	0.346	0.98

1: The heat of absorption of CO_2 at mid-loading. 2: The loadings where P_{CO2} is 0.5, 1.5, and 5 kPa at 40 ℃ corresponds to lean, mid-, and rich loading, calculated from the empirical models. 3: moles of CO_2/kg (water+amine). 4: 7 m MEA. 5: 8 m PZ.

2.3.5.2 Carnot Cycle Derivation

Equation (2-12) can also be derived from the following process. As shown in Figure 2-19, (1+m_{CO2}(gram)/1000) kg of CO_2 loaded rich amine solution was chosen as the system. The equilibrium CO_2 partial pressure at T and T+dT are $P^*(T)$ and $P^*(T+dT)$, respectively. In step 1 the rich amine solution reversibly releases m_{CO2} g of CO_2 gas and absorbs $-\Delta H_{abs}(T)\cdot {}^{m_{CO2}}/_{44.01}$ kJ heat; the m_{CO2} g of CO_2 is at equilibrium pressure, $P^*(T)$. In step 2, the m_{CO2} g CO_2 was compressed reversibly to $P^*(T+dT)$, and the lean solution and CO_2 gas are heated to T+dT. In this step the system (1 kg lean solution + m_{CO2} g CO_2 gas) absorbs heat to increase temperature, and extra work dW is put into the system for isothermal and reversible compression. In step 3, the CO_2 gas at $P^*(T+dT)$ is absorbed into the amine solution, and releases heat of $-\Delta H_{abs}(T+dT)\cdot {}^{m_{CO2}}/_{44.01}$ kJ. In step 4 the temperature of the rich amine is reduced from T+dT to T to the initial state.

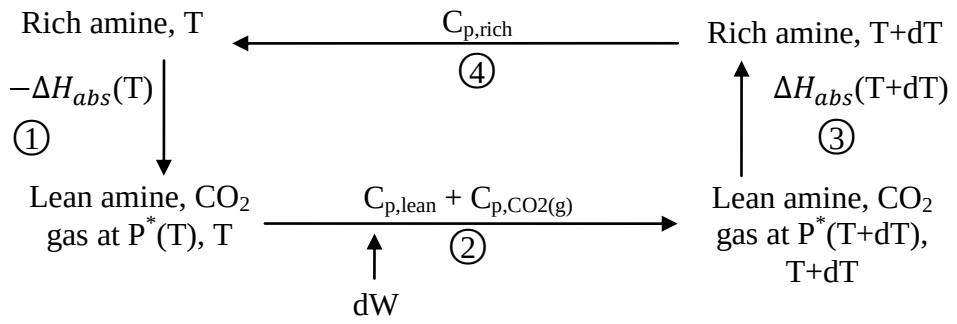

Figure 2-19: Illustration of Temperature Dependence of CO_2 Solubility and Heat of Absorption

In order to correlate enthalpy change in step 1 and 3 with the work dW in step 2, equivalent work of the cycle is calculated. The equivalent work is the largest work that can be withdrawn from heat dQ from a heat reservoir at T and can be calculated from Carnot Cycle. Assume the reference temperature is T_0, the efficiency is: $(T-T_0)/T$. Therefore, in step 1 and 3, equivalent work is $m_{CO2}/44.01 \cdot \Delta H_{abs}(T)\ (T-T_0)/T$ and $m_{CO2}/44.01 \cdot \Delta H_{abs}(T+dT)\ (T+dT-T_0)/(T+dT)$, respectively.

dW is the isothermal and reversible work to the CO_2 gas, assuming this CO_2 is an ideal gas, thus

$$dW = \frac{m_{CO2}}{44.01} RTln\frac{P^*(T+dT)}{P^*(T)} = \frac{m_{CO2}}{44.01} RTln\frac{P+dP}{P} = \frac{m_{CO2}}{44.01} RT[ln(P+dP) - lnP] = \frac{m_{CO2}}{44.01} RTdlnP \quad (2\text{-}13)$$

The heat input in step 2 and 4 are for the heating of lean solution, rich solution, and CO_2 gas. Therefore

$$Q_2 - Q_4 = (C_{p,lean}(\frac{kJ}{kg} \cdot K) \cdot 1kg + \frac{m_{CO2}\ g}{44.01g/mol} \cdot C_{p,CO2}kJ/mol)dT - C_{p,rich}(\frac{kJ}{kg} \cdot K) \cdot \left(1kg + \frac{m_{CO2}\ g}{1000g/kg}\right)dT$$

Because $C_{p,lean} \cdot 1 + \frac{m_{CO2}}{44.01} \cdot C_{p,CO2} - C_{p,rich} \cdot \left(1 + \frac{m_{CO2}}{1000}\right) \approx 0$

Thus for the cycle in Figure 2-19, the equivalent work equation is:

$$-\Delta H_{abs}(T)\cdot\frac{m_{CO2}}{44.01}\cdot\frac{T-T_0}{T}=dW-\Delta H_{abs}(T+dT)\cdot\frac{m_{CO2}}{44.01}\cdot\frac{T+dT-T_0}{T+dT} \quad (2\text{-}14)$$

dT is very small, so $\Delta H_{abs}(T)\approx\Delta H_{abs}(T+dT)$ and $T\approx T+dT$. And substitute Equation (2-13) into (2-14):

$$-\Delta H_{abs}(T)\cdot\frac{m_{CO2}}{44.01}\cdot\frac{T-T_0}{T}=\frac{m_{CO2}}{44.01}RTdlnP-\Delta H_{abs}(T)\cdot\frac{m_{CO2}}{44.01}\cdot\frac{T+dT-T_0}{T}$$

$$-\Delta H_{abs}(T)\cdot\frac{T-T_0}{T}=RTdlnP-\Delta H_{abs}(T)\cdot\frac{T+dT-T_0}{T}$$

$$\frac{\Delta H_{abs}(T)}{R}\cdot\frac{dT}{T^2}=dlnP$$

$$-\frac{\Delta H_{abs}(T)}{R}/d\left(\frac{1}{T}\right)=dlnP$$

$$-\frac{\Delta H_{abs}(T)}{R}=\frac{dlnP}{d\left(\frac{1}{T}\right)}$$

Where P is P_{CO2}.

This agrees with Equation (2-12), and the assumption made here is $f_{CO2}=P_{CO2}$ and $Q_2=Q_4$, which is reasonable when P is not very large, and dT is very small.

2.3.5.3 Inconsistency of the Measured Heat of Absorption and P_{CO2}

ΔH_{abs} by this method is the differential heat of absorption. Because of the accuracy of CO_2 partial pressure measurements, the empirical correlations show no temperature dependence of ΔH_{abs}. Figure 2-20 compares $-\Delta H_{abs}$ from the MEA empirical model and measured $-\Delta H_{abs}$ by Kim et al. (2007). The empirical model generally predicts the data, but the empirical equation does not represent the temperature dependence of the Kim data.

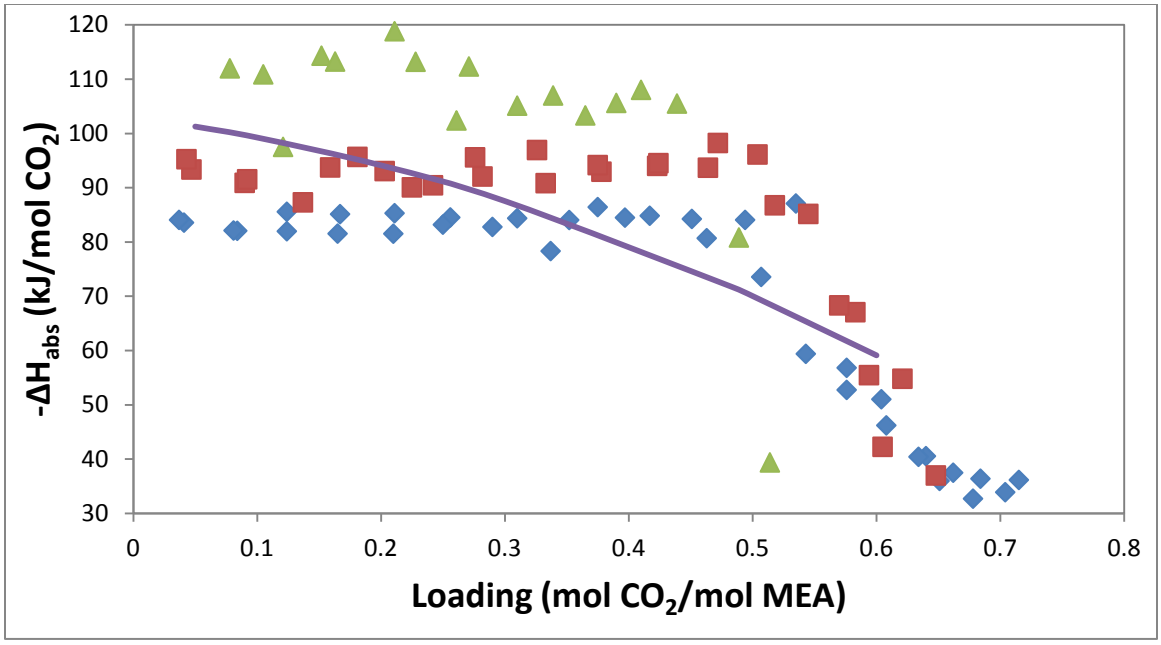

Figure 2-20: Comparison of Heat of Absorption of CO_2 in MEA. **Data points: Kim et al. (2007), ◊: 40°C, □: 80°C, Δ: 120°C; solid lines: empirical model from this work.**

To better compare measured $-\Delta H_{abs}$ from Kim et al. (2007) and the P_{CO2} data from this work, the literature $-\Delta H_{abs}$ was regressed to get a piecewise function as in Equation (2-15). Figure 2-21 shows a fit of the empirical model. A few outliers in the data were not used in the regression.

$$\begin{cases} -\Delta H_{abs} = -13.67 + 0.308T & (\alpha \leq 0.46) \\ -\Delta H_{abs} = -127.13 + 246.65\alpha + 1.02T - 1.54\alpha T & (0.46 \leq \alpha \leq 0.66) \\ -\Delta H_{abs} = 35.66 & (\alpha \geq 0.66) \end{cases} \quad (2\text{-}15)$$

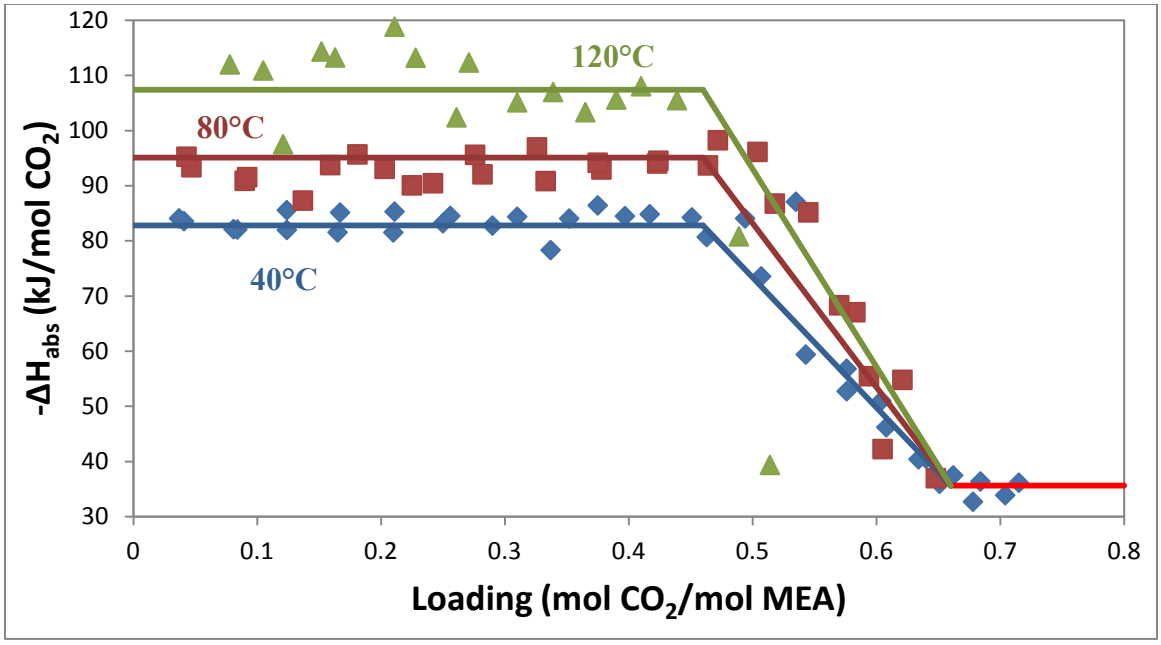

Figure 2-21: Empirical Model of Heat of Absorption of CO_2 in 7 m MEA. **Data points: Kim et al. (2007), ◊: 40°C, □: 80°C, Δ: 120°C; solid lines: empirical model Equation (2-15).**

Then Equation (2-15) was integrated to get P_{CO2}. The literature $-\Delta H_{abs}$ is at 40-120 ℃, thus P_{CO2} at 80 ℃ was chosen as the reference to calculate P_{CO2} at other temperature. The empirical model of P_{CO2} in MEA from this work was used to get P_{CO2} at 80 ℃. Figure 2-22 shows a comparison of the prediction from this integration and the experimental data by Kim et al. (2007). At 40 ℃, 80 ℃, and 120 ℃ lean loading, the model matches the data well, at 120 ℃ rich loading and at 160 ℃, the model over-predicts the data. This illustrates that the measured heat of absorption at high temperature in Kim et al. (2007) is higher than expected values from P_{CO2} measurements in this work.

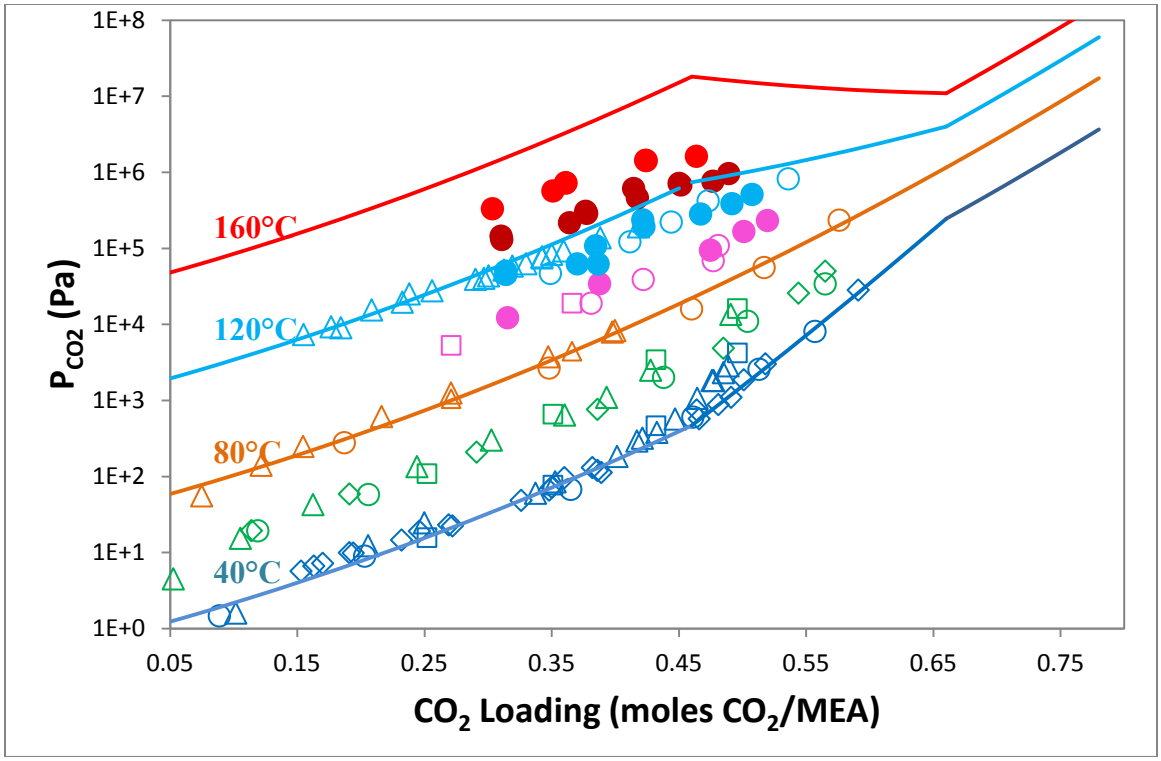

Figure 2-22: CO_2 Solubility in 7 m MEA. **●: this work; ○: Jou et al. (1995); □: Dugas et al. (2008); ◊: Hilliard (2008); Δ: Ma'mun et al. (2005); lines: Equation (2-15) integrated with the P_{CO2} empirical model.**

2.3.5.4 Inconsistency of the Measured Heat of Absorption and Specific Heat capacity

To further compare the data consistency, measured specific heat capacity was used to get the temperature dependence of $-\Delta H_{abs}$. Absorption of CO_2 at different temperature can be related with several steps shown in Figure 2-23. The dependence of C_p and ΔH_{abs} on pressure is ignored. In step 1 and 3, CO_2 is absorbed into lean amine at T_1 and T_2, respectively. C_p is the specific heat capacity. For amine solution, $C_p \approx C_v$ and can be measured by differential scanning calorimetry (DSC).

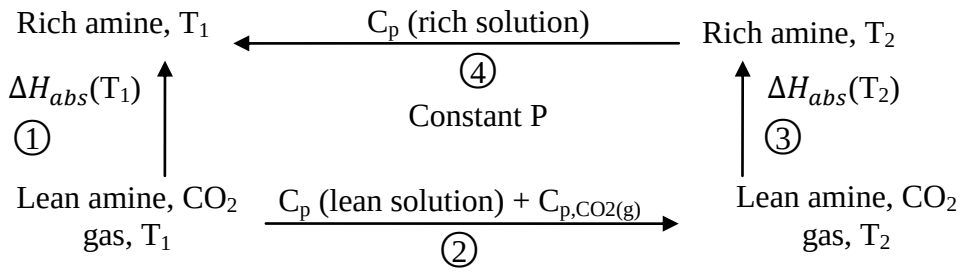

Figure 2-23: Illustration CO_2 Heat of Absorption at Different Temperature

On 1kg lean solution base, when a small amount (m_{CO2} gram) of CO_2 gas is absorbed:

$$\Delta H_{abs}(T_1)\cdot\frac{m_{CO2(g)}}{44.01}=\Delta H_{abs}(T_2)\cdot\frac{m_{CO2(g)}}{44.01}+Q_2+Q_4=\Delta H_{abs}(T_2)\cdot\frac{m_{CO2(g)}}{44.01}+\int_{T_1}^{T_2}\left[Cp(lean)+\frac{Cp_{CO2(g)}m_{CO2(g)}}{44.01}\right]dT+\int_{T_2}^{T_1}Cp(rich)\cdot(1+\frac{m_{CO2(g)}}{1000})dT \quad (2\text{-}16)$$

Using the specific heat capacity data of 7 m CO_2 loaded MEA from Hilliard (2008), a simple correlation of C_p was developed:

$$C_{p,soln}=(2.68\pm0.02)+(0.00286\pm0.00004)T+(-0.605\pm0.007)\alpha \ \text{(kJ/kg K)} \quad (2\text{-}17)$$

Where T is temperature in K, α is CO_2 loading. Figure 2-24 shows a favorable fitting of the data and Equation (2-17).

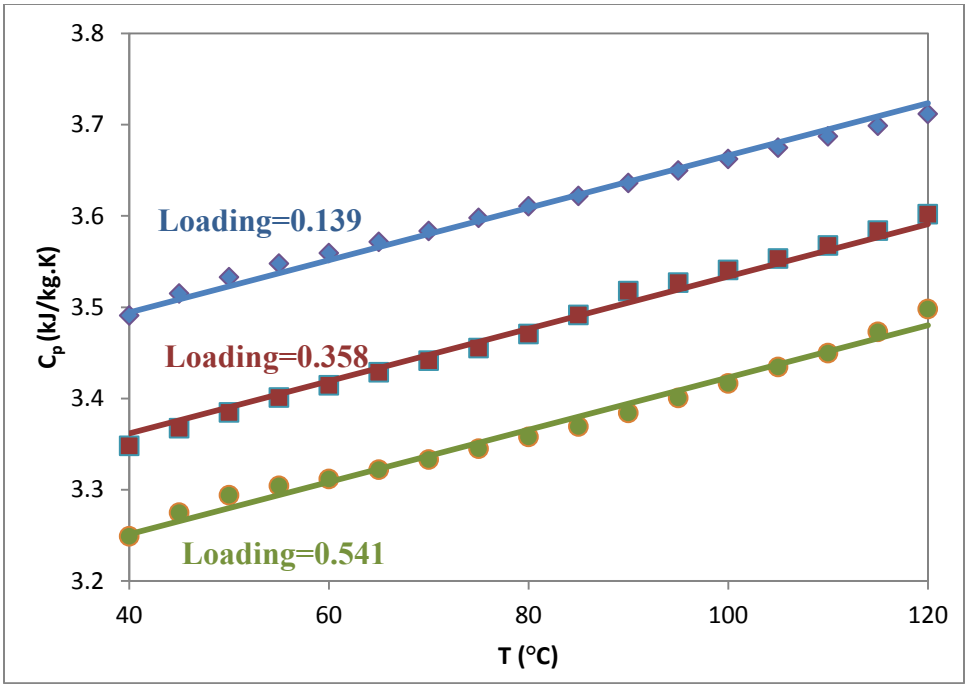

Figure 2-24: Specific Heat Capacity of 7 m MEA. **Points: Hilliard (2008) experimental data. Lines: from Equation (2-17)**

Using the C_p of CO_2 gas from DIPPR database (1998-Provo, BYU), a simple equation was correlated:

$$C_p(CO_2, g) = (0.0253 \pm 0.0005) + (4.11E-5 \pm 1.2E-6)T \quad \text{(kJ/mol K)} \qquad (2\text{-}18)$$

$-\Delta H_{abs}$ at 80 ℃ from Equation (2-15) was used as the reference state to calculate $-\Delta H_{abs}$ at other temperature and Equation (2-17) and (2-18) are used in the integration.

A calculation example of the integration is given here:

Example: at the loading of 0.35, $-\Delta H_{abs}$ at 80 ℃ from Equation (2-15), which represents Kim's experimental data, is 95.1 kJ/mol CO_2. Assume m_{CO2}=0.01 g, according to Equation (2-16):

$$-\Delta H_{abs}(120℃) = -\Delta H_{abs}(80℃) + (Q_2 + Q_4) \cdot \frac{44.01}{m_{CO2(g)}}$$

$$= 95.1 + \frac{44.01}{0.01} \cdot \int_{353.15}^{393.15} \left[Cp(lean) + \frac{Cp_{CO2(g)} 0.01}{44.01}\right] dT + \frac{44.01}{0.01} \cdot \int_{393.15}^{353.15} Cp(rich) \cdot (1 + \frac{0.01}{1000}) dT$$

According to Eq. (2-17) and (2-18),

$$Cp(lean) = 2.68 + 0.00286T - 0.605 \cdot 0.35 = 2.46825 + 0.00286T$$

$$Cp(rich) = 2.68 + 0.00286T - 0.605 \cdot \left[0.35 + \frac{0.01/44.01}{\frac{1000 \cdot 7}{1000 + 7 \cdot 61.08 + 7 \cdot 0.35 \cdot 44.01}}\right]$$

= 2.46822+0.00286T

$$Cp_{CO2(g)} = 0.0253 + 4.11E - 5T$$

Therefore,

$-\Delta H_{abs}(120℃) = 95.1 + \int_{353.15}^{393.15}[(2.46825 + 0.00286T) \cdot 4401 + 0.0253 +$

4.11E−5T−1.00001(2.46822+0.00286T)·4401dT

$= 95.1 + \int_{353.15}^{393.15}(0.0487 - (8.48E - 5)T)dT = 95.1 + 0.7 = 95.8$ (kJ/mol)

Table 2-13 compares the calculated -ΔH_{abs} from Equation (2-15) and (2-16) at the loading of 0.35. Figure 2-25 shows a comparison of -ΔH_{abs} from Equation (2-15) and (2-16) over 0-0.72 loading. The temperature dependence of calculated -ΔH_{abs} is very small compared with the measured data. Therefore, the measured -ΔH_{abs} by Kim et al. (2007) is not consistent with the measured C_p either.

If -ΔH_{abs}(40 ℃)=82.8 kJ/mol CO_2 from Equation (2-15) is used as the reference, and Equation (2-16) is used to calculate the temperature dependence of -ΔH_{abs}, the -ΔH_{abs} at 80 ℃ is about 83.6 kJ/mol CO_2 and agrees well with the -ΔH_{abs} from the P_{CO2} empirical model.

Table 2-13: Comparison of $-\Delta H_{abs}$ in 7 m MEA

	$-\Delta H_{abs}$ (kJ/mol CO_2), ldg=0.35		
	40 ℃	**80 ℃**	**120 ℃**
By Eq. (2-15)	82.8	95.1	107.4
By Eq. (2-16)	94.3	95.1	95.8
Empirical model from P_{CO2}	83.7±2		

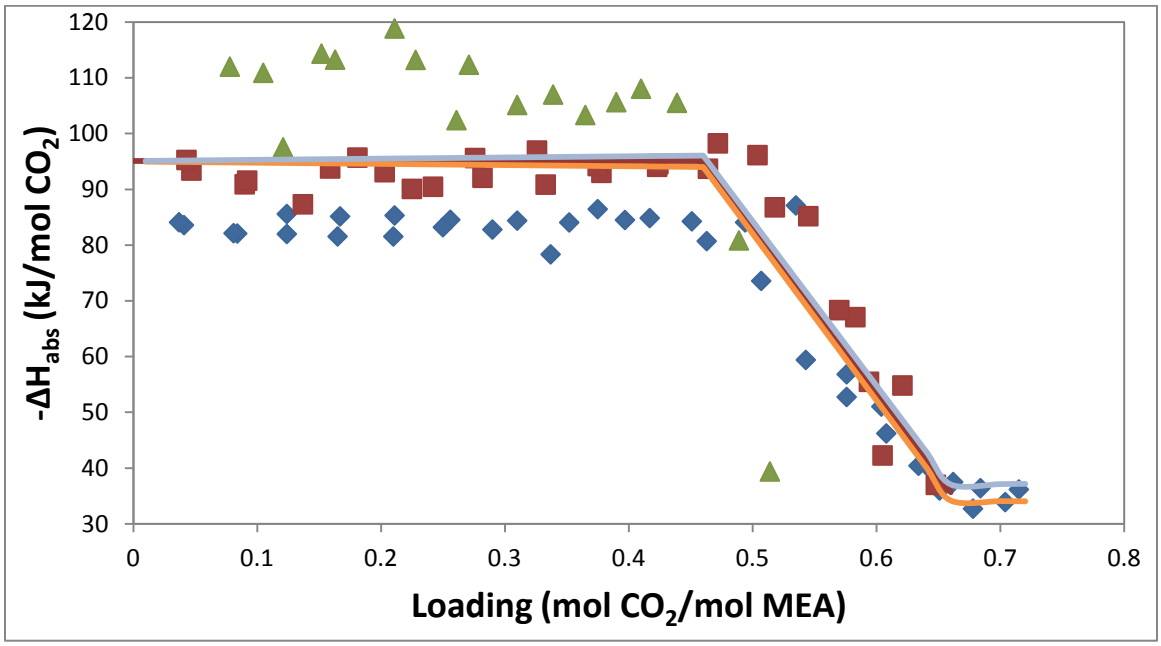

Figure 2-25: Heat of Absorption of CO_2 in 7 m MEA, Comparison of Equation (2-16) and Measured Data. **Data points: Kim et al. (2007), ◊: 40°C, □: 80°C, Δ: 120 ℃; solid lines: prediction by Equation (2-16).**

2.4 Conclusions and Recommendations

CO_2 solubility data was obtained using total pressure measurements. Empirical models as a function of temperature and loading were developed for CO_2 solubility from 40 to 191°C in aqueous MEA, PZ, 1MPZ, 2MPZ, PZ/2MPZ, DGA, PZ/1MPZ/1,4-DMPZ, and PZ/MDEA. The high temperature CO_2 solubility data for MEA is comparable to that by Jou et al. (1995) and Ma'mun et al. (2005). The high temperature data is also compatible with previous low temperature data.

For MEA and PZ, amine concentration does not have obvious effects on the CO_2 solubility.

The heat of CO_2 absorption derived from these models varies from 66 kJ/mol for 4 m PZ/4 m 2MPZ and to 72, 72, and 73 kJ/mol for MEA, 7 m MDEA/2 m PZ, and DGA.

The heat of absorption estimated from the total pressure data does not vary significantly with temperature. The temperature dependence of the heat of CO_2 absorption in MEA measured by Kim et al. (2007) is not consistent with either the measured total pressure or the measured specific heat capacity.

Chapter 3: High Temperature Amine Volatility and Specific Heat Capacity

This Chapter presents a high temperature experimental method for vapor-liquid equilibrium (VLE) of CO_2 loaded aqueous amines. It is a single vapor pass dynamic VLE apparatus with online gas sampling and analysis by FTIR. Monoethanolamine (MEA) volatility in MEA-H_2O from this work is comparable with literature data. MEA volatility in 7 molal (m, gmol/kg H_2O) MEA-CO_2-H_2O and piperazine (PZ) volatility in 5-11 m PZ-CO_2-H_2O were measured at 120 to 150 ℃, 0.24 to 0.49 CO_2 loading. At 0-0.5 loading (α), 313-413 K, 3.5-11 m MEA (mol fraction x is 0.059-0.165), MEA volatility can be expressed by $\ln(P_{MEA}/x_{MEA}) = 30.0\text{-}8153/T\text{-}2594\alpha^2/T$. At 0.25-0.4 loading, 313-423 K, 4.7-11.3 m PZ (x is 0.078-0.169), PZ volatility can be expressed by $\ln(P_{PZ}/x_{PZ}) = -123+21.6\ln T+20.2\alpha-18174\alpha^2/T$. The enthalpy of vaporization $\Delta H_{vap,MEA}$ and $\Delta H_{vap,PZ}$ have a strong dependence on speciation and free amine concentration in the solution. $\Delta H_{vap,PZ}$ has a larger dependence on CO_2 loading than $\Delta H_{vap,MEA}$ in rich solution because of the more complex speciation/reactions in PZ at rich loading.

The temperature of the DSC specific heat capacity method was extended to 150 ℃ and C_p of 8 m PZ was measured as 3.43-3.81 J/(g·K) at 70-150°C.

3. 1 Review of High T Vapor-liquid Equilibrium Measurements of Aqueous MEA and PZ

3.1.1 Amine-water

The vapor-liquid equilibrium of MEA-H_2O and PZ-H_2O has been studied. Experimental data includes total pressure and amine volatility. For the application to CO_2 capture, amine volatility is needed to estimate the amine in the purified flue gas from the absorber or the condenser of the stripper.

Total pressure measurements are usually performed in a static equilibrium cell. Touhara et al. (1982) studied the total pressure of MEA-H_2O with 0-100% MEA at 25 and 35 ℃ and the total pressure was from 0.065 to 5.623 kPa. Nath and Bender (1983) measured the total pressure of MEA-H_2O with 0-100% MEA at 60, 78, and 91.7 ℃ and the total pressure was from 1.3 to 84.7 kPa. These data can be used in thermodynamic modeling of MEA-CO_2-H_2O.

The most used method for MEA volatility measurement has been an ebulliometer or a similar equilibrium cell. After the system reaches equilibrium, vapor condensate and liquid samples are collected and analyzed by GC or titration. Cai et al. (1996) measured the binary isobaric equilibrium of MEA-H_2O at 101.33 kPa and 66.66 kPa with 0-100% MEA using a modified Rose-Williams still. Park and Lee (1997) measured VLE of MEA-H_2O with 0-100% MEA at 100-170 ℃. Tochigi et al. (1999) measured VLE of MEA-H_2O with 0-100% MEA at 90 ℃ using a modified Rogalski-Malanoski equilibrium still. Kim et al. (2008) used an ebulliometer to measure the VLE of MEA-H_2O at 40-100 ℃ with 0-56% MEA. Chemetron Corporation and Texaco Chemical had MEA volatility data for 10, 20, and 30 wt% MEA at 10-71 ℃ and the curves can be found in Figure 3-20 of *Gas Purification* (Kohl et al. 1997). Hilliard (2008) measured MEA volatility at 40-73 ℃ with 6-30 wt% MEA, using a special FTIR method with vapor phase circulation.

Most of the data above at high temperature are for high MEA concentration except in the work of Kim et al. (2008) and Hilliard (2008).

Less work has been done on PZ-H_2O vapor-liquid equilibrium. Wilson and Wilding (1994) measured total pressure of 0-100% PZ at 113 and 199 ℃. Xia et al. (1997) measured total pressure of 1.99 and 3.97 m PZ at 120 ℃. Hilliard (2008) and

Nguyen et al. (2010) measured PZ volatility in 0.9-10 m PZ at 40-70 ℃ with the same FTIR method as used in MEA-H_2O.

3.1.2 CO_2-amine-water

CO_2 loaded amines have lower amine volatility and higher total pressure than the unloaded amines. Therefore it is more difficult to measure the amine volatility in CO_2 loaded aqueous amines, especially at high temperature and pressure. Hilliard (2008) and Nguyen (2010) measured amine volatility at 40-60 ℃ in CO_2 loaded MEA and PZ using the same FTIR method as used in amine-water systems.

At high temperature, because of the high total pressure and the pressure limit of the FTIR analyzer (1-1.5 atm), vapor circulation between FTIR and the equilibrium cell becomes hard to achieve and new methods need to be developed.

Therefore in this work, a single vapor pass vapor-liquid equilibrium apparatus was set up. Vapor flowed continuously through the solution; the outlet vapor sample was depressurized and analyzed by an FTIR analyzer. MEA-H_2O vapor-liquid equilibrium was measured and compared with literature to validate the method.

3.2 Experimental Methods

3.2.1 Chemicals

Reagent chemicals were used: CO_2 (Clinical Purity, 99.5%, Matheson Tri Gas), MEA (99%, Acros Organics), anhydrous PZ (99%, Acros Organics). DDI water was used for solution preparation. Oil bath fluid: DC 200 fluid 50 CS (Dow Corning).

3.2.2 Solution Preparation

About 550 to 800 mL solution was prepared for each experiment. Amine and DDI water were weighed and combined to achieve the target molality (m). Then the

mixture was agitated by a magnetic stir bar. For PZ, the mixture was heated and stirred on a hot plate to make PZ dissolve. After the solution was clear and well mixed, it was transferred into a glass gas sparging column (for PZ the column was pre-heated) on a scale. CO_2 was sparged into the solution, and the absorbed CO_2 weight was recorded. Details can be found in the Dissertations by Hilliard (2008) and Freeman (2011).

3.2.3 Apparatus

Figure 3-1 shows the dynamic vapor-liquid equilibrium apparatus with a single vapor pass. Two 200 mL (i.d=1.5 in, depth=7 in) and one 600 mL (i.d=2.5 in, depth=8 in) stainless steel vessels (4752 and N4764-T-SS, Parr Instrument Co.) were used as equilibrium cells in series. Each cell has a split ring closure, and the maximum working pressure and temperature are 200 bar and 350 ℃. All of the vessels were submerged in an oil bath (EX-35, Thermo Fisher Scientific) for temperature control. For some experimental runs, one 200 mL and one 600 mL equilibrium cells were used. Data from these runs are presented with superscripts in the results section. Details of the equilibrium cells and the oil bath can be found in Appendix B.1 and B.2.

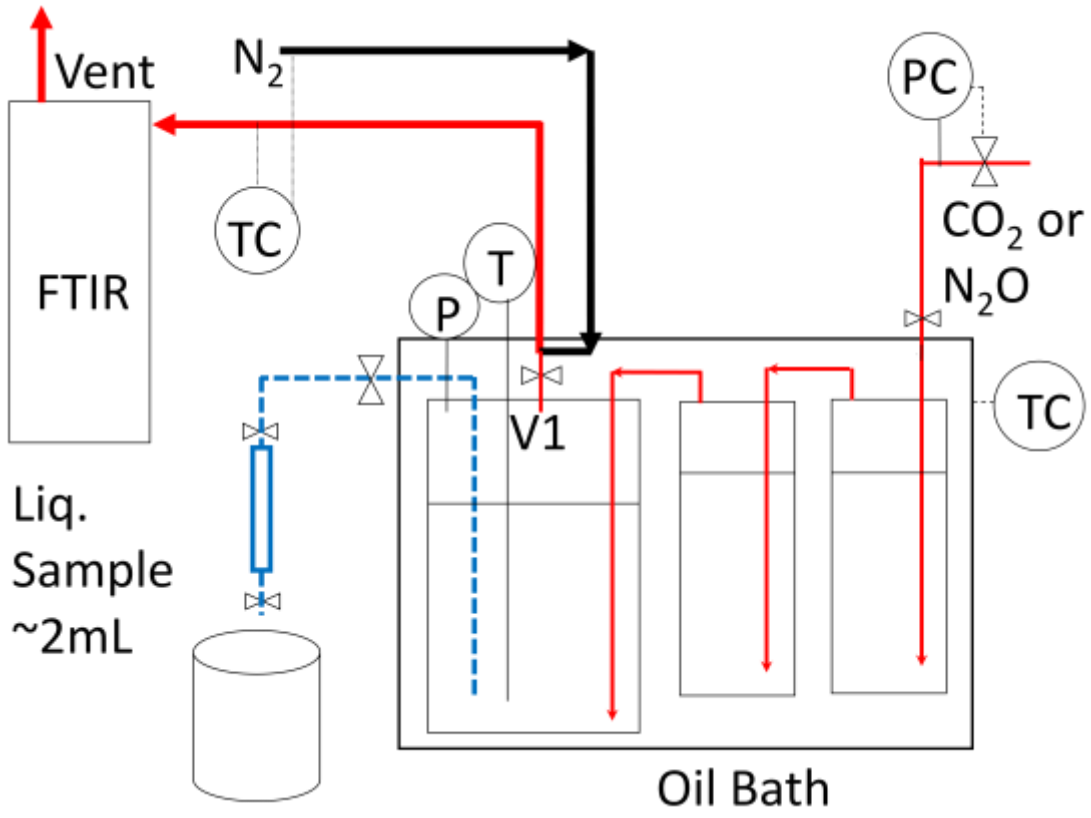

Figure 3-1: Single Vapor Pass VLE Apparatus with an Oil Bath. **Solid red line: vapor pass; dashed blue line: liquid sample pass**

The temperature of the 600 mL cell was measured by a K-type thermocouple and read by an HH506RA data logger from Omega® with 0.1 ℃ precision and the error is within ±0.6°C. A pressure transducer (Druck® PTX 611, 0–30 bar absolute) was connected to an in-house signal converter and data logger NI USB 6009. LabView® SignalExpress® software was used for data recording. The pressure data acquisition system was calibrated by a dead weight pressure tester (S/N 19189/278, by Budenberg Volumetrics, Inc.). The total pressure measurement error is ±2.4 kPa. Calibrations of the pressure transducer and the thermocouple and other details can be found in the Appendix B.3 and B.4.

3.2.4 Procedure

About 170, 170, and 450 mL of the solution was placed into the three cells, respectively. To avoid oxidative degradation, N_2 was used to purge air and then the cells were sealed and submerged under the oil.

In some experimental runs a different volume of solution was used. Figure 3-2 shows the evolution of the HTPVLE apparatus with the oil bath. By sequentially increasing mass transfer the results indicate that adequate mass transfer was achieved with two cells and high liquid level for MEA-H_2O, three cells and high liquid level for MEA-CO_2-H_2O, and two cells and mid liquid level for PZ-CO_2-H_2O.

Figure 3-2: Evolution of HTPVLE Apparatus with Oil Bath

After the temperature stabilized at the target value, the CO_2 feed valve was opened and CO_2 entered the cells. The vapor lines were made of 1/8 inch stainless steel tubes and no special spargers were used. The CO_2 feeding point was less than 0.5 in from the bottom of each cell. CO_2 feed pressure was controlled by the regulator at the cylinder.

After the temperature and pressure stabilized again, a vapor stream was continuously withdrawn from the top of the third cell, with a Swagelok® metering valve (SS-SS4-SL) for flow rate control. This vapor sample stream was 50-250 mL/min at standard pressure and was diluted by about 1.5 SLPM N_2. The N_2 flow and the stream after dilution were maintained at 180 ℃ by a 7 ft heated Teflon® line with temperature control and power supply to the Gasmet™ portable sampling system. The diluted stream was analyzed continuously by an FTIR analyzer (Gasmet™ DX-4000) with

Calcmet® software. The Swagelok® metering valve (SS-SS4-SL) was adjusted to get measurable concentrations in the FTIR.

The FTIR has a 10 meter gas sampling cell held at 180 ℃ with a working pressure of 1-2 bar. It was previously calibrated for measurements of CO_2, N_2O, MEA, PZ, and H_2O. The calibration was performed using a Gasmet calibrator with a syringe pump, a manual needle valve, and a stainless steel injection chamber. The calibration has been described previously in Goff (2005), Hilliard (2008), and Nguyen et al. (2010). Goff (2005) estimated relative expanded uncertainty in the vapor phase concentration to be ±2%. In this work, a few calibration points of MEA and PZ were checked to make sure the calibration sets were still good to use.

After the concentrations in the FTIR were stable, the vapor feeding and sampling valves were closed. The liquid sampling valves were opened quickly to let about 25–50 mL high pressure liquid flush through the 1/8 in stainless steel line, and then closed to trap about 2 mL liquid in the sample bomb. Liquid samples were then cooled to room temperature and analyzed. A cooling pack with frozen materials was applied to the liquid sampling line to reduce flashing when the sampled solution had high CO_2 loading.

For the benchmark experiments to measure MEA volatility in MEA-H_2O, N_2O instead of CO_2 was fed into unloaded aqueous MEA. The temperature for benchmark experiments was 80–140 ℃ with a 10 ℃ interval. The total pressure was controlled at 2 to 4.5 bar. No liquid sample was taken during the experiment, because MEA concentration was almost constant through a run. The reported MEA concentration at each temperature is based on samples before and after each run.

Details of solution charging, starting up, finishing, and cleaning procedures can be found in Appendix B.5.

3.2.5 Liquid Phase Analysis

3.2.5.1 CO_2 Concentration

The concentration of total CO_2 in solution was determined by Total Inorganic Carbon (TIC) analysis. The liquid samples collected through each run were gravimetrically diluted by a factor of 50-100, depending on the expected CO_2 concentration. About 20–30 μL diluted sample was injected into 30 wt% H_3PO_4 in the TIC column to release CO_2, and a continuous N_2 flow carried the CO_2 into an IR analyzer (Model 525, Horiba PIR 2000). PicoLog® software was used to record the voltage signal from the IR analyzer. In order to get a correlation curve between the voltage peak areas and carbon mass fraction, a series of calibration points were carried out at the end of each analysis by injecting known amounts of inorganic carbon standard (1000 ppm carbon, Ricca Chemical Company, Arlington, TX). Details can be found in Hilliard (2008) and Freeman (2011).

3.2.5.2 Amine Concentration

The total alkalinity of each liquid sample was determined by titration using a Metrohm-Peak 835 Titrando equipped with an automatic dispenser, Metrohm-Peak 801 stirrer, and 3 M KCl pH probe. 120-300X dilution of the sample was titrated with 0.1 N H_2SO_4 to pH 2.4. Details are available in Appendix A.3 of Hilliard (2008) and Appendix F of Sexton (2008).

3.2.6 Partial Pressure Calculation

The vapor compositions in the diluted stream were analyzed by FTIR and these were converted into concentrations in the vapor phase inside the equilibrium cell:

$$y_i = \frac{y'_i}{y'_{H_2O} + y'_{amine} + y'_{CO_2} + y'_{N_2O}} \tag{3-1}$$

y_i - mole fraction of component i in vapor

y'_i - mole fraction of component i in diluted gas.

i is water, amine, CO_2 or N_2O.

The partial pressure of each component was calculated from concentrations and total pressure using Equation 3-2:

$$P_i = P_t \cdot y_i \tag{3-2}$$

P_t - total pressure, Pa.

P_i - partial pressure of i, Pa.

i is water, amine, CO_2 or N_2O.

3.3 RESULTS

3.3.1 Benchmark – MEA Volatility in MEA-H_2O

Table 3-1 gives results for MEA volatility in MEA-H_2O.

Table 3-1: MEA Volatility in MEA-H_2O at High Temperature

2 eq. cells, high liq. level*					3 eq. cells, high liq. level				
T	**MEA**	**P_{MEA}**	**P_{H2O}**	**P_t**	**T**	**MEA**	**P_{MEA}**	**P_{H2O}**	**P_t**
℃	**m**	**Pa**	**kPa**	**kPa**	**℃**	**m**	**Pa**	**kPa**	**kPa**
99.4	6.91	434	95	95	80.5	6.89	153	44	44
120.2	6.94	1305	183	184	100.4	6.88	437	93	93
120.2	6.97	1345	207	208	120.3	6.87	1421	202	203
130.1	7.00	2085	261	263	130.1	6.86	2090	272	274
					140.2	6.86	2914	362	365

*: 2 equilibrium cells were used; filled with 170 and 450 mL solution, respectively.

Figure 3-3 compares normalized MEA volatility in 3.5-11 m MEA-H_2O from this work and literature. The literature data are comparable to these results. Hilliard's data (2008) at low temperature (<45 ℃) are not consistent with other literature and give a different slope. Simulated MEA volatility by the Hilliard Aspen Plus® MEA Model (2008) generally predicts the data from this work.

Normalized MEA volatility did not undergo any obvious change when a third cell was added with a high liquid level. Therefore we can conclude that adequate mass transfer has been obtained with two equilibrium cells, with high liquid level, for the MEA-H_2O system.

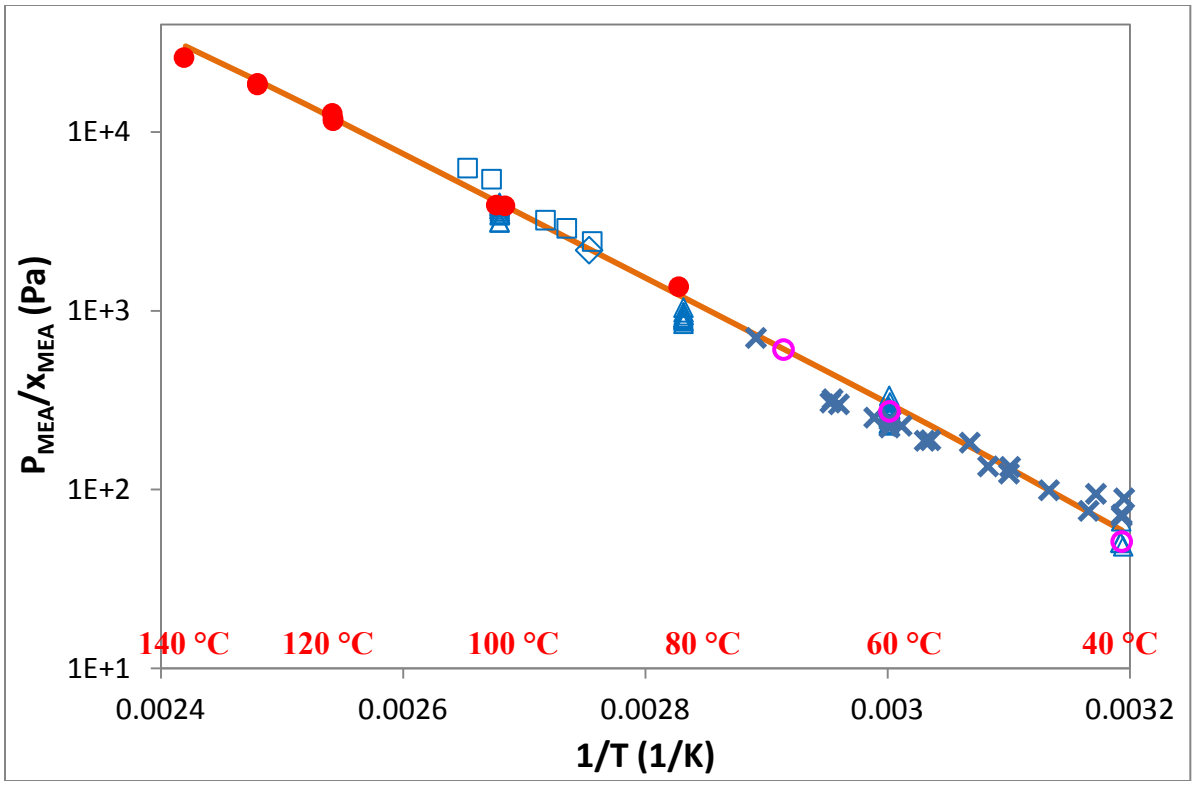

Figure 3-3: Comparison of Normalized MEA Volatility in 3.5-11 m MEA-H_2O. □: Cai et al. (1996); ○: Figure 3-20, *Gas Purification* (Kohl et al., 1997); ◊: Tochigi et al. (1999); Δ: Kim et al. (2008); X: Hilliard (2008); ●: this work; line: Aspen Plus® Hilliard Model - 7 m MEA (2008); $x_{MEA} = \frac{\text{mol of MEA}}{\text{mol of MEA+mol of } H_2O}$.

Figures 3-4 and 3-5 presented the ratio of measured P_{MEA} to simulated P_{MEA} using the Hilliard Aspen Plus® MEA model (2008). Figure 3-4 shows that the low temperature Hilliard's data below 45°C are further off the model. At low temperature (<55°C), Hilliard's measured P_{MEA} is larger than simulated P_{MEA}, while above 55 ℃,

Hilliard's measured P_{MEA} is smaller than simulated P_{MEA}. Most of Kim's data are smaller than the simulated P_{MEA} and some of the 60 ℃ data are further off. Data from the other literature and from this work are predicted by the model. Figure 3-5 shows that one series of Kim's data, which is at 60°C by comparing with Figure 3-4, has a trend to decrease as MEA concentration increases. For data from the other literature and this work, there is no obvious error associated with MEA concentration, when MEA varies from 3.5 to 11 m.

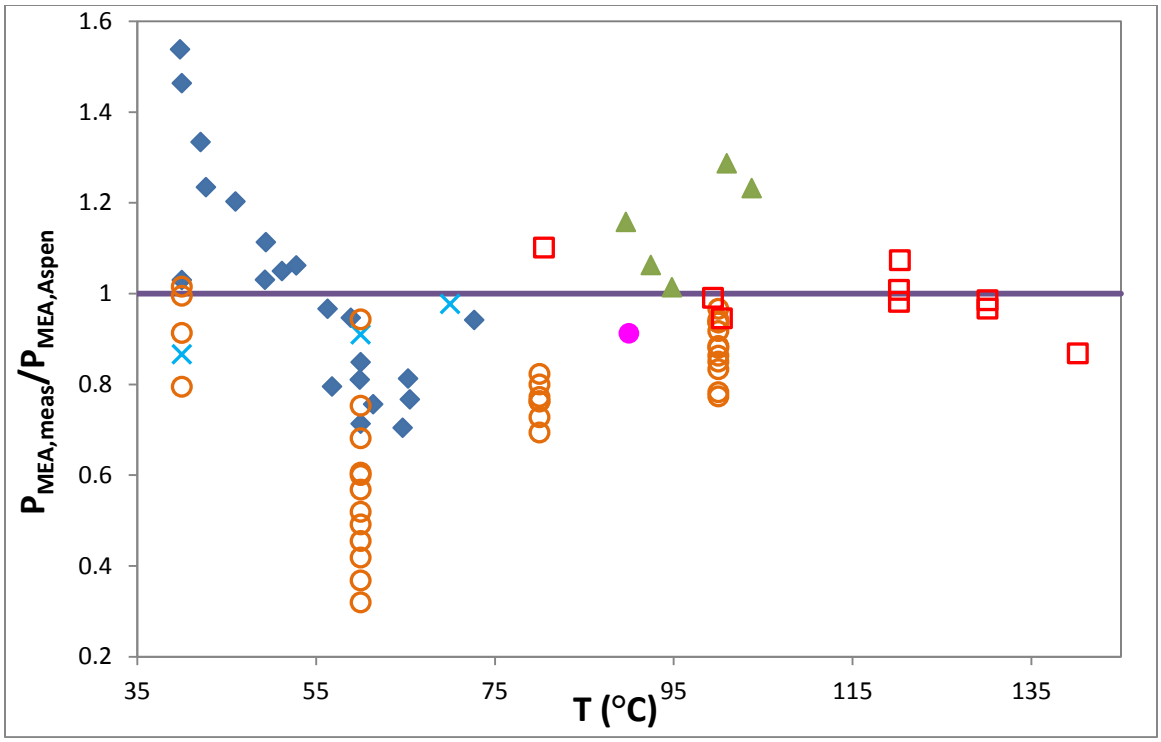

Figure 3-4: Temperature Dependence of $P_{MEA,meas}/P_{MEA,Aspen}$ in 3.5-11 m MEA.
$P_{MEA,meas}$ are experimental data and $P_{MEA,Aspen}$ are by Hilliard Aspen Plus® MEA model; ▲: Cai et al. (1996); X: Figure 3-20, *Gas Purification* (Kohl et al., 1997); ●: Tochigi et al. (1999); ○: Kim et al. (2008); ♦: Hilliard (2008); □: this work.

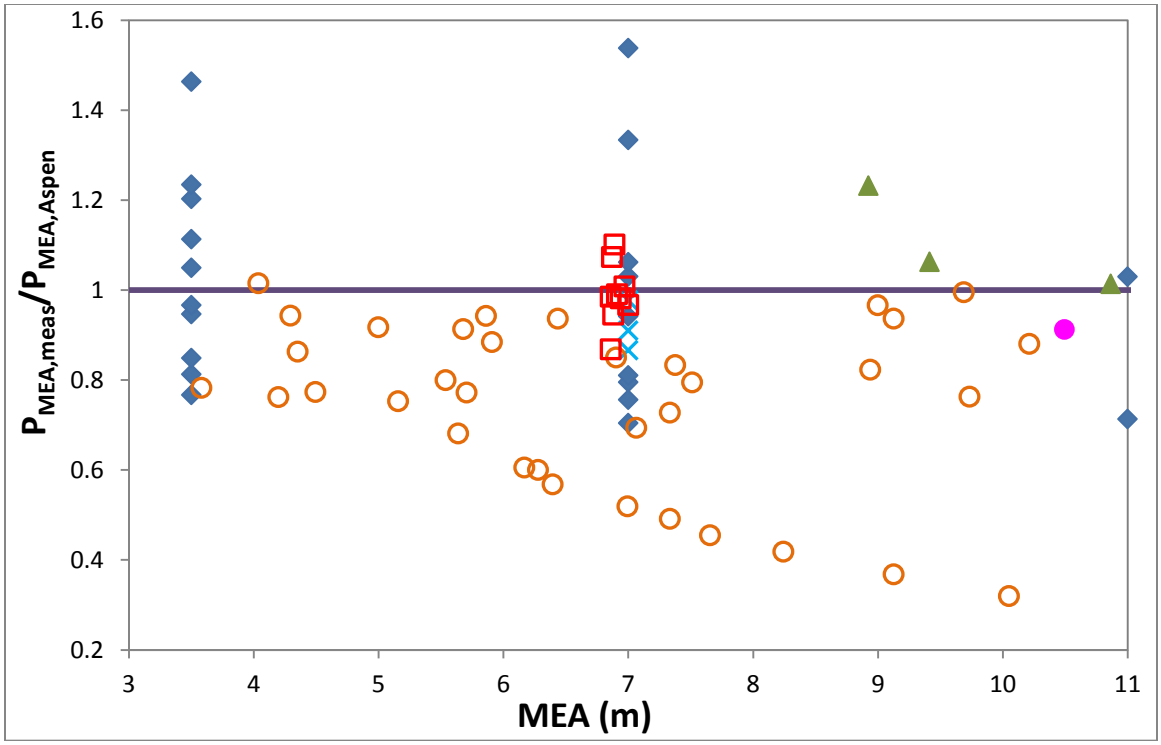

Figure 3-5: MEA Concentration Dependence of $P_{MEA,meas}/P_{MEA,Aspen}$ in MEA-H_2O, 40-140°C. **$P_{MEA,meas}$ are experimental data and $P_{MEA,Aspen}$ are by Hilliard Aspen Plus® MEA model; ▲: Cai et al. (1996); X: Figure 3-20, *Gas Purification* (Kohl et al., 1997); ●: Tochigi et al. (1999); ○: Kim et al. (2008); ♦: Hilliard (2008); □: this work.**

Figure 3-6 gives MEA volatility in 7 m solution. New data at 80 to 140 ℃ are comparable with literature data and are predicted by the Aspen Plus® Hilliard MEA Model (2008). Hilliard's data at 40 to 45°C are not consistent.

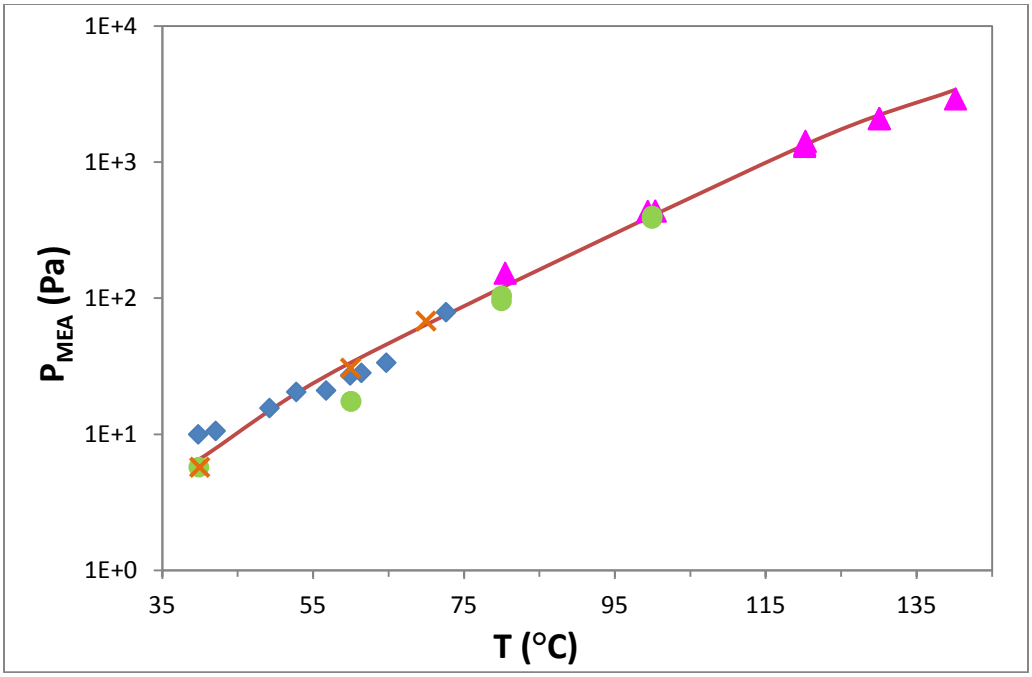

Figure 3-6: MEA Volatility in 7 m MEA. **X: Figure 3-20, Gas Purification (Kohl et al., 1997); ♦: Hilliard (2008); ●: Kim et al. (2008); ▲: this work; line: Aspen Plus® Hilliard Model – 7 m MEA (2008)**

3.3.2 MEA Volatility in MEA-CO_2-H_2O

Table 3-2 gives MEA volatility in CO_2 loaded MEA. Experiments were conducted with various CO_2 loading at 120 and 140 ℃. P_{MEA} and P_{CO2} are from vapor phase measurement. CO_2 loading (mol/mol MEA) was calculated from the empirical model of P_{CO2} in Chapter 2 (Table 2-10) using the measured T and P_{CO2}. The loading from liquid analysis was not used because of the non-systematic error with it. The analyzed loading is different from the calculated loading using the CO_2 partial pressure empirical models, and the difference does not depend on CO_2 loading or temperature. Higher pressure may result in a bigger difference, but this trend is not obvious either. This error probably comes from liquid sampling, where the pressure decreased fast from about 2-25 atm to 1 atm. Therefore, the liquid tended to flash when it flushed through the sampling line, and the composition of the liquid sample trapped in the bomb may be

different from that of the liquid phase in the equilibrium cell. Attaching a frozen pad to the liquid sampling line helped to reduce the flash, however, since the flow rate of liquid sampling was large, some of CO_2 still flashed out of the liquid. MEA concentration reported in Table 3-2 was from liquid phase analysis, assuming the flashing of MEA and water is much less than that of CO_2, making small changes in the MEA concentration.

Table 3-2: MEA Volatility in MEA-CO_2-H_2O

T	MEA	Loading*	P_{MEA}	P_{CO2}	P_{H2O}	P_t
℃	m		Pa	kPa	kPa	kPa
119.9	6.90	0.324	573	43	155	199
119.9	6.87	0.351	642	62	167	230
120.3	6.82	0.489	223	454	180	634
139.9	6.81	0.222	1627	49	326	376
140.0	6.63	0.367	1389	263	314	578
139.9	6.57	0.469	718	969	316	1286
140.3	6.86	0.467	795	966	317	1283
140.2	6.90	0.389	1110	352	324	677
120.4	7.00	0.361	610	73	169	243

*: CO_2 loading (mol/mol MEA) was calculated from the empirical model of P_{CO2} in Chapter 2 (Table 2-1) using the measured T and P_{CO2}.

The MEA volatility from this work in MEA-H_2O and MEA-CO_2-H_2O is regressed along with 50-73°C data from Hilliard (2008). Hilliard's data at lower temperature (<50 ℃) were not included because they are not consistent with other literature. Equation 3-3 is the empirical model.

$$\ln\left(\frac{P_{MEA}}{x_{MEA}}\right) = (30.0 \pm 0.3) + (-8153 \pm 96)\frac{1}{T} + (-2594 \pm 81)\frac{\alpha^2}{T} \qquad (3\text{-}3)$$

$$R^2 = 0.994$$

Using this correlation, for 7 m MEA with 0.2 and 0.5 CO_2 loading, the partial pressure of MEA is 923 and 231 Pa at 120 ℃, and 2552 and 683 Pa at 140 ℃.

Figure 3-7 compares normalized MEA volatility from this work and Hilliard data (2008) at 40 and 60 ℃. The volatility decreases with CO_2 loading, because amine reacts with CO_2 and there is less free amine in the solution as the loading increases. The Hilliard Aspen Plus® model (2008) over-predicts high temperature data at high CO_2 loading. The empirical model of Equation 3-3 fairly predicts the 60-140 ℃ data. The 40^o data from Hilliard were not regressed and are not represented by the empirical model. They do not seem to be consistent with the other data. Figure 3-8 gives the same data sets as in Figure 3-7, but uses P_{CO2} as the horizontal axis instead of CO_2 loading.

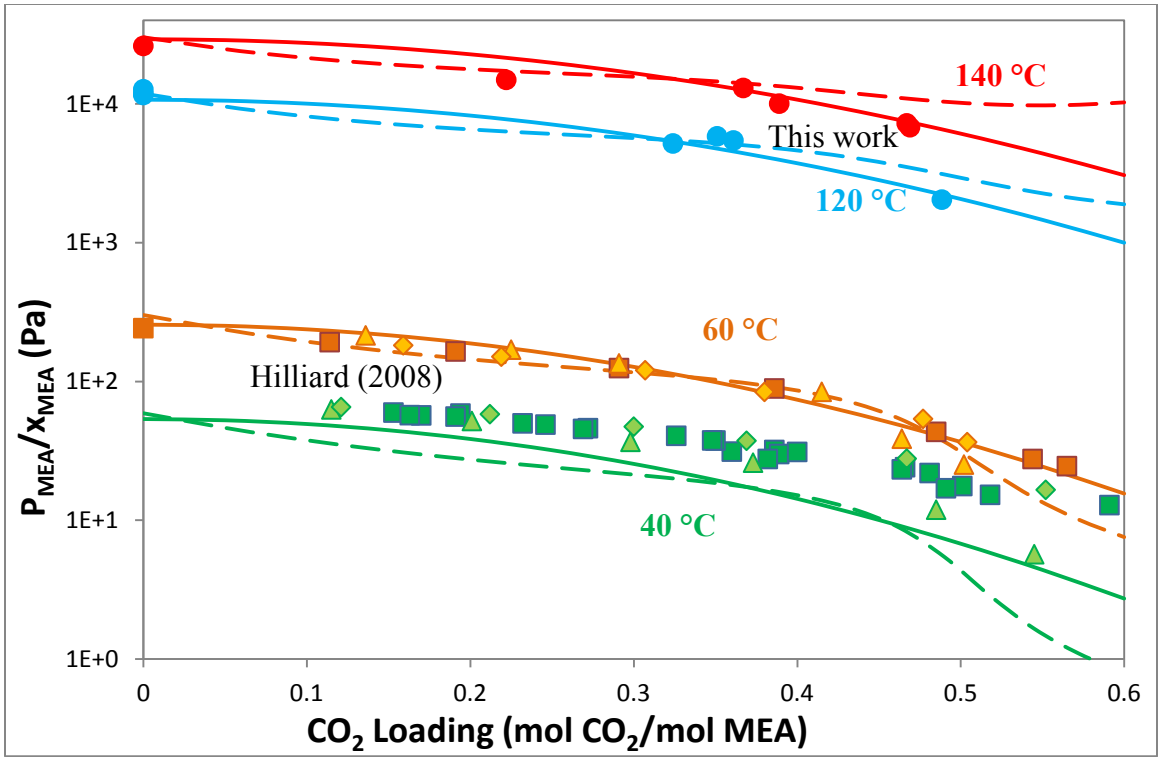

Figure 3-7: Comparison of Normalized MEA Volatility in 3.5-11 m MEA. Hilliard (2008) MEA: ♦ 3.5 m, ■ 7 m, ▲ 11 m; ●: this work; solid lines: empirical model of Eq. 3-3; dashed lines: Aspen Plus® Hilliard Model – 7 m MEA (2008). $x_{MEA} = \frac{\text{mol of total MEA}}{\text{mol of total MEA + mol of } H_2O}$.

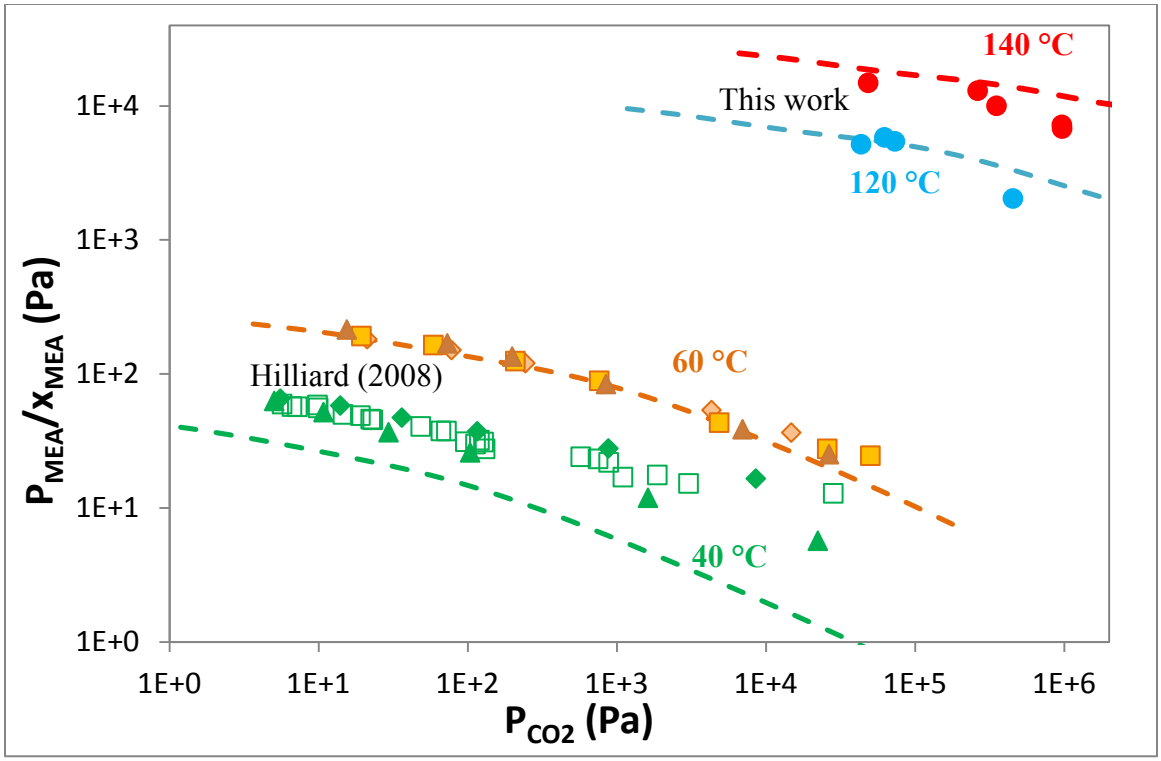

Figure 3-8: Comparison of Normalized MEA Volatility in 3.5-11 m MEA (2).
Hilliard (2008) MEA: ♦ 3.5 m, □ 7 m, ▲ 11 m; ●: this work; dashed lines: Aspen Plus® Hilliard Model – 7 m MEA (2008). $x_{MEA} = \frac{\text{mol of total MEA}}{\text{mol of total MEA + mol of } H_2O}$.

3.3.3 PZ Volatility in PZ-CO_2-H_2O

Table 3-3 gives PZ volatility in CO_2 loaded PZ. Experiments were conducted with various CO_2 loading at 120 and 150 ℃. P_{PZ} and P_{CO2} are from vapor phase measurement. As in the MEA-CO_2-H_2O system, CO_2 loading (mol/equiv. PZ) was calculated from the P_{CO2} and T with the empirical model, the equation in Table 2-10 in Chapter 2.

Table 3-3: PZ Volatility in PZ-CO_2-H_2O

T	PZ	Loading ***	P_{PZ}	P_{CO2}	P_{H2O}	P_t	T	PZ	Loading ***	P_{PZ}	P_{CO2}	P_{H2O}	P_t
℃	m		Pa	kPa	kPa	kPa	℃	m		Pa	kPa	kPa	kPa
120.0	7.74	0.391*	106	535	161	696	149.4	8.29	0.267*	2851	309	395	707
119.5	8.17	0.291*	482	91	166	257	149.8	5.91	0.391*	840	2051	493	2545
119.8	8.08	0.391*	191	528	163	691	149.7	6.11	0.239*	2078	212	419	633
118.6	8.70	0.302*	523	104	154	259	149.0	6.11	0.258*	2042	268	406	675
120.1	6.14	0.391*	130	530	178	708	149.8	4.73	0.389*	615	2004	519	2523
119.6	6.48	0.289*	338	89	170	259	149.7	4.91	0.243*	1742	223	428	653
120.1	4.89	0.391*	67	532	183	715	150.0	9.54	0.392*	1261	2112	443	2557
119.8	5.08	0.280*	232	77	179	256	149.4	10.21	0.259*	4533	275	403	683
120.4	9.86	0.397*	139	599	159	759	149.0	10.75	0.398**	1623	2234	444	2679
120.6	10.40	0.396**	142	599	158	757	148.6	11.30	0.273**	4720	324	356	685
119.3	10.65	0.305**	554	113	150	264	149.0	7.50	0.320	1730	667	381	1049
120.2	7.81	0.385	169	485	160	645	149.0	7.69	0.305	1820	533	372	907
120.3	8.02	0.327	228	174	171	344	149.2	7.80	0.278	2859	363	382	748
120.4	7.72	0.392	80	552	156	709	149.0	7.83	0.253	3617	250	363	617
120.0	7.69	0.325	176	166	158	325	149.9	7.65	0.393	1188	2140	452	2593
149.7	8.22	0.391*	1269	2064	478	2543	149.8	7.75	0.369	1459	1452	417	1871
149.5	8.76	0.261*	3139	287	397	687	149.8	7.86	0.295	2879	474	367	844
149.9	7.66	0.390*	1164	2033	474	2508	149.5	7.92	0.249	3397	242	377	623

*: 2 equilibrium cells were used, filled with 100 and 300 mL solution; **: 2 equilibrium cells were used, filled with 170 and 450 mL solution; ***: loading = mol CO_2/equivalent PZ, estimated from T and P_{CO2} using the equation in Table 2-1 in Chapter 2.

The PZ volatility from this work was regressed along with 40-65℃ data by Nguyen et al. (2010). Equation 3-4 is the empirical model.

$$\ln(\frac{P_{PZ}}{x_{PZ}}) = (-123 \pm 3) + (21.6 \pm 0.6)\ln T + (20.2 \pm 3.5)\alpha + (-18174 \pm 1933)\frac{\alpha^2}{T} \quad (3\text{-}4)$$

$$R^2 = 0.996$$

Using this correlation, for 8 m PZ with 0.3 and 0.4 CO_2 loading, P_{PZ} is 398 and 119 Pa at 120℃, and 2622 and 982 Pa at 150℃.

Figure 3-9 compares normalized PZ volatility from this work and Nguyen et al. data (2010) at 40 and 60℃. The volatility decreases with CO_2 loading, because amine

reacts with CO_2 and there is less free amine in the solution as the loading increases. The empirical model of Equation 3-4 and Aspen Plus® Fawkes Model (Frailie et al., 2010) fairly predict 40-150 ℃ data. Figure 3-10 gives the same data sets as in Figure 3-9, but uses P_{CO2} as the horizontal axis instead of CO_2 loading.

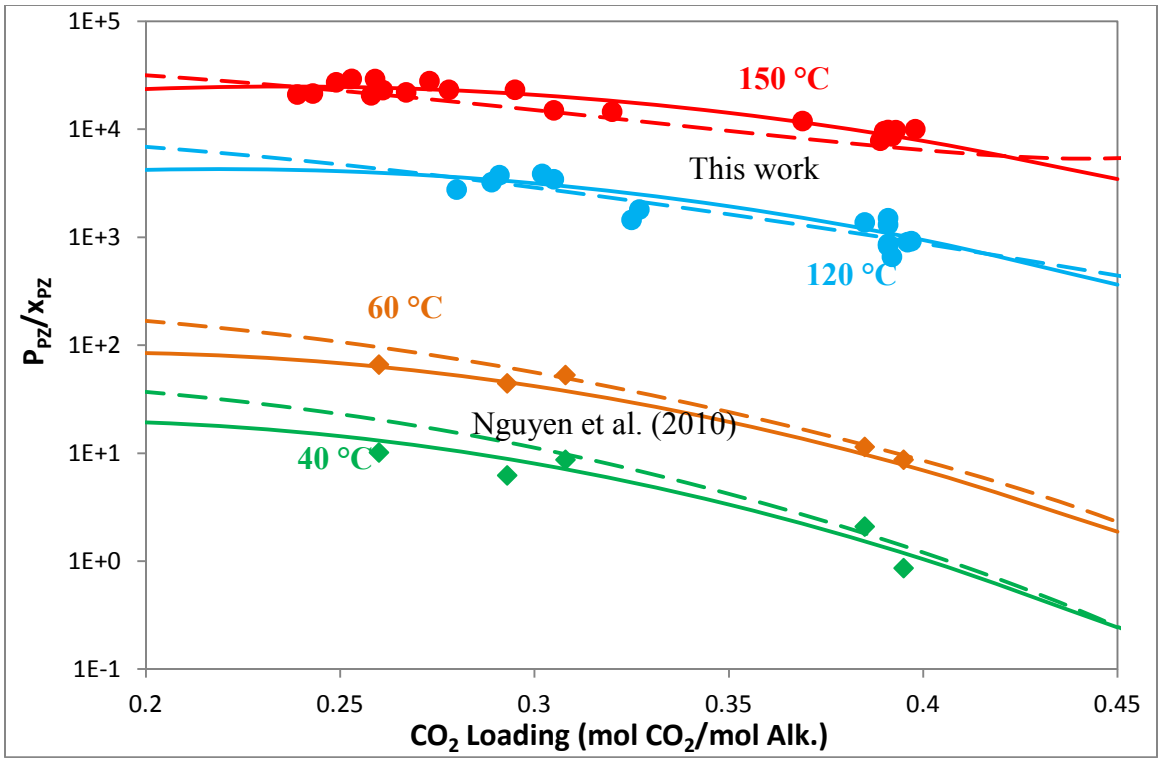

Figure 3-9: Comparison of Normalized PZ Volatility in CO_2 loaded 4.7-11.3 m PZ.
♦ Nguyen et al. (2010); ●: this work; solid lines: empirical model of Eq. 3-4; dashed lines: Aspen Plus® Fawkes Model – 8 m PZ (Frailie et al., 2010).

$$x_{PZ} = \frac{\text{mol of total PZ}}{\text{mol of total PZ + mol of } H_2O}.$$

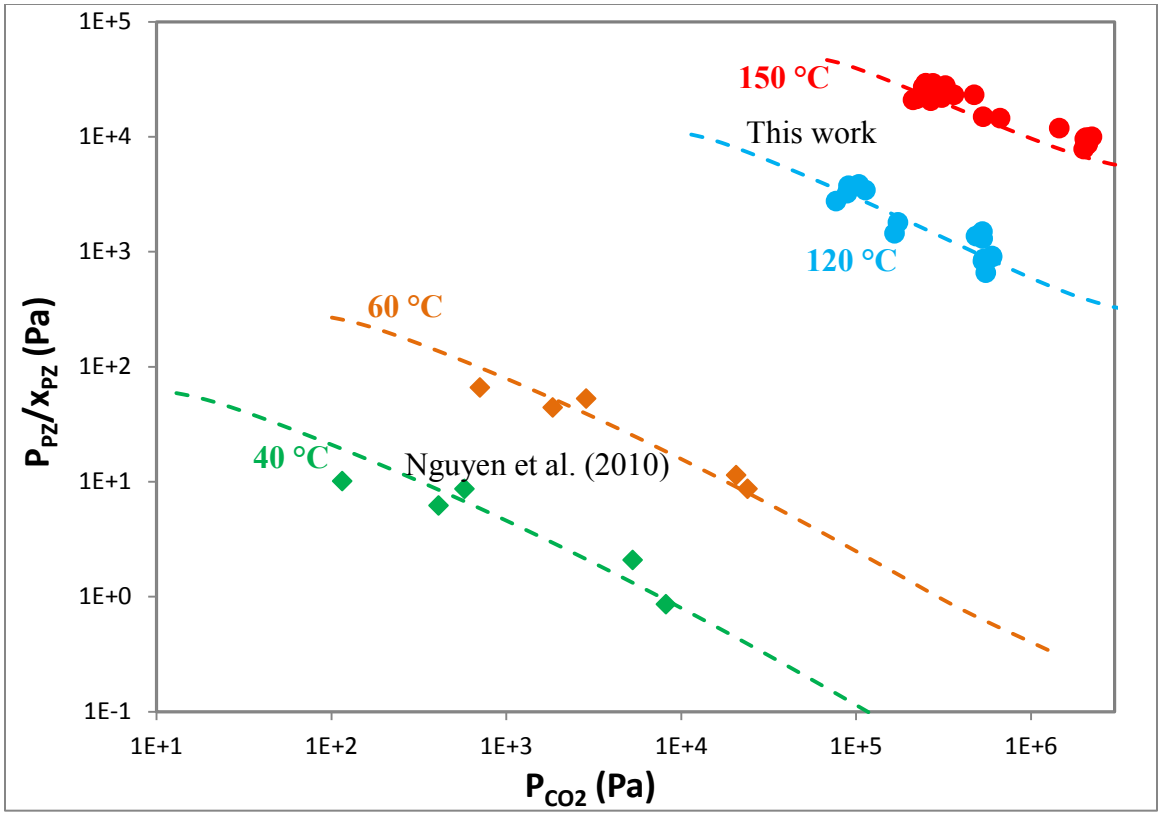

Figure 3-10: Comparison of Normalized PZ Volatility in CO_2 loaded 4.7-11.3 m PZ (2). ♦ Nguyen et al. (2010); ●: this work; dashed lines: Aspen Plus® Fawkes Model – 8 m PZ (Frailie et al., 2010). $x_{PZ} = \frac{\text{mol of total PZ}}{\text{mol of total PZ + mol of } H_2O}$.

3.3.4 Enthalpy of Vaporization

According to Equation XVIII.9 in Lewis and Randall (1923) and Equation IV.109 in Dodge (1944), the apparent enthalpy of vaporization of MEA and PZ was derived from empirical models Eq. 3-3 and 3-4, respectively.

$$\left(\frac{\partial ln f_1}{\partial T}\right)_{P,N} = \frac{H_1^* - \bar{H}_1}{RT^2}$$ Equation (XVIII.9), Lewis and Randall (1923)

Where f_1 is the fugacity of the constituent 1, $H_1^* - \bar{H}_1$ is the heat absorbed per mol when a small quantity of the constituent X_1 evaporates from the solution into a vacuum.

$$\frac{\partial ln \bar{f}_i}{\partial T} = -\frac{\bar{H}_i - \bar{H}_i^o}{RT^2}$$ Equation (IV.109), Dodge (1944)

Where $\bar{f}_i$ is the fugacity of the constituent i, $-(\bar{H}_i - \bar{H}_i^o)$ is the heat absorbed per mol when a small quantity of the constituent X_i evaporates from the solution into a vacuum.

Figure 3-11 presents the apparent enthalpy of vaporization of MEA and PZ predicted by Eq. 3-5 and 3-6, and $-\Delta H_{vap}$ from Aspen Plus® prediction by Hilliard MEA model (2008) and Fawkes model (Frailie et al., 2010).

$$\Delta H_{vap,MEA} = -R\frac{\partial \ln P_{MEA}}{\partial \frac{1}{T}} = -R*(-8153 - 2594\alpha^2) \quad (3\text{-}5)$$

$$\Delta H_{vap,PZ} = -R\frac{\partial \ln P_{PZ}}{\partial \frac{1}{T}} = -R*(-21.6T - 18174\alpha^2) \quad (3\text{-}6)$$

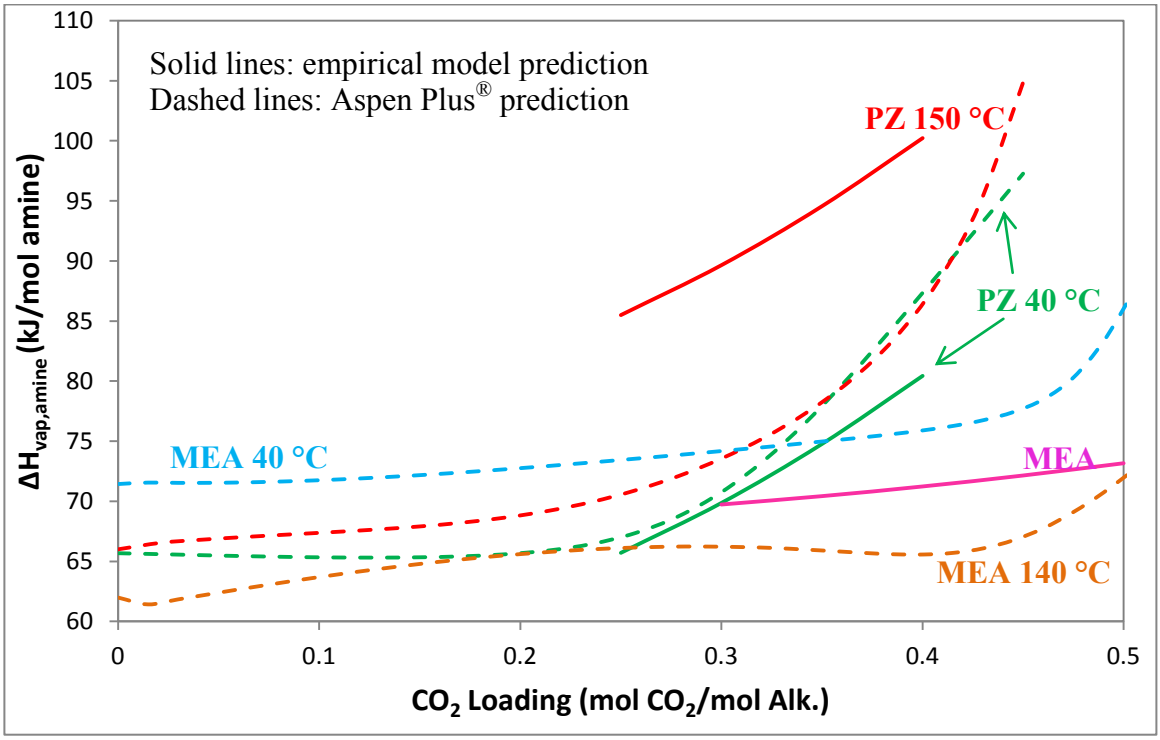

Figure 3-11: Enthalpy of Vaporization of 7 MEA and 8 mPZ. **Aspen Plus® Hilliard MEA model (2008) and Fawkes PZ model (Frailie et al., 2010) were used.**

$-\Delta H_{vap,MEA}$ does not depend on temperature, and is nearly constant over 0-0.45 CO_2 loading. $-\Delta H_{vap,PZ}$ is nearly constant below 0.25 loading, and beyond that point it increases as CO_2 loading increases. This may be because the reactions and speciation in PZ-CO_2-H_2O are more complex than that in MEA-CO_2-H_2O.

Over the practical range of CO_2 loading, there is always a significant concentration of free MEA. Therefore the heat of MEA absorption is essentially constant and corresponds to its value in MEA/H_2O.

Figure 3-12 shows the reaction stoichiometry for 8 m PZ at 40 ℃ using the Aspen Plus® Fawkes model (Frailie et al., 2010). It shows the mole change of different species when 1 mol PZ was absorbed into the solution. Figure 3-12 indicates the reactions taking place at different loading. At very lean loading (<0.1), there is significant free PZ, so its heat of vaporization is nearly constant. The stoichiometry of absorbing PZ is given by:

$$PZ(g) = PZ(aq) \quad (3\text{-}7)$$

As loading increases, more reactions take place. Starting from about 0.12 loading, the main apparent stoichiometry is:

$$PZ + HPZCOO \leftrightarrow PZH^+ + PZCOO^- \quad (3\text{-}8)$$

As CO_2 loading increases, according to Figure 3-12, one mole of HCO_3^- decrease corresponds to one mole increase in H_2O, and $PZCOO^-$ forms more than PZH^+. Therefore besides reaction 3-8, PZ starts to react with bicarbonate and $PZ(COO^-)_2$:

$$PZ + HCO_3^- \leftrightarrow H_2O + PZCOO^- \quad (3\text{-}9)$$

$$PZ + PZ(COO^-)_2 \leftrightarrow 2PZCOO^- \quad (3\text{-}10)$$

At the expected rich loading of 0.4 mol CO_2/equiv PZ and higher loading, in Figure 3-12, one mole of HCO_3^- decrease corresponds to one mole increase in H_2O and

$PZ(COO^-)_2$; $PZCOO^-$ generation is less than PZH^+. Thus besides reaction 3-8, another reaction is:

$$PZ + HPZCOO + HCO_3^- \leftrightarrow PZH^+ + H_2O + PZ(COO^-)_2 \quad (3\text{-}11)$$

Therefore the enthalpy of PZ absorption will be a function of CO_2 loading. These reactions have different temperature dependence and the changes in reactions and speciation contribute to temperature and loading effects on $-\Delta H_{vap,PZ}$.

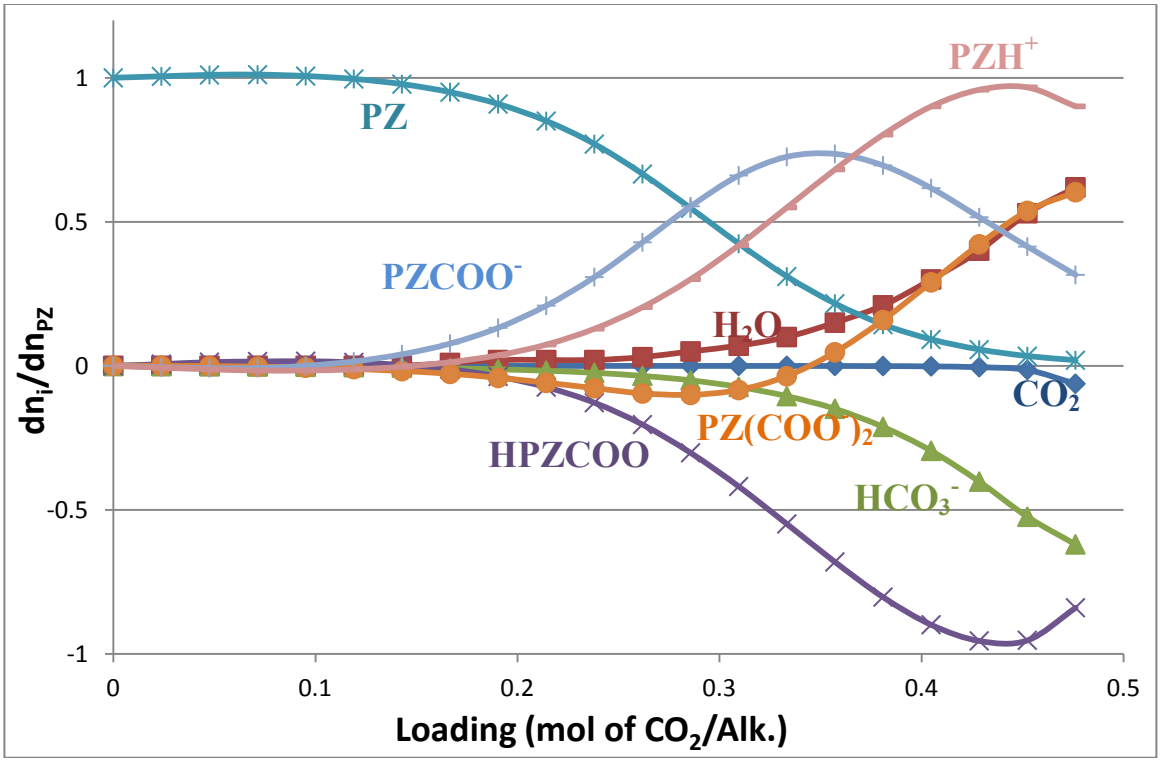

Figure 3-12: Reaction Stoichiometry for 8 m PZ at 40°C with Aspen Plus® Fawkes Model

3.4 SPECIFIC HEAT CAPACITY OF PZ-H_2O

3.4.1 Introduction

Specific heat capacity (C_p) can be used to calculate the temperature dependence of ΔH and in building the rigorous thermodynamic models. A differential scanning calorimetry (DSC) method has been previously used in the Rochelle group by Hilliard (2008) and Nguyen (Rochelle et al., 2009) for C_p measurements at 40-120°C with 3.5 and 7 m MEA-H_2O, 2 and 3.6 m PZ-H_2O, and 8-12 m PZ-CO_2-H_2O. Tables 1-6 and 1-7 give a brief literature review on specific heat capacity measurement for MEA and PZ solution.

In this work the DSC method was modified to measure C_p of 8 m PZ up to 150°C. Because of PZ solubility limits, the lower bound of temperature in this work is 70°C instead of 40°C. The higher bound is extended from 120 to 150 ℃ because in CO_2 capture process with concentrated PZ, the stripper temperature can be elevated up to 150°C. C_p of PZ-CO_2-H_2O cannot be measured at 150°C because the high total pressure exceeds the limit of the sample cells for the DSC, so C_p of unloaded 8 m PZ was measured in this work.

3.4.2 Experimental Method

This DSC method has been previously described in Hilliard (2008). It follows the ASTM E 1269-05 standard test method for determining specific heat capacity by DSC. Therefore the method will be briefly described here.

3.4.2.1 Sample Preparation

60 μL stainless steel sample pans with o-rings and lids from Perkin Elmer (#03190218) were used. PZ and DDI water were weighed and mixed to obtain the target concentration. Then the mixture was heated and stirred on a hot plate to make PZ

dissolve. After the solution got clear, an Eppendorf® pipette was used to transfer about 59.5 μL solution to the sample pan. To avoid precipitation of PZ solution in a cool pipette tip, part of the pipette tip was submerged in the heated PZ solution for a while. Then the 60 μL solution was carefully filled into the sample pan. An o-ring was placed inside the lid for sealing, and the sample pan and lid were joined together by a Perkin Elmer Quick Press (#0990-8467). All cells were sealed before going into the DSC. Figure 3-13 shows a cross view of a sample cell after sealing.

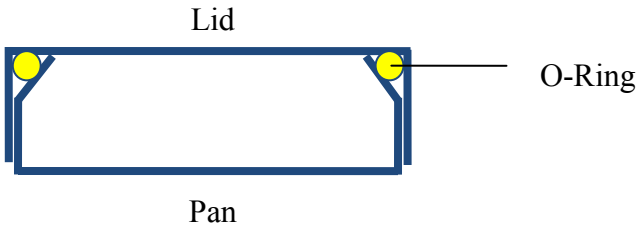

Figure 3-13: Cross View of a Sample Cell for the DSC Heat Capacity Method

3.4.2.2 Procedure

A DSC-Q100 calorimeter with a thermal analysis controller from TA Instruments was used. The equipment is located and maintained in the laboratory of Dr. Freeman's research group, the Department of Chemical Engineering at The University of Texas at Austin.

In each run, a cell containing the sample and a sealed empty reference cell were placed on the sample platforms inside the chamber of the DSC, and the heat flows to the two cells were measured. To obtain accurate results, before running the solution samples, a series of calibration runs with an empty cell, an indium sample, and an Al_2O_3 sample was performed to get the heat flow baseline, the cell constant, temperature calibration, and the sensitivity constant. The baseline was then subtracted from each sample heat profile using TA Analysis software.

The DSC program of this experiment was set up as: heat up and hold at 80°C for 5 min, cool down to 60°C and hold for 10 min, ramp the temperature up at 5°C/min to 155°C, then cool down to 40°C at the rate of 20°C/min. The heat flow from 60 to 155°C was recorded and used to get the C_p at each temperature. TA Instruments Universal Analysis 2000 was the software for analyzing the raw heat flow data.

For the 8 m PZ sample, three runs were carried out to determine the specific heat capacity.

3.4.3 Results

Table 3-4 presents the result from the specific heat capacity measurements. Figure 3-14 compares the measured C_p of 8 m PZ from this work with literature.

Table 3-4: Specific Heat Capacity of 8 m PZ

T	C_p	T	C_p	T	C_p
°C	(J/g*K)	°C	(J/g*K)	°C	(J/g*K)
70	3.43	100	3.58	130	3.71
75	3.47	105	3.60	135	3.73
80	3.49	110	3.63	140	3.76
85	3.52	115	3.65	145	3.78
90	3.54	120	3.67	150	3.81
95	3.56	125	3.69		

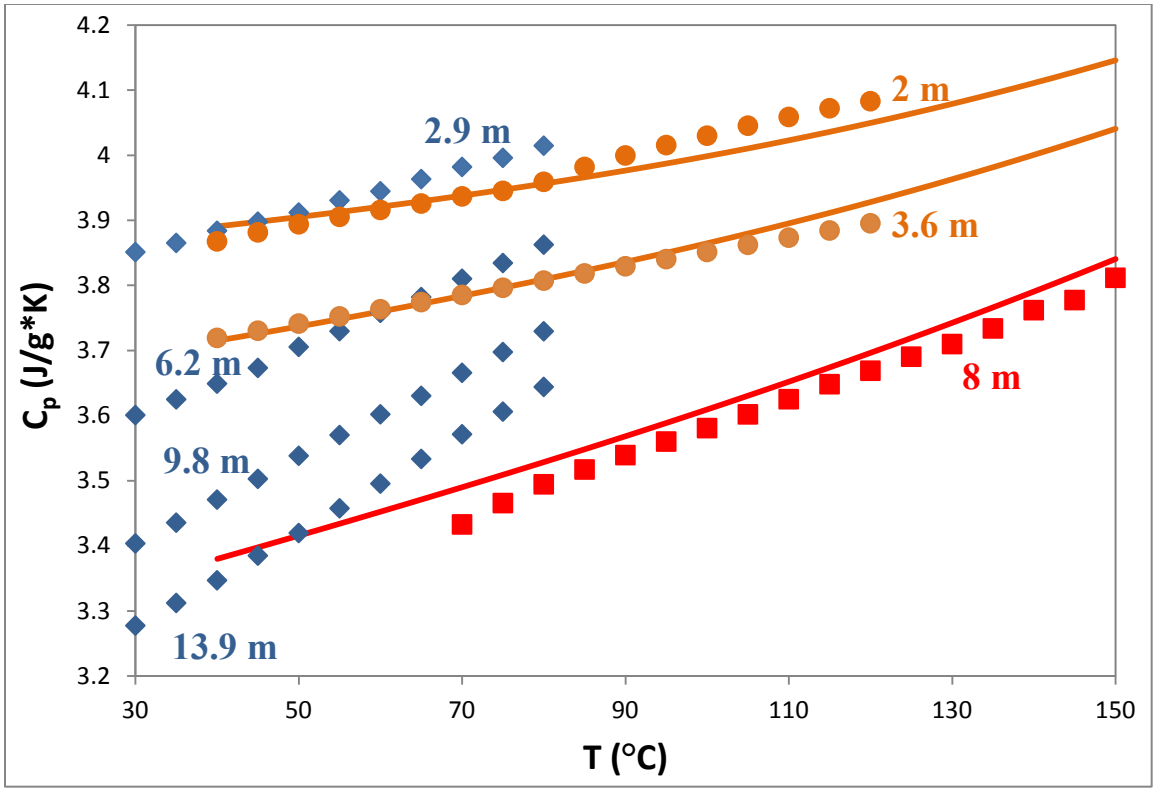

Figure 3-14: Comparison of Specific Heat Capacity of PZ-H_2O. ●: Hilliard (2008) 2 and 3.6 m PZ; ♦: Chen et al. (2010) 2.9, 6.2, 9.8, 13.9 m PZ; ■: this work 8 m PZ; solid lines: Aspen Plus® Fawkes Model 2, 3.6, 8 m PZ.

Data from Hilliard (2008) and this work have similar temperature dependence at different PZ concentration. Aspen Plus® Fawkes model generally predicts these UT data. C_p by Chen et al. (2010) has stronger temperature dependence and is higher than the UT data at the same PZ concentration. There may be some systematic error of either source of the data. Chen et al. mentioned that the PZ concentration was chosen as smaller or equal to 0.2 mol fraction (2.9-13.9 m) because of the PZ solubility limit, but according to Freeman's research (2011), at 30°C PZ is not soluble at 6.2-13.9 m concentration, and 2.9 m is on the limit of solid-liquid transition.

A small amount of water may vaporize as the temperature increases but the heat capacity measurements assume no vaporization. The water heat of vaporization was

counted in the total heat flow, thus the reported specific heat capacity of the solution may be higher than the true value. However this error can be neglected according to the following calculation.

Assume 10% of the sample cell volume is occupied by water vapor at 150°C, which is larger than the expected vapor volume. According to DIPPR (1998-Provo, BYU) water vapor pressure at 145 and 150°C is 414760 and 475090 Pa, respectively. Therefore the water in the vapor space is $60\mu L \cdot 10\% \cdot \frac{1m^3}{1e9^{\mu L}/_{m^3}} \cdot P_{H2O}(Pa)/8.314(\frac{J}{K.mol})/T(K)$, which is 7.158E-7 and 8.103E-7 mol at 145 and 150°C, respectively. Therefore, when the sample was heated from 145 to 150°C, (8.103E-7) - (7.158E-7) = 9.44E-8 mol of water was vaporized. The heat of vaporization of water is 3.8225E7 J/kmol at the average temperature 147.5°C, thus in this process $3.8225E7\frac{J}{kmol} \cdot \frac{1}{\frac{1000mol}{kmol}} \cdot (9.44E-8\,mol) = 3.61E-3\,J$ of heat was used in the vaporization of water and should be subtracted from the total heat. The average reported specific heat capacity at 145 and 150°C is 3.79 J/g·K, and the heat flow from 145 to 150°C is $3.79\frac{\text{J}}{\text{g.K}} \cdot 0.06\text{g} \cdot 5\text{K} = 1.138\,\text{J}$. Subtract the heat for vaporizing water and yield 1.134 J of heat. Therefore the more accurate heat capacity at 147.5°C is $\frac{1.134J}{0.06g \cdot 5K} = 3.78\frac{\text{J}}{\text{g.K}}$. The relative error of the reported heat capacity at 147.5°C is (3.79-3.78)/3.78=0.3%, which is very small and can be neglected.

3.5 CONCLUSIONS AND RECOMMENDATIONS

At 0-0.5 loading (α), 313-413 K, 3.5-11 m MEA (mol fraction x is 0.059-0.165), the empirical model of MEA volatility is $\ln(P_{MEA}/x_{MEA}) = 30.0\text{-}8153/T\text{-}2594\alpha^2/T$. In 7 m MEA with 0.2 and 0.5 loading, P_{MEA} is 920 and 230 Pa at 120 ℃. At 0.3-0.5 loading, the enthalpy of MEA vaporization, $-\Delta H_{vap,MEA}$, is about 70-73 kJ/mol MEA.

At 0.25-0.4 loading, 313-423 K, 4.7-11.3 m PZ (x is 0.078-0.169), the empirical model of PZ volatility is $\ln(P_{PZ}/x_{PZ}) = -123+21.6\ln T+20.2\alpha-18174\alpha^2/T$. In 8 m PZ with 0.3 and 0.4 loading, P_{PZ} is 400 and 120 Pa at 120 ℃, and 2620 and 980 Pa at 150 ℃. At 0.25-0.4 loading, $-\Delta H_{vap,PZ}$ is about 85-100 kJ/mol PZ at 150 ℃ and 66-80 kJ/mol PZ at 40 ℃.

$\Delta H_{vap,PZ}$ has a larger dependence on CO_2 loading than $\Delta H_{vap,MEA}$ in rich solution because of the more complex speciation/reactions in PZ at rich loading.

Specific heat capacity of 8 m PZ is 3.43-3.81 J/(g·K) at 70-150°C.

The liquid sampling method in the high temperature vapor-liquid equilibrium measurements needs to be modified. A better condensing system may help to reduce flashing; sampling into a vacuumed sample bomb, or sampling into a known amount of amine solution may help to get more representative samples.

Chapter 4: Thermodynamic Models of MEA-CO_2-H_2O System

This Chapter presents rigorous thermodynamic modeling of MEA-CO_2-H_2O with the Aspen Plus® electrolyte Non-Random Two Liquid (ENRTL) model. Based on the previous MEA model by Hilliard (2008) two new models were developed. One of the models includes a new species MEACOOH. Experimental CO_2 solubility, MEA volatility, total pressure, heat of absorption, specific heat capacity, and NMR speciation were compared with the model prediction. The results show that the model prediction improves by adding MEACOOH and related parameters. At high temperature or high CO_2 loading, the concentration of MEACOOH is above 1% in 7 m MEA. The sensitivity analysis shows that the heat of formation of MEACOOH has an effect on CO_2 partial pressure and heat of absorption at high temperature and high loading. Therefore MEACOOH may be considered an important species at high loading or high temperature. A profile for 11 m MEA with CO_2 solubility, MEA volatility, heat of absorption, speciation, and specific heat capacity was given by the model with MEACOOH. This work used Aspen Plus® Version 7.3.

4.1 ELECTROLYTE-NRTL MODEL

Electrolyte Non-Random Two Liquid (ENRTL) model was originally developed by Chen et al. (1979, 1982, 1986) for aqueous electrolyte systems. Mock et al. (1984, 1986) extended the model to mixed solvent electrolyte systems. It is a versatile model to count for liquid phase non-ideality over a full range of the electrolyte concentration, especially in aqueous or mixed solvent electrolyte systems. The ENRTL model was developed with the local composition concept, similar to the Non-Random Two Liquid

(NRTL) model by Renon and Prausnitz (1968). For non-electrolyte systems the ENRTL model reduces to the NRTL model.

4.1.1 ENRTL Model Framework in Aspen Plus®

4.1.1.1 ENRTL Parameters

Aspen Plus® has the built-in ENRTL model to calculate properties. The model uses interaction parameters to calculate the activity coefficients.

According to Chen et al. (1982) the excess Gibbs energy expression contains two contributions: the long-range ion-ion interactions and the local interactions. The long-range ion-ion interactions are represented by the unsymmetric Pitzer-Debye-Hückel model and the Born equation, while the local interactions are expressed by the NRTL theory. Equation (4-1) shows the excess Gibbs energy expression:

$$\frac{G_m^{*E}}{RT} = \frac{G_m^{*E,PDH}}{RT} + \frac{G_m^{*E,Born}}{RT} + \frac{G_m^{*E,lc}}{RT} \qquad (4\text{-}1)$$

Therefore

$$ln\gamma_i^* = ln\gamma_i^{*PDH} + ln\gamma_i^{*Born} + ln\gamma_i^{*lc} \qquad (4\text{-}2)$$

Where the superscript * means an unsymmetric reference state is used.

According to Aspen Plus® Help, the adjustable parameters for electrolyte NRTL model include the:

- Pure component dielectric constant coefficient of non-aqueous solvents
- Born radius of ionic species
- NRTL parameters for molecule-molecule, molecule-electrolyte, and electrolyte-electrolyte pairs

The NRTL parameters were adjusted in this work:

  - The molecule-molecule binary parameters:

$$\tau_{ij} = A_{ij} + \frac{B_{ij}}{T} + F_{ij} lnT + G_{ij} T \quad (4\text{-}3)$$

It can be used in the NRTL model as Equation 4-4 and Table 4-1 shows the corresponding parameters in Aspen Plus®:

$$ln\gamma_i = \frac{\sum_j x_j \tau_{ji} G_{ji}}{\sum_k x_k G_{ki}} + \sum_j \frac{x_j G_{ij}}{\sum_k x_k G_{kj}} \left(\tau_{ij} - \frac{\sum_m x_m \tau_{mj} G_{mj}}{\sum_k x_k G_{kj}} \right) \quad for\ T_{lower} \le T \le T_{upper} \quad (4\text{-}4)$$

Where

$$G_{ij} = \exp(-\alpha_{ij} \tau_{ij})$$

$$A_{ij} = C_{ij} + D_{ij}(T - 273.15K)$$

$$\tau_{ii} = 0$$

$$G_{ii} = 1$$

Table 4-1: Electrolyte NRTL Molecule-molecule Binary Parameters

Symbols in Eq. (4-3)	In Aspen Plus®	
	Parameters	**Default Values**
A_{ij}, A_{ji}	NRTL/1	0
B_{ij}, B_{ji}	NRTL/2	0
$\alpha_{ij} = \alpha_{ji}$	NRTL/3	0.3, 0.2, or 0.47*
-	NRTL/4	0
$F_{BB'}, F_{B'B}$	NRTL/5	0
$G_{BB'}, G_{B'B}$	NRTL/6	0

*: 0.3 for nonpolar substances; nonpolar with non-associated liquids; small deviations from ideality. 0.2 for saturated hydrocarbons with polar non-associated liquids and systems that exhibit liquid-liquid immiscibility. 0.47 for self-associated substances with nonpolar substances.

- Electrolyte-molecule pair parameters:

$$\tau_{ca,B} = C_{ca,B} + \frac{D_{ca,B}}{T} + E_{ca,B} \left[\frac{T_{ref} - T}{T} + ln\left(\frac{T}{T_{ref}} \right) \right] \quad (4\text{-}5)$$

$$\tau_{B,ca} = C_{B,ca} + \frac{D_{B,ca}}{T} + E_{B,ca}\left[\frac{T_{ref}-T}{T} + ln\left(\frac{T}{T_{ref}}\right)\right] \quad (4\text{-}6)$$

$$T_{ref} = 298.15K$$

Table 4-2 shows the corresponding parameters in Aspen Plus®.

Table 4-2: Electrolyte NRTL Electrolyte-molecule Binary Parameters

Symbols in Equation (4-5, 4-6)	In Aspen Plus®	
	Parameters	**Default Values**
$C_{ca,B}, C_{B,ca}$	GMELCC	8 and -4 for electrolyte/water pair, 10 and -2 for electrolyte/non-water solvent pair
$D_{ca,B}, D_{B,ca}$	GMELCD	0
$E_{ca,B}, E_{B,ca}$	GMELCE	0
$\alpha_{ca,B} = \alpha_{B,ca}$	GMELCN	0.2

4.1.1.2 Gibbs Free Energy and Enthalpy of Formation

Table 4-3: Parameters of Gibbs Free Energy and Enthalpy of Formation

Parameters	Description	Reference States
DGAQFM	Aqueous free energy of formation at infinite dilution, 25°C and 1 atm.	Infinite dilution in pure water at 25°C and 1 atm
DHAQFM	Aqueous heat of formation at infinite dilution.	Same as DGAQFM
DGFORM	Ideal gas Gibbs free energy of formation at 298.15 K.	The elements as ideal gases at 25°C and 1 atm
DHFORM	Ideal gas heat of formation at 298.15 K.	Same as DGFORM

4.1.1.3 Vapor Phase Calculation

The Redlich-Kwong equation-of-state is used for vapor phase calculation. The model is:

$$p = \frac{RT}{V_m - b} - \frac{a/T^{0.5}}{V_m(V_m + b)} \tag{4-7}$$

$$\sqrt{a} = \sum_i x_i \sqrt{a_i}$$

$$b = \sum_i x_i b_i$$

$$a_i = 0.42748023 R^2 T_{ci}^{2.5} / P_{ci}$$

$$b_i = 0.08664035 R T_{ci} / P_{ci}$$

4.1.1.4 Henry's Constant

The Henry's constant (H_{iA}) model is used when a dissolved gas i in solvent A is assumed a Henry's component.

$$ln\frac{H_i}{\gamma_i^{\infty}} = \sum_A w_A \, ln\frac{H_{iA}}{\gamma_{iA}^{\infty}} \tag{4-8}$$

Where w_A is a weighted average that relates to the critical volumes and mole fractions of solvents.

$$lnH_{iA}\left(T, P_A^{*,l}\right) = a_{iA} + \frac{b_{iA}}{T} + c_{iA} lnT + d_{iA} T + \frac{e_{iA}}{T^2} \quad for\ T_L \le T \le T_H \tag{4-9}$$

In this work, H_2O is the only solvent in the system. Therefore

$$ln\frac{H_i}{\gamma_i^{\infty}} = ln\frac{H_{iA}}{\gamma_{iA}^{\infty}} \tag{4-10}$$

Table 4-4: Henry's Parameters

Symbols in Equation (4-9)	In Aspen Plus®	
	Parameters	Default Values
a_{iA}	HENRY/1	-
b_{iA}	HENRY/2	0
c_{iA}	HENRY/3	0
d_{iA}	HENRY/4	0
T_L	HENRY/5	0
T_H	HENRY/6	2000
e_{iA}	HENRY/7	0

If a_{iA} is missing, $ln\frac{H_i}{\gamma_i^{\infty}}$ is set to zero and the weighting factor w_A is renormalized.

4.1.1.5 Ideal Gas Heat Capacity

Aspen ideal gas heat capacity calculation uses the following polynomial:

$$C_p^{*ig} = C_{1i} + C_{2i}T + C_{3i}T^2 + C_{4i}T^3 + C_{5i}T^4 + C_{6i}T^5 \quad C_{7i} \le T \le C_{8i} \qquad (4\text{-}11)$$

$$C_p^{*ig} = C_{9i} + C_{10i}T^{11} \quad for\ T < C_{7i} \qquad (4\text{-}12)$$

Table 4-5: Ideal Gas Heat Capacity Parameters

Symbols in Equation (4-11, 4-12)	In Aspen Plus®	
	Parameters	Default Values
C_{1i}	CPIG/1	-
$C_{2i}, \ldots, C_{6i}$	CPIG/2, …, 6	0
C_{7i}	CPIG/7	0
C_{8i}	CPIG/8	1000
C_{9i}, C_{10i}, C_{11i}	CPIG/9, 10, 11	-

4.1.1.6 Aqueous Infinite Dilution Heat Capacity

$$C_{p,i}^{\infty,aq} = C_{1i} + C_{2i}T + C_{3i}T^2 + \frac{C_{4i}}{T} + \frac{C_{5i}}{T^2} + \frac{C_{6i}}{\sqrt{T}} \quad for\ C_{7i} \le T \le C_{8i} \qquad (4\text{-}13)$$

For $T < C_{7i}\ or\ T > C_{8i}$, $C_{p,i}^{\infty,aq}$ is linearly extrapolated using the slope at C_{7i} or C_{8i}.

Table 4-6: Aqueous Infinite Dilution Heat Capacity Parameters

Symbol in Equation (4-13)	In Aspen Plus®	
	Parameters	**Default Values**
C_{1i}	CPAQ0/1	-
$C_{2i}, \ldots, C_{6i}$	CPAQ0/2,…,6	0
C_{7i}	CPAQ0/7	0
C_{8i}	CPAQ0/8	1000

4.1.1.7 Parameters for Zwitterions

Aspen Plus® has a special method to set up zwitterions. When a zwitterion is set up as a Henry's component, these parameters of the zwitterion are required: ideal gas heat capacity or aqueous infinite dilution heat capacity, molecular weight, charge (set to 0), Henry's constant, Antoine liquid vapor pressure coefficients (PLXANT), partial molal volume at infinite dilution (VLBROC), NRTL, and ENRTL parameters. HENRY/1 should be set to equal or less than -10 bar, and PLXANT/1 should be set to equal or less than -1.0E10 kPa, making the zwitterion non-volatile. NRTL and ENRTL parameters can be set to Aspen Plus® default values as in Tables 4-1 and 4-2. VLBROC can be set the same as a similar molecule for a reasonable approximation.

4.1.2 Prior Work on CO_2 Loaded Aqueous Amines

Aspen Plus® physical property databanks have included many interaction parameters and equilibrium constants regressed from previous experimental data. Better thermodynamic models can be achieved by adding new experimental data to the regressions, especially for the new solvents whose properties are not well built in Aspen Plus®.

Thermodynamic models of CO_2 loaded MEA and other amines have been studied by previous group members. Table 4-7 lists the relevant modeling work by previous researchers.

Table 4-7: Summary of Previous Thermodynamic Models for CO_2 Loaded Amines

Authors	Systems	Methods
Austgen (1991)	CO_2 and H_2S in MEA, MDEA, MDEA/MEA, MDEA/DEA	Aspen Plus® DRS
Freguia (2003)	CO_2 in MEA	Aspen Plus® DRS
Cullinane (2004)	CO_2 in PZ/K_2CO_3	Standalone FORTRAN model
Hilliard (2008)	CO_2 in MEA, PZ, K_2CO_3 and selected blends	Aspen Plus® DRS
Frailie et al. (2010)	5DeMayo (Cinco De Mayo) PZ model	Aspen Plus® DRS
Frailie et al. (2010)	Fawkes PZ/MDEA model	Aspen Plus® DRS
Plaza (2011)	Phoenix MEA model	Aspen Plus® DRS

A recent rigorous MEA model was developed by Hilliard (2008). As shown in Figures 2-6, 3-7, and 3-8, the Hilliard MEA thermodynamic model over-predicts P_{CO2} at high temperature, and misses MEA volatility data at high loading at 40-140 ℃. Some of the data incorporated in the Hilliard model were inconsistent, or may have systematic errors. There are also new literature data and high temperature data from this work on the MEA system. To achieve better predictions for the MEA-CO_2-H_2O system, in this work a series of new regressions in Aspen Plus® were done starting with the Hilliard (2008) model.

4.2 DATA REGRESSION OF MEA-H_2O SYSTEM

4.2.1 Model Development

The regression was more stable when data were regressed sequentially: pure component (amine, water), binary systems (amine-water), and then tertiary systems (amine-water-CO_2). The Hilliard MEA model (2008) was developed by this method. Since there is no new data for the pure component systems, the first step, pure MEA and water regression, was skipped in this work.

In the Hilliard (2008) MEA-H_2O model, total pressure, MEA volatility, specific heat capacity, and freezing point data were regressed. The new regression added the high temperature MEA volatility data presented in Chapter 3 and some new literature data. Table 4-8 shows the data that were used in the Hilliard (2008) model and the new model. Park and Lee (1997) data was not used in this work because of the high average absolute relative deviation (AARD) in Hilliard's MEA-H_2O model. All the data sets weighed equally in this regression. As stated in Chapter 3, the MEA volatility at low temperature by Hilliard (2008) is not consistent with other literature, thus the data below

46°C was not used in this regression. In this work MEA was defined as a Henry's component in Aspen Plus®.

Table 4-8: Data used in the MEA-H_2O Models

	Hilliard (2008)	This work
Total pressure, Nath and Bender (1983)	X	X
Total pressure, Tohara et al. (1982)	X	X
Vapor-liquid equilibrium, Park and Lee (1997)	X	
Vapor-liquid equilibrium, Tochigi et al. (1999)	X	X
Vapor-liquid equilibrium, Cai et al. (1996)	X	X
Specific heat capacity, Page et al. (1993)	X	X
Specific heat capacity, Chiu and Lee (1999)	X	X
Specific heat capacity, Weiland et al. (1997)	X	X
Specific heat capacity, Hilliard (2008)	X	X
Freezing point depression, Chang et al. (1993)	X	X
Vapor-liquid equilibrium, Kim et al. (2008)		X
Vapor-liquid equilibrium, this work		X
pK_a, Bates and Pinching (1951)	X	X
pK_a, Hamborg and Versteeg (2009)		X

4.2.2 MEA-H_2O Regression

Table 4-9 lists the regression results and standard deviation of the parameters. The other parameters CPIG/3, 4, 5, 6, NRTL/2, NRTL/6, and HENRY/4, 5, 6, were set to the default value 0.

Table 4-9: MEA-H_2O Regression Results

Parameter	Component i	Component j	Value (SI units)	Std. dev. (SI units)
CPIG/1	MEA		-171116	13222
CPIG/2	MEA		443	22
NRTL/1	MEA	H2O	-11.5	0.9
NRTL/3	H2O	MEA	0.2*	0
NRTL/5	MEA	H2O	1.8	0.2
HENRY/1	MEA	H2O	197	9
HENRY/2	MEA	H2O	-17102	458
HENRY/3	MEA	H2O	-24.2	1.3

*: set to default value 0.2.

The predicted pure MEA pressure matches the literature data as shown in Figure 4-1.

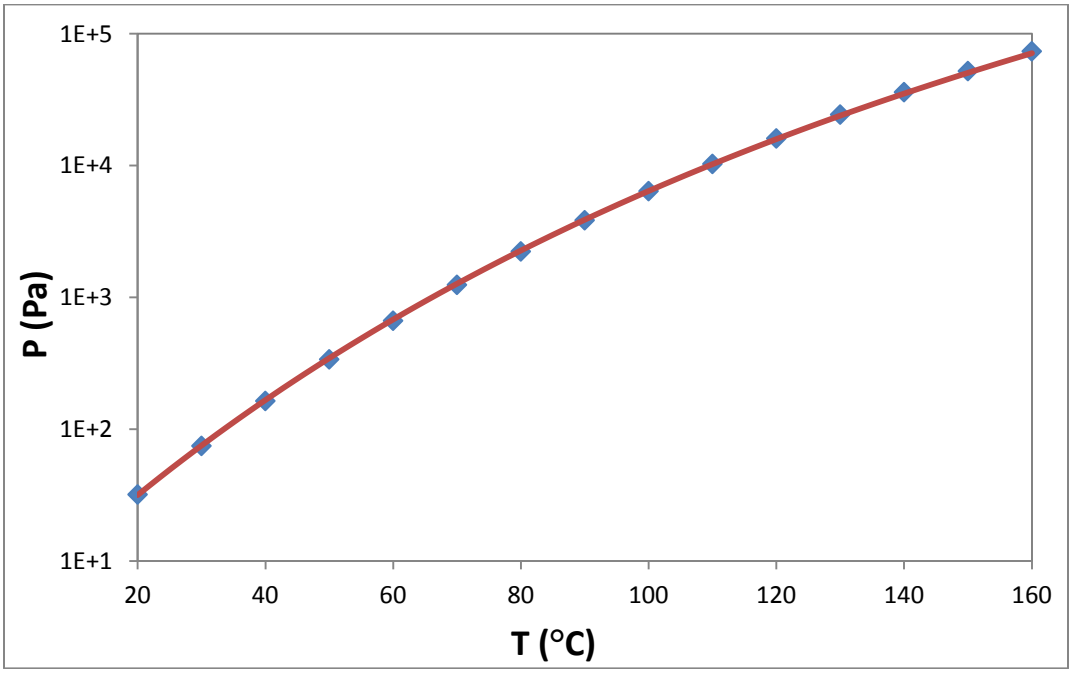

Figure 4-1: Pure MEA Vapor Pressure. **Points: experimental data from DIPPR; line: Aspen Plus® Model**

Figure 4-2 compares the new model prediction of normalized MEA volatility in 3.5-11 m MEA with the experimental data and the Hilliard's MEA model (2008).

Figure 4-3 presents the MEA volatility comparison in 7 m MEA. The major difference between the two models is at 40-60°C, because the low temperature Hilliard's MEA volatility was not used in this model. The new model fits the data and slope of the literature better than the Hilliard model at 40-70°C.

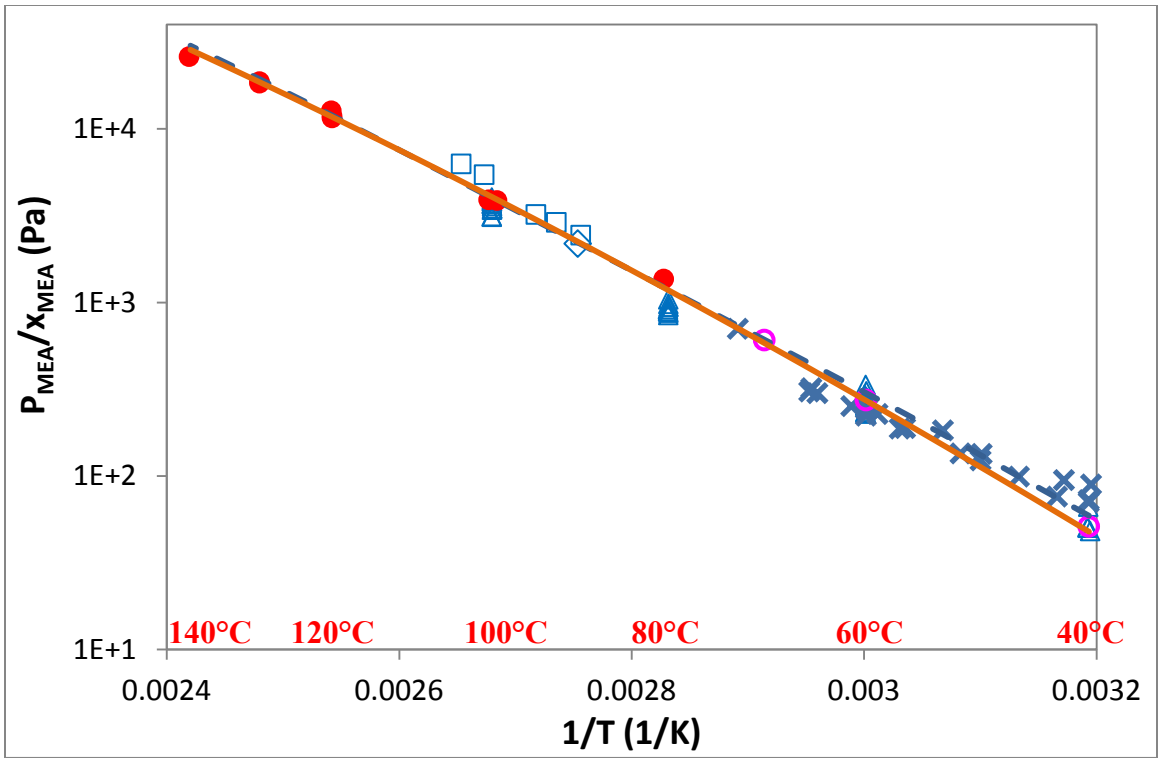

Figure 4-2: Comparison of Normalized MEA Volatility in 3.5-11 m MEA-H_2O. ○: Figure 3-20, *Gas Purification* (Kohl et al., 1997); Δ: Kim et al. (2008); □: Cai et al. (1996); ◊: Tochigi et al. (1999); X: Hilliard (2008); ●: this work; solid line: this work Aspen Plus® model – 7 m MEA; dashed line: Aspen Plus® Hilliard Model - 7 m MEA (2008); $x_{MEA} = \frac{\text{mol of MEA}}{\text{mol of MEA+mol of } H_2O}$.

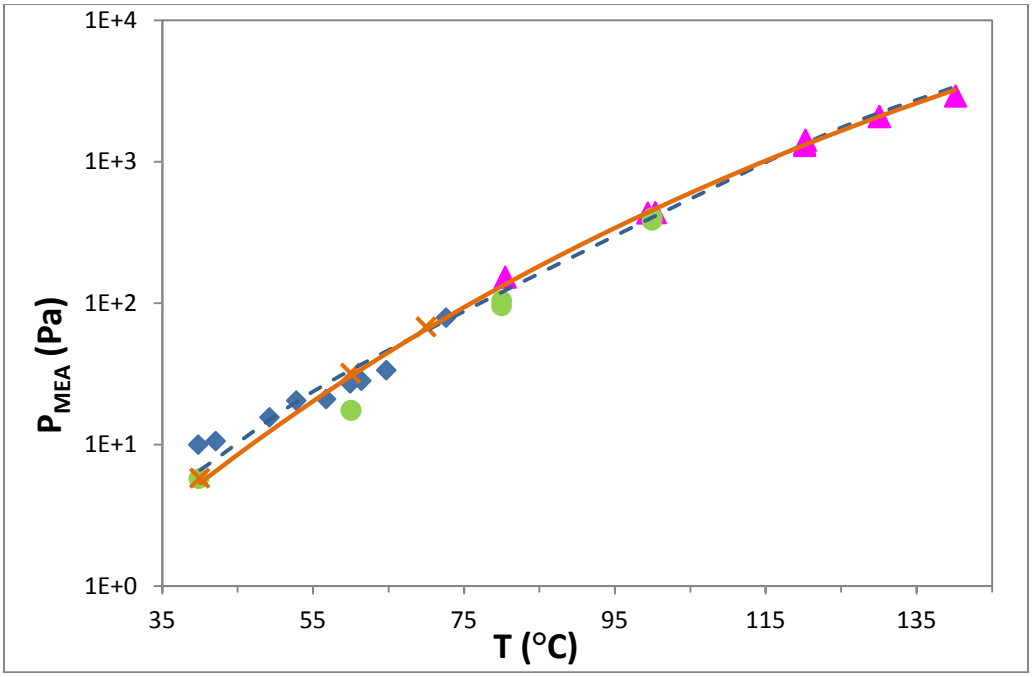

Figure 4-3: MEA Volatility in 7 m MEA. **♦: Hilliard (2008); ●: Kim et al. (2008); ▲: this work; X: Figure 3-20, *Gas Purification* (Kohl et al., 1997); solid line: Aspen Plus® model this work – 7 m MEA; dashed line: Aspen Plus® Hilliard Model – 7 m MEA (2008)**

Figure 4-4 shows the comparison of MEA partial pressure up to 31% MEA at 40-140°C. The new MEA model predicts the data well. It is better illustrated that Hilliard's MEA volatility at 40°C is inconsistent with other literature and the temperature dependence is smaller than the model prediction.

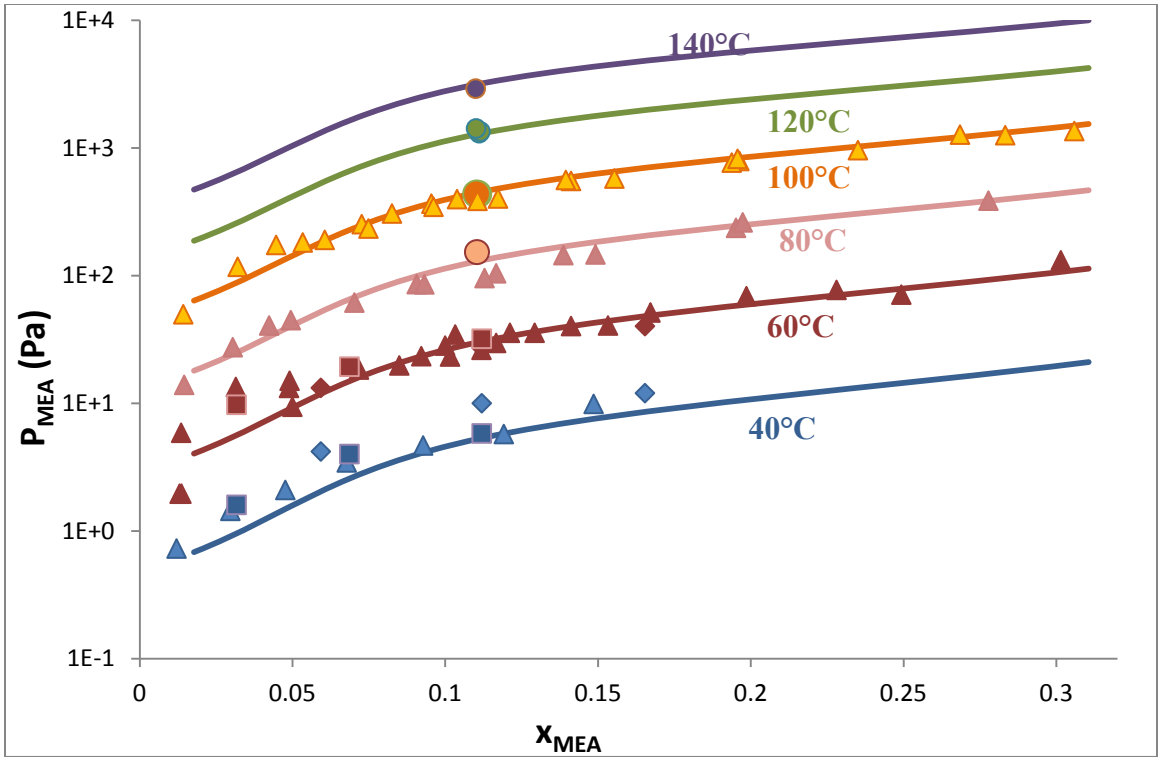

Figure 4-4: Volatility of MEA in MEA-H_2O. **♦: Hilliard (2008); ▲: Kim et al. (2008); ●: this work; ■: Figure 3-20, *Gas Purification* (Kohl et al., 1997); solid lines: Aspen Plus® model this work.**

Figure 4-5 gives the activity coefficients predicted by the new model. The reference state is pure water and infinite dilution of MEA. The activity coefficients decrease with temperature and increase with MEA.

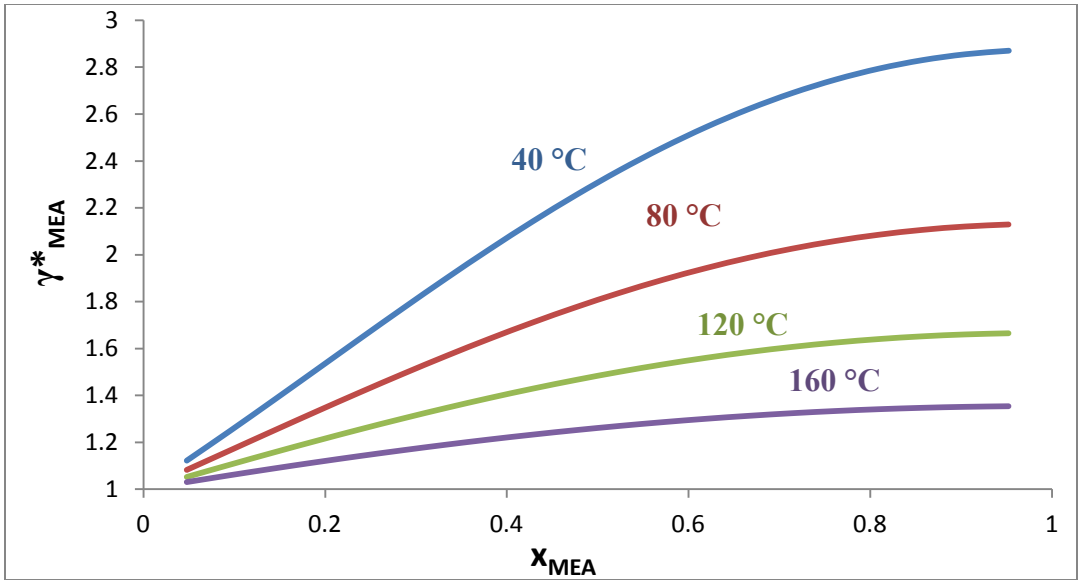

Figure 4-5: Asymmetric Activity Coefficients of MEA in MEA-H_2O

Figures 4-6 and 4-7 present the model prediction of the specific heat capacity of aqueous MEA over a wide range of temperature and MEA concentration. The model fairly predicts the data up to 40 m MEA and over 40-120°C.

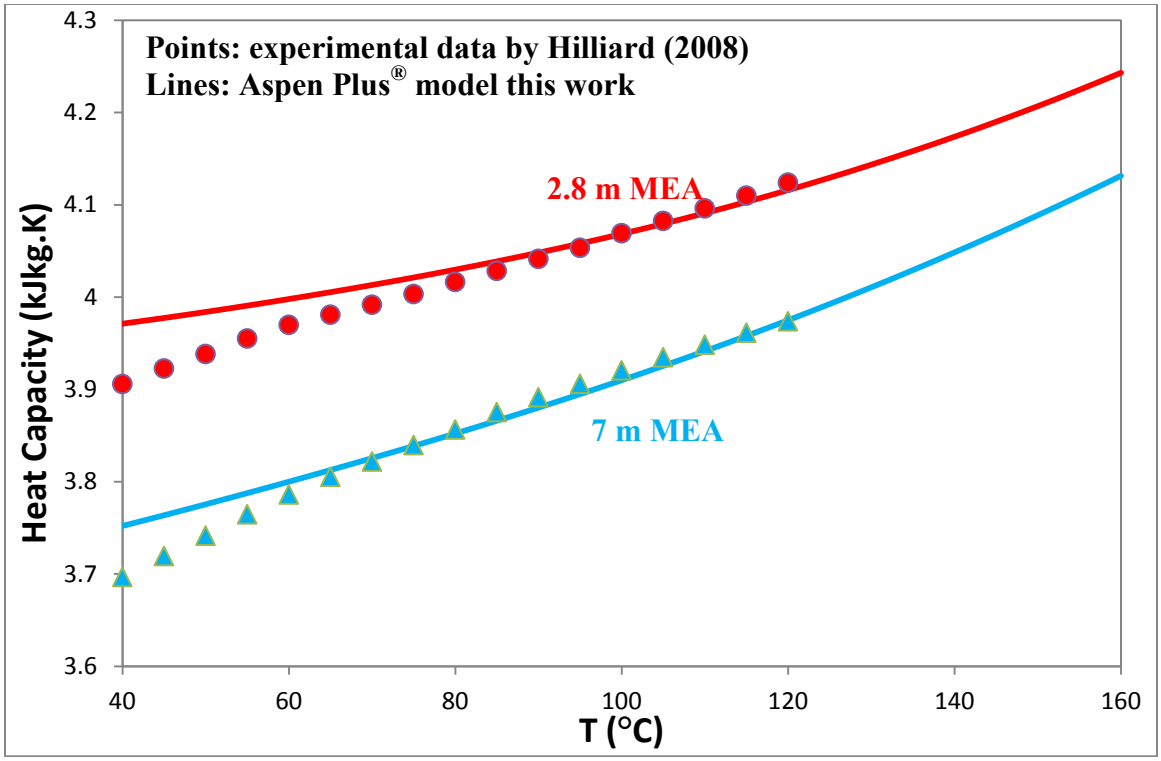

Figure 4-6: Specific Heat Capacity in MEA-H_2O

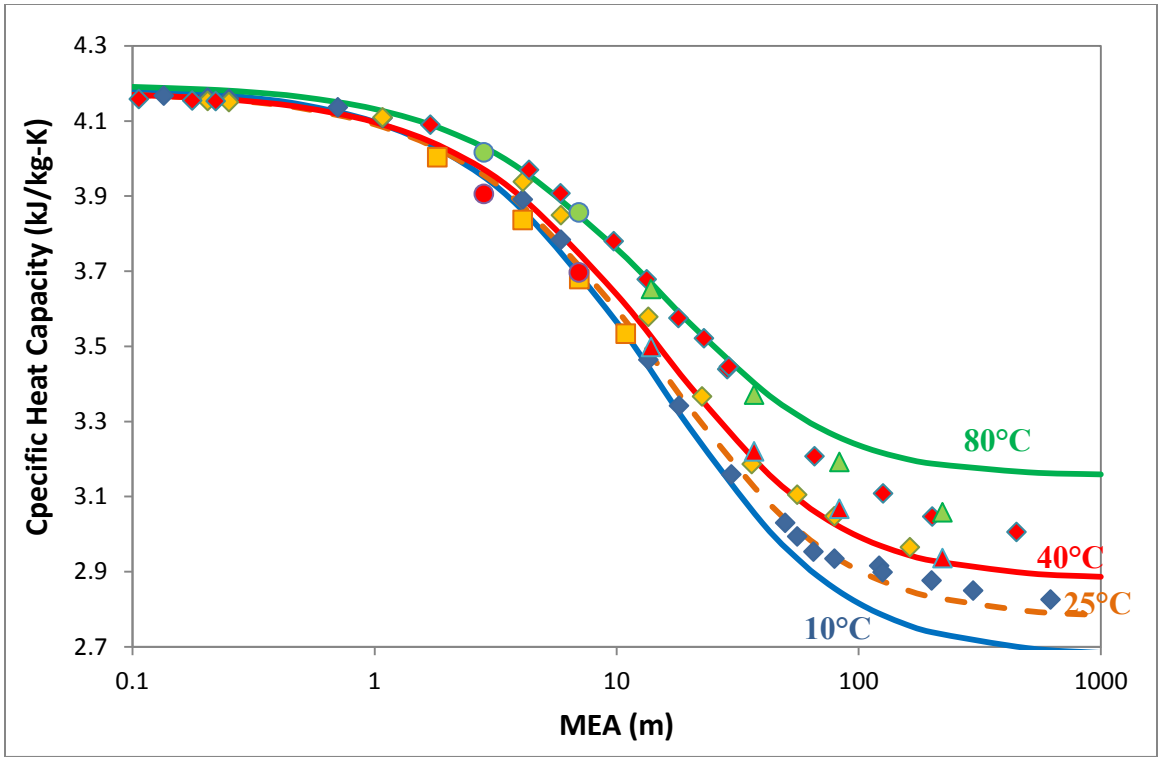

Figure 4-7: Comparison of Specific Heat Capacity of MEA-H_2O with Literature.
♦: Page et al. (1993); ■: Weiland et al. (1997); ▲: Chiu et al. (1999); ●: Hilliard (2008); Lines: Aspen Plus® Model this work

After matching the MEA volatility data and the specific heat capacity, DGAQFM and DHAQFM of $MEAH^+$ were adjusted manually to fit the pK_a of $MEAH^+$ in literature. Firstly DGAQFM was adjusted to match pK_a at 25°C, the reference temperature, then DHAQFM was adjusted to match the temperature dependence of pK_a. Figure 4-8 shows the pK_a comparison of the literature data and the model prediction. The temperature dependence fitting of this model is improved from Hilliard's MEA model (2008) because of the adding of the new high temperature experimental pK_a by Hamborg and Versteeg (2009).

$$MEA + H^+ \overset{K_a}{\leftrightarrow} MEAH^+ \tag{4-14}$$

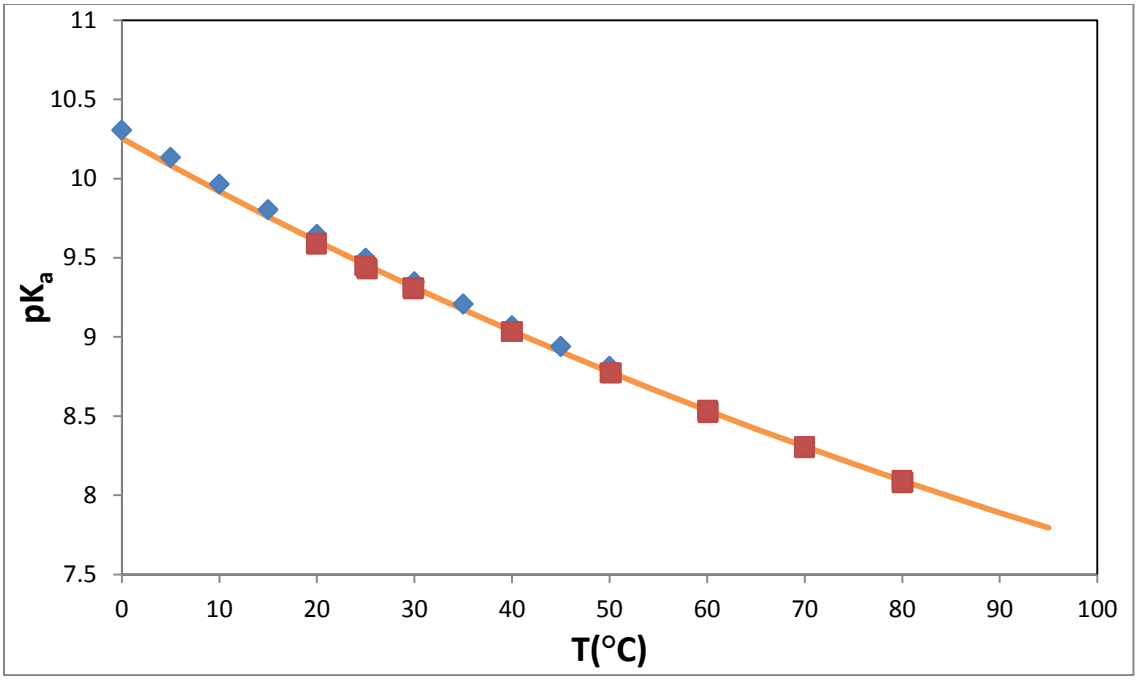

Figure 4-8: Comparison of pK_a of MEA, Molality Based, Asymmetric. ♦: Bates and Pinching (1951); ■: Hamborg and Versteeg (2009); line: Aspen Plus® model this work.

4.3 Data Regression of MEA-CO_2-H_2O without MEACOOH (Model A)

The regression of MEA-CO_2-H_2O was based on the MEA-H_2O regression in this work. To better predict all the experimental data, especially those for 7 m MEA, an additional species MEACOOH was considered for addition to the model. Therefore two different models were developed, one without MEACOOH (Model A) and one with MEACOOH (Model B). Model A will be discussed in this section and Model B will be discussed in 4.4.

4.3.1 Model A Development

In Hilliard's MEA-CO_2-H_2O model (2008), partial pressure of CO_2, MEA volatility, heat of absorption of CO_2, speciation, and specific heat capacity were regressed. However, the heat of absorption data may have systematic error as discussed in Chapter 2, MEA volatility data at below 45°C are suspicious as discussed in Chapter 3,

and there may be inconsistency among different data sets which makes the regression more difficult to converge. To reduce the complexity of the regression and reduce the inconsistency, selected data were incorporated in this work. Table 4-10 gives the data used in the three MEA models. P_{MEA} by Hilliard (2008) below 45°C was not used; P_{CO2} by Dugas et al. (2009) at 0.47 and higher loading was not used.

Table 4-10: Data used in the MEA-CO_2-H_2O Models

	Hilliard (2008)	**This work Model A**	**This work Model B**
P_{CO2}, Goldman and Leibush (1959)	X		
P_{CO2}, Lawson and Garst (1976)	X		
P_{CO2}, Lee et al. (1976), corrected	X	High loading	
P_{CO2}, Jou et al. (1995)	X	High loading	X
P_{CO2}, Ma'mun et al. (2005)	X		X
P_{CO2}, Hilliard (2008)	X	X	X
P_{MEA}, Hilliard (2008)	X	X	X
Specific heat capacity, Hilliard (2008)	X	X	X
Heat of absorption of CO_2, Kim et al. (2007)	X		
NMR speciation, Poplsteinova (2004)	X		
NMR speciation, Hilliard (2008)	X		
P_{CO2}, Dugas et al. (2009)		X	X
Total pressure, this work		X	X
P_{MEA}, this work		X	X
P_{CO2}, Aronu et al. (2011)			7 m MEA
pK_a of MEACOOH, McCann et al. (2009)			X

The data sets were assigned with different weights as in Table 4-11 to optimize the regression.

Table 4-11: Weights of the Data Sets in Model A

Data sets	Weight
Specific heat capacity in 7 m MEA, Hilliard (2008)	9
P_{CO2} in 7 and 11 m MEA, Hilliard (2008)	25
P_{CO2} in 3.5 m MEA, Hilliard (2008)	1
P_{MEA} in 7 and 11 m MEA, Hilliard (2008)	10
P_{MEA} in 3.5 m MEA, Hilliard (2008)	1
Total pressure, this work	18
P_{CO2}, Dugas et al. (2009)	8
P_{MEA}, this work	8
P_{MEA} at high loading, Hilliard (2008) and this work	18
P_{CO2} at high loading by Hilliard (2008), Lee et al. (1976) corrected, Jou et al. (1995)	10.5

Hilliard used five reactions in the model (2008):

$$H_2O \leftrightarrow H^+ + OH^- \quad (4\text{-}15)$$

$$CO_2 + H_2O \leftrightarrow H^+ + HCO_3^- \quad (4\text{-}16)$$

$$HCO_3^- \leftrightarrow H^+ + CO_3^{-2} \quad (4\text{-}17)$$

$$MEAH^+ \leftrightarrow MEA + H^+ \quad (4\text{-}18)$$

$$MEACOO^- + H_2O \leftrightarrow MEA + HCO_3^- \quad (4\text{-}19)$$

The carbonate and hydroxide concentration is very small over the whole loading range at the studied condition, thus the formation of hydroxide and carbonate (4-15) and (4-17) can be neglected. The chemical reactions were reduced to two main reactions for

easier convergence of the model. Reaction (4-20) and (4-21) are the main reactions at low and high CO_2 loading, respectively.

$$2MEA + CO_2 \leftrightarrow MEACOO^- + MEA^+ \quad (4\text{-}20)$$

$$MEA + H_2O + CO_2 \leftrightarrow MEA^+ + HCO_3^- \quad (4\text{-}21)$$

4.3.2 Model A Results

Table 4-12 lists the regression results and standard deviation of the parameters. Standard deviation 0 means the value was fixed in the final regression according to Aspen Plus® defaults or the results from a previous regression run. A very large standard deviation on the order of 1.0E11 means the value is on the regression bound or hits the limit in the data regression system in Aspen Plus®, but the value is still a good result.

Table 4-12: The Regressed Parameters of MEA-CO_2-H_2O System in Model A

#	Parameter	Component i	Component j	Value (SI units)	Standard deviation
1	DGAQFM/1	MEACOO-		-494,206,376	1,209,692
2	DHAQFM/1	MEACOO-		-731,086,866	1.13E+07
3	DHAQFM/1	MEA+		-338,000,000	12,138,474
4	CPAQ0/1	MEA+		183,474	926,721
5	CPAQ0/2	MEA+		18	526
6	CPAQ0/3	MEA+		0.47	6.83
7	CPAQ0/4	MEA+		0	0
8	CPAQ0/1	MEACOO-		-91,454	1,049,020
9	CPAQ0/2	MEACOO-		-2.7	75.5
10	CPAQ0/3	MEACOO-		0.8	7.9
11	CPAQ0/4	MEACOO-		0	0
12	GMELCC/1	H2O	(MEA+,MEACOO-)	9.42	0.80
13	GMELCD/1	H2O	(MEA+,MEACOO-)	0	0
14	GMELCE/1	H2O	(MEA+,MEACOO-)	0	0
15	GMELCC/1	(MEA+,MEACOO-)	H2O	-4.28	0.29
16	GMELCD/1	(MEA+,MEACOO-)	H2O	0	0
17	GMELCE/1	(MEA+,MEACOO-)	H2O	0	0
18	GMELCC/1	MEA	(MEA+,MEACOO-)	15.59	5.04

#	Parameter	Component i	Component j	Value (SI units)	Standard deviation
19	GMELCD/1	MEA	(MEA+,MEACOO-)	0	0
20	GMELCE/1	MEA	(MEA+,MEACOO-)	0	0
21	GMELCC/1	(MEA+,MEACOO-)	MEA	-9.23	0.58
22	GMELCD/1	(MEA+,MEACOO-)	MEA	0	0
23	GMELCE/1	(MEA+,MEACOO-)	MEA	0	0
24	GMELCC/1	H2O	(MEA+,HCO3-)	9.00	2.47
25	GMELCD/1	H2O	(MEA+,HCO3-)	0	0
26	GMELCE/1	H2O	(MEA+,HCO3-)	0	0
27	GMELCC/1	(MEA+,HCO3-)	H2O	-4.39	0.99
28	GMELCD/1	(MEA+,HCO3-)	H2O	0	0
29	GMELCE/1	(MEA+,HCO3-)	H2O	0	0
30	GMELCC/1	MEA	(MEA+,HCO3-)	12.34	9.39
31	GMELCD/1	MEA	(MEA+,HCO3-)	0	0
32	GMELCE/1	MEA	(MEA+,HCO3-)	0	0
33	GMELCC/1	(MEA+,HCO3-)	MEA	-3.47	8.81
34	GMELCD/1	(MEA+,HCO3-)	MEA	0	0
35	GMELCE/1	(MEA+,HCO3-)	MEA	0	0

Table 4-13 shows the correlation matrix of the Model A regression. The parameter number corresponds to the numbers in Table 4-12. Coefficients for non-regressed parameters are all zero and are not shown in Table 4-13.

Table 4-13: Parameter Correlation Matrix of Model A

	1	2	3	4	5	6	8	9	10	12	15	18	21	24	27	30	33
1	1.00																
2	0.04	1.00															
3	0.05	-0.95	1.00														
4	0.04	0.80	-0.84	1.00													
5	-0.08	0.14	-0.09	0.01	1.00												
6	0.00	-0.77	0.80	-0.97	-0.22	1.00											
8	-0.14	-0.69	0.68	-0.90	-0.14	0.91	1.00										
9	0.07	0.21	-0.28	0.41	-0.90	-0.21	-0.24	1.00									
10	0.14	0.60	-0.59	0.84	0.15	-0.87	-0.99	0.21	1.00								
12	0.74	-0.11	0.13	-0.13	-0.15	0.18	0.09	0.05	-0.09	1.00							
15	-0.46	0.14	-0.15	0.22	0.14	-0.26	-0.23	-0.02	0.23	-0.92	1.00						
18	-0.28	0.20	-0.24	0.07	0.03	-0.08	-0.01	0.00	0.01	-0.24	0.06	1.00					
21	-0.60	-0.01	0.04	0.03	0.09	-0.06	0.02	-0.07	-0.02	-0.71	0.62	-0.23	1.00				
24	-0.33	0.40	-0.43	0.30	0.06	-0.29	-0.25	0.06	0.24	-0.58	0.59	0.20	0.32	1.00			
27	0.23	-0.31	0.33	-0.25	-0.04	0.25	0.25	-0.05	-0.25	0.53	-0.59	-0.10	-0.31	-0.98	1.00		
30	-0.22	0.12	-0.17	-0.08	-0.04	0.08	0.06	0.02	-0.02	-0.12	0.05	0.23	-0.25	0.26	-0.24	1.00	
33	0.33	-0.40	0.45	-0.25	-0.11	0.26	0.14	-0.08	-0.08	0.31	-0.25	-0.19	0.08	-0.19	0.08	-0.49	1.00

Figure 4-9 gives the CO_2 solubility in 7 m MEA predicted by Model A. The model fits the data well up to 100°C. At 120 to 140°C low CO_2 loading and at 160°C the model over-predicts CO_2 partial pressure. This results in a high CO_2 heat of absorption at the high temperature. Figure 4-10 magnifies the high temperature / high loading part from Figure 4-9.

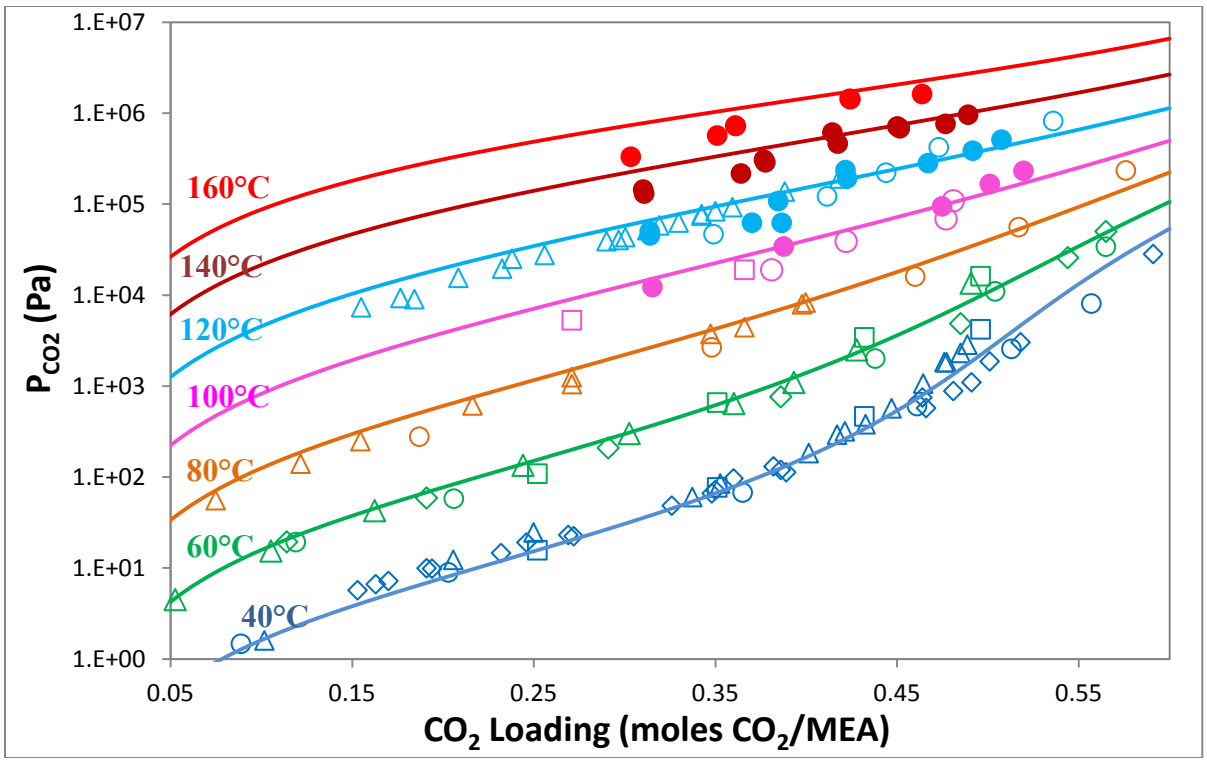

Figure 4-9: Prediction of CO_2 Solubility in 7 m MEA by Model A. **●: this work; ○: Jou et al. (1995); □: Dugas et al. (2009); ◊: Hilliard (2008); Δ: Ma'mun et al. (2005); solid lines: Model A for 7 m MEA.**

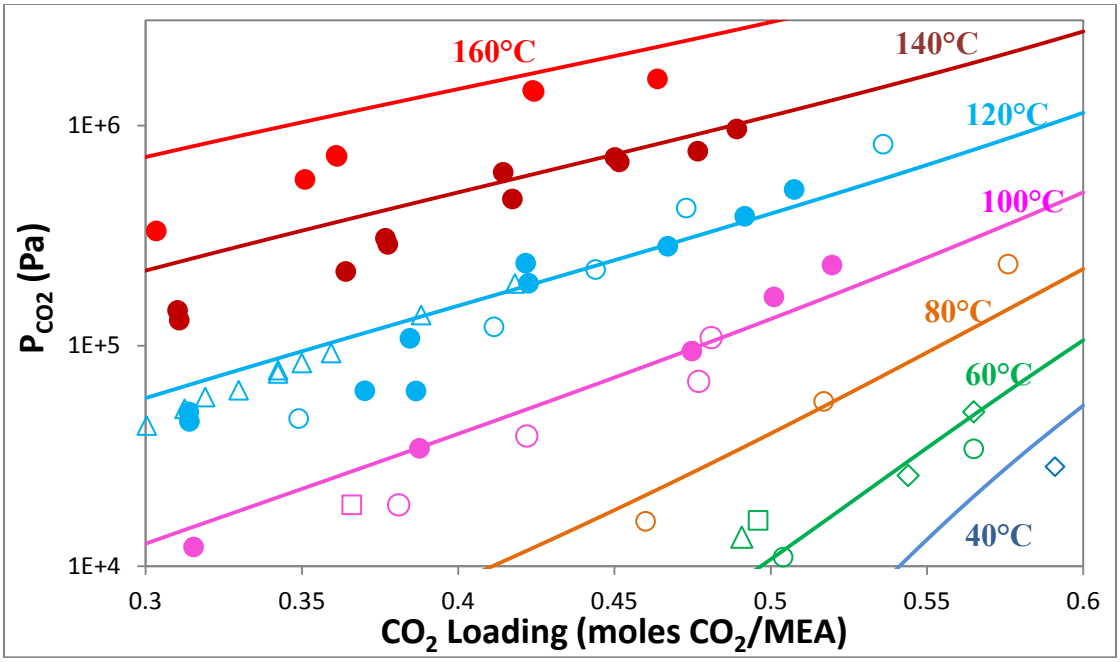

Figure 4-10: Prediction of CO_2 Solubility in 7 m MEA by Model A at High Temperature and High Loading. **●: this work; ○: Jou et al. (1995); □: Dugas et al. (2009); ◊: Hilliard (2008); Δ: Ma'mun et al. (2005); solid lines: Model A for 7 m MEA.**

Figure 4-11 compares the CO_2 heat of absorption prediction with the measured $-\Delta H_{abs}$ by Kim et al. (2007). The predicted heat of absorption was obtained by calculating P_{CO2} and the fugacity coefficient φ_{CO2} at T and T+dT in Aspen Plus® Analysis, then use the accurate form of Equation (2-12):

$$-\Delta H_{abs} = R\left(\frac{\partial ln f_{CO_2(g)}}{\partial \frac{1}{T}}\right)_{P,x} = R \cdot \frac{P_{CO2}(T+dT)\varphi_{CO2}(T+dT) - P_{CO2}(T)\varphi_{CO2}(T)}{\frac{1}{T+dT} - \frac{1}{T}}.$$

Therefore this is a differential ΔH_{abs}. The difference from the empirical derivation is that CO_2 fugacity instead of CO_2 partial pressure is used so this calculation is more accurate then the empirical model.

The predicted temperature dependence is unexpected, especially between 0.2 and 0.5 loading. The slope of $-\Delta H_{abs}$ at 120 and 160°C is too large at low loading, where -

ΔH_{abs} is expected to be relative constant. The absolute value of 40 and 80°C $-\Delta H_{abs}$ is too large compared with the measured $-\Delta H_{abs}$ by Kim et al. (2007) and the $-\Delta H_{abs}$ derived from CO_2 partial pressure in this work at lower than 0.5 loading, and is too small above 0.5 loading.

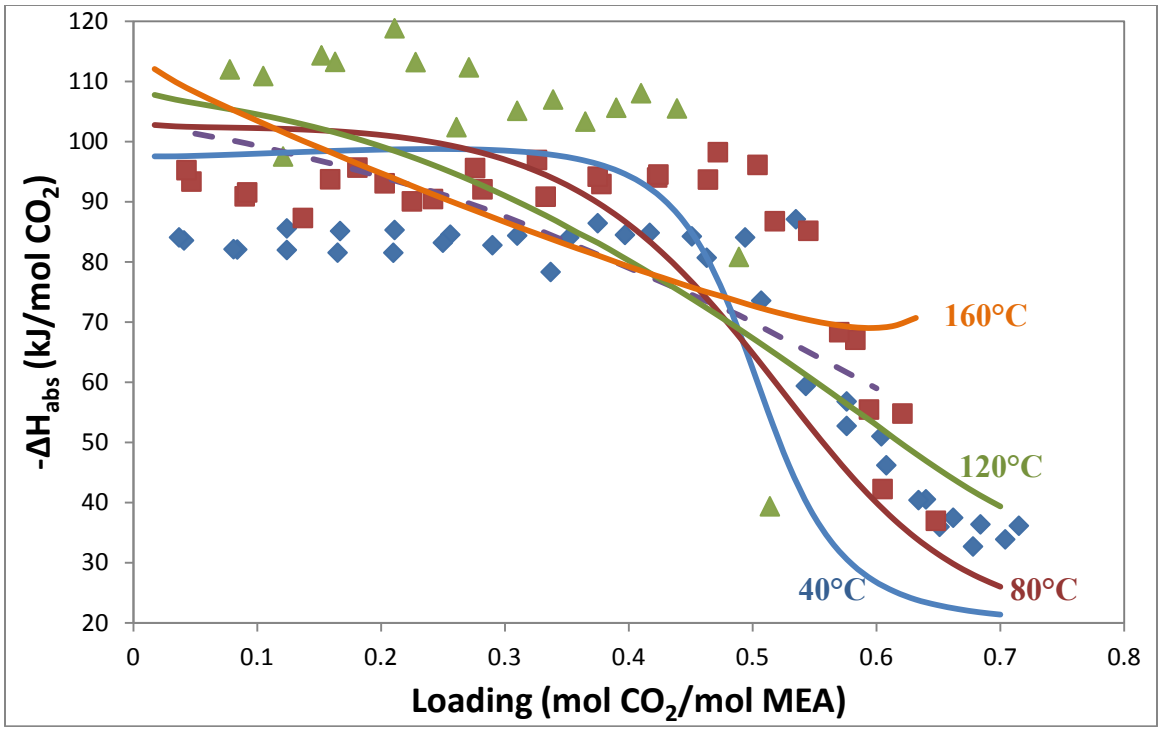

Figure 4-11: Comparison of Heat of Absorption of CO_2 in 7 m MEA with Model A.
Data points: Kim et al. (2007), ◊: 40°C, □: 80°C, Δ: 120°C; solid lines: Model A; dashed line: empirical model from this work

Figure 4-12 and Figure 4-13 show the prediction of the normalized MEA volatility by Model A. The same data sets are presented; Figure 4-13 uses CO_2 loading as the horizontal axis instead of P_{CO2}. Since the 40°C MEA volatility data were considered with error and not used in the regression, only the other temperature data were compared. Model A predicts data well at low CO_2 loading but over-predicts MEA volatility at high loading.

Figure 4-14 gives the MEA enthalpy of vaporization in 7 m MEA. $-\Delta H_{vap,MEA}$ was calculated in the same derivative method as $-\Delta H_{abs}$ of CO_2. Instead of P_{CO2} and φ_{CO2}, P_{MEA} and φ_{MEA} were obtained from Aspen Plus®. $-\Delta H_{vap,MEA}$ is larger than the value given by Hilliard's MEA model (Figure 3-11), probably because new MEA volatility data were included in Model A and previous data below 46°C were deleted from the regression. However the prediction at high CO_2 loading may not be reliable, because of the over-prediction of P_{MEA} at high loading.

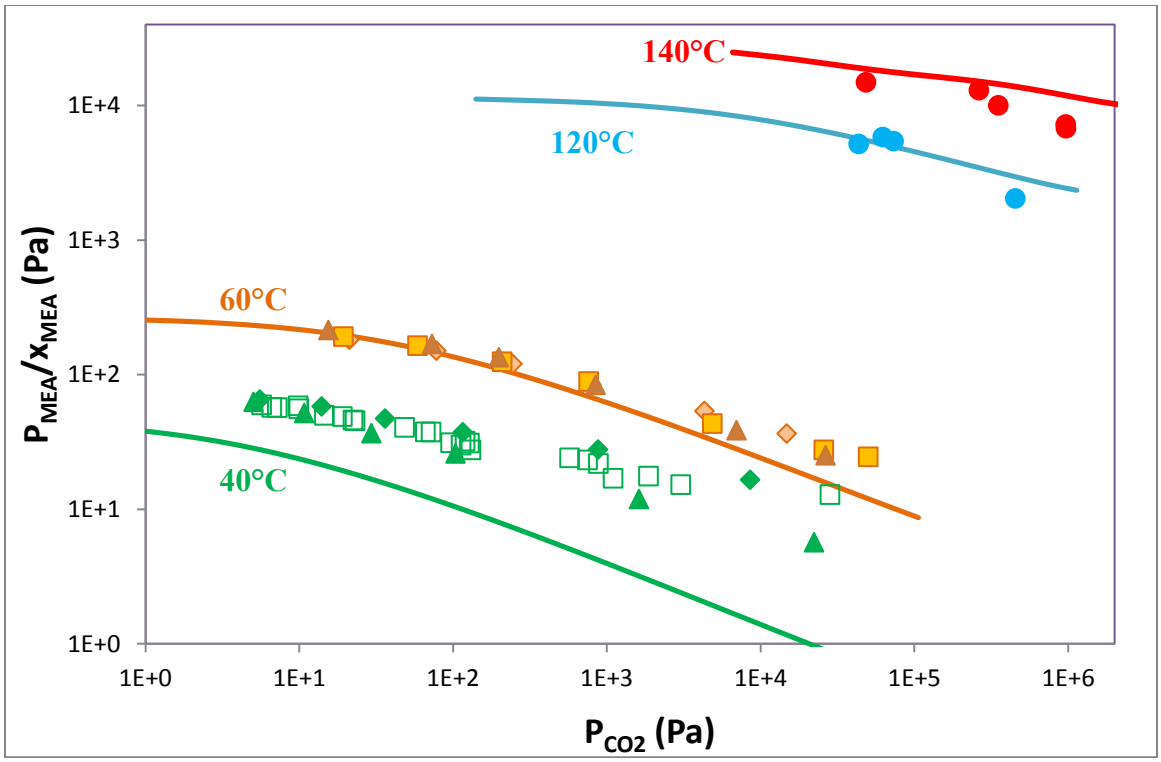

Figure 4-12: Prediction of Normalized MEA Partial Pressure over MEA-CO_2-H_2O (1) by Model A. **Hilliard (2008) MEA: ♦ 3.5 m, ■ 7 m, ▲ 11 m; ●: this work; solid lines: Model A - 7 m MEA.** $x_{MEA} = \frac{\text{mol of total MEA}}{\text{mol of total MEA + mol of } H_2O}$.

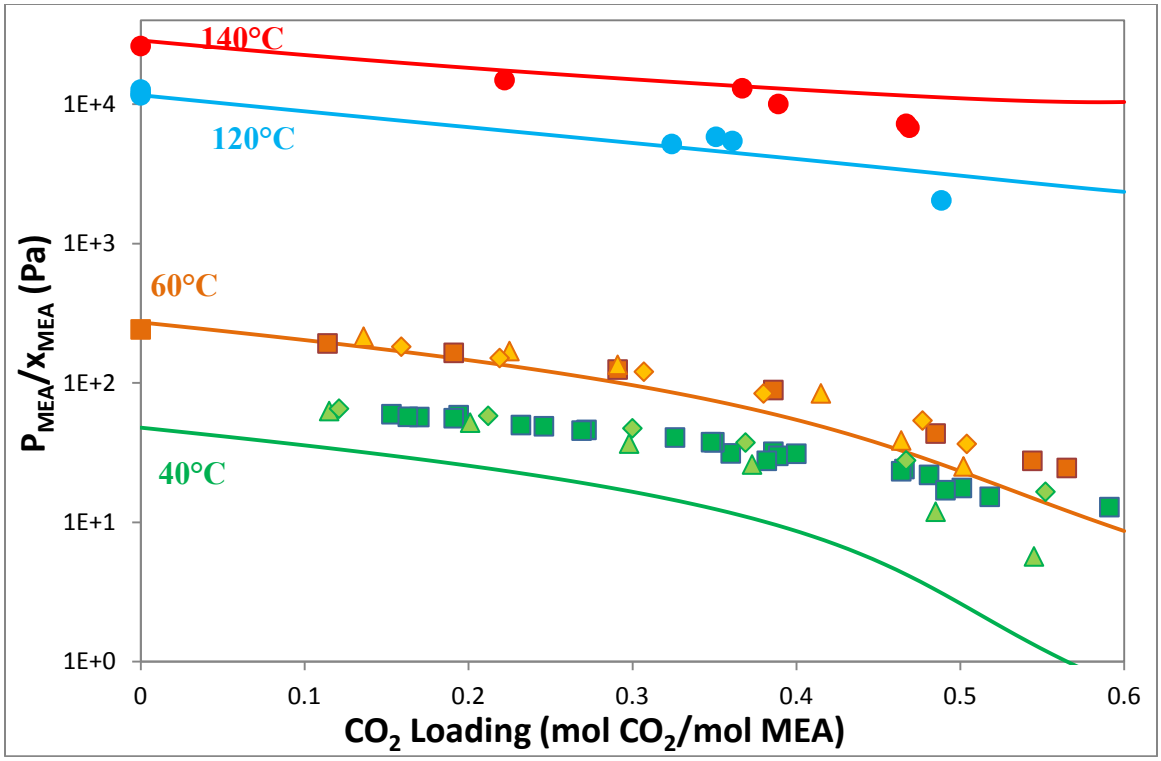

Figure 4-13: Prediction of Normalized MEA Partial Pressure over MEA-CO_2-H_2O (2) by Model A. Hilliard (2008) MEA: ♦ 3.5 m, ■ 7 m, ▲ 11 m; ●: this work; solid lines: Model A - 7 m MEA. $x_{MEA} = \frac{\text{mol of total MEA}}{\text{mol of total MEA + mol of } H_2O}$.

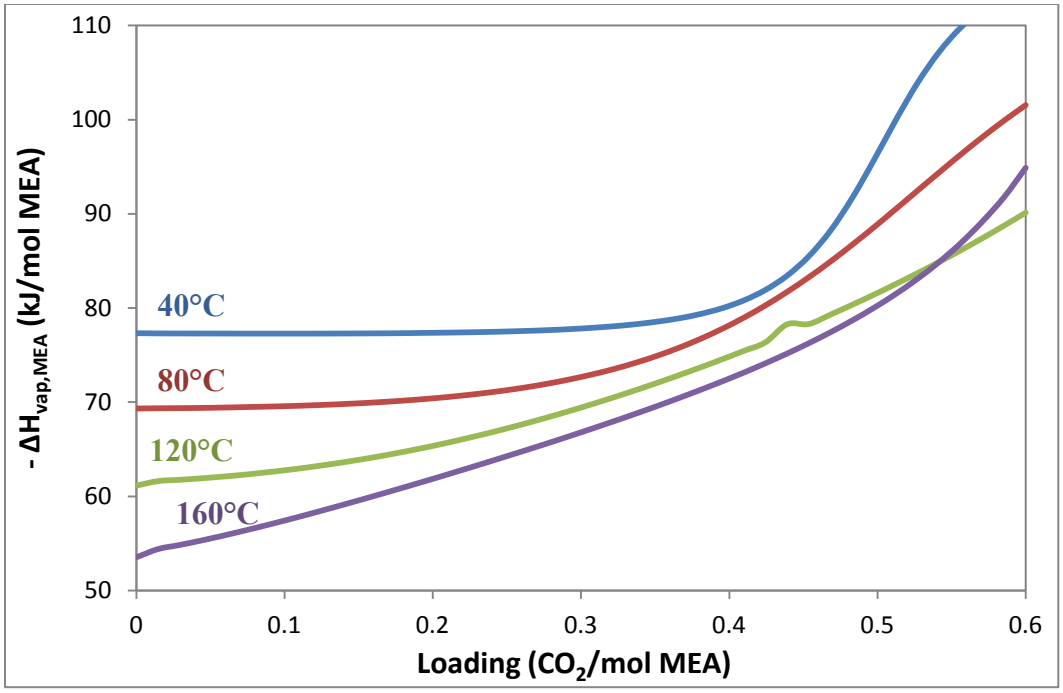

Figure 4-14: Enthalpy of Vaporization of MEA in 7 m MEA by Model A

Figure 4-15 gives the prediction of total pressure over CO_2 loaded 7 m MEA. The model predicts well at low CO_2 loading, but under-predicts the data at high loading. Considering Figure 4-9, Model A may over-predict P_{CO2} at low loading and under-predict P_{H2O} at high loading. The total pressure data by Aronu et al. (2011) was not incorporated in Model A, and there are some differences between the total pressure data by Aronu et al. (2011) and from this work as shown in Figure 4-15.

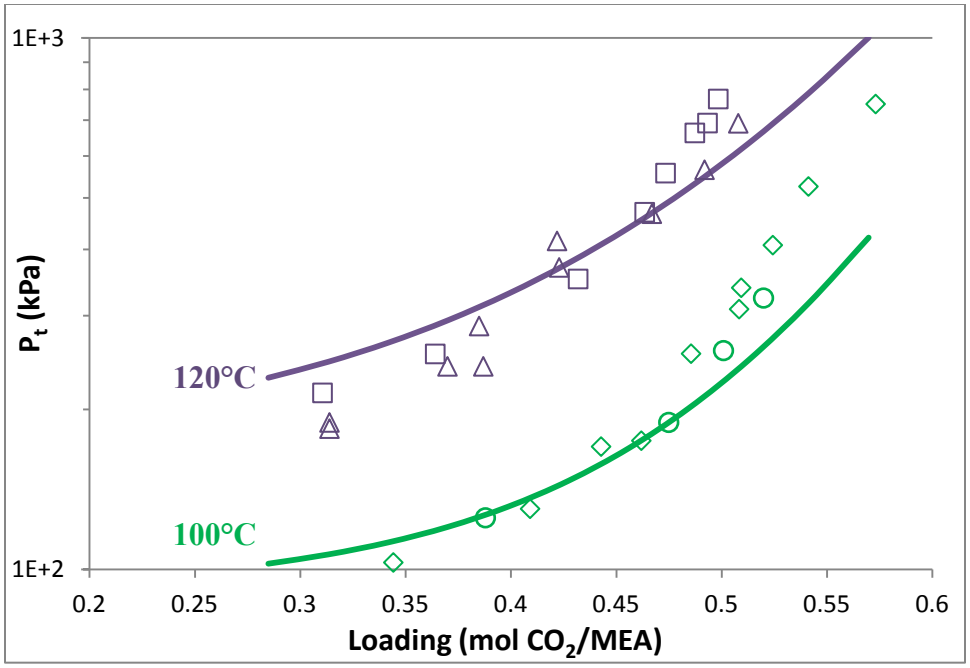

Figure 4-15: Prediction of Total Pressure in 7 m MEA by Model A. ○: 100°C this work; ◊: 100°C Aronu et al. (2011); Δ: 120°C this work; □: 120°C Aronu et al. (2011); Lines: Model A.

Figures 4-16 and 4-17 are the specific heat capacity comparison of Model A and experimental data. The model fairly predicts the data and the temperature dependence of the specific heat capacity.

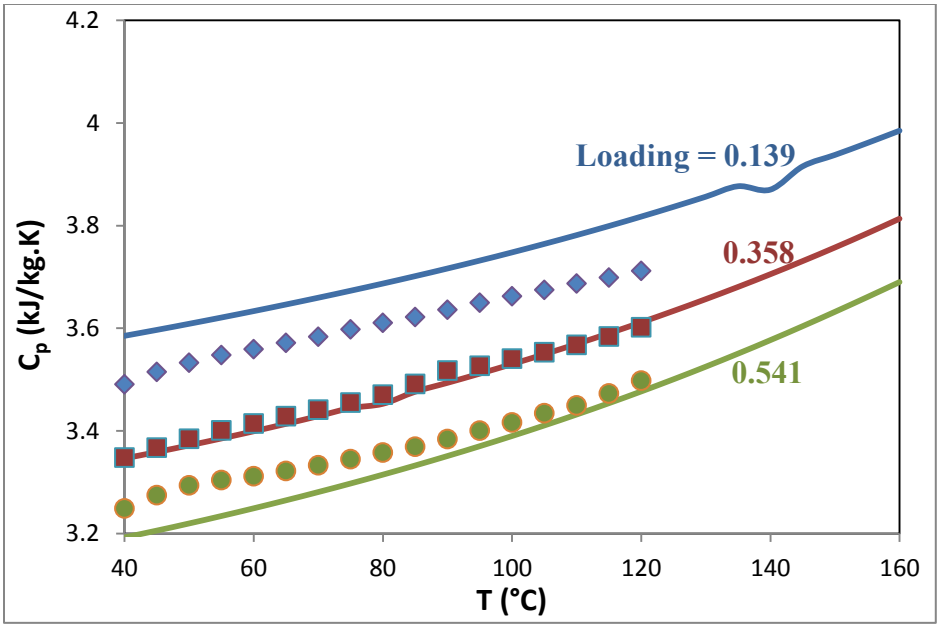

Figure 4-16: Prediction of Specific Heat Capacity of 7 m MEA by MEA-CO_2-H_2O Model A. Experimental data points (Hilliard 2008): ♦ 0.139 loading, ■ 0.358 loading, ● 0.541 loading; lines: Model A.

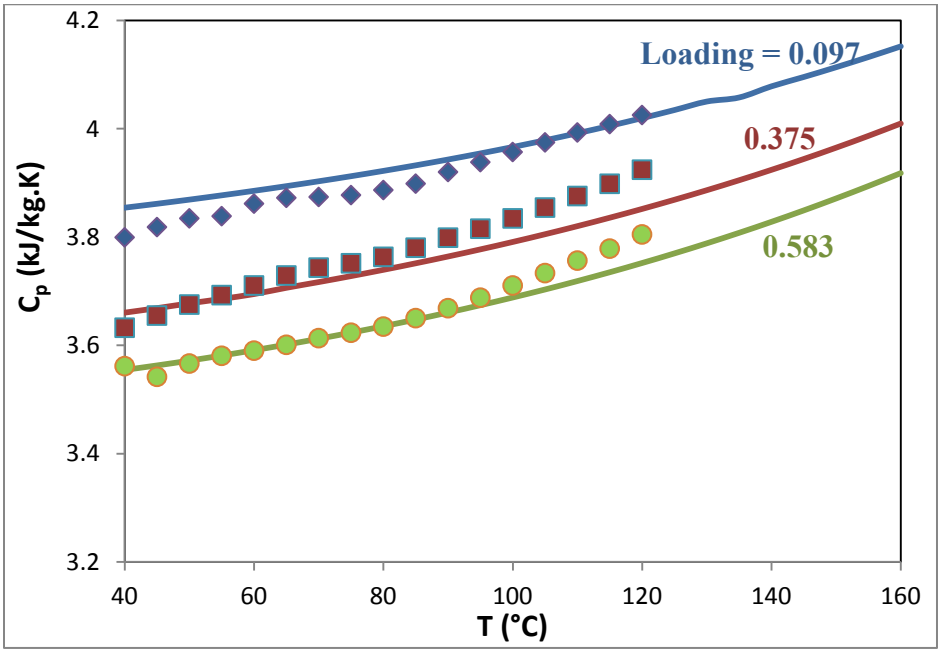

Figure 4-17: Prediction of Specific Heat Capacity of 3.5 m MEA by MEA-CO_2-H_2O Model A. Experimental data points (Hilliard 2008): ♦ 0.097 loading, ■ 0.375 loading, ● 0.583 loading; lines: Model A.

Figure 4-18 and 4-19 compare the predicted speciation by Model A and the experimental NMR data. Model A predicts the data well over the whole CO_2 loading range.

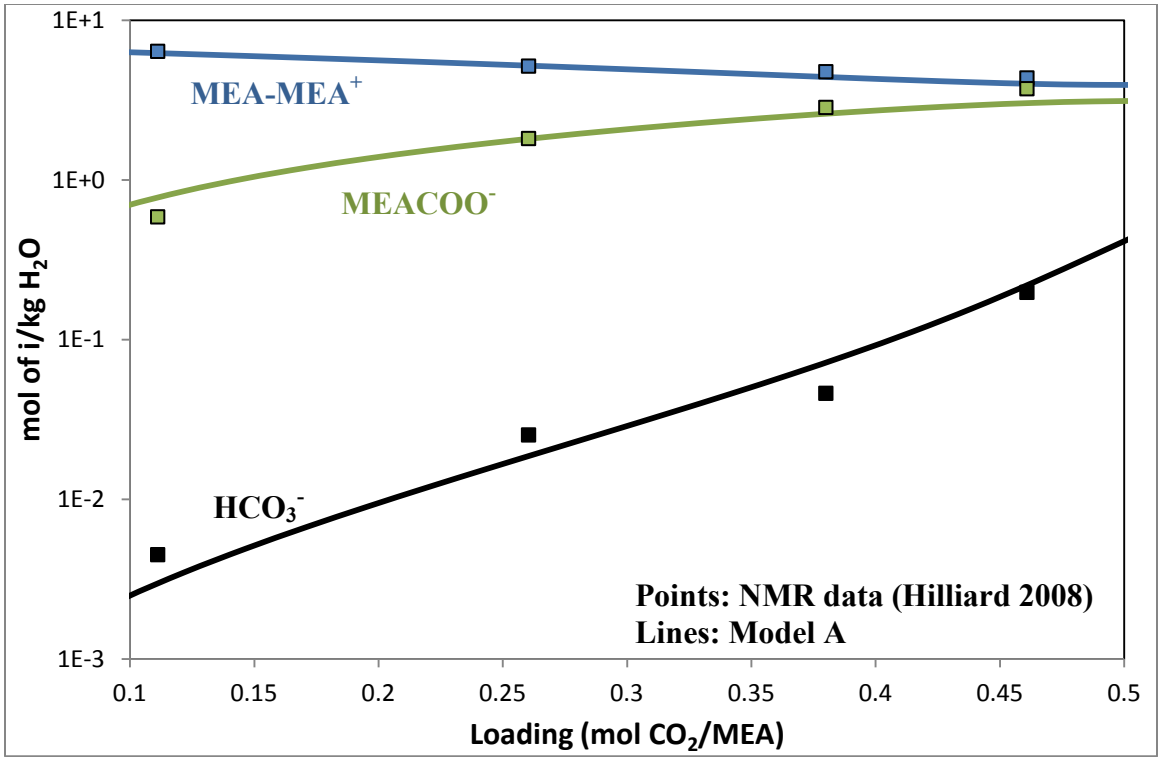

Figure 4-18: Speciation of 7 m MEA at 40 ℃ (1) by Model A

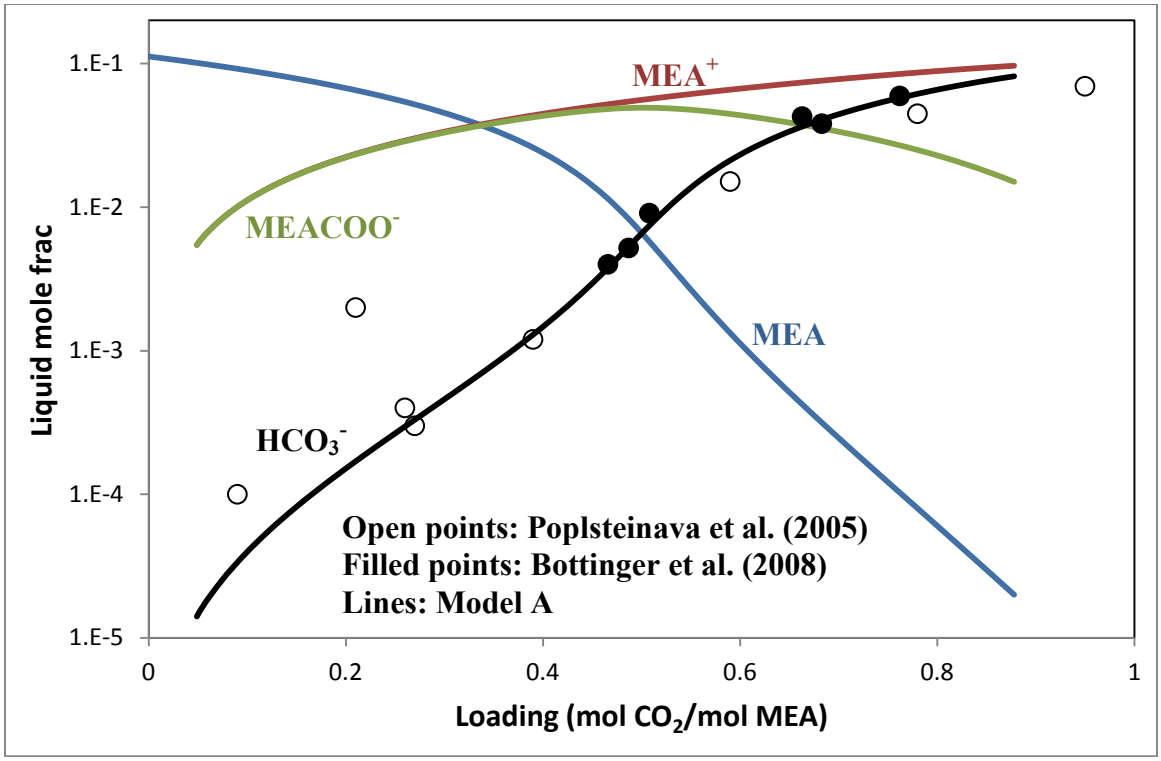

Figure 4-19: Speciation of 7 m MEA at 40 ℃ (2) by Model A

4.3.3 Model A Conclusions

For 7 m MEA, Model A predicts the CO_2 partial pressure up to 100°C, but over-predicts CO_2 partial pressure above 120°C at low CO_2 loading. Therefore as the temperature dependence of P_{CO2}, the CO_2 heat of absorption prediction by Model A is not accurate. P_{MEA} well predicted well except at high CO_2 loading. Enthalpy of vaporization of MEA is generally well-behaved but may not be accurate at high loading. Total pressure is under-predicted at 100 and 120°C at 0.48 and higher loading. Specific heat capacity at 40-120°C and speciation of CO_2 loaded MEA at 40°C are well predicted.

Therefore the major problems with Model A exist above 120°C and 0.48 CO_2 loading. To solve these problems, a new species MEACOOH was added and Model B was developed.

4.4 REGRESSION OF MEA-CO_2-H_2O WITH MEACOOH (MODEL B)

4.4.1 Model B Development

Caplow (1968) proposed the zwitterion mechanism for reactions of amines with CO_2. In this mechanism, the zwitterion MEACOOH serves as an intermediate as follows:

$$MEA + CO_2 \leftrightarrow MEACOOH \text{ (zwitterion)} \quad (4\text{-}22)$$

$$MEA + MEACOOH \leftrightarrow MEAH^+ + MEACOO^- \quad (4\text{-}23)$$

McCann et al. (2009) measured the equilibrium constants for the following reaction of zwitterion:

$$MEACOO^- + H^+ \overset{K}{\leftrightarrow} MEACOOH \quad (4\text{-}24)$$

Log K (M^{-1}) was reported as 7.49 at 30°C, which is the pK_a of MEACOOH.

Several experimental (Hikita et al. 1977 and 1979, Penny et al. 1983, Alper et al. 1990, Ali et al. 2005) and theoretical (da Silva et al. 2004, Arstad et al. 2007, Shim et al. 2009, Xie et al. 2010) studies have been done to the MEA reactions with CO_2. The other two mechanisms are:

$$MEA + CO_2 \leftrightarrow MEAH^+ + MEACOO^- \quad (4\text{-}25)$$

And

$$MEA + CO_2 \leftrightarrow MEACOOH \text{(carbamic acid)} \quad (4\text{-}26)$$

$$MEA + MEACOOH \leftrightarrow MEAH^+ + MEACOO^- \quad (4\text{-}27)$$

It was found that 2-oxazolidone was formed in the MEA thermal degradation (Polderman 1955, David 2009):

$$MEAH^+ + MEACOO^- \leftrightarrow MEA + H_2O + \quad (4\text{-}28)$$

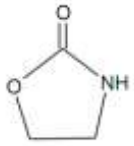

To better fit the data, a new species MEACOOH representing the above molecules zwitterion, carbamic acid, and 2-oxazolidone, was added to the MEA-CO_2-H_2O model and related parameters were added in the regression. To simplify the statement, this new species will be referred to as zwitterions or MEACOOH in this dissertation. Reaction (4-22) was added to the chemistry of the regression.

This model is referred to as Model B. The model was regressed to match the pK_a by McCann et al. (2009) as shown in Figure 4-20.

The data sets were assigned with different weights as in Table 4-14 to optimize the regression.

Table 4-14: Weights of the Data Sets in Model B

Data sets	Weight
Specific heat capacity in 7 m MEA, Hilliard (2008)	9
P_{CO2} in 7 and 11 m MEA, Hilliard (2008)	30
P_{CO2} in 3.5 m MEA, Hilliard (2008)	1
P_{MEA} in 7 and 11 m MEA, Hilliard (2008)	15
P_{MEA} in 3.5 m MEA, Hilliard (2008)	1
P_{CO2}, Jou et al. (1995)	3
P_{CO2}, Ma'mun et al. (2005)	5
Total pressure, this work	8
P_{CO2}, Dugas et al. (2009)	5
P_{CO2} in 7 m MEA, Aronu et al. (2011)	3
P_{MEA}, this work	8
P_{MEA} at high loading, Hilliard (2008) and this work	25

The following parameters of MEACOOH were set before the regression:

Molecular weight: 105.09 g/mol

Charge: 0

VLBROC: 0.0464 m^3/kmol (same as H_2O)

PLXANT/1: -1.0E20 kPa

HENRY/1 in H_2O: -10 bar

CPIG/1,2,3: 51338, -9.93, and 0.085 (same as CPAQ0/1,2,3 of $MEACOO^-$)

4.4.2 Model B Results

The regressed parameters are presented in Table 4-15. Standard deviation 0 means the parameter value was fixed in the final regression according to Aspen Plus® defaults or the results from a previous regression run. The standard deviation of DHFORM of MEACOOH was a large number on the order of 1.0E11, which means the value is on the regression bound or hits the limit in the data regression system in Aspen Plus®, but the value is still a good result. A sensitivity analysis will be performed to address the uncertainty in DHFORM of MEACOOH.

Table 4-15: Regressed Parameters in MEA-CO_2-H_2O Model B

#	Parameter	Component i	Component j	Value (SI units)	Standard deviation
1	DGAQFM/1	MEACOO-		-495,247,152	1,549,450
2	DHAQFM/1	MEACOO-		-721,181,462	31,069,098*
3	DHAQFM/1	MEA+		-339,000,000	29,274,874*
4	CPAQ0/1	MEA+		-469	4601
5	CPAQ0/2	MEA+		69	709
6	CPAQ0/3	MEA+		1.48	2.03
7	CPAQ0/4	MEA+		0	0
8	CPAQ0/1	MEACOO-		51,338	64675*
9	CPAQ0/2	MEACOO-		-9.93	114*
10	CPAQ0/3	MEACOO-		0.085	0.784*
11	CPAQ0/4	MEACOO-		0	0
12	CPIG/1	MEACOOH		51,338**	0

#	Parameter	Component i	Component j	Value (SI units)	Standard deviation
13	CPIG/2	MEACOOH		-9.93**	0
14	CPIG/3	MEACOOH		0.085**	0
15	CPIG/4	MEACOOH		0	0
16	CPIG/5	MEACOOH		0	0
17	CPIG/6	MEACOOH		0	0
18	CPIG/7	MEACOOH		0	0
19	DGFORM/1	MEACOOH		-505,389,210	6,643,988*
20	DHFORM/1	MEACOOH		-746,624,005	N/A
21	GMELCC/1	H2O	(MEA+,MEACOO-)	8.74	1.73
22	GMELCD/1	H2O	(MEA+,MEACOO-)	0	0
23	GMELCE/1	H2O	(MEA+,MEACOO-)	0	0
24	GMELCC/1	(MEA+,MEACOO-)	H2O	-4.19	0.58
25	GMELCD/1	(MEA+,MEACOO-)	H2O	0	0
26	GMELCE/1	(MEA+,MEACOO-)	H2O	0	0
27	GMELCC/1	MEA	(MEA+,MEACOO-)	6.36	2.71
28	GMELCD/1	MEA	(MEA+,MEACOO-)	0	0
29	GMELCE/1	MEA	(MEA+,MEACOO-)	0	0
30	GMELCC/1	(MEA+,MEACOO-)	MEA	-4.97	2.90
31	GMELCD/1	(MEA+,MEACOO-)	MEA	0	0
32	GMELCE/1	(MEA+,MEACOO-)	MEA	0	0
33	GMELCC/1	H2O	(MEA+,HCO3-)	10.28	1.64
34	GMELCD/1	H2O	(MEA+,HCO3-)	0	0
35	GMELCE/1	H2O	(MEA+,HCO3-)	0	0
36	GMELCC/1	(MEA+,HCO3-)	H2O	-4.73	0.75
37	GMELCD/1	(MEA+,HCO3-)	H2O	0	0
38	GMELCE/1	(MEA+,HCO3-)	H2O	0	0
39	GMELCC/1	MEA	(MEA+,HCO3-)	12.64	6.64
40	GMELCD/1	MEA	(MEA+,HCO3-)	0	0
41	GMELCE/1	MEA	(MEA+,HCO3-)	0	0
42	GMELCC/1	(MEA+,HCO3-)	MEA	0.27	2.91
43	GMELCD/1	(MEA+,HCO3-)	MEA	0	0
44	GMELCE/1	(MEA+,HCO3-)	MEA	0	0
45	GMELCC/1	MEACOOH	(MEA+,MEACOO-)	8	0
46	GMELCD/1	MEACOOH	(MEA+,MEACOO-)	0	0
47	GMELCE/1	MEACOOH	(MEA+,MEACOO-)	0	0
48	GMELCC/1	(MEA+,MEACOO-)	MEACOOH	-4	0
49	GMELCD/1	(MEA+,MEACOO-)	MEACOOH	0	0
50	GMELCE/1	(MEA+,MEACOO-)	MEACOOH	0	0

#	Parameter	Component i	Component j	Value (SI units)	Standard deviation
51	GMELCC/1	MEACOOH	(MEA+,HCO3-)	8	0
52	GMELCD/1	MEACOOH	(MEA+,HCO3-)	0	0
53	GMELCE/1	MEACOOH	(MEA+,HCO3-)	0	0
54	GMELCC/1	(MEA+,HCO3-)	MEACOOH	-4	0
55	GMELCD/1	(MEA+,HCO3-)	MEACOOH	0	0
56	GMELCE/1	(MEA+,HCO3-)	MEACOOH	0	0
57	NRTL/1	H2O	MEACOOH	0	0
58	NRTL/2	H2O	MEACOOH	0	0
59	NRTL/3	H2O	MEACOOH	0.2	0
60	NRTL/5	H2O	MEACOOH	0	0
61	NRTL/6	H2O	MEACOOH	0	0
62	NRTL/1	MEACOOH	H2O	0	0
63	NRTL/2	MEACOOH	H2O	0	0
64	NRTL/5	MEACOOH	H2O	0	0
65	NRTL/6	MEACOOH	H2O	0	0

*: The parameter was regressed in the last run with a small boundary, and the standard deviation in the last run was 0; the std. dev. in the table is from an earlier run in the progress of the regression. **: The values were set to be equal to CPAQ0/1,2,3 of $MEACOO^-$ in the last run.

Table 4-16 shows the correlation matrix of the Model B regression. The parameter number corresponds to the numbers in Table 4-15. Coefficients for non-regressed parameters are all zero and are not shown in Table 4-16.

Table 4-16: Parameter Correlation Matrix of Model B

	1	2*	3*	4	5	6	8*	9*	10*	19*	21	24	27	30	33	36	39	42
1	1.00																	
2*	-0.28	1.00																
3*	0.32	-0.99	1.00															
4	0.04	0.30	-0.24	1.00														
5	0.14	-0.37	0.31	-0.34	1.00													
6	-0.10	0.82	-0.82	0.31	-1.00	1.00												
8*	0.09	-0.88	0.87	-0.27	0.54	-0.11	1.00											
9*	0.08	0.00	0.00	-0.19	-0.45	0.75	0.25	1.00										
10*	-0.11	0.00	0.00	0.32	-0.25	-0.26	-0.89	-0.64	1.00									
19*	-0.12	-0.08	0.05	-0.49	0.36	0.14	0.05	0.00	0.00	1.00								
21	0.92	-0.25	0.27	0.02	0.14	-0.09	0.02	0.08	-0.05	-0.11	1.00							
24	-0.86	0.22	-0.24	-0.02	-0.14	0.09	-0.01	-0.08	0.04	0.11	-0.99	1.00						
27	-0.10	-0.34	0.35	-0.07	-0.06	0.06	-0.13	0.22	0.03	-0.04	0.09	-0.16	1.00					
30	0.05	0.32	-0.33	0.06	0.06	-0.06	0.13	-0.19	-0.05	0.02	-0.13	0.19	-0.99	1.00				
33	-0.41	0.39	-0.38	-0.05	-0.11	0.07	0.75	0.20	-0.68	-0.05	-0.60	0.65	-0.39	0.39	1.00			
36	0.27	-0.37	0.36	0.06	0.07	-0.04	-0.67	-0.20	0.60	0.15	0.49	-0.55	0.41	-0.41	-0.98	1.00		
39	0.11	0.52	-0.55	-0.05	0.06	-0.03	0.06	0.03	0.02	0.12	0.18	-0.20	0.43	-0.46	-0.26	0.16	1.00	
42	-0.17	-0.17	0.17	-0.62	-0.52	0.54	-0.03	0.06	-0.05	0.20	-0.15	0.14	0.11	-0.09	0.15	-0.12	-0.05	1.00

*: The coefficients of these parameters are earlier runs in the progress of the regression, not from the last run.

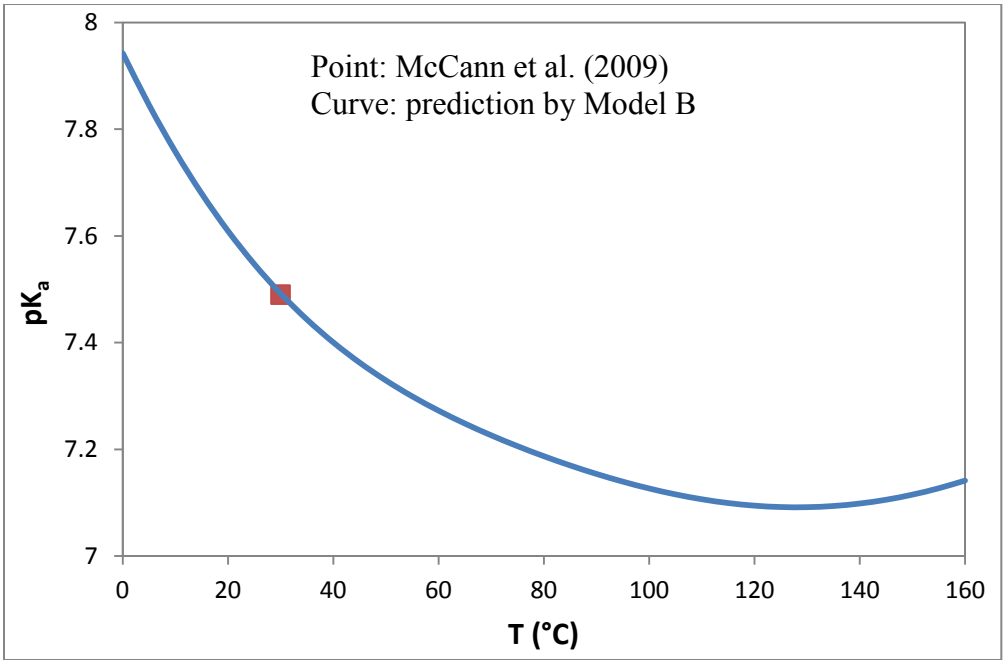

Figure 4-20: pK_a Fitting of MEACOOH, Molarity Based, Asymmetric

Figure 4-21 gives the comparison of CO_2 solubility in 7 m MEA predicted by Model A and B. Model B fits the data better than Model A at 40-160°C except a few outliers.

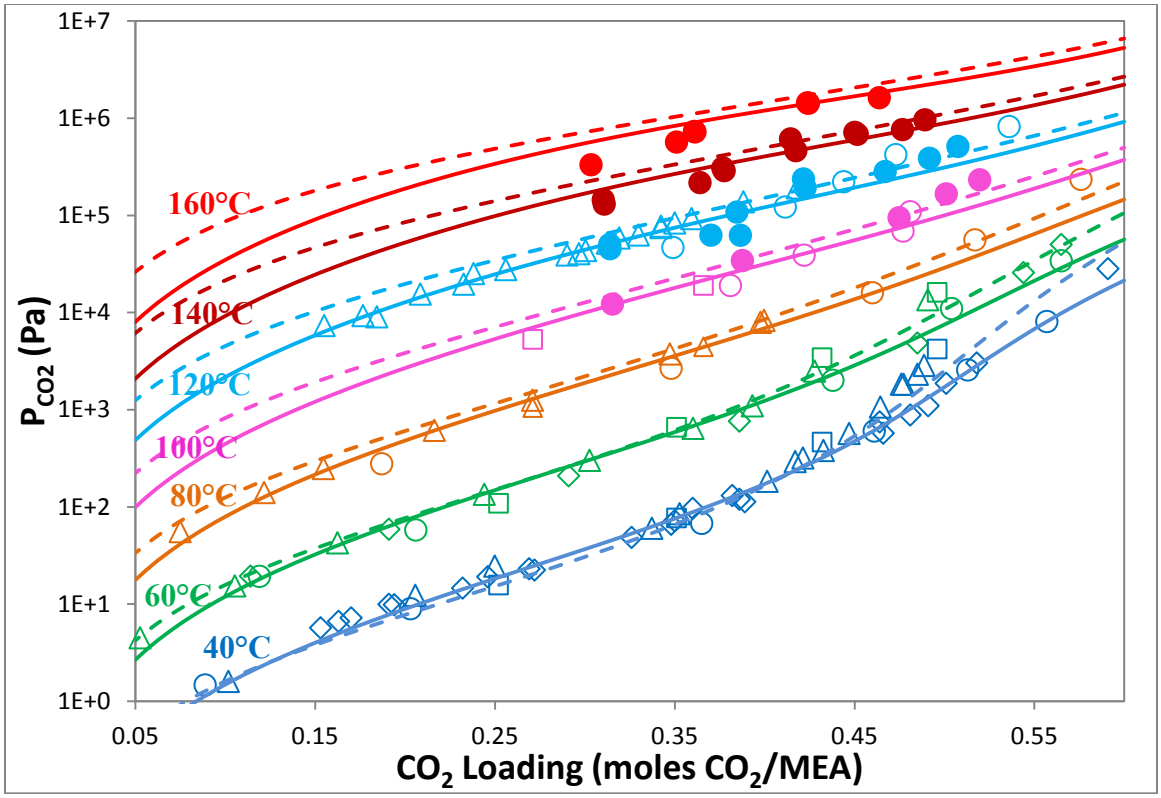

Figure 4-21: Prediction of CO_2 Solubility in 7 m MEA by Models A and B. ●: this work; ○: Jou et al. (1995); □: Dugas et al. (2009); ◊: Hilliard (2008); Δ: Ma'mun et al. (2005); solid lines: Model B for 7 m MEA; dashed lines: Model A for 7 m MEA.

Figure 4-22 compares the experimental data by Kim et al. (2007) and the prediction by Model B using the same derivative method as in Model A. The temperature dependence is reasonable; at low loading, ΔH_{abs} is relative constant. Figure 4-23 compares ΔH_{abs} from Model A, B, and the empirical model in Table 2-12. Generally, Model B predicts lower $-\Delta H_{abs}$ than Model A does below 0.5 loading, and predicts higher $-\Delta H_{abs}$ than Model A does above 0.5 loading. The temperature dependence of $-\Delta H_{abs}$ between 0.2 and 0.5 loading by Model B is more reasonable than that by Model A. The $-\Delta H_{abs}$ from the empirical model in Table 2-12 is close to the 160°C curves of Model A and B in 0.2-0.5 loading. A linear trend line of $-\Delta H_{abs}$ at 40°C in 0.2-0.5 loading from Model B will be very close to the empirical model prediction;

while a linear trend line of $-\Delta H_{abs}$ at 40°C in 0.2-0.5 loading from Model A will be higher than the empirical model prediction.

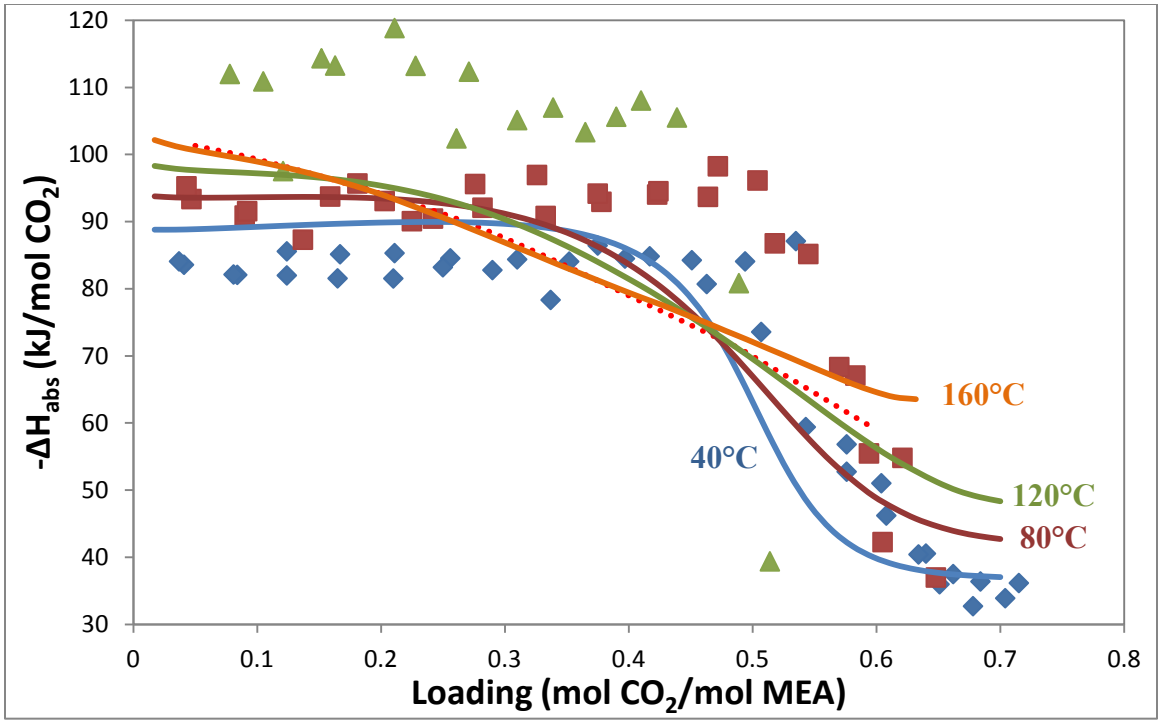

Figure 4-22: Comparison of Heat of Absorption of CO_2 in 7 m MEA by Model B.
Data points: Kim et al. (2007), ♦: 40°C, ■: 80°C, ▲: 120°C; solid lines: Model B; dotted line: empirical model from this work (Table 2-12).

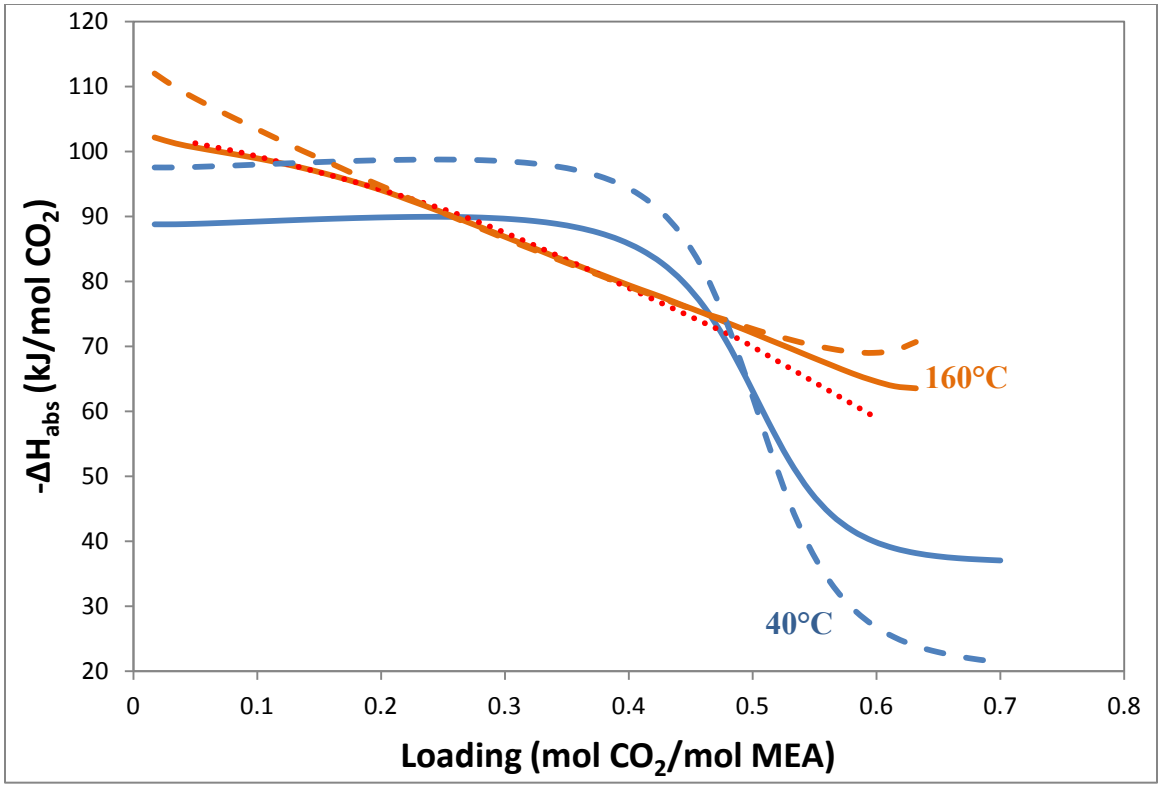

Figure 4-23: Comparison of Heat of Absorption of CO_2 in 7 m MEA. Solid lines: Model B; dashed lines: Model A; dotted line: empirical model from this work (Table 2-12).

Figures 4-24 and 4-25 compare the prediction of the normalized MEA volatility by Model A and B. The same data sets are presented; Figure 4-25 uses CO_2 loading as the horizontal axis instead of P_{CO2}. Since the 40°C MEA volatility data were considered with error and not used in the regression, only the other temperature data were compared. Model B predicts data well except a few outliers at 60 °C with high loading, where bigger experimental errors are expected. Generally Model B predicts better than Model A, compared with the experimental data. Figure 4-26 presented a favorable comparison of MEA volatility in 7 m MEA with Model B.

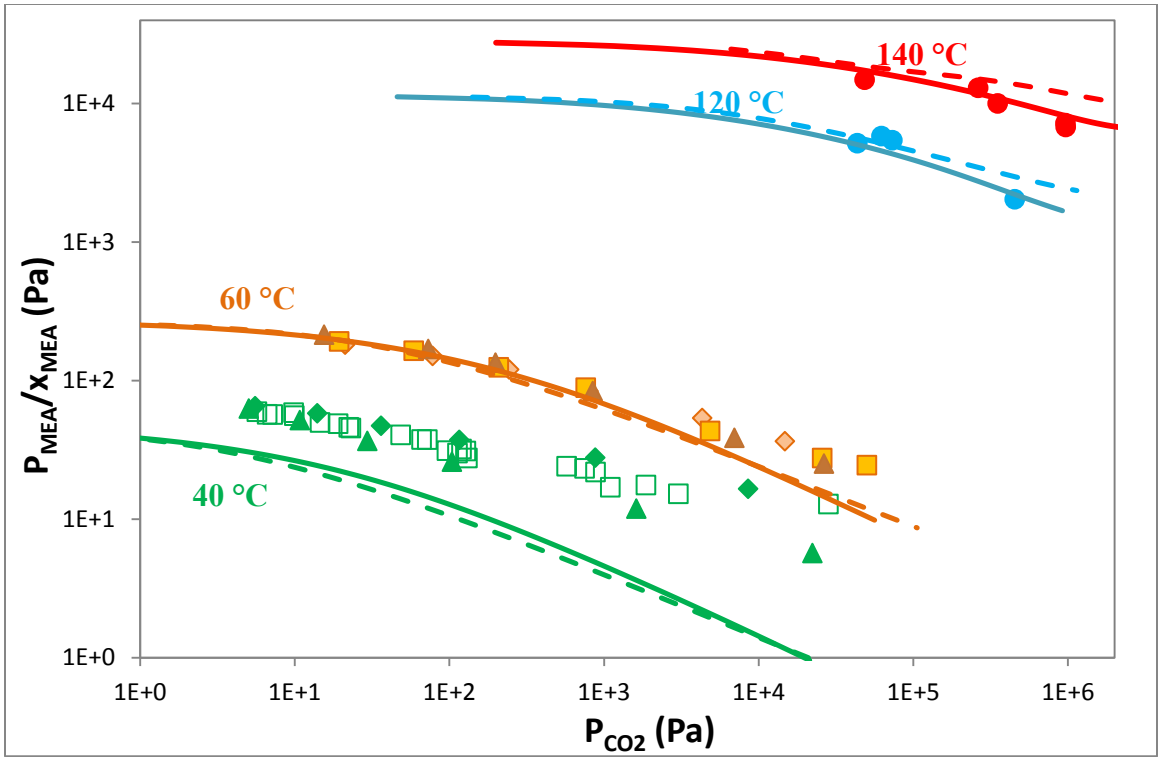

Figure 4-24: Prediction of Normalized MEA Partial Pressure over MEA-CO_2-H_2O (1) with Models A and B. Hilliard (2008) MEA: ♦ 3.5 m, ■ 7 m, ▲ 11 m; ●: this work; solid lines: Model B - 7 m MEA; dashed lines: Model A – 7 m MEA. $x_{MEA} = \frac{\text{mol of total MEA}}{\text{mol of total MEA + mol of } H_2O}$.

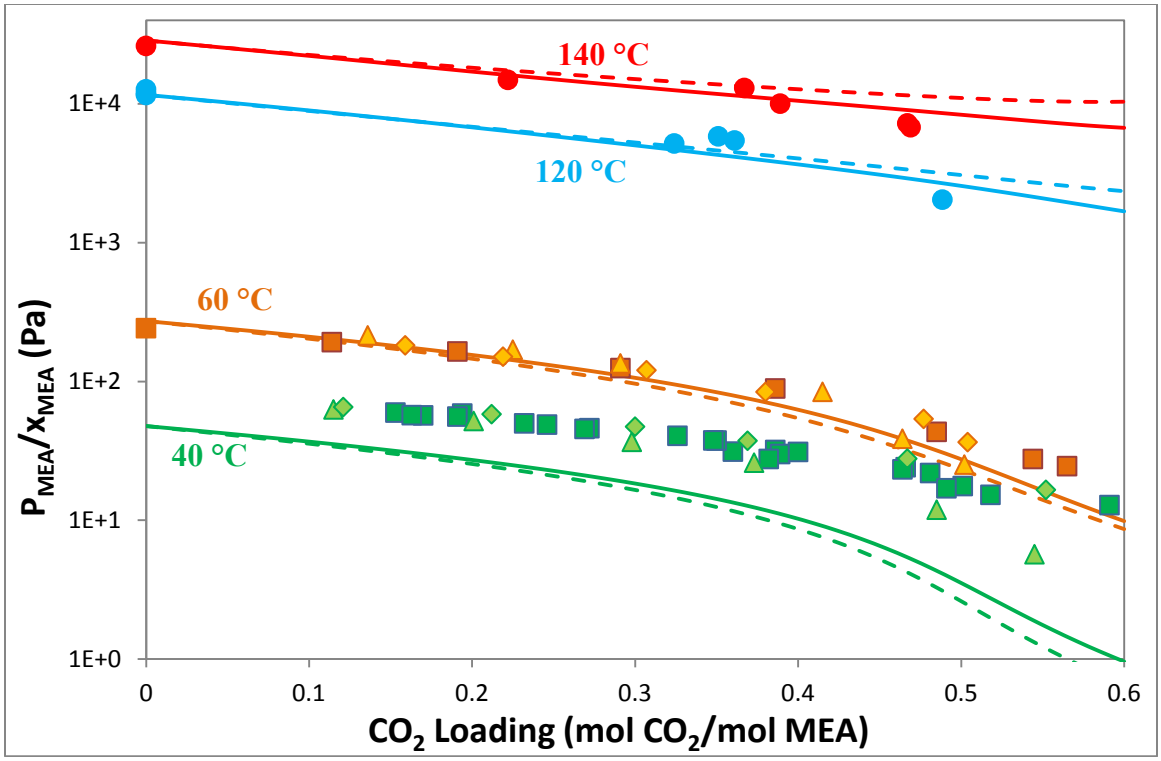

Figure 4-25: Prediction of Normalized MEA Partial Pressure over MEA-CO_2-H_2O (2) with Models A and B. Hilliard (2008) MEA: ♦ 3.5 m, ■ 7 m, ▲ 11 m; ●: this work; solid lines: Model B - 7 m MEA; dashed lines: Model A.

$$x_{MEA} = \frac{\text{mol of total MEA}}{\text{mol of total MEA + mol of } H_2O}.$$

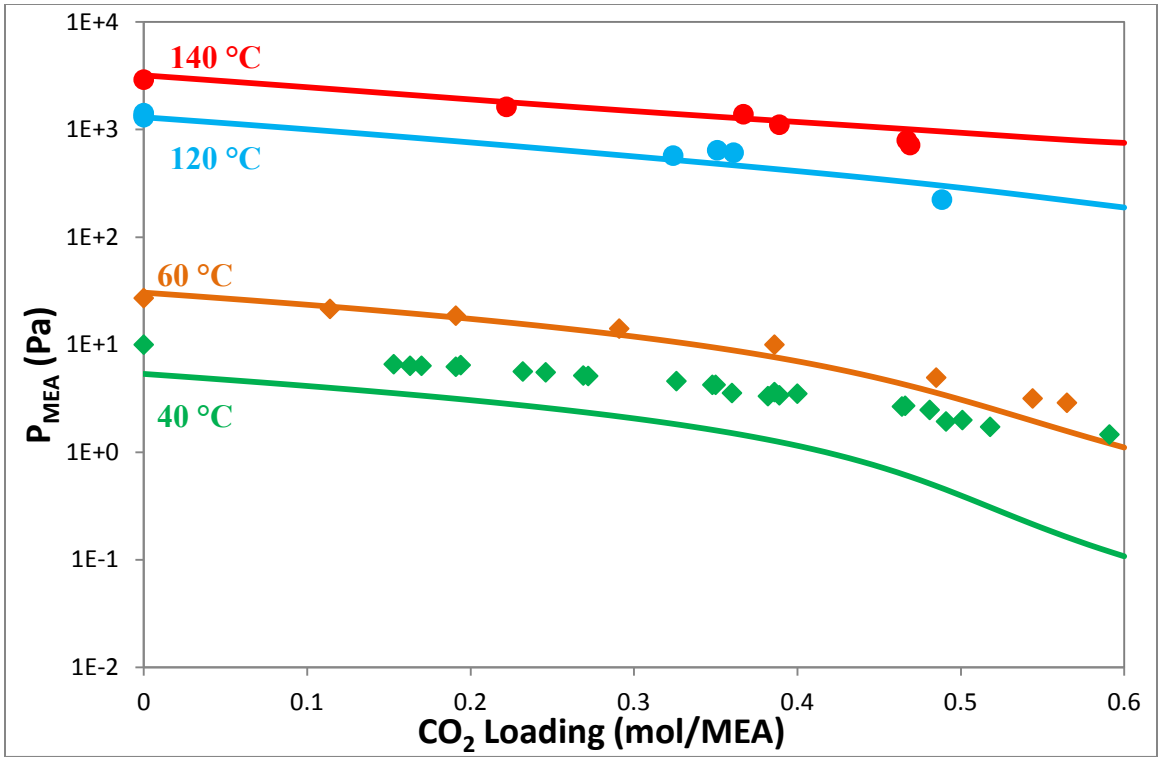

Figure 4-26: Prediction of MEA Partial Pressure over 7 m MEA by Model B. ♦: Hilliard (2008); ●: this work; lines: Model B.

Figure 4-27 gives a comparison of the MEA enthalpy of vaporization in 7 m MEA. $-\Delta H_{vap,MEA}$ was calculated using the same deferential method as in Model A. $-\Delta H_{vap,MEA}$ by Model B is larger than the value given by Hilliard's MEA model (Figure 3-11), probably because new MEA volatility data were included in Model B and previous data below 46°C were deleted from the regression. Comparing with Model A, Model B's prediction of $-\Delta H_{vap,MEA}$ is more constant at 80 to 160°C at low CO_2 loading, and is smaller within the whole studied temperature and loading range.

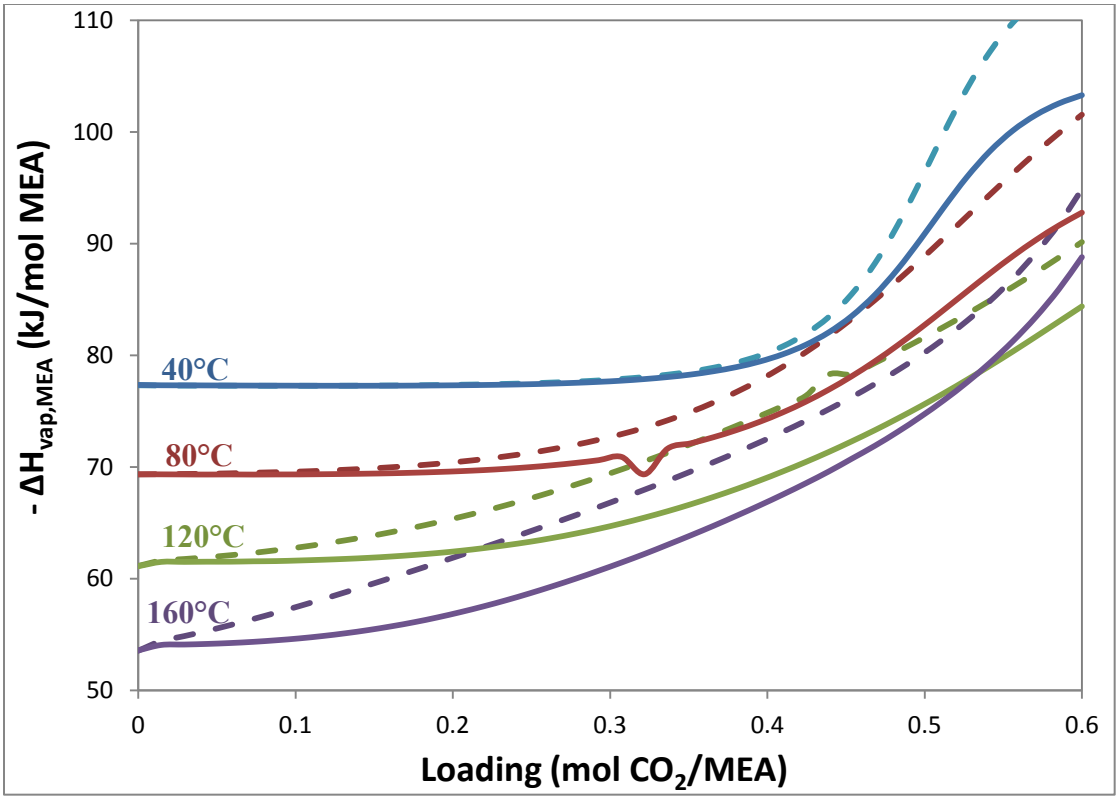

Figure 4-27: Comparison of Enthalpy of Vaporization of MEA in 7 m MEA with Models A and B. **Solid lines: Model B; dashed lines: Model A.**

Figure 4-28 gives the prediction of total pressure over CO_2 loaded 7 m MEA by Model A and B. Like Model A, Model B predicts well at low CO_2 loading, but under-predicts the data at high loading. Comparing with Figure 4-21, Model B may under-predict P_{CO2} at loading above 0.47 and at high temperature. The total pressure data by Aronu et al. (2011) was not incorporated in Model B, and there are some differences between the total pressure data by Aronu et al. (2011) and from this work as shown in Figure 4-28.

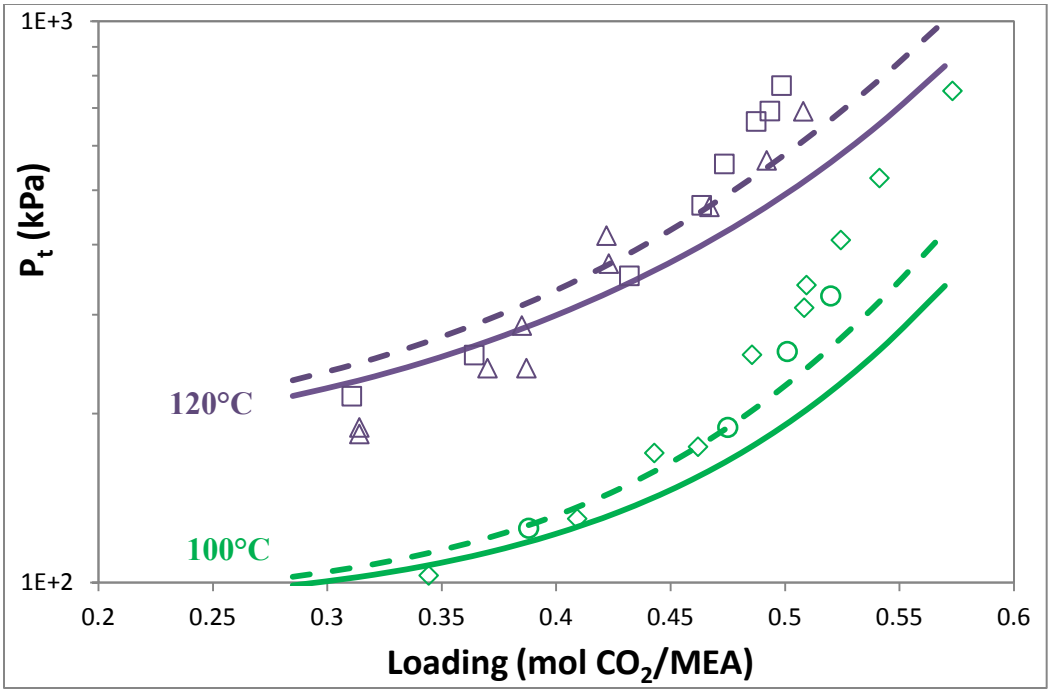

Figure 4-28: Comparison of Prediction of Total Pressure in 7 m MEA with Models A and B. **○: 100°C this work; ◊: 100°C Aronu et al. (2011); Δ: 120°C this work; □: 120°C Aronu et al. (2011); Lines: Model B.**

Figures 4-29 and 4-30 are the specific heat capacity comparison of Model A, Model B, and experimental data. Both the models fairly predict the data and the temperature dependence of the specific heat capacity.

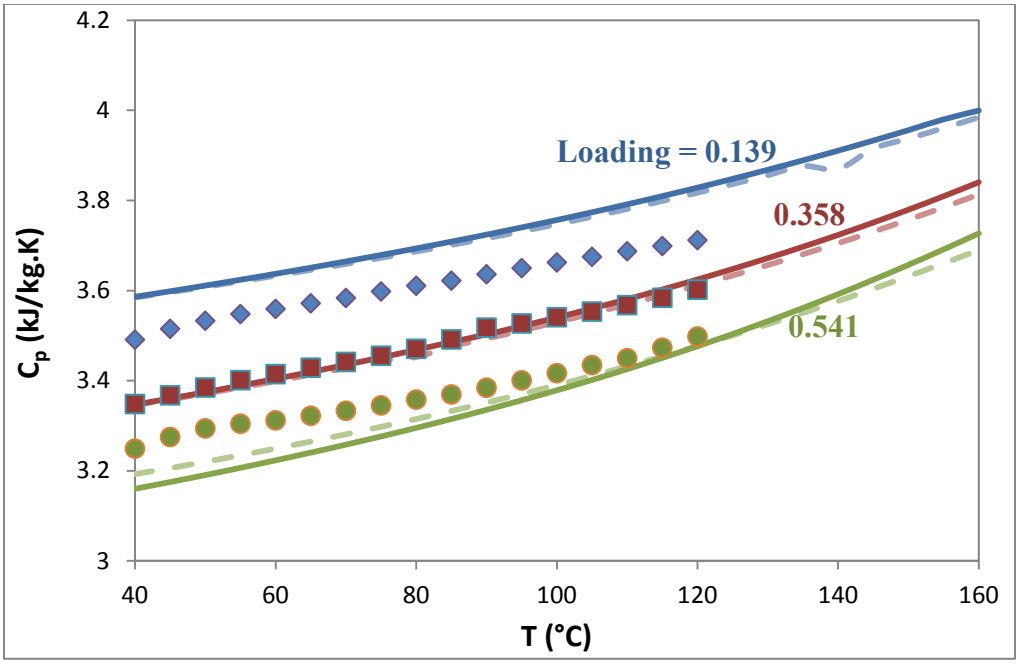

Figure 4-29: Prediction of Specific Heat Capacity in 7 m MEA by Models A and B.
Experimental data points (Hilliard 2008): ♦ 0.139 loading, ■ 0.358 loading, ● 0.541 loading; solid lines: Model B; dashed lines: Model A.

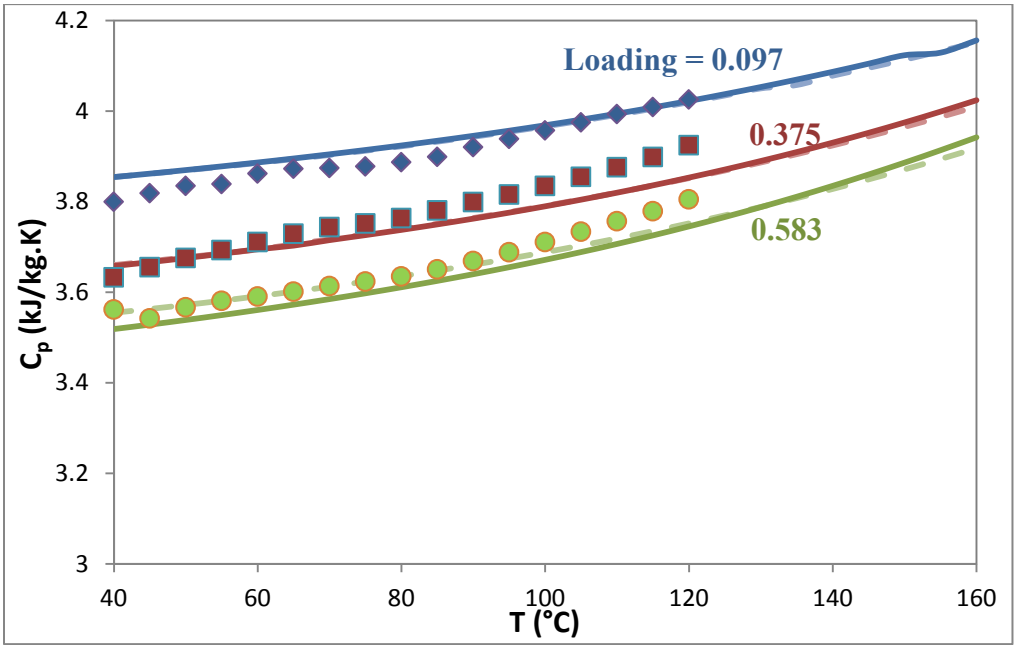

Figure 4-30: Prediction of Specific Heat Capacity in 3.5 m MEA by Models A and B.
Experimental data points (Hilliard 2008): ♦ 0.097 loading, ■ 0.375 loading, ● 0.583 loading; solid lines: Model B; dashed lines: Model A.

Figure 4-31 and 4-32 compares the predicted speciation by Model A, Model B and the experimental NMR data. Figure 4-32(b) is the enlarged high concentration and high loading part of Figure 4-32(a). The experimental data were by NMR, which cannot separate MEA from $MEAH^+$, or separate $MEACOO^-$ from MEACOOH, therefore the data reported were in concentration of MEA/$MEAH^+$, $MEACOO^-$, and HCO_3^-, and are compared with Model A and B prediction for MEA/$MEAH^+$, $MEACOO^-$/MEACOOH, and HCO_3^-, respectively. Both of the models well predict the data over the whole CO_2 loading range. Notice that the Model B predicted $MEACOO^-$/MEACOOH curve at high loading matches Poplsteinava et al. (2005) data well, and generally Model B predicts the Poplsteinava et al. (2005) data better and Model A predicts the Bottinger et al. (2008) data better. Model B under-predicts HCO_3^- concentration at low loading, but the concentration is less than 0.1% and the data scatter which reduces the importance.

Figure 4-33 shows the full speciation profile by Model B.

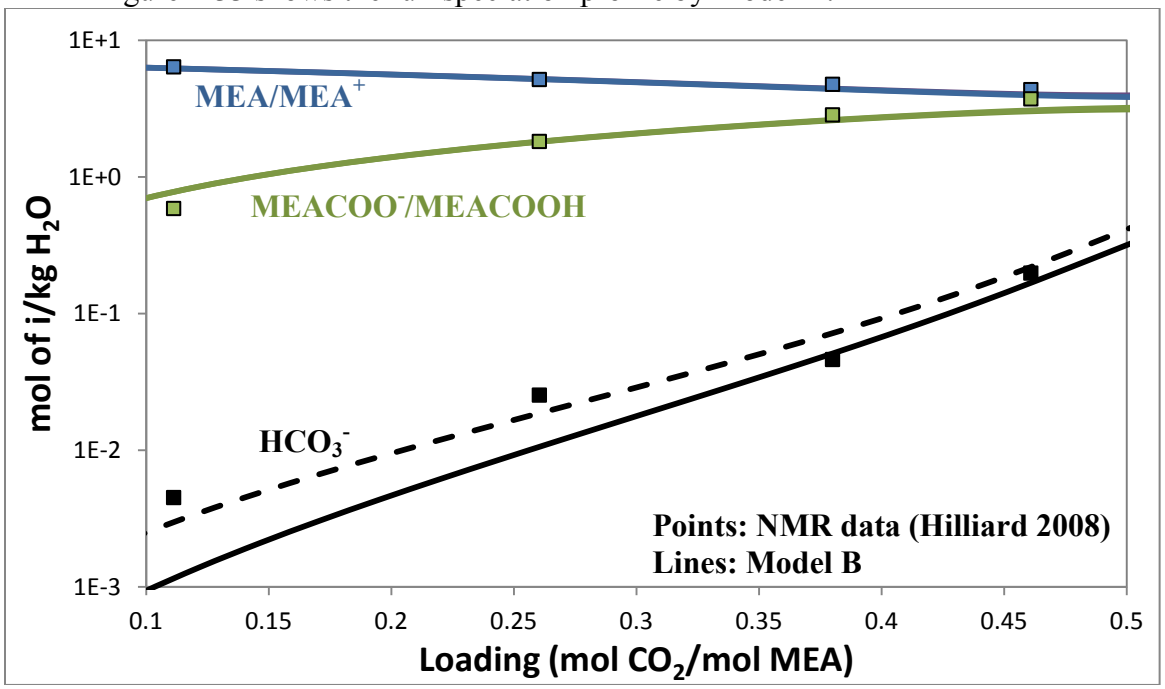

Figure 4-31: Comparison of Speciation in 7 m MEA at 40 ℃ (1) by Models A and B

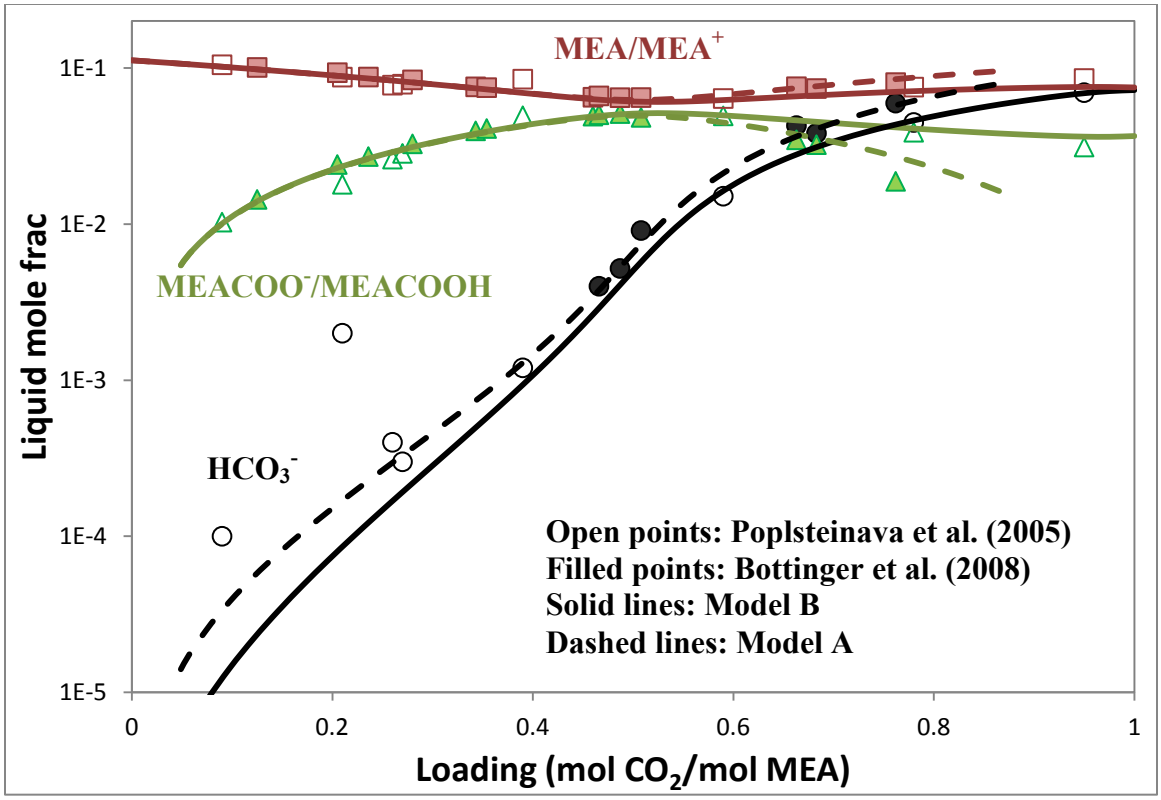

Figure 4-32 (a): Comparison of Speciation in 7 m MEA at 40 ℃ (2) with Models A and B

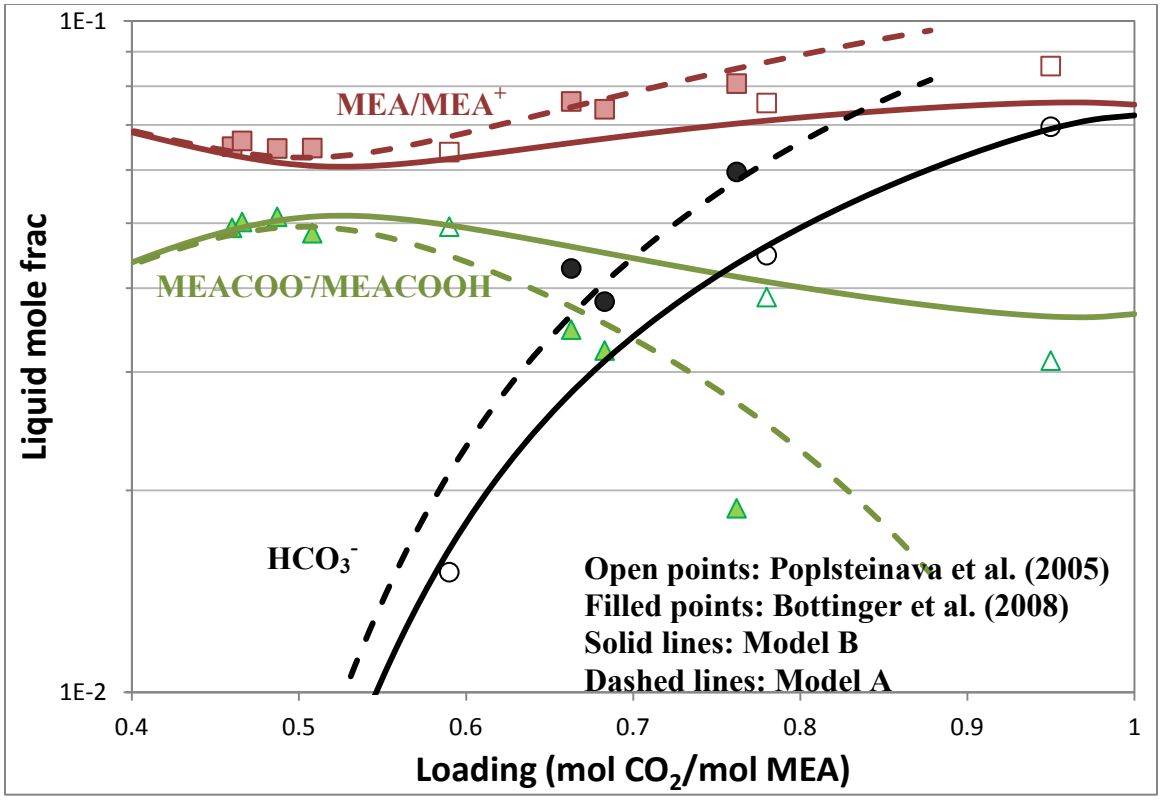

Figure 4-32 (b): Comparison of Speciation in 7 m MEA at 40 ℃ (2) with Models A and B

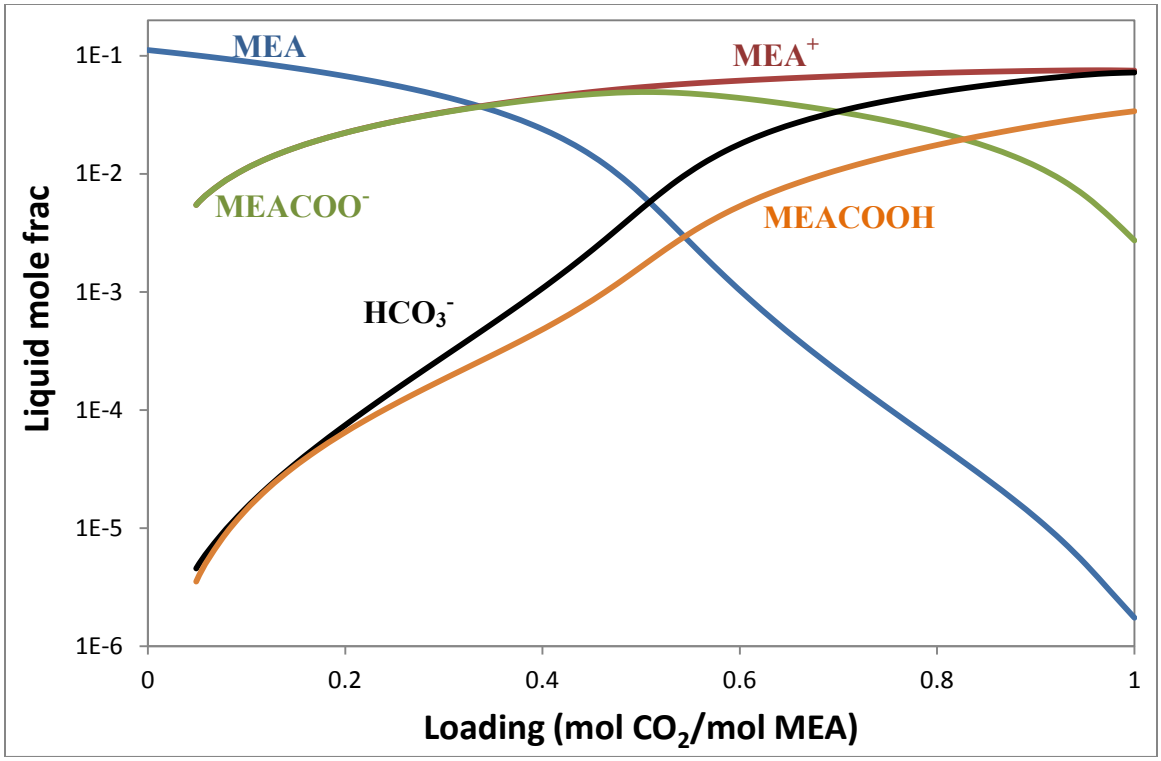

Figure 4-33: Speciation Prediction of 7 m MEA at 40 ℃ by Model B

Similarly, Figure 4-34 to 4-37 give the comparison of Model B speciation prediction and NMR experimental data. Model B predicts the data well, except for a few outliers.

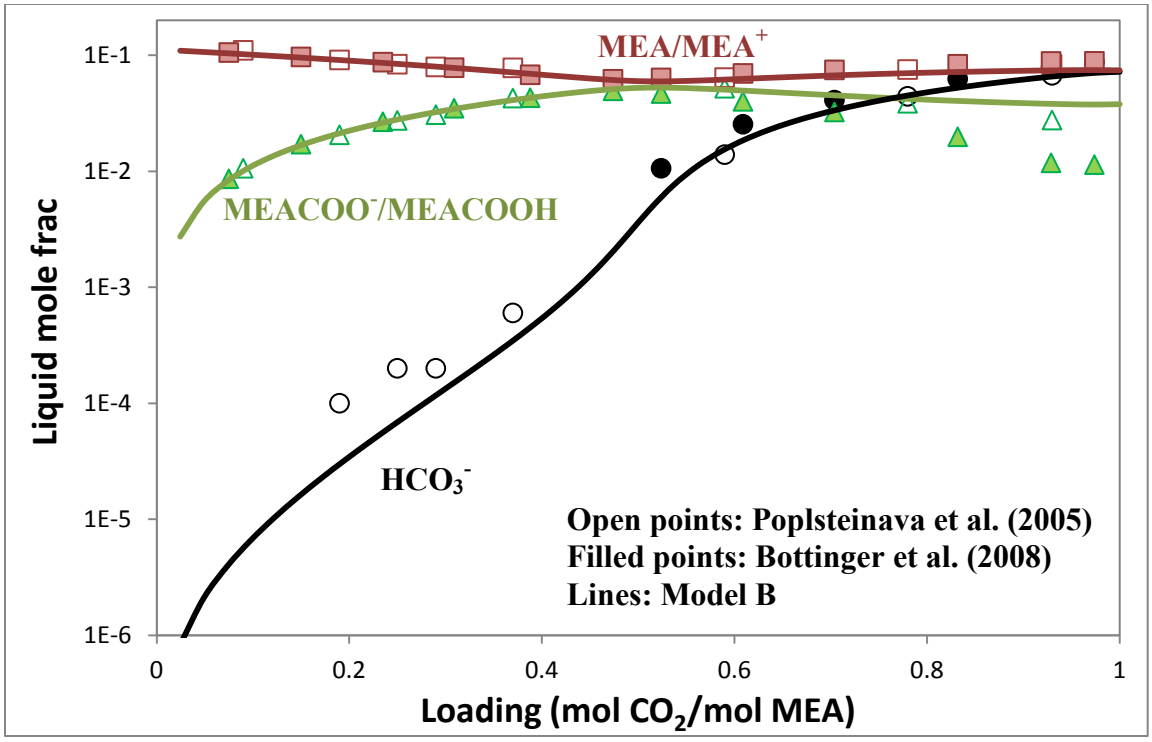

Figure 4-34: Comparison of Speciation of 7 m MEA at 20 ℃ with Model B

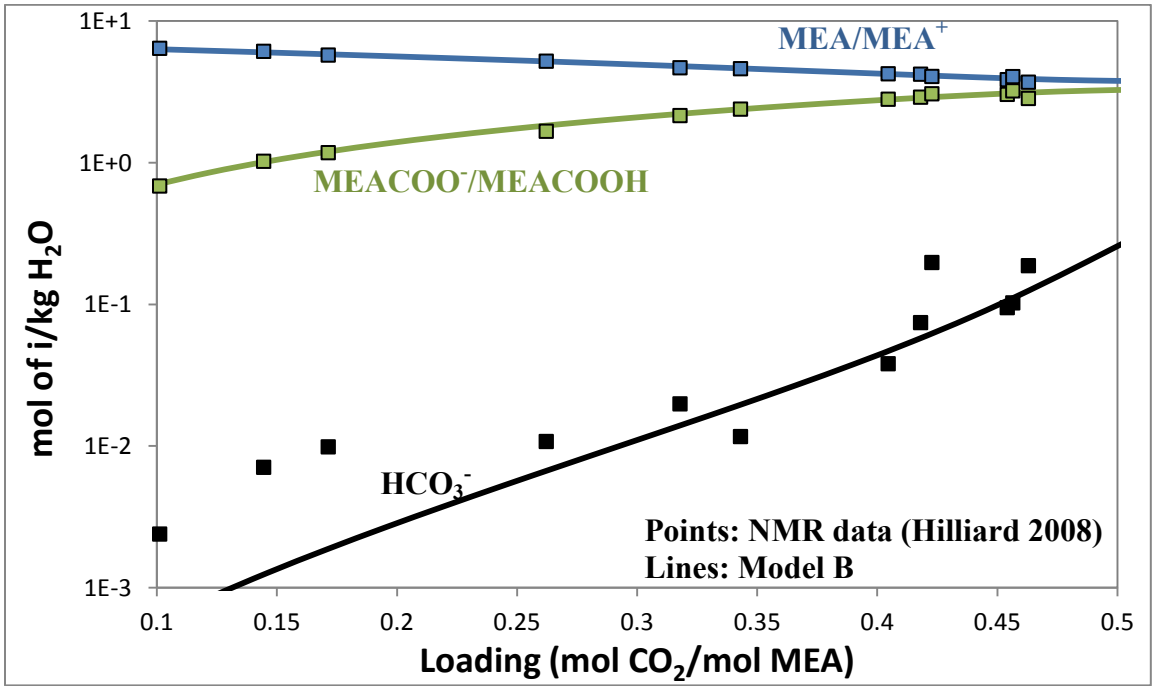

Figure 4-35: Comparison of Speciation of 7 m MEA at 27 ℃ with Model B

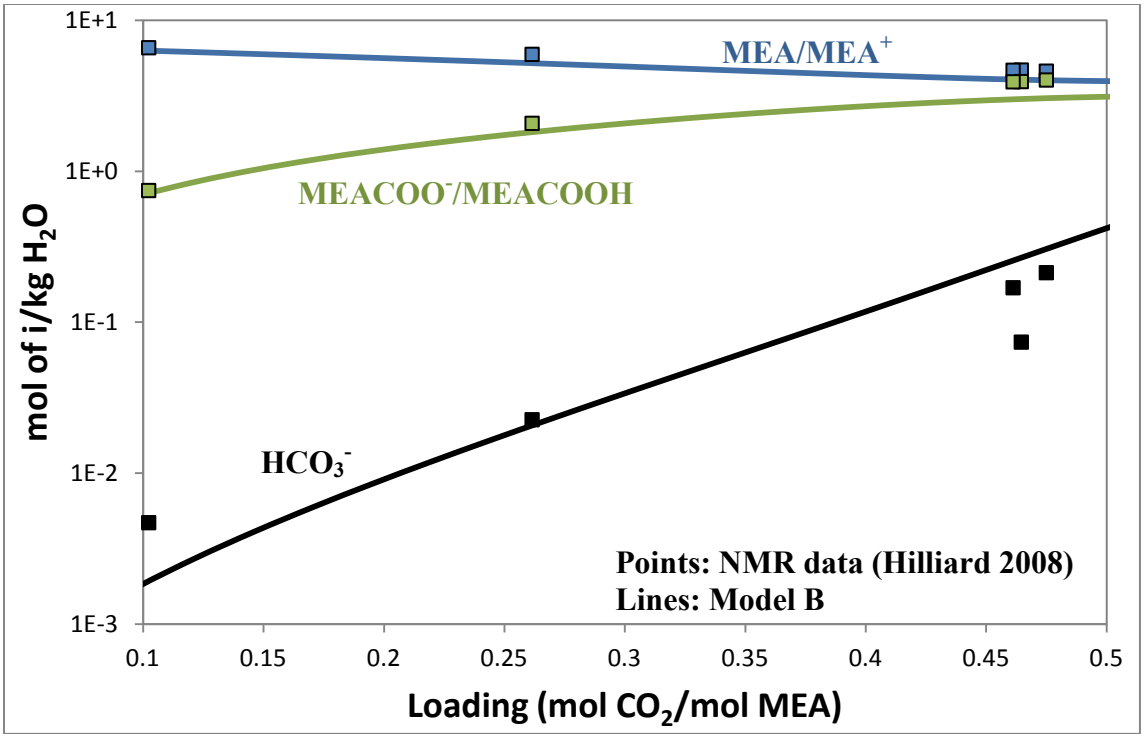

Figure 4-36: Comparison of Speciation of 7 m MEA at 60 ℃ (1) with Model B

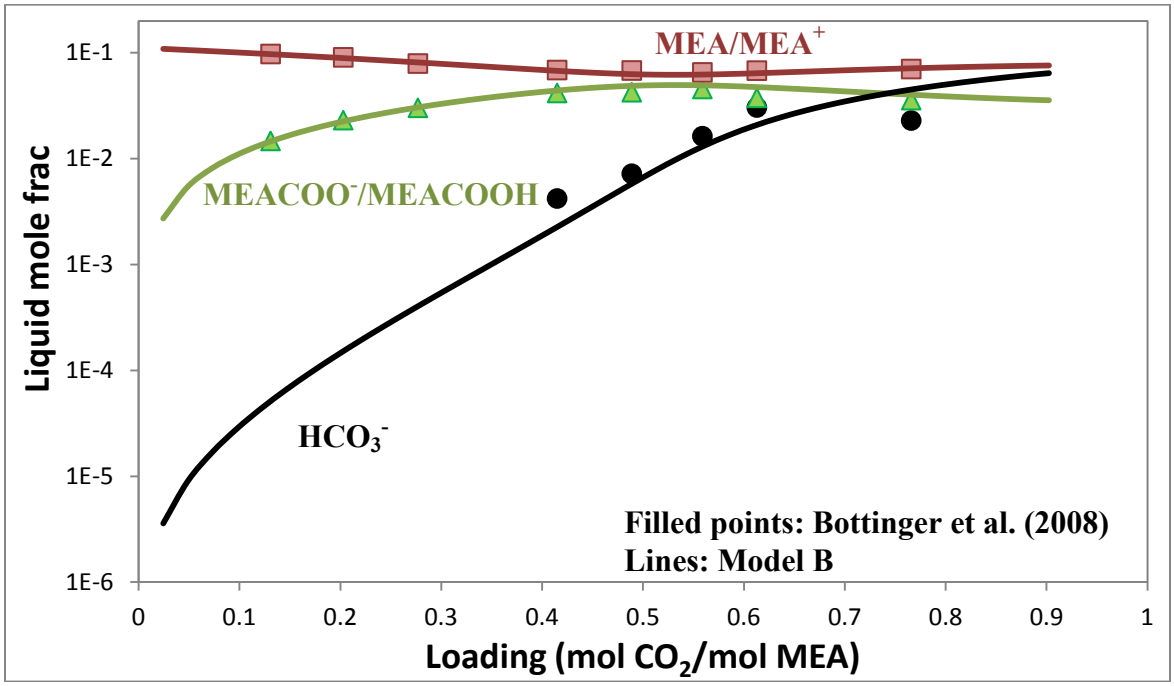

Figure 4-37: Comparison of Speciation of 7 m MEA at 60 ℃ (2) with Model B

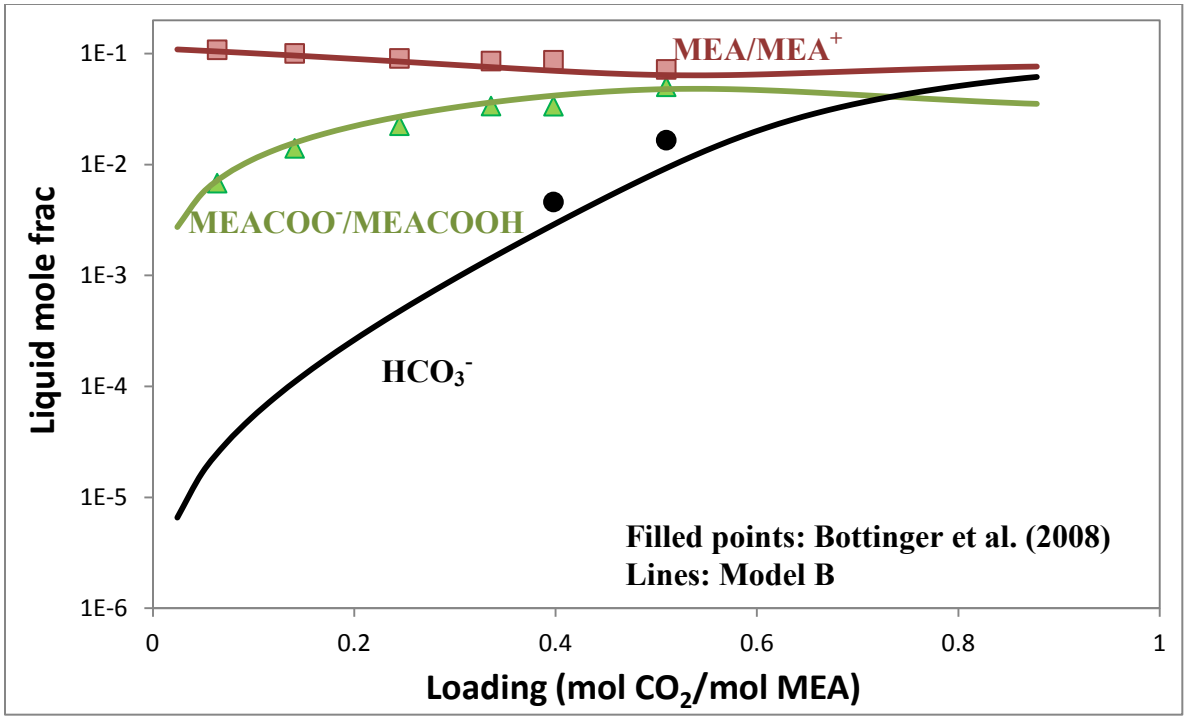

Figure 4-38: Comparison of Speciation of 7 m MEA at 80 ℃ with Model B

160°C speciation of 7 m MEA by Model B is shown in Figures 4-39 and 4-40. Comparing with 40°C speciation, less MEA reacts with CO_2 at 160°C; there is more HCO_3^- and MEACOOH at low loading and less at high loading at 160°C; there is more MEACOO- at low loading (<0.7) and less of it at high loading (>0.7) at 160°C. Therefore, in the practical rich loading range (0.45-0.55), there is more HCO_3^- and MEACOOH in the solution and this will affect other thermal properties. Figure 4-41 is the same as Figure 4-40 except for using a linear y-axis.

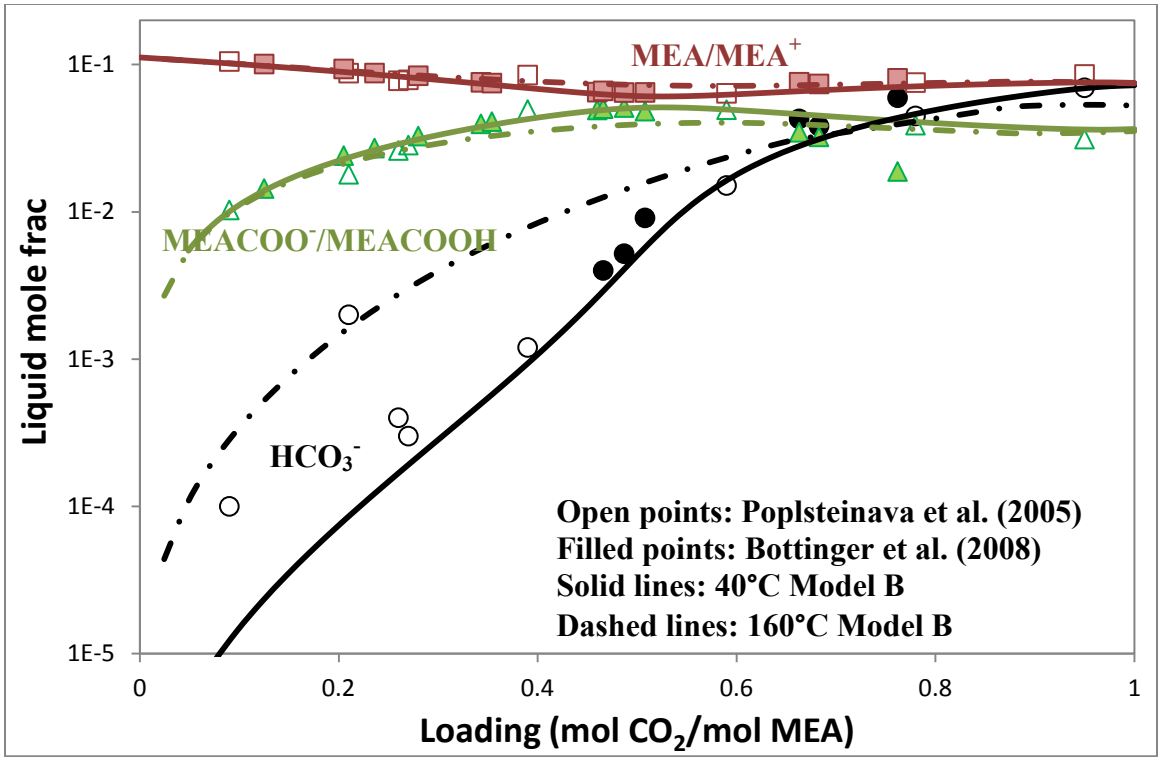

Figure 4-39: Comparison of Speciation of 7 m MEA at 40 and 160 ℃ (1) by Model B

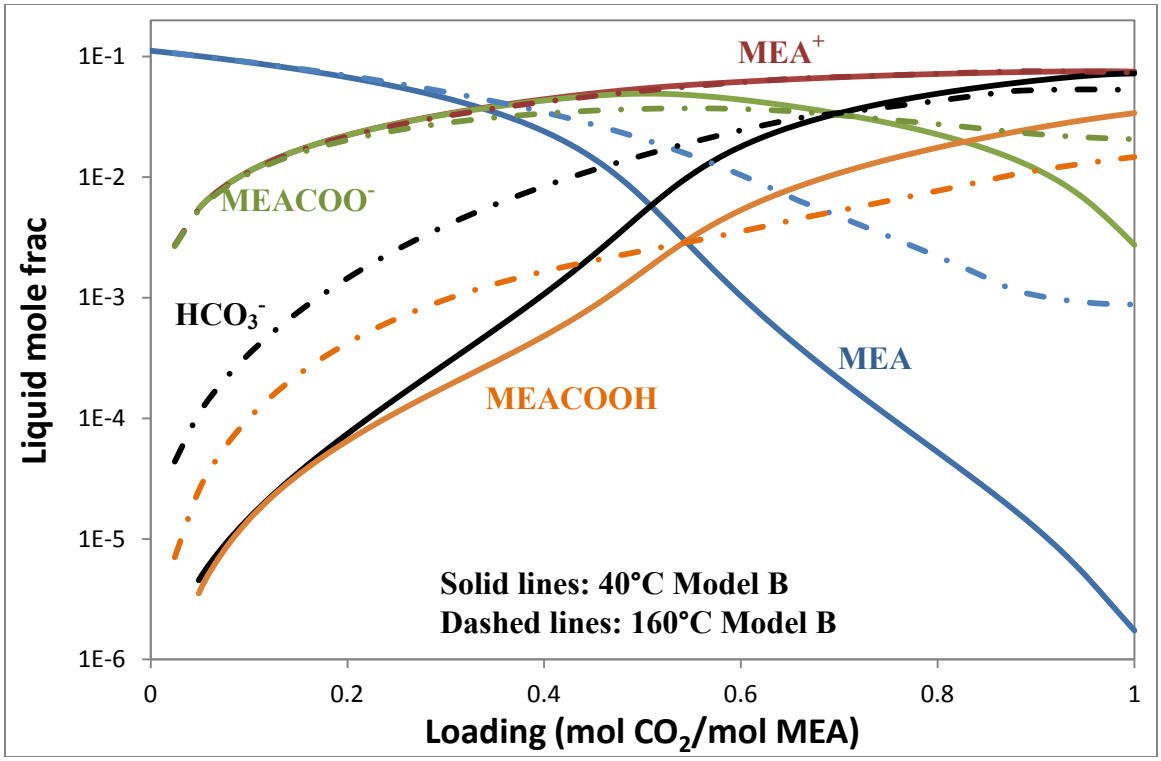

Figure 4-40: Comparison of Speciation of 7 m MEA at 40 and 160 ℃ (2) by Model B

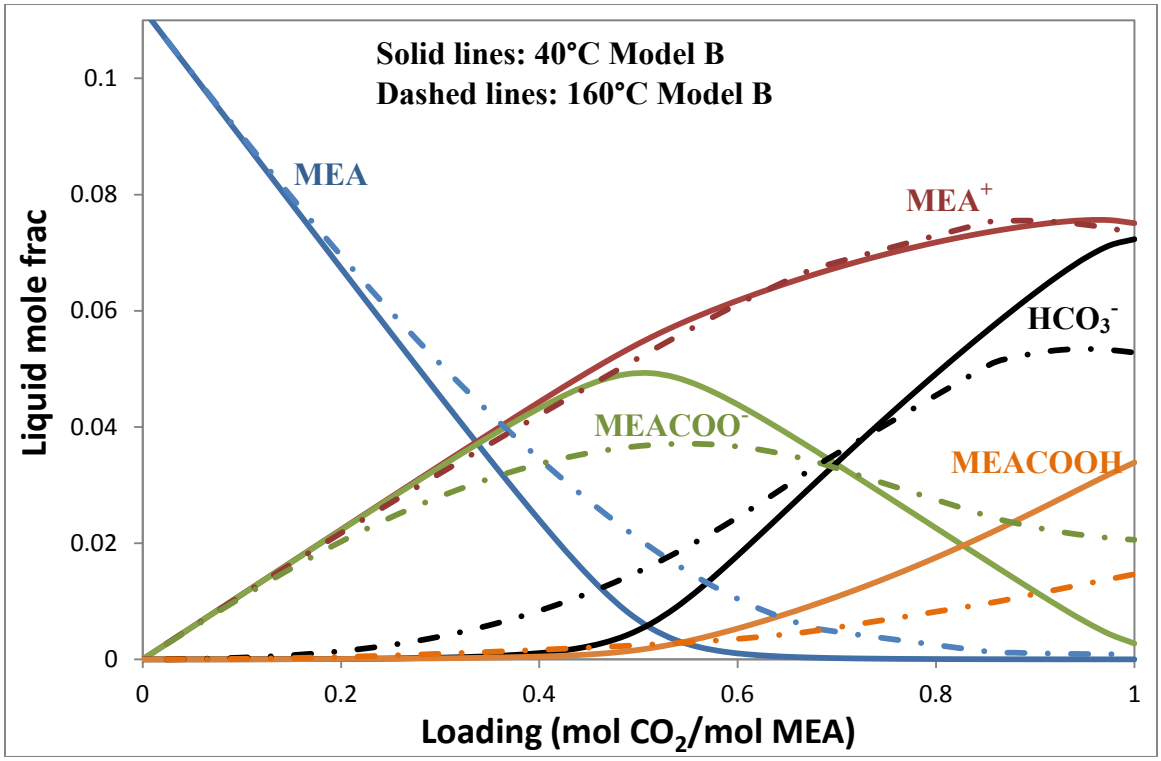

Figure 4-41: Comparison of Speciation of 7 m MEA at 40 and 160 ℃ (3) by Model B

4.4.3 Sensitivity Analysis

Because no effective standard deviation of the DHFORM of MEACOOH was given by Aspen Plus®, a sensitivity analysis was performed to the DHFORM of MEACOOH.

In Aspen Plus® Property Analysis, by changing the value of DHFORM of MEACOOH while fixing all the other parameters as in Model B, a new set of prediction can be obtained and compared with Model B and the measured data.

Table 4-17: Sensitivity Analysis of DHFORM of MEACOOH

	Value in Model B	Value in the Sensitivity Analysis	Difference
DHFORM (kJ/mol)	-746.6	-731.6	15.0

Figure 4-42 through 4-47 show the comparison of some properties between Model B and the sensitivity analysis. The new pK_a of MEACOOH at 30°C is 7.45, while it is 7.49 in Model B. And as shown in Figure 4-42, the temperature dependence of pK_a from the sensitivity analysis is larger than that in Model B. Figure 4-43 shows that after changing DHFORM of MEACOOH, the prediction curves deviate more from the experimental data, especially at high temperature and high CO_2 loading. Partial pressure of MEA changes very little in this analysis so the P_{MEA} is almost the same as in Figure 4-24 to 4-26.

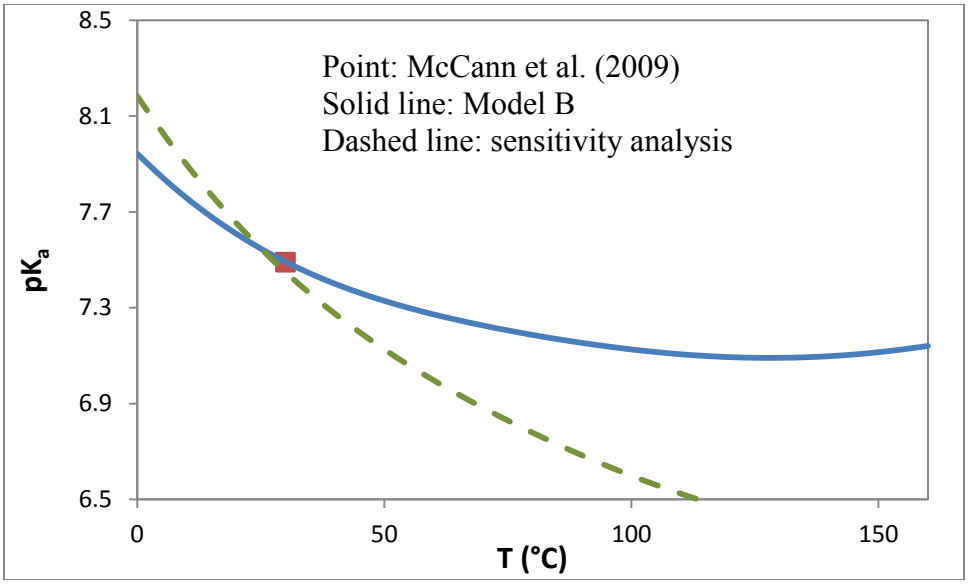

Figure 4-42 Sensitivity Analysis – pK_a of MEACOOH, Molarity Based, Asymmetric

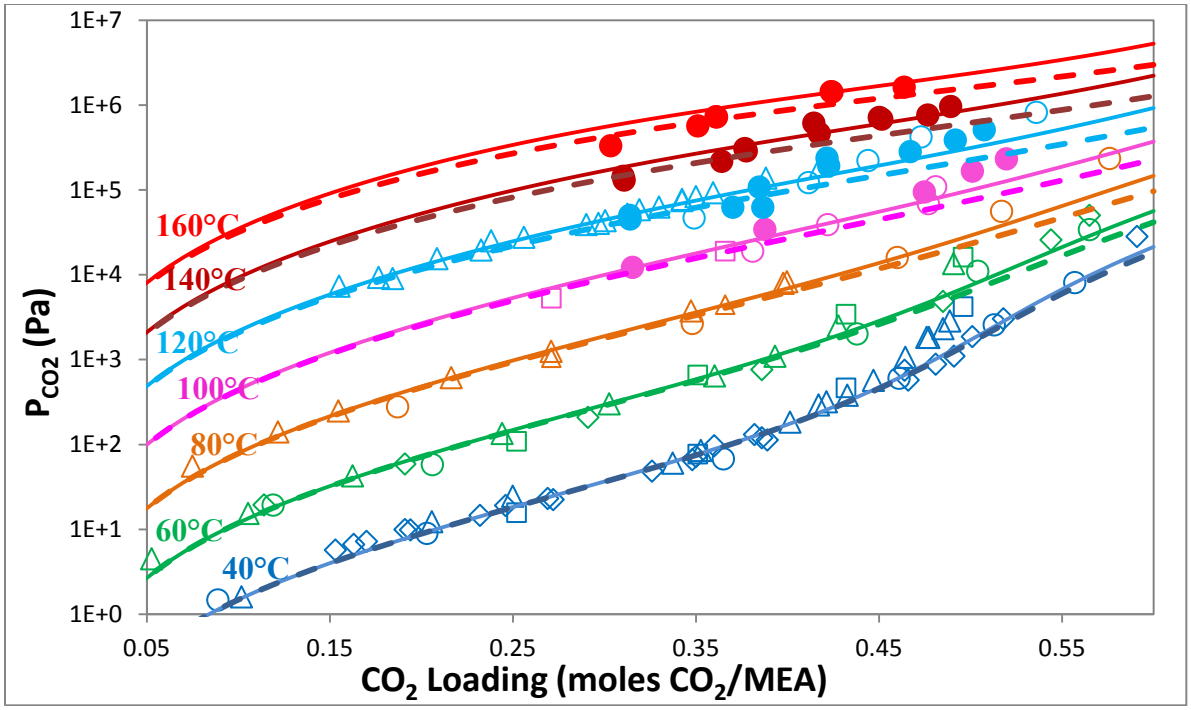

Figure 4-43: Sensitivity Analysis – CO_2 Solubility in 7 m MEA. **●: this work; ○: Jou et al. (1995); □: Dugas et al. (2009); ◊: Hilliard (2008); Δ: Ma'mun et al. (2005); solid lines: Model B for 7 m MEA; dashed lines: sensitivity analysis for 7 m MEA.**

Figure 4-44 presents the heat of absorption of CO_2 comparison. After reducing the absolute value of DHFORM of MEACOOH, $-\Delta H_{abs}$ decreases at 40 to 120°C, especially at 40 and 80°C with higher than 0.5 loading.

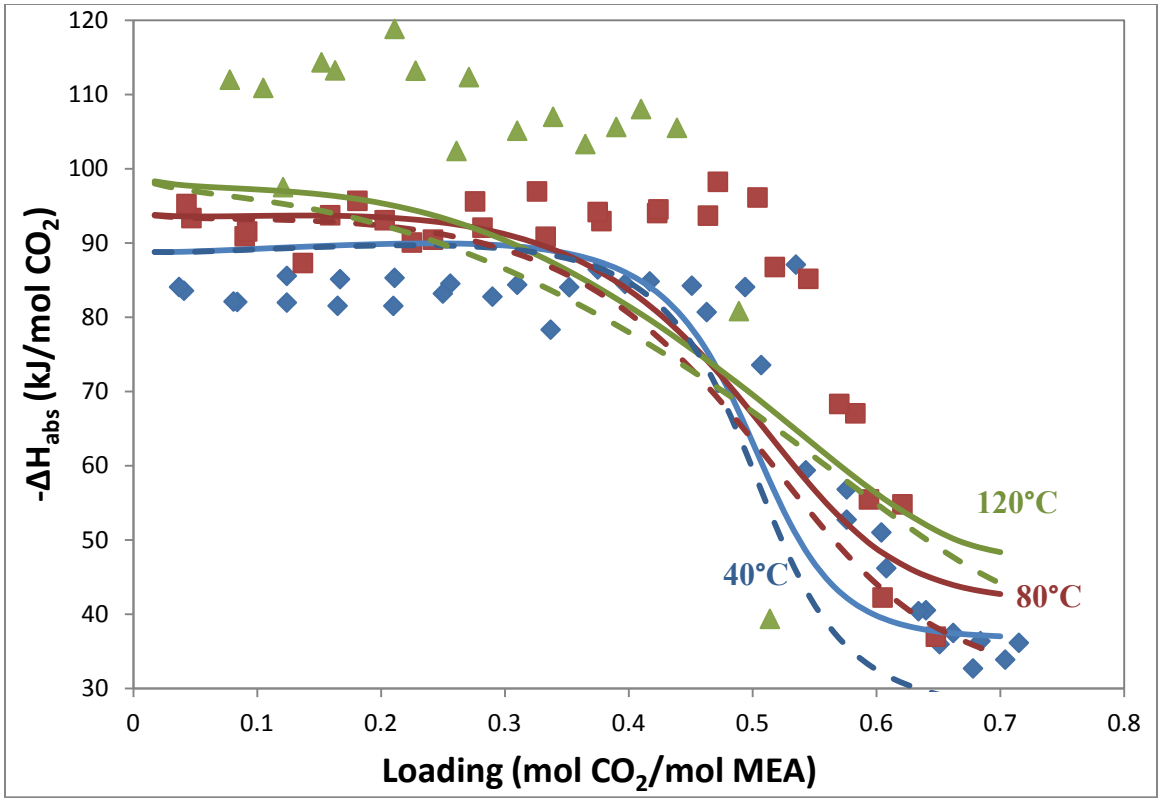

Figure 4-44: Sensitivity Analysis – Heat of Absorption of CO_2 in 7 m MEA. **Data points: Kim et al. (2007), ♦: 40°C, ■: 80°C, ▲: 120°C; solid lines: Model B; dashed line: sensitivity analysis.**

Figures 4-45 and 4-46 are the specific heat capacity analysis. C_p is further deviated from the data in the sensitivity analysis than in Model B at high temperature and high CO_2 loading.

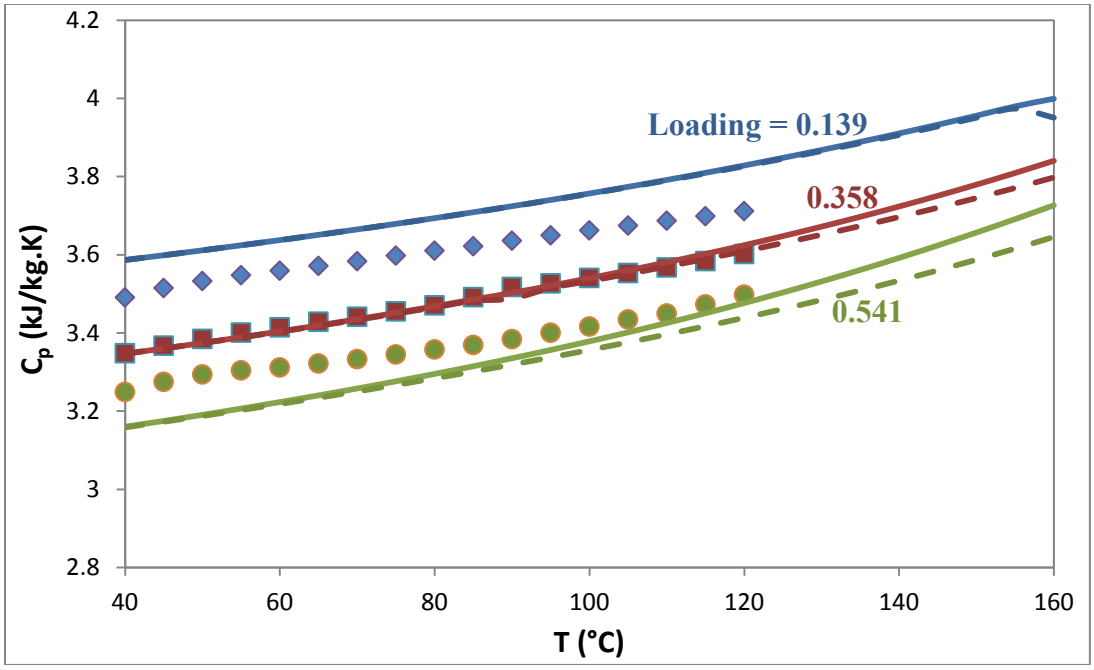

Figure 4-45: Sensitivity Analysis – Specific Heat Capacity of 7 m MEA.
Experimental data points (Hilliard 2008): ♦ 0.139 loading, ■ 0.358 loading, ● 0.541 loading; solid lines: Model B; dashed lines: sensitivity analysis.

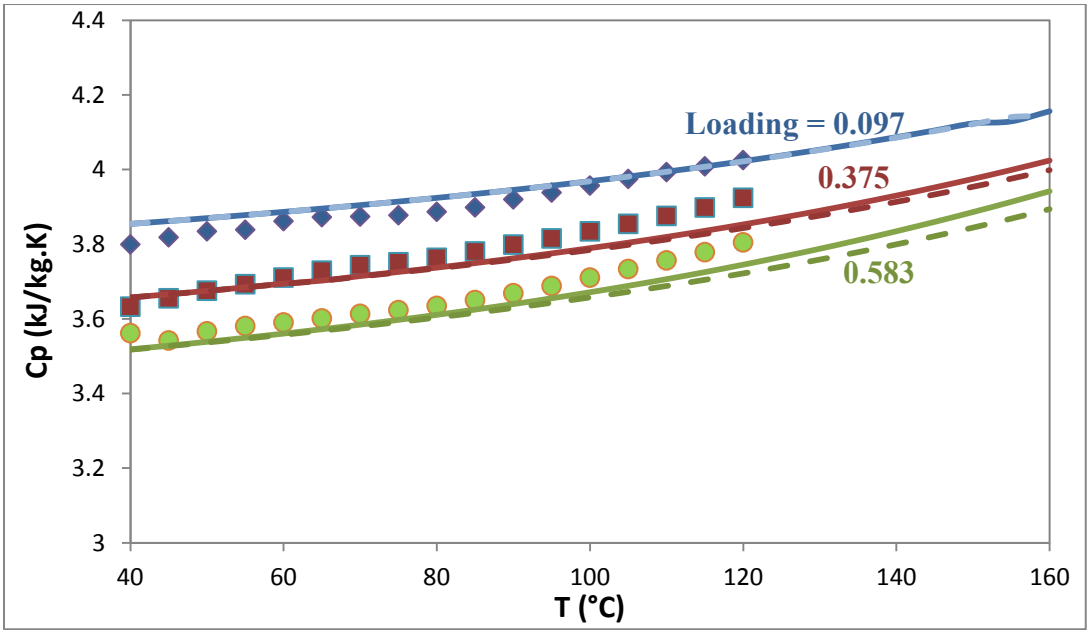

Figure 4-46: Sensitivity Analysis – Specific Heat Capacity of 3.5 m MEA.
Experimental data points (Hilliard 2008): ♦ 0.097 loading, ■ 0.375 loading, ● 0.583 loading; solid lines: Model B; dashed lines: sensitivity analysis.

Figure 4-47 is the sensitivity analysis for speciation in 7 m MEA. The differences between the results are very small, so the scale of y-axis is set to 0.01 - 0.2 to enlarge the difference on the plot. At higher than 0.6 loading, the prediction from sensitivity analysis deviates more from the experimental data and the Model B prediction.

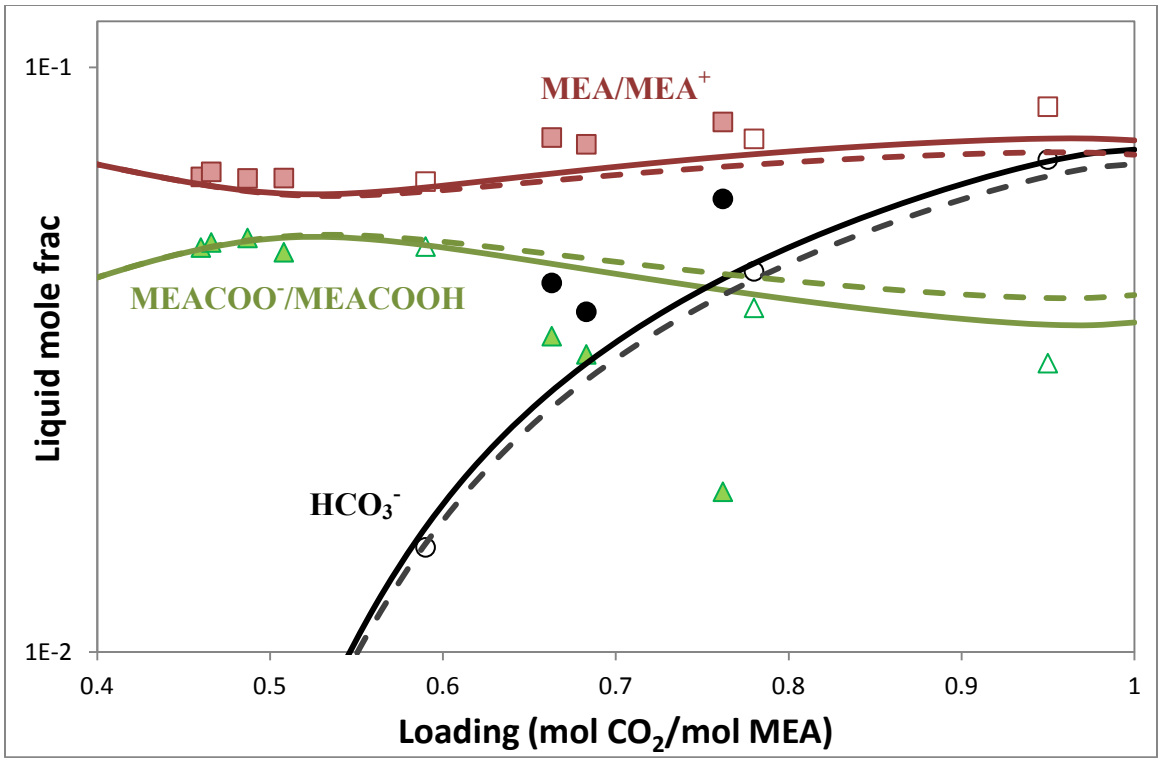

Figure 4-47: Sensitivity Analysis – Speciation in 7 m MEA at 40°C. **Open points: Poplsteinava et al. (2005); filled points: Bottinger et al. (2008); solid lines: Model B; dashed lines: sensitivity analysis.**

To conclude, after changing the value of DHFORM of MEACOOH by 15 kJ, CO_2 solubility and heat of absorption are affected more than the other properties and the prediction in the sensitivity analysis is not good to use, especially at high temperature and high loading.

4.4.4 Profile of 11 molal (40 wt%) MEA

11 m MEA or 40 wt% MEA has a high capacity, a fast reaction rate, and high heat of absorption. Assuming the lean and rich CO_2 loading corresponds to 0.5 and 5 kPa equilibrium P_{CO2} at 40°C, according to the empirical model for MEA in Table 2-11, the capacity of 7 and 11 m MEA are 0.50 and 0.66 mol CO_2 /kg (MEA+H_2O), respectively. If the stripping temperature increases from 120 to 140°C, the equivalent work of the CO_2 capture process can be reduced. The drawback of 11 m MEA is that the thermal degradation of MEA is high above 120°C. This may be solved by eliminating the residence time of high temperature processes. This section gives a profile of 11 m MEA by Model B for the design of CO_2 capture with high temperature stripping.

Figure 4-48 to 4-52 give the specific heat capacity, vapor-liquid equilibrium, heat of absorption, and speciation in 11 m MEA. In Figure 4-49 Model B prediction matches the CO_2 solubility data well except a few outliers at high loading 40 and 60°C. This may because the data incorporated in the regression in that range scatter and have two trends, as shown in Figure 4-21. Figure 4-50 presentes a favorable comparison of MEA volatility in 11 m MEA. Figure 4-51 indicates that the $-\Delta H_{abs}$ in 11 m MEA is a little larger than it is in 7 m MEA. According to Figure 4-52, in 11 m MEA, more MEACOOH is formed in the whole loading range, and it becomes an important species at high loading.

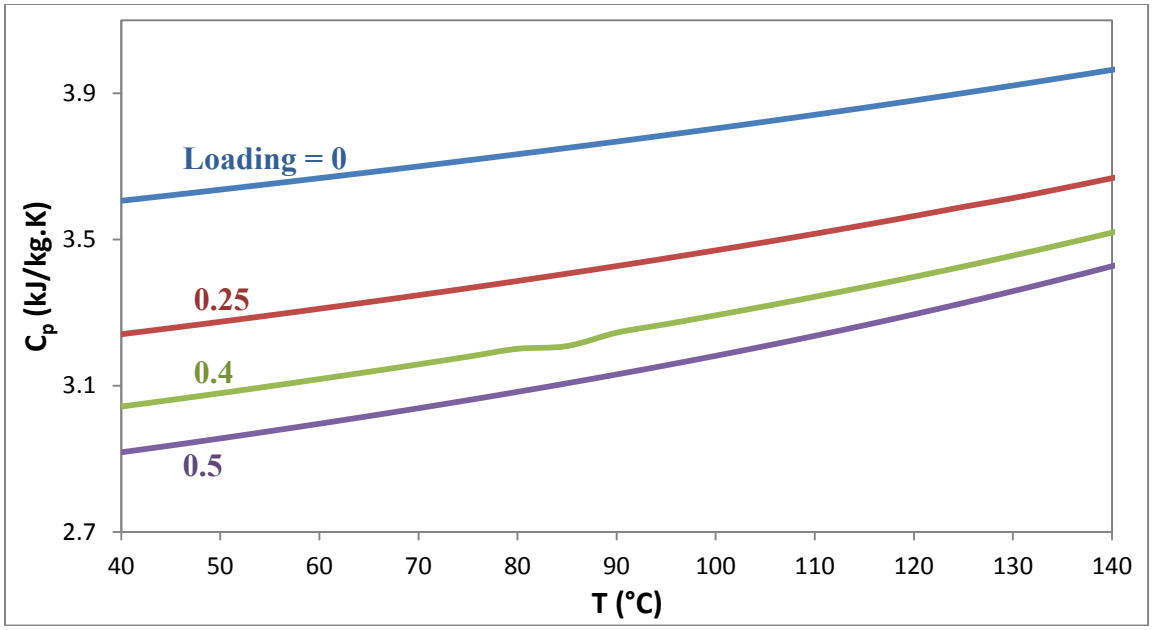

Figure 4-48: Specific Heat Capacity of 11 m MEA by Model B

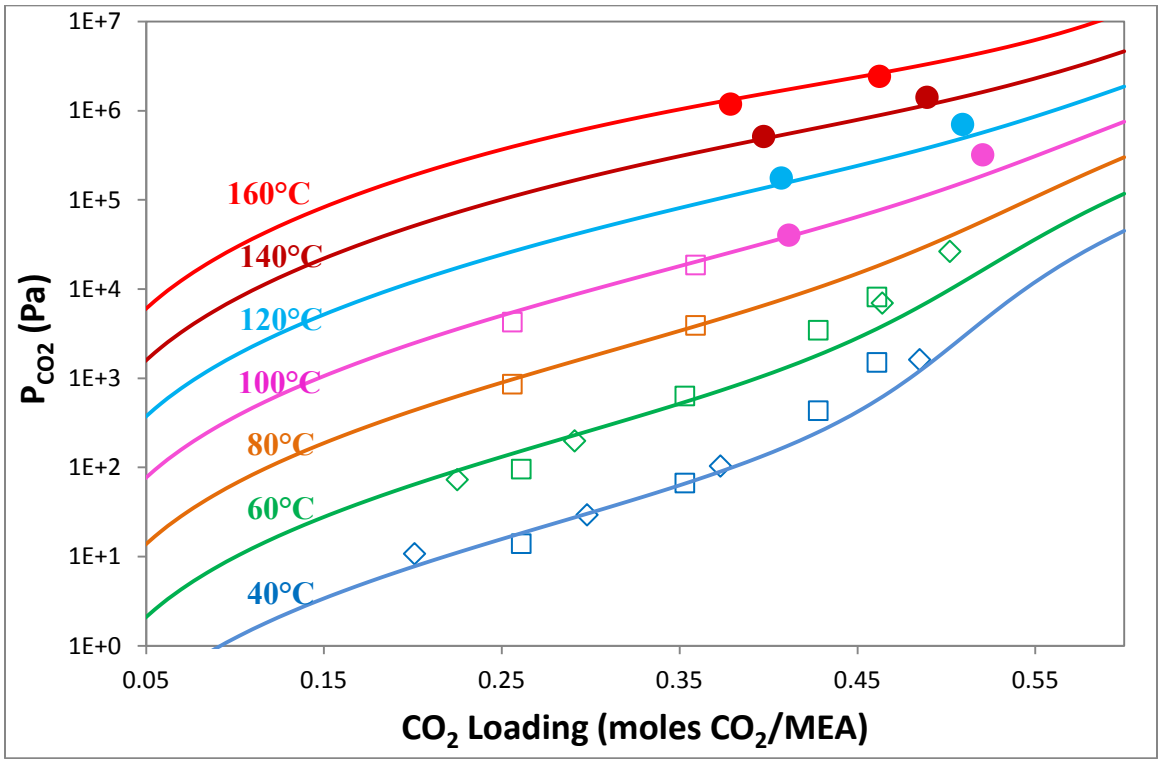

Figure 4-49: Prediction of CO_2 Solubility in 10.4-11 m MEA by Model B. ●: this work; □: Dugas et al. (2009); ◊: Hilliard (2008); lines: Model B for 11 m MEA.

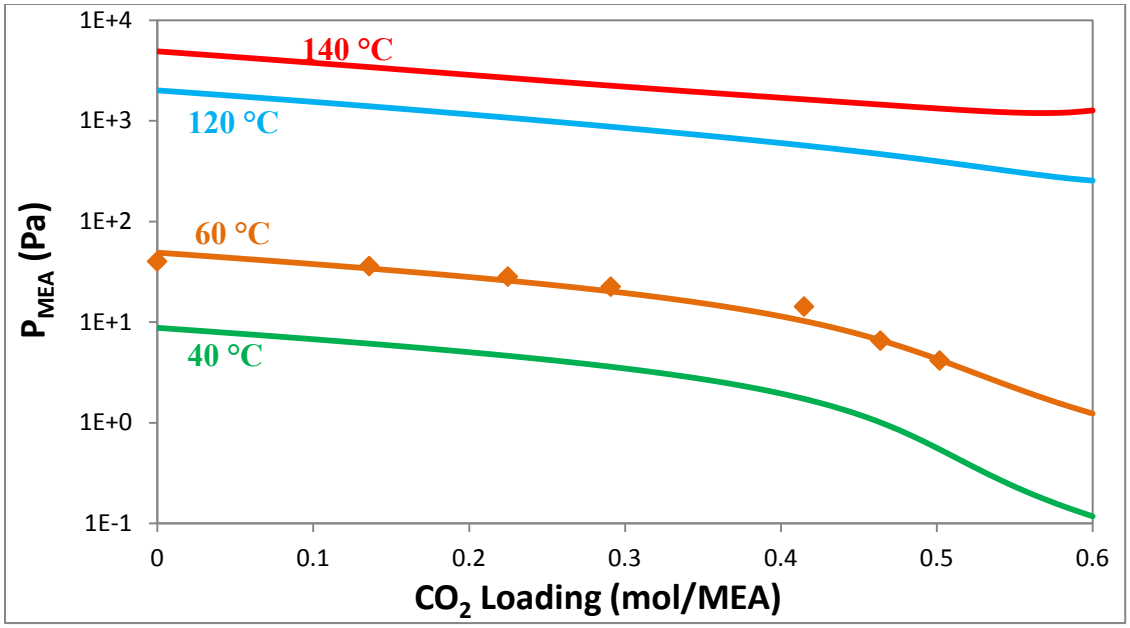

Figure 4-50: Prediction of MEA Partial Pressure over 11 m MEA by Model B.
Points: Hilliard (2008) 60°C 11 m MEA; lines: Model B - 11 m MEA.

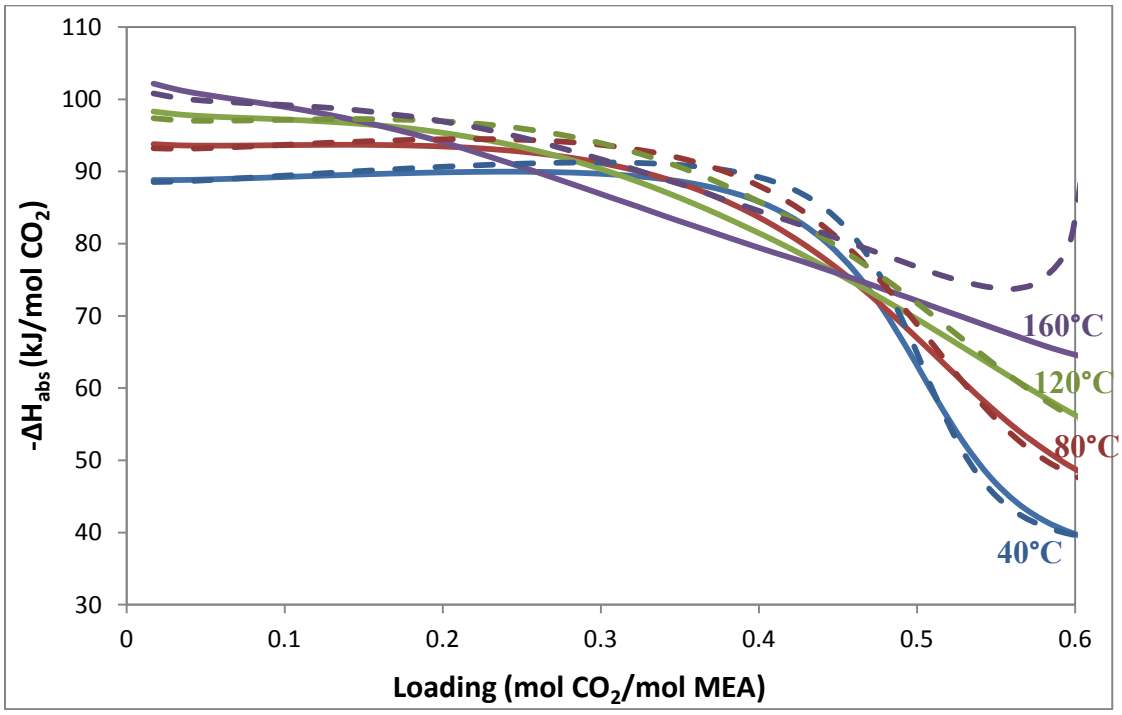

Figure 4-51: CO_2 Heat of Absorption in 7 and 11 m MEA by Model B. **Data points: Kim et al. (2007) 7 m MEA, ♦: 40°C, ■: 80°C, ▲: 120°C; solid lines: Model B - 7 m MEA; dashed lines: Model B - 11 m MEA.**

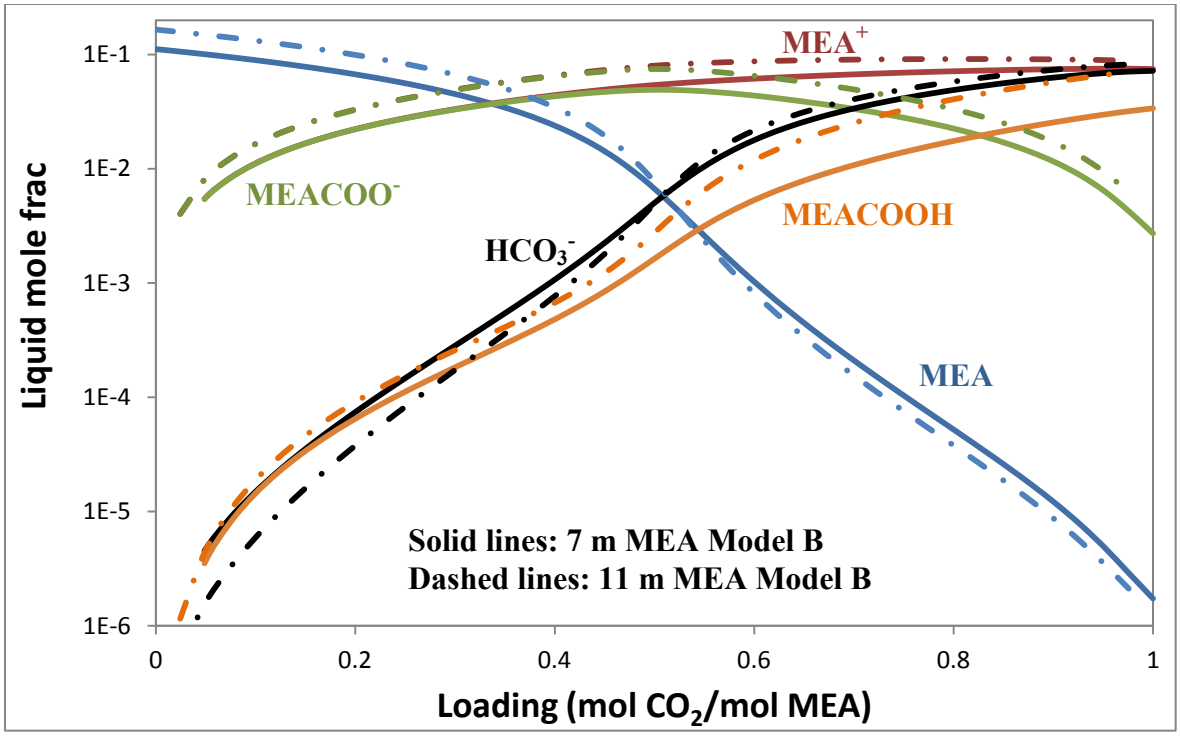

Figure 4-52: Speciation in 7 and 11 m MEA at 40°C by Model B

4.4.5 Model B Conclusions

For 7 m MEA, Model B well predicts CO_2 solubility except for a few outliers at high loading and high temperature; matches pK_a of MEACOOH; well predicts MEA volatility, specific heat capacity, and speciation. Reasonable CO_2 heat of absorption and enthalpy of MEA vaporization were obtained from Model B.

The speciation results show that at high temperature or high CO_2 loading, the concentration of MEACOOH is 0.1-3 % in 7 m MEA. The sensitivity analysis shows that the heat of formation of MEACOOH has an effect on CO_2 partial pressure and heat of absorption at high temperature and high loading. Therefore MEACOOH may be considered an important species at high loading or high temperature.

Model B also provides reasonable predictions of heat of absorption, speciation, and specific heat capacity for 11 m MEA.

4.5 CONCLUSIONS AND RECOMMENDATIONS

Two thermodynamic models in Aspen Plus® for the MEA-CO_2-H_2O system have been developed in this chapter: Model A without MEACOOH and Model B with MEACOOH. By comparing with experimental data of CO_2 solubility, MEA volatility, speciation, specific heat capacity, and total pressure, generally Model B gives a better prediction than Model A. Table 4-18 shows the result summary of Models A and B.

Table 4-18: Summary of Prediction by Models A and B

Experimental Data	Model A	Model B
P_{CO2}		Better
P_{MEA}		Better
$-\Delta H_{abs}$		Better
C_p	Similar	Similar
Speciation	Similar	Similar
P_t	Better	
pK_a of MEACOOH	-	Good

MEACOOH may be considered an important species at high temperature or high loading, when the concentration of MEACOOH is 0.1-3 % in 7 m MEA according to Model B. Model B prediction matches experimental pK_a of MEACOOH, and the measured concentration of MEACOO-/MEACOOH by NMR. The heat of formation of MEACOOH has effects on P_{CO2} and CO_2 heat of absorption, especially at high temperature and high loading. $-\Delta H_{abs}$ from Model B agrees with the $-\Delta H_{abs}$ from the empirical model developed in Chapter 2.

Although mostly developed from 7 m MEA data, Model B gives a good profile for 11 m (40 wt%) MEA.

Zwitterions may be considered to add into the thermodynamic models of other amine-CO_2-H_2O systems to get a better fitting of data at high temperature and CO_2 loading.

Chapter 5: Conclusions and Recommendations

This chapter summarizes the conclusions in total pressure experiments, high temperature vapor-liquid equilibrium experiments, and thermodynamic modeling in this work. Recommendations are made for future work.

5.1 TOTAL PRESSURE

Total pressure measurements at 100-160°C were performed with nine aqueous amine solvents: MEA, PZ, 8 m 1MPZ, 8 m 2MPZ, 4 m PZ/4 m 2MPZ, 3.75 m PZ/3.75 m 1MPZ/0.5 m DMPZ, DGA, 7 m MDEA/2 m PZ, and 5 m MDEA/5 m PZ. CO_2 partial pressure was derived from the total pressure data, and was correlated with a semi-empicial relationship: $\ln P_{CO_2}(\mathrm{Pa}) = a + b\frac{1}{T} + c\alpha + d\alpha^2 + e\frac{\alpha}{T} + f\frac{\alpha^2}{T}$, where α is the CO_2 loading (molCO_2/mol alkalinity).

For MEA and PZ, amine concentration does not have obvious effects on the CO_2 solubility when it is correlated as a function of CO_2 loading

Differential heat of absorption of CO_2 was derived from the semi-empirical models and is in the form of: $-\Delta H_{abs}(J/mol) = R(b + e\alpha + f\alpha^2)$. In this work $-\Delta H_{abs}$ varies from 66 kJ/mol for 4 m PZ/4 m 2MPZ and to 72, 72, and 73 kJ/mol for MEA, 7 m MDEA/2 m PZ, and DGA. Solvents with a higher heat of absorption may save more energy if stripping is at the same temperature.

The heat of absorption estimated from the total pressure data does not vary significantly with temperature. The temperature dependence of the heat of CO_2 absorption in MEA measured by Kim et al. (2007) is not consistent with either the total pressure CO_2 or the measured specific heat capacity.

Recommendations:

1. Increase the accuracy of total pressure measurements by the autoclave: use a platinum resistance thermometer instead of a thermocouple, keep a constant agitation rate, measure the weight of solution for each experimental run.
2. Find a more accurate way to calculate CO_2 partial pressure and to correct liquid loading: consider the non-ideality of N_2, water, amine, and CO_2 in the vapor phase.
3. Improve the semi-empirical models with more theoretical terms. This may capture a better CO_2 loading dependence of the heat of absorption at low to medium loading especially at low temperature.
4. Correlate CO_2 partial pressure with amine structures.

5.2 HIGH TEMPERATURE VAPOR-LIQUID EQUILIBRIUM

A high temperature vapor-liquid equilibrium method with online FTIR analysis was developed. Amine volatility was measured for MEA-H_2O at 80-140°C, MEA-CO_2-H_2O at 120 and 140°C, and PZ-CO_2-H_2O at 120 and 150°C.

At 0-0.5 loading (α), 313-413 K, 3.5-11 m MEA (mol fraction x is 0.059-0.165), the empirical model for MEA volatility (Pa) is $\ln(P_{MEA}/x_{MEA}) = 30.0\text{-}8153/T\text{-}2594\alpha^2/T$. In 7 m MEA with 0.2 and 0.5 loading, P_{MEA} is 920 and 230 Pa at 120 ℃. At 0.3-0.5 loading, the enthalpy of MEA vaporization, $-\Delta H_{vap,MEA}$, is 70 to 73 kJ/mol MEA.

At 0.25-0.4 loading, 313-423 K, 4.7-11.3 m PZ (x is 0.078-0.169), the empirical model of PZ volatility (Pa) is $\ln(P_{PZ}/x_{PZ}) = -123+21.6\ln T+20.2\alpha-18174\alpha^2/T$. In 8 m PZ with 0.3 and 0.4 loading, P_{PZ} is 400 and 120 Pa at 120 ℃, and 2620 and 980 Pa at 150 ℃. At 0.25-0.4 loading, $-\Delta H_{vap,PZ}$ is 85 to 100 kJ/mol PZ at 150 ℃ and 66 to 80 kJ/mol PZ at 40 ℃.

$\Delta H_{vap,PZ}$ has a larger dependence on CO_2 loading than $\Delta H_{vap,MEA}$ in rich solution because of the more complex speciation/reactions in PZ at rich loading.

The specific heat capacity of 8 m PZ is 3.43-3.81 J/(g·K) from 70 to 150°C.

Recommendations:

1. Add spargers to the gas inlet tube in each equilibrium cell to get smaller bubbles for better mass transfer.
2. The liquid sampling method needs to be modified. A better condensing system may help to reduce flashing; sampling into a vacuumed sample bomb, or sampling into a known amount of amine solution may help to get more representative samples.
3. Put better insulation to the connecting parts (the tube between the heated line and heating bath fluid) of the vapor sampling line to avoid condensing.
4. Use a better pressure controller instead of the regulator to control the feeding pressure.
5. Use a better thermometer instead of calibrating the temperature logger.
6. Redo or check the calibration of relative components in FTIR periodically.
7. Use an automatic bath fluid control system.
8. Optimize the vapor sample flow rate. It relates with temperature, pressure, and concentration of each component.
9. Measure MEA volatility in various MEA concentrations of MEA-H_2O and MEA-CO_2-H_2O.
10. Measure PZ volatility in various PZ concentrations of PZ-H_2O and PZ-CO_2-H_2O.
11. Perform the high temperature/pressure vapor-liquid equilibrium measurements with other aqueous amines.

5.3 MEA THERMODYNAMIC MODELING

Two new thermodynamic models of MEA-CO_2-H_2O were developed in Aspen Plus® starting with the Hilliard (2008) MEA model. One of them (Model B) includes a

new species MEACOOH and it gets a better prediction than the other (Model A) for CO_2 solubility, MEA volatility, speciation, heat of absorption, and other thermodynamic results. The major problems of Model A are at high temperature and high CO_2 loading.

The Model B prediction matches the experimental pK_a of MEACOOH, and measured concentration of MEACOO-/MEACOOH by NMR. In the prediction the concentration of MEACOOH is 0.1-3 % in 7 m MEA at high temperature or high loading, where the heat of formation of MEACOOH has effects on P_{CO2} and CO_2 heat of absorption. Model B solved the problems of Model A by adding MEACOOH and matched the experimental data of pK_a and speciation, therefore MEACOOH may be considered an important species at high temperature or high loading.

Although mostly developed from 7 m MEA data, Model B also gives a good profile for 11 m (40 wt%) MEA.

Recommendations:

1. Reduce the parameters in Model B regression by checking the correlation matrix and standard deviations of the parameters.
2. Find more experimental data for MEACOOH, and other related experimental data. Investigate more on the zwitterions and their effects on thermo properties of CO_2 loaded aqueous amines.
3. Zwitterions may be considered in other amine-CO_2-H_2O systems to get better thermodynamic models on a wider loading and temperature range.

Appendix A: Total Pressure Apparatus

A.1 VALIDYNE® DP15 TRANSDUCER CALIBRATION

A Validyne® DP15 transducer (±15 kPa accuracy) was calibrated by heating water and correlating the readings with known water vapor pressures from DIPPR (BYU, 1998- Provo, version 13.0). Separate calibrations were performed to the transducer with different equilibrium cells and different initial states.

A.1.1 Calorimeter

A.1.1.1 Calibration with Calorimeter - Vacuum

The following calibration was used for run MEA-1, PZ-1 and PZ-2. The vapor phase in the calorimeter was vacuumed before calibration and each experiment run, so no correction was conducted to the total pressure measured in these experiments.

Table A-1: Calibration with Calorimeter - Vacuum

Temperature (°C)	Transducer	Pressure (Pa)	Temperature (°C)	Transducer	Pressure (Pa)
100	0.005	101260	200	0.100	1551600
110	0.008	143120	190	0.080	1252500
120	0.012	198290	180	0.061	1000500
130	0.016	269710	170	0.048	790370
140	0.022	360750	160	0.038	616820
150	0.030	475090	150	0.031	475090
160	0.039	616820	140	0.022	360750
170	0.051	790370	130	0.017	269710
180	0.066	1000500	120	0.012	198290
190	0.085	1252500	110	0.009	143120
200	0.107	1551600	100	0.007	101260

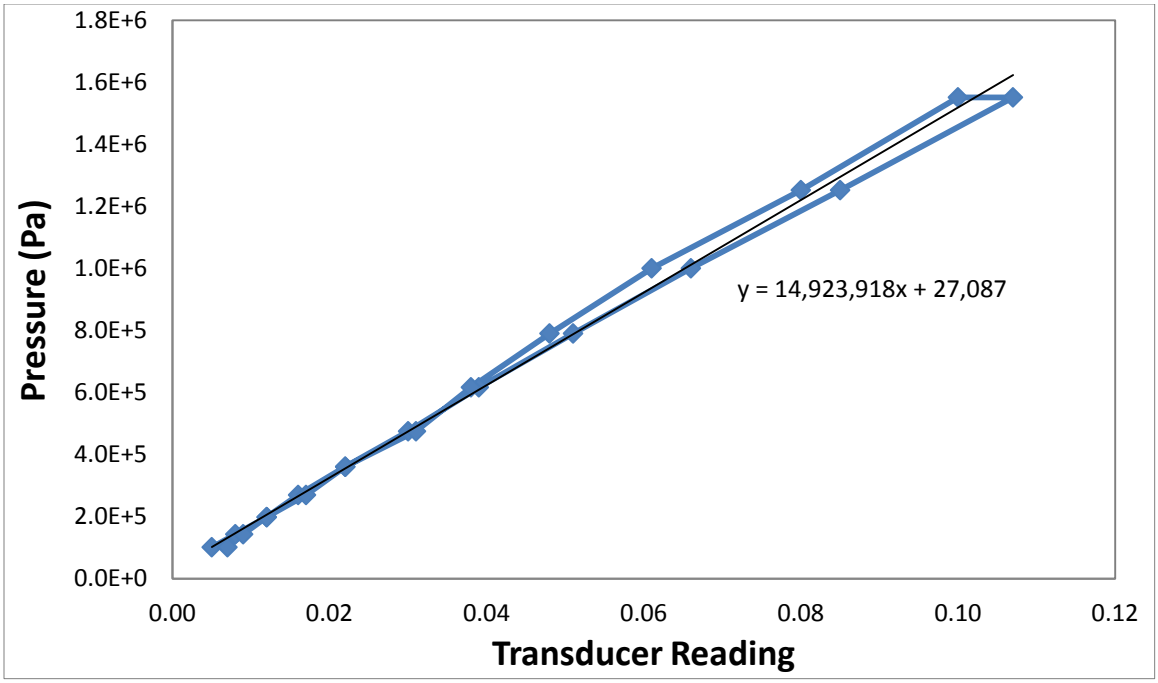

Figure A-1: Pressure Transducer Calibration with Calorimeter - Vacuum

A.1.1.2 Calibration with Calorimeter - Air

The following calibration was used for run PZ-3. 1 atm of air at room temperature was left in the cell during calibration and before the experiment run nitrogen was used to purge oxygen out. Thus corrections were made to the measured total pressure.

Table A-2: Calibration with Calorimeter - Air

T (°C)	Transducer Reading	P water (kPa)	P air (Pa)	P (Pa)	T (°C)	Transducer Reading	P water (kPa)	P air (Pa)	P (Pa)
19	0.038		101325	101325	170	0.668	790.37	153695.6	944065.6
100	0.14	101.26	129417.8	230677.8	180	0.847	1000.5	157163.9	1157664
110	0.176	143.12	132886.1	276006.1	190	1.053	1252.5	160632.1	1413132
120	0.223	198.29	136354.4	334644.4	200	1.31	1551.6	164100.4	1715700
130	0.277	269.71	139822.6	409532.6	200	1.256	1551.6	164100.4	1715700
140	0.354	360.75	143290.9	504040.9	190	1.005	1252.5	160632.1	1413132
152	0.476	501.11	147452.8	648562.8	180	0.804	1000.5	157163.9	1157664
160	0.539	616.82	150227.4	767047.4					

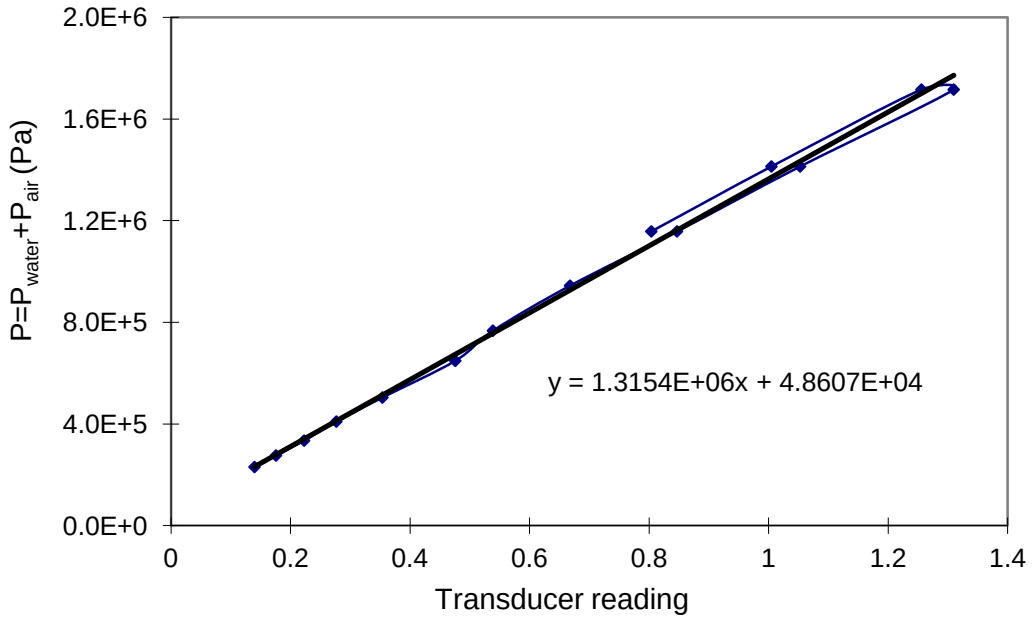

Figure A-2: Calibration with Calorimeter – Air

Calibration Calculation Example:

At 100 °C, the vapor pressure of water is 101260 kPa, the transducer reading is 0.14.

At 19 °C before calibration, the atmosphere has a reading of 0.038. Assume the air behaves as an ideal gas during calibration, according to PV=nRT, ignore the volume change, $P/P_i=T/T_i$, thus:

$$P_{air} = \frac{100 + 273.15(K)}{19 + 273.15(K)} \cdot 101325(Pa) = 129418(Pa)$$

The total pressure in the equilibrium cell at 100 °C:

$$P_{total} = P_{air} + P_{water} = 129418 + 101260 = 230678(Pa)$$

Then correlate the P_{total} with readings from the indicator and get the calibration curve in Figure A-2.

A.1.2 Autoclave

A.1.2.1 Calibration with Autoclave - Air

The following calibration was used for run MEA-2, PZ-4, and PZ-5. 1 atm of air at room temperature was left in the autoclave during calibration and before each experiment run nitrogen was used to purge oxygen out. Thus corrections were made to the measured total pressure.

Table A-3: Calibration with Autoclave - Air

T(°C)	Indicator reading	P water(Pa)	P air(Pa)	P(Pa)	T(°C)	Indicator reading	P water(Pa)	P air(Pa)	P(Pa)
28			102345	102345	190	1.047	1.25E+6	157400	1409900
102	0.175	108700	127493	236193	200	1.265	1.55E+6	160798	1712398
111	0.21	148000	130552	278552	200	1.273	1.55E+6	160798	1712398
121	0.248	204640	133950	338590	180	0.885	1.00E+6	154001	1154501
133	0.312	294800	138028	432828	159	0.59	601290	146864	748154
142	0.375	381620	141087	522707	139	0.398	350660	140067	490727
148	0.433	450160	143126	593286	121	0.276	204640	133950	338590
160	0.547	616820	147204	764024	100	0.2	101260	126813	228073
170	0.681	790370	150603	940973	190	1.079	1.25E+6	157400	1409900
159	0.55	601290	146864	748154	170	0.745	790370	150603	940973
171	0.704	809660	150942	960602	150	0.504	475090	143806	618896
170	0.681	790370	150603	940973	130	0.337	269710	137009	406719
178	0.82	955340	153321	1108661	110	0.236	143120	130212	273332
191	1.053	1.28E+6	157739	1437939					

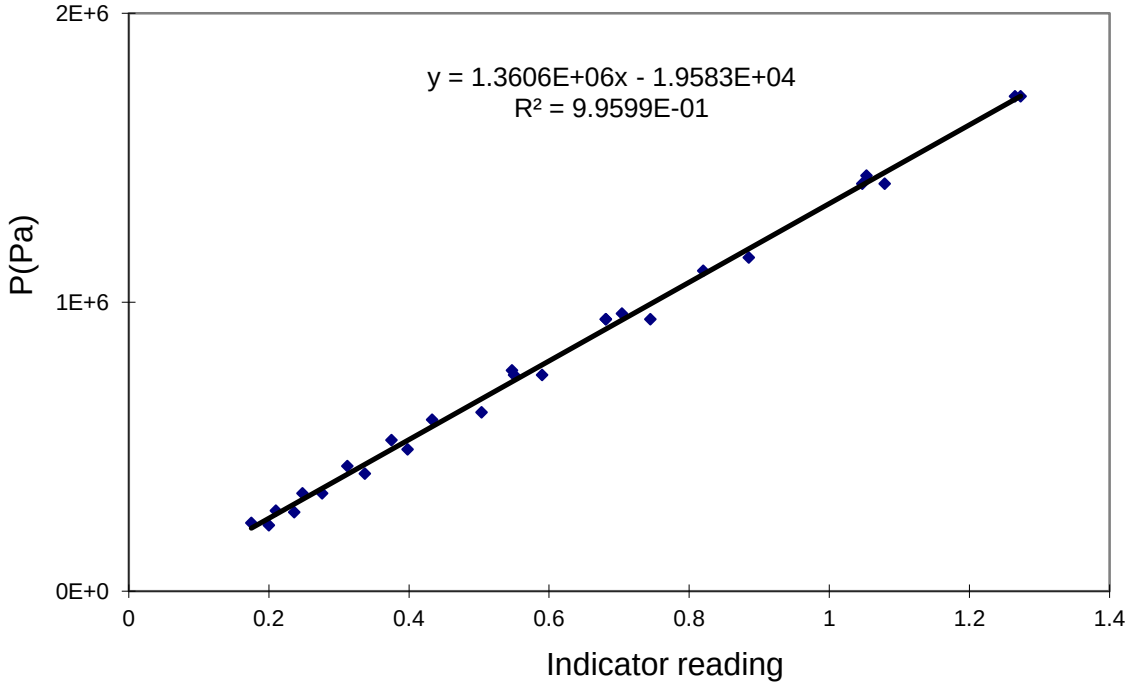

Figure A-3: Calibration with Autoclave – Air

Similar calculation was done as for the calorimeter to correct the calibration, except that the temperature is 298.15K for 1 atm air before calibration.

A.1.2.2 Calibration with Autoclave - Nitrogen

The following calibration was used for run MEA-3 and PZ-6. About 1 atm of nitrogen at room temperature was purged into the autoclave before calibration and before each experiment run. Thus corrections were made to the measured total pressure.

Table A-4: Calibration for Autoclave - Nitrogen

T(°C)	Indicator reading	P_{water} (kPa)	P_{N2}(Pa)	P(Pa)	T(°C)	Indicator reading	P_{water} (kPa)	P_{N2} (Pa)	P(Pa)
105	0.2225	120.7	128513	249213	200	1.357	1551.6	160798	1712398
110	0.242	143.12	130212	273332	190	1.131	1252.5	157400	1409900
121	0.295	204.64	133950	338590	180	0.942	1000.5	154001	1154501
131	0.351	277.88	137349	415229	169	0.769	771.45	150263	921713
140	0.417	360.75	140407	501157	160	0.6505	616.82	147204	764024

T(°C)	Indicator reading	P_{water} (kPa)	P_{N2}(Pa)	P(Pa)	T(°C)	Indicator reading	P_{water} (kPa)	P_{N2} (Pa)	P(Pa)
150	0.502	475.09	143806	618896	150	0.541	475.09	143806	618896
160	0.613	616.82	147204	764024	140	0.4505	360.75	140407	501157
171	0.7655	809.66	150942	960602	130	0.3795	269.71	137009	406719
180	0.923	1000.5	154001	1154501	120	0.322	198.29	133610	331900
190	1.1215	1252.5	157400	1409900	110	0.2775	143.12	130212	273332
200	1.364	1551.6	160798	1712398	99	0.239	97.702	126474	224176

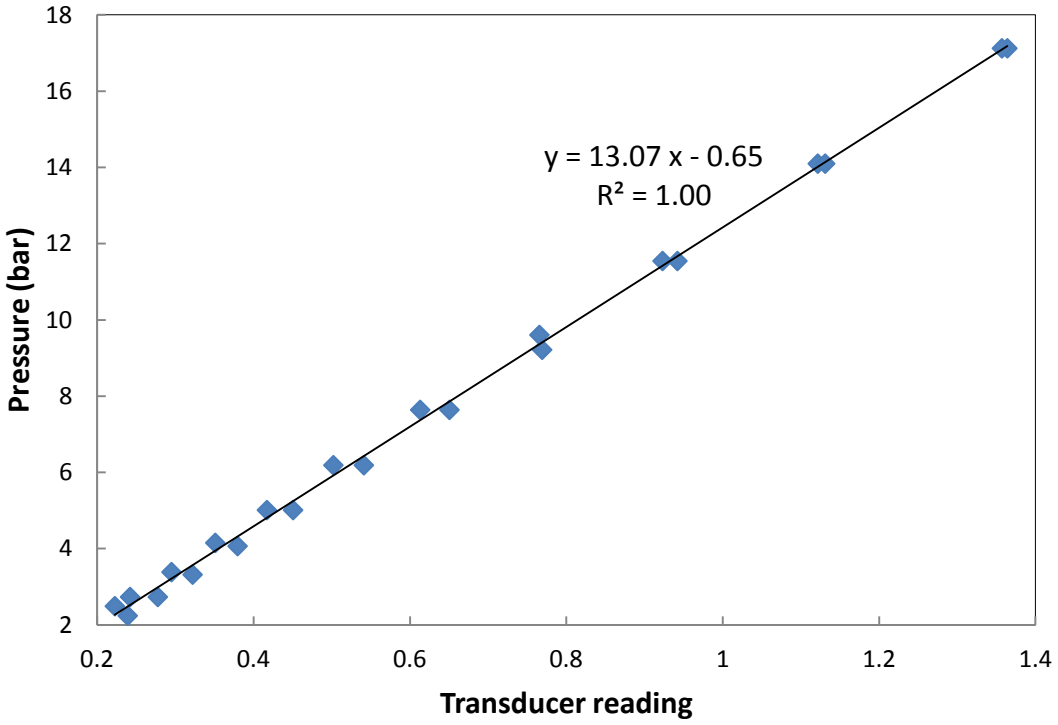

Figure A-4: Calibration with Autoclave – Nitrogen

Calibration Calculation Example:

At 105 °C, the vapor pressure of water is 120700 kPa, the transducer reading is 0.2225 (average value).

At 25 °C before calibration, the 1 atm nitrogen inside the vessel has a reading of 0.113. Assume the nitrogen behaves as an ideal gas during calibration, according to PV=nRT, ignore the volume change, $P/P_i=T/T_i$, thus:

$$P_{N_2} = \frac{105+273.15(K)}{25+273.15(K)} \cdot 101325(Pa) = 128513(Pa)$$

The total pressure in the equilibrium cell at 105 °C:

$$P_{total} = P_{N_2} + P_{water} = 128513 + 120700 = 249213(Pa)$$

Then correlate the P_{total} with readings from the indicator and get the calibration curve in Figure A-4.

A.1.2.3 Calibration with Autoclave - Vacuum

The following calibration was used for run MEA-4, MEA-5, and PZ 7-12. In the beginning of this calibration at about 110 ºC water vapor was released from a valve on top of the vessel directly to the back of hood until temperature dropped to 100 ºC. This was processed 3 times to purge all the air. So no correction was conducted to the total pressure measured in these experiments.

Table A-5: Calibration with Autoclave - Vacuum

Temperature (°C)	Transducer Reading	Pressure (kPa)
102.0	0.155	108.70
120.0	0.219	198.29
139.3	0.319	353.66
159.4	0.487	607.46
173.0	0.744	849.35
200.1	1.153	1554.90
220.8	1.719	2351.00
226.0	1.899	2593.40
209.1	1.378	1869.80
189.3	0.958	1233.40
171.2	0.659	813.56
150.6	0.434	482.78
130.9	0.292	277.05

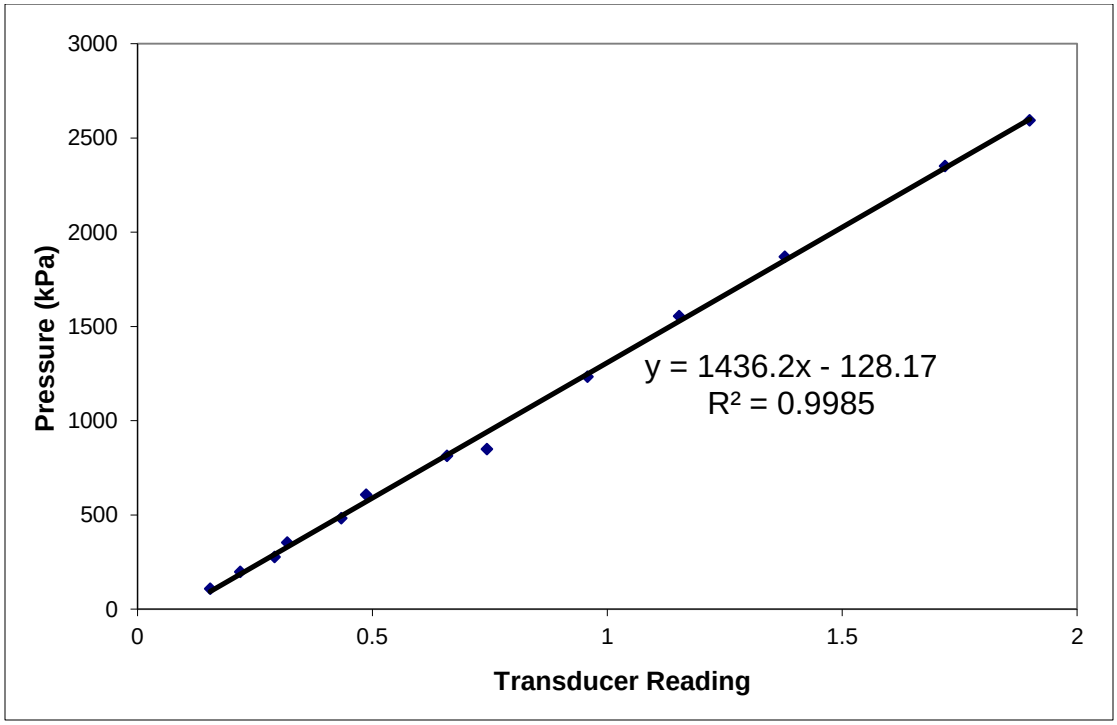

Figure A-5: Calibration with Autoclave – Vacuum

A.2 P AND T CALIBRATION WITH THE AUTOCLAVE AND LABVIEW® DATA LOGGER

The pressure transducer was calibrated with a dead weight tester. The calibration curve is shown in Figure A-6.

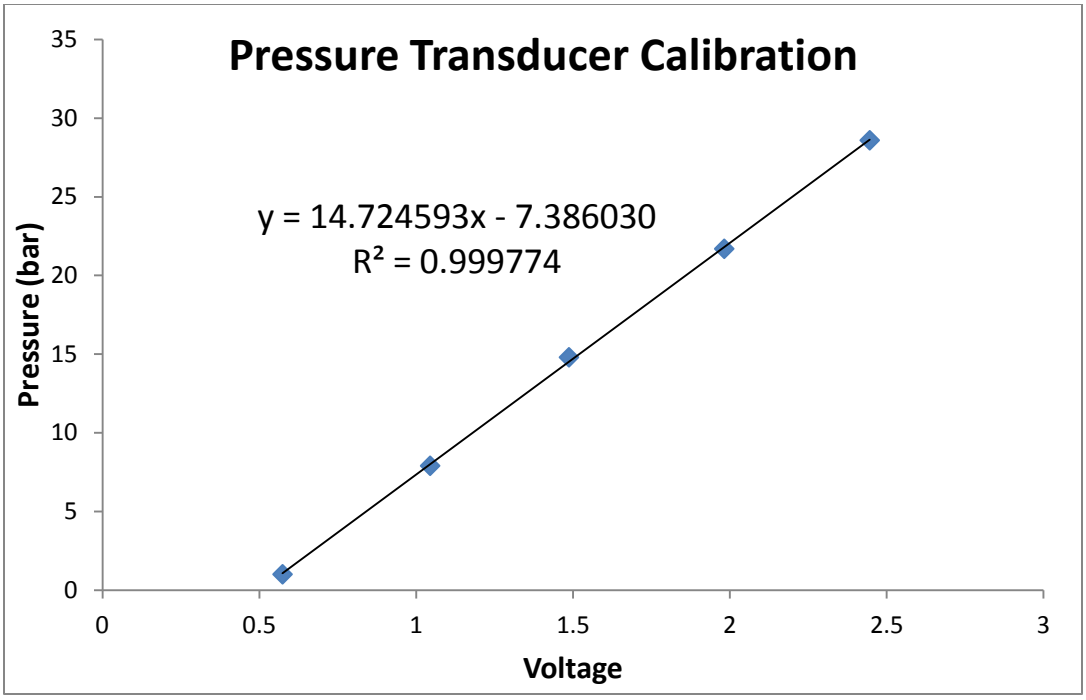

Figure A-6: Pressure Transducer Calibration with the Autoclave and LabView® Data Logger on 7/28/2009

LabView® SignalExpress® scales voltage to pressure data using the equation in Figure A.6 for the experiments before September 25th, 2009. After that an Omega® K type low noise thermocouple replaced the normal thermocouple and further pressure calibration associated with temperature measurement was performed. Pure water vapor pressure was measured at 100 to 204 °C and compared with literature data from DIPPR chemical databank. The correlation is shown in Figure A-7 below.

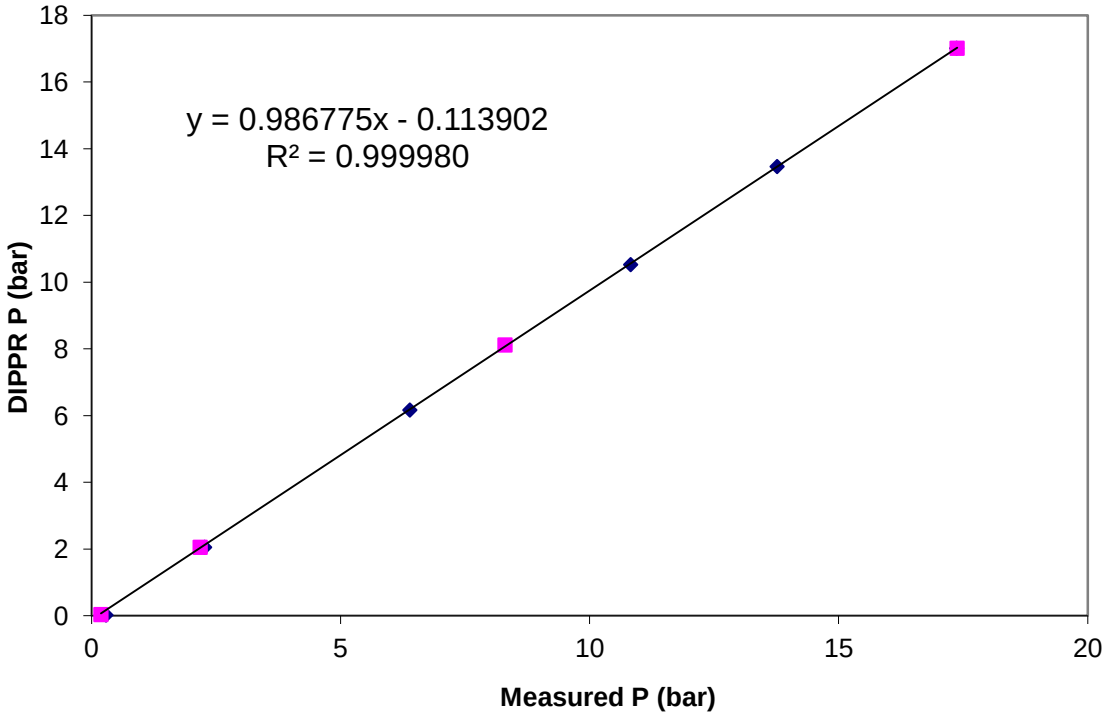

Figure A-7: Calibration of Pressure Transducer with the Thermocouple

For the experiments between September 25th 2009 and September 3rd 2010, a combination of the above two equations in Figures A-6 and A-7 was input into Signal Express® and used in total pressure experiments:

$$y = 14.529860x - 7.400745 \qquad \text{(A-1)}$$

y - pressure, bar.

x - voltage, V.

The pressure transducer calibration was repeated on September 3rd, 2010. Since then it was used in the total pressure experiments.

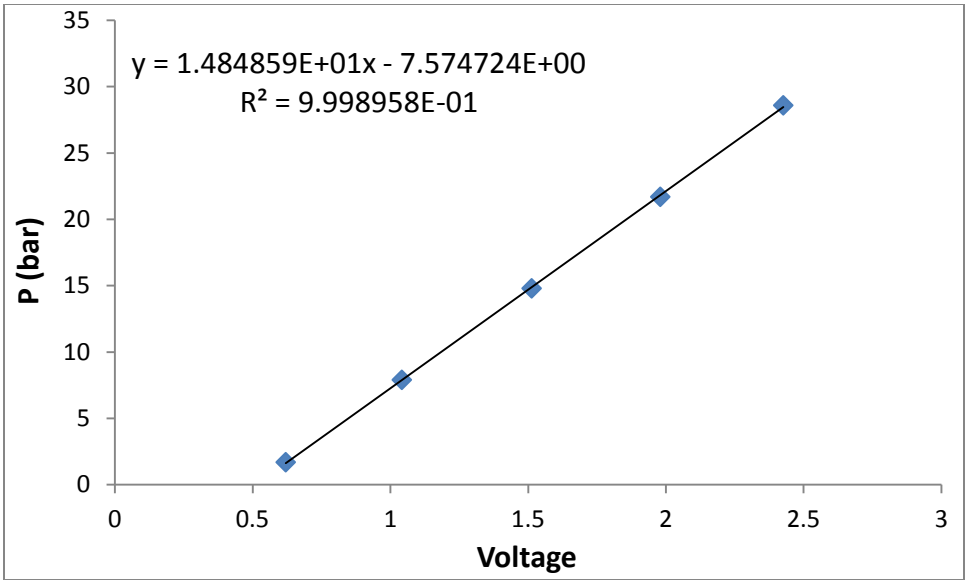

Figure A-8: Pressure Transducer Calibration with the Autoclave and LabView® Data Logger on 09/03/2010

Appendix B: High Temperature Pressure Vapor-Liquid Equilibrium Apparatus

B.1 Equilibrium Cells and Heads

Two 200 mL (i.d=1.5 in, inside depth=7 in) and one 600 mL (i.d=2.5 in, inside depth=8 in) stainless steel vessels (4752 and N4764-T-SS, Parr Instrument Co.) were used as equilibrium cells in series.

N4764-T-SS (600 mL) is a non-stirred vessel made of T316SS with the following features:

A. Head 818HC47 with only rupture disc assembly with 1000 psi rupture disc installed.
B. PTFE gasket with split ring.
C. MAWP is 3000 psi at 350 ℃.

The head 818HC47 has six openings. The openings are assigned for: gas feeding, gas sampling, rupture disc assembly, liquid sampling, thermocouple, pressure transducer and vent (share one opening by a "T" connector).

4752 general purpose vessel (200 mL) has the following features:

A. Head 428HC9 and cylinder made of T316SS.
B. PTFE flat gasket with split ring closure.
C. MAWP is 3000 psi at 350 ℃.

The head 428HC9 has two 1/8'' NPT ports. The openings are assigned for gas inlet and gas outlet, respectively.

The other tubes, valves, and fittings are from Swagelok®.

B.2 Oil Bath

DC 200 fluid 50 CS by Dow Corning was used in the oil bath (EX-35, Thermo Fisher Scientific). The bath is good for ambient +12 ℃ to 200 ℃ with a temperature

stability of ±0.01 ℃. The bath volume is 9.6 gallons, and a force/suction pump head circulates the bath fluid. Figure B-1 shows the dimensional diagram of the oil bath. The unit dimension is 52.4*28.9*64.5 (H*W*D) cm, and the bath W*L*D is 22.4*39.4*30.5 cm.

To avoid damaging the temperature control system of the bath, the level of the silicon oil (bath fluid) must be kept between the two slots in the stainless steel separating board in the oil bath. The oil expands as temperature increases, and because of the large quantity of the oil and the large temperature increase during an experiment, oil needs to be pumped in and out of the bath to maintain a good fluid level. Therefore, an oil reservoir and a peristaltic Masterflex pump (by Cole Parmer) between the bath and the reservoir were used.

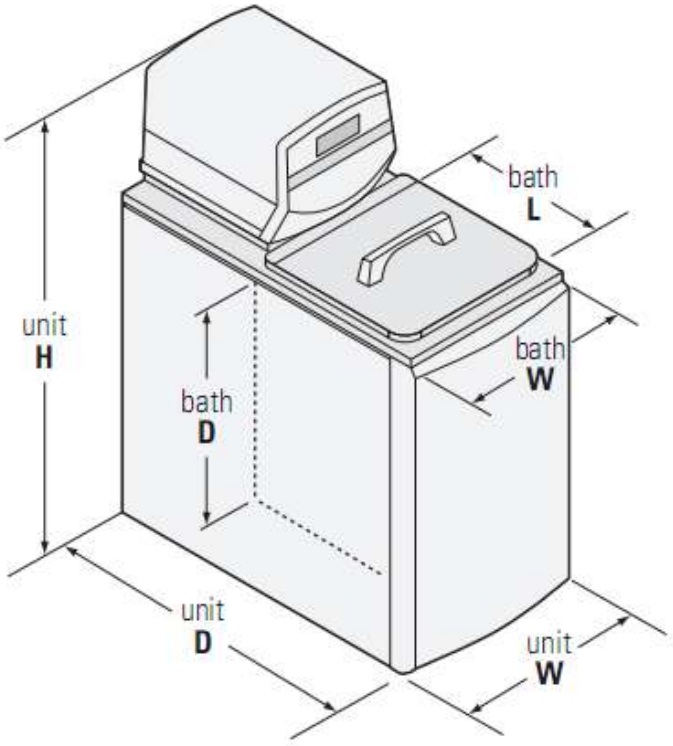

Figure B-1: NESLAB EX Dimensional Diagram (from Catalog of Thermo Scientific NESLAB™ RTE and EX Series Bath Circulators)

B.3 WIRING OF THE PRESSURE DAQ SYSTEM, CALIBRATION OF PRESSURE TRANSDUCER

A pressure transducer (Druck® PTX 611, 0–30 bar absolute) was connected to a signal converter and data logger NI USB 6009. LabView® SignalExpress® software was used for data recording. PTX611 gives signal in current. An in-house signal converter was built to convert current to voltage for data acquisition. The circuit of the data acquisition system is shown in Figure B-2.

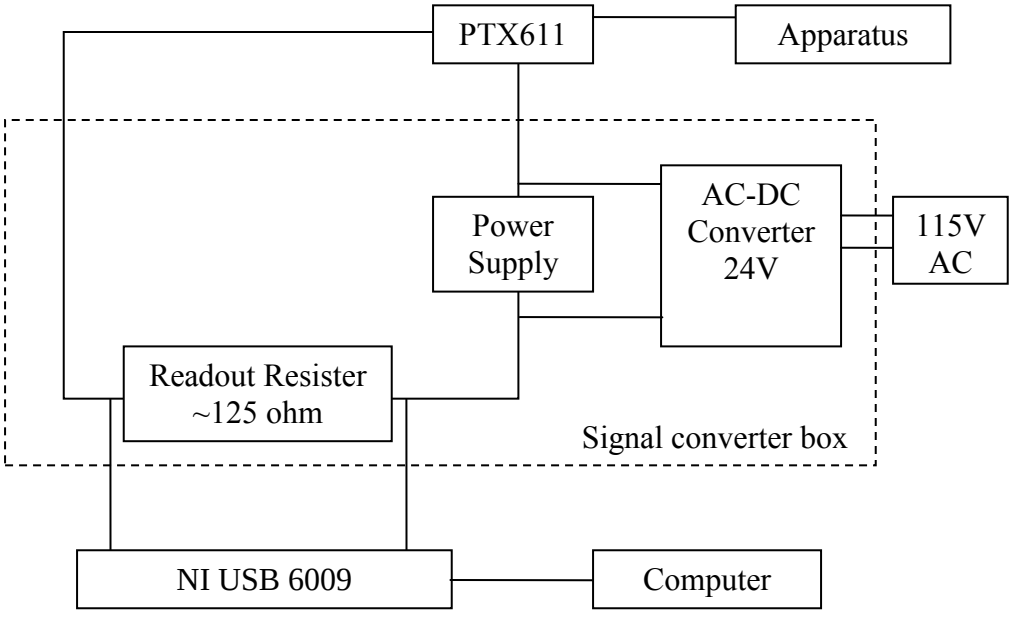

Figure B-2: Data Acquisition System of the Pressure Measurement

The pressure transducer was calibrated using a dead weight tester (S/N 19189/278, by Budenberg Volumetrics, Inc.), located and maintained in the fundamental laboratory in the Department of Chemical Engineering at The University of Texas at Austin. The transducer was connected to the dead weight tester, the pressure of which can be set by varying the weight loading. Figure B-3 is the calibration curve of the pressure and the voltage signal.

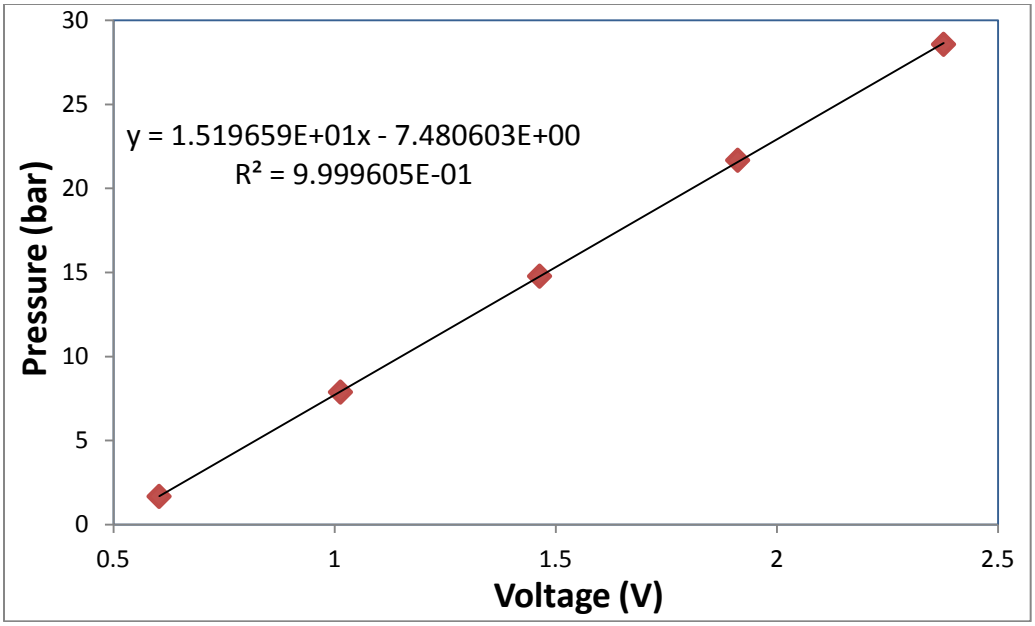

Figure B-3: Pressure Transducer Calibration on 8/17/2010

B.4 TEMPERATURE CALIBRATION

The HH506RA data logger from Omega® was found with a systematic error for temperature recording. Thus a temperature calibration was performed to the data logger.

Calibration was conducted with a Fuji Electric PXZ-4 temperature controller. Multiple thermocouples were held at the same position in the oil bath and multiple points were read by the temperature reader and the Fuji Electric PXZ-4 temperature controller. Readings from the two were correlated in Figure B-4, where the correlation equation was used in the following experiments with the HH506RA data logger.

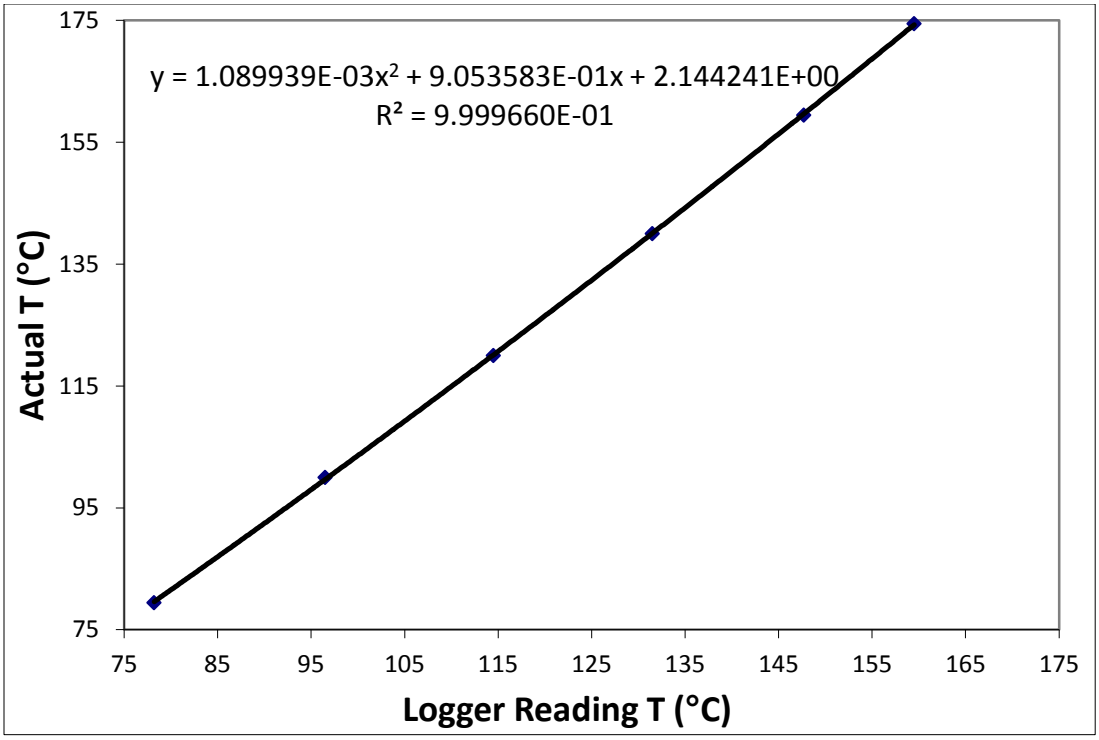

Figure B-4: Temperature Calibration for Data Logger Omega® HH506RA on 08/25/2010

B.5 Solution Charging, Starting up, Finishing, and Cleaning Procedures of the HTPVLE Experiment

B.5.1 Solution Charging and Starting of the HTPVLE Experiment

1. Pour certain amount of prepared solution into the three clean equilibrium cells. For high liquid level runs, about 170, 170, and 450 mL of the solution was added into the 200 mL, 200 mL, and 600 mL cells, respectively. For middle liquid level runs, about 100, 100, and 300 mL of the solution was added into the cells.
2. Assemble the clean covers onto the cells, make sure the o-rings are clean and in the right position, then for each cell put the two split rings on to hold the edges of the cover and the cell top, put three screws into the holes of each split ring and use a wrench to tighten the screws. This makes the sealing of the equilibrium cells.

3. Check the sealing. Close all the valves on the covers.
4. Connect N_2 to the first equilibrium cell and open the feeding valve. Let N_2 flow into the cells to increase the pressure to higher than 1 atm.
5. Close the feeding valve and disconnect N_2 line from the cells. Put the cells into the oil bath carefully. Hold the edges and 1/4'' tubes and avoid putting strength to connections of the fittings, especially the 1/8'' fittings. This process requires two people.
6. Pump silicon oil from the reservoir into the bath. As soon as the oil level reaches the lower slot in the separating board of the bath, stop pumping.
7. Turn on the bath; set the target temperature. As the temperature increases, the oil will expand; check the oil level every 20 min to make sure it is below the higher slot in the separating board of the bath. Pump oil out of the bath into the reservoir if necessary.
8. During the heating process, connect the gas line on the side of the hood to the feeding line of the first cell. Connect the FTIR heated lines to the vapor sampling line on the third equilibrium cell. Wrap insulation around the plastic tube that is not covered of the heated line.
9. After the temperature reaches the target and maintains for about 20 min, start the experiment procedure as in section 3.2.4.

B.5.2 Finishing and Cleaning Procedures of the HTPVLE Experiment

1. After one run, turn off the bath. Close all the valves.
2. When the system pressure is lower than 2 bar, for unloaded MEA solution, set the N_2O feeding pressure to be higher than the system pressure, open N_2O feeding and

keep the feeding valve open. For CO_2 loaded MEA, use N_2 or CO_2 instead of N_2O. For CO_2 loaded PZ, use N_2 instead of N_2O.

3. Leave the apparatus overnight for cooling down.
4. Close $N_2O/N_2/CO_2$ feeding, disconnect the FTIR heated lines and the feeding lines.
5. Hold the edges and ¼'' tubes of the apparatus to get it out of the bath. Put the cells in the special plastic pan for this apparatus. This process needs two people.
6. Loosen the screws of the split rings with a wrench and open up the cells. Put the covers of the cells upside down in a special plastic pan and put the pan aside.
7. Use a syringe to stir in the third equilibrium cell and collect a post-experiment liquid sample. Pour the rest solution into the waste container. Rinse each cell with running water and DI water until clean. Detergent and a brush may be used for cleaning if there is oil in the cell. The rinsing process needs two people.
8. Use paper towel and Kim Wipe to clean the inside of the covers. Use Kim Wipe to clean the edges on top of the equilibrium cells.

B.5.3 ATTENTION

1. Make sure the silicon oil level is between the two slots in the separating board of the bath when the bath is on. Low fluid level error may stop the bath from working.
2. Make sure all or the most of the vapor sampling lines are submerged under the silicon oil. This ensures the temperature control of the liquid sampling line and avoids condensing in the line.
3. Make sure the pressure in the equilibrium cells is above 1.5 atm to avoid oil leaking into the system when they are in the oil bath.

Appendix C: Raw Data

C.1 Total Pressure Experimental Data

The data here are from experiments with Validyne® DP15 transducer. The data from experiments with the PTX 611 transducer can be found directly in Chapter 2.

C.1.1 MEA-CO_2-H_2O Total P Data

MEA-4 failed so it is not listed here.

Table C-1: Raw Data for Run MEA-1

Temperature (°C)	Transducer	Pressure (Pa)	Temperature (°C)	Transducer	Pressure (Pa)
100	0.011	191250	140	0.051	788207
110	0.016	265870	130	0.034	534500
120	0.026	415109	120	0.023	370337
130	0.038	594196	110	0.015	250946
140	0.061	937446	100	0.010	176326
150	0.098	1489631			

Table C-2: Raw Data for Run MEA-2

T(°C)	Transducer	P (Pa)	$P_{corrcted}$ (Pa)	T(°C)	Transducer	P (Pa)	$P_{corrcted}$ (Pa)
101	0.257	330091	188823	160	1.593	2147173	1983628
111	0.344	448463	303420	166	1.765	2381876	2216066
121	0.467	615817	466998	161	1.615	2177106	2013184
130	0.634	843037	690820	149	1.171	1573680	1414288
140	0.870	1164139	1008146	139	0.887	1187269	1031654
150	1.191	1600211	1440443				

Table C-3: Raw Data for Run MEA-3

T(°C)	transducer reading	P_t(Pa)	T(°C)	transducer reading	P_t(Pa)	T(°C)	transducer reading	P_t(Pa)
101	0.2235	91477	160	1.15	1281241	129	0.4765	412044
111	0.275	155167	170	1.5535	1805101	120	0.378	286547
120	0.343	240791	170	1.5235	1765882	110	0.301	189520
131	0.4705	403473	160	1.156	1289085	100	0.249	125176
140	0.634	613945	150	0.878	929291			
150	0.8495	892032	140	0.6485	632901			

Table C-4: Raw Data for Run MEA-5

T(ºC)	transducer reading	P_t(Pa)	T(ºC)	transducer reading	P_t(Pa)	T(ºC)	transducer reading	P_t(Pa)
100.5	0.255	108340	150.2	0.64	644022	120.4	0.345	230689
111.3	0.291	156294	159.0	0.803	875068	109.0	0.293	159965
121.8	0.344	228767	152.0	0.671	687920	101.1	0.254	106695
131.9	0.417	330103	142.3	0.532	491656			
141.4	0.516	468989	129.9	0.409	319308			

C.1.2 PZ-CO_2-H_2O Total P Data

PZ-11 failed so it is not listed here.

Table C-5: Raw Data for Run PZ-1

Temperature (°C)	Transducer	Pressure (Pa)	Temperature (°C)	Transducer	Pressure (Pa)
100	0.011	191250	160	0.118	1788109
110	0.015	250946	150	0.084	1280696
120	0.024	385261	140	0.056	862826
130	0.032	504652	130	0.037	579272
140	0.054	832979	120	0.024	385261
150	0.086	1310544	110	0.015	250946

Table C-6: Raw Data for Run PZ-2

Temperature (°C)	Transducer	Pressure (Pa)	Corrected P (Pa)	Temperature (°C)	Transducer	Pressure (Pa)	Corrected P (Pa)
80	0.004	86783	36997	180	0.263	3952077	3888194
100	0.009	161402	108797	169	0.14	2116436	2054103
110	0.013	221098	167083	160	0.104	1579174	1518110
120	0.02	325565	270140	150	0.074	1131457	1071803
130	0.037	579272	522437	140	0.052	803131	744886
140	0.059	907598	849354	130	0.031	489728	432894
150	0.089	1355316	1295661	119	0.023	370337	315053
160	0.127	1922425	1861361	110	0.018	295718	241702
170	0.18	2713392	2650918	100	0.013	221098	168493

Table C-7: Raw Data for Run PZ-3

T(°C)	Transducer	P (Pa)	T(°C)	Transducer	P (Pa)
104	0.183	289325	160	1.460	1969091
111	0.227	347203	167	1.991	2667568
120	0.315	462958	161	1.429	1928314
130	0.452	643168	149	1.005	1370584
140	0.676	937817	139	0.670	929925
150	1.012	1379792	125	0.345	502420

Table C-8: Raw Data for Run PZ-4

T(°C)	Transducer	P_t (Pa)	Corrected P(Pa)	T(°C)	Transducer	P_t (Pa)	Corrected P(Pa)
110	0.246	315125	133868	170	1.5965	2152615	1942975
120	0.321	417170	231183	160	1.186	1594089	1389179
130	0.4275	562074	371356	150	0.842	1126042	925863
140	0.578	766844	571395	140	0.604	802219	606771
150	0.8055	1076380	876201	130	0.443	583163	392445
160	1.093	1467553	1262643	120	0.344	448463	262476
170	1.5295	2061455	1851814	110	0.267	343697	162441
174	1.774	2394121	2182589	100	0.224	285191	108666

Table C-9: Raw Data for Run PZ-5

T(°C)	Transducer reading	P_t(Pa)	P(Pa)	T(°C)	Transducer reading	P_t(Pa)	P(Pa)
81	0.2305	294035	136936	157	1.9265	2601613	2410800
89	0.287	370909	210261	150	1.6625	2242415	2054707
94	0.3335	434177	271311	139	1.2765	1717223	1534395
101	0.4075	534862	368890	130	1.0135	1359385	1180550
111	0.563	746435	576028	120	0.7715	1030120	855720
120	0.728	970934	796534	110	0.583	773647	603683
130	0.9795	1313125	1134289	100	0.4375	575680	410152
140	1.2945	1741714	1558442	90	0.3225	419211	258119
146	1.4925	2011113	1825179	82	0.256	328731	171188
150	1.6675	2249218	2061510				

Table C-10: Raw Data for Run PZ-6

T(ºC)	Transducer reading	P_t(Pa)	T(ºC)	Transducer reading	P_t(Pa)	T(ºC)	Transducer reading	P_t(Pa)
100	0.251	262580	151	1.4605	1843641	130	0.8415	1034471
110	0.3615	407013	160	1.932	2460012	120	0.625	751464
120	0.523	618119	160	1.9115	2433213	110	0.467	544933
134	0.807	989360	150	1.5205	1922081	100	0.3335	370432
140	0.9905	1229235	140	1.122	1401145			

Table C-11: Raw Data for Run PZ-7

T(ºC)	Transducer reading	P_t(Pa)	T(ºC)	Transducer reading	P_t(Pa)	T(ºC)	Transducer reading	P_t(Pa)
121	0.538	482894	161	1.863	2369457	129	0.7875	837945
137	0.9375	1050095	163	1.9655	2515848	119	0.5895	557678
146	1.239	1479419	150	1.4155	1731268	110	0.441	348092
152	1.469	1807285	139	1.048	1207975			

Table C-12: Raw Data for Run PZ-8

T(ºC)	Transducer reading	P_t(Pa)	T(ºC)	Transducer reading	P_t(Pa)	T(ºC)	Transducer reading	P_t(Pa)
100.3	0.22	74518.1	163.4	0.875	1035847	159.8	0.815	954906
110.1	0.251	139819	171.9	1.12	1388487	149.5	0.612	662796
118.5	0.288	193348	180.5	1.437	1843775	141.1	0.493	491536
129.9	0.359	294670	191.8	1.98	2623128	131.1	0.39	343991
140.9	0.466	448507	182.9	1.564	2029640			
151.5	0.62	669834	173.2	1.193	1497001			

Table C-13: Raw Data for Run PZ-9

T(ºC)	Transducer reading	P_t(Pa)	T(ºC)	Transducer reading	P_t(Pa)	T(ºC)	Transducer reading	P_t(Pa)
100.0	0.705	799937	140.6	1.720	2248496	117.8	1.006	1228207
110.0	0.850	1005924	146.7	1.954	2583187	112.2	0.864	1025533
120.0	1.090	1348350	140.5	1.701	2221231	100.6	0.626	686342
129.4	1.363	1738306	128.3	1.299	1646638			

Table C-14: Raw Data for Run PZ-10

T(ºC)	Transducer reading	P_t(Pa)	T(ºC)	Transducer reading	P_t(Pa)	T(ºC)	Transducer reading	P_t(Pa)
101.1	0.222	100211	169.4	1.125	1380592	140.0	0.512	507307
110.6	0.275	174033	180.0	1.495	1909424	130.0	0.403	353178
121.1	0.320	236125	191.1	1.988	2614787	120.0	0.324	242135
131.1	0.393	338550	180.6	1.535	1966727	108.9	0.263	157210
138.9	0.488	473104	170.0	1.164	1436458	100.6	0.232	114694
150.0	0.654	708830	160.6	0.881	1032286			
159.4	0.862	1005288	150.0	0.670	731810			

Table C-15: Raw Data for Run PZ-12

T(ºC)	Transducer reading	P_t(Pa)	T(ºC)	Transducer reading	P_t(Pa)	T(ºC)	Transducer reading	P_t(Pa)
100.0	0.279	168981	160.0	1.367	1714917	140.0	0.822	937738
109.4	0.350	268343	170.0	1.751	2263643	130.6	0.632	667468
120.0	0.461	424820	175.0	1.981	2592581	120.6	0.484	457686
130.0	0.610	636038	170.6	1.788	2316616	110.0	0.373	301209
140.0	0.802	909014	160.6	1.405	1769326	100.6	0.299	197539
150.0	1.056	1271034	148.3	1.034	1239909			

C.2 HIGH T P VAPOR-LIQUID EQUILIBRIUM RAW DATA

Table C-16: Raw Data for MEA Volatility in MEA-H_2O

Date	T(℃)	MEA	P_{MEA}	P_{H2O}	P_t
		m	Pa	kPa	kPa
20110311	99.4	6.91	434	95	95
20110311	120.2	6.94	1305	183	184
20110316	120.2	6.97	1345	207	208
20110316	130.1	7.00	2085	261	263
20110601	80.5	6.89	153	44	44
20110601	100.4	6.88	437	93	93
20110601	120.3	6.87	1421	202	203
20110602	130.1	6.86	2090	272	274
20110602	140.2	6.86	2914	362	365

Table C-17: Raw Data for MEA Volatility in MEA-CO_2-H_2O

Run #	Date	T	MEA	CO_2 Loading		P_{MEA}	P_{CO2}	P_{H2O}	P_t
		℃	m	Analyzed	Est. from P_{CO2}	Pa	kPa	kPa	kPa
MEA-S2	20110614	119.9	6.90	0.249	0.324	573	43	155	199
MEA-S2-2	20110615	119.9	6.87	0.345	0.351	642	62	167	230
MEA-S2-2	20110615	120.3	6.82	0.464	0.489	223	454	180	634
MEA-S3	20110627	139.9	6.81	0.210	0.222	1627	49	326	376
MEA-S3	20110627	140.0	6.63	0.335	0.367	1389	263	314	578
MEA-S3-2	20110628	139.9	6.57	0.427	0.469	718	969	316	1286
MEA-S4	20110701	140.3	6.86	0.486	0.467	795	966	317	1283
MEA-S4	20110701	140.2	6.90	0.408	0.389	1110	352	324	677
MEA-S4-2	20110705	120.4	7.00	0.368	0.361	610	73	169	243

Table C-18: Raw Data for PZ Volatility in PZ-CO_2-H_2O

Run #	Date	T	PZ	CO_2 Loading		P_{PZ}	P_{CO2}	P_{H2O}	P_t
		℃	m	Analyzed	Est. from P_{CO2}	Pa	kPa	kPa	kPa
PZ-F1	20101117	120.0	7.74	0.390	0.391	106	535	161	696
PZ-F1	20101117	119.5	8.17	0.290	0.291	482	91	166	257
PZ-F1	20101118	149.7	8.22	0.359	0.391	1269	2064	478	2543
PZ-F1	20101118	149.5	8.76	0.251	0.261	3139	287	397	687
PZ-F2	20101123	149.9	7.66	0.312	0.39	1164	2033	474	2508
PZ-F2	20101123	149.4	8.29	0.241	0.267	2851	309	395	707
PZ-F2	20101124	119.8	8.08	0.339	0.391	191	528	163	691
PZ-F2	20101124	118.6	8.70	0.303	0.302	523	104	154	259
PZ-F3	20101129	149.8	5.91	0.348	0.391	840	2051	493	2545
PZ-F3	20101129	149.7	6.11	0.228	0.239	2078	212	419	633
PZ-F3	20101129	149.0	6.11	0.228	0.258	2042	268	406	675
PZ-F3	20101130	120.1	6.14	0.336	0.391	130	530	178	708
PZ-F3	20101130	119.6	6.48	0.275	0.289	338	89	170	259
PZ-F4	20101202	149.8	4.73	0.340	0.389	615	2004	519	2523
PZ-F4	20101202	149.7	4.91	0.230	0.243	1742	223	428	653
PZ-F4	20101206	120.1	4.89	0.368	0.391	67	532	183	715
PZ-F4	20101206	119.8	5.08	0.284	0.28	232	77	179	256
PZ-F5	20101216	150.0	9.54	0.331	0.392	1261	2112	443	2557
PZ-F5	20101216	149.4	10.21	0.233	0.259	4533	275	403	683
PZ-F5	20101217	120.4	9.86	0.344	0.397	139	599	159	759
PZ-SP1	20110124	120.6	10.40	0.347	0.396	142	599	158	757

Run #	Date	T	PZ	CO_2 Loading		P_{PZ}	P_{CO2}	P_{H2O}	P_t
		℃	m	Analyzed	Est. from P_{CO2}	Pa	kPa	kPa	kPa
PZ-SP1	20110124	119.3	10.65	0.296	0.305	554	113	150	264
PZ-SP1	20110126	149	10.75	0.329	0.398	1623	2234	444	2679
PZ-SP1	20110126	148.6	11.30	0.234	0.273	4720	324	356	685
PZ-S1	20110707	120.2	7.81	0.382	0.385	169	485	160	645
PZ-S1-2	20110708	120.3	8.02	0.322	0.327	228	174	171	344
PZ-S2	20110712	149	7.5	0.245	0.32	1730	667	381	1049
PZ-S2	20110712	149	7.69	0.282	0.305	1820	533	372	907
PZ-S2	20110712	149.2	7.80	0.258	0.278	2859	363	382	748
PZ-S2	20110712	149	7.83	0.235	0.253	3617	250	363	617
PZ-S3	20110718	149.9	7.65	0.408	0.393	1188	2140	452	2593
PZ-S3	20110718	149.8	7.75	0.368	0.369	1459	1452	417	1871
PZ-S3	20110718	149.8	7.86	0.273	0.295	2879	474	367	844
PZ-S3	20110718	149.5	7.92	0.236	0.249	3397	242	377	623
PZ-S3-2	20110719	120.4	7.72	0.390	0.392	80	552	156	709
PZ-S3-2	20110719	120	7.69	0.316	0.325	176	166	158	325

References

Addicks J., Owren G., Tangvik K. Solubility of Carbon Dioxide and Methane in Aqueous Alkanolamine Solutions. *Proceedings of the International Gas Research Conference*, Amsterdam, November 2001.

Addicks, J. Solubility of Carbon Dioxide and Methane in Aqueous N-Methyldiethanolamine Solutions at Pressures between 100 and 200 bar. Norwegian University of Science and Technology, Department of Refrigeration and Air Conditioning, Trondheim, Norway. Ph.D. thesis. 2002.

Ali S.H. Kinetics of the Reaction of Carbon Dioxide with Blends of Amines in Amines in Aqueous Media Using the stopped-Flow Technique. *International Journal of Chemical Kinetics*. 2005, 37 (7), 391-405.

Alper E. Reaction Mechanism and Kinetics of Aqueous Solutions of 2-Amino-2-methyl-1-propanol and Carbon Dioxide. *Ind. Eng. Chem. Res.*, 1990, *29* (8), 1725-1728.

Anoufrikov Y., Kamps A.P-S., Rumpf B., Smirnova N.A., Maurer G. Solubility of H_2S in H_2O+N-Methyldiethanolamine+(H_2SO_4 or Na_2SO_4). *Ind. Eng. Chem. Res.* 2002, 41, 2571-2578.

Aronu U.E., Ghondal S., Hessen E.T., Haug-Warberg T., Hartono A., Hoff K.A., Svendsen H.F. Equilibrium in the H_2O-MEA-CO_2 System: New Data and Modeling. *Chemical Engineering Science*. Accepted.

Arstad B., Blom R., Swang O. CO_2 Absorption in Aqueous Solutions of Alkanolamines: Mechanistic Insight from Quantum Chemical Calculations. *J. Phys. Chem. A*, 2007, *111* (7), 1222-1228.

Austgen D.M., Rochelle G.T., Peng X., Chen C.C. Model of Vapor-Liquid Equilibria for Aqueous Acid Gas-Alkanolamine Systems Using the Electrolyte-NRTL Equation. *Ind. Eng. Chem. Res*. 1989, 28, 1060-1073.

Autoclave Engineers®, Zipperclave® 500&1000 mL stirred reactor, http://www.autoclaveengineers.com/ae_pdfs/SR_500_1000_Zip.pdf

Bates R.G., Pinching G.D. Acidic Dissociation Constant and Related Thermodynamic Quantities for Monoethanolammonium Ion in Water from 0 to 50°C. *Journal of Research of the National Bureau of Standards*. 1951, 46 (5), 349352.

Bishnoi S., Rochelle G.T. Absorption of Carbon Dioxide into Aqueous Piperazine: Reaction Kinetics, Mass Transfer, and Solubility. *Chemical Engineering Science.* 2000, 55, 5531-5543.

Bishnoi S. Carbon Dioxide Absorption and Solution Equilibrium in Piperazine Activated Methyldiethanolamine. The University of Texas at Austin. Ph.D. Dissertation. 2000.

Bottger A., Ermatchkov V., Maurer G. Solubility of Carbon Dioxide in Aqueous Solutions of N-Methyldiethanolamine and Piperazine in the High Gas Loading Region. *J. Chem. Eng. Data*. 2009, 54 (6), 1905-1909.

Böttinger W., Maiwald M., Hasse H. Online NMR Spectroscopic Study of Species Distribution in MEA–H_2O–CO_2 and DEA–H_2O–CO_2. *Fluid Phase Equilibria*. 2008, Vol 263, Iss 2., 131-143.

Cai ZY., Xie RJ., Wu ZL. Binary Isobaric Vapor-Liquid Equilibria of Ethanolamines + Water. *J. Chem. Eng. Data*, 1996, 41, 1101-1103.

Caplow M. Kinetics of carbamate formation and breakdown. *J. Am. Chem. Soc.* 1968, 90(24), 6795-6803.

Carson J.K., Marsh K.N., Mather A.E. Enthalpy of Solution of Carbon Dioxide in (Water + Ethanolamine, or Diethanolamine, or N-Methyldiethanolamine) at T = 298.15 K. *Journal of Chemical Thermodynamics.* 2000, 32, 1285-1296.

Chang H.T., Posey M., Rochelle G.T. Thermodynamics of Alkanolamine-Water Solutions from Freezing Point Measurements. *Ind. Eng. Chem. Res*. 1993, 32, (10), 2324-2335.

Chen C.C., Britt H.I., Boston J.F., Evans L.B. Extension and Application of the Pitzer Equation for Vapor-Liquid Equilibrium of Aqueous Electrolyte Systems with Molecular Solutes. *AIChE J*. 1979, 25, 820-831.

Chen C.C., Britt H.I., Boston J.F., Evans L.B. Local Composition Model for Excess Gibbs Energy of Electrolyte Solutions. Part 1: Single Solvent, Single Completely Dissociated Electrolyte Systems. *AIChE J.* 1982, 28, (4), 588-596.

Chen C.C. Evans L.B. A Local Composition Model for the Excess Gibbs Energy of Aqueous Electrolyte Systems. *AIChE J*. 1986, 32, (3), 444-454.

Chen X., Closmann, F., Rochelle GT. Accurate Screening of amines by the Wetted Wall Column. *GHGT-10*, 2010.

Chen X., Rochelle GT. Aqueous Piperazine Derivatives for CO_2 Capture: Accurate Screening by a Wetted Wall Column. *Chem. Eng. Res. Des*. 2011, Vol 89 (9), 1693-1710.

Chen Y-R**.,** Caparanga A.R., Soriano A.N., Li M.H. Liquid Heat Capacity of the Solvent System (Piperazine + N-Methyldiethanolamine + Water). *J. Chem. Thermodynamics*, 2010, Vol 42 (1), 54-59.

Chiu L.F., Li M.H. Heat Capacity of Alkanolamine Aqueous Solutions. *J. Chem. Eng. Data*, 1999a, 44 (6), 1396-1401.

Chiu L.F., Liu H.F., Li M.H. Heat Capacity of Alkanolamines by Differential Scanning Calorimetry. *J. Chem. Eng. Data*, 1999b, 44 (4), 631-636.

Cullinane, J.T. Thermodynamics and Kinetics of Aqueous Piperazine with Potassium Carbonate for Carbon Dioxide Absorption. The University of Texas at Austin. Ph.D. Dissertation. 2005.

da Silva E.F., Svendsen H.F. Ab Initio Study of the Reaction of Carbamate Formation from CO_2 and Alkanolamines. *Ind. Eng. Chem. Res.*, 2004, *43* (13), 3413-3418.

Dang, H. Absorption Rate and Solubility in Monoethanolamine/Piperazine/Water. The University of Texas at Austin. M.S.E. Thesis. 2000.

Davis J.D. Thermal Degradation of Aqueous Amines Used for Carbon Dioxide Capture. The University of Texas at Austin. Ph.D. Dissertation. 2009.

de Koeijer G., Solbraa E. High Pressure Gas Sweetening with Amines for Reducing CO_2 Emissions. Proceedings from IEA GHGT-7 Vancouver. 2004.

Derks P.W.J., Dijkstra H.B.S., Hogendoorn J.A., Versteeg G.F. Solubility of Carbon Dioxide in Aqueous Piperazine Solutions. *AIChE J.* August 2005, Vol 51, No. 8, 2311-2327.

Dingman J.C., Jackson J.L., Moore T.F., Branson J.A. Equilibrium Data for the H_2S-CO_2-Dyglycolamine® Agent-Water System, presented to the 62nd Annual Gas Process Association Convention, San Francisco, Mar. 14-16, 1983.

DIPPR, 1998-Provo, UT: BYU DIPPR, Thermophysical Properties Laboratory, 1998-Version 13.0.

Dodge B.F. *Chemical Engineering Thermodynamics, Chemical Engineering Series*. First Edition, McGraw-Hill Book Company, Inc. New York and London, 1944.

Dugas R.E., Rochelle G.T. Absorption and Desorption Rates of Carbon Dioxide with Monoethanolamine and Piperazine. *Energy Procedia.* 2009. Vol. 1, 1, 1163-1169.

EPA (US Environmental Protection Agency). The Experience with Emissions Control Policies in the United States. 2007. http://www.epa.gov/airmarkets/international/china/JES_USexperience.pdf

Ermatchkov V., Kamps A. P-S., Speyer D. and Maurer G. Solubility of carbon dioxide in aqueous solutions of piperazine in the low gas loading region. *J. Chem. Eng. Data*, 2006, 51 (5), 1788-1796.

Frailie P.T., Plaza J.M., Van Wagener D.H., Rochelle G.T. Modeling Piperazine Thermodynamics. *GHGT-10*. 2010.

Freeman S.A. Thermal Degradation and Oxidation of Aqueous Piperazine for Carbon Dioxide Capture. The University of Texas at Austin. Ph.D. Dissertation. 2011.

Freguia, S. Modeling of CO_2 Removal from Flue Gasses with Monoethanolamine. The University of Texas at Austin. M.S.E. Thesis. 2002.

Goff G.S. Oxidative Degradation of Aqueous Monoethanolamine in CO_2 Capture Processes: Iron and Copper Catalysts, Inhibition, and O_2 Mass Transfer. The University of Texas at Austin. Ph.D. Dissertation. 2005.

Goldman A.M., Leibush A.G. Study of the Equilibrium of Carbon Dioxide Desorption of Monoethanolamine Solutions in the Temperature Rage 75-140°C. *Tr. Gos. Nauchno-Issled. Proektn. Inst. Azotn. Promsti*. 1959, 10, 54-82.

Hamborg E.S., Versteeg G.F. Dissociation constants and thermodynamic properties of alkanolamines. *Energy Procedia*. *GHGT-9*. 2009. Vol 1, Iss 1. 1213-1218.

Hikita H., Asai S., Ishikawa H., Honda M. The Kinetics of Reactions of Carbon Dioxide with Monoethanolamine, Diethanolamine and Triethanolamine by A Rapid Mixing Method. *Chem. Eng. J*. 1977, 13 (1), 7-12.

Hikita H., Asai S., Katsu Y., Ikuno S. Absorption of Carbon Dioxide into Aqueous Monoethanolamine Solutions. *AIChE J.* 1979, 25, 793-800.

Hilliard M.D. A Predictive Thermodynamic Model for an Aqueous Blend of Potassium Carbonate, Piperazine and Monoethanolamine for CO_2 Capture from Flue Gas. The University of Texas at Austin. Ph.D. Dissertation. 2008.

Huttenhuis P.J.G., Agrawal N.J., Hogendoorn J.A., Versteeg G.F. Gas solubility of H_2S and CO_2 in aqueous solutions of N-methyldiethanolamine. *Journal of Petroleum Science and Engineering.* 2007, 55, 122-134.

International Energy Agency, CO_2 emissions from fuel combustion highlights (2009 edition), 2009.

IPCC (the Intergovernmental Panel on Climate Change). Fourth Assessment Report – Climate Change 2007. http://www.ipcc.ch/publications_and_data/publications_ipcc_fourth_assessment_report_synthesis_report.htm

Jenab M.H., Abdi M.A., Najibi S.H., Vahidi M., Matin N.S. Solubility of Carbon Dioxide in Aqueous Mixtures of N-Methyldiethanolamine + Piperazine + Sulfolane. *J. Chem. Eng. Data*. 2005, 50, 583-586.

Jenab M.H., Vahidi M., Mehrabi M. Solubility of Carbon Dioxide in Aqueous Mixtures of DIPA+MDEA and DIPA+PZ Solutions. *Journal of the Chinese Chemical Society*, 2006, 53, 283-286.

Jones J.H., Froning H.R., Claytor Jr. E.E. Solubility of Acidic Gases in Aqueous Monoethanolamine. *J. of Chem. Eng. Data*. 1959 Vol 4, No. 1, 85-92.

Jou F-Y., Mather A.E., Otto F.D. Solubility of H_2S and CO_2 in Aqueous Methyldiethanolamine Solutions. *Ind. Eng. Chem. Process Des. Dev.* 1982, 21, 539-544.

Jou F-Y., Otto F.D., Mather A.E. Vapor-Liquid Equilibrium of CO_2 in Aqueous Mixture of Monoethanolamine and Methyldiethanolamine. *Ind. Eng. Chem. Res.* 1994, 33, 2002-2005.

Jou F-Y., Mather A. E.; Otto, F. D., The Solubility of CO_2 in a 30 Mass Percent Monoethanolamine Solution. *The Canadian Journal of Chemical Engineering*, 1995, 73, 140-146.

Kadiwala S., Rayer A.V., Henni A. High Pressure Solubility of Carbon Dioxide (CO_2) in Aqueous Piperazine Solutions. *Fluid Phase Equilibria*. 2010, 292, 20-28.

Kamps A. PS., Xia J., Maurer G. Solubility of CO_2 in (H_2O + Piperazine) and in (H_2O + MDEA+ Piperazine). *AIChE Journal*. 2003, 49(10), 2662-2670.

Kim I., Svendsen H.F. Heat of Absorption of Carbon Dioxide (CO_2) in Monoethanolamine (MEA) and 2-(Aminoethyl)ethanolamine (AEEA) Solutions. *Ind. Eng. Chem. Res*. 2007, 46, 5803-5809.

Kim I., Svendsen H.F., Borresen E. Ebulliometric Determination of Vapor-Liquid Equilibria for Pure Water, Monoethanolamine, N-Methyldiethanolamine, 3-(Methylamino)-propylamine, and Their Binary and Ternary Solutions. *J. Chem. Eng. Data*, 2008, 53, 2521-2531.

Kohl AL., Nielsen RB. *Gas Purification*. Fifth Edition. Houston, Gulf Publishing Company. 1997, pp 231.

Lawson, J. D., Garst, A. W.. Gas Sweetening Data: Equilibrium Solubility of Hydrogen Sulfide and Carbon Dioxide in Aqueous Monoethanolamine and Aqueous Diethanolamine Solutions. *J. Chem. Eng. Data.* 1976, 21, (1), 20-30.

Lee J.I., Otto F.D., Mather A.E. Equilibrium between Carbon Dioxide and Aqueous Monoethanolamine Solutions. *J. Applied Chemistry and Biotechnology*. 1976, 26, 541-549.

Lee J. I., Otto F.D., Mather A.E. The Measurement and Prediction of the Solubility of Mixtures of Carbon Dioxide and Hydrogen Sulphide in a 2.5 N Monoethanolamine Solution. *The Canadian Journal of Chemical Engineering*. 1976, Vol 54, Iss. 3, 214-219.

Lewis G.N., Randall M. *Thermodynamics and the Free Energy of Chemical Substances.* First Edition, McGraw-Hill Book Company, Inc. New York and London, 1923.

Li M.-H., Chang B.-C. Solubilities of Carbon Dioxide in Water + Monoethanolamine +2-Amino-2-methyl-1-propanol. *J. Chem. Eng. Data*. 1994, 39, 448-452.

Li M.-H., Chang B.-C. Solubility of Mixtures of Carbon Dioxide and Hydrogen Sulfide in Water + Monoethanolamine + 2-Amino-2-methyl-1-propano. *J. Chem. Eng. Data.* 1995,40, 328-331.

Liu H.B., Zhang C.F., Xu G.W. A Study on Equilibrium Solubility for Carbon Dioxide in Methyldiethanolamine-Piperazine-Water Solution. *Ind. Eng. Chem. Res*. 1999, 38, 4032-4036.

Lyudkovskaya M.A., Leibush A.G. Solubility of Carbon Dioxide in Solutions of Ethanolamines under Pressure. *Zh. Prikl. Khim*. 1949, 22, 558-567.

Maddox R.N., Bhairi A.H., Deirs J.R., Thomas P.A. *Equilibrium Solubility of Carbon Dioxide or Hydrogen Sulfide in Aqueous Solutions of Monoethanolamine, Diglycolamine, Diethanolamine and Methyldiethanolamine*. GPA Research Report RR-104. Mar. 1987.

Ma'mun S., Nilsen R., Svendsen HF., Juliussen O. Solubility f Carbon Dioxide in 30 mass% Monoethanolamine and 50 mass% Methyldiethanolamine Solutions. *J. Chem. Eng. Data.* 2005, 50, 630-634.

Martin J.L., Otto F.D., Mather A.E. Solubility of Hydrogen Sulfide and Carbon Dioxide in a Diglycolamine Solution. *J. Chem. Eng. Data*, 1978, Vol. 23, No. 2, 163-164.

Mathonat C., Majer V., Mather A.E., Grolier J-P.E. Use of Flow Calorimetry for Determining Enthalpies of Absorption and the Solubility of CO_2 in Aqueous Monoethanolamine Solutions. *Ind. Eng. Chem. Res*. 1998, 37 (10), 4136-4141.

McCann N., Phan D., Wang X., Conway W., Burns R., Attalla M., Puxty G., and Maeder M. Kinetics and Mechanism of Carbamate Formation from CO_2(aq), Carbonate Species, and Monoethanolamine in Aqueous Solution. *J. Phys. Chem. A*. 2009, 113, 5022-5029.

Mock B., Evans L.B., Chen C.C. Phase Equilibria in Multiple-Solvent Electrolyte Systems: A New Thermodynamic Model. *Proceedings of the 1984 Summer Computer Simulation Conference*. pp. 558.

Mock B., Evans L.B., Chen C.C. Thermodynamic Representation of Phase Equilibria of Mixed-Solvent Electrolyte Systems. *AIChE J.* 1986, 32 (10), 1655-1664.

Muhlbauer H.G., Monaghan P.R. *Equilibrium Data for H_2S-CO_2-Monoethanolamine*. Jefferson Chemical Co, Austin, TX. 1957.

Murrieta-Guevara F., Romero-Martinez A, Trejo A. Solubilities of Carbon Dioxide and Hydrogen Sulfide in Propylene Carbonate, *N*-methylpyrrolidone and Sulfolane. *Fluid Phase Equilibria*. 1998, Vol 44, Iss. 1, 105-115.

Murrieta-Guevara F., Rebolledo-Libreros E., Trejo A. Solubility of Carbon Dioxide in Binary Mixtures of N-Methylpyrrolidone with Alkanolamines. *J. Chem. Eng. Data*. 1992, 37, 4-7.

Murrieta-Guevara F., Rebolledo-Libreros E., Trejo A. Gas Solubility of Carbon Dioxide and Hydrogen Sulfide in Mixtures of Sulfolane with Monoethanolamine. *Fluid Phase Equilibria*. 1993, Vol 86, 225-231.

Murrieta-Guevara F., Rebolledo-Libreros E., Romero-Martinez A., Trejo A. Solubility of CO_2 in Aqueous Mixtures of Diethanolamine with 2-Methyldiethanolamine and 2-Amino-2-methyl-1-propanol. *Fluid Phase Equilibria*. 1998, 150-151, pp 721-729.

Nath A., Bender E. Isothermal Vapor-Liquid Equilibria of Binary and Ternary Mixtures Containing Alcohol, Alkanolamine, and Water with a New Static Device. *J. Chem. Eng. Data*, 1983, 28, 370-375.

Nguyen T, Hilliard M.D., Rochelle G.T. Amine volatility in CO_2 capture. *International Journal of Greenhouse Gas Control*. 2010, 4, 707–715.

Page M., Huot J.Y., Jolicoeur C.A. A Comprehensive Thermodynamic Investigation of Water- ethanolamine Mixtures at 10, 25, and 40 ℃. *Can. J. Chem*. Vol. 71, 1993, 1064-1072.

Park S. B., Lee H. Vapor-Liquid Equilibria for the Binary Monoethanolamine + Water and Monoethanolamine + Ethanol Systems. *Korean Journal of Chemical Engineering*, 1997, 14, (2), 146-148.

Penny D.E., Ritter T.J. Kinetic Study of the Reaction between Carbon Dioxide and Primary Amines. *J. Chem. Soc., Faraday Trans.1*. 1983, 79, 2103.

Polderman L.D., Dillon C.P., Steele A.B. Why MEA Solution Breaks Down in Gas-Treating Service. *Oil & Gas Journal*. 1955, 54: 180-183.

Poplsteinava J., Krane J., Svendsen H.F. Liquid-Phase Composition Determination in CO_2-H_2O-Alkanolamine Systems: An NMR Study. *Ind. Eng. Chem. Res*. 2005, 44, 9894-9903.

Posey M.L. Thermodynamic Model for Acid Gas Loaded Aqueous Alkanolamine Solutions. The University of Texas at Austin. Ph.D. Dissertation. 1996.

Puxty G., Allport A., Attalla M. Vapor Liquid Equilibria Data for a Range of New Carbon Dioxide Absorbents. *Energy Procedia. GHGT-9*. 2009, 1. 941-947.

Reed R.M., Wood W.R. Recent Design Developments in Amine Gas Purification Plants. *Transactions of American Institute of Chemical Engineers*. 1941, Vol. 37, June 25, 363-383.

Renon H., Prausnitz J.M. Local Compositions in Thermodynamic Excess Functions for Liquid Mixtures. *AIChE J.* 1968, Vol. 14, No. 1, 135-144.

Robinson, D. B. *Vapor-Liquid Equilibrium Studies: GRI Project −Acid Gas Absorption*; University of Oklahoma: Norman, OK, 1993.

Rochelle GT et al. CO_2 Capture by Aqueous Absorption, First Quarterly Progress Report 2009. Luminant Carbon Management Program. The University of Texas at Austin. 2009.

Rochelle GT et al. CO_2 Capture by Aqueous Absorption, Fourth Quarterly Progress Report 2009. Luminant Carbon Management Program. The University of Texas at Austin. 2010.

Sartori G., Savage D.W. Sterically Hindered Amines for CO_2 Removal from Gases. *Ind. Eng. Chem. Fundam*. 1983, 22, 239-249.

Sexton A.J. Amine Oxidation in CO_2 Capture Processes. The University of Texas at Austin. Ph.D. Dissertation. 2008.

Shen K.P., Li M.H. Solubility of Carbon Dioxide in Aqueous Mixtures of Monoethanolamine with Methyldiethanolamine. *J. Chem. Eng. Data*. 1992, 37 (1), 96-100.

Shim J-G., Kim J-H., Jhon Y.H., Kim J., Cho K-H. DFT Calculations on the Role of Base in the Reaction between CO_2 and Monoethanolamine. *Ind. Eng. Chem. Res.*, 2009, *48* (4), 2172-2178.

Teng T-J.T., Mather A.E. Solubility of H_2S, CO_2 and Their Mixtures in an AMP Solution. *The Canadian Journal of Chemical Engineering*. 1989, Vol 67, 846-850.

Teng T-J.T., Mather A.E. Solubility of CO_2 in an AMP Solution. *J. Chem. Eng. Data*. 1990, 35, 410-411.

Tochigi K., Akimoto K., Ochi K., Liu F., Rawase Y. Isothermal Vapor-Liquid Equilibria for Water + 2-Aminoethanol + Dimethyl Sulfoxide and Its Constituent Three Binary Systems. *J. Chem. Eng. Data*. 1999, 44, (3), 588-590.

Tontiwachwuthikul P., Meisen A., Lim C.J. Solubility of CO_2 in 2-Amino-2-methyl-1-propanol Solutions. *J. Chem. Eng. Data*. 1991, 36 (1), 130-133.

Touhara H., Okazaki S., Okino F., Tanaka H., Ikari K., Nakanishi K. Thermodynamic Properties of Aqueous Mixtures of Hydrophilic Compounds 2 Aminoethanol and Its Methyl Derivatives. *J. Chem. Thermodynamics*. 1982, 14, 145-156.

Van Wagener D.H. Stripper Modeling for CO_2 Removal Using Monoethanolamine and Piperazine Solvents. The University of Texas at Austin. Ph.D. Dissertation. 2011.

Weiland R.H., Dingman J.C., Cronin D.B. Heat Capacity of Aqueous Monoethanolamine, Diethanolamine, N-Methyldiethanolamine, and N-Methyldiethanolamine Based Blends with Carbon Dioxide. *J. Chem. Eng. Data*. 1997, 42, 1004-1006.

Wilson H.L., Wilding W.V. Vapor-Liquid and Liquid-Liquid Equilibrium Measurements on Twenty Two Binary Mixtures. Experimental Results for DIPPR 1990-91 Projects on Phase Equilibria and Pure Component Properties: 1994; 63-115.

Xia J.Z., P-S Kamps A., Maurer G. Solubility of H_2S in (H_2O + Piperazine) and in (H_2O + MDEA + Piperazine). *Fluid Phase Equilibria*. 2003, 207, 23-34.

Xie H-B., Zhou Y., Zhang Y., Johnson J.K. Reaction Mechanism of Monoethanolamine with CO_2 in Aqueous Solution from Molecular Modeling. *J. Phys. Chem. A*. 2010, 114, 11844-11852.

Xu G.-W., Zhang C.-F., Qin S.-J., Guo W.-H., Liu H.-B. Gas-Liquid Equilibrium in a CO_2-MDEA-H_2O System and the Effect of Piperazine on It. *Ind. Eng. Chem. Res.* 1998, 37, 1473-1477.

Vita

Qing Xu was born in Xi'an, China. She graduated from the High School attached to the Northwestern Polytechnical University in 2002 and was admitted to Tsinghua University in Beijing without college entrance exam to study chemical engineering. She received a Bachelor of Engineering in chemical engineering from Tsinghua University in July 2006. In September 2006 she joined Dr. Rochelle's group as a Ph.D. student in the Department of Chemical Engineering at The University of Texas at Austin. In December 2008 she received an M.S.E degree in chemical engineering for the research on solvent reclaiming by crystallization of K_2SO_4. Qing has accepted full-time employment with UOP in Des Plaines, IL.

Permanent email address: qing.xu06@gmail.com

This dissertation was typed by the author.